TESLA Technical Design Report

PART II
The Accelerator

March 2001

Editors:

R. Brinkmann K. Flöttmann J. Roßbach
P. Schmüser N. Walker H. Weise

Acknowledgements

Authors

J. Andruszkow[26] A. Agababyan[12] A. Ageyev[27] J. Andruszkow[31] C. Antoine[8]
V. Aseev[30] B. Aune[8] V. Ayvazyan[54] N. Baboi[20] R. Bacher[12] J. Bahrdt[2] R. Bakker[2]
V. Balakin[5] V. Balandin[30] R. Bandelmann[12] D. Barni[22] A. Bazhan[5] M. Bernard[36]
W. Bialowons[12] G. Blair[44] D. Bloess[6] I. Bohnet[13] E. Bondarchuk[7] M. Bonezzi[22]
R. Boni[23] P. Borzemski[31] A. Bosotti[22] J. Bourdon[36] S. Bousson[28] W. Brefeld[12]
A. Brenger[12] R. Brinkmann[12] H. G. Brokmeier[49] P. J. T. Bruinsma[40] H. D. Brück[12]
S. Buhler[28] H. Burmeister[12] C. Burnton[12] T. Böckmann[12] J.-P. Carneiro[15]
M. Castellano[23] P. Castro[12] L. Catani[25] S. Celik[12] M. Champion[15] S. Chel[8] H. Chen[51]
J. Cheng[51] Y. Chernousko[27] Y. Cho[1] S. Choroba[12] A. Cianchi[25] M. Clausen[12]
A. Clozza[23] E. R. Colby[15,i] C. Crawford[15] A. Curtoni[8] W. Decking[12] P. Den Hartog[1]
Y. Derbenev[15] M. Desmons[8] A. Devred[8] G. Di Pirro[23] W. Dietzel[18] H. Dinter[12]
M. Dohlus[12] N. Doinikov[7] A. Drozhdin[15] H.-T. Duhme[12] B. Dwersteg[12] M. Ebert[12]
H.-J. Eckoldt[12] D. Edwards[15] H. T. Edwards[15] P. Emma[46] U. Engelke[12] U. Englisch[19]
K. Escherich[12] B. Faatz[12] S. Fartoukh[8] A. A. Fateev[34] J. Feikes[2] J. Feldhaus[12]
M. Ferrario[23] M. J. Fitch[53] K. Flöttmann[12] R. Follath[2] M. Fouaidy[28] W. Frentrup[2]
E. Gadwinkel[12] P. D. Gall[12] A. Gamp[12] L. Garcia-Tabares[37] T. Garvey[36] H. Gassot[28]
A. Gaupp[2] R. Gehring[16] M. Geitz[20,ii] U. Gensch[13] D. Giove[22] H.-W. Glock[29]
E. Gluskin[1] B. Goddard[6] S. Goloborodko[27] N. Golubeva[30] I. Gonin[30] V. Gorbunov[30]
C. Gourdin[8] H. Grabosch[13] D. Graef [11] W. Graeff[12] L. Grandsire[36] V. Gretchko[30]
T. Grevsmühl[12] B. Grigoryan[54] G. Grygiel[12] V. Gubarev[27] S. Guiducci[23]
A. Gössel[12] B. Günther [4] T. Habermann[4] E. Haebel[6] U. Hahn[12] M. von Hartrott[2]
W. H. Hartung[15,iii] D. Hecht[29] N. Heidbrook[12] H. Henke[48] H. Henschel[17] O. Hensler[12]
R. Hensler[12] S. Herb[12] C. Hessler[11] G. Hoffmann[12] G. Hoffstaetter[12] G. Horlitz[12]
W. Huang[51] D. Hubert[12] P. Hülsmann[33] M. Hüning[21] R. Ischebeck[21] I. Ivanov[34]
M. Jablonka[8] E. Jaeschke[2] E. Janata[19] I. Jelezov[30] K. Jensch[12] J.-P. Jensen[12]
J. M. Joly[8] M. Juillard[8] T. Junquera[28] P. Jurkiewicz[31] A. Jöstingmeier[12]
K.-P. Jüngst[16] A. Kabel[12,iv] J. Kahl[12] F.-R. Kaiser[12] H. Kaiser[12] E. Kako[35]
R. Kamps[13] T. Kamps[13] V. V. Katelev[27] M. Kauschke[50] T. Khabiboulline[30]
F. Kircher[8] J. L. Kirchgessner[42] H. Klein[33] P. Kneisel[47] J. Knobloch[42] U. Knopf[12]
V. Kocharyan[54] P. Komarek[16] D. Kong[26] D. Kostin[39] J. Kouptsidis[12] A. Kovalishin[30]
J. Kovar[12] D. Kraemer[2] M. Krassilnikov[10] L. Kravchuk[30] O. Krebs[12] G. Kreps[12]
W. Kriens[12] J. Krzywinski[32] G. Kuperman[16] M. Körfer[12] M. Lalaian[39] R. Lange[12]
B. Leblond[36] M. Leenen[12] P. Lepercq[36] J. Lesrel[28] A. Leuschner[12] M. Liepe[20]
H. Lierl[12] A. Liero[38] L. Lilje[20] T. Limberg[12] Q. Lin[51] A. Loginov[27] T. Lokajczyk[12]

H. Loos[11] R. Lorenz[13,v] J. Lorkiewicz[45] J.P. Lottin[8] A. Loulergue[8] F. Lu[12] Lu Hui Hua[26] M. Luong[8] F. Löffler[12] C. Magne[8] E. Mahner[4] J. Marini[36]
W. Maschmann[12] M. Maslov[27] G. Materlik[12] A. Matheisen[12] J. Menzel[21] E. Merker[27]
P. Michelato[22] M. Minty[12] V. Moiseev[30] C. Montag[12] A. Mosnier[8] V. Muratov[7]
G. Möller[12] W.-D. Möller[12] G. Müller[4] U.-C. Müller[12] O. Napoly[8] F. Neugebauer[13]
T. Nicol[15] U. Nielsen[19] A. Novikov-Borodin[30] A. Novokhatski[10] M. Omeich[36]
H. S. Padamsee[42] C. Pagani[22] V. Palmieri[24] R. Panvier[36] V. Paramonov[30]
J. Payet[8] M. Pekeler[12,vi] V. Peregud[7] F. Peters[12] H.-B. Peters[12] O. Peters[12]
B. Petersen[12] T. Peterson[15] A. Petrosyan[54] G. Petrosyan[54] L. Petrosyan[54] A. Petrov[7]
V. A. Petrov[34] J. Pflüger[12] B. Phung Ngoc[8] K. Pieczora[14] H. Piel[4] P. Pierini[22]
P. Pillat[12] P. Piot[12] T. Plawski[45] L. Plucinski[32] K. Polkovnikov[27] A. Popov[7]
J. Prenting[12] D. Proch[12] N. Pupeter[4] G. Pöplau[29] J. Qiao[26] H. Quack[50]
K. Rehlich[12] S. Reiche[52] P. Rejngardt-Nikulin[30] D. Renken[12] D. Reschke[12]
I. Reyzl[12] A. Richter[11] S. Riekehr[18] U. van Rienen[29] H. Riesch[13] J. M. Rifflet[8]
C. Rode[47] J. Rosenzweig[52] J. Roßbach[12] S. Roth[12] K. Rothemund[29] J. Rümmler[12]
M. Sachwitz[13] H. Safa[8] K. Saito[35] E. L. Saldin[12] W. Sandner[38] H. Sandvo[12]
C. Sanelli[23] Z. Sanok[14] J. Sarvas[43] H. Schlarb[20] G. Schmidt[12] H. von der Schmitt[12]
M. Schmitz[12] P. Schmüser[20] J. R. Schneider[12] E. A. Schneidmiller[12] R. Schnieber[49]
B. Schoeneburg[12] H.-J. Schreiber[13] S. Schreiber[12] D. Schulte[6] W. Schwarz[12,vii]
P. Schütt[10] S. N. Sedykh[34] M. Seidel[12] J. Sekutowicz[12] D. Sellmann[12] L. Serafini[22]
M. Serio[23] D. Sertore[12] S. Setzer[10] F. Sgamma[23] S. Simrock[12] W. Singer[12]
X. Singer[12] K. Sinram[12] A. Skasyrskaia[30] N. Sobenin[39] R. Sobierajski[32]
I. Sokolov[12] E. Somersalo[43] B. Sparr[12] J. B. Spelt[40] A. Stecchi[23] R. Steinbrecher[13]
F. Stephan[13] F. Stivanello[24] M. Stolper[12] T. Stoye[12] A. Swiderski[12] K. P. Sytchev[34]
V. A. Sytchev[27] A. Sytin[27] C. Tang[51] S. Tazzari[25] F. Tazzioli[23] V. Telnov[3] K. Tesch[12]
N. Tesch[12] H. Thom[13] M. Tigner[42] H. Timm[12] M. Timm[10] M. Tischer[12] F. Tonisch[13]
M. Tonutti[21] F. Toral[37] E. Trakhtenberg[1] C. Travier[8] R. Treusch[12] D. Trines[12]
V. Tsakanov[54] T. Tschentscher[12] K. Twarowski[32] M. Ukkola[43] F.-R. Ullrich[12]
G. Varisco[22] V. Verzilov[23] T. Vielitz[12] B. Visentin[8] V. Vogel[5] N. Walker[12]
G. von Walter[21] R. Wanzenberg[12] H.-P. Wedekind[12] G. Weichert[12] T. Weiland[10]
H. Weise[12] J. G. Weisend[46] M. Wendt[12] H. Wenninger[6] M. Werner[12] M. M. White[1]
I. Will[38] K. Wittenburg[12] J. Wojtkiewicz[12] S. Wolff[12] A. Wolski[9,viii] Y. Wu[40]
F. Wulf[19] G. Wöbke[12] G. Wüstefeld[2] Y. Xiang[12] I. Yazynin[27] H. Yi[51] P. Ylä-
Oijala[43] M. V. Yurkov[34] K. Zapfe[12] A Zavadtsev[39] X. Zeng[41] Q. Zhao[13] P. Zhogolev[5]
F. Zhou[12,ix] B. Zimmermann[12] S. Zintchenko[27] U. Zobjack[12] A. Zolotov[27]

1 Advanced Photon Source, Argonne National Laboratory, 9700 S. Cass Avenue, Argonne, IL 60439, USA

2 BESSY, Albert-Einstein-Strasse 15, D-12489 Berlin, Germany

3 BINP, Novosibirsk, Russia

4 Bergische Universität Wuppertal, D-42097 Wuppertal, Germany

5 Branch of the Inst. of Nuclear Physics, 142284 Protvino, Moscow Region, Russia

6 CERN, CH 1211 Geneva 23, Switzerland

7 D.V. Efremov Scientific Research Institute of Electrophysical Apparatus, St. Petersburg, Russia

8 DSM/DAPNIA, CEA Saclay, F-91191 Gif s/ Yvette, France

9 Daresbury Laboratory, Daresbury, Warrington, Cheshire, UK

10 Darmstadt University of Technology, FB18 - Fachgebiet TEMF, Schlossgartenstr. 8, D-64289 Darmstadt, Germany

11 Darmstadt University of Technology, IKP, FB 05, Schlossgartenstr. 9, D-64289 Darmstadt, Germany

12 Deutsches Elektronen-Synchrotron DESY, Notkestrasse 85, D-22607 Hamburg, Germany

13 Deutsches Elektronen-Synchrotron DESY, Platanenallee 6, D-15738 Zeuthen, Germany

14 Faculty of Physics and Nucl. Techniques, Univ. of Mining and Metallurgy, al. Mickiewicza 30, PL-30-059 Cracow, Poland

15 Fermi National Accelerator Laboratory, MS 306, P.O. Box 500, Batavia, IL 60510, USA

16 Forschungszentrum Karlsruhe, Institut f. Technische Physik, D-76021 Karlsruhe, Germany

17 Fraunhofer Institut fur Naturwissenschaftlich-Technische Trendanalysen INT, Euskirchen, Germany

18 GKSS-Forschungszentrum GmbH, D-21494 Geesthacht, Germany

19 Hahn-Meitner-Institut (HMI), Glienicker Str. 100, D-14109 Berlin, Germany

20 Hamburg University, Inst. f. Experimentalphysik, Notkestrasse 85, D-22607 Hamburg, Germany

21 III. Physik. Inst. der RWTH Aachen, Physikzentrum, D-52056 Aachen, Germany

22 INFN Milano - LASA, via Fratelli Cervi 201, I-20090 Segrate (MI), Italy

23 INFN-LNF, via E. Fermi 40, I-00044 Frascati, Italy

24 INFN-LNL, via Romea 4, I-35020 Legnaro (PD), Italy

25 INFN-Roma2, via della Ricerca Scientifica 1, I-00100 Roma, Italy

26 Inst. High Energy Physics IHEP, FEL Lab. P.O. Box 2732 Beijing 100080, P.R. China

27 Inst. High Energy Physics, 142284 Protvino, Moscow Region, Russia

28 Inst. de Physique Nucleaire (CNRS-IN2P3), F-91406 Orsay Cedex, France

29 Inst. für Allgemeine Elektrotechnik, Universität Rostock, Germany

30 Inst. for Nuclear Research of RAS, 117312 Moscow, 60th October Anniversary prospect 7A, Russia

31 Inst. of Nuclear Physics, Ul. Kawiory 26 a, 30-55 Krakow, Poland

32 Inst. of Physics, Polish Academy of Sciences, al. Lotnikow, 32/46, 02-668 Warsaw, Poland

33 Johann-Wolfgang-Goethe-Universität, Inst. für Angewandte Physik, Robert-Mayer-Str. 2-4, D-60054 Frankfurt/Main, Germany

34 Joint Inst. for Nuclear Research, 141980 Dubna, Moscow Region, Russia

35 KEK, Tsukuba, Ibaraki, 305-0801, Japan

36 Laboratoire de l'Accelerateur Lineaire, IN2P3-CNRS, Universite de Paris-Sud, B.P. 34, F-91898, Orsay, France

37 Laboratorio de Superconductividad Aplicada CIEMAT/CEDEX, Madrid, Spain

38 Max-Born-Institut, Max-Born-Str. 2a, D-12489 Berlin, Germany

39 Moscow Physical Engineering Institute, MePhI, Kashirskoe shosse 31, RU-115409 Moscow, Russia

40 NIKHEF, P.O. Box 41882, 1009 DB Amsterdam, Netherlands

41 Nat. Synchrotron Radiation Laboratory, Univ. of Science and Technology of China, Hefei, Anhui 23029, P.R. China

42 Newman Lab, Cornell University, Ithaca, NY 14850, USA

43 Rolf Nevanlinna Institute, University of Helsinki, P.O.Box 4, FIN-00014 Helsinki, Finland

44 Royal Holloway University of London, London, UK

45 Soltan Institute for Nuclear Studies, PL-05-400 Otwock-Swierk, Poland

46 Stanford Linear Accelerator Center, SLAC MS 07, 2575 Sand Hill Road, Menlo Park, CA 94025, USA

47 TJNAF, 12000 Jefferson Avenue, Newport News, Virginia 23606, USA

48 TU Berlin, Sekretariat EN2, Einsteinufer 17, D-10587 Berlin, Germany

49 TU Clausthal, Adolph-Roemer-Str. 2A, D-38678 Clausthal-Zellerfeld, Germany

50 TU Dresden, Inst. Kälte und Kryotechnik, D-01062 Dresden, Germany

51 Tsinghua University, 100084 Beijing, P.R. China

52 UCLA Dept. of Physics and Astronomy, 405 Hilgard Ave., Los Angeles, CA 90095, USA

53 University of Rochester, Dept. of Physics and Astronomy, 206 Bausch & Lomb, Rochester NY 14627, USA

54 Yerevan Physics Institute, 2 Alikhanyan Brothers str., 375036 Yerevan, Armenia

 i present address: Stanford Linear Accelerator Center, SLAC MS 07, 2575 Sand Hill Road, Menlo Park, CA94025, USA

 ii present address: Procter & Gamble, 53881 Euskirchen, Germany

iii present address: NSCL, East Lansing, Michigan 48824-1321, USA

 iv present address: Stanford Linear Accelerator Center, SLAC MS 07, 2575 Sand Hill Road, Menlo Park, CA94025, USA

 v present address: Senderbetriebstechnik Westdeutscher Rundfunk, 50600 Köln, Germany

 vi present address: ACCEL Instruments GmbH, Friedrich-Ebert-Str. 1, 51429 Bergisch-Gladbach, Germany

vii present address: University of Jena, Jena, Germay

viii present address: LBL, Berkeley, California, USA

 ix present address: CERN, CH 1211 Geneva 23, Switzerland

Administrative Support

J. Bürger, K. Desler, C. Kluth, J. Kreutzkamp, T. Lux, I. Nikodem, H. Westermann

Contents

1 Overview

1.1 Introduction

There is broad agreement in the High Energy Physics community that a linear e^+e^- collider with an initial energy of $E_{cm} = 350$–$500\,\text{GeV}$ and a luminosity above $10^{33}\text{cm}^{-2}\text{s}^{-1}$ is of fundamental importance for the future development of Particle Physics; it is in many respects complementary to the Large Hadron Collider (under construction at CERN), and should be built as the next accelerator facility. The scientific case for a next generation electron-positron collider with a centre-of-mass energy well beyond the reach of the LEP storage ring ($E_{cm} \approx 200\,\text{GeV}$) is presented in part III of this report.

The feasibility of a linear collider has been demonstrated by the successful operation of the SLAC Linear Collider (SLC). However, achieving the requirements for a next generation linear collider is by no means an easy task; in particular, high beam powers and very small spot sizes at the collision point are required to obtain a sufficiently high luminosity. Over the past decade, several groups worldwide have been pursuing different linear collider designs. The fundamental difference between TESLA and other designs is the choice of superconducting accelerating structures. The advantages of superconducting technology (summarised below) are significant and we are convinced that the machine performance potential is unrivaled by other concepts. The same arguments apply in the case of the X-ray Free Electron Laser (FEL), which is an integral part of the TESLA project. The scientific case for the FEL is presented in part V.

A first complete conceptual design of the TESLA facility was published in 1997 [1]. In this report we present the updated design of all accelerator sub-systems, and a summary of our experience gained at the TESLA test facility (TTF).

Figure 1.1.1: *The 9-cell niobium cavity for TESLA.*

TESLA uses 9-cell niobium cavities (figure 1.1.1) cooled by superfluid Helium to $T = 2\,\mathrm{K}$ and operating at L-band frequency (1.3 GHz). The design gradient at $E_{cm} = 500\,\mathrm{GeV}$ is $E_{acc} = 23.4\,\mathrm{MV/m}$ and the quality factor $Q_0 = 10^{10}$ (based on the linac layout described in chapter 3). Because the power dissipation in the cavity walls is extremely small, the accelerating field can be produced with long, low peak power RF-pulses; this results in a high RF to beam power transfer efficiency, allowing a high average beam power while keeping the electrical power consumption within acceptable limits ($\sim 100\,\mathrm{MW}$).

The high beam power is one of the ingredients for high luminosity; the second essential point for high luminosity is the extremely small beam size at the interaction point (IP). The relatively low frequency of the TESLA linac is ideally suited for accelerating and *conserving* ultra-small emittance beams. Beam dynamics issues are discussed in detail in section 3.2, but a convincing argument for the choice of low frequencies based on simple scaling laws can be made as follows: the beam accelerated in the linac induces electromagnetic fields (so-called wakefields) which act back on the beam. If the wakefields are too strong, they can degrade the quality of the beam by increasing its energy spread and transverse emittance. The longitudinal and transverse wakefields per unit length of accelerator scale approximately as f^2 and f^3 respectively: hence the wakefields in TESLA ($f = 1.3\,\mathrm{GHz}$) are considerably weaker compared to those of machines based on S-band ($f = 3\,\mathrm{GHz}$) [4] or X-band ($f = 11.4\,\mathrm{GHz}$) [2, 3] technologies. As a result, the emittance dilution can be reduced to acceptable levels in TESLA using relatively relaxed alignment tolerances for the linac components.

The choice of superconducting RF also allows us to use a long RF-pulse (1 ms) and a relatively large bunch spacing (337 ns at $E_{cm} = 500\,\mathrm{GeV}$). Three benefits result directly from this long bunch train:

- A fast (MHz) bunch-to-bunch feedback can be used to correct the orbit within one beam pulse. Such a feedback system will maintain the beams in collision at the IP, making TESLA relatively insensitive to mechanical vibrations which could otherwise lead to serious luminosity reduction.

- A head-on (zero crossing-angle) collision scheme can be used, with large-aperture superconducting quadrupoles in the interaction region.

- In the event of an emergency, a fast safety system can 'turn off' the beam within a fraction of a pulse.

The potential benefits of superconducting RF summarised above have been acknowledged since the beginning of linear collider R&D. However, in the early 1990's, the projected costs based on existing superconducting RF installations were considered too high. The main challenge for TESLA, therefore, was a reduction in the cost per unit accelerating voltage by a large factor, in order to be competitive with conventional linear collider designs. The approach adopted to reduce the cost was to:

- increase the achievable gradients available at that time (5–8 MV/m [5, 6]) by about a factor of four; and

Superconducting Cavity Performance
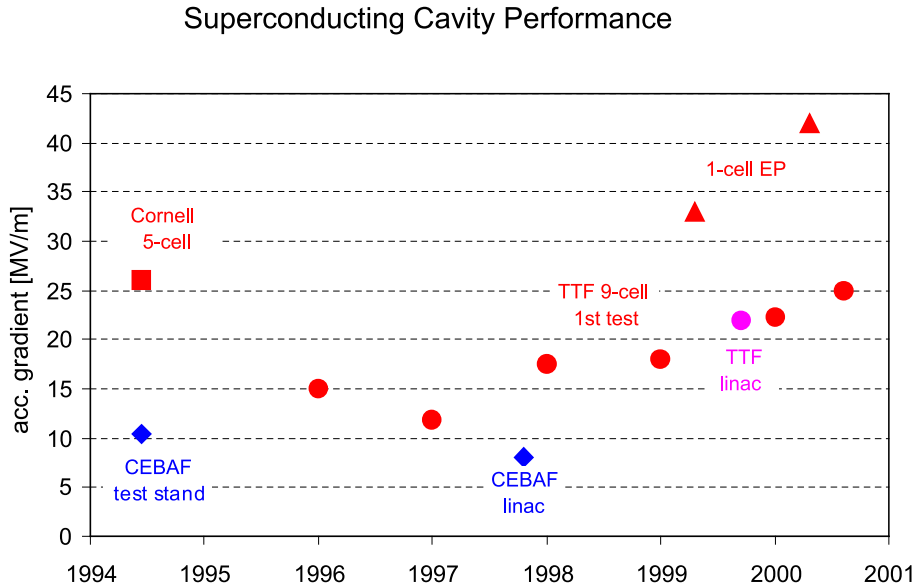
Figure 1.1.2:   *Evolution of superconducting cavity performance: red dots show the average gradient achieved with TESLA 9-cell cavities for the years 1995–2000 (first test, no additional processing), the red square shows results for 5-cell cavities at Cornell and the magenta dot depicts the average gradient measured with beam for a complete accelerator module installed at the TTF linac. Red triangles show gradients obtained with electropolished single-cell resonators (see text). Test stand and linac operation results from Jefferson Lab (CEBAF) are included for comparison (blue diamonds).*

- reduce the cost per unit length of the superconducting structures by a similar factor.

In order to demonstrate the feasibility of the high-gradient cavity technology and to create a solid basis for a reliable cost estimate of future large-scale production, the TESLA collaboration decided in 1992 to start an R&D program and to build the TESLA Test Facility (TTF) [7]. The TTF includes the infrastructure for applying different processing techniques to the niobium cavities obtained from industrial production. A detailed overview of the cavity development programme at TTF is given in chapter 2.

In the formative stages of the TESLA collaboration, three 5-cell L-band cavities were built and tested at Cornell, and reached accelerating fields of 26–28 MV/m [8]. To date, more than sixty 9-cell cavities have been processed and tested at TTF. Figure 1.1.2 shows the average gradient obtained in the years 1995–2000. Only data from the first test with cw-RF excitation are included. Several cavities reached higher performance after additional processing, but in view of future mass production, the performance obtained after a cavity has passed through the standard fabrication and treatment procedure may be considered more relevant. The steady improvement of the average gradient over the past years clearly indicates that the high performance cav-

ities required for the 500 GeV collider can now be produced with sufficient reliability. Furthermore, studies carried out together with industry have shown that the required mass production is feasible within the planned time schedule, and that the cost goal is achievable (see chapter 10).

Further progress on the cavity performance has recently been obtained by applying electropolishing to the niobium surface. Test results with single-cell resonators repeatedly show gradients above 30 MV/m [9]. The best single-cell performance obtained to date is $E_{acc} = 42$ MV/m (see chapter 2). First results for 9-cell electropolished cavities also show gradients well above 30 MV/m. We are therefore confident that the cavities in the TESLA linac will be able to operate at a gradient above 30 MV/m, allowing a significant increase in the achievable centre-of-mass energy (section 1.4).

Besides the success of the cavity development programme, the commissioning and operation of the TTF linac has been the second essential milestone reached on our way to demonstrate the feasibility of the TESLA technology. The linac [10] is constructed from accelerator modules similar to those required for the collider, and permits a full integrated system test with beam (section 2.2). We have so far tested three modules and operated the linac for more than 8,000 hours. Each 12 m long module is comprised of a string of eight 9-cell cavities (figure 1.1.3), together with beam focusing and diagnostic components. The highest average accelerating gradient measured for a module was 22 MV/m.

Our baseline design for the 500 GeV machine (chapter 3) is based entirely on the design of components installed and tested at TTF, with the exception of an optimisation of the mechanical layout of the modules (see section 3.3). The modified module improves the fill factor (ratio of active length to total length) and hence reduces the gradient required to reach the design energy within a given site length. A further improvement along the same lines is currently being developed: by grouping several cavities into a so-called superstructure (section 2.1) with minimum inter-cavity spacing, the energy reach of the machine can be maximised while at the same time reducing the cost of the RF-distribution system (reduced number of couplers). However, we have chosen to conservatively base the parameters and cost estimate for the 500 GeV machine on the TTF-like accelerator module, since as of writing, tests of the superstructure are still in preparation.

1.1.1   X-ray Free Electron Laser (FEL)

The concept of using a high energy electron linac for building an X-ray Free Electron Laser (FEL) was first developed at Stanford [11]. Due to its ability to conserve a high beam quality during acceleration, the TESLA linac is an excellent driver for an X-ray FEL. The fascinating research possibilities opened up by such a truely new kind of X-ray source and the layout of the User Facility are summarised in part V of this report. The additional accelerator components required for integration of the Free Electron Laser will be described in chapter 9.

Since the X-ray FEL concept represents a considerable extrapolation of present day FEL technology, it was considered necessary to perform a successful test of the

Figure 1.1.3: *Assembly of a string of eight 9-cell cavities in the clean room at TTF.*

Self Amplified Spontaneous Emission (SASE) FEL concept at the TTF, in a wavelength regime previously unaccessible ($\lambda \approx 100\,\text{nm}$). Lasing was first observed in February 2000, and a number of experimental studies at the TTF-FEL have since been carried out (see section 9.2). An upgrade of the TTF linac to $1\,\text{GeV}$ beam energy is in preparation, and will allow a second stage of the FEL to reach $6\,\text{nm}$ wavelength. The upgraded facility will be available for users from 2004 onwards, and will allow us to gain the operational and scientific experience needed for the operation of the proposed large-scale X-ray FEL laboratory.

1.1.2 Second interaction region (IR) and further options

Unlike a storage ring collider, a linear collider cannot serve several interaction regions simultaneously with the same beam. It is possible, however, to switch the beam between two experimental stations. We have integrated the option of a second IR in the layout of the TESLA facility. Unlike the primary IR which has a zero crossing angle, the second IR will have a crossing angle of $\sim\!34\,\text{mrad}$, and is therefore suitable for the $e\gamma$ and $\gamma\gamma$ collider modes of operation described in part VI, chapter 1. The second IR can also be used for electron-positron collisions, with the same luminosity as the primary IR (assuming that the so-called crab-crossing scheme is used). Electron-electron collisions (at one or both of the IRs) can be provided by reversing magnet polarities and adding a polarised electron source to the (nominal) positron branch of the collider. The expected performance for the $\gamma\gamma$ and e^-e^- modes of operation are included in the discussion of machine parameters in section 1.3.

In addition to collider operation, TESLA also offers options for fixed target physics.

It is possible to accelerate (in parallel with the main collider beam) a low-intensity spin-polarised electron beam which can be deflected into a separate beamline and used for a polarised target experiment (see part VI, chapter 3). Except for the additional experimental beamline and low-current polarised electron source, the impact on the accelerator itself is marginal, since the required additional RF-power is only about 10^{-3} of the nominal power.

If TESLA is built next to the DESY site, the first part of the linac can be used as an injector for the HERA electron ring, which could be operated as a pulse stretcher to deliver a continuous beam at 15–25 GeV for fixed target Nuclear Physics experiments [12]. This option provides a beam with properties very similar to the original ELFE proposal [13] and to a more recent design worked out at CERN [14]. It is described in more detail in part VI, chapter 4.

As a last possible option, the TESLA linac could be connected tangentially to the west straight section of HERA, allowing the (TESLA) electron beam to collide with protons (see part VI, chapter 2). The achievable centre-of-mass energy would exceed the present HERA energy by a factor of three to five. The most serious issue here concerns the achievable luminosity (see for example [15, 16, 17]). More detailed studies are required before a conclusion concerning the feasibility of a linac-ring e-p collider with reasonably high luminosity can be drawn.

1.2   General Layout

A sketch of the overall layout of the TESLA linear collider is shown in figure 1.2.1. In this section, a brief description of each of the sub-systems will be given, beginning with the electron and positron sources.

The electron beam is generated in a polarised laser-driven gun (section 4.2). After a short section of conventional linac, the beam is accelerated to 5 GeV in superconducting structures identical to the ones used for the main linac. The baseline design assumes that the electrons are stored in a damping ring very similar to the one required for the positron beam (see below). A novel concept for a low-emittance flat beam electron gun has recently been suggested [18], which may allow direct production of a beam of suitable quality for collider operation. The obvious cost saving makes the scheme very attractive: however, there are still several questions that need to be addressed, among them whether or not the concept can be used to produce the required *polarised* electrons.

The positron injection system has to provide a total charge of about $5 \cdot 10^{13} e^+$ per beam pulse, which is not realistically feasible with a conventional (electron on thick target) source. Instead, positrons are produced from γ-conversion in a thin target (section 4.3), after which they are preaccelerated in a conventional 200 MeV L-band linac, followed by a 5 GeV superconducting accelerator. The photons are generated by passing the high-energy electron beam through an undulator placed after the main linac, before transporting the beam to the IP. Passage through the undulator causes the energy spread in the electron beam to increase from $0.5 \cdot 10^{-3}$ to $1.5 \cdot 10^{-3}$, with
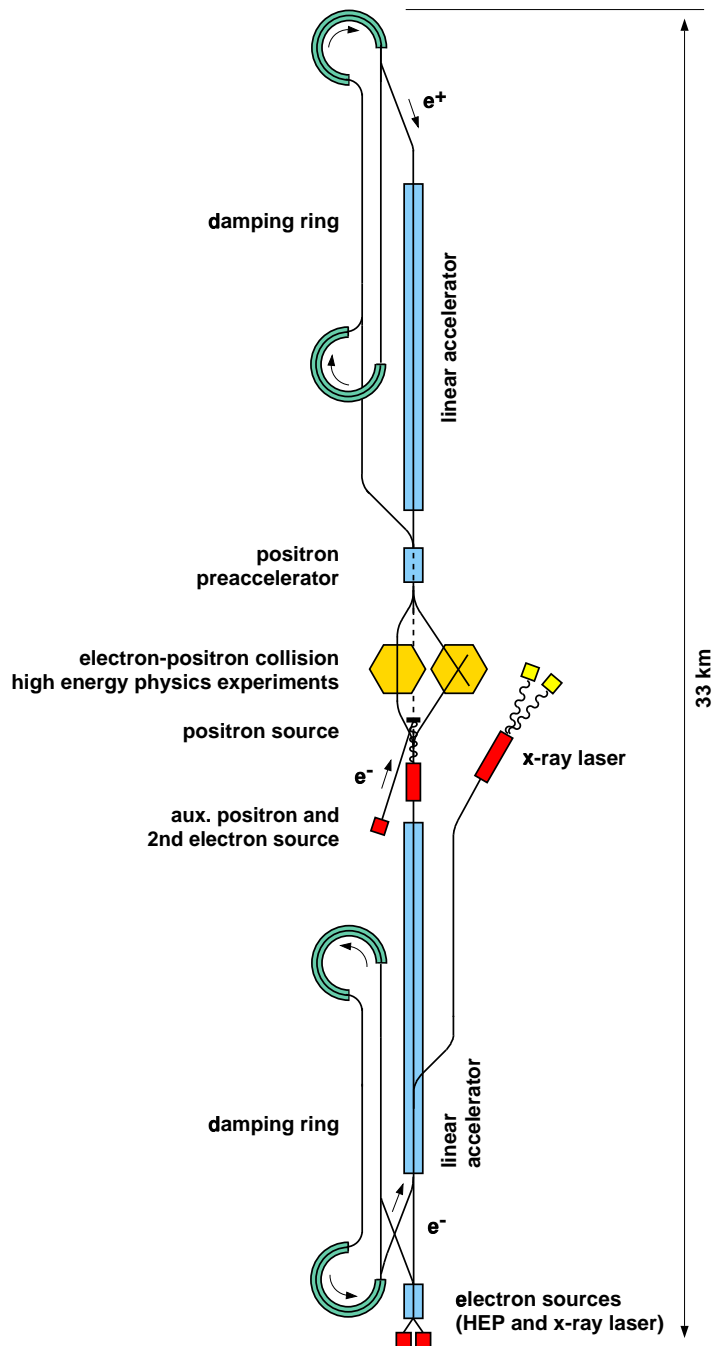
Figure 1.2.1:   *Sketch of the overall layout of TESLA.*

an average energy loss of 1.2 %, both of which appear tolerable. Locating the positron source upstream of the IP reflects a design change compared to the system described in [1], where the source was located after the IP in the spent-beam extraction line. Placing the source upstream of the IP has removed the need to collimate a substantial fraction of the high power spent-beam, which had posed technical and radiation safety problems.

The undulator-based positron source requires an electron beam energy greater than 150 GeV for full design positron beam intensity. At centre-of-mass energies below 300 GeV the luminosity is reduced due to a lower positron beam current. If lower energy running at maximum luminosity becomes important, additional electron beam pulses and bypass-beamlines are foreseen to drive the positron source independently from the (lower-energy) beam used for physics.

Besides providing a sufficiently high positron beam intensity, the undulator-based source offers several additional advantages:

- use of a thin target leads to a smaller positron beam with a smaller transverse emittance than from a conventional (thick target) source;

- the considerable investment and operating costs for a high-power electron linac needed in a conventional scheme are avoided;

- production of *polarised* positrons is possible by replacing the planar undulator with a helical undulator.

The polarised positron option is technically more ambitious and is considered a potential upgrade at a later stage of operation. The achievable polarisation ranges from 45% to 60%.

In addition to the main undulator-based source, a low-intensity auxiliary e^+ source will be installed for commissioning and machine study purposes. The auxiliary source should be capable of generating a bunch train of a few percent of the design intensity.

The positron beam is injected into the damping ring at an energy of 5 GeV. The bunch train is stored in the ring in a compressed mode, with the bunch spacing reduced by about a factor of 16; even with this compression, a large ring circumference of about 18 km is still required. To avoid building an additional large ring tunnel, a so-called 'dog bone' design is used (chapter 5). The layout has two 8 km straight sections placed entirely in the main linac tunnel; additional tunnels are only required for the 1 km circumference loops at either end. About 400 m of wiggler section are needed to achieve sufficient damping. Fast kickers are required for compression and decompression of the bunch train at injection and extraction respectively.

Despite its unconventional shape, the damping ring does not exhibit any unusual beam dynamics. The only exception, related to the large ratio of circumference to beam energy, is a large incoherent space charge tune shift. The effect can be significantly reduced, however, by artificially increasing the beam cross-section in the long straight sections.

The two main linear accelerators (chapter 3) are each constructed from roughly ten-thousand one-meter long superconducting cavities. Groups of twelve cavities are installed in a common cryostat (cryomodule); the current design is based on that used in the TTF, modified to be more compact and cost-effective. The cryomodules also contain superconducting magnets for beam focusing and steering, beam position monitors, and higher-order mode absorbers.

The RF-power is generated by some 300 klystrons per linac, each feeding 36 9-cell cavities. The required peak power per klystron is 9.5 MW, including a 10% overhead for correcting phase errors during the beam pulse which arise from Lorentz force detuning and microphonics. The high-voltage pulses for the klystrons are provided by conventional modulators: an alternative option presently under study is the use of superconducting magnet energy storage (SMES) devices, where the pulse energy is stored in the magnetic field of superconducting solenoids. The TESLA RF-system is described in detail in section 3.4.

The cryogenic system for the TESLA linac (section 8.7) is comparable in size and complexity to the one currently under construction for the LHC at CERN. Seven cryogenic plants are foreseen, each one serving a $\sim$5 km long linac subsection. The cooling capacity of the first section of the electron linac is increased to accommodate the higher load from the additional FEL beam pulses.

The beam transport between the linac and the IP (the so-called beam delivery system, described in chapter 7) consists of collimation, beam diagnostics and correction, and final focus sections. The relatively large bunch spacing of 337 ns allows a head-on collision scheme, since the beams can be safely extracted outside of the detector region and before the first parasitic bunch crossing ($\sim$50 m from the IP). Large aperture superconducting quadrupoles can be used in the IR, with one benefit being that collimation requirements upstream for protection of the experiment from background are rather relaxed. With gas scattering practically absent in the TESLA linac and weak wakefields, the expected amount of beam halo which must be collimated is expected to be small: hence background from muons originating at the collimators is unlikely to be a problem. If the loss rate at the collimators exceeds an acceptable limit (e.g. due to mis-steering or other possible failures upstream), the large bunch spacing allows a fast emergency extraction system to send the remainder of the bunch train to the main beam dump.

The design of the final focus system is essentially the same as the Final Focus Test Beam (FFTB) system successfully tested at SLAC [19]. Beam size demagnification and chromatic corrections for the TESLA design parameters are no more ambitious than at the FFTB. The beams can be kept in collision at the IP to a high precision by using a fast bunch-to-bunch feedback, which measures and corrects the beam-beam offset and crossing angle on a time scale small compared to the beam pulse length. A similar system is foreseen after the main linac, to remove possible pulse-to-pulse orbit jitter. If necessary, a fast orbit correction can also be installed at the entrance of the main linac to remove jitter generated in the injection system. A prototype of the orbit feedback system has been installed and successfully tested at the TTF linac [20].

The design of the beam delivery system is optimised for a single head-on interaction
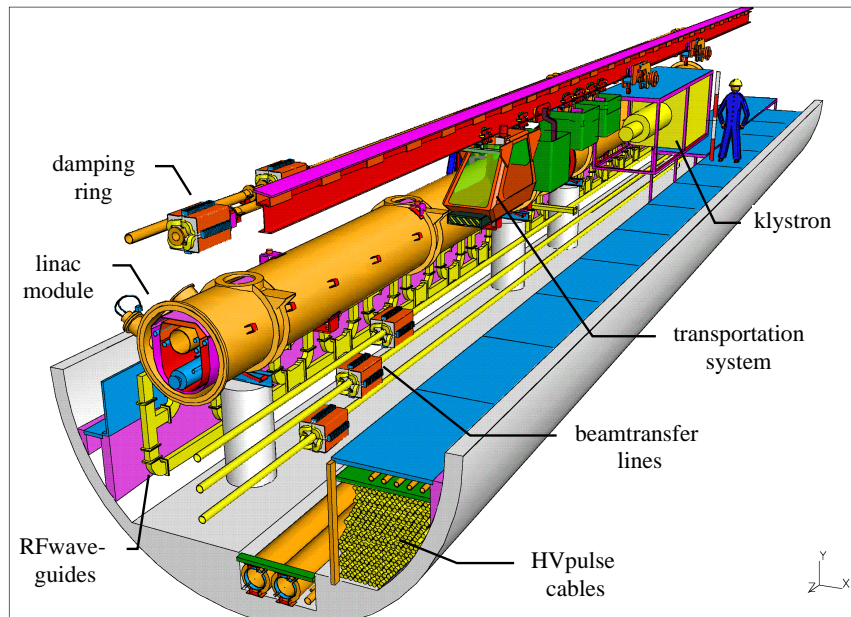
Figure 1.2.2: *Sketch of the 5 m diameter TESLA linac tunnel.*

point. The complete system of ∼3.3 km (linac to linac) will fit into a straight tunnel. All the magnet systems and beamline geometry are designed to allow an upgrade to a beam energy of 400 GeV. As previously mentioned, a second IR with a 34 mrad crossing angle is also foreseen, which could be used for $\gamma\gamma$ or $e^-\gamma$ collisions. On the electron linac side, care has been taken to place the positron source (undulator) upstream of the beam switchyard, so as not to exclude the possibility of e^+e^- collisions at the second IR.

The two linear accelerators as well as the beam delivery system will be installed in an underground tunnel of 5 m diameter (see figure 1.2.2 and section 8.2). A 2000 m^2 experimental hall is foreseen to house the detector; the hall can be extended to house a second detector should the second IR be constructed. Seven additional surface halls are required for the cyrogenic plants, spaced at intervals of about 5 km along the linacs, and are connected to the underground tunnel by access shafts. The halls will also contain the modulators which generate the HV pulses for the klystrons. The pulse transformers are placed in the tunnel close to the klystrons; the long cables required to connect the modulators to the transformers contribute a few % to the total power losses, but it is an advantage to allow access to the modulators for maintenance during machine operation. Exchange of klystrons, however, will require an interruption of the machine operation: with an energy overhead of 2% foreseen in the design, and assuming an average klystron lifetime of 40,000 hours, maintenance breaks of one day every few weeks will be necessary.

The first 3 km long section of the electron linac is used to accelerate the beam
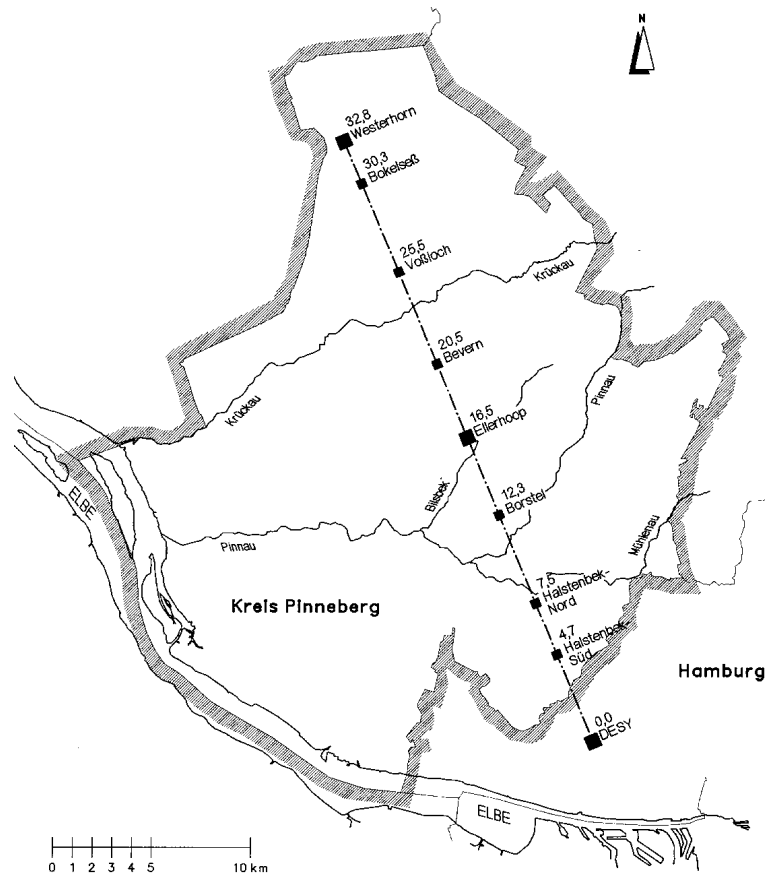
Figure 1.2.3:   *The TESLA site North-West of the DESY laboratory.*

which drives the X-ray FEL user facility. This part of the machine operates at 10 Hz — twice the nominal collider repetition rate — alternating from pulse to pulse between collider and FEL mode operation. The accelerating gradient for the FEL beam can be adjusted independently within a range of more than a factor of two (9–23 MV/m). Two extraction points are foreseen at different positions in the linac, supplying beam energies in the range 11–50 GeV to the FEL facility[1]. The extracted beams are transported in two separate transfer lines to the FEL laboratory, which is placed adjacent to the High Energy Physics experimental halls. The FEL beam requires its own low emittance source, low energy pre-accelerator and bunch compression systems. A description of the machine components related to the FEL is given in chapter 9.

Within the TESLA collaboration there is broad agreement that the facility should be constructed at an existing High Energy Physics laboratory to reduce project costs and construction time. Both DESY and FNAL have been considered as possible sites [21]. DESY as the co-ordinating laboratory in the collaboration has taken over the task of working out a detailed plan for the TESLA site North-West of the DESY

---

[1]Although the top range here is 50 GeV, the present FEL design does not require beam energies above 30 GeV.

laboratory (section 8.2). In this scenario (figure 1.2.3), the linac tunnel starts at the DESY site in a direction tangential to the west straight section of HERA, so as not to exclude the electron-proton linac-ring collider option. The central area is situated about 16 km from the DESY site in a rural part of the North German state (Bundesland) of Schleswig-Holstein, and accommodates both the collider detector hall for Particle Physics and the FEL radiation user facility.

1.3   Parameters for 500 GeV

Besides the centre-of-mass energy of the colliding beams, the second key parameter for a linear collider is the luminosity L, given by

$$L = \frac{n_b N_e^2 f_{rep}}{4\pi\sigma_x^*\sigma_y^*} \times H_D \qquad (1.3.1)$$

where

$$\begin{array}{ll}
n_b & \text{number of bunches per pulse} \\
N_e & \text{number of electrons (positrons) per bunch} \\
f_{rep} & \text{pulse repetition frequency} \\
\sigma_{x,y}^* & \text{horizontal (vertical) beam size at interaction point} \\
H_D & \text{disruption enhancement factor (typically } H_D \approx 2)
\end{array}$$

Introducing the average beam power $P_b = E_{cm} n_b N_e f_{rep}$, the luminosity can be written as

$$L = \frac{P_b}{E_{cm}} \times \frac{N_e}{4\pi\sigma_x^*\sigma_y^*} \times H_D \qquad (1.3.2)$$

An important constraint on the choice of IP parameters is the effect of beamstrahlung: the particles emit hard synchrotron radiation in the strong electromagnetic space-charge field of the opposing bunch. The average fractional beam energy loss from beamstrahlung is approximately given by [22]:

$$\delta_E \approx 0.86 \frac{r_e^3 N_e^2 \gamma}{\sigma_z(\sigma_x^* + \sigma_y^*)^2} \qquad (1.3.3)$$

where

$$\begin{array}{ll}
r_e & \text{the classical electron radius} \\
\gamma & \text{relativistic factor } E_{beam}/m_0 c^2
\end{array}$$

Beamstrahlung causes a reduction and a spread of the collision energy and can lead to background in the detector. The energy loss δ_E is therefore typically limited to a few percent. By choosing a large aspect ratio $R = \sigma_x^*/\sigma_y^* >> 1$, δ_E becomes independent of the vertical beam size and the luminosity can be increased by making σ_y^* as small as possible. Since $\sigma_y^* = (\varepsilon_{y,N}\beta_y^*/\gamma)^{1/2}$, this is achieved by a small vertical beta function at the IP (β_y^*) and a small normalised vertical emittance ($\varepsilon_{y,N}$). The lower limit on β_y^* is

given by the bunch length ('hourglass effect'); setting $\beta_y^* = \sigma_z$, the luminosity can be expressed as:

$$L \approx 5.74 \cdot 10^{20} \text{m}^{-3/2} \times \frac{P_b}{E_{cm}} \times \left(\frac{\delta_E}{\varepsilon_{y,N}}\right)^{1/2} \times H_D \qquad (1.3.4)$$

The advantages of low-frequency superconducting RF technology have already been mentioned: high RF- to beam-power efficiency; extremely small wakefields and associated linac emittance growth; fast intra-bunch feedback systems. Making use of these unique features has led to a parameter set (table 1.3.1) which clearly demonstrates TESLA's potential for high luminosity. In comparison with the earlier design [1], we achieve about a factor of five improvement in the luminosity, while maintaining a low level of beamstrahlung. The feasibility of this higher performance is supported by a careful investigation and — where necessary — optimisation of the machine subsystems.

1.3.1 Electron-electron and $\gamma\gamma$ collisions

The head-on e^+e^- interaction region can also be operated in e^-e^- mode. The disadvantage here is that the luminosity enhancement arising from self-focusing for oppositely charged bunches turns into a de-focusing effect for like charges, with $H_D < 1$. Assuming identical beam parameters, we find a luminosity seven times smaller [23] than for the e^+e^- mode (see table 1.3.1).

The photon collider option, where the electrons are converted into high energy photons by interaction with a laser beam just upstream of the IP, requires construction of the second interaction region with the large crossing angle. Unlike the e^+e^- case, the beamstrahlung constraint is not present for $\gamma\gamma$ collisions, and the horizontal beam size at the IP can be reduced still further. Table 1.3.2 lists a possible $\gamma\gamma$ parameter set which reflects the lack of the beamstrahlung constraint: the horizontal emittance is at the limit achievable with the present damping ring design, while the IP beta-functions are compatible with a final focus system design similar to the e^+e^- collider version (except, of course, for the crossing angle). Additional improvements are conceivable, but require further design studies of these sub-systems. Crab-crossing is assumed to avoid a luminosity reduction caused by the crossing angle. The actual usable $\gamma\gamma$ luminosity is smaller than the geometric value by an order of magnitude, since not all the electrons are converted by Compton scattering, and only part of the luminosity spectrum is within a few percent of the peak collision energy. For more details on the photon collider, see chapter 1 in part VI.

1.4   Energy Upgrade Potential

The length of the machine must be increased to achieve centre-of-mass energies above $\sim 1\,$TeV. However, a significant energy upgrade is possible within the site length for the current $500\,$GeV design, since:

		TESLA-500
Accelerating gradient	E_{acc} [MV/m]	23.4
RF-frequency	f_{RF} [GHz]	1.3
Fill factor		0.747
Total site length	L_{tot} [km]	33
Active length	[km]	21.8
No. of accelerator structures		21024
No. of klystrons		584
Klystron peak power	[MW]	9.5
Repetition rate	f_{rep} [Hz]	5
Beam pulse length	T_P [μs]	950
RF-pulse length	T_{RF} [μs]	1370
No. of bunches per pulse	n_b	2820
Bunch spacing	Δt_b [ns]	337
Charge per bunch	N_e [10^{10}]	2
Emittance at IP	$\gamma\varepsilon_{x,y}$ [10^{-6}m]	10, 0.03
Beta at IP	$\beta^*_{x,y}$ [mm]	15, 0.4
Beam size at IP	$\sigma^*_{x,y}$ [nm]	553, 5
Bunch length at IP	σ_z [mm]	0.3
Beamstrahlung	δ_E [%]	3.2
Luminosity	L_{e+e-} [10^{34}cm^{-2}s^{-1}]	3.4
Power per beam	$P_b/2$ [MW]	11.3
Two-linac primary electric power (main linac RF and cryogenic systems)	P_{AC} [MW]	97
e^-e^- collision mode:		
Beamstrahlung	$\delta_{E,e-e-}$ [%]	2.0
Luminosity	L_{e-e-} [10^{34}cm^{-2}s^{-1}]	0.47

Table 1.3.1: *TESLA parameters for the $E_{cm} = 500\,GeV$ baseline design. The machine length includes a 2% overhead for energy management. The klystron power and primary electric power quoted include a 10% regulation reserve.*

- Building the linac with superstructures (section 2.1) improves the fill factor — and hence the maximum energy for a fixed accelerating gradient and site length — by about 6%.

- The fundamental limit for the gradient in niobium structures at 2 K is above 50 MV/m, and at TTF several 9-cell cavities have already reached gradients around 30 MV/m. Electropolishing followed by low-temperature bake-out has yielded systematically high performance single-cell cavities (section 2.1), with gradients up to 42 MV/m.

- The Lorentz force detuning (which increases as the square of the accelerating

		TESLA-500,$\gamma\gamma$
Repetition rate	f_{rep} [Hz]	5
Beam pulse length	T_P [μs]	950
RF-pulse length	T_{RF} [μs]	1370
No. of bunches per pulse	n_b	2820
Bunch spacing	Δt_b [ns]	337
Charge per bunch	N_e [10^{10}]	2
Emittance at IP	$\gamma\varepsilon_{x,y}$ [10^{-6}m]	3, 0.03
Beta at IP	$\beta^*_{x,y}$ [mm]	4, 0.4
Beam size at IP	$\sigma^*_{x,y}$ [nm]	157, 5
Bunch length at IP	σ_z [mm]	0.3
Geometric luminosity	L_{geom} [10^{34}cm^{-2}s^{-1}]	5.8
Effective $\gamma\gamma$ luminosity	$L_{\gamma\gamma}$ [10^{34}cm^{-2}s^{-1}]	0.6

Table 1.3.2: *Beam parameters for the $\gamma\gamma$ option. The effective luminosity takes into account only the high energy peak of the luminosity spectrum ($E_{cm,\gamma\gamma} \approx 400\,GeV$), see part VI, chapter 1 for details.*

gradient) can be compensated by active mechanical stabilisation using fast piezo tuners; this reduces the need to increase the regulation RF-power overhead at higher gradients. The method was successfully demonstrated at the TTF.

As a reasonable estimate for the maximum gradient in the TESLA linac we assume $E_{acc} = 35\,\text{MV/m}$ at $Q_0 = 5\cdot10^9$. Using superstructures, the energy reach of the machine is $E_{cm} = 800\,\text{GeV}$. A parameter set for this energy is shown in table 1.4.1. The beam delivery system and the magnets in the main linac are designed to be compatible with operation up to $400\,\text{GeV}$ beam energy. Obtaining high luminosity at maximum energy requires upgrading of the cryogenic plants (approximately doubling the 2K cooling capacity) and of the RF system (doubling the number of RF stations).

It should be noted that operation above the $500\,\text{GeV}$ reference energy is already possible without any hardware modification. The cooling plant capacity has a 50% overhead in the baseline design, which allows an increase of the gradient by 20–30%[1], depending on the variation of Q_0 versus g. With constant RF-power, the beam current decreases as $I_b \propto 1/g$; this effect is counter-balanced by a stronger adiabatic damping of the emittance, so that one might expect a constant luminosity. However, since the cavity filling time increases as $g/I_b \propto g^2$, the beam pulse length and thus the luminosity goes down, putting a reasonable upper limit on the initial energy reach of the machine at about $650\,\text{GeV}$.

---

[1]Only the RF wall losses scale as g^2/Q_0, the other contributions to the 2K load (static losses, wakefields, about one half of the total load) remain unchanged.

		TESLA-800
Accelerating gradient	E_{acc} [MV/m]	35
Fill factor		0.79
Repetition rate	f_{rep} [Hz]	4
Beam pulse length	T_P [μs]	860
No. of bunches per pulse	n_b	4886
Bunch spacing	Δt_b [ns]	176
Charge per bunch	N_e [10^{10}]	1.4
Emittance at IP	$\gamma\varepsilon_{x,y}$ [10^{-6}m]	8, 0.015
Beta at IP	$\beta_{x,y}^*$ [mm]	15, 0.4
Beam size at IP	$\sigma_{x,y}^*$ [nm]	391, 2.8
Bunch length at IP	σ_z [mm]	0.3
Beamstrahlung	δ_E [%]	4.3
Luminosity	L [10^{34}cm^{-2}s^{-1}]	5.8
No. of klystrons		1240
Power per beam	$P_b/2$ [MW]	17
Two-linac primary electric power	P_{AC} [MW]	$\approx$150

Table 1.4.1: *TESLA parameters for an upgrade to 800 GeV. It is assumed that the linac is built with 2×9-cell superstructures and the RF-power has been doubled (see text).*

Bibliography

[1] R. Brinkmann, G. Materlik, J. Roßbach and A. Wagner (eds.), *Conceptual Design of a 500 GeV e+e- Linear Collider with Integrated X-ray L aser Facility*, DESY-97-048 and ECFA-97-182, 1997, chapter 3: http://www.desy.de/lc- cdr/tesla/ tesla.html.

[2] *Zeroth Order Design Report for the Next Linear Collider*, SLAC Report 474, 1996.

[3] *JLC Design Study*, KEK Report 97-1, 1997.

[4] Chapter 4 in ref. [1]: http://www.desy.de/lc- cdr/s-band/s-band.html .

[5] Y. Kimura, *Status of TRISTAN*, Proc. XVth Conf. on High Energy Accelerators, Hamburg, 1992, Vol. I, p. 72.

[6] C. E. Reece, *Operating Experience with Superconducting Cavities at Jefferson Lab*, Part. Acc. **60** (1998) 43.

[7] *Proposal for a TESLA Test Facility*, DESY TESLA-93-01, 1992.

[8] C. Crawford et al., *High Gradients in Linear Collider Superconducting Accelerator Cavities by H igh Pulsed Power to Suppress Field Emission*, Part. Acc. **49** (1995) 1.

[9] E. Kako et al., *Improvement of Cavity Performance by Electro-Polishing in the 1.3 GHz Nb S uperconducting Cavities*, Proc. Part. Acc. Conf., New York 1999, Vol. I, p. 432.

[10] D. A. Edwards (ed.), *TESLA Test Facility Linac - Design Report*, DESY TESLA-95-01, 1995.

[11] *Linac Coherent Light Source (LCLS) Design Study Report*, SLAC-R-521, 1998.

[12] N. D'Hose et al., *Prospects of Hadron and Quark Physics with Electromagnetic Probes*, Proc. of Saint-Malo Workshop, Nucl. Phys. **A622** (1997) 1c - 389c.

[13] J.M. De Conto (ed.), *Electron Laboratory for Europe - Accelerator Technical Proposal*, 1993.

[14] H. Burkhardt (ed.) et al., *ELFE at CERN*, CERN report 99-10, 1999.

[15] M. Tigner, B. H. Wiik and F. Willeke, Proc. Particle Accelerator Conf., San Fran cisco 1991, Vol. 5, p. 2910.

[16] A. K. Ciftci et al., *Linac-Ring Type Colliders: Fourth Way to TeV Scale*, DESY-97-239, 1997.

[17] R. Brinkmann, *Interaction Region and Luminosity Limitations for the TESLA/HERA e/p Collid er*, DESY-M-97-05, 1997.

[18] R. Brinkmann, Y. Derbenev and K. Flöttmann, *A Low Emittance, Flat Beam Electron Source for Linear Colliders*, Proc. 7th EPAC, Vienna 2000, p. 453.

[19] D. Burke for the FFTB Collaboration, *Results from the Final Focus Test Beam*, Proc. 4th EPAC, London 1994, Vol. I, p. 23.

[20] H.-T. Duhme et al., *Feedbackelektronik TTF*, Proc. DESY Beschleuniger-Betriebsseminar, Grömitz 2000, DESY M-00-05, p. 171.

[21] Sections 3.10.2 and 3.10.11 in ref. [1].

[22] P. Chen and K. Yokoya, *Beam-Beam Phenomena in Linear Colliders*, KEK-report 91-2, 1991.

[23] I. Reyzl and S. Schreiber, *Luminosity Issues for the e- e- Option of the TESLA Linear Collider*, Proc. 7th EPAC, Vienna 2000, p. 498.

2 Results of Superconducting Accelerator Development

2.1 Superconducting Cavities

2.1.1 Introduction

Historically, the main drawback of superconducting (sc) accelerating structures has been the low gradient of the cavities combined with the high cost of cryogenic equipment. At the time of the first TESLA workshop [1] superconducting RF cavities in particle accelerators were usually operated in the 5 MV/m regime; such low gradients would make a superconducting linear electron-positron collider non-competitive with normal-conducting colliders, and hence the ambitious design gradient of 25 MV/m was specified for TESLA. As of writing, this gradient has been exceeded in multicell niobium cavities produced by industry. In addition, the cost per unit length of the linac has been considerably reduced by applying economical cavity production methods and by assembling many cavities in a long cryostat.

The TESLA cavities are similar in layout to the 5-cell 1.5 GHz cavities of the electron accelerator CEBAF, which were developed at Cornell University and fabricated by industry [2]. At that time the cavities considerably exceeded the design gradient of 5 MV/m: hence they were considered to have a significant potential for further improvement, and the CEBAF cavity manufacturing methods were adopted for TESLA. Improved quality control of the superconducting material and of the fabrication methods were made, and important new steps were introduced into the cavity preparation:

- chemical removal of a thicker layer from the inner cavity surface;

- a 1400°C annealing with a titanium getter to improve the niobium heat conductivity and to homogenise the material;

- rinsing with ultra-pure water at high pressure (100 bar) to remove surface contaminants;

- destruction of field emitters using High Power Processing.

Application of the above techniques — combined with an extremely careful handling of the cavities in a clean-room environment — has led to accelerating fields which exceed the original TESLA-500 design goal of 25 MV/m.

The TESLA Test Facility (TTF) has been set up at DESY to provide the infrastructure for the chemical treatment, clean-room assembly, and testing of industrially

produced multicell cavities. An electron linac has been built as a test bed for the performance of the sc accelerating structures with an electron beam of high bunch charge. The linac is also equipped with undulator magnets to generate FEL radiation in the VUV regime.

2.1.2 Superconducting material

2.1.2.1 Choice of superconductor

The existing large scale applications for superconductors are magnets and accelerating cavities. A common requirement is a high critical temperature[1], but there are distinct differences concerning the critical magnetic field. In magnets operated with a dc or a low-frequency ac current, 'hard' (type I) superconductors are required, with high upper critical fields (15–20 T) and strong flux pinning in order to achieve high current density; such properties are only offered by alloys like niobium-titanium or niobium-tin. In microwave applications the limit is essentially set by the thermodynamic critical field, which is well below 1 T for all known superconductors. Strong flux pinning is undesirable as it is coupled with losses due to hysteresis. Hence a 'soft' (type II) superconductor must be used. Pure niobium is the best candidate, although its critical temperature T_c is only 9.2 K, and the thermodynamic critical field about 200 mT. Niobium-tin (Nb_3Sn) with a critical temperature of 18 K looks more favourable at first sight, however the gradients achieved in Nb_3Sn coated niobium cavities were always below 15 MV/m, probably due to grain boundary effects in the Nb_3Sn layer [3]. For this reason the TESLA collaboration decided to use niobium as the superconducting material. Among the two options — cavities made from solid niobium or by sputter-coating of a copper cavity — the solid niobium approach promised higher accelerating gradients and was adopted as the baseline for the TESLA cavity R&D program.

2.1.2.2 Microwave surface resistance

Superconductors suffer from energy dissipation in microwave fields since the radio frequency (RF) magnetic field penetrates a thin surface layer and induces oscillations of the unpaired electrons. According to the Bardeen-Cooper-Schrieffer (BCS) theory of superconductivity, the surface resistance is given by the expression

$$R_{\text{BCS}} \propto \frac{f^2}{T}\,\exp(-1.76\,T_c/T),$$

where f is the microwave frequency. For niobium the BCS surface resistance at 1.3 GHz is about 800 nΩ at 4.2 K, and drops to 15 nΩ at 2 K (see figure 2.1.1). Because of the exponential temperature dependence, operation at 1.8–2 K is essential for achieving high accelerating gradients in combination with very high quality (Q) factors. Superfluid helium is an excellent coolant owing to its high heat conductivity. In addition to the

---

[1]The High-T_c ceramic superconductors have not yet found widespread application in magnets, mainly due to technical difficulties in cable production and coil winding. Cavities with High-T_c sputter coatings on copper have shown much inferior performance in comparison to niobium cavities.
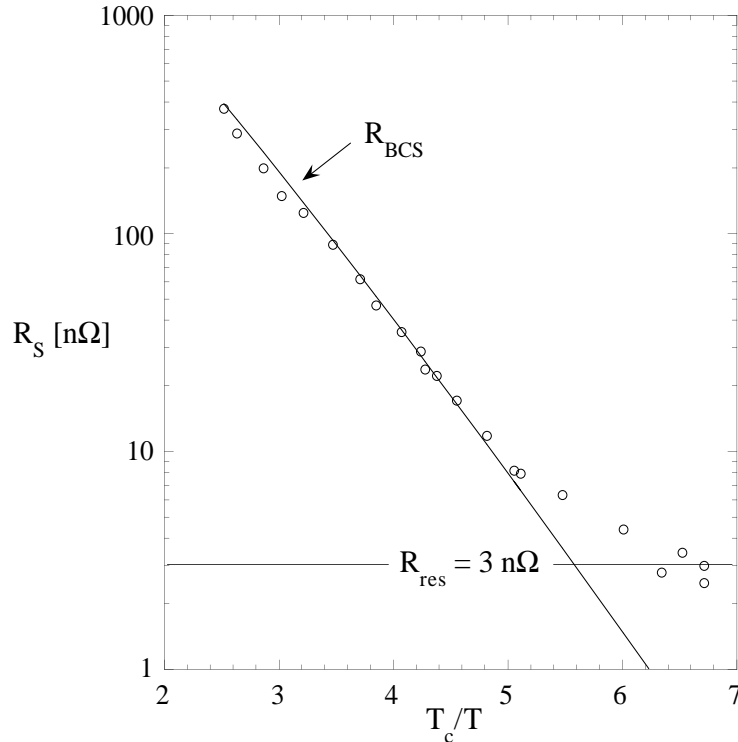
Figure 2.1.1: *The measured surface resistance of a 9-cell TESLA cavity plotted as a function of T_c/T. The residual resistance of $3\,n\Omega$ corresponds to a quality factor $Q_0 = 10^{11}$.*

BCS term there is a residual resistance R_{res} caused by impurities, frozen-in magnetic flux, or lattice distortions. This term is temperature independent and amounts to a few $n\Omega$ for very pure niobium, but increases dramatically if the surface is contaminated.

2.1.2.3   Heat conduction in niobium

The heat produced at the inner cavity surface has to be guided through the cavity wall to the superfluid helium bath. The thermal conductivity of niobium exhibits a strong temperature dependence in the cryogenic regime (see figure 2.1.2) and scales approximately with the residual resistivity ratio[1] *RRR*.

Impurities have a strong impact on the thermal conductivity, and niobium with contamination in the ppm range is required. At the niobium-helium interface a temperature jump is observed due to the so-called Kapitza resistance: for a clean niobium surface in contact with superfluid helium at $2\,K$, the effect gives a temperature rise per unit power flux of about $1.6 \cdot 10^{-4}\,K/(Wm^{-2})$ [4].

---

[1] *RRR* is defined as the ratio of the resistivities at room temperature and at liquid helium temperature. The low temperature resistivity is usually measured at $4.2\,K$, applying a magnetic field to assure the normal state.
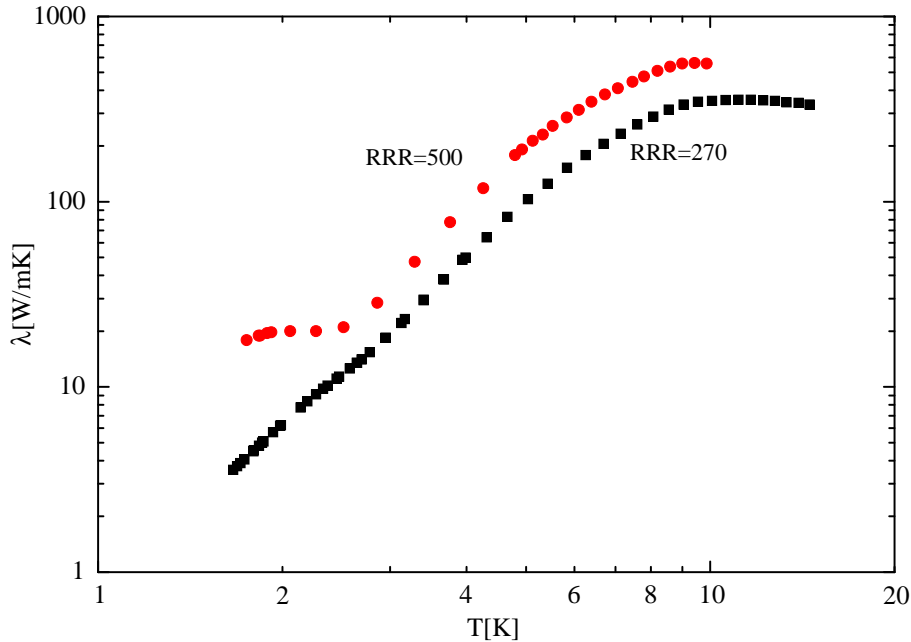
Figure 2.1.2:   *Measured heat conductivity of samples from the niobium sheets used in the TESLA cavities: before and after the 1400° C heat treatment (RRR = 280 and RRR = 500 respectively).*

2.1.2.4   Magnetic field effects

Maximum gradient. Superconductivity breaks down when the microwave magnetic field at the cavity surface exceeds a critical value. The limit is close to the thermodynamic critical field B_c (200 mT for niobium at 2 K). The corresponding accelerating field on the cavity axis is about 50 MV/m for the TESLA cavity geometry. Several authors claim that RF superconductivity persists up to a so-called 'superheating field', exceeding B_c by 20% in case of Nb: however it remains to be proven that RF cavities can be reliably operated near or even beyond B_c.

Trapped magnetic flux. Although niobium is a soft type II superconductor without strong flux pinning, weak magnetic dc fields are not expelled upon cool-down but remain trapped in the niobium. Each flux line contains a normal-conducting core. Trapped magnetic flux contributes to the surface resistance by an amount of $3.5 \, n\Omega/\mu T$ for niobium. Therefore, to achieve $Q_0 \geq 10^9$ the TESLA cavities are magnetically shielded.

2.1.3   Design of the TESLA cavities

The TESLA cavity is a 9-cell standing wave structure of about 1 m length whose fundamental TM mode has a frequency of 1300 MHz. The cavity is made from solid niobium and is bath-cooled by superfluid helium at 2 K. Each cavity is equipped with:

a helium tank; a tuning system driven by a stepping motor; a coaxial RF power coupler; a pickup probe; and two higher-order mode (HOM) couplers.

2.1.3.1   Choice of frequency and cavity geometry

Cost economy in a long linac calls for a small cavity design and consequently a frequency well above the 350 to 500 MHz used in storage rings like LEP or HERA. The frequency can not be made arbitrarily high, however, because of the f^2 dependence of the BCS surface resistance, which at 3 GHz already limits the attainable gradient to about 30 MV/m [5]. Another reason to stay below 3 GHz is the wakefields which scale with the second to third power of the frequency ($W_{\parallel} \propto f^2$, $W_{\perp} \propto f^3$). The optimum frequency is in the 1.5 GHz regime; the choice for 1.3 GHz was motivated by the availability of high power klystrons.

A multicell structure is needed to maximise the active acceleration length in a linac. An upper limit on the number of cells per cavity is given by the requirements of field homogeneity throughout the structure and the absence of trapped modes (see below). A 9-cell structure is close to the optimum. A side view of the TTF cavity with the beam tube sections and the coupler ports is shown in figure 2.1.3.

The cells have a spherical contour near the equator for low multipacting sensitivity, and a large iris radius to reduce wakefield effects. The resonator is operated in the π-mode with 180° phase difference between adjacent cells. The cell length is determined by the condition that the electric field has to be inverted in the time a relativistic particle needs to travel from one cell to the next. The end cells have a slightly different shape to ensure equal field amplitudes in all 9 cells. In addition there is a small asymmetry between the left and right end cell which reduces trapping of higher-order modes. The important cavity parameters are listed in table 2.1.1.

2.1.3.2   Lorentz-force detuning and cavity stiffening

The RF electromagnetic field exerts Lorentz forces on the currents induced in a thin surface layer, resulting in a deformation of the cells in the μm range. The computed frequency shift at 25 MV/m is 900 Hz for an unstiffened cavity of 2.5 mm wall thickness. The bandwidth of the cavity equipped with the main power coupler ($Q_{ext} = 2.5 \cdot 10^6$) is about 520 Hz (FWHM): hence a reinforcement of the cavity is needed to reduce the detuning. Niobium stiffening rings are welded in between adjacent cells as shown in figure 2.1.4. They reduce the frequency shift by a factor of two[1].

2.1.4   Cavity fabrication and treatment

The superconducting resonators are fabricated from bulk niobium by electron-beam (EB) welding of deep-drawn half cells. The tubes for the beam pipes and the coupler ports are made by back extrusion and are joined to the cavity by EB welds.

---

[1]Part of the remaining shift is due to an elastic deformation of the tuning mechanism.

type of accelerating structure	standing wave
accelerating mode	TM_{010} , π-mode
fundamental frequency	$1300\,\mathrm{MHz}$
nominal gradient E_{acc} for TESLA-500	$23.4\,\mathrm{MV/m}$
quality factor Q_0	$> 10^{10}$
active length L	$1.038\,\mathrm{m}$
cell-to-cell coupling k_{cc}	$1.87\,\%$
iris diameter	$70\,\mathrm{mm}$
R/Q	$1036\,\Omega$
E_{peak}/E_{acc}	2.0
B_{peak}/E_{acc}	$4.26\,\mathrm{mT/(MV/m)}$
tuning range	$\pm\,300\,\mathrm{kHz}$
$\Delta f/\Delta L$	$315\,\mathrm{kHz/mm}$
Lorentz force detuning constant K_{Lor}	$\approx 1\,\mathrm{Hz/(MV/m)^2}$
Q_{ext} of input coupler	$2.5 \cdot 10^6$
cavity bandwidth at $Q_{ext} = 2.5 \cdot 10^6$	$520\,\mathrm{Hz}$ FWHM
fill time	$420\,\mu\mathrm{s}$
number of HOM couplers	2

Table 2.1.1:   *Parameters of the 9-cell cavity (note that we adopt here the definition of shunt impedance by the relation $R = V^2/P$, where P is the dissipated power and V the peak voltage in the equivalent parallel LCR circuit).*
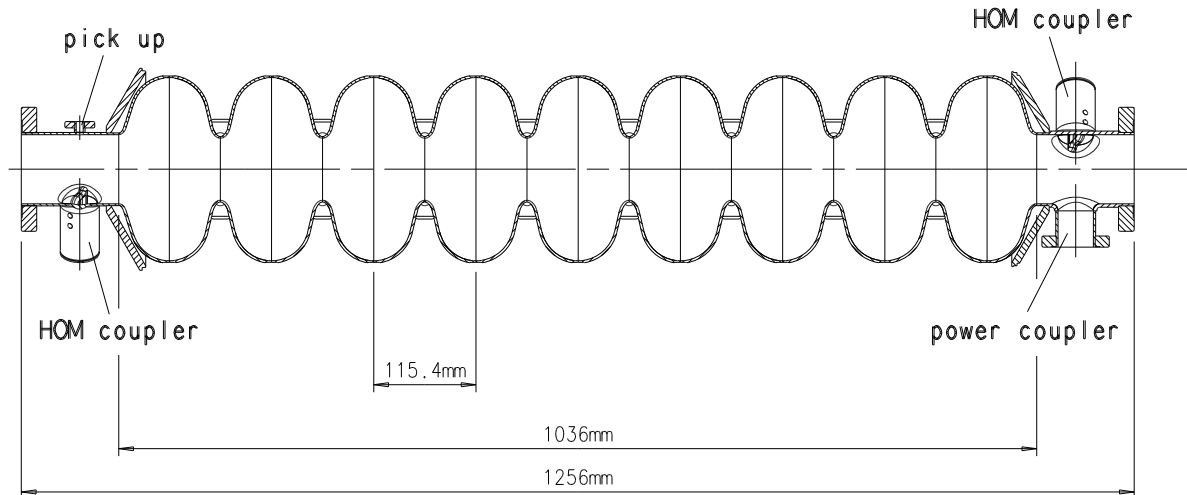
Figure 2.1.3:   *Side view of the 9-cell cavity with the main power coupler port and two higher-order mode couplers.*
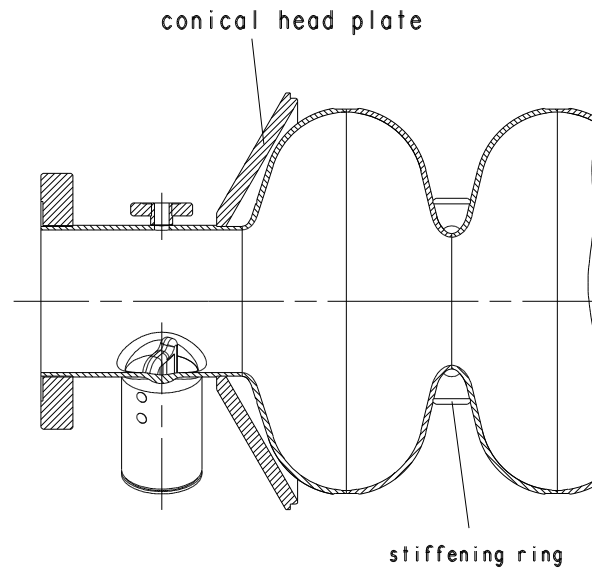
Figure 2.1.4: *End section of a cavity with stiffening ring and conical head plate for welding into the helium tank.*

Impurity content in ppm (wt)				Mechanical Properties	
Ta	≤ 500	H	≤ 2	Residual resistivity ratio RRR	≥ 300
W	≤ 70	N	≤ 10	grain size	$\approx 50\ \mu$m
Ti	≤ 50	O	≤ 10	yield strength	> 50 MPa
Fe	≤ 30	C	≤ 10	tensile strength	> 100 MPa
Mo	≤ 50			elongation at break	30 %
Ni	≤ 30			Vickers hardness HV 10	≤ 50

Table 2.1.2: *Technical specification for niobium used in TESLA cavities.*

2.1.4.1   Niobium specification

The niobium specification for the TESLA cavities is listed in table 2.1.2. The most important metallic impurity in niobium is tantalum, with a typical concentration of 500 ppm. The interstitially dissolved gases (mainly oxygen) act as scattering centres for the unpaired electrons and reduce the thermal conductivity. The niobium ingot is out-gassed by several melting cycles in a high vacuum electron beam furnace. The interstitial oxygen, nitrogen and carbon contamination is reduced to a few ppm.

The Nb ingots are forged and rolled into sheets of 2.8 mm thickness. After rolling the Nb sheets are first degreased and cleaned by chemical etching. The sheets are then annealed for 1–2 hours at 700–800°C in a vacuum oven at 10^{-5}–10^{-6} mbar to achieve full recrystallization and a uniform grain size of about 50 μm. The finished Nb sheets are eddy-current checked for defects like cracks or foreign inclusions which might impair the superconducting properties.

2.1.4.2   Cavity fabrication

Cavity fabrication is a delicate procedure, requiring intermediate cleaning steps and a careful choice of the weld parameters to achieve full penetration of the joints. First, two half cells are connected at the iris; the stiffening rings are welded in next. At this point weld shrinkage may lead to a slight distortion of the cell shape which needs to be corrected. Particularly critical are the equator welds which are made from the outside, and a reliable method for obtaining a smooth weld seam at the *inner* cavity surface was required. A two-pass procedure was developed, where 50% of the power is applied to the first weld pass, and 100% on the second. In both cases, a slightly defocused electron beam rastered in an elliptic pattern is used. The electron-beam welding technique of niobium cavities has been perfected in industry to such an extent that the weld seams do not limit cavity performance below $\sim$30 MV/m.

A challenge for a welded construction are the tight mechanical and electrical tolerances. These can be maintained by a combination of mechanical and radio frequency measurements on half cells and by careful tracking of weld shrinkage. The procedures established during the TTF cavity fabrication are suitable for large series production, requiring quality assurance measurements only on a small sample of cavities.

The cavities are equipped with niobium-titanium flanges at the beam pipes and the coupler ports[1]. NbTi can be electron-beam welded to niobium and possesses a surface hardness equivalent to that of standard UHV flange material (stainless steel 316 LN/ DIN 1.4429). Contrary to pure niobium, the alloy NbTi (ratio 45/55 by weight) shows no softening after the heat treatment at 1400°C and only a moderate crystal growth. O-ring type aluminum gaskets provide reliable seals in superfluid helium.

2.1.4.3   Cavity treatment

A layer of 100–200 μm is removed in several steps from the inner cavity surface to obtain good RF performance in the superconducting state. The standard method applied at DESY is called Buffered Chemical Polishing (BCP) [6], and uses an acid mixture of HF (48%), HNO_3 (65%) and H_3PO_4 (85 %) in the ratio 1:1:2. The acid is cooled to 5°C and pumped through the cavity in a closed loop. After rinsing with ultra-pure water and drying in a class 100 clean room, the cavities are annealed at 800°C in an Ultra High Vacuum (UHV) oven to out-gas dissolved hydrogen and relieve mechanical stress in the deep drawn niobium. In a second UHV oven the cavities are heated to 1350–1400°C at which temperature the other dissolved gases diffuse out of the material, and the residual resistivity ratio RRR increases by about a factor of two to around 500. To absorb the oxygen diffusing out of the niobium and to prevent oxidation by the residual gas in the oven (pressure $< 10^{-7}$ mbar), a thin titanium layer is evaporated on the inner and outer cavity surface (Ti being a stronger getter than Nb). The titanium layer is later removed by 80 μm and 20 μm BCP of the inner and outer cavity surface respectively. This high-temperature treatment with Ti getter is referred to as post-purification. A severe drawback of post-purification is the considerable grain growth

---

[1]Except the first production series.
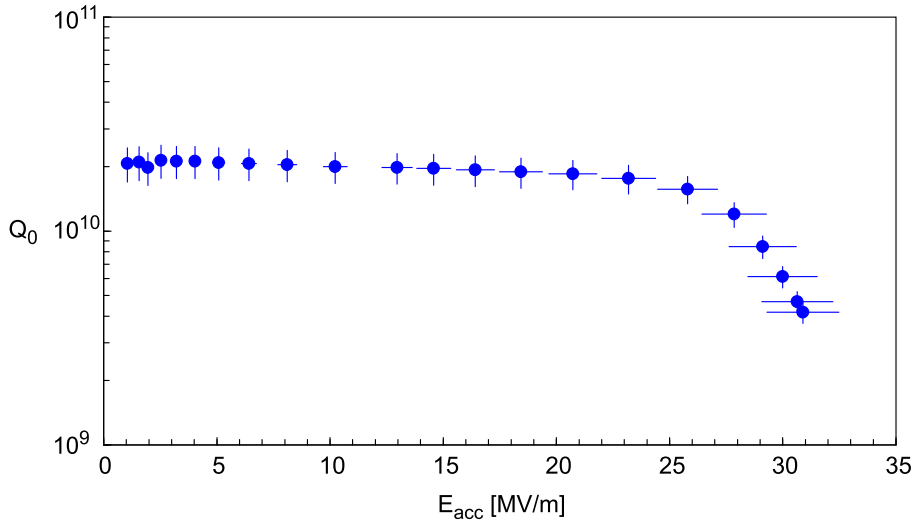
Figure 2.1.5:   *Excitation curve of a high-performance 9-cell cavity. The cavity was cooled by superfluid helium of 2 K. The systematic rms errors in the determination of the accelerating field and the quality factor are indicated.*

of the niobium: post-purified cavities are vulnerable to plastic deformation and have to be handled with great care.

After the final heat treatment, the cavities are mechanically tuned to adjust the resonance frequency to the design value and to obtain equal field amplitudes in all 9 cells. This is followed by a light BCP, three steps of high-pressure water rinsing (100 bar), and drying in a class 10 clean room. The final acceptance step is an RF test in a superfluid helium bath cryostat.

2.1.5   Cavity performance and quality control measures

2.1.5.1   Practical limitations of superconducting cavities

Figure 2.1.5 shows the 'excitation curve' of a high-performance 9-cell resonator; plotted is the quality factor Q_0 as a function of the accelerating electric field E_{acc}. An almost constant high value of more than 10^{10} is observed up to 25 MV/m. The drop of Q_0 at higher gradients indicates that even the best multicell cavities are still far from reaching the theoretical limit of about 50 MV/m: the performance is limited because the superconducting surface is not perfect.

The fundamental advantage of superconducting cavities is their extremely low surface resistance at 2 K leading to RF losses which are 5 to 6 orders of magnitude lower than in copper cavities. The drawback is that even tiny surface contaminations are potentially harmful as they decrease the quality factor and may even lead to a thermal breakdown (quench) of the superconductor due to local over-heating. Perfect cleaning of the inner cavity surface is of utmost importance. Cavity treatment and assembly is therefore carried out in clean rooms conforming to semiconductor standards.

Two frequently encountered effects which degrade performance are field emission of electrons and multipacting. Field emission of electrons from sharp tips has been a notorious limitation of high-gradient superconducting cavities. In field-emission loaded cavities the quality factor drops exponentially above a certain threshold field and X-rays are observed. There is ample evidence that small particles or dust on the cavity surface act as field emitters. High quality cleaning (e.g. by rinsing with high-pressure ultra-pure water) is the most effective remedy [7]. Using high-pressure rinsing it has been possible to raise the threshold for field emission in multicell cavities from about $10\,\mathrm{MV/m}$ to more than $20\,\mathrm{MV/m}$ in the past few years. Remaining emitters can often be destroyed by 'conditioning' the cavity with short RF pulses of high instantaneous power [8] (up to $500\,\mathrm{kW}$ for a $1\,\mathrm{m}$ long TESLA cavity).

2.1.5.2   Results from the first series of TTF cavities

The first series of 27 nine-cell resonators, fully equipped with flanges for the main power and higher-order mode couplers, were produced by four European companies during the years 1994/95. These cavities were foreseen for installation in the TTF linac with a gradient of at least $15\,\mathrm{MV/m}$ at $Q_0 > 3 \cdot 10^9$. In the specification given to the companies, however, no guaranteed gradient was required. According to the test results at TTF these resonators fall into four classes:

(1) 16 cavities without any known material and fabrication defects, or with minor defects which could be repaired;

(2) 3 cavities with serious material defects;

(3) 6 cavities with imperfect equator welds;

(4) 2 cavities with serious fabrication defects (not fully penetrated electron beam welds or with holes burnt during welding; these were rejected).

The test results for the cavities of class 1 in a vertical bath cryostat with superfluid helium cooling at $2\,\mathrm{K}$ are summarized in figure 2.1.6. With the exception of two cavities, the TTF design goal of $15\,\mathrm{MV/m}$ is exceeded. Nine of the resonators achieve the more demanding TESLA specifications of $E_{acc} \geq 23.4\,\mathrm{MV/m}$ at $Q_0 \geq 1 \cdot 10^{10}$.

The excitation curves of the class 2 cavities (figure 2.1.7) are characterized by sudden drops in quality factor with increasing field, and rather low maximum gradients. Temperature mapping revealed excessive heating at isolated spots; an example is shown in figure 2.1.8a. An eddy-current scan, performed at the Bundesanstalt für Material-forschung in Berlin (BAM), showed a pronounced signal at the defect location. With X-ray radiography (also carried out at BAM) a dark spot with a size of 0.2–0.3 mm was seen (figure 2.1.8b), indicating an inclusion of foreign material with a higher nuclear charge than niobium. Using X-ray fluorescence at HASYLAB the inclusion was identified as tantalum.

The six cavities in class 3 were all produced by one company and exhibited premature quenches at gradients of 10–14 MV/m, and a slope in the excitation curve $Q(E)$
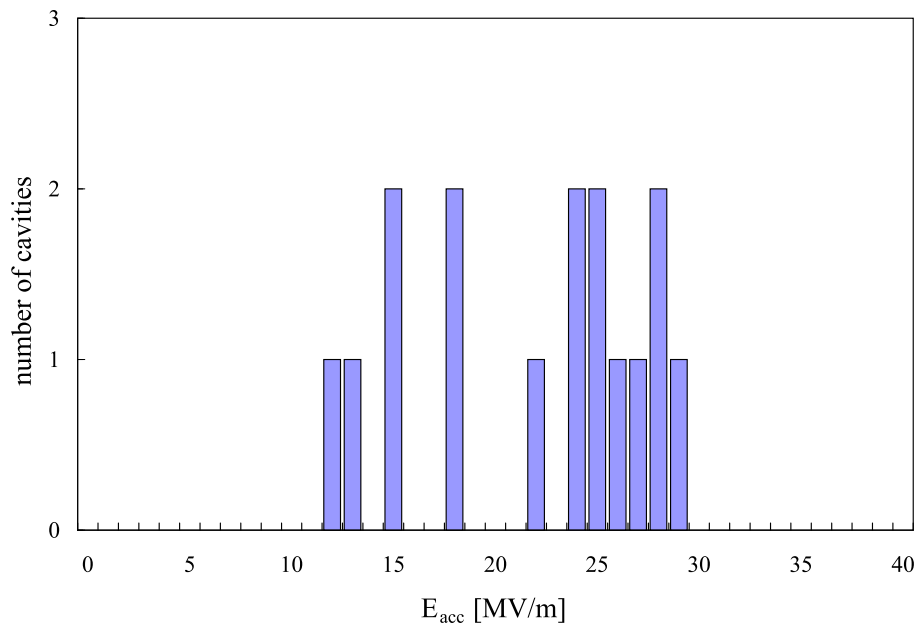
Figure 2.1.6:   *Distribution of maximum gradients for the resonators of class 1, requiring a quality factor $Q_0 \geq 1 \cdot 10^{10}$.*
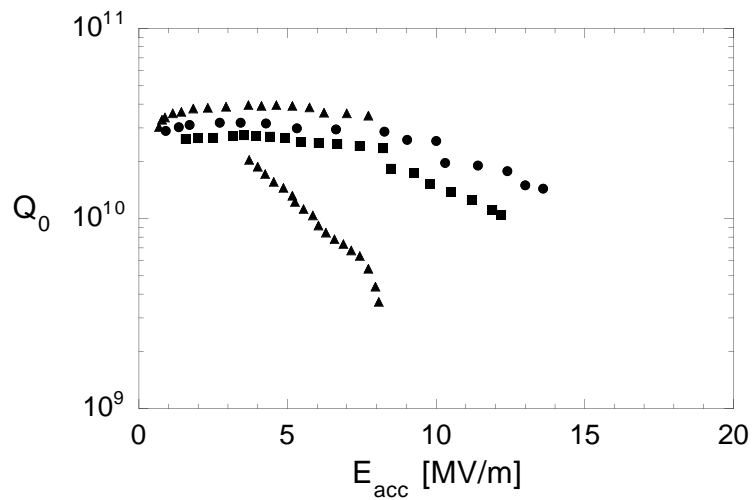
Figure 2.1.7:   *Excitation curves of the three cavities with serious material defects (class 2). Cavity C5 (▲) exhibited a jump in quality factor.*

(a)   (b)
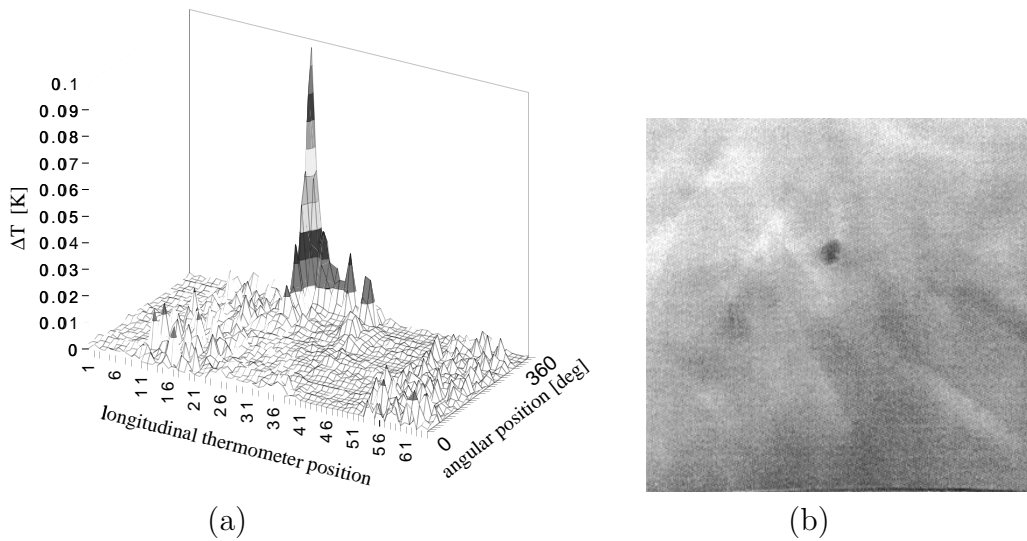
Figure 2.1.8:   (a) Temperature map of cell 5 of cavity C6 showing excessive heating at a
localized spot. (b) Positive print of an X-ray radiograph showing the 'hot spot' as a dark
point.
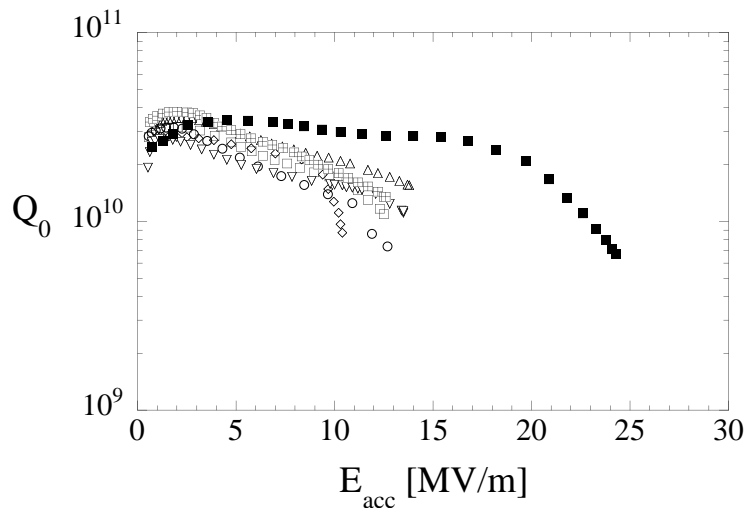
Figure 2.1.9:   Excitation curves of the six cavities with imperfect equator welds (class 3).
Also shown is a resonator (■) made later by the same company, observing stringent
cleaning procedures at the equator welds.

(figure 2.1.9). Temperature mapping revealed strong heating at several spots on the equator weld and pointed to contamination of the weld seam. A new resonator manufactured by the same company — after observing stringent cleaning procedures of the weld region — showed high performance, achieving 24.5 MV/m (see figure 2.1.9). Later cavities made by the same company showed still better performance.

2.1.5.3   Diagnostic methods and quality control

The deficiencies encountered in the first series production of TTF cavities initiated the development of several diagnostic methods and quality control procedures.

Electron microscopy. Scanning electron microscopy with energy-dispersive X-ray analysis (EDX) is used to identify foreign elements on the surface. Only a depth of about $1\,\mu$m can be penetrated, so one has to remove layer by layer to determine the diffusion depth of titanium or other elements. The titanium layer applied in the high temperature treatment was found to extend to a depth of about $10\,\mu$m in the bulk niobium. The sensitivity of the EDX method is limited and a Ti fraction below $0.5\,\%$ is undetectable. Auger electron spectroscopy offers higher sensitivity and showed titanium migration at grain boundaries to a depth of $60\,\mu$m: hence a layer of this thickness must be removed from the RF surface by BCP after post-purification with Ti getter.

Eddy-current scan. Microscope methods are restricted to small samples and cannot be used to study entire cavities. In addition the methods are far too time-consuming to check large niobium sheets. A practical device for the quality control of all niobium sheets going into cavity production is a high-resolution eddy-current system developed at BAM. The apparatus operates similar to a turn table and permits a high scanning speed (about 10 minutes for a 260 mm diameter disk). A two-frequency principle is applied: scanning with high frequency (about 1 MHz) allows detection of surface irregularities, while the low frequency signal (about 150 kHz) is sensitive to bulk inclusions. The performance of the eddy-current scanning device was verified with a Nb test sheet containing implanted tantalum deposits of 0.2 to 1 mm diameter.

2.1.5.4   Second and third series of TTF cavities

The niobium sheets were all eddy-current scanned to eliminate material with tantalum or other foreign inclusions before the deep drawing of half cells. More than $95\,\%$ of the sheets were found free of defects, the remaining ones showed grinding marks, imprints from rolling or large signals due to small iron chips. Most of the rejected sheets were recoverable by applying some chemical etching. The eddy-current check has proven to be an important quality control procedure, not only for the cavity manufacturer but also for the supplier of the niobium sheets.

Stringent requirements were imposed on the electron-beam welding procedure to prevent the degraded performance at the equator welds encountered in the first series. After mechanical trimming, the weld regions were cleaned by a light chemical etching followed by ultra-pure water rinsing and clean-room drying. The cleaning process was performed not more than 8 hours in advance of the EB welding.
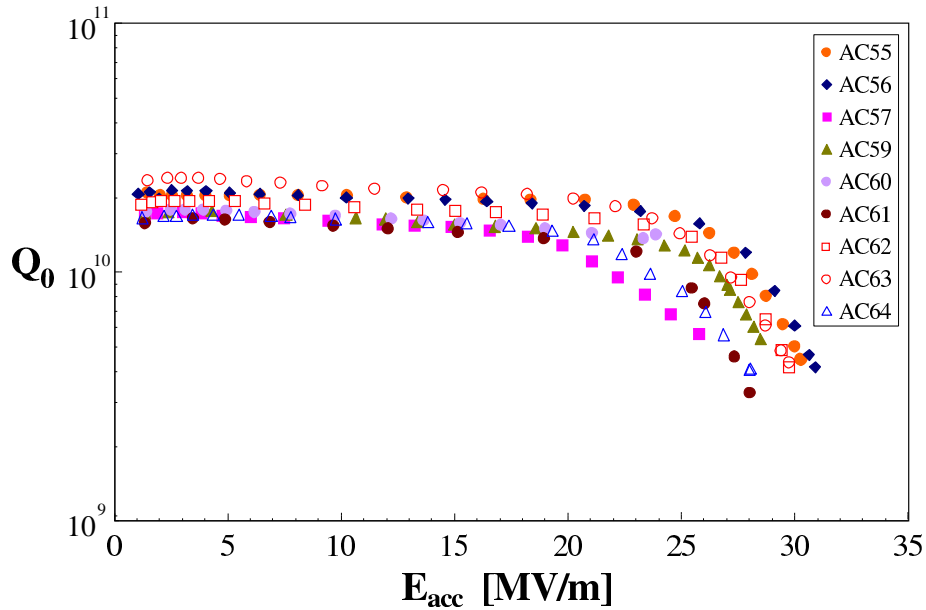
Figure 2.1.10:   *Excitation curves of cavities of the third production series.*

Since implementing these two additional quality control measures, no foreign material inclusions nor weld contaminations have been found in new cavities tested so far.

2.1.5.5   Test results in vertical cryostat

All new cavities were subjected to the standard treatment described in section 2.1.4.3, including the post-purification with titanium getter at 1400°C. In the second series there was one cavity with a serious weld defect (a repaired hole in an equator weld). The average gradient of the remainder is $23.3 \pm 2.3\,\mathrm{MV/m}$ at $Q_0 \geq 1 \cdot 10^{10}$. From the third series (produced by one company), nine cavities have been tested to date (see figure 2.1.10). They exceed the TESLA-500 specification: the average gradient at $Q_0 \geq 1 \cdot 10^{10}$ is $26.1 \pm 2.3\,\mathrm{MV/m}$ and the average quality factor at the design gradient of $23.4\,\mathrm{MV/m}$ is $Q_0 = (1.39 \pm 0.35) \cdot 10^{10}$.

As of writing, five cryogenic modules each containing eight 9-cell resonators have been assembled. Figure 2.1.11 shows the performance of the cavities in the three production series and of those installed in the five cryomodules. In both cases the average gradient exhibits a clear trend towards higher values, and the spread in gradient across the cavities (as indicated by the error bars) is shrinking. The most recent cavities exceed the $23.4\,\mathrm{MV/m}$ operating gradient of TESLA-500 by a comfortable margin.

2.1.5.6   Tests with main power coupler in horizontal cryostat

After having passed the acceptance test in the vertical bath cryostat, the cavities are welded into their liquid helium container and equipped with the main power coupler.
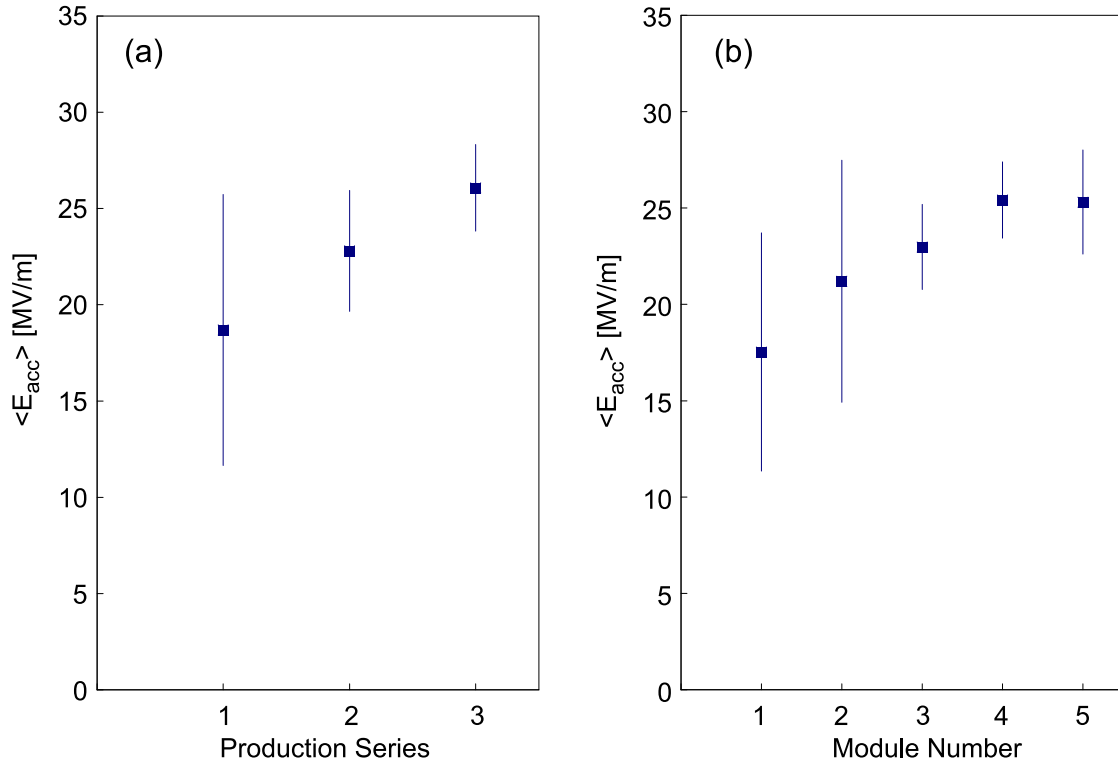
Figure 2.1.11:   *Average accelerating gradients at $Q_0 \geq 10^{10}$ measured in the vertical test cryostat of: (a) the cavities in the three production series; and (b) the cavities installed in the first five cryogenic modules for TTF (see also [9]).*

The power coupler is adjusted to an give an external Q^1 of typically $3 \cdot 10^6$. The accelerating fields achieved in the vertical and the horizontal test are well correlated as shown in figure 2.1.12. In a few cases a reduced performance was seen, usually caused by field emission. Several cavities improved their performance in the horizontal test because of operation with short (millisecond) pulses[2] instead of the continuous wave (cw) operation in the vertical cryostat. The results show that the good performance of the cavities is maintained by taking care to avoid dust contamination during mounting of the helium vessel and power coupler.

In one of the cryomodules installed in the TTF linac the maximum usable gradient was determined for each of the eight cavities, restricted by a minimum quality factor of $1 \cdot 10^{10}$ to restrict the heat load on the helium system. The average gradient was $23.6 \, \mathrm{MV/m}$, indicating that installation of the individual cavities into a module does not degrade their performance.

---

[1]In the vertical test, a weakly coupled input antenna is used whose external Q is less than the Q_0 of the cavity.

[2]the addition of the main power coupler allows the use of short pulses.
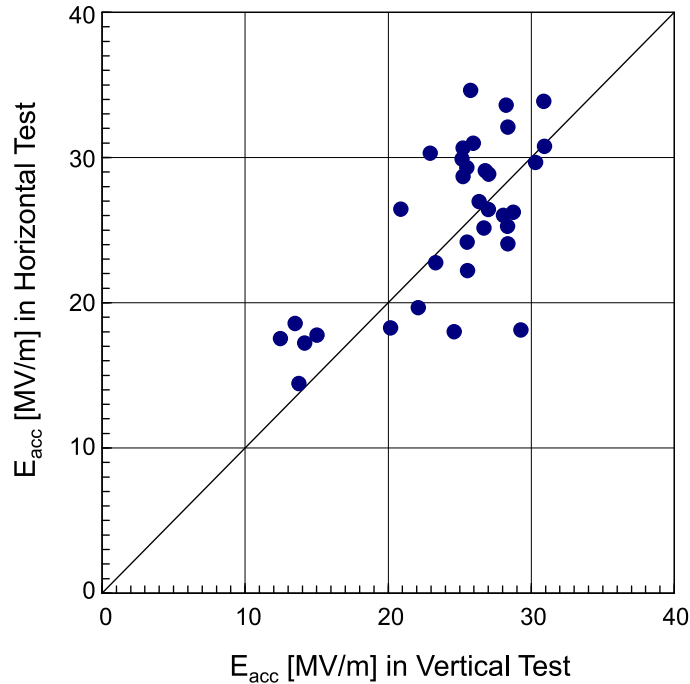
Figure 2.1.12:   *Comparison of vertical and horizontal test results at 2 K. The average accelerating field achieved in the vertical test with continuous wave (cw) excitation is 24.5 MV/m, in the horizontal test with pulsed excitation 25.5 MV/m. The RF pulse has a rise time of 500 μs and a flat top of 800 μs.*

2.1.6   Cavities of ultimate performance

The design c.m. energy of 500 GeV corresponds a gradient of 23.4 MV/m in the present nine-cell cavities with a reduced beam pipe length. The cavities from the third industrial production exceed this value by a comfortable margin, and consequently TESLA-500 can be realized with the present cavity fabrication and preparation methods. The energy upgrade to 800 GeV (section 1.4) requires use of the so-called 'superstructure', where the effective acceleration length is increased by combining together several multicell cavities with reduced inter-cavity spacing (section 2.1.8). The accelerating field gradient required is then 35 MV/m, which represents a significant increase compared to the performance achieved so far. Three main obstacles might prevent us from approaching the superconductor limit of ≈ 50 MV/m in multicell niobium cavities:

- foreign material contamination in the niobium;

- insufficient quality and cleanliness of the inner RF surface; and

- quality of the welds.

The first two points are being addressed by on-going R&D programs (section 2.1.6.1). The feasibility of so-called 'seamless' cavities to avoid welding is also being investigated

(section 2.1.6.4).

While material problems may represent a significant challenge to achieving the required cavity performance for the 800 GeV upgrade, a fundamental limitation is given by the effect of Lorentz-force detuning, which must be reduced to allow efficient 35 MV/m operation in the linac (section 2.1.6.3).

2.1.6.1   Quality improvement of niobium and post-purification

As already discussed, niobium for microwave resonators has to be of extreme purity for two reasons: dissolved gases like hydrogen, oxygen and nitrogen impair the heat conductivity at liquid helium temperature; and contamination by normal-conducting or weakly superconducting clusters close to the RF surface may cause a premature breakdown of the superconducting state. The niobium for the TTF cavities was processed in industry with plants which are in addition used for other metals. For the large series production of cavities needed for the TESLA collider, it would be economical to install dedicated facilities for the niobium refinery and the forging and sheet rolling operations. A substantial improvement in material quality can be expected from specialized installations which are designed for the highest cleanliness, and which are free of contamination by other metals. The same applies for the electron-beam welding machines which must conform to Ultra High Vacuum standards: such a high-quality EB welding machine will be installed at DESY in early 2001 to be used in the cavity R&D program.

The recent TTF cavities have been made from eddy-current checked niobium with gas contents in the few ppm range and an RRR of 300. Ten 9-cell cavities have been tested before and after the 1400°C heat treatment which raises the RRR to more than 500. The average gain in gradient was 4 MV/m. The result implies that, with the present surface preparation by chemical etching, the heat treatment is an indispensable step in achieving the TESLA-500 goal. From tests at KEK there is some evidence that the tedious and costly 1400°C heat treatment may not be needed in cavities prepared by electropolishing (see below).

2.1.6.2   Electrolytic polishing (electropolishing)

The Buffered Chemical Polishing (BCP) used at TTF to remove a 100–200 μm thick damage layer produces a rough niobium surface with strong grain boundary etching. An alternative method is 'electropolishing' (EP) in which the material is removed in an acid mixture under current flow. Sharp edges and burrs are smoothed out and a very glossy surface can be obtained. In figure 2.1.13 BCP and EP treated niobium samples are compared.

Electropolishing of niobium has been already used in the 1970's to obtain high magnetic surface fields in small X-band cavities (see references in [6]). But it is only recently that this method has been developed to a high standard at the KEK laboratory in Japan [10]. The electrolyte is a mixture of H_2SO_4 (95 %) and HF (46 %) in a volume ratio of 9:1. The bath temperature is 30–40°C. The process consists of two alternating steps [11, 6]: oxidation of the niobium surface by the sulphuric acid under current flow
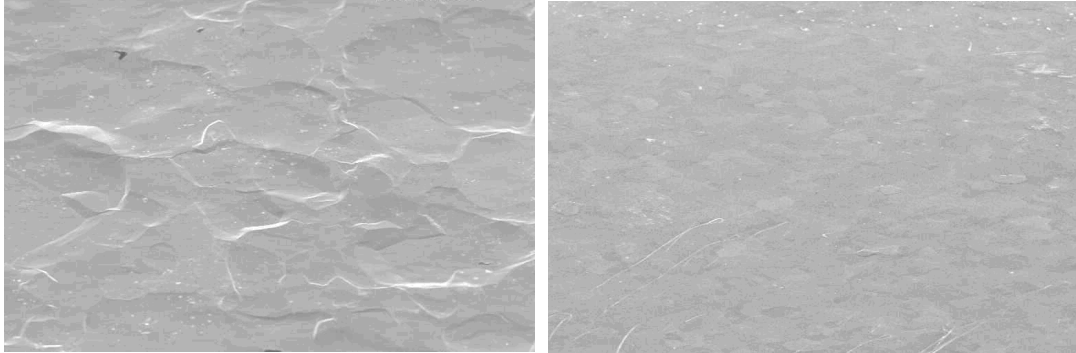
Figure 2.1.13:   *SEM micrographs of niobium surface after BCP (left) and EP (right). The average surface roughness is 1 μm in the left and 0.1 μm in the right sample. Height of micrograph is 500 μm (Courtesy of CERN).*

(current density about $500 \, \text{A/m}^2$); and dissolving of the Nb_2O_5 by the hydrofluoric acid. The rate of material removal is around $40 \, \mu$m per hour.

Since 1995 gradients above $35 \, \text{MV/m}$ have been routinely obtained at KEK in several electropolished L-band single-cell niobium cavities [12]. Most of these cavities were made from RRR 200 material and not subjected to a high temperature heat treatment for post-purification. A KEK-Saclay collaboration demonstrated that EP raised the accelerating field of a 1-cell cavity by more than $7 \, \text{MV/m}$ with respect to BCP. When the electropolished surface was subjected to a subsequent BCP, the cavity suffered a clear degradation in RF performance which could be recovered by a new EP [13]. Thus there is strong evidence that EP is the superior surface treatment method.

CERN, DESY, KEK and Saclay started a joint R&D program with EP of half cells and 1-cell cavities in August 1998. Gradients between 35 and $42 \, \text{MV/m}$ are now routinely being achieved [14] (see figure 2.1.14). The current program focuses on cavities made from niobium with $RRR = 300$. An important goal is to determine whether or not the high gradients so far achieved can be obtained without the time-consuming $1400°$C heat treatment.

Recently it has been found that an in-situ baking of the evacuated cavity at 100–$150°$C (following the EP and clean water rinsing) is an essential step in reaching higher gradients without a strong degradation in quality factor [15]. The underlying mechanism is not yet understood. The baking was applied to all single-cell cavities.

The transfer of the EP technique to multicell cavities requires considerable investment. In a first test a 9-cell TESLA resonator has been electropolished by a Japanese company, improving its performance from 22 to $32 \, \text{MV/m}$ (figure 2.1.15). An EP facility for 9-cell cavities is under construction at DESY. Given the results obtained so far, it is likely that EP will form an essential part of producing cavities capable of achieving the $35 \, \text{MV/m}$ operating gradient needed for TESLA-800.
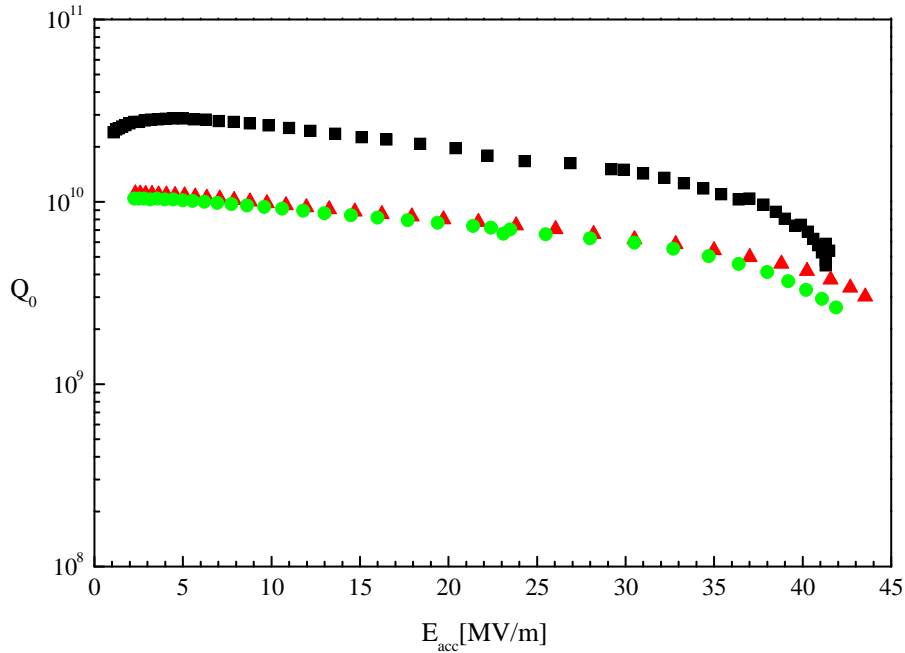
Figure 2.1.14:   *Excitation curves of three electropolished single-cell cavities without heat treatment at 1400° C. The tests have been performed in different cryostats and under slightly different conditions (magnetic shielding, helium temperature).*

2.1.6.3   Frequency stability of the cavities

The pulsed operation leads to a time-dependent frequency shift of the 9-cell cavities. The stiffening rings joining neighbouring cells are adequate to keep this 'Lorentz-force detuning' within tolerable limits up to the nominal TESLA-500 gradient of 23.4 MV/m. To allow for higher gradients the stiffening must be improved[1], or alternatively, the cavity deformation must be compensated. The latter approach has been successfully demonstrated using a piezoelectric tuner [17] (see figure 2.1.16). The result indicates that the present stiffening rings augmented by a piezoelectric tuning system will permit efficient cavity operation at the TESLA-800 gradient of 35 MV/m.

2.1.6.4   Seamless cavities

To explore the feasibility of cavities without weld connections in the regions of high electric or magnetic RF fields, the TESLA collaboration has pursued two alternative 'seamless' production methods: spinning and hydroforming.

   Spinning. At the Legnaro National Laboratory of INFN in Italy, the spinning technique [18] has been used to deform flat niobium disks into 1.3 GHz cavities. A very high degree of material deformation was needed, leading to a rough inner cavity

---

[1]The reinforcement of niobium cavities by a plasma-sprayed outer copper layer has been investigated at Orsay [16].
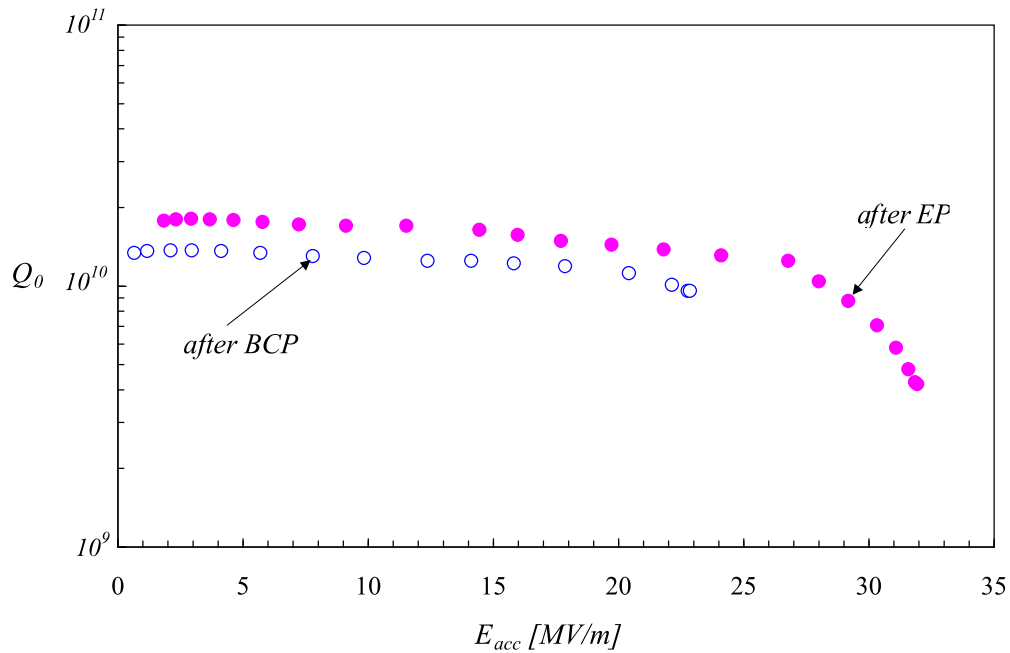
Figure 2.1.15:   *Excitation curve of a TESLA 9-cell cavity after buffered chemical polishing (BCP) and electropolishing (EP), but before application of the baking procedure.*
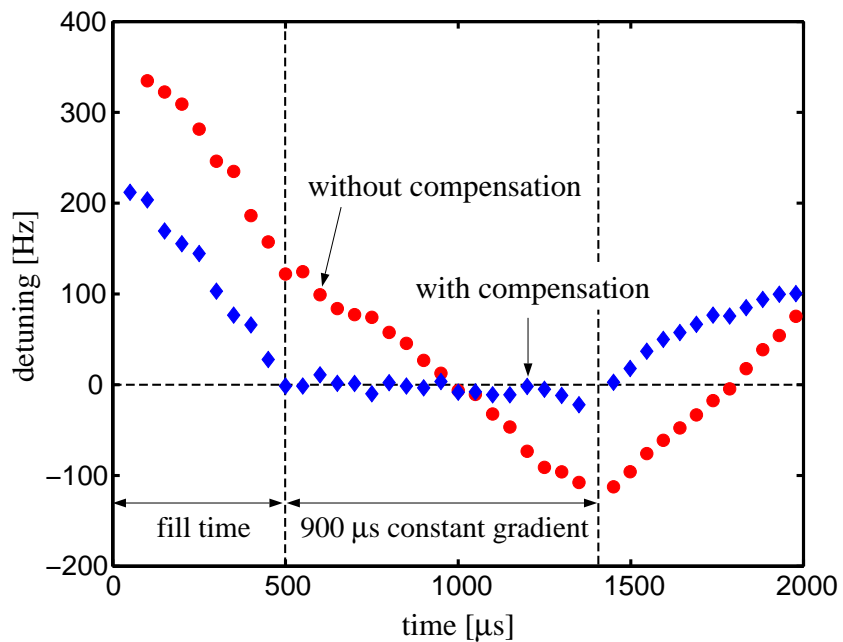
Figure 2.1.16:   *Piezoelectric compensation of the Lorentz-force induced frequency shift in pulsed-mode cavity operation. The accelerating field is 23.5 MV/m.*
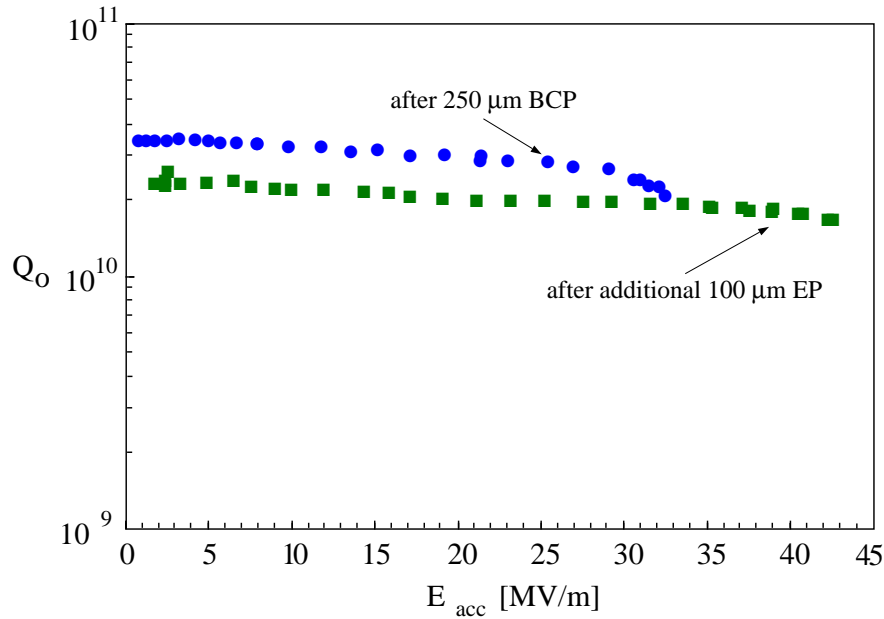
Figure 2.1.17:   *Excitation curve of a hydroformed 1-cell cavity after BCP and EP. Preparation and measurement of the cavity was carried out by P. Kneisel at Jefferson Laboratory.*

surface. After mechanical grinding and heavy etching (removal of more than $500\,\mu$m), gradients of the order of $25\,$MV/m were obtained [20]. With an electropolished cavity, up to $38\,$MV/m have been achieved [19]. Presently 1-cell, 3-cell and 9-cell cavities are being produced from seamless Nb tubes with an RRR of 300; in this case the amount of deformation will be much less and a smoother inner surface can be expected.

Hydroforming. The deformation of a seamless niobium tube into a cavity by hydrostatic pressure is being studied in collaboration with industry. Starting from a tube of intermediate diameter, the first step is to reduce the diameter at the iris and then to expand the tube in the equator region. The deformation process is first modeled on a computer, using measured strain-stress and plastic flow characteristics of the niobium tubes to be used. The shaping of the tube into an external mould is done under computer control by applying internal over-pressure and at the same time compression along the axis direction. The deformation is done in small steps with a strain rate below 10^{-3}/s, following the procedure established in the simulation.

Two cavities were hydroformed at DESY from RRR 100 tubes of $134\,$mm diameter and $2\,$mm wall thickness. One cavity was produced at a company (Butting) from a deep drawn RRR 200 niobium tube of $156\,$mm diameter and $3\,$mm thickness. An intermediate annealing was not needed. The DESY cavities were post-purified at a temperature of $1400°$C with titanium getter, increasing the RRR to more than 300. They achieved accelerating fields of 33 and $32\,$MV/m respectively at $Q_0 = 2 \cdot 10^{10}$. One cavity was then electropolished at KEK (removing $100\,\mu$m) and reached the record

value[1] of $E_{acc} = 42\,\text{MV/m}$ [21] (see figure 2.1.17). The most remarkable observation is that the excitation curve $Q_0(E)$ is almost flat up to the highest field.

2.1.6.5   Niobium sputtered cavities

Recent investigations at CERN [22] and Saclay [23] have shown that 1.3–1.5 GHz single-cell copper cavities with a niobium sputter layer of about $1\,\mu\text{m}$ thickness are able to reach accelerating fields in the order of 20–25 MV/m. This is a considerable improvement in comparison with the LEP cavities but still almost a factor of two below the performance of solid niobium cavities. Moreover the quality factor is continuously decreasing with rising gradient. At present there is no experimental evidence to suggest that Nb sputtered copper cavities have the potential of achieving the TESLA-800 goal.

2.1.7   Auxiliary systems and components

2.1.7.1   Helium vessel and tuning system

The cavity is welded into a cylindrical vessel which contains the superfluid helium needed for cooling and serves as part of the tuning mechanism. The tank is made from titanium whose thermal contraction is almost identical to that of niobium. A titanium bellows allows the length to be adjusted by the mechanical tuner.

Tuning the cavity to its nominal operating frequency is a challenging task since the cavity length must be adjusted with sub-micron accuracy. The tuning system used at TTF consists of a stepping motor with a gear box and a double lever arm. The moving parts operate at 2 K in vacuum. The frequency tuning range is $\pm 300\,\text{kHz}$ with a resolution of 1 Hz. The tuners in the TTF linac have been working for two years with high reliability. For TESLA a more compact tuning system is under development which incorporates a piezoelectric crystal for fast frequency adjustment (feedback).

2.1.7.2   Main power coupler

For TTF several coaxial power input couplers have been developed [24, 25, 26, 27, 28], consisting of a cold section which is mounted on the cavity in the clean room and closed by a ceramic window, and a warm section which contains the transition from the coaxial line to the waveguide. The latter part is evacuated and sealed against the air-filled wave guide (WR 650) by a second ceramic window (see figure 2.1.18). The elaborate two-window solution was chosen for protection of the cavity against contamination during mounting in the cryomodule, and against a window fracture during linac operation.

Bellows in the inner and outer conductors of the coaxial line of the coupler allow a few mm of motion between the cold mass and the vacuum vessel when the cavities are cooled from room temperature to 2 K. A low thermal conductivity is achieved by using stainless steel pipes and bellows with a 10–$20\,\mu\text{m}$ copper plating at the radio frequency surface. Lower values than the design heat loads of 6 W at 70 K, 0.5 W at 5 K and 0.06 W at 2 K have been achieved in practice.

---

[1]as of writing
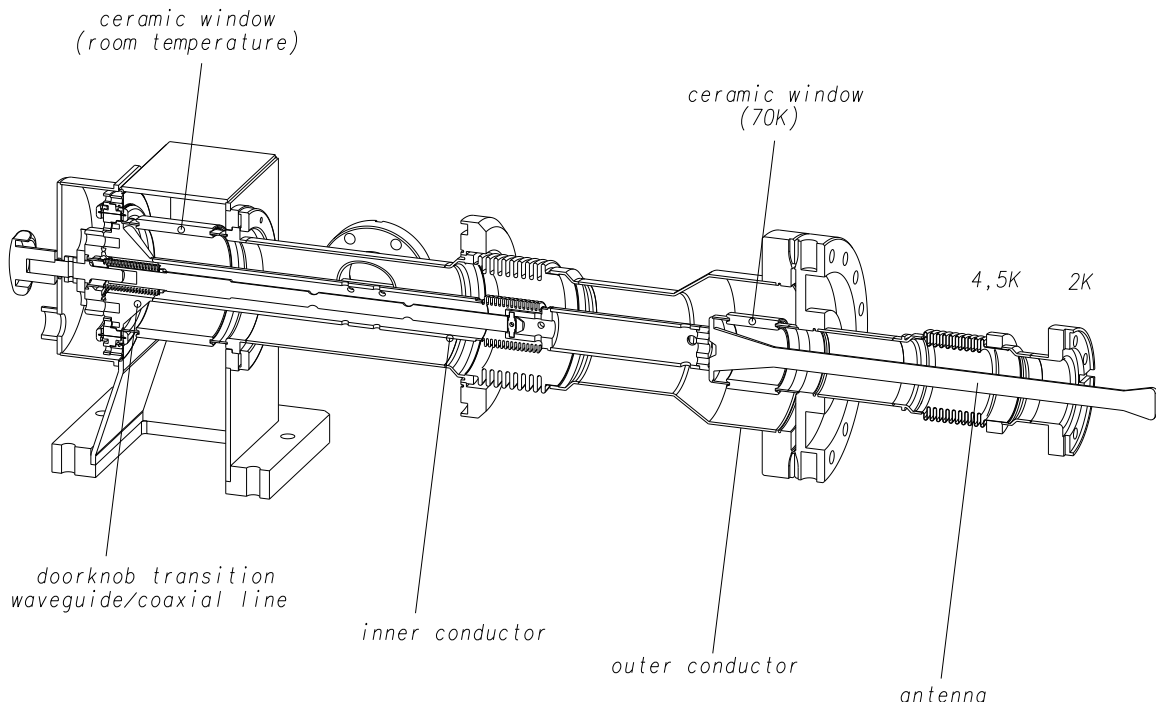
Figure 2.1.18:   *The coaxial power input coupler (version III) for the TTF cavities. The coaxial part is thermally connected to the 4.5 K and 70 K radiation shields of the cryostat. The input antenna is movable to vary Q_{ext} in the range $(1-6) \cdot 10^6$.*

The most recent coupler (version III) features two cylindrical Al_2O_3 windows which are insensitive to multipacting resonances [29], and are coated with titanium nitride to reduce the secondary electron emission coefficient [30]. The coaxial line is also insensitive to multipacting resonances, and a further suppression is achieved by applying a dc bias voltage (up to 5 kV) to the inner conductor; such a bias was originally proposed at INP Novosibirsk and has proven very beneficial in the case of the LEP couplers [31].

An instantaneous power of 230 kW has to be transmitted to provide a gradient of 23.4 MV/m for a 950 μs long beam pulse of 9.5 mA. The filling time of the cavity amounts to 420 μs, and the decay time (after the beam pulse) is an additional 500 μs. The external quality factor of the coupler is $Q_{ext} = 2.5 \cdot 10^6$ at 23.4 MV/m. By moving the inner conductor of the coaxial line, Q_{ext} can be varied in the range $(1–6) \cdot 10^6$ to cope with different beam loading conditions and to facilitate an in-situ high power processing of the cavities at RF power levels up to 1 MW. This feature has proven extremely useful on several occasions to eliminate field emitters that entered the cavities at the last assembly stage.

All couplers needed some conditioning but then performed according to specification. During experimental tests at TTF, the couplers were able to transmit up to 1.5 MW of RF power in travelling wave mode.
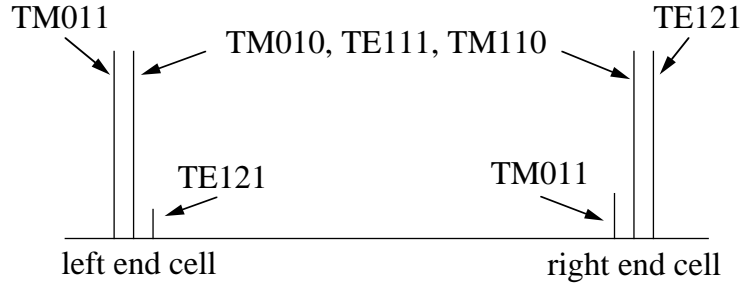
Figure 2.1.19: *Effect of asymmetric end cell shaping on various modes. The main accelerating mode TM_{010} and the higher modes TE_{111} and TM_{110} are not affected while TM_{011} is enhanced in the left end cell, TE_{121} in the right end cell. Using HOM couplers at both ends, all higher-order modes can be extracted.*

2.1.7.3   Higher-order mode couplers

The intense electron bunches excite eigenmodes of higher frequency in the resonator which must be damped to avoid multibunch instabilities and beam breakup. This is accomplished by extracting the stored energy via higher-order mode (HOM) couplers mounted on the beam pipe sections of the nine-cell resonator. A problem arises from 'trapped modes' which are concentrated in the centre cells and have a low field amplitude in the end cells. An example is the TE_{121} mode. By an asymmetric shaping of the end half cells one can enhance the field amplitude of the TE_{121} mode in one end cell, while preserving the field homogeneity of the fundamental mode and the good HOM coupling to the untrapped modes TE_{111}, TM_{110} and TM_{011}. The effects of asymmetric end cell tuning are sketched in figure 2.1.19.

The two polarization states of dipole modes in principle require two orthogonal HOM couplers at each side of the cavity. In a string of cavities this complexity can be avoided since the task of the 'orthogonal' HOM coupler is taken over by the HOM coupler of the neighboring cavity. The design of the HOM coupler is shown in figure 2.1.20. The superconducting pickup antenna is well cooled and insensitive to γ radiation and electron bombardment. A tunable 1.3 GHz notch filter suppresses power extraction from the accelerating mode to less than 50 mW at 23.4 MV/m.

2.1.8   The superstructure concept

2.1.8.1   Limitation on number of cells per cavity

A fundamental design goal for a linear collider is to maximize the active acceleration length in the machine and to reduce the cost of the radio frequency system. Hence it is desirable to use accelerating structures with as many cells as possible both to increase the filling factor and to reduce the number of power couplers and wave guide components. However, the number of cells per cavity (N) is limited by the conditions of field homogeneity and the presence of trapped modes. For a standing-wave structure
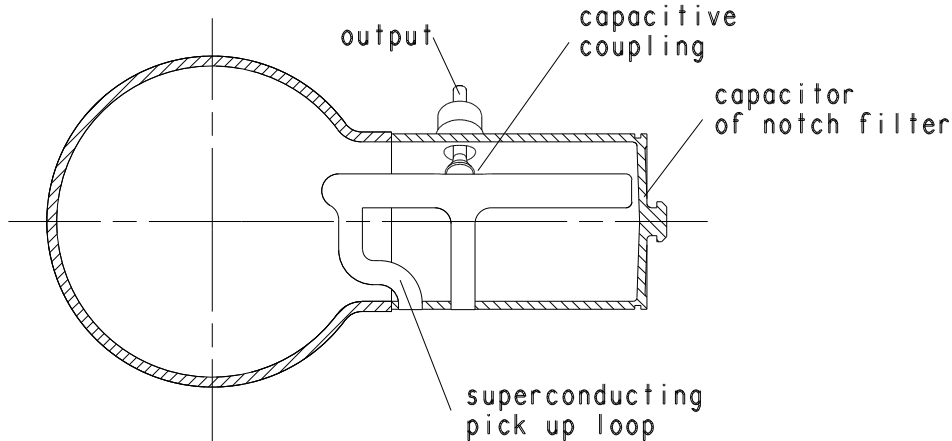
Figure 2.1.20:   *Cross-section of the higher order mode (HOM) coupler.*

operated in the π-mode, a frequency error δf in an individual cell results in an error in the accelerating field amplitude (δA_{cell}) of

$$\delta A_{cell} \propto \frac{N^2 \, \delta f}{k_{cc}},$$

where k_{cc} is the cell-to-cell coupling. The sensitivity of the field pattern to small perturbations grows quadratically with the number of cells. The probability of trapping higher-order modes within a structure also increases with N; such modes with a small field amplitude in the end cells are difficult to extract by the HOM couplers. In superconducting cavities these modes are particularly dangerous because of their long damping times: the modes persist over a significant portion of the bunch train, causing emittance dilution (beam break-up, see section 3.2).

The 9-cell structure chosen for TESLA is a good compromise between the conflicting requirements of optimum filling factor, field homogeneity and absence of trapped modes. In the TESLA Test facility linac each cavity is equipped with its own input coupler and tuning system. The cavities are connected by beam tube sections and bellows with a total length of $3/2\,\lambda$, where $\lambda = 0.223\,\mathrm{m}$ is the RF wavelength. The tube diameter ($78\,\mathrm{mm}$) is below cutoff for $1.3\,\mathrm{GHz}$: hence there is no power flow from one cavity to the next. For the baseline design of TESLA-500 the 9-cell cavity concept with individual power coupler is maintained, but the interconnection is shortened to improve the filling factor of the machine and to reduce the nominal accelerating gradient from 25 to $23.4\,\mathrm{MV/m}$.

2.1.8.2   The superstructure

The limitations on the number of cells per cavity can be circumvented by joining several multicell cavities to form a so-called superstructure [32]. Short tubes of sufficient diameter ($114\,\mathrm{mm}$) enable power flow from one cavity to the next. Two types of
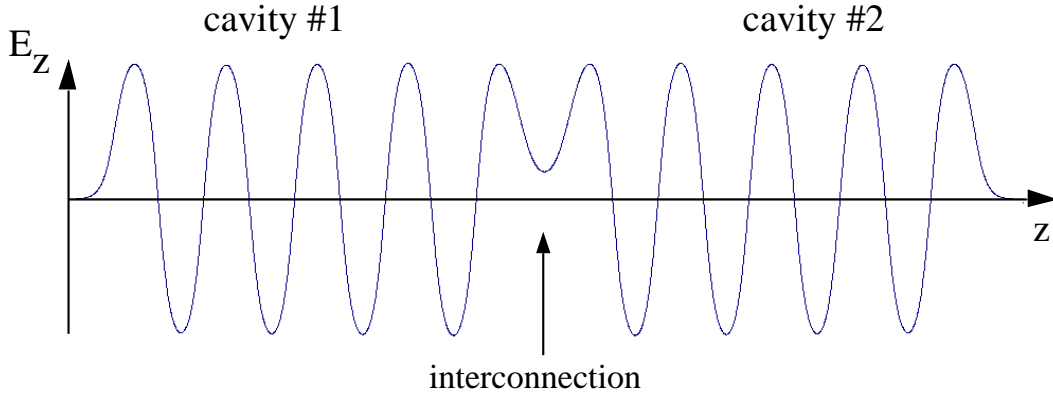
Figure 2.1.21: E_{acc} along the axis of a 2×9-cell superstructure.

superstructures have been investigated in detail: Superstructure I consisting or four 7-cell resonators; and, more recently, Superstructure II consisting of two 9-cell resonators. The chain of cavities is powered by a single input coupler mounted at one end. HOM couplers are located at the interconnections and at the ends. All cavities are equipped with their own tuners. The cell-to-cell coupling is $k_{cc} = 1.9\,\%$, while the coupling between two adjacent cavities is a superstructure is two orders of magnitude smaller at $k_{ss} \approx 3 \cdot 10^{-4}$: due to this comparatively weak inter-cavity coupling the issues of field homogeneity and HOM damping are much less of a problem than in a single long cavity with $N = 28$ or 18 cells. The shape of the centre cells is identical to those in the 9-cell TTF structures while the end cells have been redesigned to accommodate the larger aperture of the beam tube. The radio frequency properties of both superstructures are summarised in table 2.1.3.

2.1.8.3   Electrical properties of a superstructure

Field profile. Synchronism between the relativistic bunches and the accelerating field requires a length of $\lambda/2$ for the shortest interconnection. When N is an odd number, the (π-0) mode (cell-to-cell phase advance is π and cavity-to-cavity phase advance is zero) can be used for acceleration. The field profile of this mode is shown in figure 2.1.21.

The cavities are tuned to equal field amplitude in all cells and are then welded into their liquid helium tanks and joined to form the superstructure. It has been verified that the pre-tuning of the cavities can be preserved during the assembly steps. The equalisation of the field amplitudes across the cavities is then accomplished by a method resembling the standard bead pull technique used to homogenise the field in a multicell cavity. By means of the mechanical tuners the cavities are changed in volume one after the other by a given amount and the resulting frequency shifts of the (π-0) mode recorded. A perturbation calculation allows the required adjustments to be determined. The method has been validated by tests using a copper model of the superstructure and by computer simulations. The tuning can be carried out on the cleaned and evacuated superstructure, and requires only one pickup probe for all the

Parameter	4×7cell	2×9cell
sensitivity factor, N^2/k_{cc}	2600	4300
cell-to-cell coupling k_{cc}	1.9 %	1.9 %
cavity-to-cavity coupl. k_{ss}	3.6· 10^{-4}	2.8· 10^{-4}
(R/Q) cavity	736 Ω	986 Ω
E_{peak}/E_{acc}	2.0	2.0
B_{peak}/E_{acc}	4.18 $\frac{\text{mT}}{\text{MV/m}}$	4.18 $\frac{\text{mT}}{\text{MV/m}}$
distance to next resonance	158 kHz	330 kHz

Table 2.1.3:   *RF parameters of the superstructures.*

cells.

Induced energy spread in a bunched beam. The main concerns for a chain of cavities fed by a single input coupler is the flow of the RF power through the interconnecting beam pipes, and the time needed to reach equal field amplitude in all cells during pulsed-mode operation. The power flow has been extensively studied [33, 34] with two independent codes, HOMDYN and MAFIA. The relative spread in energy gain in a train of 2820 bunches is predicted to be less than 10^{-4} (figure 2.1.22), indicating that the energy flow is sufficient to refill the cells in the time interval between two adjacent bunches.

In superstructure I (4×7 cells) the main power coupler must transmit 675 kW of travelling wave power at 500 GeV c.m. energy and 1080 kW at 800 GeV. For Superstructure II (2×9 cells) the numbers are 437 kW and 705 kW, respectively. The TTF couplers have been tested up to 1500 kW and are therefore sufficient to feed either type of superstructure. To provide an additional safety margin for the operation at 35 MV/m (TESLA-800) the diameter of the cold coupler section will be increased from 40 mm to 60 mm.

The higher-order modes have been extensively studied for Superstructure I. Nearly all modes propagate through the 114 mm diameter beam pipe and are efficiently damped with 5 HOM couplers mounted at the three interconnections and at both end tubes. The details of the dipole mode impedances differ somewhat from the 9-cell cavity, but the overall effect on the beam dynamics is similar [35].

2.1.8.4   Technical and economical aspects of the superstructures

The baseline design of TESLA-500 rests on the well-established 9-cell TTF cavity technology with individual power couplers but a reduced length of the interconnection (283 mm instead of 346 mm for beam pipes and bellows). The two superstructures under consideration improve the filling factor by 6 % and require a factor of 2–3 fewer main power couplers in the machine. Keeping the total length of the collider constant, the superstructures allow us to reach the 500 GeV c.m. energy with a gradient of 22 MV/m, compared to 23.4 MV/m with individual 9-cell cavities. In table 2.1.4 the important parameters of the three versions of the TESLA accelerating system are
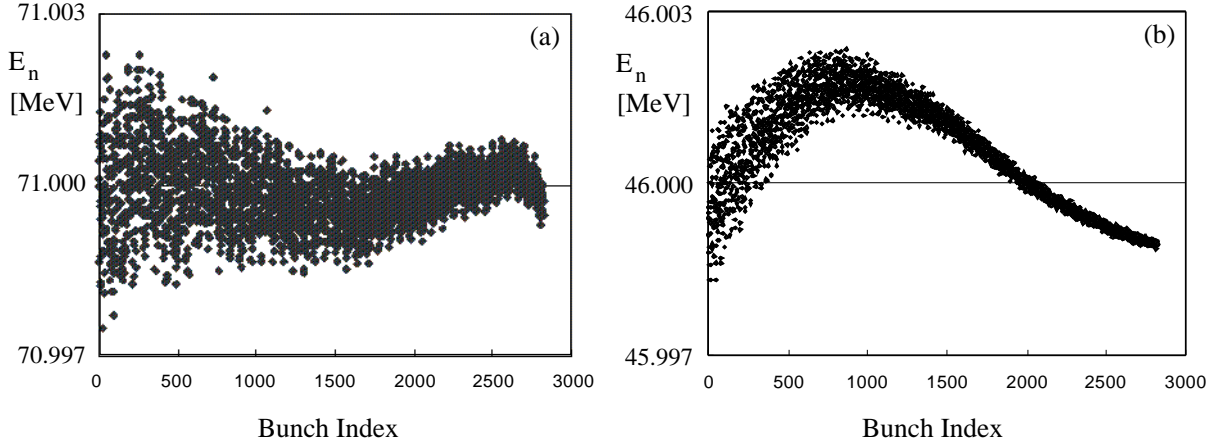
Figure 2.1.22: *Computed energy gain E_n for a train of 2820 bunches in: (a) Superstructure I (nominal gain 71 MeV); and (b) Superstructure II (nominal gain 46 MeV).*

Layout	L_{active} [m]	E_{acc} [MV/m]	no. of power coupl.	no. of HOM coupl.	no. of tuners	filling factor L_{active}/L_{total} [%]	P_{trans} [kW]
9-cell	1.04	23.4	20592	41184	20592	78.6	232
4×7-cell	3.23	22.0	7032	35160	28128	84.9	675
2×9-cell	2.08	22.0	10926	32778	21852	84.8	437

Table 2.1.4: *Different layouts of the TESLA accelerating system. The numbers refer to TESLA-500. P_{trans} is the power per RF coupler transmitted to a 9.5 mA beam.*

compared.

Superstructure I. The 4×7-cell structure appears most attractive in terms of cost reduction: 7000 superstructures would be needed and the same number of power couplers. On the other hand, the cavity comprises of only 7 cells, so the number of helium vessels and tuning systems is higher than with 9-cell cavities. A clear disadvantage is the large overall length of 3.86 m which makes chemical and heat treatments of the entire structure difficult.

Superstructure I was proposed first and extensive RF measurements have been performed on a copper model. A niobium prototype is in preparation for a beam test in the TTF linac. In this prototype the 7-cell cavities are joined by superconducting flanges. The third generation of TTF input coupler and five HOM couplers will be
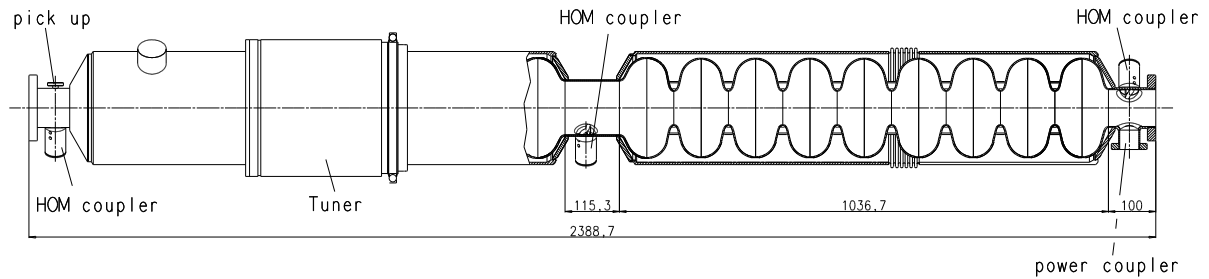
Figure 2.1.23:   *Superstructure II consisting of two 9-cell resonators joined by a 114 mm diameter beam pipe.*

used. The beam test is scheduled for beginning of 2002 and will help verify the energy spread computations and the RF measurements on the copper model. In addition the performance of the HOM couplers, which are exposed to a higher magnetic field due to the enlarged beam tube diameter, can be tested. Another goal is to validate the proposed tuning method when the structure is installed in the linac.

Superstructure II. The combination of two 9-cell resonators (see figure 2.1.23) achieves the same high filling factor[1] of 85 % but is only 2.39 m long. This structure can be chemically treated and handled with an upgraded version of the facilities at TTF. Therefore no new welding and preparation techniques will be needed for the assembly, which means that the excellent performance obtained with the single 9-cell cavities can also be expected from the superstructure. Electropolishing of the 2.39 m long unit should also be possible. The only disadvantage in comparison with superstructure I is the higher number of power couplers, but this has to be balanced against the lower number of tuners and helium vessels. Superstructure II will need about eighteen months of R&D before it can go into series production: as of writing, it is expected to become the preferred solution for the TESLA collider.

2.1.9   Summary of TESLA acceleration system layout

In this section we briefly summarize the layout of the superconducting cavity system for TESLA. Details can be found in the previous sections.

Baseline design. TESLA-500 can be safely realized using the existing 9-cell TTF cavities with a reduced length of the interconnecting beam pipes. In the third series of industrially produced cavities for TTF the required accelerating field of 23.4 MV/m is exceeded by an ample safety margin. Each of the cavities is equipped with its own power coupler. The couplers built for TTF can transmit far higher RF power levels than needed for the TESLA-500 beams. It should be noted that cavities, couplers and other auxiliary systems like helium vessel, frequency tuner and HOM couplers have been thoroughly tested with beam in the TTF linac and are suitable for the TESLA

---

[1]The filling factor defined here does not include additional lengths for magnets and module interconnections.

collider.

Improvement in surface quality by electropolishing. The essential step towards TESLA-800 is a new preparation method: the present chemical etching of the inner cavity surface will be replaced by electropolishing which leads to a much smoother surface. An electropolishing apparatus for 9-cell cavities and 2×9-cell superstructures is under development at DESY. According to numerous tests with 1-cell cavities, improved performance can be expected from the new technique with gradients in the 35–40 MV/m regime.

Superstructure. The active acceleration length in the TESLA machine can be increased by 6 % when two 9-cell cavities are joined by a very short beam pipe to form a superstructure. The nominal gradient for TESLA-500 is thereby reduced to 22 MV/m. Only one power coupler per superstructure is needed, resulting in a factor of two saving in power couplers and other wave guide components. About 18 months of R&D are required to make this option ready for series production.

The TESLA cavity system. The basic acceleration unit for TESLA will most likely be the 2×9-cell superstructure with a surface preparation by electrolytic polishing. According to present knowledge the TESLA-800 operating gradient should be safely achievable. The auxiliary components and systems (e.g. main power and HOM couplers, tuners) developed for TTF are already adequate for TESLA-500 and need only moderate improvement for TESLA-800. The TTF cavity stiffening scheme combined with a piezo-electric tuner will provide sufficient frequency stability at the TESLA-800 gradient of 35 MV/m.

Currently only cavities made from solid niobium offer the potential for achieving gradients of 35 MV/m, and this is the technology of choice for TESLA.

2.2   Integrated System Test

2.2.1   TESLA Test Facility — overview

The major challenge for the TESLA collaboration was to prove the feasibility and reliability of achieving accelerating gradients well above 20 MV/m, i.e. high enough for the 500 GeV linear collider. The TESLA Test Facility linac (TTFL) at DESY was constructed to show that the high gradients achieved in the cavities could be maintained during assembly into a linac test string, and then successfully operated with auxiliary systems to accelerate an electron beam to a few hundred MeV. The basic characteristics of the TTFL were designed to be as consistent as possible with the parameters of the TESLA linear collider design.

The original proposal for the TTF [36] was for a linac test string of four cryogenic modules, each containing eight superconducting nine-cell TESLA structures. The initial design goal was 15 MV/m, which was at that time substantially higher than superconducting cavities operated at other accelerator laboratories. Shortly after finishing the first design of the TTFL, it became clear that the test linac would be almost ideal to drive a Free Electron Laser (FEL) based on the principle of Self Amplified Spontaneous Emission (SASE): therefore the overall layout was changed and the FEL became
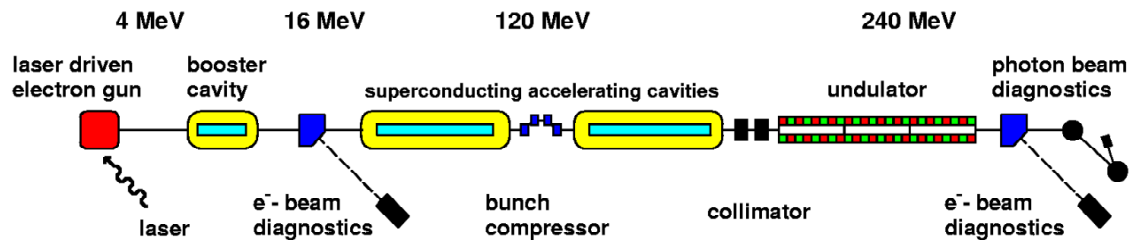
Figure 2.2.1: *Schematic layout of the TESLA Test Facility Linac (TTFL). The total length is ~120 m.*

part of the TTF project [37, 38].

The TTF (linac) programme for the accelerator modules was planned to check many of the aspects of operation in the linear collider:

- gradient achievable in a standard linac module;

- input coupler and higher-order mode (HOM) coupler performance;

- radio frequency (RF) control of multi-cavity systems;

- Lorentz force detuning and microphonic noise effects;

- RF conditioning of cavities and couplers;

- vacuum performance / failure recovery potential;

- cryostat design and cryogenic operation / heat load;

- dark current;

- energy and beam position feedback and control;

- alignment.

The TTF Linac was constructed to gain experience with the new components (cavities, klystrons, diagnostics, etc.) during continuous long term operation. As of writing, the total beam time at the TTFL was about 8,000 h. In addition, important experience with the FEL operation was obtained [39] (see also chapter 9).

2.2.2   Layout of the TTF linac

The TTF linac at DESY has been designed, built, installed and operated by the TESLA collaboration. The schematic of the linac is shown in figure 2.2.1.

The TTFL in its present set-up consists of the following sections:

- injector area;

- two accelerator modules;

- bunch compressor section;

- collimator section;

- undulator; and

- high energy beam analysis area together with the photon beam diagnostics.

The injector area includes the electron gun, the superconducting capture cavity, focusing lenses, and beam diagnostic equipment for the full characterisation of the electron beam properties. The capture cavity is identical to one of the standard nine-cell structures in the main linac. The principal parameters of the injector are listed and discussed in the following sections.

The two installed cryomodules (each 12.2 m in length) comprise the main body of the linac (figure 2.2.2). Each cryomodule contains eight nine-cell cavities, a superconducting quadrupole / steerer package, and a cold cavity type beam position monitor. Each accelerating structure has an input coupler for RF power, a pickup antenna to measure the cavity field amplitude and phase, two HOM damping couplers, and a frequency tuning mechanism. The two cryomodules are connected by a cryogenic line bypassing the bunch compressor.

The bunch compressor section between the two cryomodules is used to reduce the electron bunch length produced in the electron gun by roughly a factor of four. The shortening of the bunch increases the peak bunch current to several hundred amps, which is required for a high gain of the FEL.

A collimator section in front of the undulator protects the vacuum system as well as the permanent magnets of the undulator. Because of the small electron beam diameter in the undulator, a beam loss in this approximately 15 m long section would be a high risk for the linac vacuum system. Radiation from beam losses could also cause a reduction of the magnetisation of the permanent magnet material in the undulator.

The undulator consists of three sections, each 4.5 m in length. The sinusoidal magnetic field has a period of 2.73 cm. Focusing of the beam is accomplished using additional permanent quadrupole magnets. Beam position monitors and wire scanners are installed between each section and in front and behind of the complete undulator. Additional beam position monitors within the undulator sections themselves can be used for improving the needed overlap between the magnetic axis of the undulator, the electron beam, and the emitted photon beam.
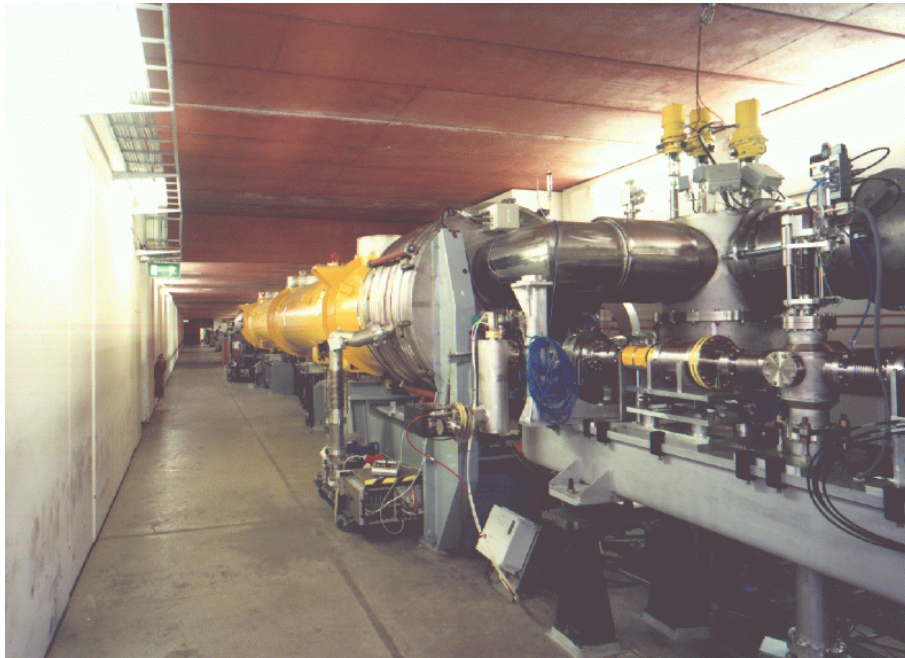
Figure 2.2.2: *View into the TTF Linac tunnel. The electron beam (already accelerated by the capture cavity) comes from the right and is injected into the first accelerator module, which can be seen in the background (yellow vessel).*

The high energy beam analysis area allows the full analysis of the electron beam parameters. Transverse profile, divergence, energy, energy spread, and bunch charge can be measured bunch by bunch. Other measurements (e.g. bunch length) require a scan over several bunches. The photon diagnostic section downstream of the undulator allows the full characterisation (intensity, time structure, and spatial distribution) of the FEL photon beam.

2.2.3   Parameters of the TTF linac

The design parameters for the TTF Linac are summarised in table 2.2.1. The achieved parameters listed summarise the results of the year 2000 run. A description of the various experiments, component development, and achievements is presented in the following sections.

2.2.4   Electron gun

The test of superconducting cavities with the design bunch charge and beam pulse current and length was planned as part of the TTF program. A radio frequency (RF) gun is the state-of-the-art way to generate this electron beam. Furthermore, the X-ray FEL requires bunches of sub-picosecond length at 1 nC charge. At present only laser-driven RF photocathode guns are capable of producing such ultrashort bunches. The

Injector		TTF Linac design/achieved	
		Inj. I	Inj. II
Injector Energy [MeV]		10 / 12	20 / 16
Norm.Emittance [pi mm mrad]			
at 37 pC (only Inj.I)		5 / 3	
at 8 nC (only Inj.II)			20 / 15
at 1 nC (only Inj.II)			2 / 4
Bunch frequency [MHz]		217 / 217	1-9 / 0.1-2.25
Bunch charge [nC]		0.037 / 0.037	1-8 / 0.1-10
Linac	**TESLA**	**TTF Linac designed / achieved**	
Linac Energy [MeV]	250000	255 / 300	
RF frequency [GHz]	1.3	1.3	
Accel.Gradient [MV/m] with beam	23.4	15 / 14, 19, 22	
Unloaded quality factor [10^{10}]	1.0	0.3 / > 1.0	
No. of Cryomodules	2628	4 / 3 + 2	
Energy Spread, single bunch rms	5×10^{-4}	$\approx 10^{-3}/10^{-3}$	
Energy variation, bunch to bunch	5×10^{-4}	$\approx 2 \times 10^{-3}$ / 2×10^{-3}	
Bunch length, rms [μm]	300	1000 / 400	
Beam current [mA]	9.5	8 / 8	
Beam macro pulse length [μs]	950	800 / 800	

Table 2.2.1: *TESLA-500 – TTF Linac parameters comparison.*

small emittance can be preserved by rapidly accelerating the electrons to relativistic energies where the effects of space charge forces become small. For these reasons an RF gun was chosen as the electron source for the TTF linac, although the specified beam macro pulse length of $800\,\mu$s presented a considerable challenge.

Since the development of the RF gun required some time, a thermionic gun was used in the first injector (INJ1) [40] of the TTF linac. The grid of the thermionic gun was modulated with a subharmonic of the main RF frequency, $1300/6 = 217\,$MHz, to produce an $800\,\mu$s long train of electron bunches with a charge of $37\,$pC, a length of $660\,$ps and a spacing of $4.6\,$ns. After electrostatic acceleration to $250\,$keV the electrons were injected into a $217\,$MHz copper cavity where a velocity modulation was imposed on the particles to achieve a longitudinal compression in the following drift space. A superconducting 9-cell cavity, the booster cavity in figure 2.2.1, raised the energy to $12\,$MeV. This electron beam has been used to commission the TTF linac and to check many technical components. In particular it has been possible to operate the super-conducting cavities with full beam loading [41] and to verify the proper functioning of the klystron, the high power RF distribution system and the digital RF control system. Furthermore, first studies of higher-order modes and multibunch effects were made using this injector (see below).

The development of an RF gun was started at FNAL, based on the existing design of operating RF guns at BNL and Los Alamos. Later, an alternative design was

pursued at DESY [43] which tried to optimise the gun with respect to the FEL beam emittance requirements: a coaxial RF input coupler was used, which improved the axial symmetry of the accelerating field and gave more freedom to optimize the pattern of the superimposed magnetic field at the cathode (i.e. the position of focusing solenoids).

The main challenges of the RF gun development were:

- the long macro pulse of $800\,\mu$s length;

- the high gradient of $35\,$MV/m at the cathode surface;

- a long life time of Cs_2Te cathodes with high quantum efficiency;

- experience with a cathode preparation system [44].

In addition, the development of a UV laser with sufficiently high power and a pulse structure suitable to produce the required electron beam time structure [45] presented a considerable challenge.

The FNAL RF gun has been in use at DESY since 1998. The laser, RF supply ($\sim 2.2\,$MW), amplitude and phase controller, water cooling system, and cathode preparation and handling system are all used routinely. At gradients above $30\,$MV/m we routinely have $800\,\mu$s long RF pulses in the gun. The dark current (typically $100\,\mu$A) at the gun exit is low enough to scrape off. The laser produces the required pulse structure, although for FEL operation the pulse length should be shortened. Gun conditioning is, however, problematic and generally time consuming, and additional minor design problems are still under investigation. Details of the results of the operation of the FNAL RF gun are given in [46]. Further R&D on the gun and beam transport to the first accelerating module will be carried out using the DESY RF gun [47].

2.2.5 Booster cavity and low energy beam analysis area

The approximately $4\,$MeV electron beam from the RF gun is injected into the booster cavity which is a standard nine-cell TESLA cavity. This cavity was one of the first prepared for the TTFL. Its field emission onset is about $14\,$MV/m. A feedback system [48] allows the cavity to operate with an amplitude stability better than 0.1%, and a phase stability of better than $1°$. The cavity was operated with full beam loading and with the design beam parameters. The typical beam energy downstream of the capture cavity is $16\,$MeV.

The beam transport system at $16\,$MeV consists of a magnetic dipole chicane, a spectrometer section ending at a beam dump, and the straight matching section to the first accelerator module. The chicane was installed to study bunch shortening at low energies. The challenge facing the injector beam transport is to achieve a low emittance as well as a short bunch length under the presence of large space charge forces. At $1\,$nC the optimized normalized emittance was measured at $4\,$mm mrad, and at 8 nC approximately $15\,$mm mrad [49, 50].

The spectrometer arm is used to tune the injector with respect to energy and energy spread. At $16\,$MeV beam energy the optimized relative energy spread was measured at $0.2\,\%$ (rms).

2.2.6   Accelerator modules

The layout of the TTF linac accelerator modules is very similar to the layout for the TESLA main linac, which is described in detail in section 3.3. The main difference is the length, which is about 12 m for the TTF modules and about 17 m for TESLA. The reason is that the TTF modules accommodate eight 9-cell cavities whereas 12 cavities are foreseen for the TESLA linac modules.

Results of measurements of the static heat load at the various temperature points are listed in table 2.2.2. The somewhat higher value at 2 K with respect to the design heat load is due to the cables for additional diagnostics (e.g. temperature sensors, vibration sensors), which will not be present in the TESLA linac modules.

	static load (design)	static load (meas.)
at 2 K / Watts	2.8	4
at 4.5 K / Watts	13.9	13
at 70 K / Watts	76.8	78

Table 2.2.2: *Summary of TTF heat load for one accelerator module.*

As of writing five accelerator modules have been built since the beginning of the TTF programme. Three of them have been installed in the TTFL; the last two are foreseen for the extension of the linac to higher energies. Cavities operated in the TTFL have shown slightly lower gradients compared to the vertical or horizontal cavity tests (see figure 2.1.11 in section 2.1.5.5); this is because of different field emission onsets, and because the operation of several cavities connected to one single klystron is limited by the worst cavity. The maximum gradients achieved (at quality factors higher or equal to the design value of $Q_0 = 10^{10}$) with the three modules are given in table 2.2.3.

In the linac a total of 16 cavities are driven by one klystron. The cavities have been routinely operated at a gradient of ≈ 15 MV/m providing a 260 MeV beam for different experiments including stable FEL operation. The achieved relative amplitude stability of 2×10^{-3} and absolute phase stability of $0.5°$ complies with the requirements. Residual fluctuations are dominated by a repetitive component which can be further reduced be using an adaptive feedforward, significantly surpassing the design goals (see section 3.4 and [51]).

module No.	module name	RF test ($Q_0 > 10^{10}$)	beam operation
1	1 (ACC1 old)	17.5	14
2	2 (ACC2)	21.2	19
3	3 (ACC1 new)	23.6	22
4	4	25.4	to be tested
5	1*	25.3	to be tested

Table 2.2.3: *Gradients achieved in the TTF Linac accelerator modules.*

One of the major challenges for the RF control of superconducting cavities is the Lorentz force detuning: the electromagnetic field inside the structures deforms the cavity causing it to detune. The frequency change scales with the square of the accelerating gradient and depends on the mechanical stiffness of the cavities. At high gradients the frequency change is comparable with the bandwidth, and the stabilization of the field amplitude requires additional RF power. Recently an active system was successfully tested which compensates the frequency detuning by means of a piezoelectric tuner (see section 2.1).

The transport of very low emittance beams along the TESLA linac requires transverse higher-order mode (HOM) damping: the HOM Q values should not exceed $\sim 10^5$. HOM couplers mounted on the beam tubes of the TESLA nine-cell superconducting cavities are foreseen for this purpose. So-called 'trapped' modes whose energy is concentrated in the central cells of the cavity can only be detected using the accelerated electron beam [52]. In a dedicated experiment using an intensity-modulated beam from injector-I, a high-order 2585 MHz dipole mode was found with a Q factor up to 9×10^5 [53]. The mode could be identified with the highest mode of the third dipole passband. The high Q factor is outside the specifications for the TESLA linac, but is expected to be avoidable by a better control of the cavity's geometry or a slight re-positioning of the HOM coupler (or both).

One of the measurements performed with long beam pulses is shown in figure 2.2.3. An almost 800 μs long macro pulse comprising 1800 bunches with more than 3 nC bunch charge each was accelerated in the TTF Linac. With the macro pulse current being about 8 mA, the bunch charge was stable within $\sim$10%, the achieved energy stability was σ_E/E=0.07%. The above mentioned RF control of the superconducting cavities was used together with a beam loading compensation.

2.2.7   Bunch Compressor

The free-electron laser operation mode of the TTFL requires short electron bunches with high intensity. Therefore a bunch compressor is inserted between the two accelerating modules to increase the peak current of the bunch up to 500 A, corresponding to 0.25 mm bunch length (rms) for a 1 nC bunch with Gaussian density profile. The compression is achieved by making use of the path length difference for particles of different energy in a bending magnet system (chicane). By accelerating the bunches slightly off-crest in the RF wave, particles in the bunch head have a lower energy than in the tail and thus travel a longer distance in the chicane.

It is routinely verified that a large fraction of the bunch charge is compressed to a length below 0.4 mm (rms) [54]. In addition there are indications that the core is compressed even further, giving an estimated peak current of 400 ± 200 A. At these short bunch lengths, coherent synchrotron radiation produced in the magnetic chicane may affect the emittance and the energy spread of the bunch [55].
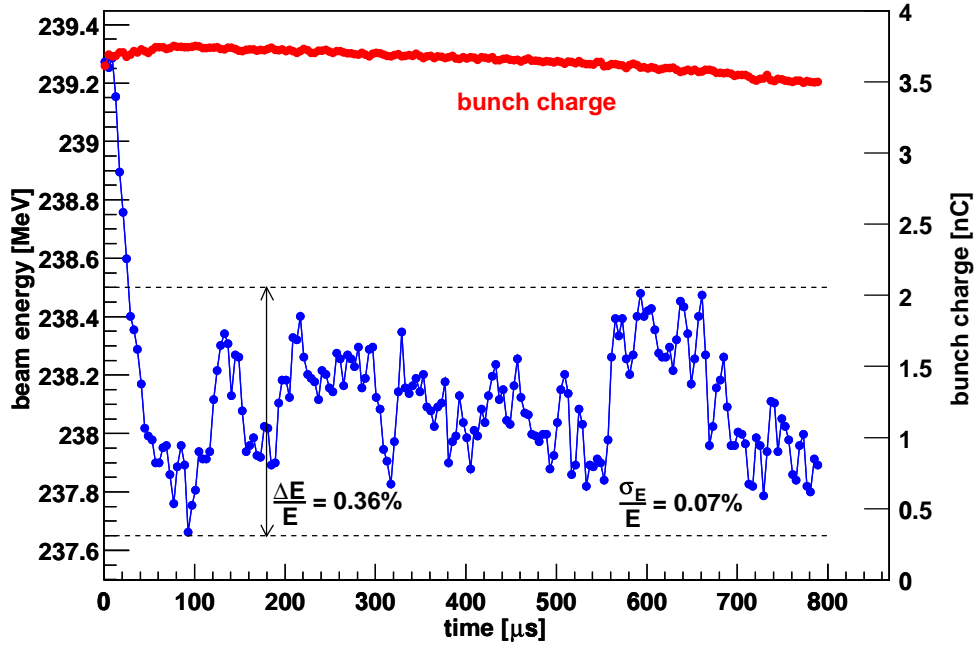
Figure 2.2.3: *Acceleration of long macro pulses. The beam energy and the bunch charge within one single macro pulse are shown. The RF control system was operated with beam loading compensation. The bunch spacing was 444 ns.*

2.2.8   Collimator

The second installed accelerator module of the TTFL is followed by a collimator section which combines the transverse matching of the electron beam to the undulator with the protection of the undulator vacuum chamber and magnets. As a consequence of the small beta function in the undulator — typically $1\,\mathrm{m}$, corresponding to an rms beam sizes of $\sim 100\,\mu\mathrm{m}$ — it only requires 10 bunches with $1\,\mathrm{nC}$ charge to burn a hole into the vacuum chamber. In addition radiation damage of the Sm_2Co_{17} permanent magnets in the undulator from either beam halo (dark current) or direct beam loss could degrade the field quality. The collimator consists of a pair of spoiler / absorber units, and the optics (quadrupole settings) is matched so that the physical apertures of the downstream undulator lie within the collimator shadow.

2.2.9   Undulator

The undulator is a $12\,\mathrm{mm}$ gap permanent magnet device which uses a combined function magnet design [56]. It has a period length of $27.3\,\mathrm{mm}$ and a peak magnetic field of $0.46\,\mathrm{T}$, resulting in an undulator parameter of K = 1.17. The beam pipe diameter in the undulator ($9.5\,\mathrm{mm}$) [57] is much larger than the beam diameter ($300\,\mu\mathrm{m}$). Electron beam focusing is achieved by integrated quadrupoles producing a gradient of $12\,\mathrm{T/m}$ superimposed on the periodic undulator field. The undulator system is subdivided

into three segments, each 4.5 m long and containing 10 quadrupole sections, i.e. 5 full focusing-defocusing (FODO) cells. The FODO lattice periodicity runs smoothly from segment to segment. There is a spacing of 0.3 m between adjacent undulator segments for diagnostics (e.g. wire scanners [58]). The total length of the undulator section is 14.1 m. The vacuum chamber incorporates beam position monitors and orbit correction magnets (one for each quadrupole).

The first observation of SASE in a free-electron laser was at the beginning of year 2000 (see section 9.2 and [39]). The emitted radiation was in the Vacuum Ultraviolet range between 80 nm and 180 nm wavelength. Later in the year, the SASE gain was increased to approximately 10^5. For the radiation intensity measurements different detectors were used [59].

2.2.10 Beam diagnostics

The high energy beam analysis area at the end of the TTFL allows the full analysis of the electron beam parameters. Transverse profile and beam divergence are measured using optical transition radiation (OTR) screens [60] as well as diffraction radiators [61]. Energy and energy spread are measured in the dispersive section again using OTR screens. A system combining the readout of different toroid monitors installed in all sections (from the gun to the beam dump) measures the beam intensity and monitors the transmission along the linac; together with a number of photo-multipliers, it forms part of the interlock system and protects the TTFL against excessive beam losses.

The above measurements can be made on a single bunch: measurement of the bunch length requires averaging over several bunches. A bunch length monitor using interferometry of coherent transition radiation is located downstream of the second accelerator module.

The symbiosis between the accelerator module test and FEL operation has proven useful with respect to the development of new diagnostic techniques. The measurement of wakefields excited by bunches of different length [62] and the test of a beam trajectory monitor for the TTF FEL undulator [63] are two good examples.

Bibliography

[1] Proceedings of the 1st TESLA WORKSHOP, CLNS-90-1029, edited by H. Padamsee, Cornell University, USA, 1990.

[2] C. Reece et al., *Performance Experience with the CEBAF SRF Cavities*, Proc. Particle Accelerator Conference and International Conference on High Energy Accelerators, Dallas 1995, p. 1512.

[3] G. Müller, Proc. 3rd Workshop on RF Superconductivity, ANL-PHY-88-1, Argonne, USA, 1988, edited by K.W. Shepard, p. 331.

[4] A. Boucheffa et al., Proc. 7th Workshop on RF Superconductivity, CEA/Saclay 96 080/1, Gif-sur-Yvette, France, 1995, edited by B. Bonin, p. 659.

[5] H. Padamsee, J. Knobloch and T. Hays, *RF Superconductivity for Accelerators*, John Wiley, New York, 1998.

[6] P. Kneisel, Proceedings of the Workshop on RF Superconductivity, KFK 3019, Karlsruhe, Germany, 1980, p. 27.

[7] Ph. Bernard et al., *Superconducting Niobium Sputter-Coated Copper Cavities at 1500 MHz*, Proc. 3rd EPAC, Berlin 1992, p. 1269.

[8] C. Crawford et al., *High Gradients in Linear Collider Superconducting Accelerator Cavities by High Pulsed Power to Suppress Field Emission*, Particle Accelerators **49** (1995) 1.

[9] M. Liepe, *Pulsed Superconductivity Acceleration*, Proc. 20th International Linac Conference, Monterey 2000, to be published.

[10] K. Saito et al., Proc. 4th Workshop on RF Superconductivity, KEK Report 89-21, p. 635, Tsukuba, Japan, 1989.

[11] L. Ponto and M. Hein, External Report from Bergische Universität Wuppertal, WUB 86-17, Wuppertal, Germany, 1986.

[12] K. Saito et al., Proc. 8th Workshop on RF Superconductivity, Abano Terme, Italy 1997, edited by V. Palmieri and A. Lombardi, published in Particle Accelerators **60** (1998) 193.

[13] E. Kako et al., *Improvement of Cavity Performance in the Saclay/Cornell/DESY's SC Cavities*, Proc. 9th Workshop on RF Superconductivity, Santa Fe, USA, 1999 (to be published).

[14] L. Lilje et al., *Electropolishing and in-situ Baking of 1.3 GHz Niobium Cavities*, Proc. 9th Workshop on RF Superconductivity, Santa Fe, USA, 1999 (to be published).

[15] B. Visentin et al., *Cavity Baking: A Cure for the High Accelerator Field Q_0 Drop*, Proc. 9th Workshop on RF Superconductivity, Santa Fe, USA, 1999 (to be published).

[16] S. Bousson, *Advances in Superconducting RF Cavity Stiffening by Thermal Spraying*, Proc. 9th Workshop on RF Superconductivity, Santa Fe, USA, 1999 (to be published).

[17] M. Liepe, W.D. Moeller, S.N. Simrock, *Dynamic Lorentz Force Compensation with a Fast Piezoelectric Tuner*, DESY TESLA-01-03, 2001.

[18] V. Palmieri, in Proc. 8th Workshop on RF Superconductivity, Abano Terme, Italy, 1997, edited by V. Palmieri and A. Lombardi, p. 553 and LNL-INFN (Rep) 133/98.

[19] V. Palmieri et al., *Spun TESLA-type Cavities: Results from a Worldwide Collaboration*, LNL INFN (REP) 176/2001.

[20] P. Kneisel, V. Palmieri and K. Saito, *Development of Seamless Niobium Cavities for Accelerator Application*, Proc. 9th Workshop on RF Superconductivity, Santa Fe, USA, 1999 (to be published).

[21] W. Singer, I. Gonin, I. Jelezov, H. Kaiser, T. Khabibuline, P. Kneisel, K. Saito, X. Singer, *Hydro Forming of TESLA Cavities at DESY*, Proc. 7th EPAC, Vienna 2000.

[22] C. Benvenuti et al., *High-Q, High Gradient Niobium-Coated Cavities at CERN*, Proc. 9th Workshop on RF Superconductivity, Santa Fe, USA, 1999 (to be published).

[23] P. Bosland, A. Aspart, E. Jacques and M. Ribeaudeau, IEEE Transactions on Applied Superconductivity, ASC'98, Vol. 9, 896 (1999).

[24] M. Champion et al., TESLA Input Coupler Development, Proc. Particle Accelerator Conf., Washington 1993, Vol. II, p. 809.

[25] S. Chel et al., *Power Coupler Development for SC Cavities*, Proc. 5th EPAC, Sitges 1996, p. 2088.

[26] S. Chel et al., *Status of the TESLA Power Coupler Development Programme in France*, Proc. 6th EPAC, Stockholm 1998, p. 1882.

[27] S. Chel et al., *Coaxial Disc Windows for a High Power Superconducting Cavity Input Coupler*, Proc. 18th Particle Accelerator Conf., New York 1999, p. 916.

[28] W. D. Möller, *High Power Coupler for the TESLA Test Facility*, Proc. 9th Workshop on RF Superconductivity, Santa Fe, USA, 1999 (to be published).

[29] M. Ukkola and P. Ylä-Oijala, *Numerical Simulation of Electron Multipacting in TTF III Cold Window with a DC Bias*, Helsinki Institute of Physics, Finland, Technical Report, 2000.

[30] S. Michizono, A. Kinbara et al., *TiN Film Coatings on Alumina Radio Frequency Windows*, J. Vac. Sci. Technol. **A 10** (4) 1992.

[31] J. Tückmantel et al., *Improvements to Power Couplers for the LEP2 Superconducting Cavities*, Proc. Particle Accelerator Conference and International Conference on High Energy Accelerators, Dallas 1995, Vol III, p. 1642.

[32] J. Sekutowicz, M. Ferrario, C. Tang, *Superconducting superstructure for the TESLA collider: A concept*, Phys. Rev. ST Accelerators and Beams 2:062001, 1999.

[33] M. Ferrario, A. Mosnier, L. Serafini, F. Tazzioli, J.M. Tessier, *Multi-Bunch Energy Spread Induced by Beam Loading in a Standing Wave Structure*, Particle Accelerators **52** (1996) 115.

[34] M. Dohlus, H. W. Glock, D. Hecht and U. van Rienen, *Filling and Beam Loading in TESLA Superstructures*, DESY TESLA-98-14, 1999.

[35] N. Baboi, R. Brinkmann, M. Liepe and J. Sekutowicz, *HOM Damping Requirements for the TESLA Superstructures*, Proc. 7th EPAC, Vienna 2000, p. 2016.

[36] *Proposal for a TESLA Test Facility*, DESY TESLA-93-01, 1992.

[37] TESLA Collaboration, ed. D.A. Edwards, *TESLA Test Facility Linac - Design Report*, DESY TESLA-95-01, 1995.

[38] *A VUV Free Electron Laser at the TESLA Test Facility - Conceptual Design Report*, DESY TESLA-FEL-95-03, 1995.

[39] J. Andruszkow et al., *First Observation of Self-Amplified Spontaneous Emission in a Free-Electron Laser at 109 nm Wavelength*, Phys. Rev. Lett. **85** (2000) 3825.

[40] B. Aune, M. Jablonka, J. M. Joly and E. Klein, *A Low Charge per Bunch Injection Line for the TESLA Test Facility*, DESY TESLA-93-04, 1993.

[41] T. Garvey et al., *First Beam Tests of the TTF Injector*, Proc. Particle Accelerator Conference, Vancouver 1997, p.2823.

[42] E. Colby, *Experimental Testing of the TTF RF Photoinjector*, Proc. Particle Accelerator Conference, Vancouver 1997, p.2873.

[43] B. Dwersteg et al., *RF Gun Design for the TESLA VUV Free Electron Laser*, Proc. 18th International FEL Conference, Rome 1996, p.93.

[44] P. Michelato et al., *Cs_2Te Photocathode for the TTF Injector II*, Proc. 5th EPAC, Sitges 1996, p.1510.

[45] S. Schreiber et al., *Running Experience with the Laser System for the RF Gun Based Injector at the TESLA Test Facility Linac*, Nucl.Instr. and Methods **A445** (2000) 427.

[46] S. Schreiber for the TESLA Coll., *First Experiments with the RF Gun Based Injector for the TESLA Test Facility Linac*, Proc. Particle Accelerator Conference, New York 1999, p. 84.

[47] F. Stephan et al., *Photo Injector Test Facility under Construction at DESY Zeuthen*, FEL'2000 Conference, submitted to NIM.

[48] A. Mosnier et al., *RF Control System for the SC Cavity of the TESLA Test Facility Injector*, Proc. Particle Accelerator Conference, Vancouver 1997, p.2311.

[49] Ph. Piot et al., *Transverse Phase Space Studies in TTF Photoinjector During Run 00-01: A Comparison between Simulation and Experiment*, DESY TESLA-FEL-00-04, 2000.

[50] M. Geitz et al., *Phase Space Tomography at the TESLA Test Facility Linac*, Proc. Particle Accelerator Conference, New York 1999, p.2175.

[51] S.N. Simrock et al., *Design of the Digital RF Control System for the TESLA Test Facility*, Proc. 5th EPAC, Sitges 1996, p. 349.

[52] S. Fartoukh, *A New Method to Detect the High Impedance Dipole Modes of TESLA Cavities*, DESY TESLA-98-13, 1998.

[53] S. Fartoukh et al., *Evidence For a Strongly Coupled Dipole Mode with Insufficient Damping in TTF First Accelerating Module*, Proc. Particle Accelerator Conference, New York 1999, p. 922.

[54] M. Geitz et al., *Sub-Picosecond Bunch Length Measurement at the TESLA Test Facility*, Nucl. Instr. and Methods **A445** (2000) 343.

[55] M. Dohlus et al., *Optimal Beam Optics in the TTF-FEL Bunch Compression Section: Minimizing the Emittance Growth*, Proc. Particle Accelerator Conference, New York 1999, p. 1650.

[56] Y.M. Nikitina, J. Pflüger, *Two Novel Undulator Schemes With Quadrupolar Focusing for the VUV-FEL at the TESLA Test Facility*, Nucl. Instr. and Methods **A375** (1996) 325.

[57] U. Hahn et al., *Design and Performance of the Vacuum Chambers for the Undulator of the VUV FEL at the TESLA Test Facility at DESY*, Nucl. Instr. and Methods **A445** (2000) 442.

[58] G. Schmidt et al., *First Results of the High Resolution Wire Scanners for Beam Profile and Absolute Beam Position Measurement at the TTF*, FEL'2000 Conference, submitted to NIM.

[59] Ch. Gerth et al., *Photon Diagnostics for the Study of Electron Beam Properties of a VUV SASE FEL at DESY*, FEL'2000 Conference, submitted to NIM.

[60] M. Castellano et al., *Time Resolved Energy Measurement of the TESLA Test Facility Beam Through the Analysis of Optical Transition Radiation Angular Distribution*, Proc. Particle Accelerator Conference, New York 1999, p. 2196.

[61] M. Castellano et al., *Bunch Length Measurements at TTF Using Coherent Diffraction Radiation*, Proc. 7th EPAC, Vienna 2000, p. 1699.

[62] M. Huening et al., *Experimental Setup to Measure the Wake Fields Excited by a Rough Surface*, Nucl.Instr. and Methods **A445** (2000) 362.

[63] S. Hillert et al., *The Beam trajectory Monitor for the TTF-FEL at DESY*, Proc. 7th EPAC, Vienna 2000, p 1803.

3 Main Linac

3.1 Introduction

In this chapter, we describe the layout and the properties of the main linacs, in which the electron and positron beams are accelerated from 5 to 250 GeV at a gradient of E_{acc}=23.4 MV/m. The electron and positron linacs have a total length of 14.4 km each, including a $\sim$2 % overhead for energy management in case of klystron failures. The 10,296 9-cell cavities per linac are contained in cryomodules (12 cavities per module, see section 3.3), which also house the focusing quadrupoles, steering magnets, and beam position monitors (BPM).

The radio frequency (RF) system (section 3.4) consists of 286 10 MW klystrons per linac (including overhead), which are installed in the tunnel and connected to the pulsed power supplies (modulators) in the external service halls by high voltage cables. The linac is operated at a pulse rate of 5 Hz, except for the first 3 km of the electron linac where the pulse rate is doubled to accelerate both the collider beam and the beam driving the X-ray Free Electron Laser (chapter 9). The flexibility of the RF control system allows independent adjustment of the accelerating gradient for the alternating collider and FEL beam pulses.

The small design emittance requires careful control of the beam dynamics in the linac. This important issue is discussed in the following section.

3.2 Beam Dynamics

To achieve the desired high luminosity, long trains of bunches with small transverse emittances are required. In this section, emittance preservation during acceleration in the main linac is discussed. The primary sources of transverse emittance dilution in a high energy linear accelerator are the transverse wakefields excited in the accelerating sections in the presence of imperfections, and the dispersive errors caused by the focusing magnets. For TESLA, the low RF frequency and corresponding large irises of the accelerating structures result in much smaller wakefield kicks for a given misalignment than in higher frequency room-temperature designs. Furthermore, a given dispersion generates less emittance blow-up, because the beam energy spread is kept small along most of the accelerator. The small wakefields and low energy spread ultimately result in relatively relaxed alignment tolerances for the various components (focusing magnets, beam position monitors, accelerating structures), for which modern optical survey techniques in combination with the standard beam-based alignment

	Collider	FEL
Accelerating gradient E_{acc} [MV/m]	23.4	9.2–23
Injection energy E_i [GeV]	5	2.5
Bunch charge N_e [10^{10}]	2.0	0.63
Bunch spacing Δt_b [ns]	337	93
Bunch length σ_z [μm]	300	25–50
Norm. design emittance ϵ_x, ϵ_y [10^{-6}m]	10, 0.03 (at IP)	1.5 (at undulator)
Norm. emittance at injection ϵ_x, ϵ_y [10^{-6}m]	8, 0.02	0.9
Beam size at injection $\sigma_{x,i}$, $\sigma_{y,i}$ [μm]	320, 16	150
Beam size at linac exit $\sigma_{x,f}$, $\sigma_{y,f}$ [μm]	60, 3	$\approx$35–60
Initial uncorr. energy spread $\sigma_{E,i}/E$ [%]	2.5	0.1
Off-crest RF phase Φ_{RF} [°]	5	0–30
Correlated energy spread δ_{cor} [10^{-4}]	3	10–1
Total spread $\sigma_{E,f}/E$ at linac exit [10^{-4}]	6	10–1.5

Table 3.2.1: *Overview of beam parameters in the main linac.*

procedures are sufficient. Table 3.2.1 lists all important linac parameters relevant to beam dynamics issues for both the HEP and FEL beams.

3.2.1   Beam optics

The beam is kept focused in the linac by means of a FODO lattice, which is characterised by its phase advance and beta functions. The wakefields are sufficiently small that suppression techniques such as Balakin-Novokhatski-Smirnov (BNS) damping [1] are not required, and a relatively large beta function and a weak beta scaling with energy can be used. The wakefield effects are dominant for large beta values (less quadrupoles) whereas the chromatic effects are dominant for small beta values (more quadrupoles). The TESLA lattice represents an optimised solution which balances the two contributions to the transverse emittance growth. The linac is divided into two sections:

- from 5 to 125 GeV, a FODO cell with $\beta_{max} = 127$ m and a cell length of 65 m is used, which is constructed from four accelerator modules;

- from 125 to 250 GeV, a longer cell (96 m) with $\beta_{max} = 167$ m is used, constructed from six modules.

The phase advance per cell is 60° in both cases. There are 365 FODO cells in total, so that the phase advance over the entire linac is about $60 \times 2\pi$. The maximum required quadrupole field at 400 GeV is 47 T/m for a magnetic length of 0.6 m. For orbit correction, every quadrupole contains a vertical correction coil, with an additional horizontal coil for every second (horizontally focusing) quadrupole. The vertical coils are also used to provide the small deflection required to follow the curvature of the earth, for
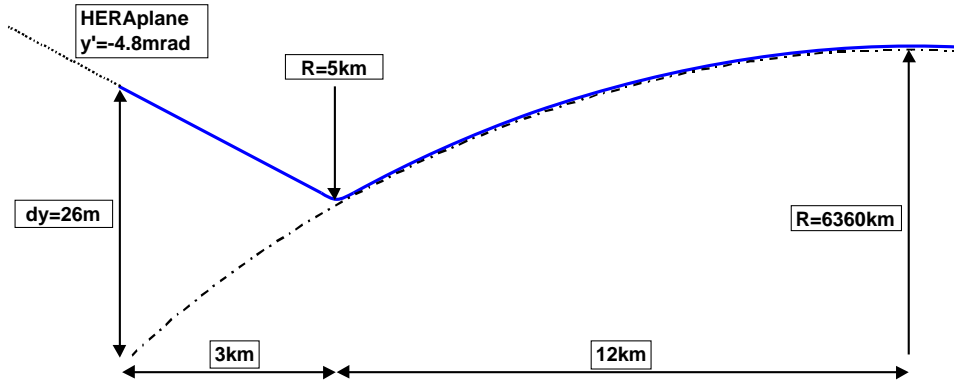
Figure 3.2.1:   *Vertical profile of the beam orbit (blue line) in the electron linac.*

which a maximum integrated field gradient of 0.01 Tm is required (at 400 GeV). The
effect of synchrotron radiation emitted in the steering magnets on the beam emittance
and energy spread is negligible.

In the first 3 km section of the electron linac, the 60°-lattice is also suitable for
the FEL beam over most of its foreseen energy range. At low FEL energy operation
(corresponding to an accelerating gradient of 9.2 MV/m, as compared to 23.4 MV/m
for the High Energy Physics beam), a reduction to 45° per cell *for the high-energy beam*
is necessary to avoid over-focusing of the lower-energy FEL beam, which sees a phase
advance of 118° per cell (see also chapter 9). In addition, simultaneous operation of
two very different energy beams in a linac which follows the curvature of the earth
leads to intolerable systematic dispersive orbit offsets [2]. To avoid the latter effect, we
have chosen to align this section of the linac along an exact straight line (in contrast
to the previous layout [3]). Figure 3.2.1 shows the geometry. The beam line starts in
the plane of the HERA ring, which is tilted with respect to the horizontal plane by an
angle of -8 mrad. The transition to the line following the earth's curvature is provided
by an achromatic bend insertion directly after the high-energy FEL beam extraction
point. The emittance increase due to synchrotron radiation is negligible for the 50 GeV
beam, and is still tolerable for the case of the linac-ring e-p collider option, where a
beam of several hundred GeV would have to pass through this bending section in the
opposite direction.

3.2.2   Single bunch effects

We consider first the short-range wakefield effects: as a bunch travels through the ac-
celerating structures, wakefields are excited which act back on the bunch itself. The
longitudinal wakefields affect the energy of the particles along the bunch, leading to a
so-called correlated energy spread. For a beam which is off-axis in a cavity, the trans-
verse wakefields tend to deflect the tail of the bunch away from the axis, resulting in a
'banana shape' of the bunch and a corresponding increase of the transverse emittance.
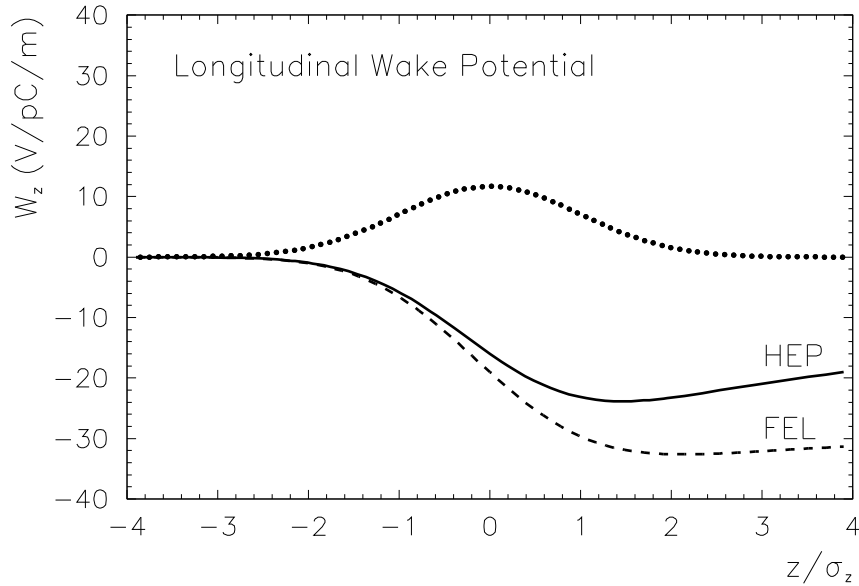
Figure 3.2.2:   *Longitudinal wake potential for $\sigma_z = 300\mu m$ (High energy Physics beam, HEP) and $\sigma_z = 25\mu m$ (Free Electron Laser beam, FEL). The dotted line indicates the charge distribution of the bunch.*

3.2.2.1   Longitudinal single bunch dynamics

The longitudinal wakefields for the TESLA 9-cell cavities and a short bunch length ($\sigma_z < 1\,\mathrm{mm}$) have been carefully calculated. As the bunch travels through the cavities, the wakefield changes, and only reaches a steady state after passing through a number of structures. To correctly determine this steady state wake for the long periodic array of cavities in the linac, the computations were carried out for a chain of up to 16 cavities [5, 6]. From these calculations an analytic approximation for the point charge wake function per unit length of accelerating structure was derived:

$$w(s) = -38.1 \left[\frac{\mathrm{V}}{\mathrm{pC} \cdot \mathrm{m}}\right] \left(1.165 \cdot \exp\left(-\sqrt{\frac{s}{3.65 \cdot 10^{-3}\,\mathrm{m}}}\right) - 0.165\right).$$

The corresponding wake potentials for Gaussian bunches of length $\sigma_z = 300\,\mu m$ (HEP collider beam) and $\sigma_z = 25\,\mu m$ (FEL beam) are shown in figure 3.2.2.

   The correlated energy spread induced by longitudinal wakefields can be minimised by running the bunch at the optimal RF-phase. This method works well for the $500\,\mathrm{GeV}$ collider parameters, but is less efficient for the FEL beam due to the short bunch (see figure 3.2.3 and table 3.2.1). In addition to the correlated energy spread induced by the wakefields and the curvature of the applied RF, there is an initial uncorrelated energy spread present in the injected beam (generated in the bunch compressor), which decreases adiabatically with acceleration. At injection, this energy spread is 2.5% and 0.1% for the collider and FEL beams respectively, and must be included in the
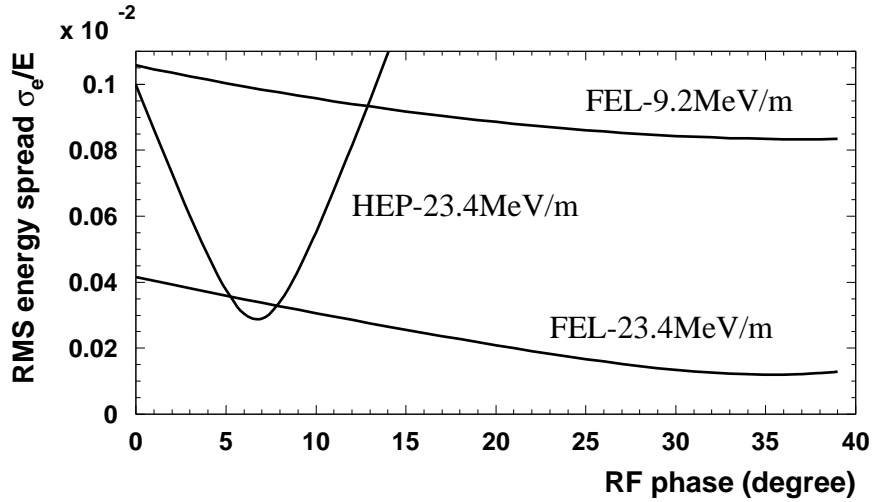
Figure 3.2.3:   *Correlated rms energy spread as a function RF-phase for the High Energy Physics (HEP) (E_{acc}=23 MV/m) and Free Electron Laser (FEL) (E_{acc} =9.5–23 MV/m) beams.*

calculations of chromatic emittance growth.

3.2.2.2   Transverse single bunch dynamics

For beam dynamics studies in the transverse plane, we need the transverse wake excited by a point-like charge (Green's function), while cavity codes only give the transverse bunch wake of a displaced bunch. The transverse impulse factor $k_\perp$ (a quantity proportional to the total transverse momentum given to the bunch by its own wake) has been computed for different bunch lengths [4, 3]. A fit of $k_\perp$ suggests a $\sigma_z^{1/2}$ dependence. The corresponding required delta wake per unit length is deduced from the fit of the transverse impulse factor:

$$W_\perp(s) = 1290 \sqrt{s/\mathrm{m}} - 2600 \, s/\mathrm{m} \qquad (\mathrm{V/pC/m^2})$$

where s is the position *behind* ($s > 0$) the exciting point-like charge. When a bunch is injected off-axis, it performs a betatron oscillation about the central orbit. The tail particles of the bunch are then resonantly driven by the wakefield excited by the head particles. As a result, the amplitude of the oscillation grows rapidly as the beam travels down the linac. This effect leads to a tolerance on the allowed amplitude of the betatron oscillation. For the high-frequency machines, the wakefields are strong and the corresponding amplitude tolerance very tight, and BNS damping must be used to reduce the resonant effect. BNS damping works by making the head more energetic than the tail of the bunch, and the transverse wake effect is then partially compensated by the chromatic phase advance of the trailing particles. The disadvantage of BNS is the relatively large correlated energy spread that is required, which results in a
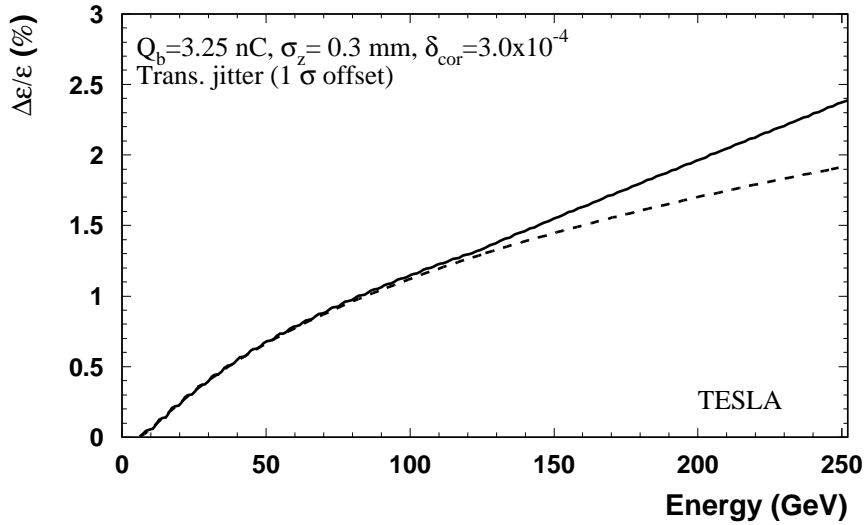
Figure 3.2.4:   *Vertical emittance growth from transverse wakefields with a beam offset equal to the rms vertical beam size. Full line: focusing lattice with β-step at half of linac length, dashed line: constant-β lattice.*

larger dispersive emittance dilution due to quadrupole misalignments. Fortunately, BNS damping is not required for TESLA due to the weak wakefields, and the energy spread can then be kept at its minimum value along the entire linac. Figure 3.2.4 shows the development of the emittance growth along the linac for the linac lattice as described above, with an initial beam offset equal to a one rms beam size and no BNS damping. We note that even without BNS damping, the final emittance growth from the transverse wakefield is less than 2.5%. When the initial uncorrelated bunch energy spread is taken into account, an additional emittance dilution occurs due to chromatic filamentation. Performing the calculation again for one σ_y injection error yields $\Delta\epsilon_y/\epsilon_y=6\%$. For the FEL beam, the emittance growth is below 1%.

Next, we study the emittance growth caused by the transverse wakefields of randomly misaligned cavities. The average emittance dilution for the collider beam, calculated from 50 different random seeds of cavity misalignments with $\delta y_c=0.5\,\mathrm{mm}$ (rms), is $\Delta\epsilon_y/\epsilon_y=7\%$ (see figure 3.2.5). The effect is negligible for the FEL beam. A further reduction of emittance growth is possible by using a non-dispersive orbit bump method: with only two closed bumps at different positions in the linac we obtain a residual emittance dilution at the end of the linac of $\Delta\epsilon_y/\epsilon_y \approx 1\%$. While it may be questionable whether the emittance can be measured with an accuracy of less than 1%, the bump method can still be useful for an empirical optimisation of the collider luminosity.

In order to avoid a continually growing trajectory in the presence of quadrupole alignment errors, the beam must be steered all along the linac. The simplest trajectory correction is the so-called 'one-to-one' method, where the dipole correctors steer the
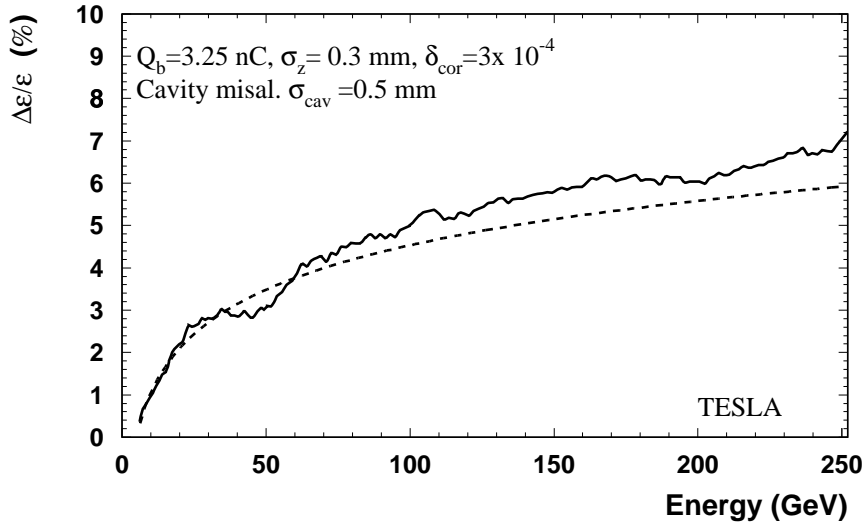
Figure 3.2.5:   *Vertical emittance growth obtained from computer simulation of 50 random seeds of cavity misalignments (δy_c=0.5 mm rms). The dashed curve is the analytical prediction from a two-particle model.*

beam to the magnetic centres of the quadrupoles using BPM measurements. Since the actual orbit will then follow the BPM misalignments, dispersive errors will arise. The realistic alignment errors after installation and survey of the linac modules are 0.3 mm (rms) for the quadrupoles and 0.1 mm (rms) for the BPMs with respect to the quadrupole centres. From simulations of the current lattice, the mean emittance growth due to the above random alignment errors — and after one-to-one steering — is one order of magnitude larger than the vertical design emittance. While this is acceptable for the initial commissioning of the machine, more elaborate correction algorithms are required for high luminosity operation:

- initial beam-based alignment techniques; and

- dispersion-free (DF) steering.

Beam-based alignment differs from the more standard optical alignment (survey) techniques in that the misalignments are deduced from BPM measurements with different beam trajectories. Beam-based alignment and correction has been developed and applied at the Stanford Linear Collider (SLC), the Final Focus Test Beam (FFTB), and several electron storage rings (for example see [7, 8, 9, 10, 11]), and can be considered a well established technique. The basic idea behind all the methods is to effectively replace the absolute error of an orbit measurement by the *relative* error of the BPM (i.e. its resolution), which is much smaller than the absolute BPM misalignment. For example, in the 'shunt' technique the strength of a single quadrupole is changed and the variation of the orbit downstream is measured. If the beam is steered through the magnetic centre of the quadrupole, the difference orbit becomes zero. The BPM next

to the quadrupole then shows its relative offset with respect to the quadrupole centre, with a precision equal to the BPM resolution. In contrast to this local method, the dispersion free (DF) steering algorithm [12] uses the variation of the strength of all quadrupoles simultaneously in the entire linac or a sub-section of it. The applied correction algorithm aims at minimising the measured difference orbit and thus effectively eliminates the absolute BPM offsets. We have investigated both the shunt method and the DF algorithm and found that a BPM [13] resolution of $10\,\mu$m (rms) is sufficient to limit the dispersive emittance growth in the linac to a few %. The results of computer simulations for the DF method are shown in figure 3.2.6. The dispersive emittance growth obtained by averaging over 50 random seeds of misalignments amounts to 1% for an iterative procedure, in which the DF-algorithm is applied to sections of 20 FODO cells per step (see [14] for details). The residual orbit deviations after DF-correction yield an additional emittance growth from the transverse wakefield of 2% (figure 3.2.6).

In addition to a transverse alignment error, the cavity can be tilted longitudinally. The accelerating field then gives an additional transverse kick to the beam, with a strength which depends on the longitudinal position in the bunch. The tolerance on the cavity angle error has been estimated from numerical simulations at $0.5\,$mrad.

3.2.3   Multi-bunch effects

The TESLA beam pulse is composed of many bunches. Each bunch feels the accumulated effects of the long-range wakefields of all the preceding bunches. As a result, the amplitude of oscillation of the bunches increases rapidly as the bunch train travels down the linac. This phenomenon, called multi-bunch beam breakup (BBU), sets the tolerance on the cavity alignment with respect to the beam axis. In addition the bunch-to-bunch energy deviation will introduce a multi-bunch emittance growth, analogous to the single bunch dispersive dilution already mentioned.

3.2.3.1   Longitudinal multi-bunch dynamics

The inter-bunch energy spread should be smaller than the single-bunch energy spread in order to avoid strong additional chromatic effects. The multi-bunch energy spread is mainly produced by the transient beam loading in the accelerating structures. Fortunately, the high beam loading will be compensated in the standing-wave TESLA cavities by matching the power extracted by the beam to the RF power supplied by the klystron. A residual energy gain variation along the beam pulse is mainly caused by Lorentz force detuning and microphonics in the cavities, and RF mismatches; these will be suppressed by a feedback system down to $5\cdot10^{-4}$. The dispersive orbit variation over the bunch train is then of the order of a few tenths of the vertical beam size (rms). This does not present a problem in the linac and, since the energy variation takes place on a time scale much longer than the bunch spacing, it will be removed by the fast orbit correction feedback in the beam delivery system (chapter 7).

Because of the natural frequency spread of the longitudinal higher-order modes
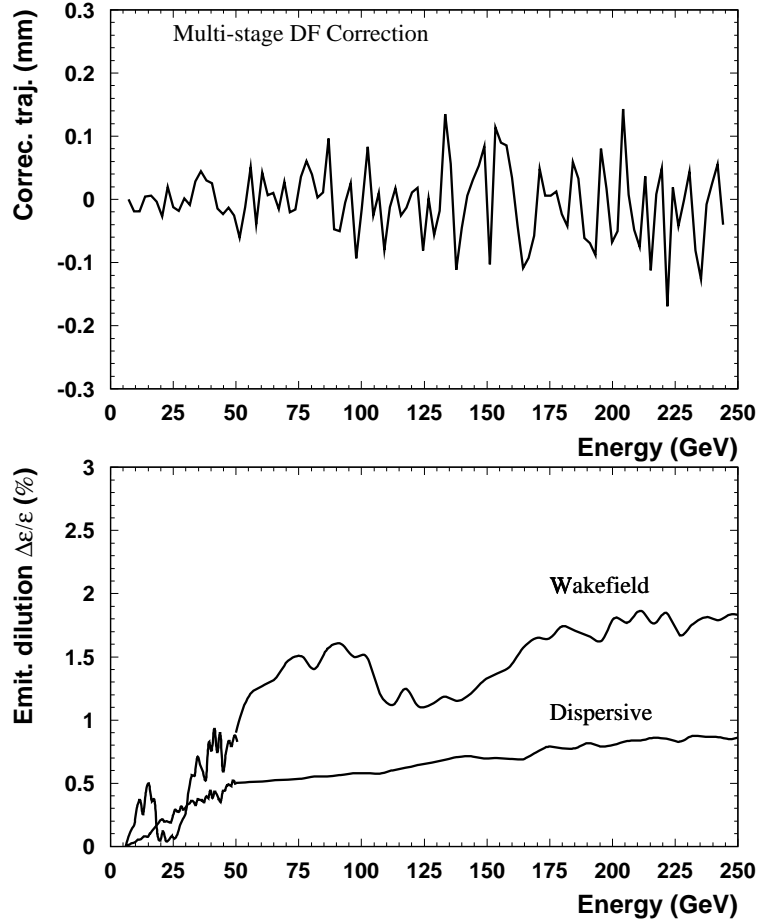
Figure 3.2.6:   *Beam orbit (upper figure) and emittance growth (lower figure) after multi-stage dispersion free correction.*

(HOM), the resulting energy kicks given to the bunches of the train cancel out, and the total effect is therefore negligible.

3.2.3.2   Transverse multi-bunch dynamics

With a train of bunches, the long-range wakefields excited by each bunch will act on the subsequent bunches. The major effect comes from the multi-bunch beam break-up (or cumulative BBU) instability. Two methods are used to suppress the effects of cumulative BBU: cavity detuning and damping. The required random detuning of the transverse HOMs is naturally provided by cavity fabrication errors. As long as the bunch displacements are small, the effective wake is the average of the individual modes over many structures. For a Gaussian distribution of errors (HOM frequencies) and an infinite number of cavities, the effective wake would be reduced by the factor

$$\exp\left[-1/2(\sigma_\omega \tau)^2\right],$$

Frequency (ave. meas.) [GHz]	Loss factor (simulation) [V/pC/m^2]	R/Q (simulation) [Ω/cm^2]	Q (meas.)
TE$_{111}$-like			
1.6506	19.98	0.76	$7.0 \cdot 10^4$
1.6991	301.86	11.21	$5.0 \cdot 10^4$
1.7252	423.41	15.51	$2.0 \cdot 10^4$
1.7545	59.86	2.16	$2.0 \cdot 10^4$
1.7831	49.20	1.75	$7.5 \cdot 10^3$
TM$_{110}$-like			
1.7949	21.70	0.77	$1.0 \cdot 10^4$
1.8342	13.28	0.46	$5.0 \cdot 10^4$
1.8509	11.26	0.39	$2.5 \cdot 10^4$
1.8643	191.56	6.54	$5.0 \cdot 10^4$
1.8731	255.71	8.69	$7.0 \cdot 10^4$
1.8795	50.80	1.72	$1.0 \cdot 10^5$
TE-like			
2.5630	42.41	1.05	$1.0 \cdot 10^5$
2.5704	20.05	0.50	$1.0 \cdot 10^5$
2.5751	961.28	23.80	$5.0 \cdot 10^4$

Table 3.2.2: *Dipole modes with highest loss factors of the 9-cell cavities as used for the multi-bunch beam dynamics simulations. The average frequencies and the Q values are taken from measurements at the first 3 TTF modules. The loss factors were obtained from MAFIA simulations.*

where σ_ω is the rms angular frequency spread and τ the elapsed time. In reality, the averaging is performed over a finite number of sections and the wake envelope does not vanish completely, but re-coheres at a later time: therefore, in order to reduce the effective wake for the rest of the long TESLA bunch train, a small damping is required. The lower the quality factor Q, the less will the excited field persist over the bunch train. The quality factors of the modes are reduced by means of HOM dampers, which are mounted at both ends of a TESLA cavity. The parameters of the dipole modes used for the multi-bunch calculations (frequency, geometric impedance and Q) are given in table 3.2.2. The assumed damping, with Q values of around or below 10^5 for the highest R/Q modes, are in agreement with measurements made at the TTF. For a few of the cavities installed in the TTF linac, one dipole mode (at 2.58 GHz) has shown a Q value higher than assumed [15]: however, it is expected that by a better control of the mechanical tolerances of the cavities or a re-arrangement of the HOM-couplers (or both), this can be cured. We shall also see below that most of the BBU effect can be removed by the fast intra-train orbit correction system, so that it remains uncritical even in the case of a higher Q.
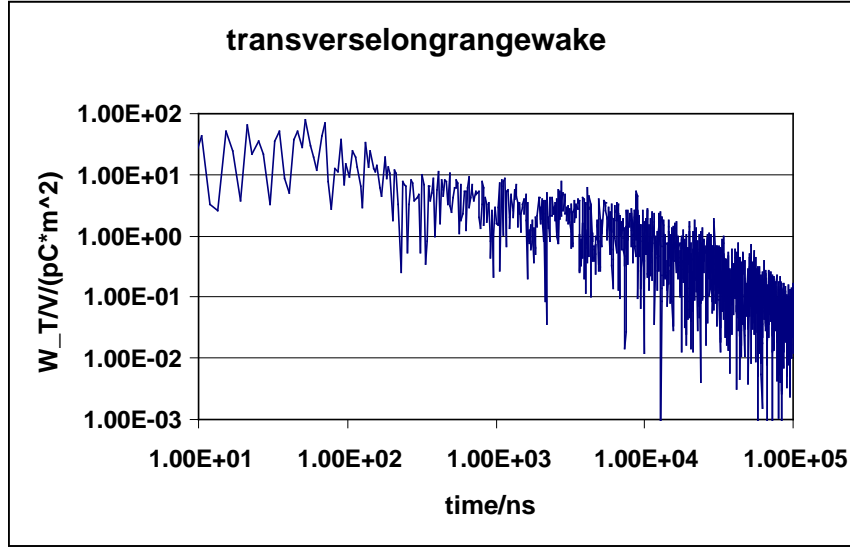
Figure 3.2.7: *Transverse long-range wake, calculated with the HOMs listed in table 3.2.2, and averaged over 36 cavities with a frequency spread of 0.1%.*

The effective dipole wake after detuning and damping is plotted in figure 3.2.7. After one bunch spacing (337 ns) the wake has decreased by an order of magnitude, and after about 100 μs the HOM damping becomes effective. The multi-bunch emittance growth for the whole train has been obtained from computer simulations, and is shown in figure 3.2.8 (averaged over 10 different random seeds of cavity misalignment, with δy_c =0.5 mm rms, no quadrupole misalignments). The mean value of the relative multi-bunch emittance growth is only 3%. The corresponding rms bunch orbit offsets are about two tenths of the beam size, sufficiently small to avoid an additional contribution to the single bunch emittance growth.

One of the advantages of the long TESLA pulse is that even with weak damping, a 'steady state' of HOM excitation is reached after a small fraction ($\sim$10%) of the bunch train. This can be seen in figure 3.2.9, where the individual orbit offsets of the bunches at the end of the linac are shown. Since only the fluctuation of the bunch offsets (and angles) around the average orbit matters for the emittance dilution, the rapid transition to a steady state helps to limit the BBU-driven emittance dilution to a tolerable value. We should point out that even a less favourable situation (e.g. when some of the HOMs have higher Q-values than expected, or the machine is operated with shorter pulses) does not present a serious problem regarding the multi-bunch dynamics, since the pattern of bunch offsets is essentially static, i.e. reproducible from pulse to pulse. It can therefore be removed by the fast orbit correction system after the linac, operating in a feed-forward mode. We have investigated with computer simulations the stability of the bunch orbit offsets with respect to the average orbit under the influence of ground motion, injection errors and bunch-to-bunch charge fluctuation [17]. One
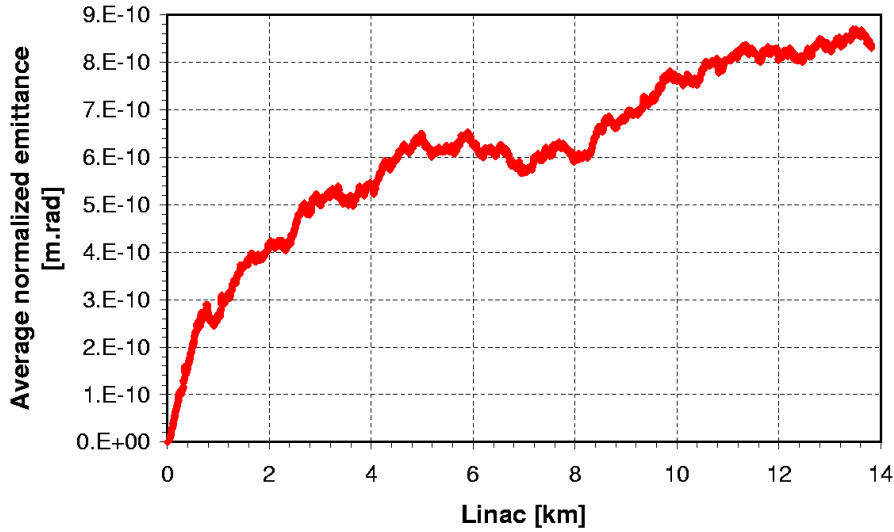
Figure 3.2.8:   *Multi-bunch emittance growth along the linac, averaged over 10 random seeds of cavity misalignments ($\delta y_c = 500$ μm).*

such simulation result is shown in figure 3.2.9 for the example of a one σ_y injection error. The entire bunch train at the end of the linac is shifted because of the coherent betatron oscillation, but the pattern of orbit offsets due to HOMs remains almost unchanged: after subtracting the average orbit difference, the change in the individual bunch offsets is less than $10^{-2}\sigma_y$ rms from all of the above mentioned effects.

3.2.3.3   Orbit stability

Ground motion is of major concern because it will over time displace the quadrupoles, which in turn will dilute the beam emittance in the linac through dispersive effects. Numerous power spectra of ground motion have been measured at different sites. At low frequency, the motion can be quite large and is usually described by the 'ATL' rule, which states that the relative rms displacement Δy of two points separated by a distance L and after a time T (A is a constant which depends on the geology of the considered site) is given by

$$\Delta y^2 = A \cdot T \cdot L.$$

Slow orbit correction (feedback) can be used up to a frequency of some small fraction of the repetition rate (=5 Hz). At higher frequencies, the ground motion (vibration) amplitude falls off rapidly, but occurs too fast to use beam orbit feedback with simple steering magnets.

We have derived realistic estimates of orbit stability in the TESLA linac from ground and orbit motion measurements in the HERA storage ring (see for example [18, 19]). From these data, we can characterise the high frequency regime by an uncorrelated quadrupole vibration with an rms amplitude of $\Delta y_Q = 50$–100 nm. This causes an orbit
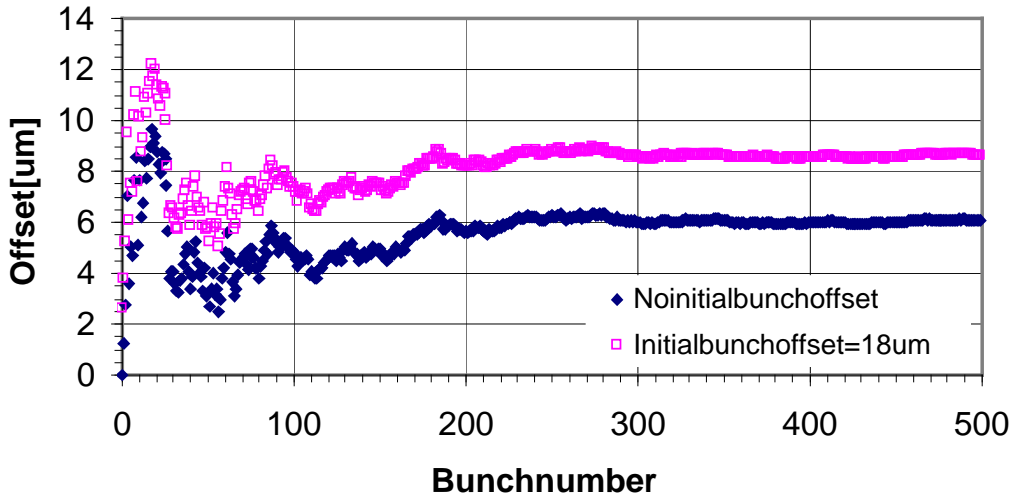
Figure 3.2.9: *Orbit offsets in µm of the first 500 bunches at the end of the linac. The lower curve shows the effects of cavity misalignments only ($\Delta y_c = 0.5\,mm\ rms$, one seed). The upper curve shows the effects of the same misalignments, but with an additional one σ_y injection error of the beam (coherent betatron oscillation).*

jitter Δy_{rms} at the end of the linac of

$$\Delta y_{rms} \approx 0.03\mu\mathrm{m} \cdot \frac{\Delta y_Q}{\mathrm{nm}}, \tag{3.2.1}$$

corresponding to 0.5–1 times the beam size $\sigma_{y,f}$. This jitter does not present a problem for the beam dynamics in the linac itself, but it has to be corrected by the fast intra-train orbit feedback system in the beam delivery system in order to keep the beams in collision with the required accuracy (see chapter 7). On a longer time scale, slow diffusive ground motion (ATL) becomes the dominant effect. From the HERA data we obtain $A \approx 4 \cdot 10^{-6}\ \mu\mathrm{m}^2/\mathrm{s/m}$. The calculated orbit drift at the end of the linac is then

$$\Delta y_{rms} \approx \sigma_{y,f} \cdot \sqrt{t/30\mathrm{s}}.$$

This drift is sufficiently slow to be able to use steering magnets for maintaining the beam on the 'golden' orbit, previously established by beam-based alignment and DF steering. After a longer time, when the position drift of the quadrupoles (and BPMs) becomes comparable to the BPM resolution, additional dispersive emittance growth is generated and the beam-based alignment has to be repeated. With the above assumption on diffusive ground motion, the dispersion free steering algorithm has to be applied on average about once per month.

3.2.4   Concluding remarks

The beam dynamics studies in the main linac have shown that with realistic assumptions on the alignment accuracy and orbit diagnostics precision, the small vertical beam emittance can be preserved. We expect a total emittance growth with respect to the design value at the IP of about 10%, which is well within the emittance growth budget of a factor of 1.5 between the damping ring and the IP. However, one has to be careful with the interpretation of the emittance dilution obtained here. The single bunch transverse wakefield kicks and dispersive effects from the longitudinal wakefield have not 'filamented' at the end of the linac, i.e. there remains a longitudinal-transverse correlation ('banana effect'). In the regime of high disruption parameter, the beam-beam interaction tends to amplify such correlated distortions in the bunches and the resulting luminosity reduction can be larger than naively estimated by using the *projected* emittance to determine the effective beam size at the IP. This question is in more detail discussed in chapter 7.

3.3   Accelerator Modules (Cryomodules)

The design of the so-called cryomodules has been primarily driven by the need to reduce costs compared to existing superconducting cavity systems. The module described here is based on the $3^{\rm rd}$ cryomodule generation of the TESLA Test Facility [20, 21]. Except for the length (≈ 17 m compared to 12 m for a TTF module), only minor modifications to the design have been made.

   Present day superconducting cavity systems tend to have many separate cryogenic supply boxes and associated warm-to-cold transitions, which represent a significant fraction of the cost. The concept adopted here is to significantly reduce this number by having a single long continuous string of about 2.5 km — called a cryogenic unit — which is connected to one cryogenic supply box at the beginning and one end box. Long modules will be built consisting of twelve 9-cell cavities, a quadrupole, steering coils and a beam position monitor (BPM); the helium distribution system needed to operate the superconducting cavities and magnets at 2 K is also integrated into the module. The modules are then connected together to form a cryogenic unit.

3.3.1   The Cryostat

Figure 3.3.1 shows a longitudinal view of a cryomodule. The 300 mm diameter helium gas return pipe (GRP) is the main support structure for the string of cavities and magnets. The GRP is supported from above by three posts which provide the necessary thermal insulation to room temperature. The posts are fastened to large flanges on the upper part of the vacuum vessel by adjustable suspension brackets, allowing the axis of the cavities and quadrupoles to be correctly aligned, independent of the flange position.

   The support system is designed to allow the GRP to contract/expand longitudinally with respect to the vacuum vessel during thermal cycling. The centre post is fixed to
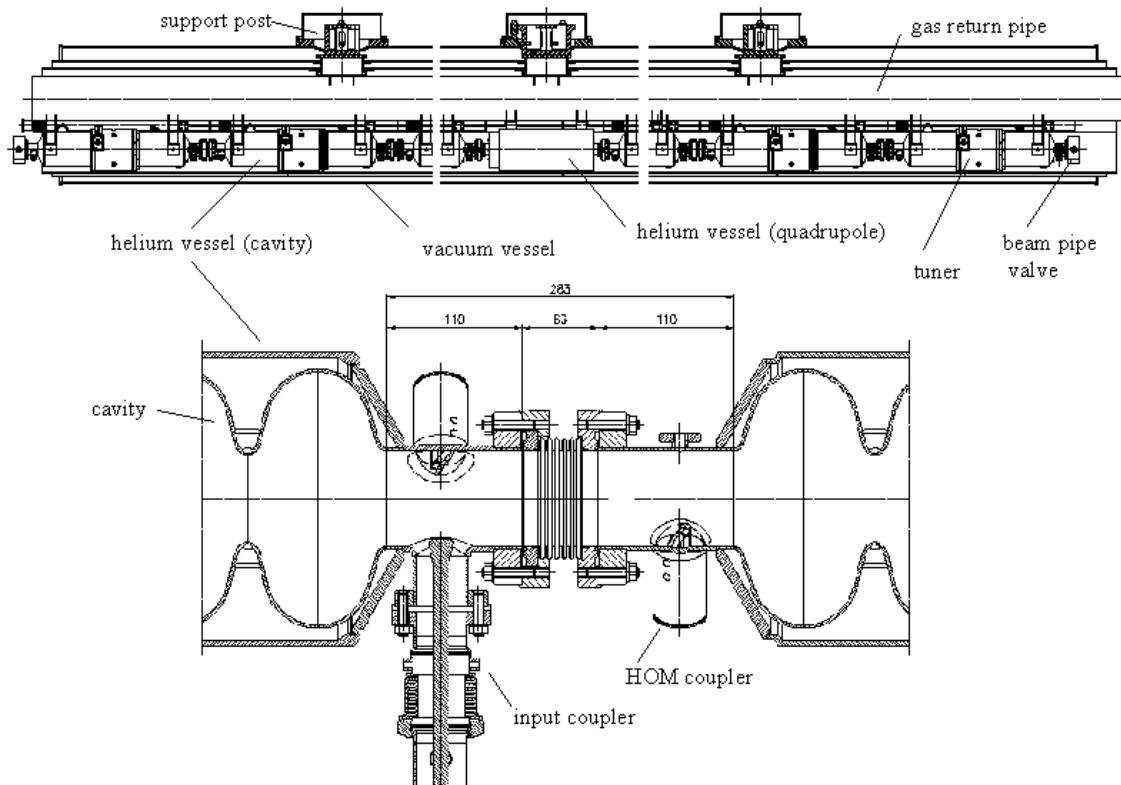
Figure 3.3.1: *Longitudinal view of a cryomodule.*

the vacuum vessel, while the two end brackets can move in the axial (z) direction to accommodate differential shrinkage. A post consists of a fiberglass pipe terminated by two shrink-fit stainless steel flanges. Two additional shrink-fit aluminum flanges are provided to allow intermediate heat flow intercept connections to the 5–8 K and 40–80 K thermal shields; the exact location of these flanges has been optimised to minimise the heat leakage. In addition, the post diameter has been optimised to prevent possible excitation of mechanical eigenfrequencies.

Each of the 12 cavities is encased in a titanium helium vessel, attached to the GRP by means of stainless steel brackets connected to four titanium pads on the vessel itself; each bracket is equipped with a longitudinal sliding mechanism and adjusting screws and pushers for alignment. A mechanical and a piezo-electric tuner are mounted to the vessel [22]. The inter-cavity spacing — which accommodates RF- and HOM-couplers and a flanged bellows — amounts to 283 mm.

Manually operated valves required by the clean-room assembly terminate the beam pipe at both module ends. The valves are fitted with simple RF shields [23].

During cool down the two ends of the $\sim$17 m long gas return pipe move by up to 26 mm toward the centre of the module. To keep the cold input coupler head of each cavity fixed longitudinally within an accuracy of 1 mm, each cavity is anchored to a long invar rod attached to the longitudinal centre of the gas return pipe.

The beam pipe interconnection between the cryomodules consists of a 0.38 m long section that incorporates a Higher Order Mode (HOM) absorber, a bellows, and a vacuum pumping port; the latter will be connected to a flange in the vacuum vessel every ninth cryomodule.

The cryostat includes two aluminum radiation shields operating in the temperature range of 5–8 K and 40–80 K respectively. Each shield is constructed from a stiff upper part (divided into two halves), and 12 (or 13) lower sections (according to the number of the cold active components, e.g. cavities, magnets). The upper parts are supported by the intermediate flanges on the fiberglass posts; they are screwed to the centre post but can axially slide on the other two posts, to which they are still thermally connected. The new 'finger welding' technique — successfully demonstrated at TTF — is used both to connect each thermal shield to its properly shaped aluminum cooling pipe, and the lower shield parts to the upper ones.

Blankets of multi-layer insulation (MLI) are placed on the outside of the 5–8 K and the 40–80 K shields. The 5–8 K shield blanket is made of 10 layers while the 40–80 K blanket contains 30 layers. In addition the cavity and quadrupole helium vessels, gas return pipe and 5–8 K pipes are wrapped with 5 layers of MLI to reduce heat transfer in the event of a vacuum failure.

Figure 3.3.2 shows a cross section of the cryomodule. The cryostat outer vacuum vessel is constructed from carbon steel and has a standard diameter of 38″. Adjacent vacuum vessels are connected to each other by means of a cylindrical sleeve with a bellows, which is welded to the vessels during installation. Radiation shield bridges are also provided. In the event of accidental spills of liquid helium from the cavity vessels, a relief valve on the sleeve together with venting holes on the shields prevent excessive pressure build-up in the vacuum vessel. Wires and cables of each module are extracted from the module using metallic sealed flanges with vacuum tight connectors. The insulating vacuum system will be pumped during normal operation by permanent pump stations located every 250 m. Additional pumping ports are located every 50 m for movable pump stations, which are used for initial pump down, and in the case of a helium leak. The RF power coupler needs an additional vacuum system on its room temperature side; this is provided by a common pump line for all 12 couplers per module, equipped with an ion getter and a titanium sublimation pump.

The following helium lines are integrated into the cryomodules:

- The 2 K forward line transfers pressurised single phase helium through the cryomodule to the end of the cryogenic unit.

- The 2 K two phase supply line (made from titanium) is connected to the cavity and magnet helium vessels. It supplies the cavities and the magnet package with liquid helium and returns cold gas to the 300 mm GRP at each module interconnection.

- The 2 K GRP returns the cold gas pumped off the saturated He II baths to the refrigeration plant. It is also a key structural component of the cryomodule (see above text and section 3.3.3).
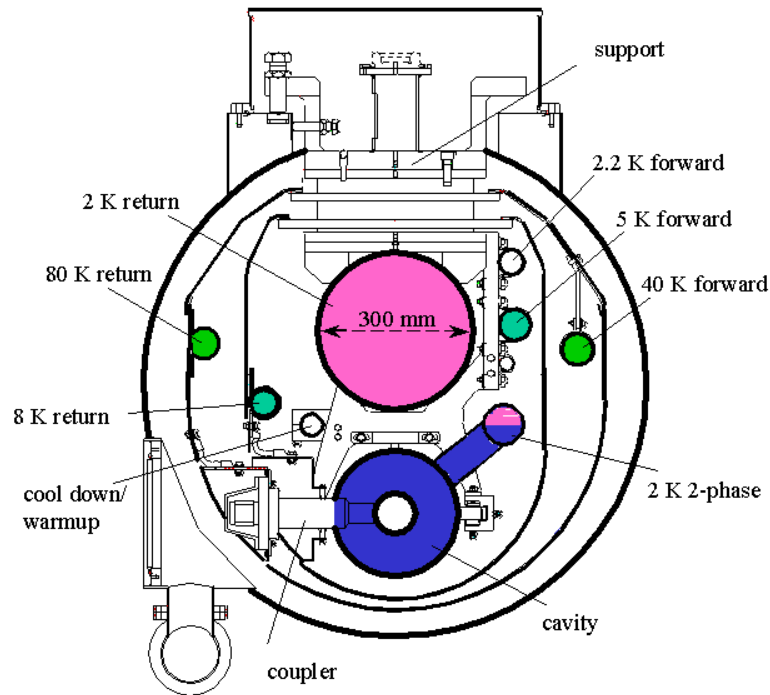
Figure 3.3.2:   *Cross section of cryomodule.*

- The 5–8 K forward and return lines. The 5 K forward line is used to transfer the He gas to the end of the cryogenic unit. The 5–8 K return line directly cools the 5–8 K radiation shield and, through the shield, provides the heat flow intercept for the main coupler and diagnostic cables, and the higher-order mode (HOM) absorber located in the module interconnection region.

- The 40–80 K forward and return lines. The 40 K forward line is used to transfer He gas to the cryogenic unit end and cools the high temperature superconductor (HTS) current leads for the quadrupole and correction magnets. The 40–80 K return line directly cools the 40–80 K radiation shield and the HOM absorber and, through the shield, provides an additional heat flow intercept for the main coupler and diagnostic cables.

- The warm-up/cool-down line connects to the bottom of each cavity and magnet helium vessel. It is used during the cool down and warm up of the cryostat.

The helium lines connected to the cavities and the magnets withstand a pressure of 4 bar; all other cryogenic lines withstand a pressure of 20 bar. The helium lines of

adjacent modules are connected by welding, as was done for the HERA superconducting magnets. Transition joints (similar to those used in the HERA magnets) are used for the aluminum to stainless steel transition on the thermal shield cooling lines.

The cryostat maintains the cavities and magnets at their operating temperature of 2 K. A low static heat load is an essential feature of the cryostat design; the total heat load is dominated by the RF losses, and is thus principally determined by cavity performance. Table 3.3.1 shows the calculated heat load for a cryomodule with cavities operating at the nominal accelerating gradient of 23.4 MV/m (21.1 MV/m is assumed as the maximum gradient for the FEL operation).

The short bunches in TESLA excite wake fields in a very wide frequency range which will be absorbed in the structure walls and therefore contribute to the cryogenic losses. Table 3.3.2 shows the single bunch losses calculated from the monopole short range wake [5, 6]. The effect of losses in a frequency range beyond the threshold for Cooper pair breakup (about 750 GHz) in superconducting niobium has been investigated in [24]: in a quasi-periodic string of 9-cell cavities the temperature rise of the inner cavity surface and the resulting Q_0 drop are negligible.

Most losses occur at lower frequencies where the conductivity of the superconducting surfaces is several orders higher than that of normal conducting walls. Part of this power is extracted by input- and HOM-couplers, but high frequency fields will propagate along the structure and be reflected at normal and superconducting surfaces [25]. In order to reduce the losses at normal conducting surfaces at 2 K and 4 K, a special HOM absorber is foreseen which operates at 70 K, where the cooling efficiency is much higher. The absorber basically consists of a pipe of absorbing material mounted in a cavity-like shielding, and integrated into the connection between two modules. As the inner surface area of this absorber (about $280 \, cm^2$) is small compared to that of all the normal conductors in one cryomodule, the absorber has to absorb a significant part of all the RF power incident upon it. In field propagation studies, which assume a gas-like behaviour for photons, it has been shown that an absorber with a reflectivity below 50% is sufficient [25]. Theoretical and experimental studies have suggested that the required absorption may be obtained with ceramics like MACOR [25, 26] or with artificial dielectrics [27].

The axes of the 12 cavities must be aligned to the ideal beam axis to within ± 0.5 mm, and quadrupole axes to within ± 0.2 mm. The quadrupoles have an additional 'roll' tolerance of ± 0.1 mrad.

The ambient magnetic field in the cavity region must not exceed $0.5 \, \mu$T to preserve the low surface resistance. At TTF this has been achieved by demagnetising the vacuum vessel (made of soft steel) before assembly of the cryomodule, and placing a passive shield (made of Cryoperm) around each cavity helium vessel.

Several types of cryomodule are required in the machine:

- 1004 standard linac modules with 12 cavities and a length of 15.927 m;

- 742 standard linac modules with an additional quadrupole and corrector coil package (package length 0.864 m, which increases the module length by 0.801 m),

	static [W]	dynamic [W], 23.4 MV/m, $Q_0 = 1 \cdot 10^{10}$, 5 Hz, high energy beam	add. dynamic [W], 21.1 MV/m, $Q_0 = 1 \cdot 10^{10}$, 5 Hz, FEL beam
2 K			
RF load	–	4.95	3.99
supports	0.60	–	–
input coupler	0.76	0.14	0.14
HOM coupler	0.01	$0.27^{a)}$	$0.27^{a)}$
HOM absorber	0.14	0.02	0.01
beam tube bellows (12)	–	0.24	0.20
HOM to structure	–	1.68	0.86
instrumentation cable	0.13	–	–
current leads	0.10	0.01	–
sum	**1.74**	**7.31**	**5.47**
5–8 K			
radiation	1.95	–	–
supports	2.40	–	–
input coupler	2.05	1.19	1.15
HOM coupler	0.40	$2.66^{a)}$	$2.66^{a)}$
HOM absorber	3.13	0.77	0.37
instrumentation cable	1.39	–	–
sum	**11.32**	**4.62**	**4.18**
40–80 K			
radiation	44.99	–	–
supports	6.00	–	–
input coupler	21.48	59.40	48.89
HOM coupler	2.55	13.22	13.22
HOM absorber	-3.27	15.27	8.07
instrumentation cable	5.38	–	–
current leads	13.00	5.00	–
sum	**90.13**	**92.89**	**70.18**

Table 3.3.1: *Calculated heat loads for 17 m long cryomodule with quadrupole. $^{a)}$ Worst case estimate, assuming resonant excitation of monopole modes.*

	collider operation	FEL operation
total losses	23.3 W	14.2 W
losses above 10 GHz	12.7 W	9.4 W
losses above 750 GHz	< 0.001 W	0.5 W

Table 3.3.2: *Monopole single bunch losses in one cryomodule.*

are required every second module up to 125 GeV, and thereafter every third module;

- 27 cryomodules with 8 cavities and one quadrupole package are required for the FEL injector and the positron pre-accelerator; and

- 8 cryomodules with 4 cavities and 4 quadrupole packages are required for the positron pre-accelerator (see chapter 4).

In about every tenth cryomodule (the shortest cooling loop), three cryogenic valves (one JT-valve), three flow-meters and some instrumentation will be incorporated. This avoids extra string connection boxes which would require extra space (and cost).

3.3.2 Quadrupole and Correction Magnets

The quadrupole package is shown in figure 3.3.3. It consists of:

- a cos2Θ type quadrupole;

- correction dipoles for vertical and horizontal beam deflection;

- an iron yoke with shrink cylinder surrounding the magnet coils;

- a helium vessel;

- an RF beam position monitor (BPM);

- current leads.

To simplify the system, the quadrupole packages are cooled with 2 K super-fluid helium in the same manner as the cavities. Because of the small stored energy, the pressure in the 2-phase supply line will not increase beyond 3 bar during a quench. The magnet parameters are listed in table 3.3.3.

3.3.2.1 Quadrupoles

The linacs contain quadrupoles with a maximum gradient of 60 T/m (field integral 31.2 T). The quadrupoles are located at the centre of the cryomodules (generally underneath the central support post) to guarantee high positional accuracy. The operating current is limited to 100 A for cost reasons (minimum heat loads and low cost

quadrupole coil (cos2Θ, 2 layer)		
inner coil radius RQi	45	mm
outer coil radius RQo	66	mm
coil straight section length	520	mm
coil total length	626	mm
nominal gradient	60	T/m
max. field at conductor	3.6	T
operating temperature	2.0	K
nominal current	100	A
number of turns/pole	1007	
inductance	~ 3.2	H
dipole coils, vert./horiz. (cosΘ, single layer)		
inner coil radius RDi1	67	mm
outer coil radius RDo1	68	mm
inner coil radius RDi2 (in every 2nd package)	69	mm
outer coil radius RDo2 (in every 2nd package)	70	mm
coil straight section length	520	mm
coil total length	626	mm
max. field on axis	0.074	T
max. field at conductor	3.6	T
operating Temperature	2.0	K
max. current	40	A
number of turns(1)/pole	99	
number of turns(2)/pole	102	
inductance/coil	~ 29	mH
iron yoke		
inner yoke radius RYi	71	mm
outer yoke radius RYo	121	mm
yoke length	520	mm
helium vessel		
outer radius RVo	145	mm
inner beam pipe radius Rbi	39	mm
helium vessel length	666	mm
field quality (at $R_0 = 30$ mm)		
skew quadrupole (a_2)	$3 \cdot 10^{-4}$	
higher harmonics of quadrupole	10^{-3}	
alignment error (angle)	0.1	mrad rms

Table 3.3.3:   *Main parameters of the superconducting magnet package.*
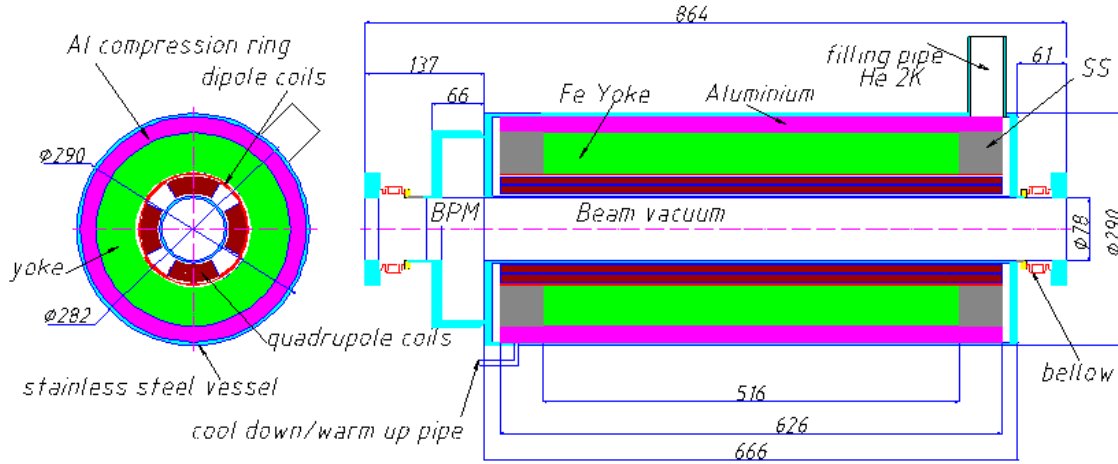
Figure 3.3.3:   *Cross-section and longitudinal cut of superconducting magnet package.*

power supplies). The superconducting coils are of the cos2Θ type, wound in double layers from a flat ribbon made from electrically insulated superconducting wires. The coil has a large inductance ($\sim 3.2\,\mathrm{H}$), and a quench must be detected fast so that an external dump resistor can be switched into the circuit for protection.

3.3.2.2   Correction dipoles

The correction dipoles have a maximum field of $0.074\,\mathrm{T}$ (field integral $0.038\,\mathrm{Tm}$), which can correct a maximum beam offset (at $E_{beam} = 400\,\mathrm{GeV}$) of $\pm 3\,\mathrm{mm}$ per correction coil. There is one correction coil for vertical beam deflection in every magnet package and one for horizontal beam deflection in every second package. The coils are wound from a round multi-filament wire in a single layer on top of the quadrupole coils. The maximum dipole current is $40\,\mathrm{A}$.

3.3.2.3   Iron yoke and shrink cylinder

The coil package is surrounded by a yoke made from $5\,\mathrm{mm}$ thick carbon steel laminations. At the coil ends the carbon steel is replaced by stainless steel. The laminations are held together by rods, and a shrink cylinder made from aluminum is placed around the yoke in order to apply the necessary force on the coils.

3.3.2.4   Helium vessel

The quadrupole, together with the correction dipole coils and associated yoke, are assembled in a helium vessel which consists of the electrically insulated beam pipe, the outer vessel, and the end plates of which one is part of the BPM. The beam pipe has bellows at both ends, and both the beam pipe and bellows are copper plated from inside. The outer vessel contains keys for proper alignment of the interior yoke and

coils, and there are fiducial marks for alignment on the outside of the end plates. The end plates are covered with soft steel magnetic mirror plates to reduce the fringe fields.

3.3.2.5   Beam position monitor

The BPM is of the pill box type, and is attached to the end plate of the helium vessel. It is copper plated on the inside and equipped with two antennas for each transverse direction (x and y). The beam position measurement resolution is $10\,\mu$m and the installation tolerance with respect to the quadrupole axis is 0.1 mm.

3.3.2.6   Current leads

The coils will be powered through current leads made from HTS in the low temperature region, and from normal conducting material in the upper part. For reasons of simplification and to avoid many valves in the tunnel, there is no gas cooling foreseen. The heat flow in the upper end of the HTS part is intercepted at 50 K from the 40–80 K forward line.

3.3.2.7   Quadrupole support and alignment

The quadrupole package is rigidly mounted to the 300 mm diameter GRP. The package is located underneath the centre post, which assures minimum motion during operation.

The relatively tight tolerances on the quadrupole field and BPM alignment have a major impact on their fabrication:

- the coils will be fabricated with high precision using precise tooling (radii and coil angles with tolerances of 0.02 mm);

- the yoke laminations will be fabricated by punching or fine blanking, assuring high accuracy;

- the helium vessel must be accurately fabricated and precisely assembled with the aid of pins, keys and reference targets at the end plates;

- the field axis and orientation will be accurately measured and referenced before and during installation;

- the BPM will be machined with high precision as an integral part of the helium vessel end plate.

In addition, the shrinking process during cool down leads to a tight fit between coils and yoke, which further assures the alignment.

3.3.3   Assembly and alignment

The design of the cryomodule — including fabrication procedures and tolerances — is the key factor to obtaining the required alignment precision for cavities and magnets, while at the same time limiting the costs. The final alignment of the individual active components is performed once the string of cavities is out of the clean room and anchored to the supporting GRP. The alignment of the GRP, via three Taylor-Hobson spheres, is then used to reference the axis of the active components. Assembly and cool down do not affect this external reference, except for a predictable and reproducible parallel vertical motion.

A crucial step in cutting the production cost was to relax the general tolerances of the GRP and of the vacuum vessel, while using a long milling machine to precisely reference (after welding of ancillary components) all the important axes and planes. In particular, the GRP is now fabricated according to the standard tolerances for a high quality welded pipe ($\pm 5\,$mm), including straightness. After welding of the cavity supports, lower post flanges and end flanges, the axis is defined on the milling machine according to the end flange centres and transferred to the lower post flanges. The interconnection bellows, properly fastened, are already included to minimize the inter-module lateral forces. The pipe is then turned and the cavity supports referenced to the defined GRP axis. A similar procedure is also applied to the vacuum vessel to reference the coupler ports and upper flanges to the vessel axis. After welding and before milling, a stress relief is performed on the GRP to avoid permanent deformation induced by thermal cycling.

The stretched wire measurements at TTF show that these procedures lead to the required accuracy.

The module assembly is performed in three major steps:

1. the cavity string is prepared in the class 10 clean room, pre-aligned and closed;

2. the string is then transferred to the assembly area where it is attached to the aligned GRP;

3. each cavity and quadrupole is aligned with respect to the GRP using the three optical targets on the posts (Taylor-Hobson spheres) and then fixed.

The module can now be moved and the alignment recovered through the external targets. The last step is performed in a third assembly station where, after the assembly of the thermal shields, a long fixed cantilever and a movable cart are used to insert the cold mass into the vacuum vessel. Module alignment in the linac is made using three optical targets placed on the vacuum vessel and referenced to those on the GRP.

3.4   RF System

3.4.1   Overview

The RF system consists of 286 stations per electron and positron main linac, each of which provides power at 1.3 GHz to a total of 36 accelerating cavities (three cryomodules, see section 3.3). The peak RF power needed for one superconducting cavity at full gradient and maximum beam current (23.4 MV/m and 9.5 mA) is 231 kW; the nominal peak power needed for 36 cavities is therefore 8.3 MW. Taking into account a regulation reserve of 10% for phase and amplitude control and another 6% for circulator and waveguide losses, a total of 9.7 MW is required. The RF pulse length is 1.37 ms, which includes the beam pulse length of 950 μs, and the cavity fill time of 420 μs. The repetition rate is 5 Hz for the major part of the linac: the 5–50 GeV section stations will run at 10 Hz to alternate between FEL and Linear Collider operation.

During the beam pulse the fluctuations of the accelerating field (defined as the vector sum of the fields in the 36 cavities) must be kept small. The major sources of field perturbations which have to be controlled by the low level RF system are fluctuations of the resonance frequency of the cavities and fluctuations of the beam current. Changes in resonant frequency result from deformations of the cavity walls induced by mechanical vibrations (microphonics) or the gradient dependent Lorentz force. Slow changes in frequency — on the time scale of minutes or longer — are corrected by a frequency tuner, while faster changes are counteracted by fast amplitude and phase modulation of the incident RF power.

The main components of the RF system are the modulators and klystrons. The modulator converts AC line power into high voltage pulse power; its main components are a high voltage power supply, a high voltage pulser unit and a pulse transformer. The klystron generates pulsed RF power from (pulsed) high voltage power, which is then distributed to the cavities by a system of waveguides. The circulators in the distribution system protect the klystron from reflected power. The low level RF system controls the shape, amplitude and phase of the RF. Various auxiliary devices for the klystron and modulator are also required. An interlock system protects the linac and the RF stations in case of malfunction.

In order to provide RF power for the entire linac at a centre of mass energy of 500 GeV, 560 RF stations are required. The number of installed systems will be 572 to provide an overhead for energy management in case of klystron failures. For the 800 GeV upgrade, the number of stations will be doubled to 1144. With the exception of the high voltage power supplies and pulser units for the modulators, the RF stations will be installed in the tunnel with a separation of 50 m (25 m for the 800 GeV). The high voltage power supplies and pulsers for the modulators will be installed in the access halls, which are separated by about 5 km. The connection between the pulser and pulse transformer will be accomplished by high voltage pulse power cables. There will also be additional cable connections for the interlock system between the halls and the tunnel. The number of modulators per hall will be typically 100.

In the remainder of this section, the various subsystems forming one RF station

Figure 3.4.1:   *Cathode of the multibeam klystron.*

will be described.

3.4.2   High power RF source

Comparison of different types of klystrons constructed and built so far have shown that a low microperveance of the klystron electron beam ($p = 10^6 \times I/V^{3/2}$, where I and V are the klystron beam current and voltage respectively) results in a high efficiency [28, 29]. This is due to lower space charge forces in the beam, which make the bunching easier and more efficient. For a single beam klystron at very high output power, the demand for high efficiency leads to low microperveance and hence to very high voltage, resulting in a reduced reliability. The solution is to use a multibeam klystron, where many small low voltage, low microperveance beams are used in parallel in one vacuum vessel. With a multibeam klystron, an efficiency of 70% or more seems to be feasible, compared to a typical maximum of 45% for a 5 MW single beam klystron.

Figure 3.4.1 shows the cathode of the multibeam klystron constructed and built by Thomson Tubes Electroniques [30]. Seven beams are produced by the cathode and accelerated by the klystron gun. Each beam has a microperveance of 0.5. The beams share common cavities but have independent drift tube sections. After RF extraction in the output cavity, the spent electron beams are absorbed in the collector.

Figure 3.4.2 shows the complete TH1801 multibeam klystron (without solenoid). Two output waveguides are required to handle the RF power of 2×5 MW in the output

Figure 3.4.2:   *The Thomson TH1801 multibeam klystron.*

windows. The total height of the klystron is 2.5 m. The klystron was successfully tested and is now in use at the TTF. It achieved an output power of 10 MW with an efficiency of 65%. Table 3.4.1 summarises the design parameters and the parameters achieved with the prototype tests. More detailed information can be found in [31].

The gain of 48 dB means that the drive power is below 160 W, and solid state amplifiers can be used; they will be installed near to the klystrons in the tunnel. The klystrons will be mounted horizontally together with the pulse transformer inside a container. The complete assembly will be transported using the monorail system to its location in the tunnel, and then installed below the walk way. The goal for klystron lifetime is 60,000 h, but a conservative 40,000 h is used for the estimation of the rate of klystron exchange in the linac tunnel.

	Design	Measurement
Operation Frequency	1300 MHz	1300 MHz
RF Pulse Duration	1.5 ms	1.5 ms
Repetition Rate	10 Hz	5 Hz
Cathode Voltage	110 kV	117 kV
Beam Current	130 A	131 A
HV Pulse Duration	1.7 ms	1.7 ms
No. of Beams	7	7
Microperveance	3.5	3.27
No. of Cavities	6	6
Max. RF Peak Power	10 MW	10 MW
RF Average Power	150 kW	75 kW
Efficiency	70%	65%
Gain	48 dB	48.2 dB
Solenoid Power	4 kW	6 kW

Table 3.4.1: *Design and measured parameters of the multibeam klystron (see [31] for details).*

3.4.3   Modulator

3.4.3.1   Overview

The modulator converts AC line voltage to pulsed high voltage in the 120 kV range to be applied to the klystron cathode. The pulse shape must be as rectangular as possible. The flat top ripple should not exceed ±0.5% in order to limit phase and amplitude variations of the klystron RF output. The rise and fall times of the pulse should be as short as possible to maximise the total efficiency. The pulse-to-pulse stability must be better than ±0.5%. In case of klystron gun sparking, the energy deposited into the spark must be limited to a maximum of 20 J. These and other requirements are summarised in table 3.4.2.

Various types of modulators meeting these requirements are conceivable; the most promising solution (with respect to cost, ease of design, and reliability) is a bouncer modulator consisting of a DC high voltage power supply, a pulser unit and a pulse transformer [32]. Several modulators of the bouncer type were built and are in use at the TTF. A detailed description of the modulator is given in [33, 34, 35, 36].

A modulator based on the Superconducting Magnetic Energy Storage (SMES) principle as a possible alternative will be tested at TTF. Here a superconducting solenoid is used instead of a capacitor bank for the intermediate energy storage [37].

	Typical	Maximum
Klystron Gun Voltage	115 kV	120 kV
Klystron Gun Current	130 A	140 A
High Voltage Pulse Duration (70% to 70%)	< 1.7 ms	1.7 ms
High Voltage Rise and Fall Time (0 to 99%)	< 0.2 ms	0.2 ms
High Voltage Flat Top (99% to 99%)	1.37 ms	1.5 ms
Pulse Flatness During Flat Top	< ±0.5%	±0.5%
Pulse-to-Pulse Voltage fluctuation	< ±0.5%	±0.5%
Energy Deposit in Klystron in Case of Gun Spark	< 20 J	20 J
Pulse Repetition Rate for 90% of the Modulators	5 Hz	5 Hz
Pulse Repetition Rate for 10% of the Modulators	10 Hz	10 Hz
Transformer Ratio	1 : 12	
Filament Voltage	9 V	11 V
Filament Current	50 A	60 A

Table 3.4.2:   *Modulator requirements.*
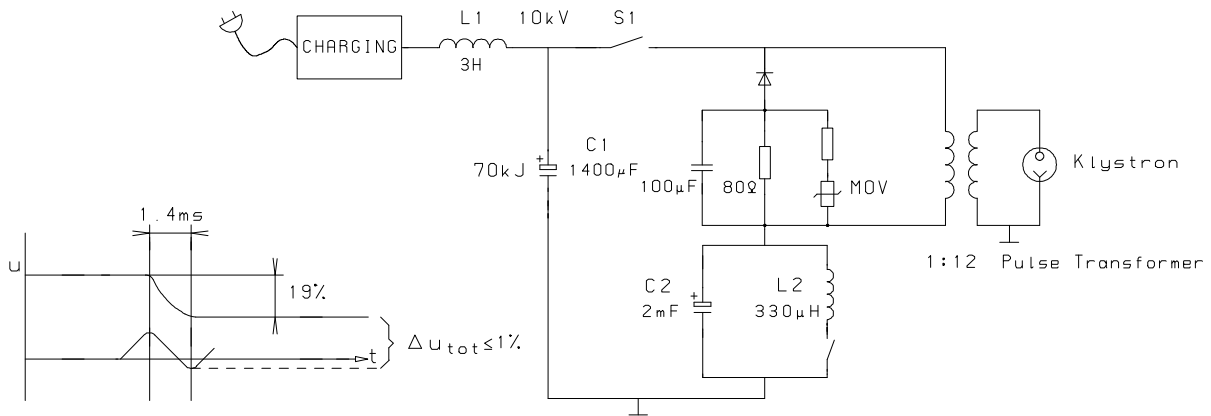
Figure 3.4.3:   *Modulator circuit (conceptual).*

3.4.3.2 Bouncer pulser

The bouncer modulator solution is sketched in figure 3.4.3. During operation the DC power supply keeps capacitor C1 charged to the 10 kV level. The output pulse is started by closing S1, connecting C1 to the pulse transformer primary. Semiconductor devices like Isolated Gate Bipolar Transistors (IGBT) or Integrated Gate-Commutated Thyristors (IGCT) can be used for the switches. The pulse is terminated after 1.57 ms (1.37 ms flat top + ∼0.2 ms rise time) by opening S1. The nominal current switched by S1 is 1.56 kA. The primary pulse of 10 kV is stepped up by the 1:12 pulse transformer to the klystron operating level (maximum 120 kV).

During the pulse, capacitor C1 discharges by 19% of its initial voltage, putting an intolerable slope on the output pulse. To correct the slope to the 1% level without

resorting to a 29 mF capacitor at the C1 location, a bouncer circuit is used: this is a resonant LC circuit, which creates a single sine wave with a period of 5 ms and an amplitude at the 1 kV level. The bouncer is triggered slightly before the main pulse so that the linear (bipolar) portion of the cycle compensates the slope from C1. The size of the pulser units are $2.8\,\mathrm{m\,(L)} \times 1.6\,\mathrm{m\,(W)} \times 2.0\,\mathrm{m\,(H)}$, and will be installed in the access halls (typically 100 per hall).

3.4.3.3   Pulse transformer

The output pulse of the pulser unit has a maximum amplitude of 10 kV, and must be transformed to the 120 kV level by means of a pulse transformer. The transformer should not significantly distort the rectangular pulse. The rise time of the high voltage pulse is mainly determined by the transformer's leakage inductance, which must therefore be kept to a minimum. Several transformers with leakage inductances slightly above $300\,\mu\mathrm{H}$ have been built and operated at TTF. Some new transformers having even less than $200\,\mu\mathrm{H}$ are now available and will be used at TTF. The voltage level of 120 kV requires the transformer to be installed in a tank filled with transformer oil; the klystron socket housing the cathode will be installed in the same tank.

The pulse transformer tanks have the dimensions $3.2\,\mathrm{m\,(L)} \times 1.2\,\mathrm{m\,(W)} \times 1.4\,\mathrm{m\,(H)}$, and weigh 6.5 t each. They will be installed below the walk way in the tunnel.

3.4.3.4   Pulse cable

The energy transport from the modulator to the transformer will be done via pulse cables. The maximum distance between the modulators in the service halls and the pulse transformers in the tunnel is $\sim 2.8\,\mathrm{km}$. The required cross section of the copper current lead is $300\,\mathrm{mm}^2$ per conductor. In order to transmit the high voltage pulse without significantly distorting the pulse shape (especially at the leading edge of the pulse), the cable impedance must be matched to the klystron impedance, and the skin effect must be minimized. To achieve this, four coaxial cables will be used, each having a conductor cross section of $75\,\mathrm{mm}^2$, and an outer diameter of 30 mm. The cable construction is shown in figure 3.4.4. The cable impedance Z_0 of the four cables equals $6.45\,\Omega$. Coaxial cables are used to prevent electromagnetic noise in the tunnel. The inner lead is at high potential (12 kV); the outer lead is at the potential of the bouncer circuit ($\pm$ 2 kV). VPE will be used as insulation material, and an aluminium foil shield and a protective outer coating help to minimise the risk of fire. Additional line matching to the pulse transformer will be done via an RC network. The power losses in the cable will be 2% on average. Simulation results and further information on the cable are given in [38].

The cables will be placed in cable trays welded to steel anchor plates integrated into the tunnel wall. They will be cooled by natural air convection.
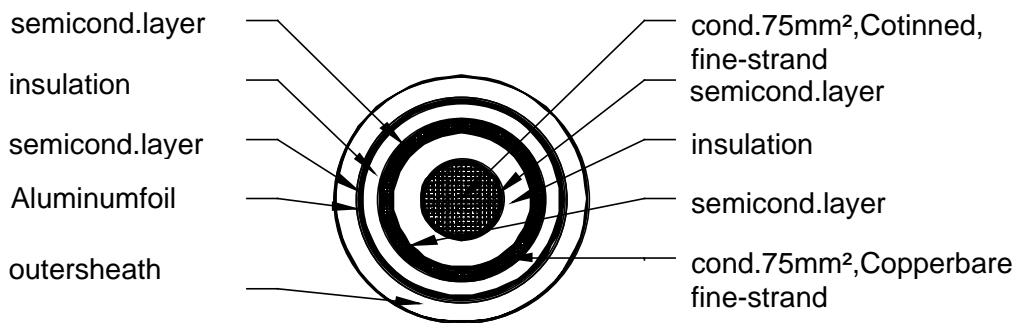
Figure 3.4.4: *Construction of the pulse cable.*

3.4.3.5   High voltage power supply

The high voltage power supply — which charges the main capacitor of the pulser — has to meet two requirements:

- the capacitor has to be charged to an accurate value of voltage in order to obtain the same voltage at the klystron from pulse to pulse; and

- the low repetition frequency of 5 Hz and 10 Hz respectively has to be suppressed in order not to produce disturbances in the mains.

The amount of allowed disturbance is defined by the German norm VDE 0838 or the equivalent European norm EN 61000. For the 5 Hz and 10 Hz repetition rate of TESLA, the allowed amount of distortion (D) is 0.5% of the short circuit power. TESLA will have a distributed power system with a voltage of 20 kV. In each service hall a maximum of 100 modulators are to be installed having an average real power consumption of up to 15 MW. The service halls have a short circuit power (S_{sc}) of approximately 200 MVA: therefore from $D = \Delta S / S_{sc} \leq 0.5\%$ it follows that the allowed variation of the input power must be $\Delta S \leq 1$ MVA per hall or ≤ 10 kVA per RF station. The corresponding input power variation for a single modulator must be less than 6.5% of its nominal power (changes in reactive power included).

Each modulator will have a separate switch mode power supply. The input will be the standard grid three phase voltage. The voltage output is 12 kV, and the nominal power of each supply is 150 kW at 5 Hz (300 kW at 10 Hz) repetition rate. The power supply is built in modules, ensuring a high reliability. Buck converters will be used as switch mode units; series resonant converters are a possible alternative. The advantages of this solution are:

- the system has a high redundancy — failure of one modulator or power supply leaves the other modulators unaffected;

- failure of one single power supply module still allows the modulator to be operated;

- each power supply can be regulated independently with a high regulation dynamics;

- the low voltage level means the switch gear is available as a low-price commercial off-the-shelf component;

- no additional high-voltage safety requirements are necessary during maintenance or replacement of a power supply.

The power supply is regulated by digital self-learning regulation of the input power, made possible by the high regulation dynamics. In addition, the voltage at the capacitor bank at the trigger time of the pulse will be regulated to within 0.5%.

The size of the high voltage power supply is $1.2\,\text{m}\,(\text{L}) \times 1.6\,\text{m}\,(\text{W}) \times 2.0\,\text{m}\,(\text{H})$. Further information about the power supplies can be found in [39].

3.4.3.6   Auxiliary power supplies

In addition to the main high voltage power supplies, operation of the klystron and modulator require additional auxiliary supplies for:

- the klystron focusing solenoid;

- the klystron filament;

- the klystron vacuum pump; and

- the core bias for the pulse transformer.

The auxiliary power supplies will be installed below the walk way in the tunnel.

3.4.4   Power requirements

The klystrons must deliver the maximum RF power of 9.7 MW when required, taking into account the regulation reserve of 10% for phase and amplitude control and 6% for losses in the waveguide distribution. To allow for the regulation, the klystron must be run slightly below saturation, and the efficiency drops from the design (saturation) value of 70% by a few percent. Taking this into account, we assume a klystron efficiency of 65%; a corresponding klystron voltage of 117 kV is then required. The high voltage pulse of the modulator meets the requirement during the flat top but not during the rise and fall times. The pulse rise time is of the order of $200\,\mu\text{s}$: however the average rise time of the HV pulse at the klystrons will be greater than $200\,\mu\text{s}$ because of the long cables between the pulse forming units in the service buildings, and the pulse transformer-klystron units in the tunnel.

Since the first $420\,\mu\text{s}$ of the RF pulse will only be used to fill the superconducting cavities with power, it can already start during the rise time of the high voltage pulse: the klystron RF output power during the rise time will be lower than that during the flat top, but can still be used to fill the cavities. The RF pulse can be started when the

Peak RF power per RF station	9.7 MW
Duty cycle	0.685%
Average RF power available per RF station	66 kW
Klystron efficiency	65%
Modulator efficiency	85%
Total efficiency	55%
AC power per RF station	120 kW
Auxiliary power per RF station incl. LLRF and waveguide tuner	14 kW
Total wall plug power per station	134 kW
Number of active stations	560
Total wall plug power	75 MW

Table 3.4.3:   *Efficiencies and power requirements of the RF system.*

klystron voltage reaches 80% of the flat top voltage — about 100 μs after the beginning of the high voltage pulse. The klystron output power at this voltage is about 4 MW. The RF phase shift of ∼320° in about 200 μs due to the changing klystron voltage can be compensated by the low level RF control system. In this way, the rise time efficiency[1] of the modulator can be increased to 96%. The electronic efficiency of the modulator is 90%. Taking into account the additional ohmic losses of 2% in the pulse cables, this results in a total modulator efficiency of 85%.

In order to generate 9.7 MW in a 1.37 ms long RF pulse at 5 Hz repetition rate, an average primary AC power of 120 kW per RF station is required. In addition, 14 kW for the auxiliary power supplies must be added. The total average AC power required for 560 active RF stations is therefore 75 MW. Table 3.4.3 summarises the power requirements for RF generation in the main linac. An additional 6 MW AC power must be added to these numbers for the FEL operation.

3.4.5   Modulator and klystron protection and control

A comprehensive interlock system is required for the reliable and safe operation of the RF system. In the event of a klystron gun spark, the energy deposited in the spark must be kept below 20 J to avoid damage of the klystron gun. The response to a spark will be an immediate opening of the relevant IG(B)CT switch to disconnect the capacitor bank from the sparking klystron. The energy stored in the transformer leakage inductance and power transmission cable is dissipated in two networks: one at the cable end near the IG(B)CT consisting essentially of a reverse diode and a resistor; the second made up by an 80 Ω resistor across the transformer primary and by a 100 μF capacitor which limits the peak inverse voltage at the primary to 800 V when the IG(B)CT is opened. In addition a crowbar is fired. Other important interlocks are: cooling water flow and

---

[1]defined as the ratio of the energy per high voltage pulse used for RF generation, to the total energy per high voltage pulse.

temperature; focusing solenoid current; vacuum. Additional interlock conditions result from: sparks in the RF distribution system; reflected power; RF leaks; power couplers; and cryogenics.

In order to meet the different safety requirements, several different interlock techniques will be used. The interlock which inhibits RF operation during tunnel access is accomplished by two separate and independent hard-wired systems, which switch off the klystron RF drive power and the modulators high voltage power supply.

The technical interlock — which protects the linac and the RF station in case of malfunction — will be realized using programmable logic controller (PLC) and system-on-programmable-chip (SOPC) techniques. Both systems are industrial standards, and help is available for planning, structure and programming. In addition hardware for almost all applications can be obtained from several manufactures. Besides system protection and providing start up and shut down procedures for the RF stations, the interlock system will offer comprehensive diagnostics of the RF systems. It will measure and diagnose parameters, and adjust set points within certain limits for each RF station and its subsystems. Communication with the accelerator main control system will be accomplished by a VME bus.

The interlock system will be divided into two units: one installed in an electronic rack in the tunnel near to the klystron, and another installed near to the pulser and the high voltage power supply unit in the access hall. Connection and communication between these two units are accomplished by glass fiber cables, allowing fast transfer of the interlock signals. To reduce the number of interconnecting cables, the interlocks of each unit are summarised into categories, and only these sum interlocks will be exchanged between units. Each unit is connected via its own VME bus to the main control system.

3.4.6   RF waveguide distribution system

Figure 3.4.5 illustrates the RF distribution concept. The 10 MW multibeam klystron has two RF output windows and has to supply 36 9-cell cavities, installed in three modules. The RF distribution is based on two symmetrical systems, each supplying 18 cavities. A linear system branching off identical amounts of power for each cavity from a single line by means of directional couplers will be used; it matches the linear tunnel geometry best and leads to lower waveguide losses than a tree-like distribution system, because long parallel waveguide lines can be avoided. Such a system is already in use for the HERA superconducting RF system and has also been successfully tested at TTF.

Circulators are indispensable: they have to protect the klystron against reflected power at the start and end of the RF pulse, and during the filling time of the cavity. In conjunction with load resistors and the power input coupler, the circulators define the loaded cavity impedance as seen by the beam.

Only 4% of the average power generated by one klystron is lost in the waveguides, with an additional 2% in the circulators. Thermal expansion will result in an RF phase shift of 6° and 12° for operation at full power and pulse duration at 5 Hz and 10 Hz
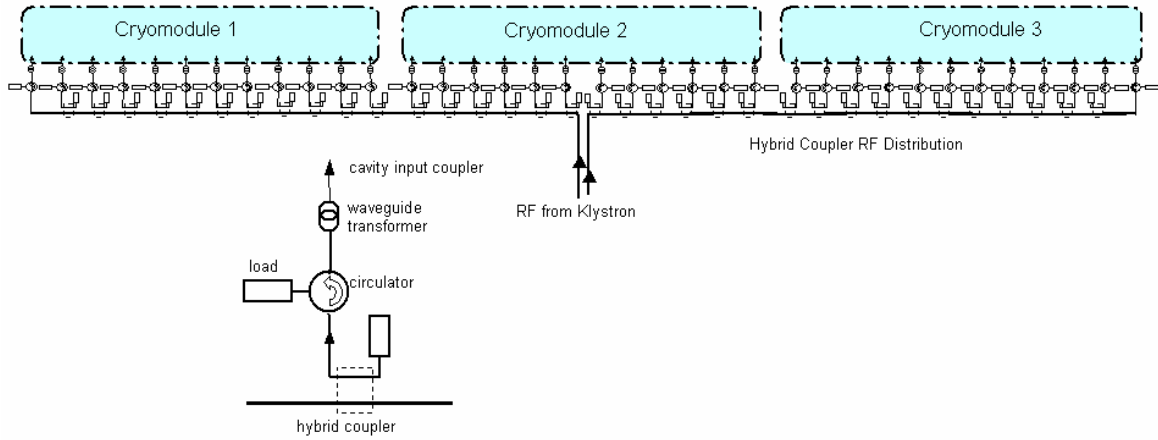
Figure 3.4.5:   *RF waveguide distribution of one RF station.*

respectively. The phase shift can be compensated easily by the waveguide transformers (three-stub waveguide transformer) installed between the circulators and each cavity. The waveguide transformers provide an impedance matching range from $1/3\,Z_W$ to $3.0\,Z_W$ and the possibility of $\pm 50^0$ phase adjustment. Each stub is equipped with a motor which is controlled by the low level RF system.

The RF distribution system will be equipped with several interlock sensors, e.g. reflected power, sparking and RF leakage. Similar systems are in use at TTF.

3.4.7   Low level RF

3.4.7.1   Control requirements

The requirements for amplitude and phase stability of the vector-sum of 36 cavities are driven by the maximum tolerable energy spread in the beam. It is desirable to keep the bunch-to-bunch energy spread below the single-bunch energy spread of $5 \cdot 10^{-4}$ in order to assure that the bunch-to-bunch chromatic effects will not be a dominant emittance growth factor. The bunch-to-bunch rms energy error due to *systematic* errors of all the klystrons can be suppressed to the level of $3 \cdot 10^{-4}$: The tolerance for the *uncorrelated* random errors of each individual klystron is set such that the total rms error is not greater than the systematic error. If N_k is the number of klystrons per linac ($N_k = 280$), then the maximum allowed uncorrelated error for each klystron is $\sqrt{N_k} \times 3 \cdot 10^{-4} \approx 5 \cdot 10^{-3}$.

In the following the layout of the RF control system is summarised; more details can be found in refs. [3, 40, 41, 42, 43, 44].

3.4.7.2   RF control design considerations

An important constraint is that the RF power needed for control should be minimized. The RF control system must also be robust against variations of system parameters

such as beam loading and klystron gain, especially close to klystron saturation. The pulsed structure of the RF power and the beam current, which are shown in figure 3.4.6, imposes demanding requirements on the RF control system. Amplitude and phase control is obviously needed during the flat top of $950\,\mu$s when the beam is accelerated, but it is equally desirable to control the field during cavity filling to ensure proper beam injection conditions and to minimize the RF power during filling.
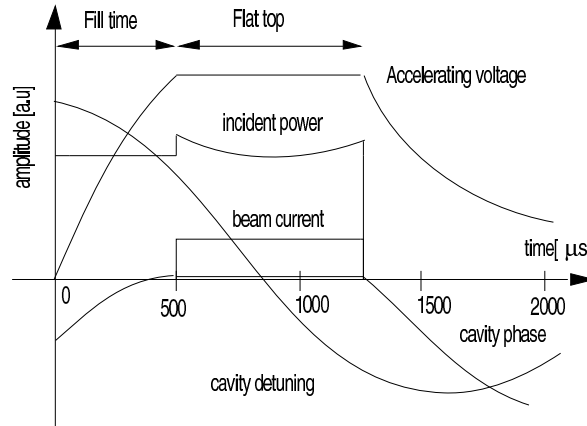
Figure 3.4.6:   *Various parameters related to the pulsed cavity fields in the superconducting cavities of the TESLA Test Facility.*

As a result of Lorentz force detuning and microphonics, the amplitude and phase errors are of the order of 5% and 20 degrees respectively. These errors must be suppressed by a factor of at least 10, and the loop gain must be adequate to meet this goal. Fortunately, the dominant source of errors is repetitive (Lorentz force and beam transients) and can be significantly reduced by the use of feedforward.

3.4.7.3   Design of the TESLA RF control system

Fast amplitude and phase control of the cavity field can only be accomplished by modulating the signal driving the klystron, and hence systematically affects all the associated 36 cavities. A so-called I/Q modulator is used to control both the in-phase (I) and quadrature (Q) components of the cavity field[1]. This scheme minimizes coupling between the loops and guarantees control in all four quadrants. The overall scheme of the RF control system is shown in figure 3.4.7.

Digital I/Q detectors are used for the cavity field, incident and reflected waves. The RF signals are converted to an intermediate frequency of 250 kHz and sampled at a rate of 1 MHz (i.e. two consecutive data points describe I and Q of the cavity field). The I and Q component are multiplied by 2×2 rotation matrices to correct the phase offsets

---

[1]I and Q are the two cartesian components of the cavity voltage, from which the amplitude and phase can be readily obtained.
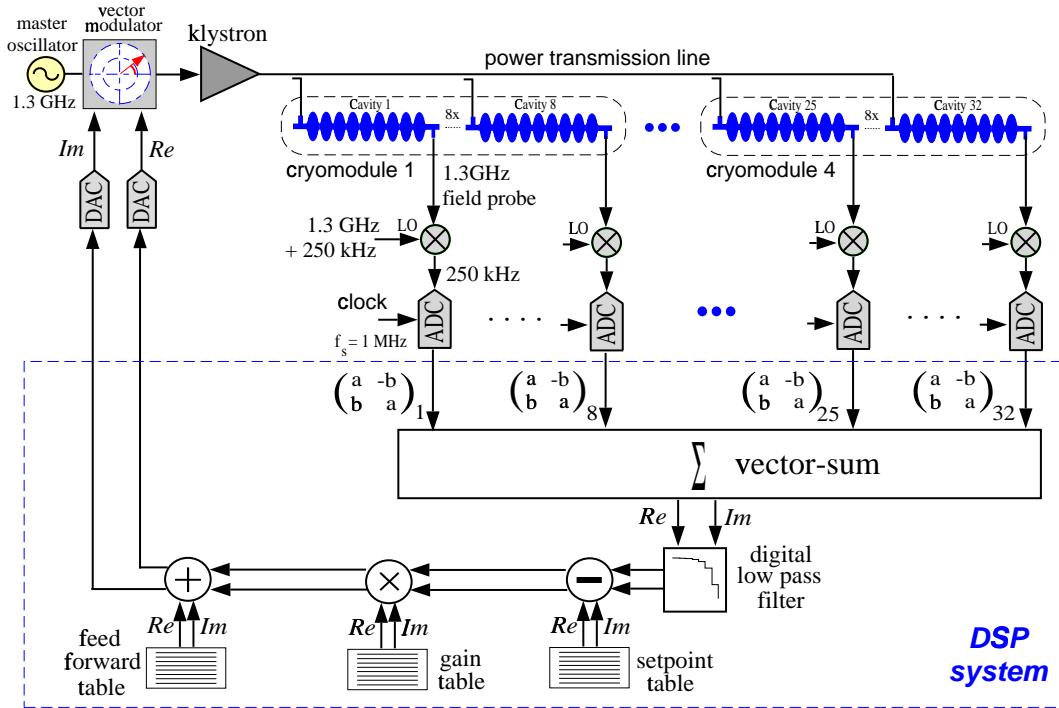
Figure 3.4.7: *Schematic of the digital RF feedback system.*

and to calibrate the gradients of the individual cavity probe signals. The vector-sum is calculated and corrected for systematic measurement errors. Finally the set point is subtracted and the compensator filter is applied to calculate the new actuator setting (I and Q control inputs to a vector modulator). Feedforward is added from a table in order to minimize the control effort. The feedforward tables are adaptively updated to reflect slowly changing parameters such as average cavity detuning, changes in klystron gain, phase shift in the feedforward path, and general changes in operating parameters. The operation of the more than 560 linac RF systems will be highly automated by the implementation of a finite state machine, which has access to high level applications including the adjustment of the loop phase, vector-sum calibration, frequency and waveguide tuner control, and exception handling.

3.4.7.4   Measured RF control performance at the TTF

The purpose of the TTF is to demonstrate that all major accelerator sub-systems meet the technical and operational requirements of the TESLA linear collider. Currently the TTF linac is operated with one klystron driving 16 cavities. The cavities have been routinely operated at a gradient of 15 MV/m providing a beam energy of 260 MeV. The requirements of $\sigma_A/A < 2 \cdot 10^{-3}$ for amplitude stability and of $\sigma_\Phi < 0.5^0$ phase stability have been achieved with feedback only, the stability being verified by beam measurements. The residual fluctuations are dominated by a repetitive component which is further reduced using the adaptive feedforward by about one order of magni-
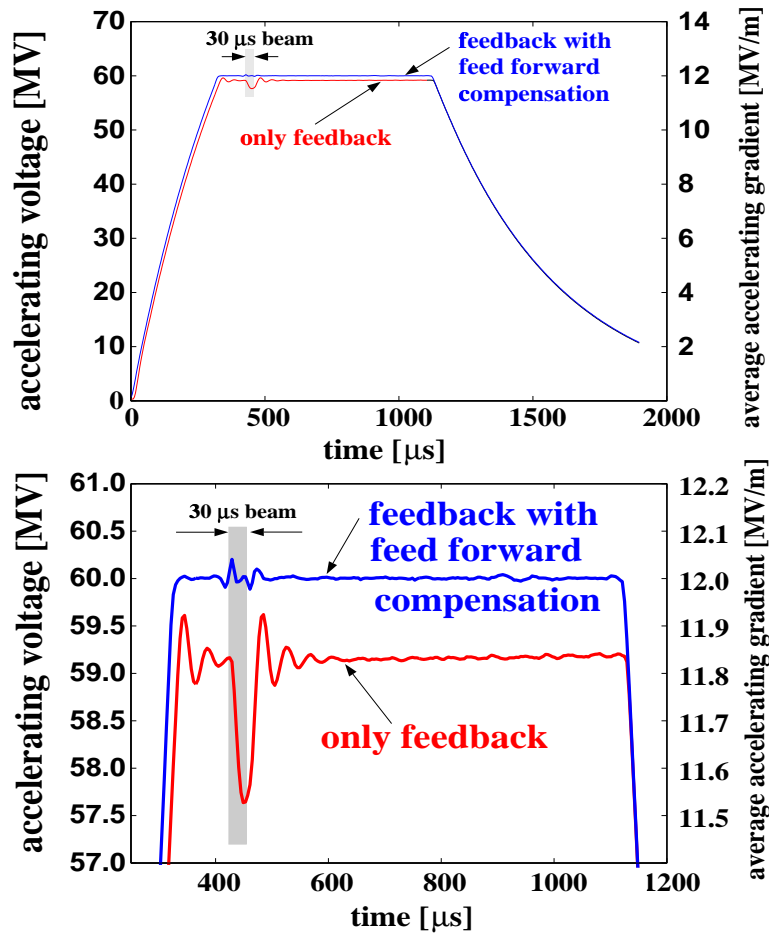
Figure 3.4.8:   *Field stability with and without adaptive feed forward.*

tude, thereby exceeding the design goals significantly. The high degree of field stability
achieved is mainly due to the low microphonic noise levels. A typical result of measured
field stability with and without the adaptive feedforward is shown in figure 3.4.8.

3.4.8   RF components test hall

During the installation of the RF system for the linac, all incoming RF components
will be received, inspected, tested and prepared for installation in a components test
hall. After installation is complete, the hall will be used for maintenance work and
storage of spare components required during linac operation. In addition, the hall will
still continue to be used to receive klystrons delivered by industry at a rate of about
ten per month. The additional investment for the test hall is included in the total RF
system cost estimate.

Bibliography

[1] V. Balakin, A. Novokhatski, V. Smirnov, *VLEPP: Transverse Beam Dynamics*, Proc. 12th Int. Conf. on High Energy Accelerators, Fermilab 1983, p. 119.

[2] V. Tsakanov, *Beam Dynamics Study for TESLA with the Integrated FEL*, DESY TESLA-99-21, 1999.

[3] R. Brinkmann, G. Materlik, J. Roßbach and A. Wagner (eds.), *Conceptual Design of a 500 GeV e+e- Linear Collider with Integrated X-ray Laser Facility*, DESY-97-048 and ECFA-97-182, 1997, chapter 3.

[4] A. Mosnier, *Longitudinal and Transverse Wakes for the TESLA Cavity*, DESY TESLA-93-11, 1993.

[5] A. Novokhatski, M. Timm and T. Weiland, *Single Bunch Energy Spread in the TESLA Cryomodule*, DESY TESLA-99-16, 1999.

[6] A. Novokhatski, M. Timm and T. Weiland, *Transition Dynamics of the Wake Fields of Ultra Short Bunches*, DESY TESLA-00-03, 2000.

[7] C. E. Adolphsen et al., *Beam Based Alignment Technique for the SLC Linac*, SLAC-PUB-4902, 1989.

[8] R. Assmann, T. Chen, F. J. Decker, M. Minty, T. Raubenheimer and R. Siemann, *Quadrupole Alignment and Trajectory Correcton for Future Linear Colliders: SLC Tests of a Dispersion-Free Steering Algorithm*, Proc. Int. Wokshop on Accelerator Alignment, Tsukuba 1996, KEK-95-12, p. 463.

[9] P. Tenenbaum et al., *Beam-Based Alignment of the Final Focus Test Beam*, SLAC-PUB-7058, 1995.

[10] M. Böge et al., *Application of a Beam Based Alignment Technique for Optimizing the Electron Spin Polarization at HERA*, Proc. 5th EPAC, Sitges 1996, Vol. I, p. 439.

[11] R. Assmann, P. Raimondi, G. Roy and J. Wenninger, *A Method for Simultaneous Optimisation of Orbit and Dispersion in Storage Rings*, Proc. 7th EPAC, Vienna 2000, p. 1462.

[12] T. Raubenheimer and R. D. Ruth, *A Dispersion Free Trajectory Correction Technique for Linear Colliders*, Nucl. Instr. Meth. **A 302** (1991) 191.

[13] C. Magne and M. Wendt, *Beam Position Monitors for the TESLA Accelerator Complex*, DESY TESLA-00-41, 2000.

[14] G. A. Amatuni, V. G. Khachatryan, V. Tsakanov and R. Brinkmann, *On the Single Bunch Emittance Preservation in TESLA*, DESY TESLA-01-02, 2001.

[15] S. Fartoukh et al., *Evidence for a Strongly Coupled Dipole Mode with Insufficient Damping in the TTF First Accelerating Module*, Proc. Particle Accelerator Conf., New York 1999, p. 922.

[16] N. Baboi, M. Dohlus, H.-W. Glock, C. Magne, A. Mosnier and O. Napoly, *Investigation of a High-Q Dipole Mode at the TESLA Cavities*, Proc. 7th EPAC, Vienna 2000, p. 1107.

[17] N. Baboi and R. Brinkmann, *Higher Order Mode Effects and Multi-Bunch Orbit Stability in the TESLA Main Linac*, DESY TESLA-00-28, 2000.

[18] R. Brinkmann and J. Roßbach, *Observation of Orbit Motion in HERA Covering Eight Decades in Frequency*, Nucl. Instr. Meth. **A 350** (1994) 8.

[19] V. Shiltsev, B. Baklakov and P. Lebedev, *Measurements of Ground Vibrations and Orbit Motion in HERA*, DESY HERA-95-06, 1995.

[20] J. G. Weisend II, R. Bandelmann, D. Barni, M. Bonezzi, G. Grygiel, R. Lange, C. Pagani, B. Petersen, P. Pierini, D. Sellmann, S. Wolff, *The TESLA Test Facility (TTF) Cryomodule: A Summary of Work to Date*, Proc. CEC/ICMC 1999, Montreal 1999, published in Advances in Cryogenic Engineering **45A** (2000) 825.

[21] C. Pagani, D. Barni, M. Bonezzi, J. G. Weisend II, *Further Improvements of the TESLA Test Facility (TTF) Cryostat in View of the TESLA Collider*, Proc. CEC/ICMC 1999, Montreal 1999, published in Advances in Cryogenic Engineering **45A** (2000) 939.

[22] M. Liepe, W.D. Moeller, S.N. Simrock, *Dynamic Lorentz Force Compensation with a Fast Piezoelectric Tuner*, DESY TESLA-01-03, 2001.

[23] M. Dohlus, H.P. Wedekind and K. Zapfe, *Wakefield Induced Losses in the Manual Valves of the TESLA Cryomodule*, DESY TESLA-00-39, 2000.

[24] R. Brinkmann, M. Dohlus, D. Trines, A. Novokhatski, M. Timm, T. Weiland, P. Huelsmann, C. Rieck, K. Scharnberg, P. Schmueser, *THz Wakefields and Their Effect on the Superconducting Cavities in TESLA*, Proc. 7th EPAC, Vienna 2000, p. 2028.

[25] A. Joestingmeier, M. Dohlus, C. Cramer, *Photon Diffusion Model for TTF2*, DESY TESLA-00-11, 2000.

[26] A. Joestingmeier, M. Dohlus, M. Wendt, C. Cramer, *Theoretical and Practical Investigations Concerning the Design of a HOM Broadband Absorber for TESLA*, DESY TESLA-00-10, 2000.

[27] B. Mikijeli, I. Campisi, *Developement of an Artificial Dielectric Ceramic for the use at CEBAF*, Proceedings of the Workshop on Microwave-Absorbing Materials for Accelerators, CEBAF, 1993.

[28] C. Bearzatto, M. Bres, G. Faillon, *Advantages of Multiple Beam Klystrons*, ITG Garmisch-Partenkirchen, May 4 to 5, 1992.

[29] R. Palmer, *Introduction to Cluster Klystrons*, Proceedings of the International Workshop on Pulsed RF Power Sources For Linear Colliders, RF93, Protvino, July 1993, p. 28.

[30] A. Beunas, G. Faillon, *10 MW/1.5 ms, L-band Multi-beam Klystron*, Proc. Conf. Displays and Vacuum Electronics, Garmisch-Partenkirchen, Germany, April 29-30 1998.

[31] A. Beunas, G. Faillon, S. Choroba, A. Gamp, *A High Efficiency Long Pulse Multi Beam Klystron for the TESLA Linear Collider*, DESY TESLA-01-01, 2001.

[32] W. Bothe, *Pulse Generation for TESLA, a Comparison of Various Methods*, DESY TESLA-94-21, 1994.

[33] H. Pfeffer, C. Jensen, S. Hays, L. Bartelson, *The TESLA Modulator*, DESY TESLA-93-30, 1993.

[34] D. A. Edwards (ed.), *The TESLA Test Facility LINAC-Design Report*, DESY TESLA-95-01, 1995.

[35] H. Pfeffer, L. Bartelson, K. Bourkland, C. Jensen, Q. Kerns, P. Prieto, G. Saewert, D. Wolff, *A Long Pulse Modulator for Reduced Size and Cost*, presented at the 21st Int. Power Modulator Symposium, Costa Mesa, CA, June 1994.

[36] H. Pfeffer, L. Bartelson, K. Bourkland, C. Jensen, P. Prieto, G. Saewert. D. Wolff, *A Second Long Pulse Modulator For TESLA Using IGBTs*, Proc. 5th EPAC, Sitges 1996, p. 2585.

[37] K.P. Juengst, G. Kuperman, R. Gehring, *SMES Based Power Modulator - Status Dec. 2000*, Reports of Forschungszentrum Karlsruhe, FZKA 6568, Jan. 2001.

[38] H.-J. Eckoldt, *Pulse Cables for TESLA*, DESY TESLA-00-35, 2000.

[39] H.-J. Eckoldt, N. Heidbrook, *Constant Power Power Supplies for the TELSA Modulator*, DESY TESLA-00-36, 2000.

[40] M. Liepe, S. N. Simrock, *Adaptive Feed Forward for Digital RF Control System at the TESLA Test Facility*, Proc. 6th EPAC, Stockholm 1998, p. 1735.

[41] M. Hüning, S. N. Simrock, *System Identification for the Digital RF Control at the TESLA Test Facility*, Proc. 6th EPAC, Stockholm 1998, p. 1732.

[42] S. N. Simrock, I. Altmann, K. Rehlich, T. Schilcher, *Design of the Digital RF Control System for the TESLA Test Facility*, Proc. 5th EPAC, Sitges 1996, p. 349.

[43] S. N. Simrock, T. Schilcher, *Transient Beam Loading based Calibration of the Vector- Sum for the TESLA Test Facility*, Proc. 5th EPAC, Sitges 1996, p. 1866.

[44] B. Aune et al., *Superconducting TESLA Cavities*, Published in Phys.Rev.ST Accel.Beams 3:092001, 2000.

4 Injection Systems

4.1 Introduction

The injection system must provide the electrons and positrons for the beams of the two linacs. The low-energy beams must be accelerated to 5 GeV before being first injected into damping rings to reduce their emittances (chapter 5), after which they are sent through bunch compressors (chapter 6) before injection into the main linacs.

The electron linac will be supplied with beam from three separate injectors, depending on the mode of operation:

- a polarised electron gun for the collider;

- a laser driven RF gun for the collider;

- a laser driven RF gun for the free electron laser (FEL, section 9.3).

Although the polarised injector is intended as the primary source for the collider, the RF gun can be used as a commissioning gun and as a backup to the polarised source: this is particularly prudent given the additional complexity and R&D required for the polarised gun, whereas the RF gun (unpolarised) source is essentially a copy of the TTF gun. The use of two different RF guns for the collider and FEL is a result of the different beam characteristics for optimal performance of the two modes of operation.

The three electron sources share a common superconducting electron injection linac (based on the main linac design, see chapter 3) for acceleration to 5 GeV. For convenience, the beams from the three sources are injected into the 5 GeV linac at a common nominal energy of 500 MeV.

The positron source is based on the concept of high-energy photon conversion into e^+e^- pairs in a thin rotating target. This scheme has the advantage of a low heat load on the target and a relatively high capture efficiency. The photons are generated by sending the high energy electron beam (150–250 GeV) through a long planar undulator magnet placed upstream of the interaction point. The generated positron beam has a large longitudinal and transverse emittance, and solenoids are required for focusing; this precludes the use of a superconducting accelerator, and normal-conducting copper cavities must be used. The copper cavities can also withstand the relatively high particle losses expected in the region. An adiabatic matching device adapts the phase space of the beam emerging from the target to the acceptance of the solenoid focused linac. After acceleration to 250 MeV, the positron beam is further accelerated in a

superconducting linac (the positron injection linac) to an energy of 5 GeV. Replacing the planar undulator magnet by a helical undulator will open up the possibility of generating polarised positron beams.

It is inconvenient to use the high energy electron beam for positron production during the commissioning and initial 'tuning' phase of the positron linac. Therefore, for tuning purposes it is planned to construct an *auxiliary* low intensity positron source, based on a 500 MeV electron beam striking the same target. The electron beam is generated from a source of the same type used for the main electron injector. This source (without the conversion target) could also be used in an alternative commissioning scheme, where the positron systems would be operated with electrons (note that switching magnet polarities in the various sub-systems is also required for the e^-e^- and $\gamma\gamma$ collider modes of operation).

4.2 The Electron Injectors

Figure 4.2.1 shows the overall concept of the electron injector complex foreseen for TESLA. The three electron sources can be installed in tunnels at different depths below ground level, one above the other. Alternatively, the three injectors can be placed at the same depth with the main axis shaft leading to one injector and with tunnels connecting the injectors together. A pulsed bending magnet will be used to select which injector provides beam to the 5 GeV injector linac for a given pulse. Two of the electron injectors will require an additional dipole. Since beam quality is most critical for the FEL, the FEL injector will be placed on the same axis as the linac. The injectors will be separated from the injector linac tunnel by an access shaft which will allow equipment installation for the linac. Access for installation and maintenance of the injectors will be via the common shaft at the gun end.

All klystrons will be housed together in a suitable location outside of the tunnel. Because of the critical nature of the injector operation, several additional back-up klystrons will also be installed, allowing fast switching in the event of a failure.

4.2.1 Unpolarised injector

4.2.1.1 RF gun and booster cavity

The advances in the field of laser driven RF guns make them attractive candidates for the unpolarised electron source. The TTF photoinjector gun [1] serves as a basis for the TESLA gun, and consists of a normal conducting 1-1/2 cell L-band standing wave cavity operated in TM_{010} mode. Solenoidal focusing is used to provide emittance compensation against the detrimental effects of space charge [2]. A high cathode gradient (35 MV/m) is needed to ensure good beam quality; this gradient is achieved by powering the gun with a 4.5 MW klystron, resulting in an output energy of approximately 4 MeV.

The TTF gun uses a Cs_2Te photocathode, which has a high quantum efficiency (> 1%) and long life-time (> 1000 h) [3]. The life-time is critically dependent on
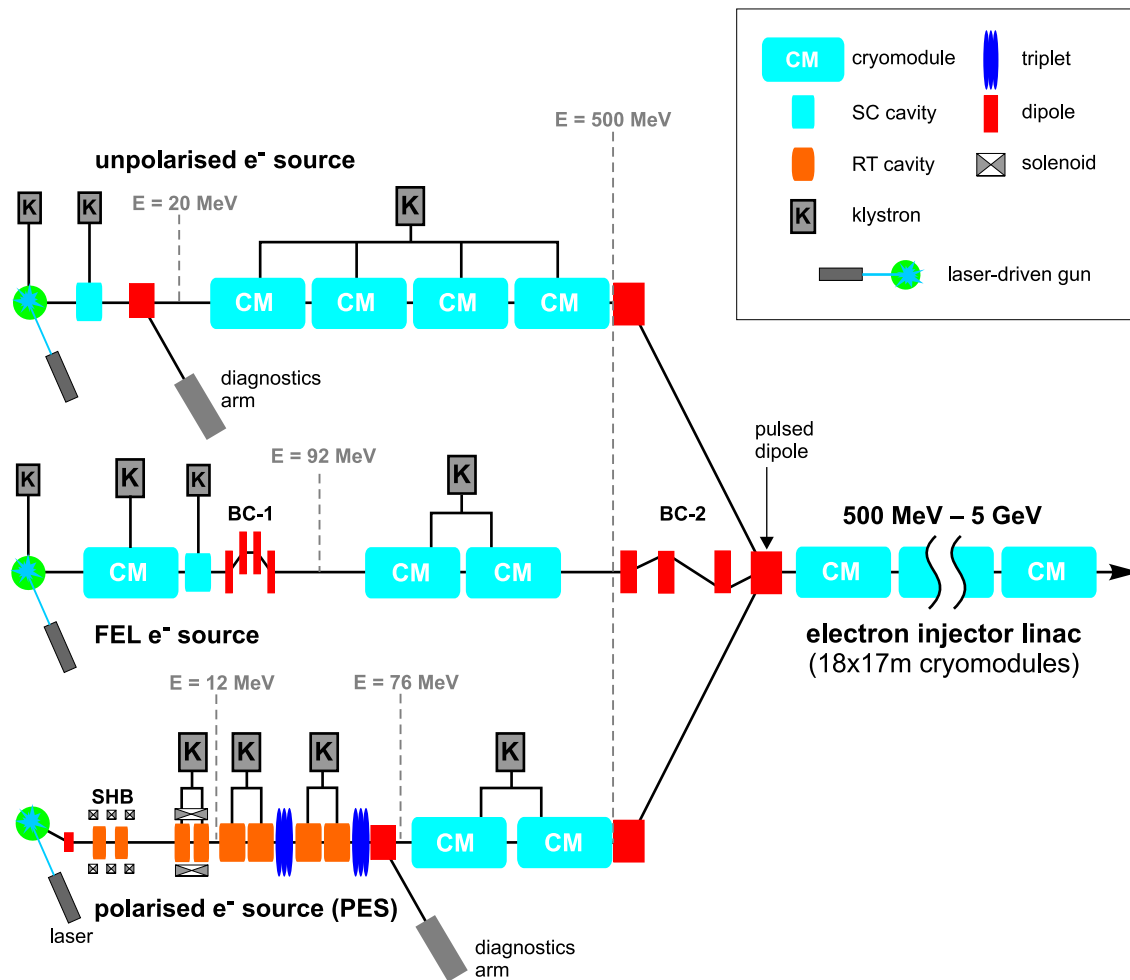
Figure 4.2.1: *Schematic of the electron injector complex (see relevant sections for details). Note that not all components are shown.*

the vacuum quality inside the gun, and so a photocathode preparation and 'load-lock' system is necessary to maintain ultra-high vacuum conditions while changing cathodes. Such systems have already been developed for TTF [4]. The laser required to provide the beam time structure for TESLA has also been developed for the TTF linac and is described below.

Similar to the TTF scheme, the electrons leaving the gun are are 'boosted' to an energy of 20 MeV by a single superconducting (SC) 9-cell cavity. The booster cavity needs a dedicated klystron of relatively low power ($< 200\,\text{kW}$). A low level RF control system using digital signal processors has been developed at TTF to maintain the phase and amplitude constant during the 1 ms pulse. The gun-booster assembly will be separated from the rest of the injector by a short dipole spectrometer which will allow the quality of the 20 MeV beam to be checked when necessary.

The TTF gun provides symmetric normalised horizontal and vertical emittances of

Parameter	TESLA 500	TESLA 800
wavelength	<270 nm	
Train rep. rate	5 Hz	3 Hz
Pulse Train Structure:		
Pulse train length	950 μs	860 μs
No. of pulses per train	2820	4886
Pulse spacing	337 ns	176 ns
Pulse energy	3 μJ	2 μJ
Pulse length	10 ps (sigma)	
Spot radius on cathode	3 mm (flat top)	
Synchronization	to reference RF signal	
Phase stability	< 1 ps (rms)	
Energy stability	< 5 % (rms)	
Control	fully remote	
Maintenance downtime	<1 %	

Table 4.2.1: *Basic specifications of the laser system for the unpolarised electron source. The differences in the pulse train structure for both TESLA-500 and TESLA-800 are shown.*

typically 10 mm mrad at 4 nC; this exceeds the required value for the vertical emittance at the interaction point by almost two orders of magnitude, and thus a damping ring is required. A potential alternative 'flat beam' gun is currently under study, which might provide asymmetric beams with sufficiently low vertical emittance to remove the need for the electron damping ring, or at least simplify it. Some details can be found in [5].

4.2.1.2   Laser for the unpolarised RF gun

The laser system for the unpolarised source is based on the photoinjector laser system used at the TTF. A description of the laser and a discussion of the experience with its operation can be found in [18]. Basic specifications of the TESLA laser system are listed in table 4.2.1.

An important feature of the laser system is the generation of a stable ∼1 ms long train of UV laser pulses synchronized with the RF of the accelerator. Currently available lasers can produce the required bunch charge when used in combination with a Cs_2Te-photocathode with a quantum efficiency of ∼1%. At TTF, such cathodes have been operated for several thousands of hours with a stable quantum efficiency of 0.5 %. With this number, a single UV laser pulse energy in the μJ-range has to be achieved, which the TTF laser can already supply.

The laser is based on flashlamp pumped Nd:YLF rods lasing at 1047 nm. This material has a long fluorescence lifetime, high induced emission cross-section, and very small thermal lensing — all of which are favorable for long pulse trains. A mode-
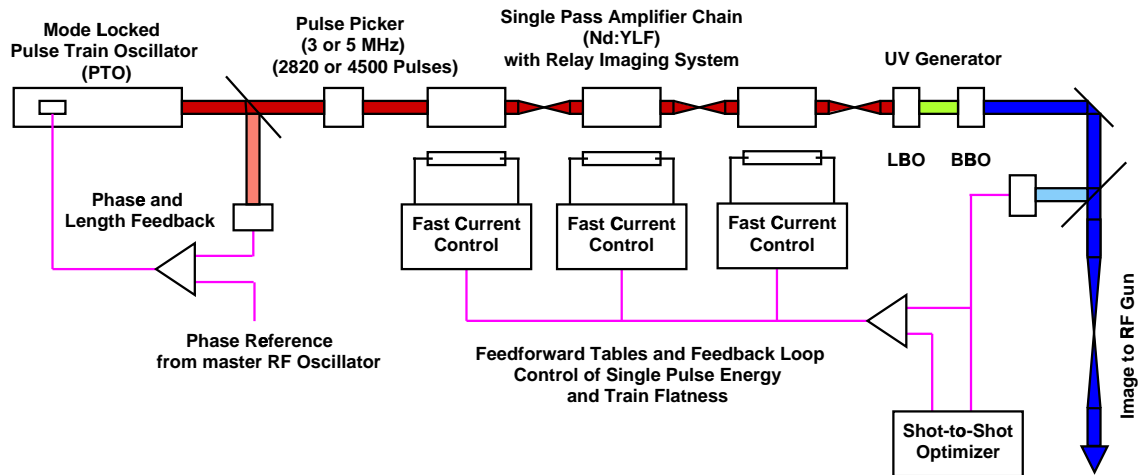
Figure 4.2.2: *Schematic of the laser system for the unpolarised RF gun source.*

locked pulse train oscillator (see figure 4.2.2) synchronized with the reference RF signal generates a pulse train with a suitable multiple of the required pulse train frequency (e.g. 30 MHz). A Pockels-cell based pulse picker running at 3 MHz for TESLA-500 (5 MHz for TESLA-800) forms the required pulse train. At TTF, a Pockels-cell is being operated at 2.25 MHz, and 9 MHz is in preparation. The train is amplified by a single pass amplifier chain to 150 μJ per pulse, corresponding to an average laser beam power of 2 W. The UV wavelength (262 nm) is generated with two non-linear crystals (e.g. LBO and BBO). The conversion efficiency is in the range of 10 %, and an energy stability in the UV of ±5 % (rms) is achievable. The bandwidth of Nd:YLF is sufficiently large to obtain a pulse length of 10 ps. The laser system will be fully remote controlled. At TTF, the photoinjector laser system has achieved an availability close to 99 %.

4.2.1.3 The 500 MeV pre-accelerator linac

Acceleration to 500 MeV takes place in four TTF type accelerator modules, each containing eight 9-cell cavities. The modules are driven by a single 10 MW klystron operating well below its maximum power capacity. The use of four modules implies a very moderate accelerating gradient for the pre-accelerator ($\sim$ 15 MV/m) in comparison with the main linac[1].

4.2.2 Polarised electron injector

A specific study for a TESLA polarised electron gun has not yet been carried out. The design for TESLA gun is therefore based on the parameters of the gun proposed for

---

[1]It should be noted that the choice of using four 12 m long TTF-like modules in the injection system design is not crucial, and they could easily be replaced by three 17 m modules of the standard main linac type (section 3.3)

Parameters	units	TESLA	NLC
Gun bunch charge	nC	4.5	
Bunch FWHM at gun	ns	2	0.7
Peak current	A	2.25	6.4
Cathode bias voltage	kV	-120	
Edge emittance	mm·mrad	8	
Beam radius	mm	12	
Envelope angle	mrad	10	
Bunch # per pulse		2820	90
Bunch spacing	ns	337	1.4
Pulse length	μs	950	0.13
Repetition rate	Hz	5	120

Table 4.2.2: *Specifications for TESLA and NLC polarised electron source.*

the NLC project [8], which is specified to deliver approximately the same bunch charge (table 4.2.2).

The TESLA time structure is quite different from the NLC: a specifically developed laser is required for the longer macropulse. We have assumed an initial bunch length of 2 ns rather than 700 ps for NLC. The transverse emittance is assumed to be the same which is a conservative assumption due to the smaller TESLA peak current. The longer initial bunch excludes the use of the NLC scheme for the prebunching section: therefore prebunching cavities of a lower frequency are chosen which follow the design for the S-Band collider Test Facility injector, described in [20].

4.2.2.1 Polarised electron gun

Polarised electrons are produced by illuminating a GaAs cathode with circularly polarised laser light. GaAs photocathodes require ultra-high vacuum conditions ($< 10^{-11}$ mbar) which are not compatible with high gradient RF gun operation. Although work is in progress to develop a polarised RF gun, we will consider here only a polarised gun based on the technology developed for SLC [7] and under further development for NLC [8].

The TESLA gun is operated with 1 ms long high voltage pulses of 120 kV with a repetition rate of 5 Hz. The accelerating field is 1.8 MV/m, the perveance $0.3 \, \mu$A/V$^{3/2}$. The strained-lattice GaAs cathode has a large surface area of 3 cm^2, and is illuminated by circularly polarised laser light of 840 nm wavelength.

The gun is equipped with a load-lock system which allows the cathode to be retracted while maintaining the ultra-high vacuum in the gun. To simplify the load-lock system, an inverted insulator geometry is foreseen [9].

To avoid damage of the cathode by ion bombardment, the dark current must be kept as low as possible; this requires low fields at the electrodes, and a careful processing of the gun. The SLC gun operates at 120 kV with a dark current of less than 50 nA, and the highest field on the electrodes is 7 MV/m [7]. The TESLA gun will be operated at

a gradient of only 1.8 MV/m (as discussed for the NLC gun) which should significantly reduce the dark current.

The low accelerating gradient limits the extractable beam current due to space charge effects. The current can be estimated using the Child-Langmuir law: a typical perveance of $0.3 \, \mu A/V^{3/2}$ yields a current of 12.5 A at 120 kV.

A more severe limitation specific to GaAs-type cathodes is the so-called 'cathode charge limit', which is in fact a current density limit [10]. The limitation is typical for semiconductor cathodes with a negative electron affinity surface. In order to achieve a high electron extraction probability, an alkali coating is applied to the surface of the GaAs crystal[1]. This limit can be estimated using SLC data [12]: the SLC gun has a current density limit of $3.3 \, A/cm^2$. For the TESLA cathode with a surface area of $3 \, cm^2$, the extractable current is limited to 10 A which is below the previous limit set by the perveance.

With a bunch charge of 3.2 nC (2.2 nC for TESLA 800), a bunch length of at least 320 ps is required to keep the peak current below the 10 A limit. A bunch length of 2 ns has been chosen to ease the design of the laser system.

For multibunch operation, an additional effect related to the cathode charge limit becomes important. The effect causes a considerable reduction in bunch charge for pulse trains with very small bunch spacing. Experiments at the SLC have shown that the recovery time of the cathode is between of 10 to 100 ns, depending on the cathode thickness [7]. Fortunately, the bunch spacing at TESLA is large, 337 ns (189 ns for TESLA 800), so that the cathode can easily recover between bunches.

A high degree of polarisation is required to fully explore the physics potential of the collider. At SLC, 80 % polarisation with a strained lattice GaAs cathode has been achieved, but with a quantum efficiency of only 0.1% [13]. The quantum efficiency determines the required laser power, and hence has a direct impact on the design of the laser system. Maintaining good quantum efficiency requires a careful control of the vacuum, which should be kept below $10^{\cdot-11}$ mbar at all times. Regular coating of the cathode by cesium may also be necessary.

In the NLC proposal, the gun is placed at a 20° angle to the injector axis, an arrangement that we will also adopt. The arrangement has several advantages: shielding of the cathode from reverse dark current produced by the downstream cavities; allowing installation of a second gun (a backup PES or a thermionic grid gun); and allowing space for a polarimeter.

4.2.2.2   Polarised gun laser

Most polarised electron sources use Ti:Sapphire lasers with a wavelength around 800 nm. The lasers have a sufficient bandwidth to tune the wavelength to optimize the electron beam polarisation.

TESLA requires a long laser pulse train of 1 ms, consisting of several thousand pulses with an energy of $\sim 5 \, \mu J$ per pulse. A laser system delivering such a pulse structure is commercially not available and requires considerable R & D. Presently, a

---

[1]A discussion of the theory of the effect can be found in [11].

Parameter	TESLA 500	TESLA 800
Wavelength	780 to 850 nm	
	tunable to < 10 nm	
Train rep. rate	5 Hz	3 Hz
Polarisation	circular	
	switchable	
Pulse Train Structure:		
Pulse train length	950 μs	850 μs
No. of pulses per train	2820	4500
Pulse spacing	337 ns	189 ns
Pulse energy	4.6 μJ	3.2 μJ
Pulse length	700 ps to 2 ns (sigma)	
Spot radius on cathode	10 mm (flat top)	
Synchronization	to reference RF signal	
Phase stability	< 200 ps (rms)	
Energy stability	$< 5\%$ (rms)	
Control	fully remote	
Maintenance down time	$<1\%$	

Table 4.2.3: *Basic specification of the laser system for the polarised electron source. The differences in the pulse train structure for TESLA-500 and TESLA-800 are shown.*

laser system for the photoinjector test stand at DESY-Zeuthen is under development [14], which will serve as a test bed for the polarised gun laser. The basic specification of the laser system is given in table 4.2.3.

There are several disadvantages of the choice of Ti:Sapphire with respect to the long TESLA pulse train. The life-time of the upper laser level is only 3.2 μs, and hence the pump energy can only be stored for a short fraction of the pulse train. In addition, flashlamp pumping is not efficient. Consequently it is necessary to provide a complete laser system to pump the Ti:Sapphire for every bunch of the train. The pump lasers will be very similar to the laser for the unpolarised source: a mode-locked Nd:YLF laser with the required pulse train structure will be doubled in frequency to produce the green wavelength necessary for pumping.

Thermal properties — like thermal lensing — are also not favorable for Ti:Sapphire. Its strong thermal lensing will lead to a variation of the focusing of the laser beam during the pulse train resulting in an undesired non-uniformity, which must be compensated.

Other laser materials which are tunable in the required wavelength range are Cr:LiCAF and Cr:LiSAF. They have the advantage of low thermal lensing and the possibility of pumping by flashlamps or laser diodes [15]. Mode locked Cr:LiSAF lasers and regenerative amplifiers have been successfully built [16], but high quality materials are still difficult to obtain. A laser based on Cr:LiSAF/Cr:LiCAF is discussed in the

proposal for the TTF laser system [17].

A third possibility under study is based on an energy upgraded version of the laser proposed for the unpolarised source (section 4.2.1.2): the second and third harmonic of the fundamental laser wavelength (1047 nm) is converted to 840 nm by optical parametric amplification.

4.2.2.3   Polarised electron pre-accelerator linac

The low energy electrons produced by the polarised source cannot be directly injected into superconducting cavities because solenoids are required for transverse focusing. The electrons are first accelerated in normal-conducting copper cavities until the divergence of the beam is small enough that solenoid focusing is no longer required. Because the gun produces a long initial bunch length (2 ns), a prebunching and bunching system is also required.

The injector linac for the polarised electron beam will include:

- a prebunching and bunching section;

- an accelerating section;

- a matching and analysing section; and

- two accelerator modules to reach 500 MeV.

The injection linac is described in more detail in [19].

The prebunching section

We use two sub-harmonic prebunching cavities (SHB) working at 1/12 and 1/3 of the injector linac frequency, i.e. 108 and 433 MHz respectively. Simulations with the PARMELA code have been performed, assuming an initially uniform longitudinal distribution[1] of charges with a length of 2 ns. The optimum modulating peak voltages of the 108 MHz and 433 MHz cavities were found to be 40 kV and 44 kV respectively. The bunches are compressed to ∼190 ps rms at the entrance to the second cavity, and to ∼50 ps rms at the buncher entrance.

The power requirements have been scaled from the data for the buncher cavity used in the low charge TTF injector [21]; this cavity operates at 217 MHz and can handle a 1 ms long RF macropulse. We expect a shunt impedance R_s=4.4 MΩ for the 108 MHz cavity and R_s=8.8 MΩ for the 433 MHz cavity. The required peak power is then 360 W and 220 W respectively.

The bunching section

The cavities for the bunching section have to withstand 1 ms long RF pulses and a 0.5% duty cycle, which implies severe thermal loads. Requirements for copper cavities having

---

[1]A Gaussian distribution does not significantly change the results.

Parameters	units	Type #1	Type #2
RF frequency	GHz	1.3	
Structure type		standing wave	
Dissipated power	MW	<4	
Aperture	mm	52	
Number of cells		5	17
Shunt impedance	MΩ/m	31.9	35.4
Accelerating gradient	MV/m	<14.8	<8.5
Length	m	0.576	1.96

Table 4.2.4:   *Main characteristics of the accelerating structures for the bunching section.*

Parameters	units	results
Energy	MeV	11.3
Charge	nC	3.7
Phase extension (rms)	deg	5.3
Bunch length (rms)	mm	3.4
Energy spread (rms)	keV	45
Normalised emittance (rms)	mm mrad	42.5
Beam size σ_x	mm	2.6
Beam angular spread σ_{xp}	mrad	0.7

Table 4.2.5: *Summary of PARMELA simulations results at the buncher exit.*

high gradient and high average power also appear in the design of the positron pre-accelerator (PPA) (section 4.4), where new RF cavities (so-called CDS structures [34]) have been proposed. They have a high shunt impedance and can dissipate 30 kW/m. In addition they have a large iris aperture. The characteristics of the cavities used here are summarised in table 4.2.4.

The bunching section comprises two 5 cell cavities (type #1, see table 4.2.4), separated by a distance of $\lambda/2$ (115.3 mm) and sharing the power of one 10 MW klystron. The cavities are capable of producing up to 14.8 MV/m, but to provide a safety margin, simulations have been made using only 12 MV/m in each cavity.

In the simulations we assume for simplicity a 0.75 m long drift space between the source exit and the first prebuncher cavity, with one solenoidal lens in the middle. The lens is used to focus the beam into the first prebunching cavity.

The fields are optimised to achieve a minimum transverse emittance (figure 4.2.3). The magnetic field starts from about 50 Gauss after the first prebuncher, increases linearly to about 130 Gauss at the buncher entrance, where it then increases sharply to a value of 500 Gauss and stays constant over the length of the two buncher cavities. Steep transitions are necessary to fulfil the Brillouin conditions for laminar flow. The transitions are created using magnetically shielded solenoids. Simulation results obtained with PARMELA at the buncher exit, are summarised in table 4.2.5.
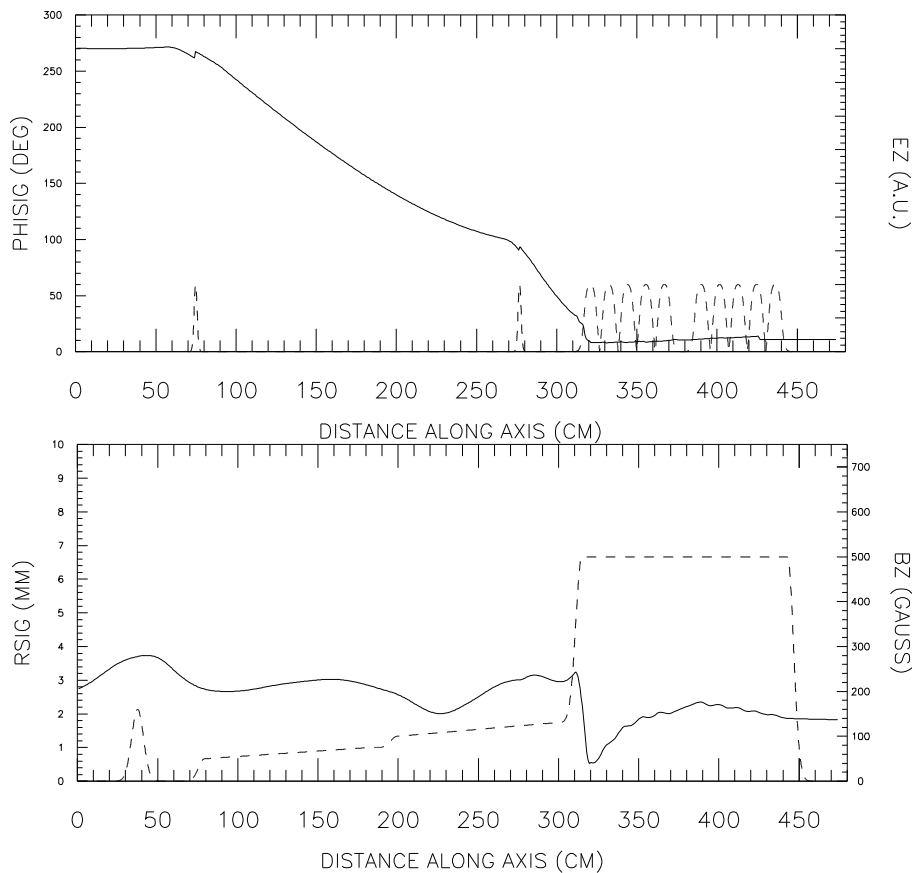
Figure 4.2.3:   *RMS beam radius and bunch length variation along the prebunching and bunching sections. The axial electric field (top) and the magnetic focusing field (bottom) are shown.*

Acceleration prior to injection into the SC linac

The choice of beam energy at the entrance of the first accelerator module of the injector linac is defined by the (non-normalised) beam emittance, which must be small enough to allow the beam to be easily transported through the module. As a goal, we have chosen the TTF injector normalised emittance of 20 mm·mrad for 8 nC bunches at 20 MeV, corresponding to a (un-normalised) emittance of 0.5 mm mrad at injection into the first cryomodule.

After the buncher, the beam energy is ~12 MeV. To provide the necessary acceleration, we will use the 17-cell cavities (table 4.2.4), which provide more energy than the 5-cell ones. One pair of cavities — powered with one standard 10 MW klystron — can give an energy gain of 32 MeV. Table 4.2.6 shows the expected beam emittance after one, two or three such units. One unit, resulting in a beam energy of 44 MeV, is sufficient to adiabatically damp the initial emittance to below the required 0.5 mm mrad (un-normalised): using two such pairs (76 MeV) provides a large and sufficient margin.

	E (MeV)	Norm. emittance	emittance
TTF injector	20	20.	0.5
proposed buncher	12	42.5	1.74
+ 1 klystron	44	42.5	0.49
+ 2 klystrons	76	42.5	0.28
+3 klystrons	108	42.5	0.20

Table 4.2.6: *Compared emittance (in mm mrad) of the TTF injector and of the proposed linac for beams of increasing energy.*

A spectrometer arm will be installed between the room temperature section and the SC linac so that the former can be independently operated and tuned. Two triplets are required for beam matching into the SC linac. A triplet is also necessary between the pairs of type #2 PPA cavities.

The 500 MeV superconducting linac

To achieve the required energy of 500 MeV, the SC linac has to provide 424 MeV to complement the 76 MeV from the room temperature section. Two standard linac cryomodules operated at a conservative gradient of 17.8 MV/m are used. One 10 MW standard klystron is sufficient to power both modules (see figure 4.2.1).

4.2.3   Electron source for the free electron laser (FEL)

The FEL source is treated in section 9.3. We mention it here only for completeness. It employs a 1-1/2 cell RF gun producing a 6.6 MeV beam which is subsequently injected into an accelerator module. The beam which exits the module at 155 MeV is slightly decelerated in a third harmonic (3.9 GHz) superconducting cavity which serves to correct the non-linear energy distribution of the beam. The FEL source also requires the use of a magnetic bunch compressor at an energy of 140 MeV as well as a further compressor at 500 MeV. To provide space for the compressors, only 3 modules are used in the FEL injector. The average gradient required in the last two modules is 25 MV/m. The 500 MeV bunch compressor will be based on the design used in the TTF linac.

4.2.4   The 5 GeV electron injector linac

The common injector linac accelerates the beam energy from 500 MeV to the damping ring energy of 5 GeV. It is a short version of the TESLA main linac and uses the same technology described in chapter 3. The energy gain of 4.5 GeV will be provided by 18×17 m modules (section 3.3) running at a gradient of $E_{acc} = 20$ MV/m and powered by six 10 MW klystrons. If one klystron fails, the linac can still be operated by increasing the gradient in the remaining sections (15 modules driven by 5 klystrons, corresponding to 24 MV/m).

For the FEL beam the injector linac is operated at lower gradient. We presently assume an FEL beam energy of 2.5 GeV at the injector linac exit (E_{acc}=8 MV/m), but there is a large flexibility to adjust this energy if desired.

The focusing is provided by a FODO structure with two accelerator modules per cell (one quadrupole in every module). The phase advance is 45° for the collider beam and up to about 100° per cell for the FEL beam.

4.3   Positron Source

A fundamental intensity limit for conventional positron sources is given by the thermal stress in the conversion target due to the energy deposition of the primary electron beam. For TESLA the target can be rotated within the long bunch train. With a target velocity of 50 m/s the heat load of about 100 bunches contributes to the thermal stress at a given position on the target. Table 4.3.1 compares the design parameters of TESLA with parameters reached at the SLC positron source, which has the highest intensity to date. The SLC source operates close to the stress limit of the target, and an extension of this technology by the required two orders of magnitude in intensity seems unrealistic. Therefore a new concept based on the conversion of high-energy undulator radiation in a thin target has been developed [22, 23]. The scheme also allows the possibility to produce polarised positrons; but since the technological demands for a polarised source are much higher than for an unpolarised source, only the latter will be considered for the initial TESLA run. The polarised source is considered as a possible upgrade to the machine at a later date.

parameter	SLC	TESLA
No. of positrons per pulse	$(3\text{--}5) \times 10^{10}$	5.6×10^{13}
No. of bunches per pulse	1	2820
pulse duration	3 ps	0.95 ms
bunch spacing	8.3 ms	337 ns
repetition frequency	120 Hz	5 Hz

Table 4.3.1: *Comparison of TESLA and SLC positron source parameters.*

4.3.1   General layout

A schematic of the source is shown in figure 4.3.1. The source is designed to produce twice as many positrons as required. In contrast to the original proposal in the CDR [6], the high-energy electron beam upstream of the interaction point (IP) is now used to generate high-energy photons in an undulator section positioned just downstream of the main linac. The original concept of using the spent electron beam (i.e. after collision) placed too many constraints on the design of the extraction line, and in particular suffered from unacceptably high distributed particle losses. Moving the e^+
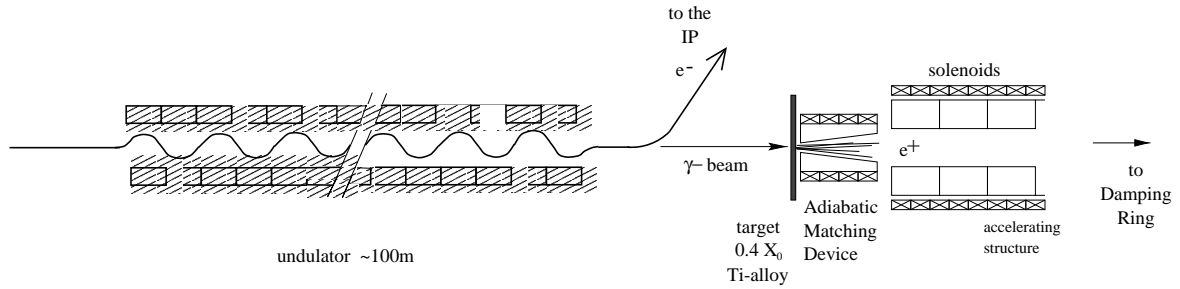
Figure 4.3.1: *Sketch of the positron source layout.*

source upstream of the IP has significantly simplified the extraction line and reduced the associated losses (see section 7.6). In addition, using the very high quality electron beam from the linac as opposed to the severely disrupted beam after the IP has increased the likelihood of realising a polarised positron source. The disadvantages of the location in front of the IP are that extra space and a positron transfer line to the other side of the interaction point (detector) are required. The undulator also slightly degrades the quality of the incoming electron beam, but the effects are considered acceptable.

The geometry of the source and the electron optics has been designed to accommodate the polarised source upgrade. For polarised positrons, the divergence of the high-energy photons from the helical undulator must be dominated by the $1/\gamma$ characteristic angle of the radiation, and only have a small contribution from the electron phase space. With the opening angle of the photons fixed by the electron beam energy, the beam size on the target is then only a function of distance. With a $250\,\mathrm{GeV}$ electron beam, corresponding to an angle of $1/\gamma \approx 2\,\mu\mathrm{rad}$, a drift length to the target of $314\,\mathrm{m}$ is required to achieve the necessary target beam size of $0.7\,\mathrm{mm}$ (see section 4.3.7).

With the geometry and electron optics fixed by the polarised source, the unpolarised source requires a rather weak, long planar undulator $(K \leq 1)$[1] to keep the $0.7\,\mathrm{mm}$ beam size at the target. The photons are used to produce electron-positron pairs in the thin conversion target. The conversion of photons — rather than electrons as in a conventional source — leads to a small optimal target thickness of 0.4 of a radiation length (X_0). The conversion efficiency in a thin target depends only weakly on the target material: thus a low Z material such as titanium with a high specific heat capacity can be chosen. An additional advantage of the thin target is the smaller multiple-scattering which results in a higher capture efficiency. Both effects help to reduce the heat load on the target. The target has to rotate with a high velocity in order to withstand the long beam pulse.

The capture optics behind the target is of a conventional design. Since the positrons

---

[1] The K-value of an undulator is defined as: $K = eB\lambda_u/(2\pi m_e c)$, where B indicates the amplitude of the magnetic field and λ_u the undulator period. The K-value determines the spectral characteristics of the device and the opening angle of the radiation. For $K > 1$ the opening angle is K/γ.

have a broad distribution of transverse and longitudinal momenta, they must first be accelerated in RF cavities embedded in a solenoid field. The acceptance of a solenoid channel is characterised by a large transverse size and a small divergence, while the positrons emerging from the target have a small transverse size and a large divergence. To match the positrons to the acceptance of the solenoid, an adiabatic matching device (AMD) is used. It consists of a solenoid field which starts with a high initial field and tapers down adiabatically to the constant end field. After the AMD the positron beam will be captured and pre-accelerated to $\approx 250\,\mathrm{MeV}$ in the normal conducting positron pre-accelerator (PPA). The beam is then transported through a transfer line under the detector hall, to the superconducting positron injector linac, where it is accelerated to $5\,\mathrm{GeV}$ and injected into the damping ring (chapter 5).

The safety factor of two in the positron production rate is valid for $250\,\mathrm{GeV}$ electron beam energy. When operating at a lower energy (i.e. lower centre of mass energy at the IP) this margin is reduced due to the strong dependence of positron production on photon energy. Without modifications, the source can be used down to about $160\,\mathrm{GeV}$ (just below the top quark pair production threshold) without a significant intensity drop (the yield at this energy is ~ 1). In order to recover a high luminosity at even lower energy, e.g. at the Z^0 resonance, a scheme can be used in which the first part of the main linac ($\approx 50\,\mathrm{GeV}$) accelerates the beam used for collisions, while the remainder ($\approx 200\,\mathrm{GeV}$) accelerates the drive beam for the positron source. This option requires an additional drive beam injector and a $\sim 50\,\mathrm{GeV}$ transfer line.

In the following sections, the various components of the positron source will be discussed in more detail.

4.3.2   Permanent magnet planar undulator

With a K-value of about 1 the spot size of the photon beam on the target is $0.7\,\mathrm{mm}$, large enough to keep the thermal stress in the target low and small enough to obtain a high capture efficiency of the optics behind the target. The advantage of the planar undulator over the helical undulator required for the polarised positrons is the easier technology (permanent as opposed to superconducting magnets) and the accessibility from the side (important for field measurements, beam diagnostics pumping etc.).

The gap size of the undulator (in terms of nominal electron beam size) must be larger than the apertures defined by the downstream halo collimation system in the beam delivery system ($13\sigma_x \times 80\sigma_y$, section 7.5). Table 4.3.2 lists parameters of permanent magnet undulators with varying gap size and $K = 1$. With an elliptical vacuum chamber of half-gap $5\,\mathrm{mm\,(h)} \times 1.5\,\mathrm{mm\,(v)}$, the (normalised) aperture is $79\sigma_x \times 350\sigma_y$, significantly larger than the collimation aperture.

With a vertical gap size of $5\,\mathrm{mm}$ a field of $0.75\,\mathrm{T}$ can be reached. The corresponding energy of the first harmonics is $28\,\mathrm{MeV}$ and the required undulator length is $100\,\mathrm{m}$ in this case. Note that due to the higher harmonics of the undulator radiation a significant amount of positrons are produced with an energy larger than $28\,\mathrm{MeV}$.

gap [mm]	λ_u [cm]	B_{max} [T]	E_1 [MeV]
4.0	1.25	0.85	31.6
4.5	1.34	0.8	29.5
5.0	1.42	0.75	27.8

Table 4.3.2: *Parameters of the planar undulator.*

4.3.3   Influence of the undulator on the electron beam parameters

The main effect of the undulator on the electron beam is the mean energy loss of 1.2% (3 GeV) which has to be compensated by the main linac. The beam quality is deteriorated mainly in the longitudinal phase-plane by an increased energy spread of 0.15% as compared to 0.05% without the undulator [31].

The relative increase in horizontal transverse emittance from a perfect undulator is $\sim 3 \times 10^{-5}$ and can be ignored. Typical errors of the undulator magnets of $\Delta B/B = 1\%$, $\Delta\lambda_u/\lambda_u = 1\%$ and an rms rotation angle of 1 mrad lead to additional relative emittance contributions of $\sim 2 \times 10^{-3}$ and $\sim 1 \times 10^{-3}$ for the horizontal and vertical plane respectively [32].

4.3.4   Target

The positron production rate in the conversion target has been calculated with the code EGS4 [25] — a general purpose package for the Monte-Carlo simulation of electromagnetic showers. The optimum target thickness in terms of positron yield for a titanium alloy target is $0.4\, X_0$ (1.4 cm). The production rate in a titanium target is about 16% lower than in tungsten, but the higher heat capacity (by a factor of five) and the excellent mechanical properties of titanium allow much higher particle densities inside the target. The target has to rotate with a high velocity in order to avoid an overlapping of all bunches within one RF pulse. A velocity of about 50 m/s at the circumference of the target is necessary to spread out a single bunch train over a distance of 5 cm; this can be achieved with a target of 80 cm diameter rotating at 1210 revolutions per minute. The maximum heat load reached then corresponds to $\sim$100 bunches overlapping at the same location, giving a temperature rise of about 420°C. The diameter is chosen to evenly distribute the heat load over the entire circumference of the target over many 5 Hz pulses. The average heat load amounts to 5 kW. Cooling by radiation might be sufficient in the case of the large target wheel, but this needs further investigation. Cooling with water is possible with a vacuum feed-through based on a design from CERN [28], which uses differential pumping.

4.3.5   The adiabatic matching device (AMD)

The particles which emerge from the target have to be accelerated in a cavity embedded in a solenoid field for focusing: it is here that the final emittance and the efficiency of the positron source are defined. Because the multiple-scattering is reduced in a thin

target (compared to the thick target of conventional sources), the transverse momenta of the positrons emerging from the target are smaller, resulting in a higher capture efficiency. In order to match the phase space of the positron beam (characterized by a small spot size and a large divergence) to the acceptance of the solenoid (large spot size and a small divergence), a matching section is introduced between the converter target and the first accelerating cavity. The matching section consists of a so-called adiabatic matching device (AMD), a tapered solenoid starting with a high initial field and tapered adiabatically down to the constant end field. The acceptance of the system is matched to the acceptance of the damping ring so that no further particle losses occur in the ring itself.

Two mechanisms lead to an emittance growth of the positron beam in the matching device and hence to additional particle losses:

- emittance growth due to non-adiabatic fields; and

- bunch lengthening due to path length and velocity differences.

A solution for the particle motion in an adiabatically varying solenoid field has been found [29], from which the optimum on-axis field distribution for the matching device along the longitudinal coordinate z is given by:

$$B(z) = \frac{B_i}{1 + g \cdot z},$$

where B_i is the initial solenoid field and g the taper parameter. The condition for an adiabatic field variation is then given by $(gP)/(eB_i) \ll 1$ ($P =$ particle momentum). In order to fulfil this condition for particles with higher energy the taper parameter g has to be small: however, this means that the matching section becomes long, and the bunch lengthening becomes stronger. An optimum is reached with $g = 30\,\mathrm{m}^{-1}$ in the present design. An overall capture efficiency of 16% can be reached with an initial field of 6 T. Fields of up to 8 T have already be realised [30] and 10 T seems feasible: however, since the bunch train is long the production of a higher field with a pulsed device is more difficult, and a lower field seems to be more reasonable.

Table 4.3.3 lists the important parameters of the positron source.

4.3.6   Low intensity auxiliary source

For the commissioning of the various positron accelerator systems, a source which works independent of the main electron linac is desirable. An electron beam of 500 MeV is sufficient to produce a few per cent of the design positron current using the same thin titanium target and the capture optics of the high intensity source. The heat load on the target is high, but does not reach the limits discussed in [23]. The electron source is a copy of the main electron injector (see section 4.2).

It is foreseen to use the same gun as the (second) electron source when TESLA is operated as a $\gamma\gamma$ or e^-e^- collider. It should be noted that in these cases, a polarised electron source is required.

Undulator	
peak field	0.75 T
period length	14.2 mm
gap height	5 mm
γ-spot size on target	0.7 mm
photon beam power	135 kW
Target	
material	Ti-alloy
thickness	1.42 cm $(0.4 X_0)$
pulse temperature rise	420 K
av. power deposition	5 kW
Adiabatic Matching Device	
initial field	6 T
taper parameter	30 m^{-1}
end field	0.16 T
capture cavity iris radius	23 mm
General	
capture efficiency	16%
No. of positrons per electron	2
norm. e^+-beam emittance	0.01 m
total energy width	± 30 MeV
required D.R. acceptance	0.048 m

Table 4.3.3: *Overview of the positron source main parameters.*

4.3.7   Potential upgrade to a polarised positron source

The proposed positron source opens up the possibility to produce polarised positrons: circularly polarised photons produced by high-energy electrons in a helical undulator convert to polarised e^+e^- pairs in the target [22, 23]. However, the technological challenges of a polarised source are far more demanding than for the unpolarised source, and the polarised source is considered as a potential future upgrade.

In order to produce circularly polarised photons, a short period helical undulator of about 100 m length has to be used instead of the planar wiggler. Since only the on-axis photons are completely circularly polarised, off-axis photons have to be collimated; this requires that the photon beam spot size at the target is dominated by the natural opening angle of the radiation ($\sim 1/\gamma$). The distance between the undulator and the target has to be large (>150 m) to achieve the required target photon beam size (0.7 mm), and the electron beam divergence in the undulator has to be small compared to $1/\gamma$. The parameters of the helical undulator are demanding and have so far not been demonstrated. With a period length of 1 cm an on-axis field of 1.3 T has to be reached. The parameters can currently only be realised with superconducting technology at a gap radius of about 2 mm [33]. A detailed design of such an undulator with the required parameters is still to be done.

The collimation of a large fraction of the photons — necessary to increase the degree of polarisation — requires the development of high-power collimators. The average power deposition in the collimators can reach several $100\,\mathrm{kW}$. The polarisation of the circularly polarised photons is transferred to the electron-positron pairs during pair production. For the calculation of the processes in the target the EGS4 code has been extended [23]. The code includes polarisation effects for pair production, bremsstrahlung and Compton scattering. Simulation results indicate a maximum longitudinal positron polarisation of 45–60%.

4.4   Positron Injection System

The positron injection system consists of three sections:

- a normal conducting pre-accelerator which captures the positrons, separates them from the electrons and the photon beam, and accelerates them up to an energy of $250\,\mathrm{MeV}$;

- a long transfer line which guides the positrons below the experimental hall to the other side of the IP;

- a superconducting accelerator to bring the positrons to the damping ring energy of $5\,\mathrm{GeV}$.

The layout and the main results of the optimisation of the complete positron injection system are presented below. For further scientific and technical details of the design we refer to the detailed reports [34, 35].

4.4.1   Positron pre-accelerator (PPA)

The purpose of the PPA is to provide a maximum capture efficiency for that part of the emerging positron beam which is within the damping ring acceptance; this 'useful' part of the beam has an energy spread $\Delta E/E_f = \pm 6\%$ for the PPA output energy of $250\,\mathrm{MeV}$ and a phase spread $\Delta \varphi = \pm 7.5^o$ with respect to the PPA RF-frequency of $1.3\,\mathrm{GHz}$. The total normalised transverse e^+ beam emittance is limited by $\varepsilon_x < 0.036\mathrm{m}$, $\varepsilon_y < 0.036\mathrm{m}$, and $\varepsilon_x + \varepsilon_y < 0.048\,\mathrm{m}$ for the PPA and other parts of the injector. The capture efficiency is defined as the ratio of the number of positrons inside this acceptance to the total number of positrons escaping from the target.

The general layout of the PPA is shown in figure 4.4.1. The PPA is a standing-wave normal-conducting linac. The front end of the PPA consists of acceleration cavities embedded in a focusing solenoid. The first two cavities (figure 4.4.2) have a high accelerating gradient ($E_{acc} = 14.5\,\mathrm{MV/m}$), to reduce bunch lengthening, whereas the others have moderate gradients ($E_{acc} = 8.5\,\mathrm{MV/m}$) to reduce RF power consumption. Each cavity is powered by one standard TESLA $10\,\mathrm{MW}$ klystron through a single RF coupler (figure 4.4.2). An additional bunch length reduction is achieved by inserting the first cavity into the AMD by $\approx 60\,\mathrm{cm}$.
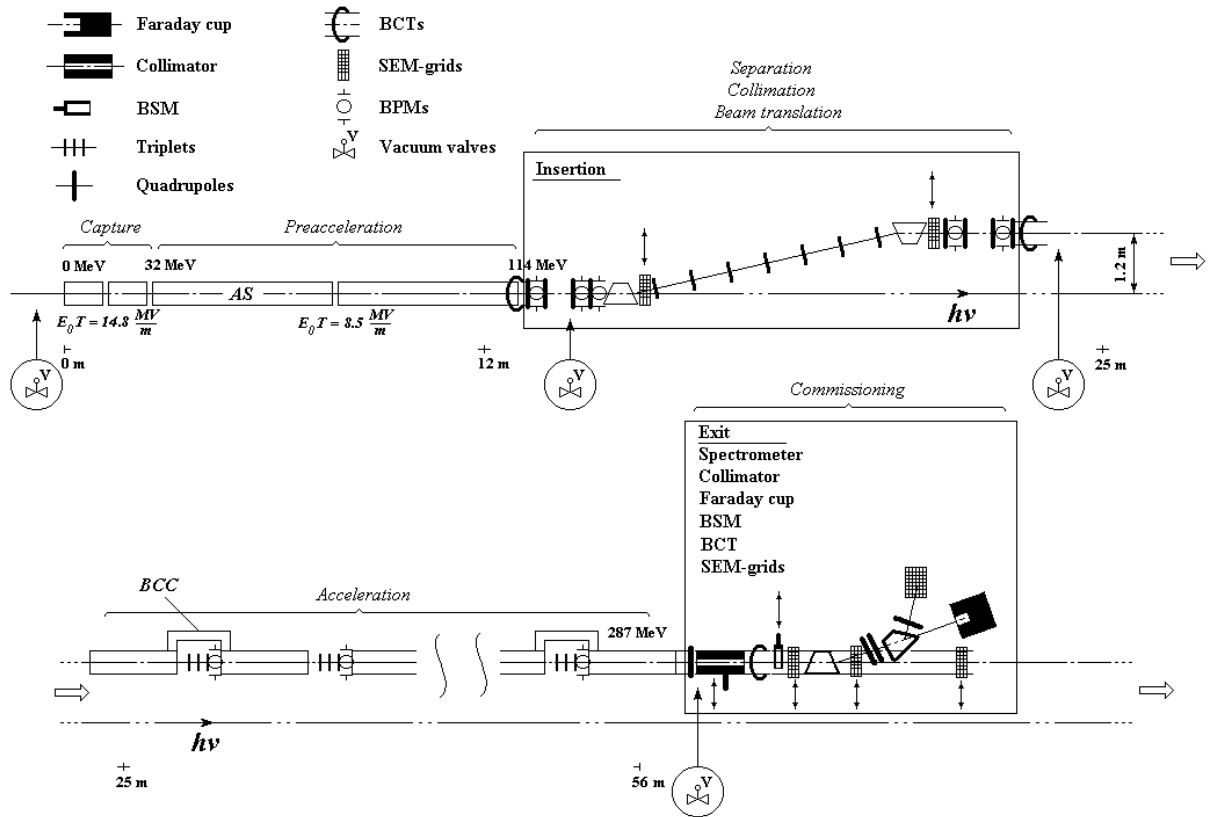
Figure 4.4.1: *Conceptual layout of the PPA.*

With the long RF pulse (950μs flat-top) and repetition rate of 5 Hz, the achievable gradients in the first and second cavity of the PPA are limited by RF power and heat load restrictions. Three dimensional thermal stress analysis indicates that stable and reliable cavity operation with a heat load of about 30 kW/m is possible, corresponding to an accelerating gradient $E_{acc} = 14.5$ MV/m [34, 36].

About 65% of the incoming positrons and 76% of the incoming electrons will be lost in the AMD and the first four cavities, resulting in an enhanced radiation level and additional heating.

Located downstream of the PPA (at a positron beam energy of 114 MeV) is a magnetic insertion to separate the positrons and the remaining electrons. The insertion makes a parallel translation of the PPA axis by a distance of 1.2 m; this provides a sufficient clearance for the photon beam and allows collimation of the positron beam. The insertion has a standard achromatic design with two bend dipoles and matching sections at both ends (figure 4.4.3). Non-linear chromatic effects are the dominant factors for the final beam quality when transporting the low energy beam with high relative energy spread [35]. The total positron losses in the separator (composed mainly of particles with a large momentum deviation) are estimated at ~8.4 % of the incoming
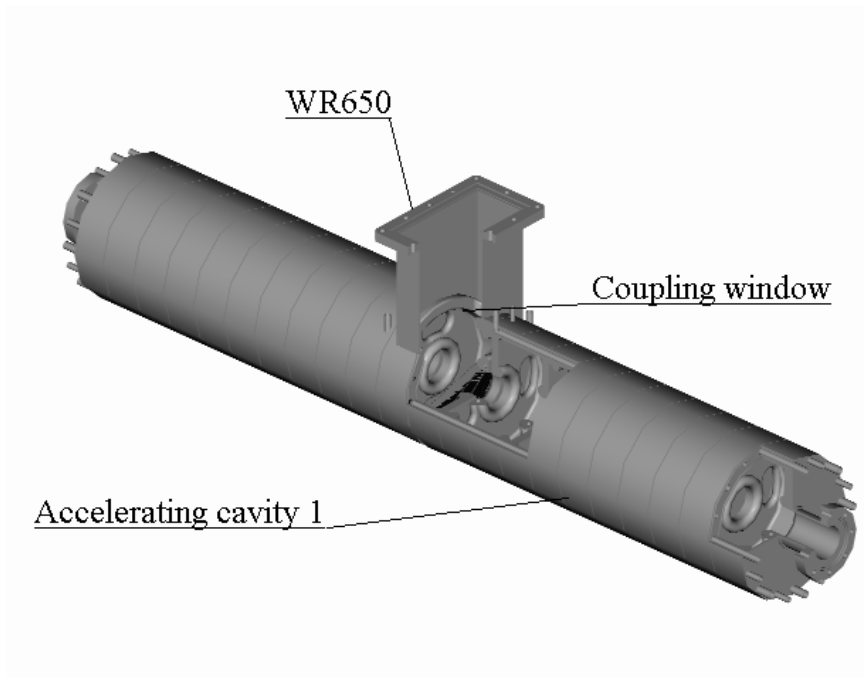
Figure 4.4.2: *Short accelerating cavity for the first part of the PPA.*
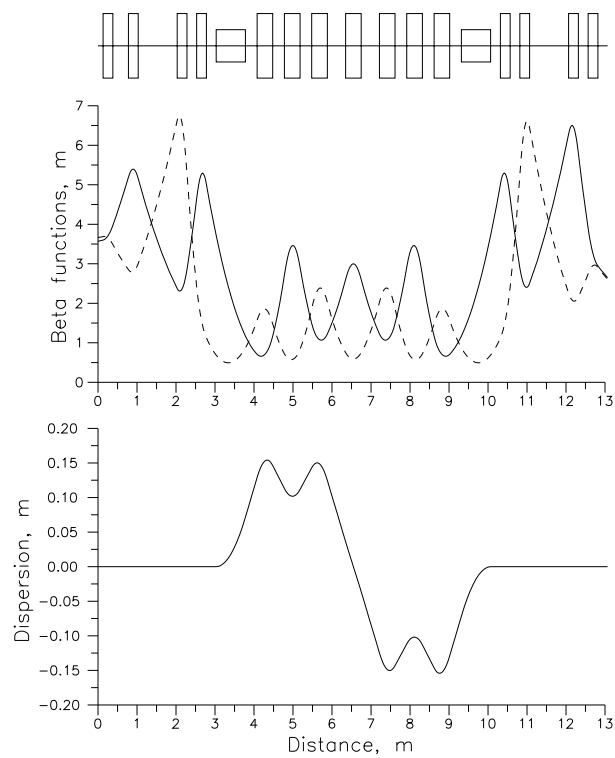
Figure 4.4.3: *Optical functions in the separator section.*
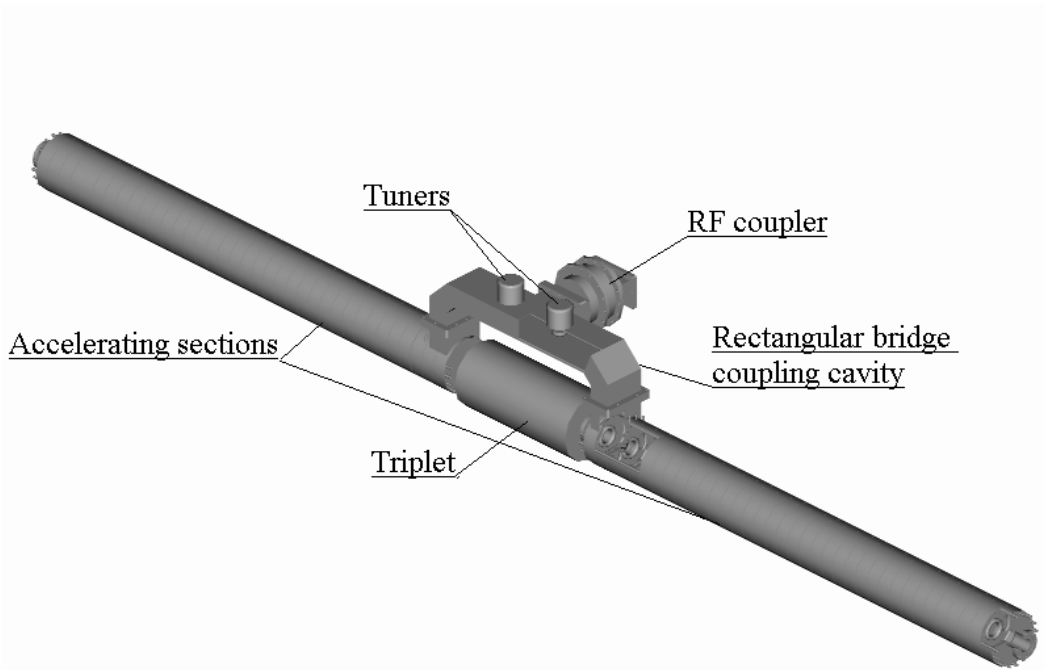
Figure 4.4.4: *Accelerating cavity in the downstream part of the PPA.*

e^+ beam. Behind the first dipole of the separator there is a dump system, which can handle the residual e^- beam up to an average power of 12–15 kW.

After the separator the positron beam has practically a single-bucket structure (the first e^+ bunch has $\sim$ 99.3% of the total number of positrons); the population of neighbouring RF-buckets present before the insertion [34] has practically vanished. The downstream part of the PPA consists of five cavities with moderate gradient (8.5 MV/m). Each cavity has two accelerating sections (figure 4.4.4). The transverse focusing is accomplished using quadrupole triplets, placed between the sections, which are separated by a drift space of $4\lambda_{RF}$. To combine two sections into a single resonant system, bridge coupling cavities are used. Each cavity is powered by one 10 MW klystron. The phase space distribution at the PPA exit is shown in figure 4.4.5.

The main PPA parameters are listed in table 4.4.1. The total PPA length is 55 m and the transverse dimensions are small enough to allow clearance to the neighbouring magnets of the high-energy electron switch-yard and beam delivery system (see chapter 7). The nine klystron stations (plus one spare for fast exchange in case of a failure) will be placed in the second-IR switch-yard shaft which also houses the positron target.

The coils of all magnetic elements placed in areas with large particle losses (the solenoid in the first part of the PPA, quadrupoles and bending magnets in the PPA insertion) have to be made from a special cable with mineral insulation.

Due to the strong non-linear effects in the magnetic insertion, this area is equipped
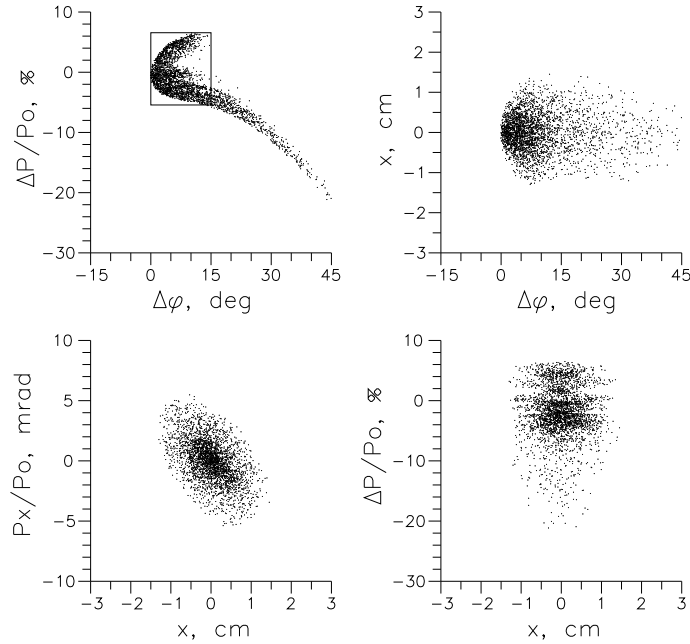
Figure 4.4.5: *Positrons phase space plots at the PPA exit.*

Parameter	value
Final energy E_f, MeV	287
Total capture efficiency, %	21.3
Solenoid length, m	~11.4
Solenoid field, T	0.22
Number of quadrupoles	42
Number of dipoles	2
Number of klystrons	9
Total length, m	~55.5

Table 4.4.1:   *The main parameters of the PPA.*

with instrumentation to verify the beam parameters. All quadrupoles have integrated position monitors. In addition, two secondary emission (SEM) grid monitors are foreseen behind the bending magnets for beam profile measurements. A complete set of beam monitors is foreseen at the PPA exit, mainly for linac commissioning. The PPA subsystems are described in detail in [34] and [35].

4.4.2   Shielding requirements for the target and PPA area

Since the energy of the undulator photons is below the muon production threshold of 210 MeV, no muons will be produced in the target. Therefore the major radiation source during operation is the photon induced neutron production in the target,

adiabatic matching device, and the first section of the accelerator. To protect the surrounding environment from the high neutron flux, these components will be embedded in a concrete cave of up to 1.5 m wall thickness. The embedded section will be assembled on a common girder and all connections (power cables, cooling water etc.) will be outside of the cave. The shielding requirements for the downstream sections are more relaxed and can be realised with concrete blocks (in the separation and collimation section) or lead walls. The induced activity after 5000 hours of operation can be shielded with lead of ≤ 15 cm thickness even in the target area. In case of a failure it is foreseen to exchange complete sections (girders) rather than single components.

4.4.3   Low-energy transfer line

The general layout of the transfer line is shown in figure 4.4.6. The line must:

- use the existing TESLA tunnel (with the exception of the bypass section);

- provide a vertical bypass section between the two main dump halls, that passes under the detector hall;

- provide adjustable matching to the beam parameters at the PPA exit and superconducting accelerator entrance;

- not introduce dispersion (except in the bypass section);

- keep the bunch length constant.
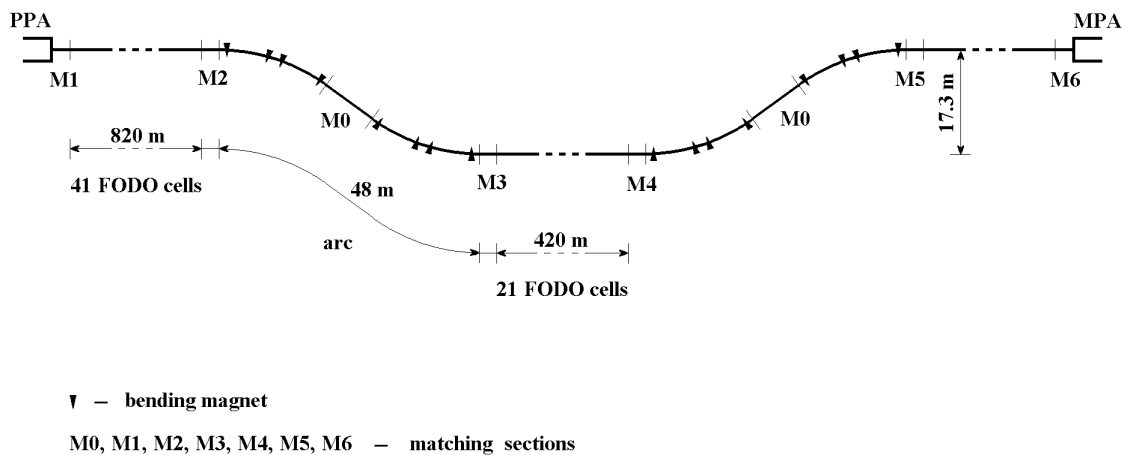
Figure 4.4.6: *Schematic layout of the low-energy transfer line.*
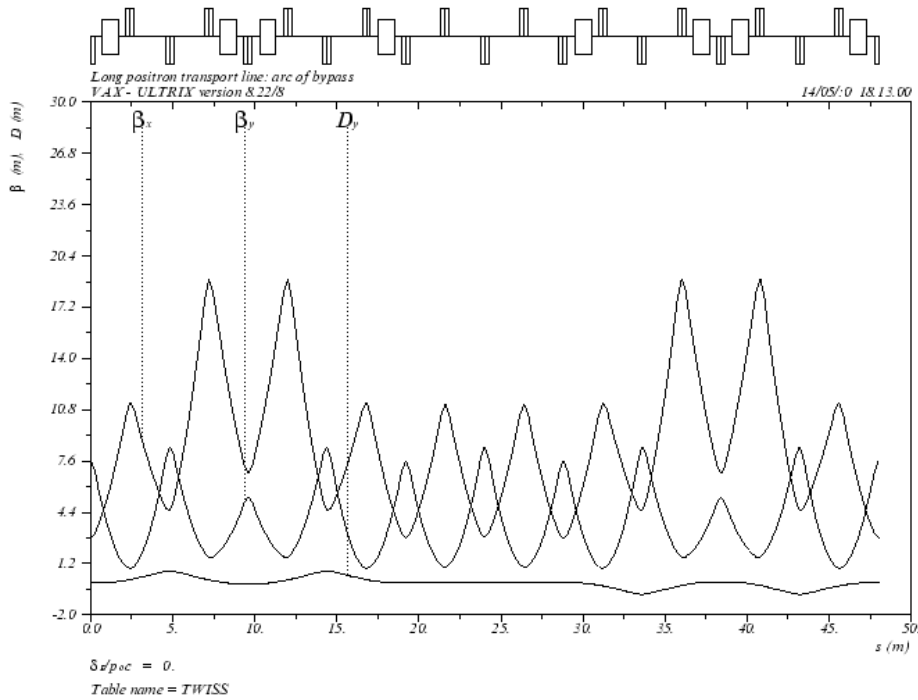
Figure 4.4.7: *Optical functions along one bypass arc.*

There are a few special aspects which complicate the design of the transport system:

- the transfer line is long, and therefore the aperture versus the number of magnets needs to be optimised; and

- it must transport a beam with large transverse emittance and a large energy spread, resulting in large magnet apertures and a quasi-isochronous bypass design.

For the long straight sections a FODO type structure is used. The parameters of the FODO cell have been optimised with respect to the maximum beam size, maximum tolerable modulation of the β-function, and the number of quadrupoles in the line.

As a result of various studies the following scheme has been chosen for the bypass. Each arc of the bypass section consists of two quasi-isochronous cells connected by a matching section (figure 4.4.7). It is convenient to construct the matching section from the same FODO cells (without bending magnets) used in the isochronous cells. Two quasi-isochronous cells plus two FODO matching cells are sufficient to reach a (downward) vertical displacement of 17.3 m. The quasi-isochronous cells of the bypass are based on a modified four-cell FODO structure with missing magnets. The longitudinal dispersion (R_{56}) of the bypass and hence of the complete transfer line is tunable and can be used to further compress the bunch.

Parameter	Value	Unit
Kinetic energy	287	MeV
Total length	2208.3	m
Length of bypass arc	48	m
Translation base	17.3	m
Normalised emittances		
horiz.	0.036	m
vert.	0.036	m
Energy spread	±0.06	
Number of quadrupoles	276	
Number of dipoles	16	

Table 4.4.2: *Main parameters of the low-energy positron transfer line.*

The main parameters of the transfer line are summarised in table 4.4.2. All quadrupoles have the same dimensions, differing only in the gradient G_0, and can be divided in two groups: those with low gradient $G_0 \leq 0.3\,\text{T/m}$, (211 units); and those with moderate gradient $0.3\,\text{T/m} \leq G_0 \leq 1.5\,\text{T/m}$ (65 units). The DC power required for one low gradient FODO quadrupole is 60 W. The lenses can be made without water cooling to reduce costs. The aperture diameter for all quadrupole lenses is equal to 0.16 m, providing a 1.7 safety factor with respect to the full size of the beam for the FODO cells and more than a factor of two for all matching and bypass quadrupoles (except for four quadrupoles in each bypass arc). This choice is a reasonable compromise between the safety factor and the number of magnetic elements. Other details of the transfer line design are described in [35].

4.4.4   Superconducting positron injector linac (PIL)

The general layout of the positron injector linac is shown in figure 4.4.8. The linac is based on the standard TESLA nine-cell superconducting accelerating structure. Due to the large transverse emittances of the e^+ beam the transverse focusing in the linac is based on superconducting quadrupole doublets. The safety factor, calculated as a ratio of the inner radius of an element to the maximum beam envelope in that element, is >2. Two types of cryomodules[1] are assumed in the design: the first type (CM-1) contains four accelerating structures and four doublets, while the second one (CM-2) consists of eight structures and a single doublet [35]. The design of the doublets is based on the main linac quadrupole. It is possible to keep the gradient to $\sim 60\,\text{T/m}$ with an effective length of $\sim 200\,\text{mm}$ for each quadrupole in the CM-2 modules: thus these doublets have the same length as the standard linac quadrupole. The doublets for the CM-1 type modules are longer and replace every second accelerating cavity. Eight

---

[1]The design of the positron pre-accelerator has been based on TTF-like 12 m long modules. It is also conceivable to use the standard 17 m long modules as in the main linac, thus avoiding building two types of modules of different length.
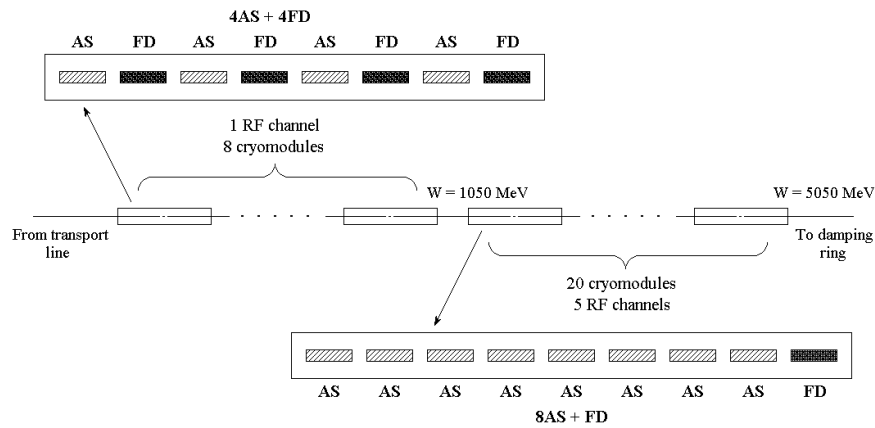
Figure 4.4.8: *Conceptual layout of the sc positron injector linac (AS = accelerating structure, FD = quadrupole doublet).*
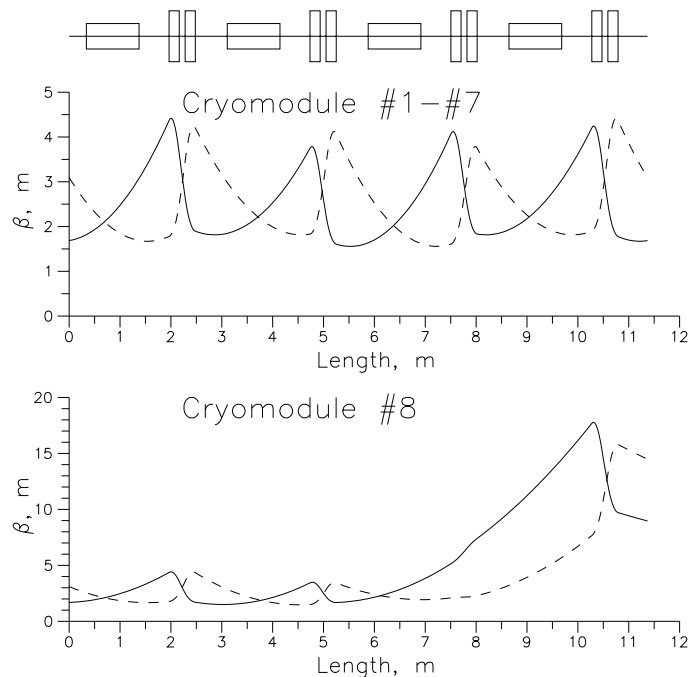
Figure 4.4.9: *β-functions for the eight CM-1 modules.*

CM-1 type modules are used in the first part of the injector linac (up to a positron energy of $\approx 1\,\mathrm{GeV}$). The eighth module is used as a matching module (figure 4.4.9). The remainder of the linac (up to $5\,\mathrm{GeV}$) is constructed from 20 CM-2 modules. The standard TESLA RF distribution scheme and hardware are used.

The general parameters of the injector linac are listed in table 4.4.3. More details of the injector linac design can be found in ref [35].

Cryomodule CM-1	
Number of cryomodules	8
Cryomodule length [m]	11.368
Energy gain per cryomodule [MeV]	100
Number of quadrupole doublets	4
Number of accelerating sections	4
Cryomodule CM-2	
Number of cryomodules	20
Cryomodule length [m]	12.352
Energy gain per cryomodule [MeV]	200
Number of quadrupole doublets	1
Number of accelerating sections	8
Final beam energy [GeV]	~ 5.08
Total length [m]	~ 338
Safety factor	> 2
Total number of klystrons	6
Total number of cryomodules	28
Total number of quadrupole doublets	52
Total number of accelerating sections	192

Table 4.4.3:   *The main parameters of the positron injector linac.*

4.4.5   Summary of the positron injector

In this final section we briefly summarise the major points of the positron production system. Details can be found in the preceding sections.

The positron injector consists of several essentially different parts: a normal conducting positron pre-accelerator (PPA); a low-energy transport line (including bypass sections); and a superconducting injector linac. The parameters for each sub-system are optimised to obtain an effective, technically realisable and cost-effective solution.

The PPA is a standing-wave normal-conducting linac; its design is based on experience from existing linear accelerators and standard TESLA RF equipment. The low-energy transfer line magnets have conservative cost-effective parameters. The sc injector linac is based on standard TESLA/TTF equipment.

The total positron transmission of the injector from the target to the exit of the pre-accelerator is estimated at $\approx 16\%$. This value is sufficient to provide the necessary positron intensity for the 500 GeV collider with a safety

Bibliography

[1] S. Schreiber et al. , *Performance Status of the RF-Gun Based Injector of the TESLA Test Facility Linac*, Proc. 7th EPAC, Vienna 2000, p. 309.

[2] B. E. Carlsten, *New Photoelectric Injector Design for the Los Alamos National Laboratory XUV Fel Accelerator*, Nucl. Instr. Meth. **A285** (1985) 313.

[3] P. Michelato, C. Pagani, D. Sertore, A. di Bona, S. Valeri, *Characterization of Cs_2Te photoemissive film: Formation, spectral responses and pollution*, Nucl. Instr. Meth. **A 393** (1997) 464.

[4] P. Michelato et al., *High Quantum Efficiency Photocathode Preparation System for TTF Injector II*, Proceedings of the 21st International FEL Conference, Hamburg 1999, Vol. II, p.97.

[5] R. Brinkmann et al., *A Flat Beam Electron Source for Linear Colliders*, DESY TESLA-99-09, 1999.

[6] R. Brinkmann et al. (Eds.), *Conceptual Design of a 500 GeV e^+e^- Linear Collider with Integrated X-ray Laser Facility*, Vol. I, DESY report 1997-048 and ECFA 1997-182, 1997.

[7] R. Alley et al., *The Stanford Linear Accelerator Polarised Electron Source*, Nucl. Inst. and Meth. **A 365**, p.1 (1995)

[8] The NLC Design Group, *Zeroth-Order Design Report for the Next Linear Collider*, SLAC Report 474, pp 28-34 (1996)

[9] M. Breidenbach et al., *An Inverted-geometry, High Voltage Polarized Electron Gun with UHV Load Lock*, Nucl. Instrum. And Meth. **A 340** (1994)

[10] M. Woods et al., *Observation of a Charge limit for Semiconductor Photocathodes*, J. Appl. Phys. **73** 8531 (1993)

[11] W. E. Spicer and A. Herrera-Gomez, *Modern Theory and Applications of Photocathodes*, SLAC-PUB-6306 and Proc. SPIE 2022 51 (1993)

[12] D. Schultz et al., *The Polarized Electron Source of the Stanford Linear Accelerator Center*, SLAC-PUB-6606, August 1994; presented at 17th International Linear Accelerator Conference (LINAC 94), Tsukuba, Japan, 21-26 Aug (1994)

[13] J. E. Clendenin, *Polarized Electron Sources*, SLAC-PUB-95-6842, May 1995 and Proc. of Particle Accelerator Conference PAC 95, Dallas, Texas, 1-5 May 1995, pp 877-881 (1995)

[14] F. Stephan et al., *Photo Injector Test Facility under Construction at DESY Zeuthen*, Proc. Free Electron Laser Conf., 13-18 Aug. 2000, Durham, North Carolina.

[15] W. Koechner, *Solid-State Laser Engineering*, Berlin 1999, p. 406.

[16] White et al., *120-fs Terawatt $Ti : Al_2O_3/Cr : LiSrAlF_6$ Laser System*, Opt. Lett.
17 1067 (1992);
Ditmire, Perry, *Terawatt $Cr : LiSrAlF_6$ Laser System*, Opt. Lett. **18** (1993) 426.

[17] I. Will, P. Nickles, W. Sandner, *A Laser System for the TESLA Photo-Injector*,
Internal Design Study, Max-Born-Institut, Berlin, 1994.

[18] *Running Experience with the Laser System for the RF Gun based Injector at the
TESLA Test Facility Linac*, Nucl. Instrum. Meth. **A445** (2000) 427.

[19] A. Curtoni, M. Jablonka, *Study of the TESLA preaccelerator for the polarized
electron beam*, DESY TESLA-01-22, 2001.

[20] R. Brinkman et al. (Eds.), *Conceptual Design Report of a 500 GeV e^+e^- Linear
Collider*, Vol. II, DESY 1997-048, p. 697-726.

[21] D. A. Edwards (Eds.), *TESLA TEST FACILITY design report*, DESY TESLA-
95-01, 1995, p. 57-92.

[22] V. E. Balakin and A .A. Mikhailichenko, *The Conversion System for Obtaining
High Polarized Electrons and Positrons*, Preprint INP 79-85, 1979.

[23] K. Flöttmann, *Investigations Toward the Development of Polarized and Unpo-
larized High Intensity Positron Sources for Linear Colliders*, DESY-93-161, 1993.

[24] R. Brinkmann, J. Pflüger, V. Shiltsev, N. Vinokuro, P. Vobly, *Wiggler Options
for TESLA Damping Ring*, DESY-TESLA-95-24, 1995.

[25] W. Nelson, H. Hirayama and D. Rogers, *The EGS4 Code System*, SLAC-265,
1985.

[26] S. Ecklund, *Positron Target Materials Tests*, SLAC Collider Note-128, 1981.

[27] E. M. Reuter and J. A. Hodgson, *3D Numerical Thermal Stress Analysis of the
High Power Target for the SLC Positron Source*, SLAC-PUB-5370, 1991.

[28] P. Sievers and M. Höfert, *A Megawatt Electron Positron Conversion Target — A
Conceptual Design*, Proc. 1st EPAC, Rome 1988.

[29] R. H. Helm, *Adiabatic Approximation for Dynamics of a Particle in the Field of
a Tapered Solenoid*, SLAC-4, 1962.

[30] H. Ida, *Present R&D Status of Positron Sources for JLC-1 and ATF*, presented at
6th International Workshop on Linear Colliders, Tsukuba 1995.

[31] E. L. Saldin, E. A. Schneidmiller, M. V. Yurkov, *Calculation of Energy Diffusion in an Electron Beam due to Quantum Fluctuations of Undulator Radiation*, DESY TESLA-FEL 96-05, 1996.

[32] R. Glantz, *A Feasibility Study of High Intensity Positron Sources for the S-Band and TESLA Linear Colliders*, DESY-97-201, 1997.

[33] K. Flöttmann, S. Wipf, *Field Enhancement of a Superconducting Helical Undulator with Iron*, DESY TESLA-96-05, 1996.

[34] K. Flöttmann, V. Paramonov ed., *Conceptual design of a Positron Pre-Accelerator for the TESLA Linear Collider*, DESY TESLA-99-14, 1999.

[35] K. Flöttmann, V. Paramonov ed., *Conceptual Design of a Positron Injector for the TESLA Linear Collider*, DESY TESLA-00-12, 2000.

[36] V. Paramonov, I. Gonin, *3D Thermal Stress Analysis for the CDS Structure*, Proc. 7th EPAC, Vienna 2000, p. 1990.

5 Damping Ring

5.1 Introduction

Damping rings are necessary to reduce the emittances produced by the particle sources to the small values required for the linear collider. Emittance reduction is achieved via the process of radiation damping, i.e. the combination of synchrotron radiation in bending fields with energy gain in RF cavities. The design of the damping ring has to ensure a small emittance and a sufficient damping rate.

One of the main design criteria for the damping ring comes from the long beam pulse: a 1 ms pulse containing 2820 bunches, corresponding to an approximately 300 km long bunch train. To keep the damping ring length reasonable, the bunch train has to be stored in a compressed mode with a much smaller bunch spacing than in the rest of the accelerator. Consequently each bunch has to be individually injected and ejected. The ring length is then given by the bandwidth of the injection and extraction system. A bandwidth of 50 MHz (bunch spacing of 20 ns) requires a ring length of 17 km. To avoid the cost for an additional 17 km of ring tunnel, most of the damping ring will be in the form of straight sections installed in the linac tunnel [1]. Short return arcs requiring additional tunnels provide about 12 % of the circumference.

The ring energy is 5 GeV; this is a compromise between the need for higher energy to reduce space charge effects (see section 5.3.1) and damping wiggler costs, and a preferable lower energy which reduces the RF power needs and eases the design of the damping ring arcs.

The design of low emittance arcs with sufficiently high bending fields to provide enough damping becomes increasingly difficult at higher energies: thus the majority of the damping (95%) is supplied by long damping wigglers. The final extracted transverse emittance (ε_f) is given by

$$\varepsilon_f = \varepsilon_{eq} + (\varepsilon_f - \varepsilon_{eq})e^{-2T/\tau_D}$$

where ε_i and ε_{eq} are the initial (injected) emittance and the equilibrium emittance respectively, τ_D is the damping time and T is the storage time (200 ms). The initial normalised positron emittance is 0.01 m, and $\sim$7 damping times (28 ms) are required to achieve the final design normalised emittance of 2×10^{-8} m. The injected electron beam — having been produced by a photoinjector as opposed to a target — has a much better beam quality ($\gamma\varepsilon_i \approx 10^{-5}$ m), and only requires 4 damping times. This provides an opportunity for cost saving by reducing the amount of wiggler in the straight sections, and subsequently reducing the RF power needs.

Energy E	$5\,\mathrm{GeV}$
Circumference C	$17\,\mathrm{km}$
Hor. extracted emittance $\gamma\varepsilon_x$	$8 \times 10^{-6}\,\mathrm{m}$
Ver. extracted emittance $\gamma\varepsilon_y$	$0.02 \times 10^{-6}\,\mathrm{m}$
Injected emittance $\gamma\varepsilon_{x(y)}$	$0.01\,\mathrm{m}\ (10^{-5}\,\mathrm{m})$
Number of damping times n_τ	$7.2\ (4.0)$
Cycle time T_c	$0.2\,\mathrm{s}$
Damping time τ_d	$28\,\mathrm{ms}\ (50\,\mathrm{ms})$
Number of bunches n_b	2820
Bunch spacing $\Delta\tau_b$	$20 \times 10^{-9}\,\mathrm{s}$
Number of particles per bunch N_e	2.0×10^{10}
Current	$160\,\mathrm{mA}$
Energy loss/turn	$21\,\mathrm{MeV}\ (12\,\mathrm{MeV})$
Total radiated power	$3.2\,\mathrm{MW}\ (1.8\,\mathrm{MW})$
Tunes Q_x, Q_y	72.28, 44.18
Chromaticities ξ_x, ξ_y	-125, -68
Momentum compaction α_c	0.12×10^{-3}
Equilibrium bunch length σ_z	$6\,\mathrm{mm}$
Equilibrium momentum spread σ_p/P_0	$0.13\,\%\ (0.1\,\%)$
Transverse acceptance $A_{x|y}$	$0.05\,\mathrm{m}\ (0.012\,\mathrm{m})$
Momentum acceptance A_p	$1\,\%\ (0.5\,\%)$

Table 5.1.1: *Parameters for the TESLA positron damping ring. Where different, values for the electron damping ring are given in parentheses.*

A summary of the main parameters of the damping ring is given in table 5.1.1. Figure 5.1.1 shows a sketch of the positron damping ring, with the long straight section, injection/ejection sections, wigglers, and RF placed in the main linac tunnel. Slight modifications of the arc geometry would allow the wiggler to be placed in the arc tunnel.
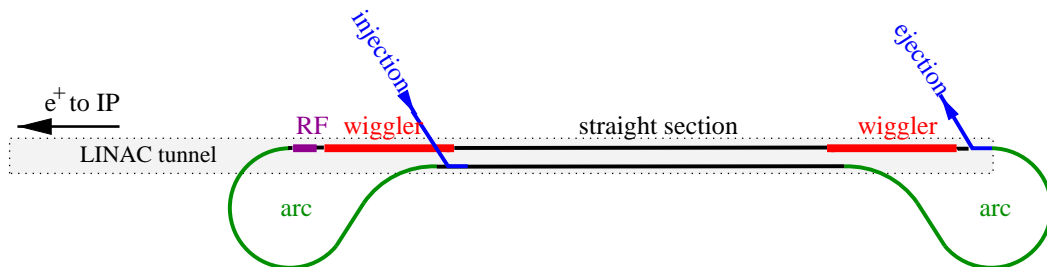
Figure 5.1.1: *Conceptual layout of the positron damping ring. The electron ring is similar with the exception that the injection point is located close to the indicated ejection position at the beginning of the linac.*

The damping ring lattice can be divided into three separate parts:

- the arcs;

- the wiggler sections; and

- the long straight sections in the linac tunnel.

The optics of each of these sections will be described in section 5.2. The investigation of beam dynamics, including space charge effects, dynamic aperture and tolerances, is summarised in section 5.3. Collective effects are discussed following the description of the RF system in section 5.4. Some aspects of the injection and ejection kicker system and basic timing requirements are covered in section 5.5. A summary of the technical layout including detailed drawings of the magnets and vacuum system is given in section 5.6; it also includes the layout of the arc tunnel and a summary of the infrastructure needs of the damping ring.

5.2   Lattice Layout and Optics

5.2.1   Arc lattice

The arc lattice is designed as a minimum emittance cell with a $6\,^\circ$ dipole flanked by quadrupole doublets, allowing the phase advance to be changed if desired. The drift space between the two outer focusing quadrupoles provides space for the focusing sextupole at the point of highest horizontal dispersion and β-function. In order to achieve a reasonable bunch length (6 mm), the dipoles are made long (9 m) to increase the momentum compaction factor. The resulting cell length is 15.2 m. In addition, the relatively large cell length results in larger dispersion and β-functions, which reduces the sextupole strength [3].

Figure 5.2.1 shows the optical functions and the geometry of one arc cell. Table 5.2.1 summarises the parameters of the damping ring arcs.

Cell length	15.2 m
Cell phase advance $\mu_x/2\pi$, $\mu_y/2\pi$	0.4 ,0.1
Total number of cells	100
Length of one arc	950 m
Total chromaticity contribution ξ_x, ξ_y	-90 , -35
Total energy loss contribution	1.1 MeV/turn
Total horizontal emittance contribution	2.0×10^{-6} m

Table 5.2.1: *Arc parameters.*
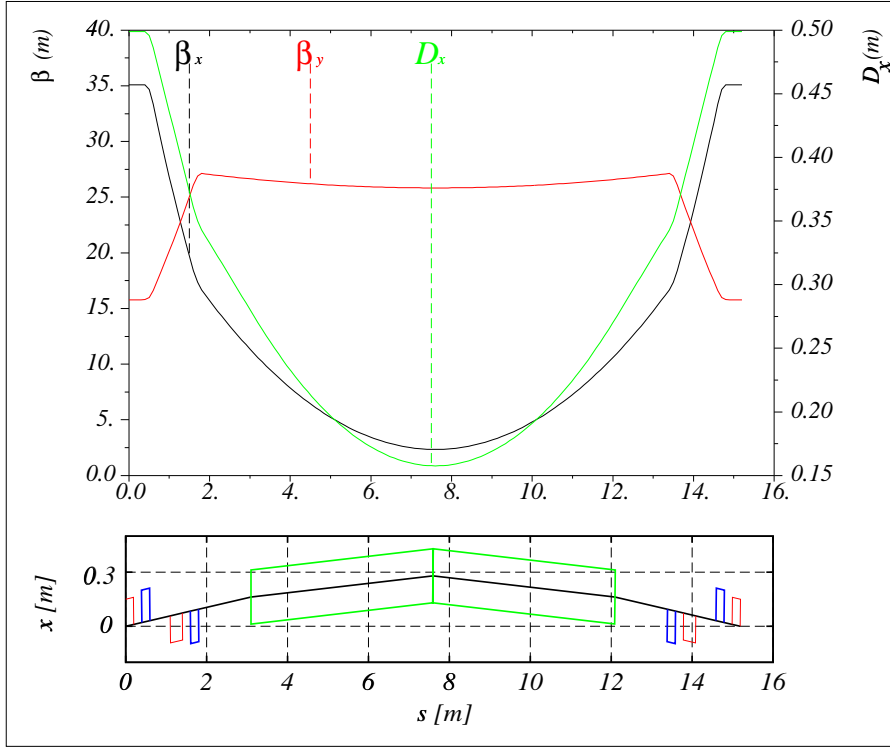
Figure 5.2.1: *Upper plot: horizontal (black), vertical (red) β-functions and horizontal dispersion (green). Lower plot: arc cell geometry showing the location of dipoles (green), quadrupoles (blue) and sextupoles (red).*

5.2.2   Straight section

The long straight section consists of FODO cells of approximately 100 m length with a phase advance of $\mu_{x,y}/2\pi = 0.125$. The choice of both length and phase advance is a compromise between the need to keep the magnet apertures small (smaller β-functions), and a small contribution to the overall chromaticity of the ring (larger β-functions).

The TESLA tunnel follows the curvature of the earth, and thus the straight sections require vertical bending. The emittance contribution of the vertical bending magnets is negligible, but care has to be taken to have no vertical dispersion in the wiggler and arc sections.

Cell length	100 m
Cell phase advance $\mu_x/2\pi$, $\mu_y/2\pi$	0.125, 0.125
Total number of cells	140
Chromaticity contribution ξ_x, ξ_y	$-18, -18$

Table 5.2.2: *Parameters for the damping ring straight sections.*

	Permanent magnet	Electro- magnet
Cell length	12.2 m	
Cell phase advance $\mu_x/2\pi$, $\mu_y/2\pi$	0.075 ... 0.3, 0.125	
Cell chromaticity ξ_x, ξ_y	–0.05 ... –0.32, –0.14 ... –0.28	
Maximum vertical beta	18 ... 28 m	
Energy loss contribution	19.1 MeV/turn	
Radiated power (160 mA)	3 MW	
Total number of cells	45	36
Horizontal emittance contribution	$(7.8 ... 2.5) \times 10^{-6}$ m	$(20.7 ... 6.5) \times 10^{-6}$ m

Table 5.2.3: *Wiggler section parameters for both electromagnet and permanent magnet designs.*

5.2.3   Wiggler cell

To achieve the desired (positron) damping time of 28 ms, the wigglers have to provide a total second field integral $\int B^2 dl \approx 605\,\mathrm{T^2 m}$. Wiggler designs based on electromagnets [2] and permanent magnets [4] have been studied. The basic parameters of the wigglers are given in table 5.6.2. The wigglers can be embedded in either a FODO or triplet focusing lattice, depending on the wiggler length and gap. The final extracted horizontal emittance can be adjusted by changing the average horizontal β-function.

5.3   Beam Dynamics

5.3.1   Space charge effects

The direct space charge force is the collective force of all the particles in the bunch acting on one particle. It is proportional to the particle density in the bunch. The space charge force causes a shift in each particle's tune, leading to an incoherent tune spread within the bunch. With the nominal damping ring parameters the maximum vertical space charge tune shift before ejection (when the beam is smallest) is $\Delta Q_y \approx 0.23$; this relatively large value results primarily from the unusually large ratio of ring circumference to energy, and is one of the reasons for preferring a higher ring energy.

The effect of the large incoherent tune spread has been simulated with the computer code MAD [5], including an extension which simulates the non-linear space charge kicks at each element in the ring [6]. The results suggest that a maximum tune shift of 0.1 is tolerable [7], and hence a reduction of more than a factor of two is required.

Because the long straight sections account for ∼90% of the ring circumference, they are also responsible for the major part of the space charge effects: thus increasing the transverse beam size (i.e. decreasing the charge density) in the straight sections can significantly reduce the incoherent tune shift. Full local transverse coupling in the
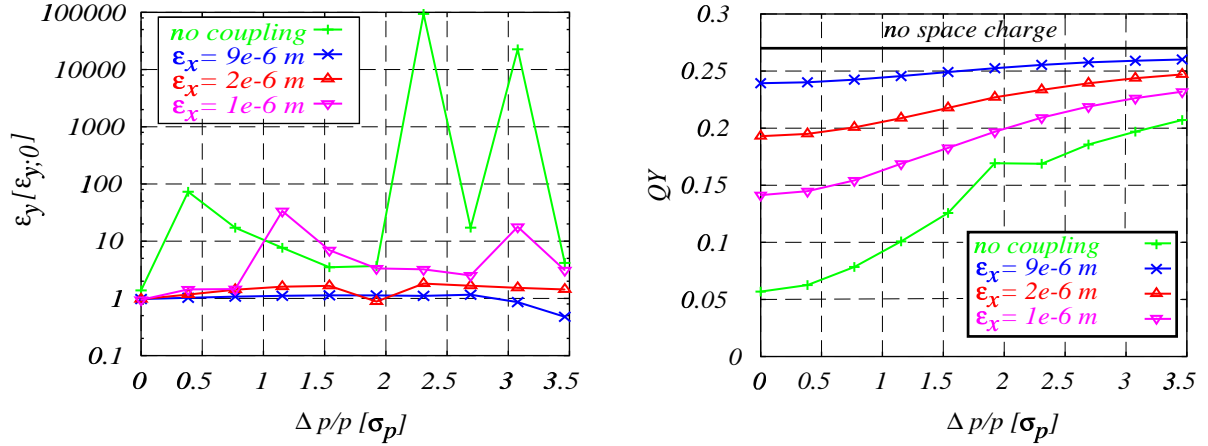
Figure 5.3.1: *Effect of direct space charge force on a single particle in a beam with various horizontal emittances. The test particle performs longitudinal and transverse oscillations with an initial energy offset $\Delta p/p$ and an an initial amplitude corresponding to the nominal vertical emittance. Left: average relative change of vertical action variable (invariant amplitude squared) Right: change of vertical tune.*

straight sections ($\tilde{\varepsilon}_x = \tilde{\varepsilon}_y = \varepsilon_x/2$, where $\tilde{\varepsilon}_{x,y}$ are the *projected* emittances) can reduce the vertical space charge tune shift by as much as a factor of five. The local coupling is provided by two skew-quadrupole insertions placed at the beginning and end of each section.

The effect of the coupling insertion on the beam has been simulated with tracking calculations including space charge forces. The phase and amplitude of a particle was recorded turn by turn under various conditions. The test particle had an initial fractional tune of $\nu_y = 0.27$.

The results for various initial energy offsets ($\Delta p/p$) are shown in figure 5.3.1. With no coupling insertion, the maximum tune (figure 5.3.1 right) shift for the synchronous particle in the centre of the bunch is 0.21, and the amplitude (figure 5.3.1 left) shows a marked increase when crossing resonances. The coupling insertion reduces the maximum tune shift to 0.035, and suppresses the amplitude growth. Figure 5.3.1 also indicates that at a maximum tune shift of 0.1 (corresponding to a four times smaller horizontal emittance) only small amplitude growth is observed.

5.3.2   Dynamic acceptance

The dynamic acceptance of the damping ring has been investigated with particle tracking including synchrotron oscillations. Random offsets and roll angles have been given to sextupoles and quadrupoles to simulate realistic optics deviations and coupling. The wiggler has been simulated by an array of hard-edge dipole magnets. The physical aperture of the ring has been simulated in the tracking by applying a maximum transverse amplitude limit.
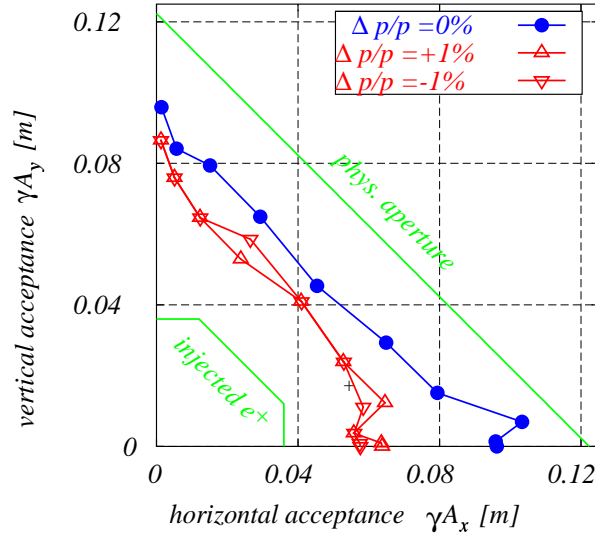
Figure 5.3.2: *Dynamic acceptance of the damping ring. The simulations include quadrupole and sextupole alignment errors which result in an average emittance coupling of 1 %, and the real physical aperture as the maximum amplitude limit. The phase space volume of the incoming beam as defined by acceptance of the positron pre-accelerator (see section 4.4) is also shown.*

The dominant source of non-linear beam dynamics are the strong sextupoles in the damping ring arcs; these sextupoles have to provide the chromaticity correction for the complete ring. Multipole errors of the ring magnets can be kept small ($\leq 10^{-3}$ of the design field) by proper design and manufacturing procedures. Sets of particles with various initial ratios of their horizontal and vertical emittances have been tracked over 512 turns (roughly 1 damping time). Two chromatic sextupole families and a second-order dispersion suppressor (to reduces the second-order dispersion in the straight sections) were applied. The results are plotted in figure 5.3.2. The dynamic acceptance achieved is sufficient to accommodate the injected positron beam.

5.3.3 Tolerances

The TESLA damping ring requires a small emittance ratio of 0.2 % at extraction. This ratio has been achieved in present day synchrotron radiation sources and collider rings [8, 9, 10]. Tight alignment tolerances and a high resolution orbit measurement system are crucial.

Vertical emittance is generated through betatron coupling and residual vertical dispersion. Betatron coupling can be reduced with the help of skew-quadrupoles. Minimising spurious vertical dispersion in the wigglers is especially important: here the vertical rms dispersion has to be corrected to the 1 mm level. An algorithm which performs a simultaneous orbit and dispersion correction has been studied. The simulations included alignment errors assigned to all machine elements (as summarised in

Transverse position of elements	0.1 mm
Roll angle	0.2 mrad
BPM resolution	0.01 mm
BPM resolution wiggler section (averaging mode)	0.001 mm

Table 5.3.1: *Alignment tolerances for the damping ring.*

table 5.3.1). Successive steps of the correction algorithm were applied until no further reduction of the residual rms orbit and dispersion were achieved. Studies using many random error seeds showed that the required vertical emittance was obtained on average. Correcting the dispersion to the required 1 mm in the wiggler sections requires a relative orbit measurement with a precision of $\sim 1\mu$m. Beam position monitors (BPM) with a resolution of $10\,\mu$m will be used in the damping ring. For the high-precision dispersion measurement the accuracy can be achieved by averaging.

The dispersion can also be corrected using empirical tuning of the vertical beam size (emittance) with the appropriate dispersion generating orbit bumps; this method has the advantage of not requiring an explicit measurement of the dispersion function.

An important concern is the orbit stability over various time scales. For long-term stability a diffusion-like orbit drift caused by slow uncorrelated ground motion must be taken into account. An orbit correction back to the 'golden' orbit is necessary every few minutes to avoid unacceptable vertical emittance blow-up. For this task a BPM resolution of $10\,\mu$m is sufficient once the vertical emittance has been optimised (i.e. the 'golden' orbit established). On the short time scale the influence of time varying stray fields in the long straight sections is a concern. With no active correction applied to the orbit, the stray field amplitude has to be smaller than a μT. This is in contradiction to measurements on the DESY site, where field amplitudes up to several μT have been observed in typical accelerator environments. Thus a fast orbit feedback has to control the resulting residual orbit in the wiggler and arc sections of the ring.

5.4   RF System and Collective Effects

5.4.1   RF system

The RF System of the damping ring is based upon the following main parameters:

RF Frequency:	500 MHz
Total RF peak voltage:	50 MV
Beam energy loss per turn:	20.3 MeV
Average beam current:	160 mA
Synchrotron radiation power:	3.2 MW

The RF system makes use of 12 superconducting (SC) cavities of the same type developed for CESR [11] and KEK-B [12], and is sketched in figure 5.4.1. Three 1.2 MW
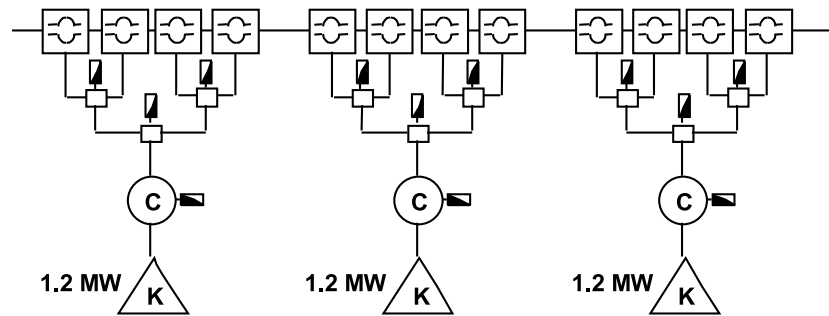
Figure 5.4.1: *Damping ring RF system based on single cell SC cavities.*

klystrons are used.

The SC cavities are single cell Niobium 500 MHz resonators, each housed in its own liquid helium cryostat. Large diameter beam tubes permit the higher order modes (HOMs) to propagate out of the cavities, where they are damped using dissipative material applied to the inner surface of both beam tubes just outside the cryostat at room temperature [13, 14]. Such HOM dampers have been very effective in CESR and KEK-B, and can dissipate up to 10 kW of parasitic power. The quality factor (Q) of the parasitic modes is reduced to a few hundred over the bandwidth 1–3 GHz.

As of writing, the achievable RF field in 500 MHz SC cells is very close to 15 MV/m (i.e. 4.5 MV/cell). To reach these gradients requires high residual resistivity ratio (RRR) Niobium, improved cavity heat treatment and operation at a temperature of 2 K. Twelve cavities would provide up to 54 MV. At 2 K, the cavity Q_0 can be close to 10^{10}. With $R/Q = 45\Omega$ per cell ($R = V^2/2P$), the power loss per cell will be ≤ 30 W at 15 MV/m. The CESR cryostat design, which operates at 4.2 K, has to be re-designed for 2 K operation, where static heat losses of 30 W should be achievable. The total cooling power of 720 MW at 2 K will be provided by the main linac refrigerators.

The 3.2 MW required for the beam will be shared among the twelve cavities, and the input RF power per coupler is therefore 270 kW; this is below the power handling capability (in traveling wave mode) of RF windows already developed and tested at other laboratories [12, 15]. Powerful klystrons (1.2 MW/cw at 500 MHz) are produced by industry and operate routinely at KEK. With a klystron efficiency $\eta \approx 60\%$, the total power required by the RF is 6.5 MW.

The heat load for the conventional cooling is mainly the klystron tubes, and is about 2.5 MW. Each cavity cryostat is equipped with a pair of 300 l/s vacuum ion pumps. Two additional 60 l/s pumps are connected to the waveguide power coupler.

5.4.2 Coupled bunch instabilities

The longitudinal and transverse instability growth rates due to the higher-order modes with Q-values of about 100 are of the same order or smaller than the damping rate: therefore a broadband multibunch feedback system may not be necessary, or at least would only require a small damping rate. Multibunch feedback systems with much larger bandwidths than that required for the damping ring are nowadays in routine

Operating frequency	500 MHz
Max RF cavity field	15 MV/m
Cell active length	0.3 m
Number of cavities	12
Total RF voltage	54 MV
RF-to-beam power	3.2 MW
RF cell R/Q	45 Ω
Q_0 at 2 K	$\leq 10^{10}$
Power loss/cell	≤ 30 W
Power per coupler	270 kW
Input coupler Q_{ext}	1.1×10^6
Klystron power	1.2 MW
No. of klystrons	3
Primary power for RF	6.5 MW
Cryostat static losses	≤ 30 W
Cryo-power per cavity	≤ 60 W
Total power at 2 K	≤ 720 W
Water cooling dissipation	2.5 MW

Table 5.4.1: *Damping ring RF system parameters.*

operation in high-current storage rings.

In the transverse plane, coupled bunch instabilities are also strongly driven by the resistive wall effect of the vacuum chamber. The transverse resistive wall impedance of the aluminium vacuum chamber yields ≈ 3200 MΩ for the mode number which is equal to the integer part of the transverse tune. This mode gives the largest growth rate of $\approx 2000\,\text{s}^{-1}$. The instability is easily damped with a low-bandwidth feedback.

The interaction of a train of electron bunches with an ion cloud can give rise to a fast single pass coupled bunch instability (Fast Beam Ion Instability [16]). The ion production rate can be estimated based on the residual gas properties and yields upper limits for the allowable vacuum pressure. Computer simulations have shown that the instability is avoided at a nitrogen equivalent pressure of $P_{N_2} \approx 10^{-9}$ mbar [17].

Positron bunches interact with photo-electrons [18, 19, 22]. The creation of electron clouds depends on many parameters, for example: vacuum chamber design and material; external fields; residual gas properties. Electron cloud instabilities have been observed in modern high-current positron storage rings, and can be cured by weak external magnetic fields which confine the photo-electrons to the vacuum chamber surface. The impact of the electron cloud instability on the positron damping ring needs to be investigated in more detail.
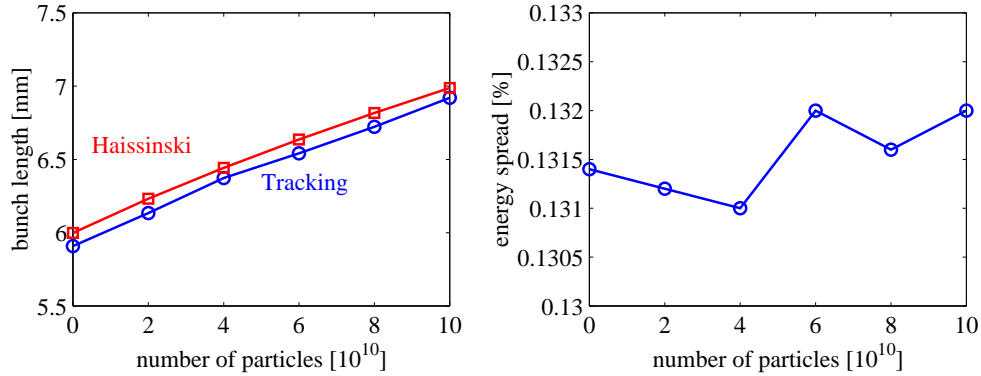
Figure 5.4.2: *Bunch length and energy spread as a function of the number of particles within the bunch. Tracking calculations and Haissinski equation solution are based on the impedance model described in table 5.4.2.*

| | | $Z_{||}/n$ | $k_{||}$ |
		mΩ	V/pC
	RF cavities	2.0	8.8
Non-inductive	Resistive wall	5.4	8.9
	Kickers	≈ 17	≈ 39
	Total	≈ 25	≈ 57
	Bellows	≈ 11	≈ 3.4
Inductive	BPMs	≈ 12.5	≈ 1.7
	Other components	≈ 5	≈ 1.5
	Total	≈ 28.5	≈ 6.6
All components			≈ 64

Table 5.4.2: *Contributions to the longitudinal broadband impedance. $Z_{||}/n$ is the longitudinal impedance divided by the mode number n, and $k_{||}$ the longitudinal loss factor.*

5.4.3   Single bunch effects

The longitudinal single bunch dynamic is influenced by the wakefields generated in the various ring components. Estimates of the different contributions to the impedance budget are given in table 5.4.2.

The effective broadband impedance of the damping ring vacuum system is 25 mΩ, which is below the microwave instability threshold [20] of 61 mΩ. The purely inductive part of the impedance does not contribute to the microwave instability but can lead to bunch lengthening. Tracking calculations in the longitudinal phase space [21] show a bunch lengthening of up to 5 % for an initial bunch length of 6 mm and 2.0×10^{10} particles per bunch (see figure 5.4.2). The energy spread stays constant, indicating the absence of an instability.

The transverse broadband impedance can give rise to the mode-coupling instability. Estimations of the instability threshold and the impedance contributions show that this is of no concern for the damping ring [22].

5.5   Injection and Extraction System

5.5.1   Kicker

The damping ring injection/extraction scheme requires a kicker system with a bandwidth of 50 MHz. The kick strength for both injection and ejection is $\theta \approx 0.6$ mrad or $\int Bdl \approx 0.01$ Tm at 5 GeV and $\beta_{kicker} = 50$ m. To ensure an ejected beam stability of $< 0.1\sigma_x$, the amplitude stability of the kicker system has to be 7×10^{-6} Tm for both the maximum deflection and the remaining ripple after the kicker pulse; this corresponds to a relative stability of 7×10^{-4} at maximum deflection. Reduction of the relative stability requirement cannot be achieved using (for example) an orbit bump at the ejection septum, since the full aperture of the machine is required for the undamped bunches[1].

A traveling wave kicker showing the required time response has been built and successfully tested [23]. Other concepts like C-yoke kickers around either a sputtered ceramic vacuum chamber or a stripe chamber are under consideration. The necessary pulser technology exists and tests will be performed in 2002. Depending on the chosen kicker/pulser technology, 20–40 kickers are required per ring.

5.5.2   Timing

The timing scheme for the positron damping ring is primarily constrained by the fact that the electron bunches are used to generate the positrons. For the nth 5 Hz pulse, the electron bunches generate the corresponding positron bunches for the next $(n+1)$ pulse: these bunches must be stored in the damping ring, and are injected into the empty bucket created when the corresponding positron bunch for the nth pulse was extracted. This free bucket in the damping ring train must therefore perform 1.5 turns, before being filled again with a new (undamped) bunch.

The positron production scheme leads to the following constraints for the damping ring design and overall collider layout [24]:

- the damping ring circumference, injection position, and harmonic number are fixed;

- the longitudinal position of the main e^+e^- interaction region and the optional second interaction region can only differ by an integer number of half the linac bunch spacing ($\sim$50 m);

- any gap in the damping ring fill (for ion clearing) will be transferred into missing bunches in the linac bunch train.

---

[1]Damped and undamped bunches are simultaneously present in the ring.

5.6   Technical Layout

5.6.1   Magnets

The damping ring uses conventional water cooled magnets. The main parameters and the number of magnets for each family of the two arcs, wiggler sections and long straight sections of a single damping ring are listed in table 5.6.1. A laminated yoke for both dipoles and multipoles has been foreseen. Bending dipoles and steering magnets have C-shaped cross-sections, while multipole magnets can be split in half to allow easy assembly of the vacuum chamber. The coils have been designed to minimise the power dissipation by keeping the current densities below $2.5\,\mathrm{A/mm^2}$. Figure 5.6.1 shows a bending magnet while figure 5.6.2 shows a typical quadrupole and sextupole. Two-dimensional codes for basic dimensioning of all the magnets have been used: however the design of the pole profiles needs further optimisation to minimise the non-linear magnetic fields. The mechanical length of each type of magnet has been scaled from experience. Detailed three-dimensional simulations must be performed to set the final dimensions.

Special girders, where magnets, vacuum chambers and pumps, etc. are assembled and carefully aligned outside the tunnel, have been designed to reduce the installation time inside the tunnel.

Two alternative designs for the damping wigglers have been studied: permanent magnet [4] and electromagnetic technology. A schematic view of the permanent magnet wiggler is shown in figure 5.6.3; its advantages are compact size and low operating costs. On the other hand, an electromagnetic wiggler is tunable and less sensitive to radiation damage. The specific design of the electromagnetic wiggler magnet is shown in figure 5.6.4. Due to cost and space constraints, the maximum current density is limited to $8.6\,\mathrm{A/mm^2}$. The power requirements for the electromagnetic wiggler is $6.8\,\mathrm{MW}$, corresponding to $85\,\%$ of the total power required by all the magnets. Therefore the permanent magnet wiggler has been chosen as the reference design for the damping ring. Radiation damage will be avoided by means of collimation and an active protection system.
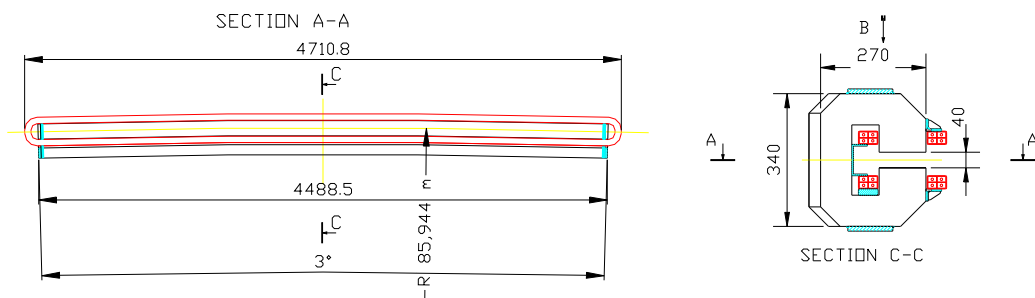
Figure 5.6.1: *Bending magnet.*

Bending magnets	Quantity	Mag. length [m]	Defl. angle [deg]	Mag. field [T]	Gap [mm]	Ampere turns [A]	Power/ magnet [W]
	216	4.5	3	0.194	40	6176	2557

Quadrupoles	Quantity	Mag. length [m]	Max. gradient [T/m]	Bore radius [mm]	Ampere turns/pole [A]	Power/ magnet [W]
Arc	456	0.2	21.7	24	4973	631
Arc match	38	0.3	10.3	24	2361	258
Wiggler	70	0.2	14.2	18	3254	270
Wiggler match	16	0.4	10.9	28	3400	270
Long straight	269	0.2	7.5	52	8070	1085

Sextupoles	Quantity	Mag. length [m]	Max. gradient $[\,T/m^2]$	Bore radius [mm]	Ampere turns/pole [A]	Power/ magnet [W]
SF	204	0.3	101.7	24	187	46
SDA	96	0.4	130.1	24	240	78
SDB	12	0.2	130.1	24	240	43

Steering magnets	Quantity	Mag. length [m]	Nom. field [T]	Gap [mm]	Ampere turns [A]	Power/ magnet [W]
Arc, wiggler	360	0.1	0.08	120	8620	190
Long straight	269	0.1	0.003	105	288	2

Table 5.6.1: *Damping ring magnet parameters.*

Wigglers	Quantity	Period length [mm]	# of periods	Max. Field [T]	$\frac{\int B^2 dl}{\left[\frac{T^2 m}{m}\right]}$	Gap [mm]	Ampere turns/ pole [A]	Power/ magnet [W]
Electro-magnetic	72	550	8	1.8	2.1	25	20500	94000
Permanent magnet	90	400	12	1.67	1.37	25		

Table 5.6.2: *Wiggler magnet parameters for both the electromagnetic and permanent magnet wiggler.*
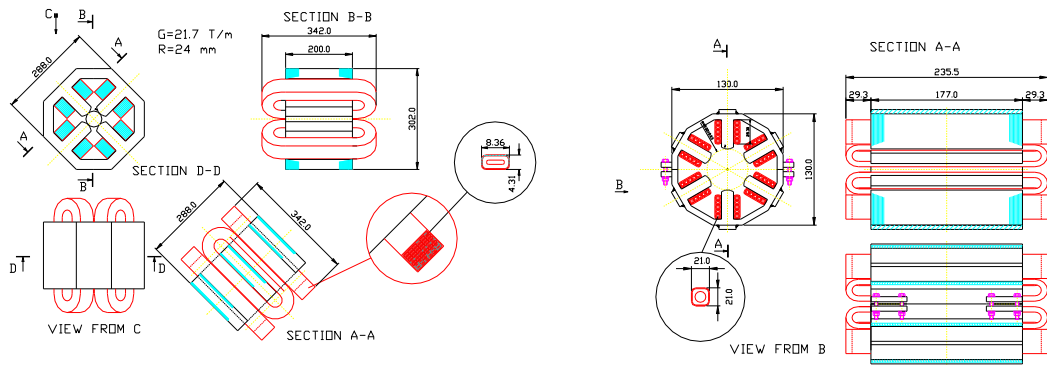
Figure 5.6.2: *Typical quadrupole magnet (left) and sextupole magnet (right).*
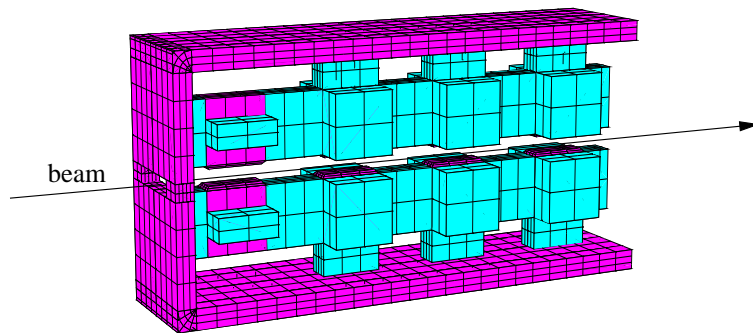
Figure 5.6.3: *Partial view of the permanent magnet wiggler.   The permanent magnet material is drawn in blue and the iron poles and yoke in magenta. The side yoke plates which enclose the whole structure are not shown.*
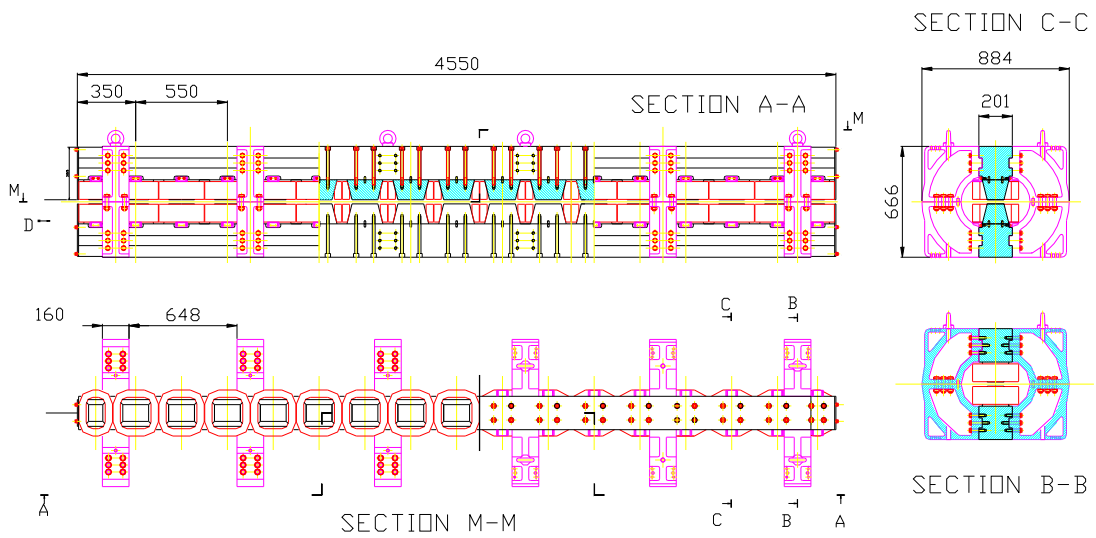
Figure 5.6.4: *Electromagnetic wiggler.*

5.6.2   Vacuum system

The vacuum system has been designed to achieve a mean pressure inside the vacuum chamber of $\sim 10^{-8}$ mbar in the arc sections, and $\sim 10^{-9}$ mbar in the long straight sections.

5.6.2.1   Residual gas sources

The residual gas inside the vacuum chamber has a contribution from two sources: thermal out-gassing and synchrotron radiation photo-desorption. The thermal out-gassing contribution is proportional to the inner surface of the vacuum chamber and strongly depends on the surface condition and treatment. A reasonable estimate of the thermal gas load is in the range from 10^{-10} to 10^{-11} mbar l/s cm^2 for a well cleaned surface. The synchrotron radiation photo-desorption contribution is proportional to the photon flux emitted by the particle beam, and is a function of the beam dose.

The synchrotron radiation properties of the dipole and wiggler are given in table 5.6.3. After a beam dose of about 50 Ah, it is reasonable to consider a desorption coefficient of about 3×10^{-6} molecules per photon. The total gas load contributions are given in table 5.6.4.

	Dipole	Wiggler	
Photon flux at 160 mA	5.4×10^{18}	3×10^{19}	photons/magnet/s
Synchrotron radiation power	860	34	kW/magnet
Maximum surface power density	190	1	kW/mm^2

Table 5.6.3: *Synchrotron radiation properties for dipoles and wigglers.*

Thermal	6×10^{-4}	mbar l/s
Dipole	1.3×10^{-4}	mbar l/s
Wiggler	1.2×10^{-4}	mbar l/s

Table 5.6.4: *Contributions to the total gas load.*

5.6.2.2   Vacuum chamber

The vacuum chamber in the bending magnets (see figure 5.6.5) accommodates a distributed pumping system. A suitable RF screen will be used to separate the beam channel from the pumping chamber. A cooling channel is present to remove the synchrotron radiation power load. In the straight sections between dipoles, the vacuum chamber is circular with a cooling channel on one side (see figure 5.6.5). In the two 7 km long straight sections the vacuum chamber is essentially a pipe of 100 mm outside diameter and 2 mm thickness, and no cooling is needed. In the wiggler sections, the

vacuum chamber has a central beam channel and two ante-chambers (see figure 5.6.6), where the synchrotron radiation fan travels before being stopped by absorbers. The vacuum chamber inside the quadrupole has a cross section as shown in figure 5.6.6. Downstream of each wiggler is a water cooled synchrotron radiation absorber with a pumping station, as shown in figure 5.6.7. All vacuum chambers are constructed from an aluminium alloy.
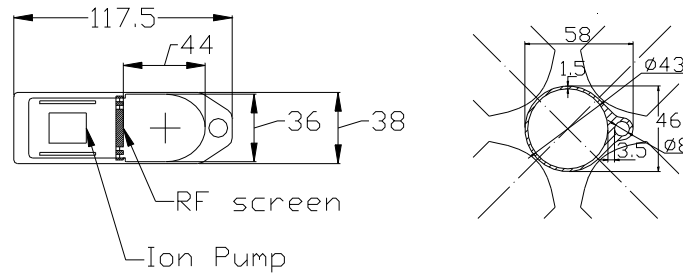
Figure 5.6.5: *Dipole vacuum chamber with distributed ion pump (left), and quadrupole vacuum chamber (right).*
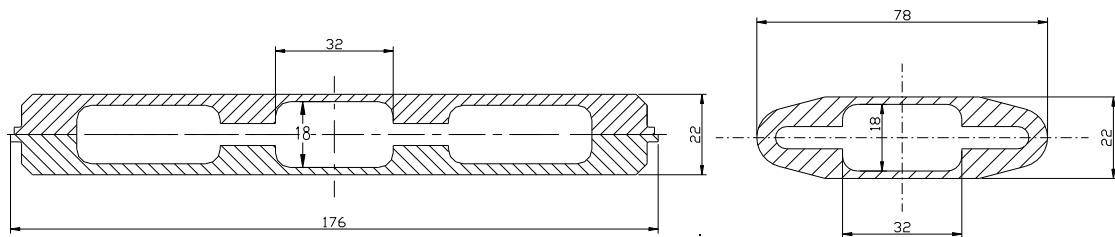
Figure 5.6.6: *Wiggler vacuum chamber with ante-chamber (left), and wiggler cell quadrupole vacuum chamber (right).*
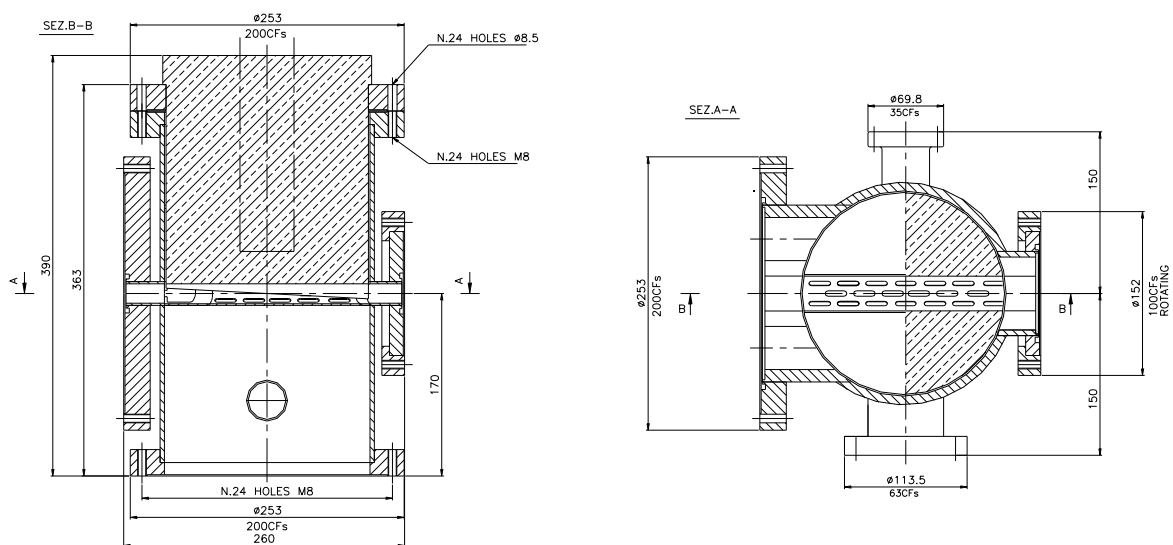
Figure 5.6.7: *Synchrotron radiation absorber.*
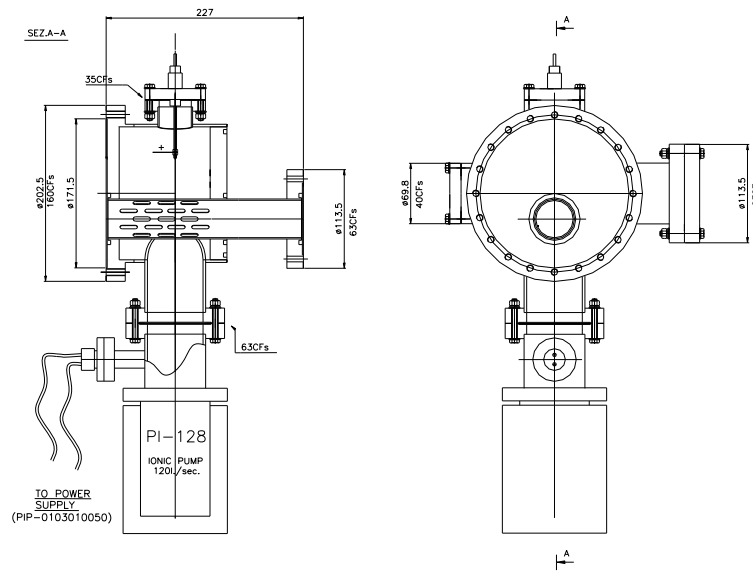
Figure 5.6.8: *Typical pumping station.*

5.6.2.3   Vacuum pumps

Table 5.6.5 lists the pumps required for the damping ring. The lumped vacuum pumps
are connected to the chamber by means of a special RF-screened vacuum port (figure
5.6.8). The section has two flanges to connect the pump and a vacuum gauge, and a
third flange which connects to a valve used during pump down.

Location	Quantity	Item	Pumping rate [l/s]
Arcs	216	distributed sputter ion pumps	190
	368	lumped sputter ion pumps	120
Wigglers	72	lumped sputter ion pumps	400
RF cavities	24	lumped sputter ion pumps	400
Long Straights	1876	titanium sublimation pumps	1000
	1876	lumped sputter ion pumps	60

Table 5.6.5: *Required pump installation.*

5.6.2.4   Bellows

Installed on the arc vacuum chambers are 662 bellows with a 43 mm inside diameter.
The vacuum chamber for the long straight sections contains 1876 bellows with a 96 mm
inside diameter (see figure 5.6.9). Each bellow is provided with a sliding contact RF
screen.
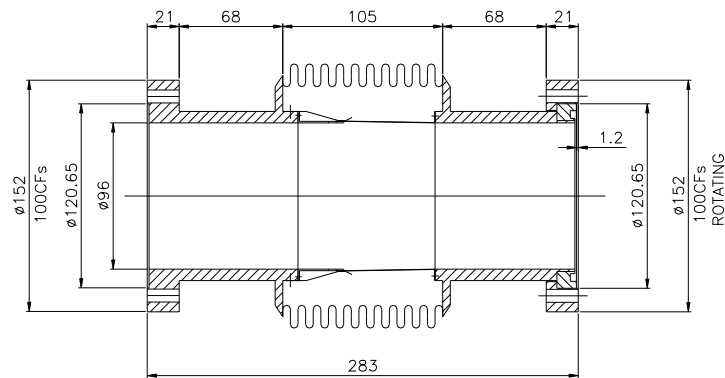
Figure 5.6.9: *RF screened bellows.*

5.6.2.5 Gate valves

Electro-pneumatic all-metal gate valves with RF contact are used to section the vacuum chamber. The number, type and location of the valves are given in table 5.6.6.

Location	Quantity	Item
Arcs	30	electro-pneumatic gate valves DN 63 with RF contact
Long Straight	60	electro-pneumatic gate valves DN 100 with RF contact
RF section	6	electro-pneumatic gate valves DN 200 with RF contact

Table 5.6.6: *Location, type and number of vacuum valves required.*

5.6.3 Infrastructure

5.6.3.1 Arc tunnel layout

The damping ring arc is located in a tunnel with 3 m inner diameter (see figure 5.6.10). This tunnel is connected at two positions to the main linac tunnel.

Each arc is equipped with a monorail transportation system capable of transporting material, components and people as shown in figure 5.6.10. The components are directly hung on the rail axis while people and generic materials can be carried on a trolley running on the tunnel side-walk. The system is powered by sliding contacts at 400 V. The main characteristics of the transportation system are:

Velocity:	5–50 m/min
Monorail loading capacity:	10 t (5 t per crane)
Trolley loading capacity:	4 people plus 1500 kg
Transversal stroke:	±100 mm on the tunnel axis

Additional infrastructure in the arcs consists of:

- a compressed air distribution line running along the whole arc;
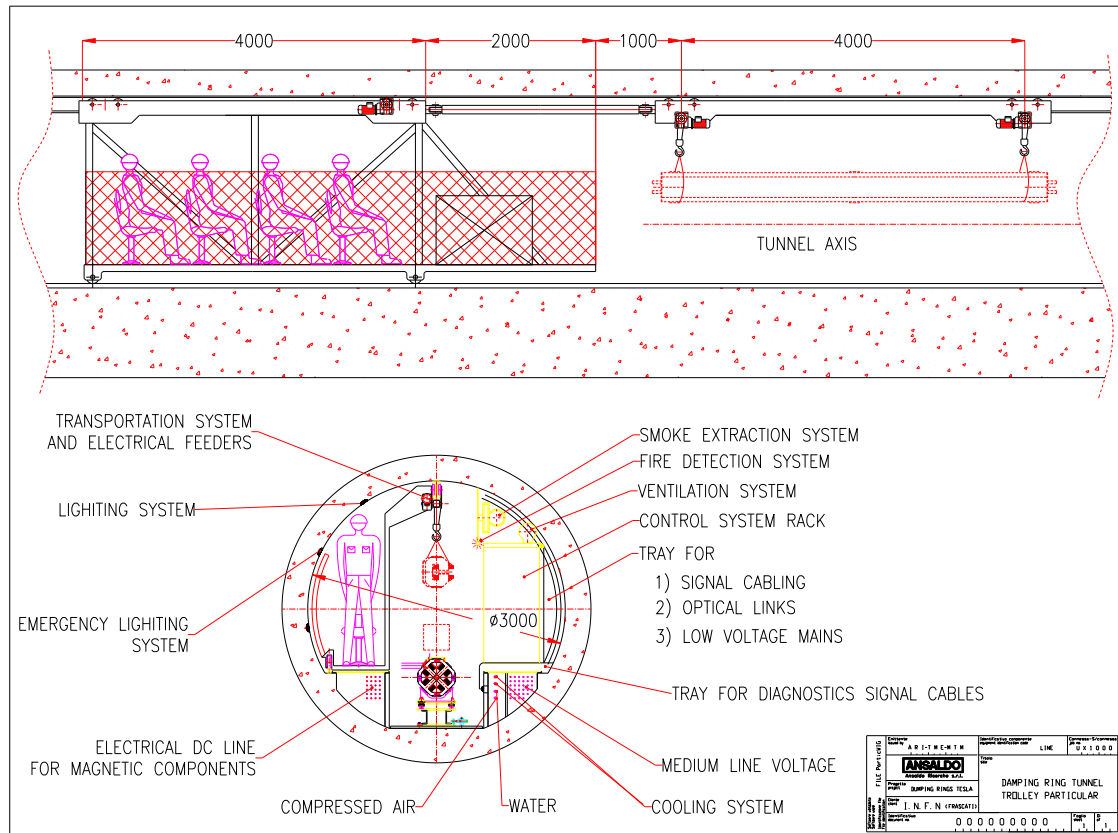
Figure 5.6.10: *Arc tunnel cross section.*

- a fire detection and extinguishing system;

- normal and emergency lighting, and an optical video circuit;

- a ventilation and air extraction system.

5.6.3.2   Electrical services and cooling systems

The electrical power needs for the damping rings are summarised in table 5.6.7, while the conventional cooling system requirements are summarised in table 5.6.8 (the cooling capacity of 720 MW for the superconducting RF cavities will be provided by the main linac refrigerators). More detailed information can be found in sections 8.4 and 8.5. The electron damping ring needs less damping (see section 5.1), i.e. the total power loss due to synchrotron radiation is smaller. Consequently the electric power consumption of the RF system and the cooling capacity are reduced.

	Positron ring	Electron ring
RF klystrons	6.5 MW	4.3 MW
Magnet power supplies	2.0 MW	
Other systems	0.5 MW	
Total	9.0 MW	6.8 MW

Table 5.6.7: *Electrical power needs of damping ring systems.*

	Positron ring	Electron ring
RF klystrons	3.3 MW	2.2 MW
Synchrotron radiation	3.2 MW	2.1 MW
Magnets and power supplies	2.0 MW	
Total	8.5 MW	6.3 MW

Table 5.6.8: *Cooling capacity for damping rings.*

Bibliography

[1] K. Flöttmann, J. Rossbach, *Emittance Damping Considerations for TESLA*, DESY 93-023, 1993.

[2] C. Sanelli et. al., *Technical Layout of the TESLA Damping Ring*, LNF-01/003 (IR), 2001.

[3] W. Decking, *Optical Layout of the TESLA 5 GeV Damping Ring*, DESY TESLA-01-11, 2001.

[4] M. Tischer, J. Pflüger, W. Decking, *A Permanent Magnet Wiggler Design for the TESLA Damping Ring*, DESY TESLA-00-20, 2000.

[5] H. Grote, F. Iselin, *The MAD Program*, CERN/SL/90-13(AP), 1996.

[6] F. Ruggiero, F. Zimmermann, *Consequences of the Direct Space Charge Effect for Dynamic Aperture and Beam Tail Formation in the LHC*, Proc. Part. Acc. Conf., New York 1999, p. 2626.

[7] W. Decking, R. Brinkmann, *Space Charge Problems in the TESLA Damping Ring*, Proc. 7th EPAC, Vienna 2000, p. 1024.

[8] R. Nagaoka, *Work Carried Out at the ESRF to Characterise and Correct the Coupling*, Proc. 7th EPAC, Vienna 2000, p. 131.

[9] E.B. Blum, *Operation of a Low Emittance Lattice at the NSLS X-RAY Ring*, Proc. Part. Acc. Conf., New York 1999, p. 2304.

[10] M. Zobov, *Status Report on DAΦNE Performance*, Proc. 7th EPAC, Vienna 2000, p. 43.

[11] E. Chojnacki, J. Sears, *Superconducting RF Cavities and Cryogenics for CESR III Upgrade*, Cornell SRF 990716-09, 1999.

[12] T. Tajima et al., *The Superconducting Cavity System for KEKB*, Proc. Part. Acc. Conf., New York 1999, p. 440.

[13] T. Tajima et al., *Development of HOM Damper for B-Factory (KEKB) Superconducting Cavities*, KEK Preprint 95-77, 1995.

[14] S. Belomestnykh et al., *Comparison of the Predicted and Measured Loss Factor of the Superconducting Cavity Assembly for the CESR Upgrade*, Cornell SRF 950406-04, 1995.

[15] E. Chojnacki et al., *Tests and Designs of High-power Waveguide Vacuum Windows at Cornell*, Part. Accel. **61** (1998) 309.

[16] T.O. Raubenheimer and F. Zimmermann, *A Fast Beam - Ion Instability in Linear Accelerators and Storage Rings*, SLAC-PUB-95-6740 and Phys. Rev. **E 52** (1995) 5487.

[17] C. Montag, *Simulation of the Fast Beam-Ion Instability in the TESLA Electron Damping Ring*, DESY TESLA-00-16, 2000.

[18] K. Ohmi, *Beam-Photoelectron Interactions in Positron Storage Rings*, Phys. Rev. Lett. **75:8** (1995) 1526.

[19] K. Ohmi and F. Zimmermann, *Head-Tail Instability Caused by Electron Clouds in Positron Storage Rings*, Phys. Rev. Lett. **85:18** (2000) 3821.

[20] A. Chao, *Physics of Collective Beam Instabilities in High Energy Accelerators*, John Wiley & Sons Inc., 1993.

[21] C. Burnton, *Tracking Studies in the Longitudinal Phase Space for the TESLA Damping Ring Design*, DESY TESLA-98-15, 1998.

[22] V.D. Shiltsev, *TESLA Damping Ring Impedances: Preliminary Design Considerations*, DESY TESLA-96-02, 1996.

[23] B.I. Grishanov, F.V. Podgorny, J. Ruemmler, V.D. Shiltsev, *Very Fast Kicker for Accelerator Applications*, DESY TESLA-96-11, 1996.

[24] W. Kriens, *Basic Timing Requirements for TESLA*, DESY TESLA-01-10, 2000.

6 Bunch Compressor and Transfer to Main Linac

6.1 Introduction

The equilibrium bunch length in the damping ring (DR) is 6 mm, too long by an order of magnitude for optimum collider performance ($\sigma_z = 0.3\,\mathrm{mm}$). Hence the bunch must be compressed longitudinally by a factor of $\sim$20 before being injected into the main linac.

Compression is achieved by introducing an energy-position correlation along the bunch length using an RF section, followed by a dispersive beamline with an energy dependent path length: in this way, the tail of the bunch can be made to follow a shorter path than the head, and the bunch becomes shorter. For the dispersive (compressing) beamline, a simple wiggler chicane will be used.

In addition to the bunch compressor, the ring-to-linac transfer line also includes the following sections:

Spin rotator The particle spin orientation in the damping ring must be vertical to preserve the polarisation. To adjust the spin vector to the required orientation at the collision point, a so-called spin rotator is required. The system consists of a combination of dipole and superconducting solenoid magnets.

Coupling correction section The large horizontal to vertical emittance ratio requires a high degree of betatron coupling control. A section containing skew-quadrupoles provides a sufficient empirical correction of the cross-plane coupling.

Diagnostic and collimation section The transfer line includes a diagnostic section which allows continuous monitoring of the beam phase space. The diagnostics serve as a quality control for the complete injection system. For commissioning and tune up a beam dump downstream of the diagnostic section is foreseen. The section also contains the collimators which remove the beam halo before injection into the main linac, decreasing the particle flux at the post-linac collimation system in the beam delivery section, and protecting the accelerating structures in the linac.

Fifteen-degree arc Before injection into the main linac, the TESLA tunnel bends 15° with a 500 meter radius. An achromatic optics is required to transport the large energy spread in the beam ($\sim$3% rms), without causing significant transverse emittance growth.

horizontal emittance $\gamma\epsilon_x$	$8 \times 10^{-6}\,\mathrm{m}$
vertical emittance $\gamma\epsilon_y$	$0.02 \times 10^{-6}\,\mathrm{m}$
initial bunch length σ_{z_i}	$6 \times 10^{-3}\,\mathrm{m}$
initial energy spread σ_{δ_i}	$0.13\,\%$
beam energy E_0	$5\,\mathrm{GeV}$
final bunch length σ_{z_f}	$0.3 \times 10^{-3}\,\mathrm{m}$
final energy spread σ_{δ_f}	$2.7\,\%$
compression ratio	20

Table 6.2.1:   *Beam parameters before and after the TESLA bunch compressor.*

6.2   Bunch Compressor

A detailed description of the bunch compressor can be found in [1]. Here only a brief overview is given.

The first stage of bunch compression is to introduce a longitudinally correlated energy spread in the bunch; this is accomplished by injecting the bunch into an accelerating section at a phase close to the zero-crossing of the RF waveform. The bunch is then compressed by transporting it through a dispersive section, constructed from a series of magnetic chicanes, which provides the necessary path length dependence on energy.

From the conservation of longitudinal emittance, we can immediately write down the final relative (rms) energy spread (σ_{δ_f}, $\delta \equiv \Delta p/p$) of the beam:

$$\sigma_{\delta_f} = \sigma_{\delta_i} \cdot \frac{\sigma_{z_i}}{\sigma_{z_f}},$$

where σ_{z_i} is the initial (DR) bunch length, σ_{z_f} the final (compressed) bunch length, and σ_{δ_i} the initial (DR) rms relative energy spread. Hence the RF must increase the energy spread of the bunch by the same factor as the bunch is compressed (~ 20).

The change in path length (Δl) with energy due to a dispersive beamline is normally expressed as a series expansion:

$$\Delta l = R_{56}\delta + T_{566}\delta^2 + ...$$

For the coefficients we adopt the matrix convention defined in [2]. For small δ, we can use the linear approximation. For a given bunch compression and associated final energy spread, the required R_{56} is given by

$$R_{56} = \frac{\sqrt{\sigma_{z_i}^2 - \sigma_{z_f}^2}}{\sigma_{\delta_f}}.$$

For a linear compressor, a coefficient $R_{56} \approx 0.22\,\mathrm{m}$ would be required. The basic parameters for the TESLA bunch compressor are given in table 6.2.1 [1].
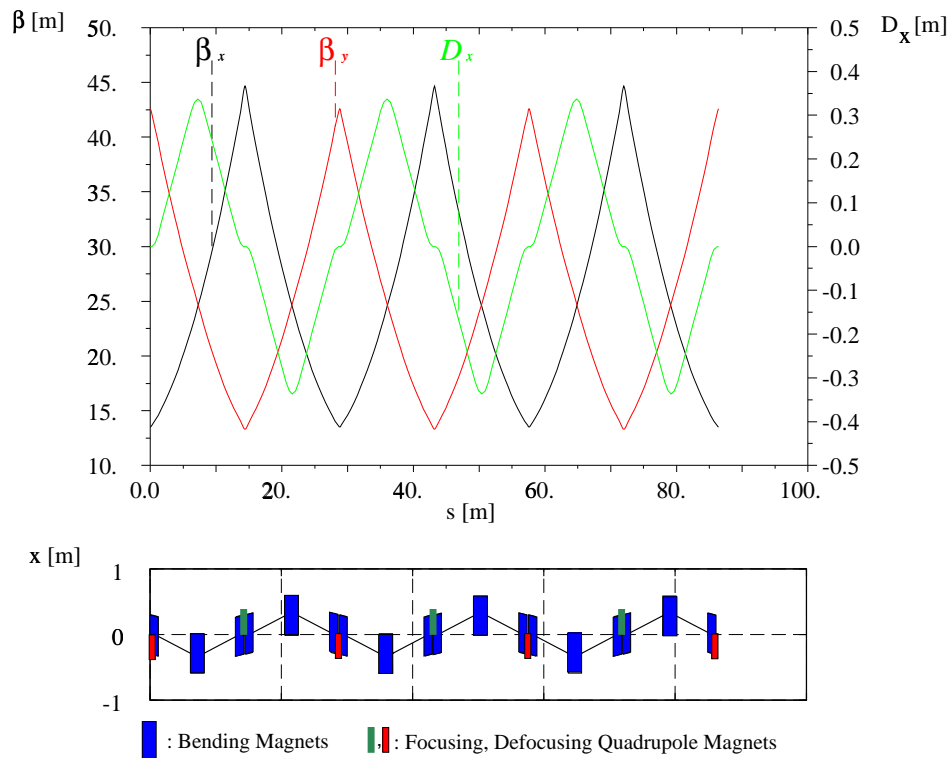
Figure 6.2.1: *Optical functions and floor plan of the wiggler bunch compressor: horizontal (black) and vertical (red) betatron function and horizontal dispersion (green).*

The large rms energy spread of $\sim 3\%$ in the magnetic compression section means that the non-linear terms in the path length (T_{566}) can no longer be ignored. The δ^2 term causes a non-linear deformation of the phase space during compression, which increases the final bunch length. A useful figure of merit is the ratio $r = T_{566}/R_{56}$, which ideally should be made as small as possible.

In addition to the above considerations, the compressor system must not cause any significant transverse emittance growth. There are two mechanisms by which emittance growth can occur:

- chromatic aberrations — most notably non-linear dispersive effects in the horizontal plane — which must be made small owing to the 3% energy spread in the beam;

- the effects of coherent and incoherent synchrotron radiation (CSR and SR respectively), which constrain the strength of the bending magnets and the overall length of the system.

Figure 6.2.1 shows the magnetic wiggler system for the compressor. It consists of bending magnet chicanes (wiggler type) embedded in a FODO structure. No additional
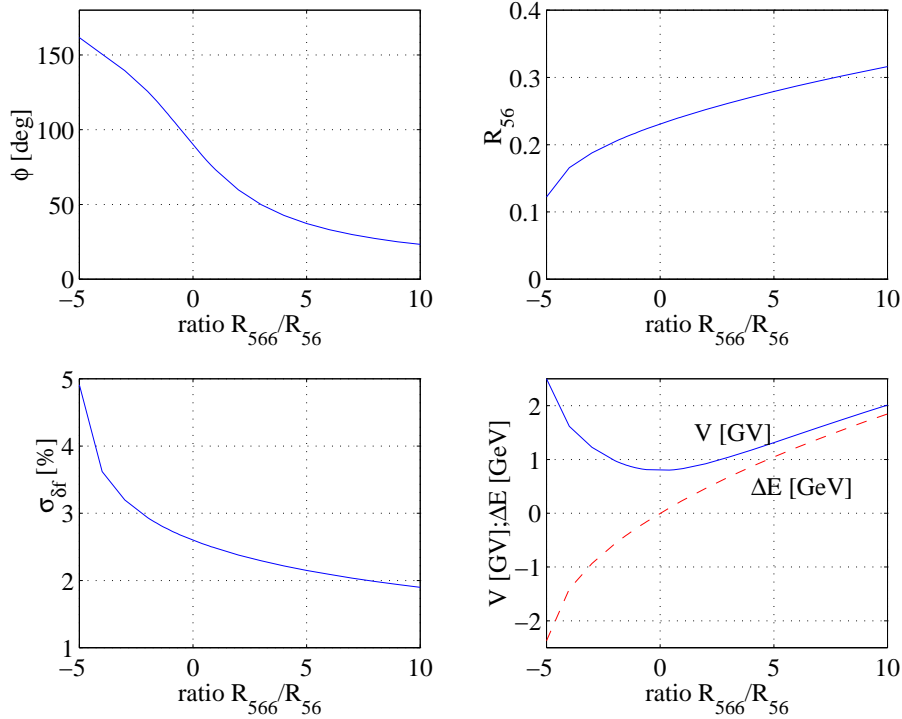
Figure 6.2.2: *Accelerating phase (upper left), longitudinal dispersion R_{56} (upper right), final energy spread (lower left), and effective accelerating voltage (lower right) as a function of $r = T_{566}/R_{56}$. The final bunch length is $300\,\mu$m.*

optical elements are included between the bending magnets of each individual wiggler section. As a result, the dispersion is zero at every quadrupole, and no higher-order dispersion is generated.

The disadvantage of a wiggler-based system is that the ratio r is fundamentally fixed at a value of $\approx -3/2$, and cannot be influenced by the design parameters. For an energy spread of 3% the value is too large to be left uncorrected, since the non-linear effects would significantly increase the final bunch length.

To compensate the effect of the δ^2 term, we use the curvature of the RF in the upstream accelerator section. By adjusting the phase of the bunch away from the zero-crossing of the RF (i.e. away from the linear slope), a non-linear energy correlation along the bunch length can be introduced. By a careful choice of parameters, this correlation can offset the effects of the non-linear path length in the wiggler section (to second-order in δ). Figure 6.2.2 shows the accelerating phase, gradient, and R_{56} necessary to cancel the second-order terms for various ratios $r = T_{566}/R_{56}$. For a negative value of r as we have here, the beam has to be decelerated on average to achieve the desired correction. Details of the compensation scheme can be found in [1, 3, 4].

The parameters for the wiggler-based compressor are presented in the table 6.2.2. The required peak voltage of the RF before the wiggler is $890\,$MV at a phase $\phi =$

longitudinal dispersion R_{56}	$0.215\,\mathrm{m}$
final energy spread $\sigma_{\delta f}$	$2.8\,\%$
total RF voltage V_{RF}	$890\,\mathrm{MV}$
RF phase angle ϕ_{RF}	$113\,^\circ$
total chicane length	$86.4\,\mathrm{m}$
SR induced emittance growth $\Delta\varepsilon_x/\varepsilon_{x0}$	0.02%

Table 6.2.2: *Basic parameters of the wiggler bunch compressor.*
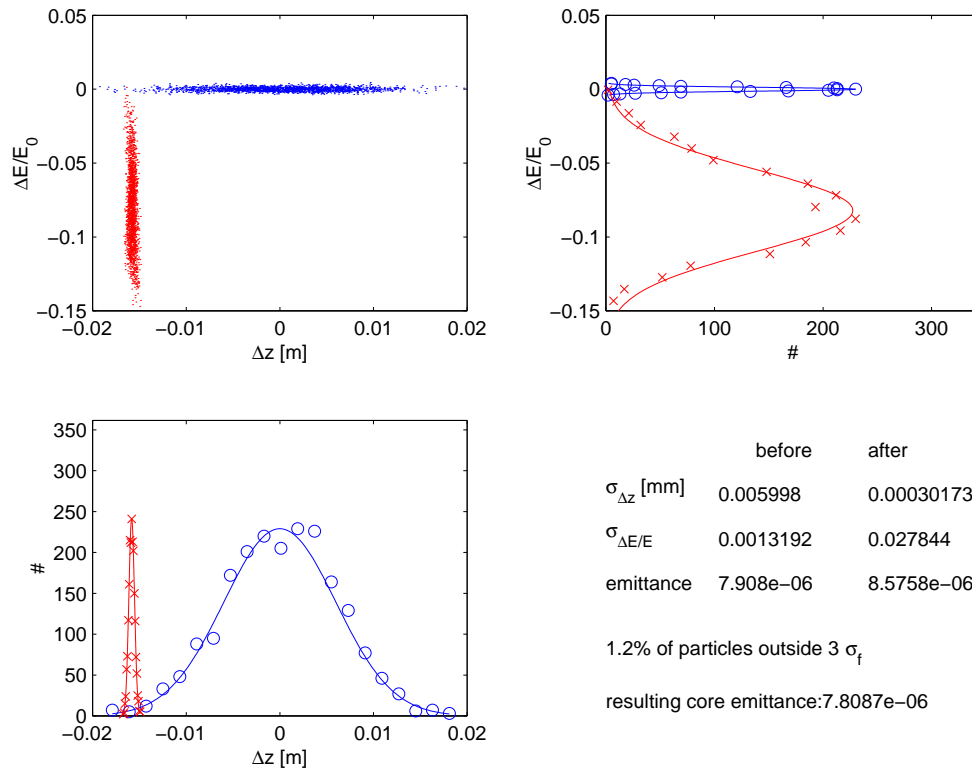
Figure 6.2.3: *Longitudinal phase space before (blue) and after (red) the bunch compressor.*

113°; this voltage will be provided by three TESLA accelerating modules with an average gradient of $23.8\,\mathrm{MV/m}$. The average energy loss is $0.4\,\mathrm{GeV}$ which has to be compensated by two additional accelerating modules. The optimised value of $R_{56} = 0.215\,\mathrm{m}$ reflects a small change from the previous value of $0.22\,\mathrm{m}$ due to the non-linear compensation scheme. The total length of the bunch compressor (including three accelerating modules) is $\approx 140\,\mathrm{m}$. The maximum deviation from the central axis is $0.3\,\mathrm{m}$, which should fit easily into the main linac tunnel.

To check the performance of the compressor, six-dimensional particle tracking using the code MAD[5] was performed. Figure 6.2.3 shows the longitudinal phase space before and after the bunch compressor. No significant transverse emittance growth was observed.
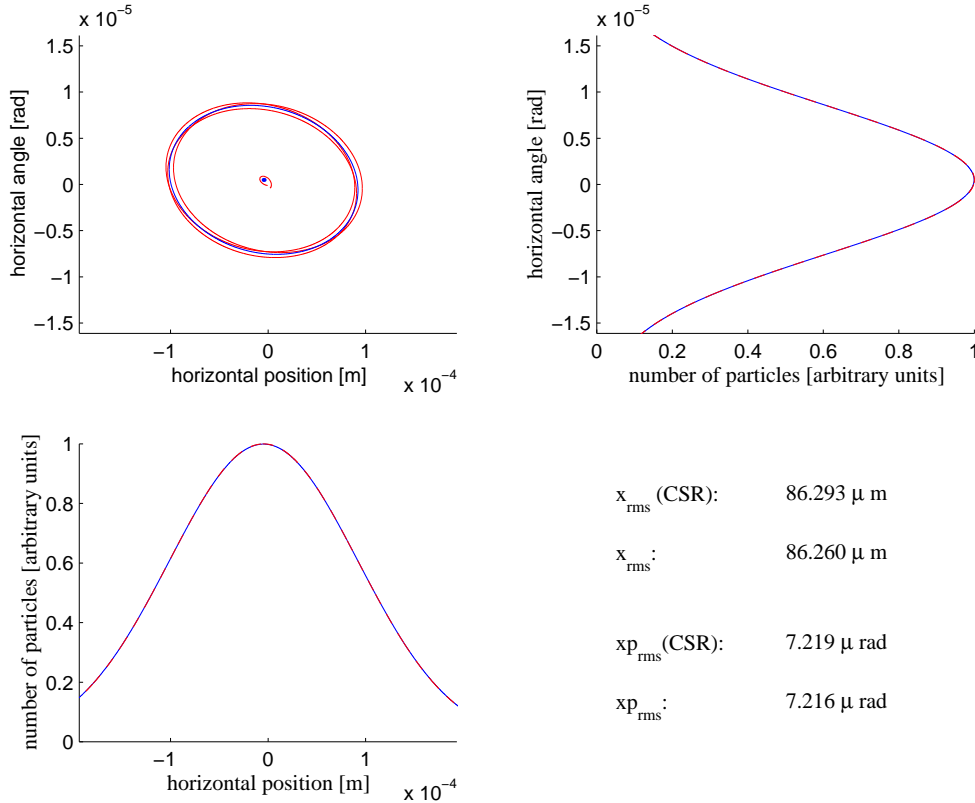
Figure 6.2.4: *TraFiC4-calculation of emittance growth due to Coherent Synchrotron Radiation effects. Shown are horizontal phase space and projections (red lines/dots: with CSR, blue lines/dots: without CSR). Upper left: horizontal phase space with longitudinal bunch slice centres and 1σ-ellipses. Upper right: projection of particle angles. Lower left: projection of particle positions.*

As a final check on the wiggler performance, a calculation of emittance growth due to Coherent Synchrotron Radiation (CSR) effects was made using the code TraFiC4[43]. CSR effects cause an emittance growth which is correlated along the bunch length similar to single bunch wakefield effects in the linac. At the compressor exit, the correlated normalised emittance is about 2.5×10^{-7} m, the uncorrelated emittance is preserved and the projected emittance grows by less than 1%. Figure 6.2.4 shows the horizontal phase space and its projections at the end of the compressor.

6.3   Spin Rotator

The spin rotation is constructed from superconducting solenoids and a normal conducting bend section (arc), located upstream of the bunch compressor. A system consisting only of normal conducting vertical and horizontal bending magnets (a so-called 'half-serpent' $90°$ spin rotator) is not an option for TESLA, since long dipoles ($\sim$150 m) would be required to reduce emittance growth due to synchrotron radiation [7, 8].

longitudinal dispersion R_{56}	$0.005\,\text{m}$
maximum spin rotation in solenoid $\nu_{solenoid}$	$90°$
total arc bend angle ϕ	$8.0°$
spin rotation angle in the arc ν_{arc}	$90°$
total length of rotator system L_{tot}	85m
SR induced emittance growth $\Delta\epsilon_x/\epsilon_{x0}$	0.02%

Table 6.3.1: *Basic spin rotator parameters.*

Since the damped beam is flat ($\epsilon_y/\epsilon_x \ll 1$) the cross-plane coupling induced by the solenoids must be compensated. This is achieved by a spin rotator unit constructed from two identical superconducting solenoids, separated by a short beamline whose (transverse) optics form a $-I$ transformation; this effectively cancels the betatron coupling, while the spin rotation of the two solenoids add. A single unit can rotate the spin around the longitudinal axis by up to 90°. The complete spin rotator is constructed from three sections:

- an initial solenoid pair, which rotates the spin around the local longitudinal (z) axis by $\pm90°$;

- a normal conducting horizontal arc, which further rotates the spin around the vertical axis by 90°; and

- a final solenoid pair, providing an additional rotation about the z-axis by $\pm90°$.

With the above combination of rotations, all possible spin orientations can be achieved.

The focusing effect of the solenoids is corrected with four matching quadrupoles per paired solenoid section. The matching quadrupoles are positioned between the solenoid sections and the central arc (see figure 6.5.1). With the solenoids at maximum field strength, the chromatic emittance growth is $\sim 1\%$ ($\sigma_{\delta_i} \approx 0.13\%$). The parameters of the spin rotator system are given in table 6.3.1.

6.4   Auxiliary Beamline Sections

6.4.1   Coupling correction section

In order to empirically correct anomalous cross-plane coupling due to either damping ring extraction or spin rotator errors, a coupling correction section of the type proposed in [9] is included. The system is constructed from four skew-quadrupoles with zero nominal strength. The betatron phase advance between the first and second skew quadrupoles, and the third and fourth skew-quadrupoles is $\Delta\psi_x = \Delta\psi_y = \pi/2$; the second and third are separated by $\Delta\psi_x = \pi, \Delta\psi_y = \pi/2$ such that the four skew quadrupoles orthogonally control the four coupled correlations in the beam: $\langle x'y\rangle$, $\langle xy'\rangle$, $\langle xy\rangle$ and $\langle x'y'\rangle$. Using skew-quadrupoles with a length of $0.1\,\text{m}$, $\pm0.1\,\text{T}$ pole-tip

field and a $0.01\,\mathrm{m}$ pole-tip radius, a factor of about two in emittance increase can be corrected per skew-quadrupole.

6.4.2 Diagnostic and collimation section

A wire-array emittance measurement station [9] is located downstream of the wiggler section. The section is design to continuously monitor the matching and emittance of the beam before being injected into the linac. A wire-array station is constructed from a series of n FODO cells, with a profile monitor (wire[1] scanner) located at each vertically focusing quadrupole ($\hat{\beta}_y$). A minimum of $n = 3$ scanners are required to uniquely determine the emittance of the beam. To add some statistical redundancy, we choose $n = 4$. The optimal phase advance per cell is then given by $\pi/n = \pi/4$.

The nominal rms beam size at the monitors is $5\,\mu\mathrm{m}$ vertically and $70\,\mu\mathrm{m}$ horizontally. A correctly matched beam is easily identified since the beam size (for a single plane) is identical at each of the four wire scanners. The cross-plane coupling can not be accurately determined using this system: however, by simply minimizing the vertical emittance (flat beam) with the four skew-quadrupoles in the upstream coupling correction section, all coupling can be corrected (with some iteration necessary in extreme cases). A direct measurement of the coupled correlations in the beam can be made by using six wire scanners with similar phase advances if necessary [9].

Transverse phase space collimation is obtained by placing four mechanical spoiler pairs in a FODO lattice with appropriate phase advance. Energy collimation is done in the fifteen-degree arc.

6.4.3 Fifteen-Degree Arc

The fifteen-degree arc is necessary to accommodate the special tunnel geometry required for the option of colliding TESLA bunches with HERA proton beams. The arc is constructed from an achromatic lattice with an energy acceptance of $\pm 10\%$. Strong focusing, chromatic correction using sextupole magnets, and small cell length is needed to prevent emittance growth. The bending magnets are vertically focusing (combined function) to maintain sufficient dynamic aperture by reducing the vertical betatron function. Figure 6.4.1 shows the optical functions of one achromatic cell. Figure 6.4.2 shows the results of tracking simulations for a beam with an energy spread of 3% rms. The longitudinal dispersion R_{56} is small ($0.002\,\mathrm{m}$) and affects the bunch length by less than 5%.

6.5 Beamline Geometry

Figure 6.5.1 shows the floor plan of the entire tunnel in the electron damping ring extraction and injection region. The floor plan starts at the '$500\,\mathrm{MeV}$ point', where

---

[1]by wire we refer to either a mechanical wire device or a laser wire.
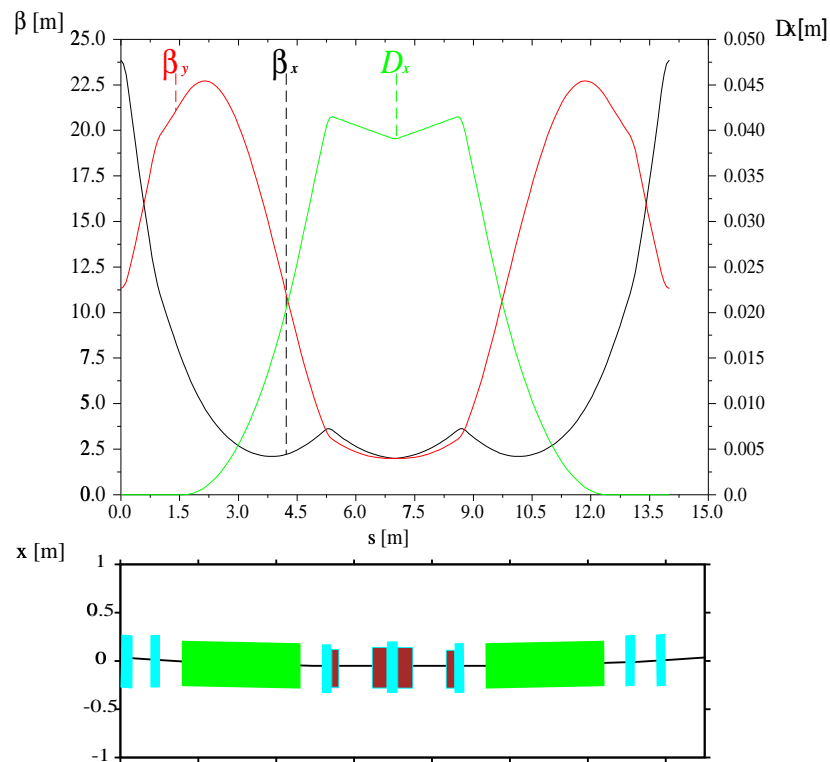
Figure 6.4.1: *Optical functions and floor plan of one achromatic arc cell. Dipoles are green, quadrupoles blue and sextupole magnets are brown.*

the various pre-accelerator linacs deliver the bunch trains for TESLA collider and FEL operation to the 5 GeV electron injector linac (section 4.2).

At the exit of the injector linac, a horizontal dipole pulsed at 5 Hz[1] deflects the collider pulses into a vertical transfer line which then (horizontally) injects the beam into the damping ring. The damping ring is situated about two meters above the main linac axis.

After ∼200 ms the beam is horizontally ejected from the damping ring, and deflected down to the level of the main linac, where it is injected into the spin rotator and the bunch compressor. This beamline runs parallel to the injector linac. Figure 6.5.2 shows a cross-section of the tunnel. To allow a clear passage, the tunnel monorail (chapter 8) has to move to the side by 0.7 m in the area of the spin rotator.

After passing though the bunch compressor, diagnostics and collimation section and fifteen-degree arc, a second 5 Hz pulsed dipole joins the trajectories of the collider and FEL beams together before they are injected into the main linac.

The positron system is essentially the same as that described above. The geometry

---

[1]The injector linac runs at 10 Hz, alternately accelerating bunches for the collider and the FEL. Only the beam for the collider is injected into the damping ring.
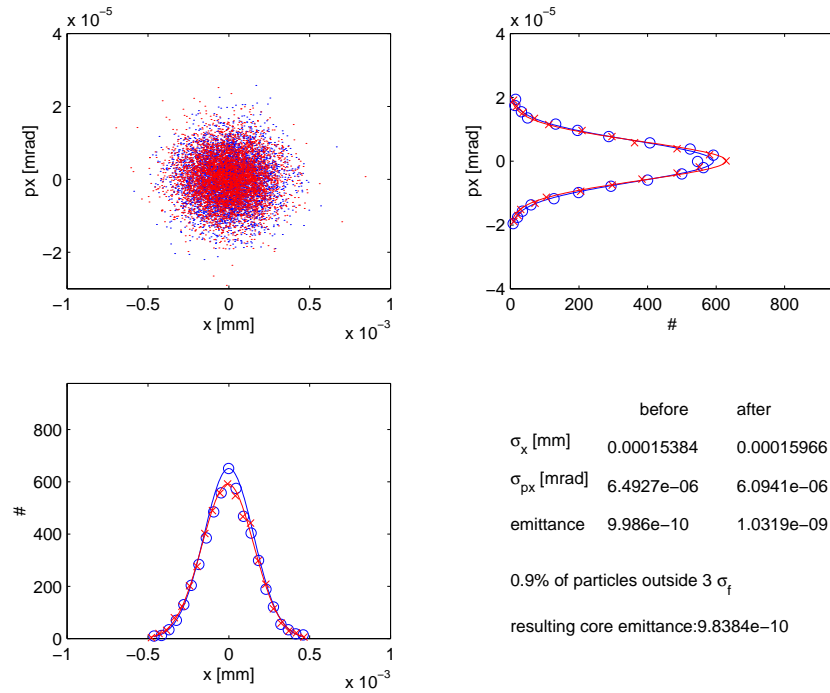
Figure 6.4.2: *Horizontal phase space before (blue) and after (red) tracking through the fifteen-degree arc. The rms energy spread of the beam is 3%.*

is simplified, however, since the positron injector linac is located at the opposite end of the damping ring (at the high-energy end of the main linac). In addition, there is no FEL beamline and the fifteen-degree arc is not needed.

6.6   Magnet and RF Systems Summary

The complete list of magnets and RF modules (and their specifications) for the entire ring-to-linac transfer line is given in table 6.6.1.
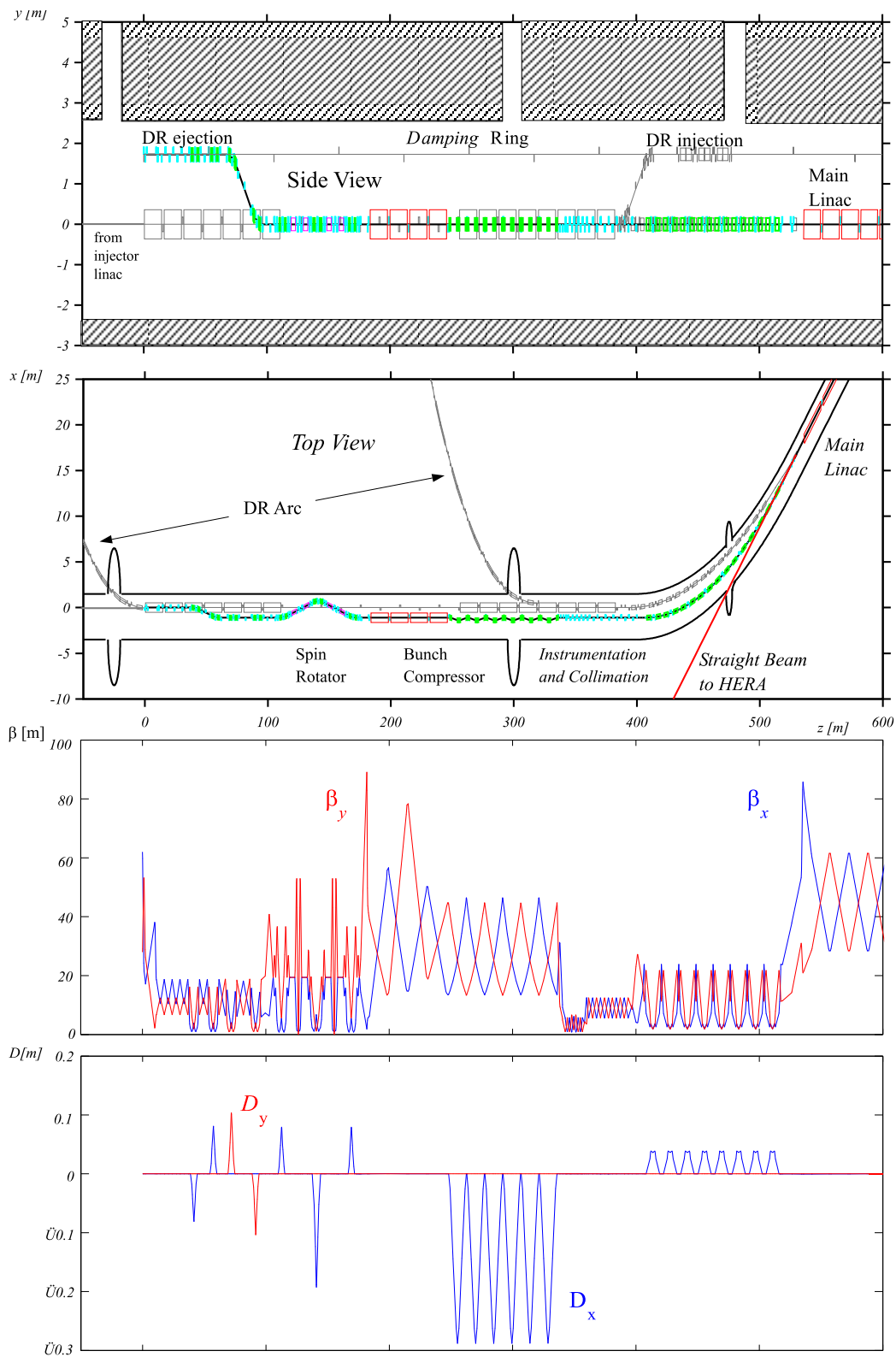
Figure 6.5.1: *Floor plan, betatron functions and dispersion for the complete beamline. In the floor plan, bending magnets are green, quadrupoles blue, RF cavities red and solenoid magnets magenta. The damping ring components and those of the injector linac are shaded in grey.*
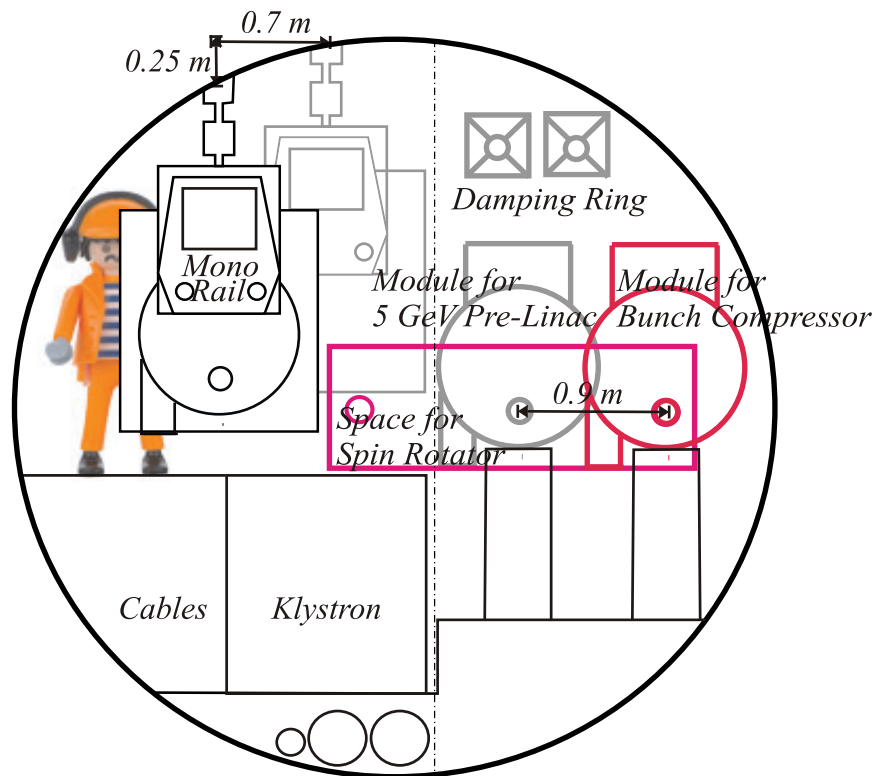
Figure 6.5.2: *Cross-section of the TESLA tunnel in the electron damping ring injection/ejection region, looking upstream towards the injector. The RF modules of the two beam lines are interleaved (see figure 6.5.1).*

Bending Magnets	Quantity	Mag. Length [m]	Defl. Angle [deg]	Mag. Field [T]	Gap [mm]
horizontal dogleg	4	1.0	2	0.582	20
vertical dogleg	4	1.25	2.5	0.582	20
spin rotator	4	0.75	2	0.776	20
	4	1.5	4	0.776	20
bunch compressor	12	1.075	3.2	0.785	20
	6	2.15	6.4	0.785	20
15 degree arc	16	3.0	0.9375 with 2.5 T/m gradient	0.091	20

Quadrupoles	Quantity	Mag. Length [m]	Max. Gradient [T/m]	Bore [mm]
	170	0.2–0.4	25.0	20

Sextupoles	Quantity	Mag. Length [m]	Max. Gradient [T/m^2]	Bore [mm]
15 degree arc	32	0.4	850	20

Solenoids	Quantity	Mag. Length [m]	Nom. Field [T]	Bore [mm]
spin rotator	4	3.55	3.8	20

RF-Modules	Quantity	Number of Cavities	Max. Gradient [MV/m]
bunch compressor	3	12	23.8

Correctors	Quantity	Mag. Length [m]	Max. Defl. [deg]	Max. Field [T]	Gap [mm]
	120	0.1	0.009	0.025	20

Table 6.6.1: *Transfer line magnet parameters.*

Bibliography

[1] W. Decking, G. Hoffstätter, T. Limberg, *Bunch Compressor for the TESLA Linear Collider*, DESY TESLA-00-40, 2000.

[2] K. Brown, *A First- and Second-Order Matrix Theory for the Design of Beam Transport Systems and Charged Particle Spectrometers*, SLAC Report-75, 1982.

[3] P. Emma, *Bunch Compressor Beamlines for the TESLA and S-Band Linear Colliders*, DESY TESLA-95-17, 1995.

[4] P. Emma, *Bunch Compressor Options for the New TESLA Parameters*, DESY TESLA-98-31, 1998.

[5] H. Grote and F. Iselin, *The MAD Program*, CERN/SL/90-13(AP), 1996.

[6] M. Dohlus, A. Kabel and T. Limberg, *Efficient Field Calculation of 3D Bunches on General Trajectories*, Nucl. Instr. Meth. **A445** (2000) 338.

[7] P. Emma, *A Spin Rotator System for the NLC*, NLC-NOTE 7, 1994.

[8] T. Fieguth, *Snakes, Serpents, Rotators and the Octahedral Group*, SLAC-PUB-4195, 1987.

[9] M. D. Woodley, P. E. Emma, *Measurement and Correction of Cross Plane Coupling in Transport Lines*, Proc. 20th Int. Linac Conference, Monterey, CA, Aug. 2000, LINAC2000-MOC19, SLAC-PUB 8581, 2000.

7 Beam Delivery System

7.1 Introduction

The Beam Delivery System (BDS) transports the beams from the exit of the linacs to the interaction point (IP), where they are brought into collision, and then safely extracted and dumped in high-power beam dumps. The BDS serves several important functions. It must:

- produce the necessary strong demagnification of the beams, resulting in the 550 nm×5 nm beam spots at the IP;

- maintain the beams in collision using active stabilisation (feedback);

- cleanly extract the strongly disrupted beams after the IP, and transport them to high-power dumps;

- provide a high level of machine (and detector) protection, in the event of a linac fault resulting in a beam with either a large energy error or a large orbit deviation or both;

- provide collimation of large amplitude particles (the so-called beam halo) coming out of the linac, which would cause significant background in the physics detector;

- provide diagnostics (emittance measurement) for the linac;

- include a switch-yard to separate the beamline serving the (optional) second interaction region (IR).

In addition to the above, the *electron* BDS must also accommodate the undulator-based positron source (section 4.3), which is located at the exit of the electron linac.

In this chapter, an overview of the TESLA BDS sub-systems is given. Many of the basic concepts and design constraints have been covered in the original Conceptual Design Report (CDR)[83]: since then, however, new concepts and philosophies have been adopted, and the system described here is significantly different from the one described in the CDR. The chapter is divided into seven sections which reflect the primary functions of the BDS:

- Section 7.2 acts as an introduction to the entire system, covering the lattice, optics, magnets and vacuum systems.

- Section 7.3 covers the luminosity stability issues, with emphasis on the various feedback systems that need to be implemented in order to achieve the required high luminosity. Effects of vibration and ground motion are also discussed.

- Section 7.4 deals with the important considerations related to the IR (machine-detector interface), and particular beam-beam effects.

- Section 7.5 gives an overview of the beam halo collimation system, which uses mechanical spoilers to physically 'scrape' the halo particles off the beam. Machine protection issues are also covered in this section.

- Section 7.6 discusses both the charged-particle spent-beam extraction system and the beamstrahlung extraction system.

- Finally, section 7.7 covers the concept and design of the high-power main beam dump.

The chapter is intended to be a comprehensive overview of the current design and philosophy of the TESLA BDS: more detailed information on particular sub-systems or components can be found in the supplied references.

7.2 Magnet Lattice and Optics

The following sections provide an overview of the main features of the primary e^+e^- BDS up to the IP. The main extraction line system will be dealt with separately in section 7.7.

7.2.1 Basic layout and geometry

The TESLA BDS for the primary e^+e^- IR is $3436\,\mathrm{m}$ in length (linac to linac). The IR itself sits slightly off-centre, with the e^- and e^+ delivery systems being $1759\,\mathrm{m}$ and $1677\,\mathrm{m}$ in length respectively. The slight asymmetry is due to the undulator-based e^+ source at the exit of the e^- linac (see section 4.3). From the first bend magnet in the switch-yard (section 7.2.2) both lattices are identical.

Figure 7.2.1 plots $\sqrt{\beta_{x,y}}$ and the dispersion function (D_x) for the BDS (e^-). The various modules which separate out the functionality of the BDS are clearly marked:

e^+ **source undulator** Contains space for the e^+ source undulator (section 7.2.2).

Switch-yard Arc A double bend achromat arc which acts as a switch to a second IR and allows enough clearance for the e^+ source photon target (section 7.2.2).

Magnetic Energy Spoiler (MES) A dispersive section containing non-linear elements which 'blow up' the beam at the downstream energy collimator in the event of a large energy error (section 7.2.3).
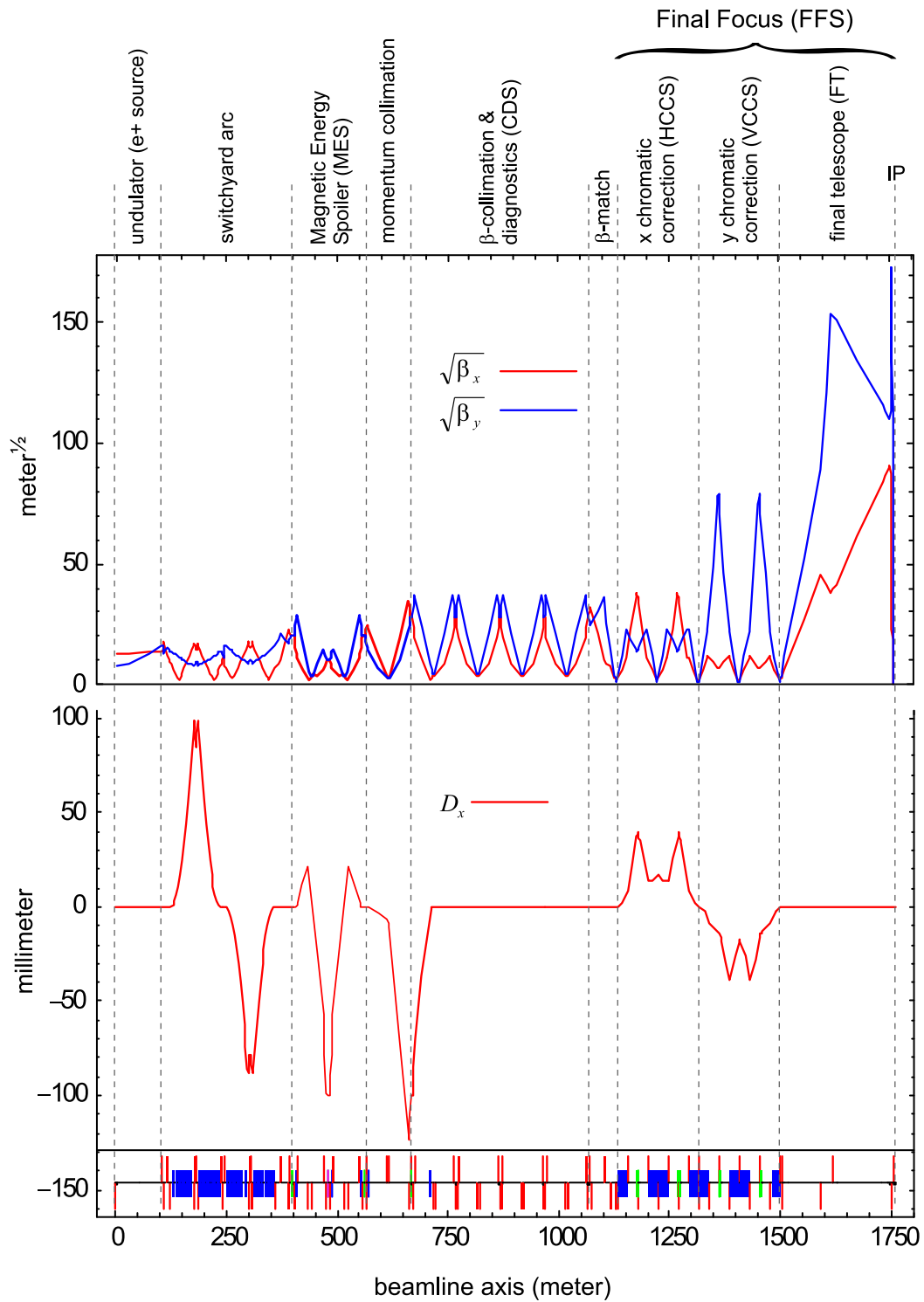
Figure 7.2.1: *Optics functions for the TESLA BDS (e⁻).*
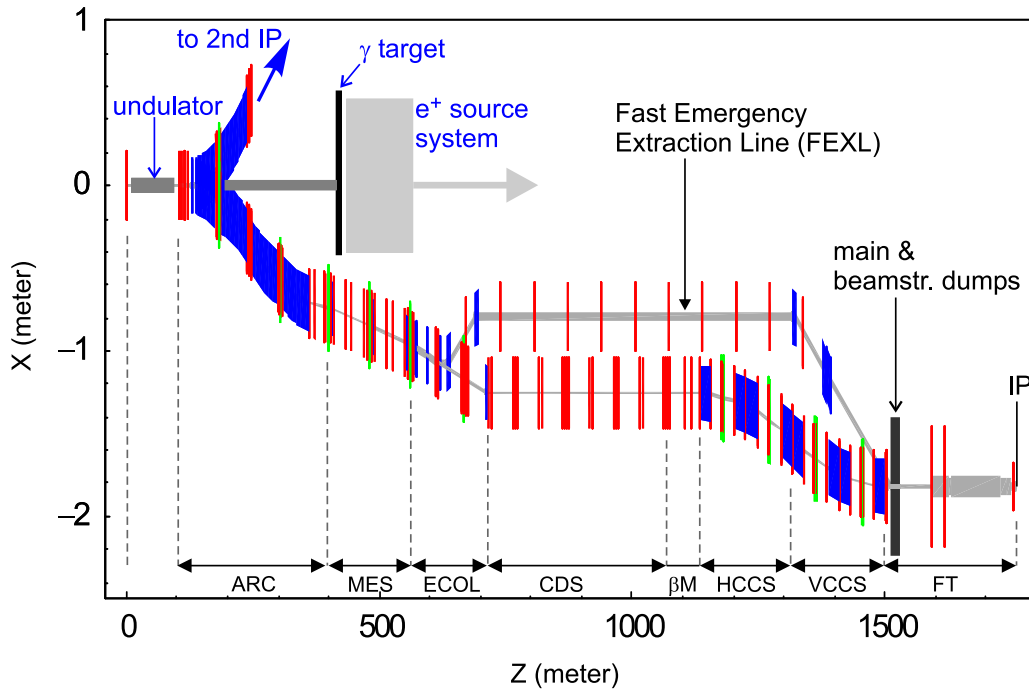
Figure 7.2.2: *Geometry of the primary e^- BDS from linac to IP.*

Momentum Collimation A point of high dispersion where the primary energy collimator will be placed (section 7.2.3).

Collimation and Diagnostics Section (CDS) A repetitive lattice where a series of spoilers and absorbers are used to collimate the beam halo. This section will also support the primary emittance measurement station (section 7.2.4).

β-Match Matching from the CDS to the entrance (image point) of the Final Focus System.

Final Focus System (FFS) A second-order achromatic telescope system which focuses the beam at the IP (section 7.2.5).

Figure 7.2.2 shows the geometry of the electron BDS, including the Fast Emergency Extraction Line (FEXL, section 7.2.6), and an indication of the location of the positron source system (section 4.3). The IP has a transverse offset with respect to the linac of 1.82 m, and the net bending angle is zero. Figure 7.2.3 shows the complete BDS layout (linac to linac), including the optional second IR.

7.2.2   Positron source undulator and beam switch-yard

In the case of the e^- BDS, the undulator for the e^+ source is installed directly after the linac. The matching from linac to undulator is designed to reduce the e^- phase space contribution to the total photon spot size at the target to less than one-fifth (a
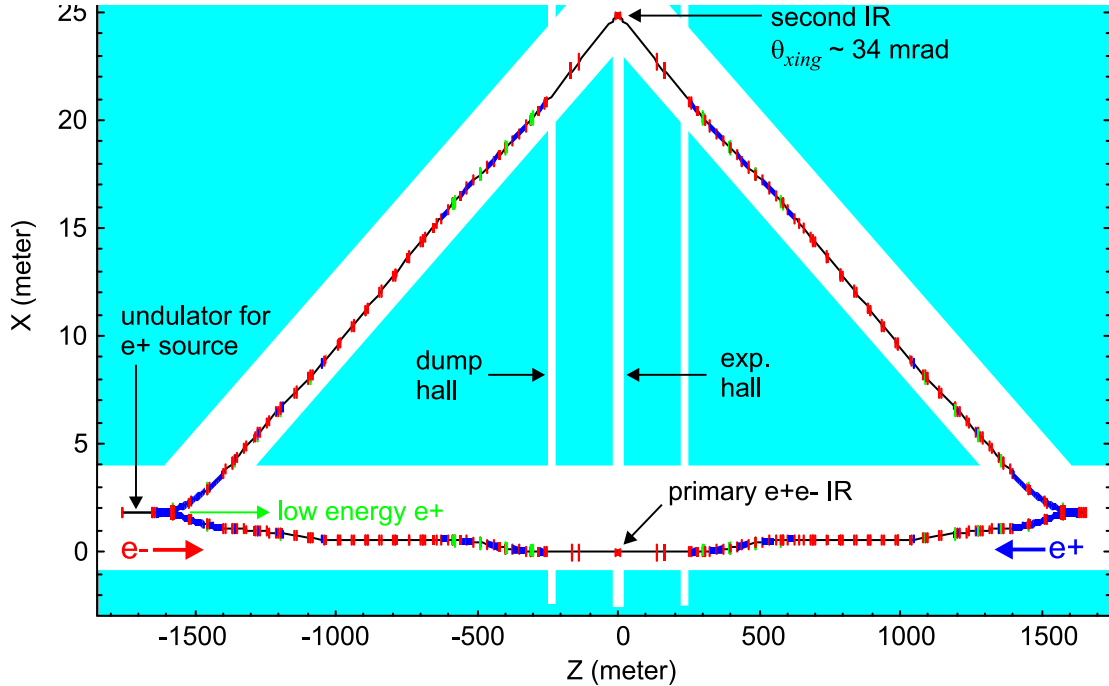
Figure 7.2.3: *Geometry of the TESLA BDS, including the second IR.*

necessary constraint for polarised e^+ production). Details of the e^+ source are covered in section 4.3. The undulator increases the relative energy spread in the beam to about 0.15%, as compared to $< 0.05\%$ coming out of the linac; this increase has consequences for the magnet stability tolerances and luminosity stabilisation (section 7.3).

Immediately after the undulator, the beam switch-yard steers the e^- beam to either of the two foreseen interaction regions (figure 7.2.4). The switch-yard is placed after the undulator so as not to exclude the possibility of $e^+ e^-$ collisions at the second IR. The two primary constraints for the design of the switch-yard arcs are:

- the emittance growth due to synchrotron radiation should be kept to an acceptable minimum; and

- the arc geometry should allow enough clearance for the photon target and the associated e^+ capture system (section 4.3).

The first 24 dipole magnets are common to both beamlines, after which the transverse clearance is enough to separate the two (see 7.2.7 for magnet details). The use of iron-core electromagnets precludes fast intra-bunch switching between the two IRs, but could in principle allow switching at 5 Hz.

The lattice is based on a double-bend achromat system used in modern light sources to significantly reduce the horizontal emittance growth from synchrotron radiation effects. Figure 7.2.5 shows the emittance growth along the entire BDS beamline: the
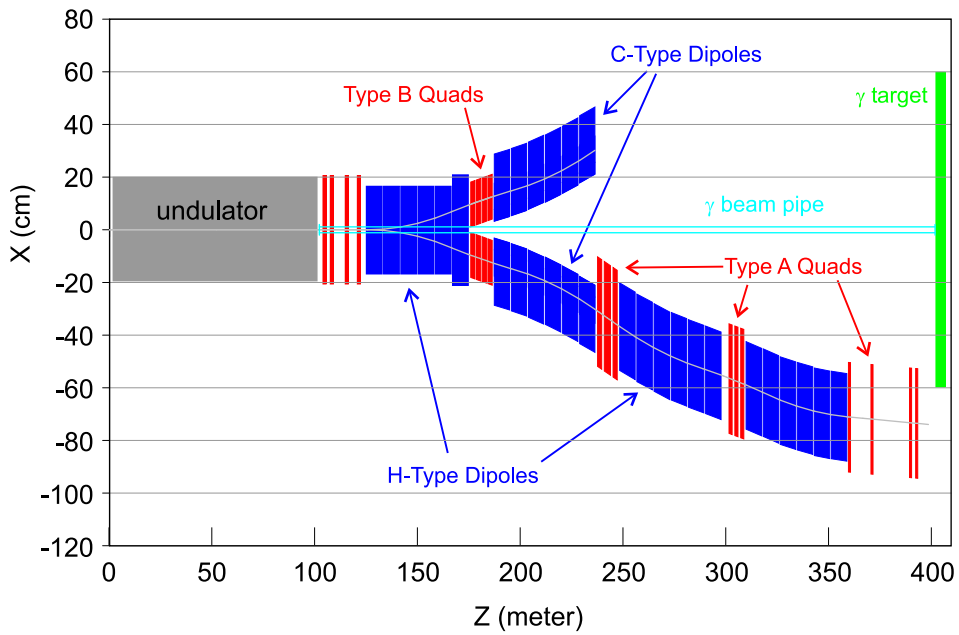
Figure 7.2.4: *The BDS switch-yard, showing the location of the photon beamline and target.*
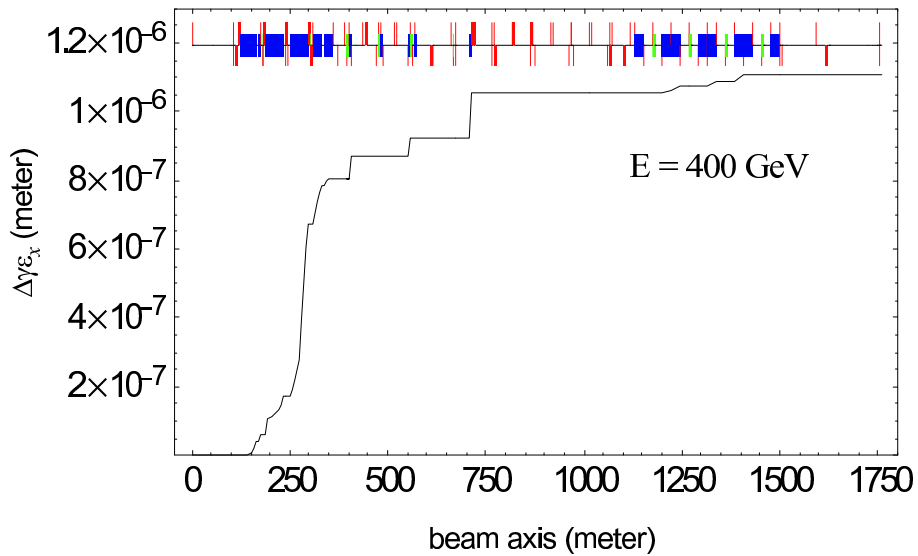
Figure 7.2.5: *Horizontal emittance growth for the entire BDS, and a beam energy of 400 GeV (design emittance $\gamma\epsilon_x = 8 \times 10^{-6}$ m).*

largest contribution comes from the arcs, but the total effect is still less than 14% at 400 GeV which is considered acceptable.

A complete and detailed description of the BDS switch-yard system can be found in [2].

7.2.3   Energy collimation and magnetic energy spoiler (MES)

The system is characterised by the double peaked dispersion function (after the switch-yard arc, see figure 7.2.1). The first peak is the so-called magnetic energy spoiler (MES), which forms part of the machine protection (MP) system. It is primarily intended to protect the downstream (mechanical) energy spoiler from being damaged by a direct hit from an off-energy beam. In the event of a beam energy error (>2%), The MES serves two related MP functions:

- a BPM placed at the high dispersion peak is used to send a signal to the downstream fast kicker system of the Fast Emergency Extraction Line (FEXL, section 7.2.6), causing the remainder of the bunch train to be safely extracted to the main dump;

- the non-linear magnets in the system significantly increase the vertical beam size on the face of the downstream energy spoiler, allowing the spoiler to survive a few bunches from the train.

Section 7.5 covers the collimation system in more detail, while the FEXL is covered in section 7.2.6.

7.2.4   Collimation and diagnostics section (CDS)

In the CDR [83] version of the BDS, the collimation system and diagnostic sections were separated. In the current system, the betatron collimation system and the main emittance measurement station have been combined into a single beamline. Betatron collimation is now performed at intervals of 45° phase advance, at locations of relatively large beam size ($\sigma_{x,y} = 127, 7\,\mu$m at 250 GeV). Such a lattice also provides for an efficient emittance measurement station as described in [4], using profile monitors close to each spoiler location. For the monitors themselves, both flying carbon-wire monitors [5] and laser-wires [6] are envisaged, the latter being used during nominal luminosity (high current) operation. A more detailed description of the lattice can be found in section 7.5.

7.2.5   Final focus system (FFS)

The FFS focuses the beams down to the required $\sigma_x = 550$ nm and $\sigma_y = 5$ nm at the IP (250 GeV). The optics is based on that used for the SLC final focus system [7] and the final focus test beam (FFTB) [8]. The demagnification is performed by a point-to-point telescope system (Final Telescope, FT). Upstream of the FT are two dispersive
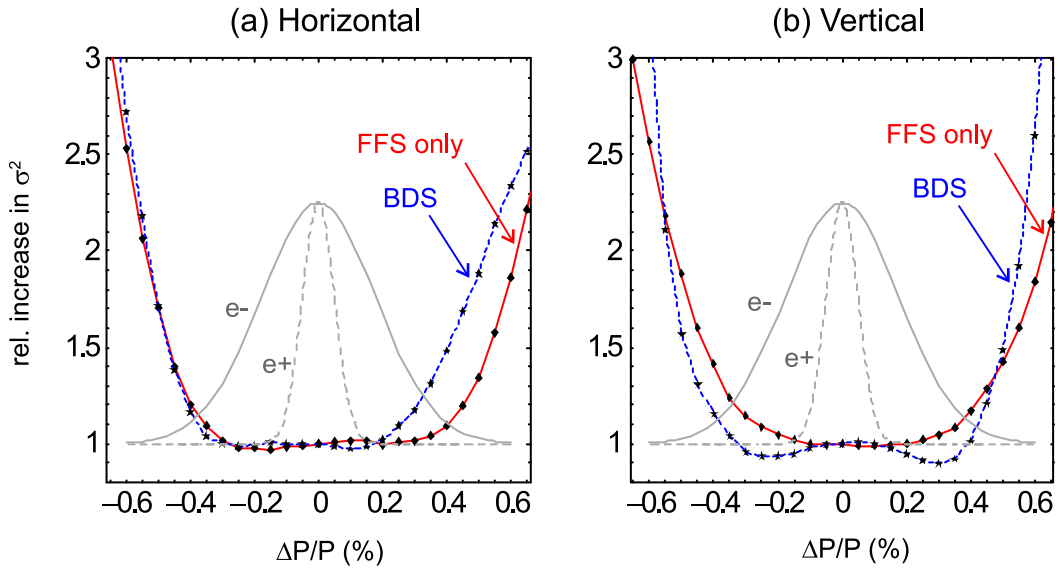
Figure 7.2.6: *Energy bandwidth for the (a) horizontal and (b) vertical plane. The bandwidth for the entire BDS and only the FFS are indicated. The energy profile of both e^- and e^+ are also shown for comparison.*

sections referred to as the horizontal (HCCS) and vertical (VCCS) chromatic correction sections, where pairs of strong sextupoles separated by a $-I$ transformation are used to correct (to second-order) the strong chromaticity of the final doublet. Figure 7.2.6 shows the momentum bandwidth for the BDS; the bandwidth due only to the FFS is also shown for comparison.

To allow a clear extraction path for the beamstrahlung to the main dump hall ($\sim$250 m from the IP), the length of the FT has been significantly increased beyond that which would naturally be required (see section 7.7). In order to re-establish the correct optics and required bandwidth, an additional weak doublet is now required approximately 130 m upstream of the final doublet. The length of the FFS system is now approximately 700 m long, compared to $\sim$500 m for the system described in the CDR [83].

7.2.6   Fast emergency extraction line (FEXL)

The fast emergency extraction line is primarily intended to extract the remainder of the bunch train safely to the main dump (section 7.7) in the event of a machine protection trip. In addition, it will serve as a by-pass system during commissioning. Figure 7.2.7 shows the overall concept of the FEXL, while the exact geometry can be seen in figure 7.2.2.

The extraction point for the FEXL is placed just downstream of the MES (section 7.5.3). Should an off-energy bunch train exit the linac ($|\Delta E/E| > 2\%$), the BPM at the non-zero dispersive point in the MES can send a signal to the fast kicker system,
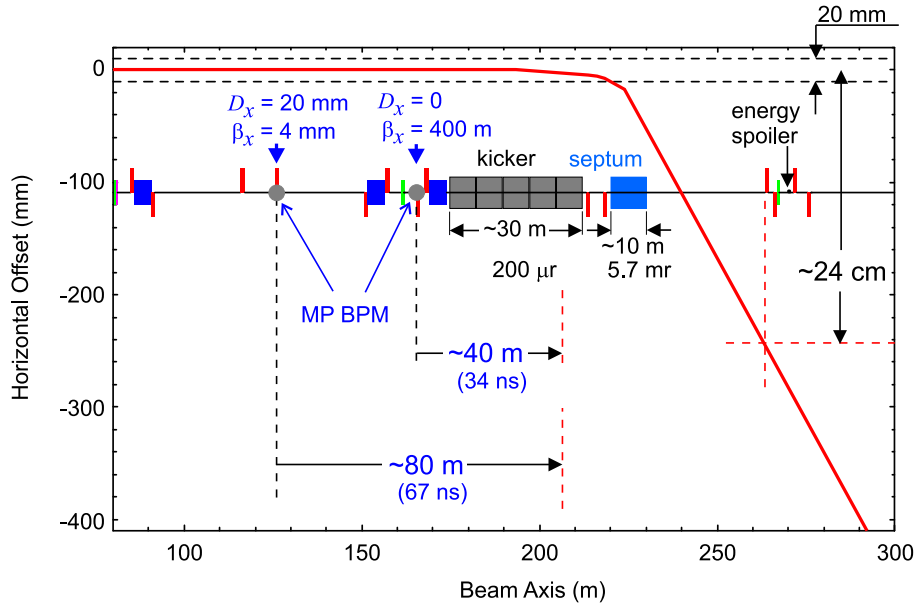
Figure 7.2.7: *Concept of the fast extraction (machine protection) system. Two machine protection (MP) BPMs are used to generate fast emergency signals, which can then be transmitted downstream to the fast kicker. Given the signal delay times, it is expected that (at the most) two bunches will be allowed through.*

approximately 80 m downstream[1]. Since the signal and beam travel in the same direction, the delay[2] is of the order of $\sim$67 ns. A second BPM at a zero-dispersion point with $\beta_{x,y} = 400$ m is used to detect pure betatron (orbit) errors: the delay in this case is $\sim$34 ns. The kicker system comprises of 30×1 m kicker modules, giving a total kick of $\sim$200 μr, with a rise time of 100 ns [9]. Allowing an additional 100 ns for signal processing, the total signal delay time is $\sim$270 ns, which is still less than the bunch spacing of 337 ns. Hence only one (two at the most) bunches will be allowed through, before the remainder of the bunch train is safely extracted. When the FEXL is used as a commissioning line, two weak dipoles magnets are switched on to provide the same kick geometry as the kicker system.

The design of the lattice (including the septum magnet), is constrained by the following requirements:

- a –2% to –5% beam energy error[1] ;

- a possible failure of one kicker module (–3.5%);

- a kicker flat-top of $\pm$2%

---

[1]The FEXL can also be triggered by other machine protection signals, e.g. loss monitors.

[2]Assuming a cable signal velocity of 0.8c

[1]Although positive energy errors >2% can occur under certain circumstances, they are considered far less likely than a negative energy error.

- $\pm 0.5\%$ power-supply stability.

The beam is extracted horizontally, and then transported by a FODO system to a section comprising both a horizontal and vertical bend, which steer the beam down (~ 15 mrad) to the main dump. The optics is arranged to produce a beam size on the dump window that is larger than the required single pulse limit (see section 7.7).

A more detailed description of the FEXL system can be found in [10].

7.2.7   Magnet systems

Table 7.2.1 shows the basic magnet family types for the main BDS lattice. The magnets have been designed for cost-effective manufacture by:

- reducing the number of magnet families to a minimum; and

- restricting the power-supply requirements to those of standard commercially available supplies.

In particular, all dipole magnets are 1.8 m in length and have an aperture (vertical gap) of 20 mm: the long dipoles required in the arcs and CCS are then constructed from strings of these dipoles, allowing the necessary spacing for coils, vacuum pumps etc. Both an H-type and a C-type magnet have been designed.

Quadrupoles and higher-order multipoles are characterised by the standard apertures (diameters) of 20 mm, 40 mm and 140 mm. Figure 7.2.8 shows examples of cross-sections of some of the BDS magnets.

The total of 288 magnets in the main lattice are grouped into circuits where possible, resulting in 52 power-supplies, which themselves are grouped into three stability ratings (see 7.3). The magnets have power ratings ranging from 0.05–84 kW, with a more typical value of a few kW. The total power consumption for the main BDS lattice magnets is ~ 0.5 MW (one side).

Both the FEXL and the main extraction line contain strong dipoles (~ 1.4 T) which require a large amount of power. The power requirement for both extraction lines is $\sim 2 \times 1.5$ MW. The total power requirement for a single BDS (main lattice, FEXL and main extraction) is therefore ~ 4 MW, which includes ~ 0.5 MW for losses in power supplies, re-cooling etc.

Most of the power-supplies will be located in the tunnel close to the associated magnets to reduce cable lengths (costs). A redundancy system is foreseen where an emergency supply can be remotely 'switched in' should a supply in the tunnel fail, avoiding the need to access the tunnel directly. The failed supply can then be repaired during a routine scheduled maintenance break.

A complete description of all the BDS magnets, including detailed drawings and specifications, can be found in [11, 12, 13]. Details of the power supply system can be found in [28].

(a) narrow switchyard
quadrupole

(b) Ø20mm quadrupole
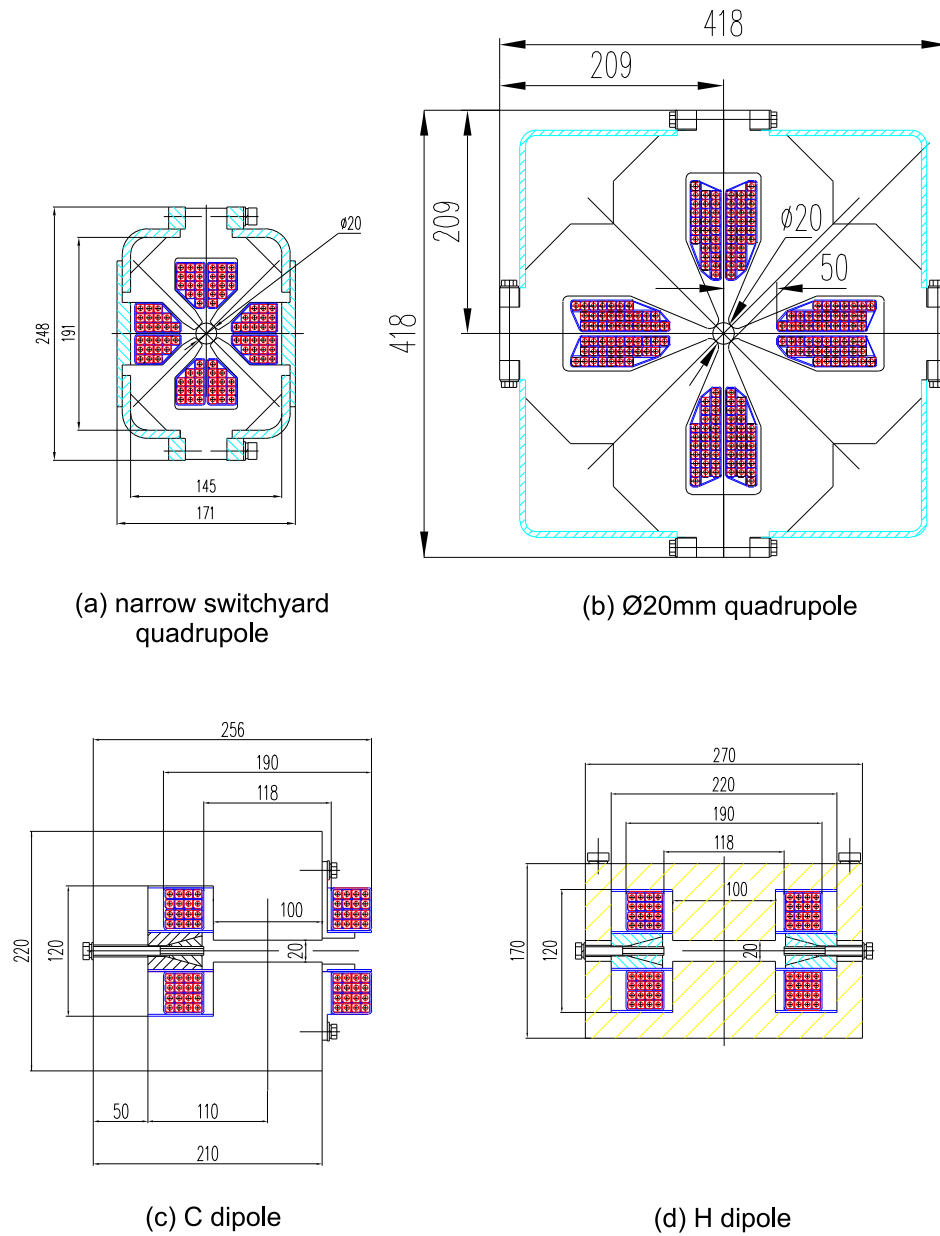
(c) C dipole

(d) H dipole

Figure 7.2.8: *Cross-sections of four of the BDS magnets (taken from [11]): (a) Special narrow quadrupole used in the switchyard arcs (20 mm) (section 7.2.2); (b) standard 20 mm quadrupole; (c) C dipole (20 mm); (d) H dipole (20 mm). Dimensions are in mm.*

Magnet	Type	length (m)	Aperture (mm)	Field (Tesla)	No.	Total
dipoles	H septum	1.8	20	0.12	24	185
	H (or C)	1.8	20	0.24	161	
quadrupoles	A	0.5	20	0.83	4	90
		1.0	20	1.14	48	
		1.5	20	1.14	16	
		2.0	20	1.02	14	
	B	1.5	20	0.79	4	
	C	0.5	40	0.72	2	
	D	2.0	140	0.75	2	
sextupole	E	0.5	20	0.26	2	12
		1.0	20	0.34	2	
		2.2	20	1.05	8	
octupole	F	0.5	20	0.29	1	1
					total:	288

Table 7.2.1: *Main magnets for a single BDS (not including extraction lines or the superconducting final doublet). Type refers to the magnet cross-section type; length to the core length; aperture is either the vertical gap height (dipoles), or the pole-tip diameter (quadrupoles, sextupoles and octupoles); field is the maximum pole-tip field for a beam energy of 400 GeV.*

7.2.8 Vacuum system

The vacuum system is required to maintain an average pressure of 10^{-8} mbar (CO equivalent)[1]. The vacuum chamber is constructed from stainless steel, which is copper coated on its inner surface to reduce the effects of resistive-wall wakefields on the beam. Ion getter pumps are used to maintain the vacuum. The design of the system is cost optimised by trading off the size of the pumps against the number required per meter of vacuum chamber. Because the magnets typically have small apertures (e.g. 20 mm diameter), the cross-section of the vacuum chamber is increased to 35 mm (where needed) to reduce the number of pumps; the transitions are tapered to reduce geometric wake effects. A total of ∼380 pumps are required, with capacities of 2 l/s, 20 l/s, and 125 l/s. Particular attention is paid to the region between the strong sextupole pairs in the HCCS and VCCS (section 7.2.5), where there is a tight tolerance on the allowed wakefield kicks: here the magnet aperture cross-section of 20 mm is maintained throughout the region to reduce geometric transitions. A complete detailed description of the vacuum system can be found in [14].

---

[1]The pressure is calculated from limits on hard Coulomb gas scattering of the high-energy beam.

7.3   Luminosity Stabilisation

The combination of strong focusing and relatively large β-functions in the BDS result in some of the tightest alignment and field tolerances in the entire machine. There has been much work reported on the effects of ground motion and vibration in beam delivery systems (for TESLA see for example [83, 15, 16]). In this section a comprehensive summary of the necessary stabilisation and tolerances for the TESLA BDS will be given. Due to the large aspect ratio $\sigma_x^*/\sigma_y^* = 550/5$, only effects in the vertical plane are generally considered.

When discussing luminosity stability, it is useful to separate out those losses due to beam-beam separation at the IP, and those due to an increase in beam size at the IP (bearing in mind that $L \propto 1/(\sigma_x^*\sigma_y^*)$). The mechanisms must then be further characterised by their time scales:

- those errors which occur on a time scale too fast to be actively compensated for (high frequency), or

- those which occur slowly enough to be corrected (low frequency).

For the case of ground motion and vibration, two correction (feedback) systems will be used:

- a fast (MHz) inter-bunch feedback system for correcting the beam-beam separation and collision angle at the IP;

- a slower ($<0.1\,\mathrm{Hz}$) orbit correction system for the entire BDS, which effectively keeps the beam centred in each magnet.

The IP inter-bunch feedback system (section 7.3.1) keeps the beams in collision. Since it works on a bunch-to-bunch time scale (337 ns), it effectively corrects all frequency components from d.c. to $\sim$170 kHz. The slow orbit correction system (section 7.3.3) addresses slow ground motion drifts which perturb the orbit in the BDS, causing aberrations such as spurious dispersion to increase the beam size at the IP. Due to the 5 Hz repetition rate, the slow feedback can only be expected to correct frequencies below 1 Hz, and probably realistically only below $\sim$0.1 Hz. The effects of aberrations caused by magnet vibration — and subsequent orbit motion — above $\sim$1 Hz are currently not corrected for; these effects are summarised in section 7.3.2.

Section 7.3.4 briefly summarises the power supply tolerance (field stability) requirements. The final section (7.3.5) discusses luminosity tuning knobs, and requirements for beam-based alignment.

7.3.1   IP fast-feedback system

Due to the high vertical disruption parameter at the IP ($D_y \approx 25$), the luminosity is extremely sensitive to small offsets in both beam-beam displacement and crossing
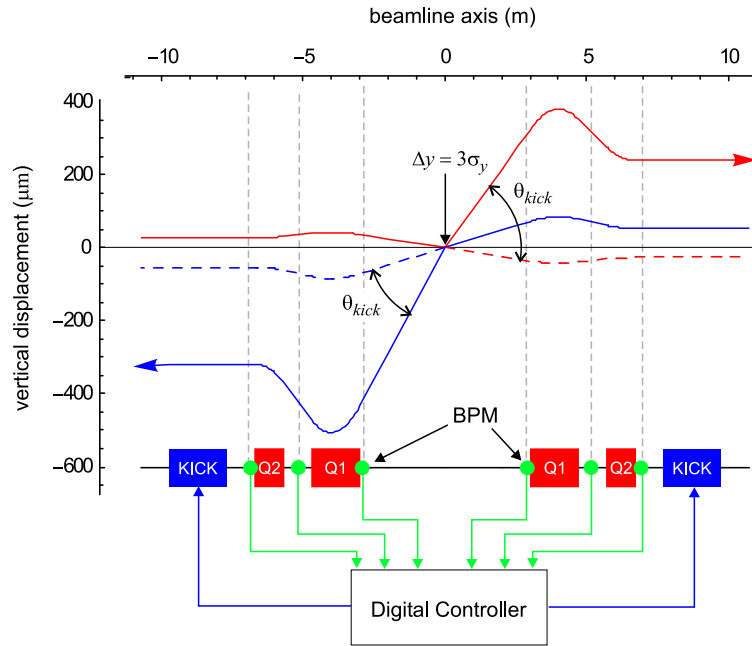
Figure 7.3.1: *The IP fast feedback system. The red and blue rays represent an example having a $3\sigma_y^*$ offset at the IP (corresponding approximately to a $10\sigma_{y'}^*$ kick). The dotted lines represent the trajectories with no beam-beam kick. Initial (example) IP angles are 1 and $2\sigma_{y'}^*$ for red and blue respectively.*

angle (see section 7.4). As a result, the collisions must be maintained to within $\sim 0.1\sigma$ in both offset and angle, or $0.5\,\text{nm}$ and $1.2\,\mu\text{rad}$ respectively.

Figure 7.3.1 illustrates the concept for the IP beam separation feedback system. The large TESLA bunch spacing of $337\,\text{ns}$ allows the use of a digital controller. Fast kickers ($\sim 100\,\text{ns}$) are used to make the necessary corrections. The feedback signal is derived directly from the strong beam-beam kick which both beams experience when they do not collide head-on[1]. Figure 7.3.2 shows the expected beam-beam kick versus beam separation for the design parameters. Since the feedback uses a linear algorithm, the slope of the beam-beam kick curve at $\Delta y = 0$ is used to calculate the offset; this approach has the advantage of making the feedback response as fast and accurate as possible for small beam-beam offsets, while having the disadvantage of a relatively long response time for larger offsets.

Two BPMs placed approximately $3\,\text{m}$ away from the IP on either side are used to measure the beam-beam kick. Four more BPMs placed between and upstream of the final quadrupoles as shown in figure 7.3.1 can also be used. The BPMs need a spatial resolution of $5\,\mu\text{m}$ and a time resolution of $20\,\text{ns}$, the latter arising from the arrival time of the opposing bunch. For the primary BPMs ($3\,\text{m}$), directionally coupled strip-line devices are currently considered, while for the other BPMs re-entrant cavities of the

---

[1]Such a feedback system based on the beam-beam kick was successfully used at the SLC [17].
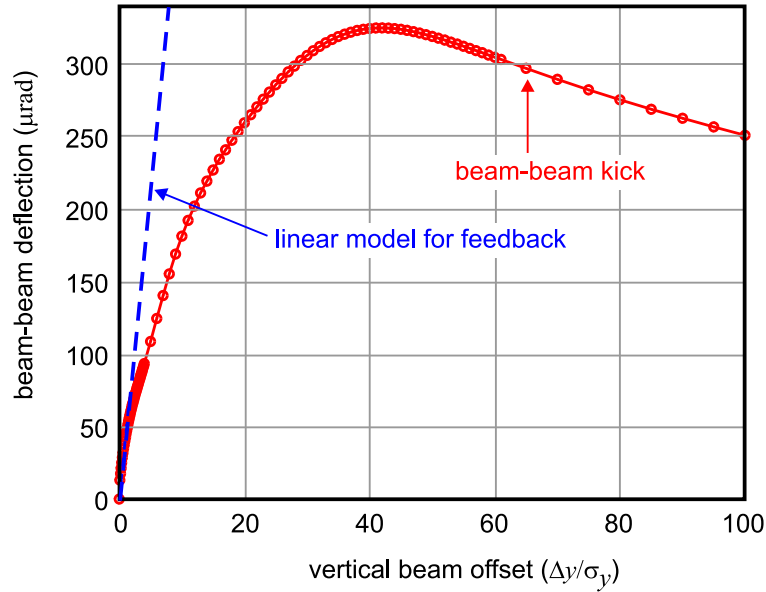
Figure 7.3.2: *The beam-beam kick as a function of the relative offset for the nominal 250GeV beam parameters (calculated using GUINEA-PIG[18]). The linear feedback model is also indicated.*

type currently used at TTF will be used [19] (see section 7.4.4 for more details on the IR region).

The fast kickers are based on an actual design currently being used in the TTF feedback test setup [20, 21]. They have a rise time of ~100 ns and a kick strength of ~0.12 μr/m (at 250 GeV). One-meter long kickers will be placed either side of the IR, which is sufficient to correct up to ~ $100\sigma_y$ beam-beam separation: an RMS of ~$30\sigma_y$ is expected from calculations based on 70 nm RMS quadrupole vibration [16].

The time response of the feedback system is determined by the total delay time of the loop. The actual feedback algorithm currently favoured is a proportional-integral (PI) controller, giving a good d.c. rejection (step response) without compromising the high frequency attenuation. The current (simulated) system shows a damping of frequencies below ~170 kHz with approximately 15 dB per decade.

Figure 7.3.3(a) shows simulation results of the response to a $100\sigma_y$ step-function (including errors). The bunch train also contains the expected bunch-to-bunch offsets due to multi-bunch wakefield effects in the linac (see section 3.2). The initial offset is reduced by three orders of magnitude within ninety bunches, or 3% of the bunch train. After that, the bunches are controlled with the required $0.1\sigma_y$, corresponding to a luminosity loss of less than 10%.

Figure 7.3.3(b) shows the response of the angle feedback. To adjust the angle at the IP, a kicker must be placed at an IP image point upstream of the VCCS, so that the resulting kick is achromatic. An image-point in the β-matching section offers a relatively large β_y function (~52 m). Three one-meter kickers can correct ~130 μrad,
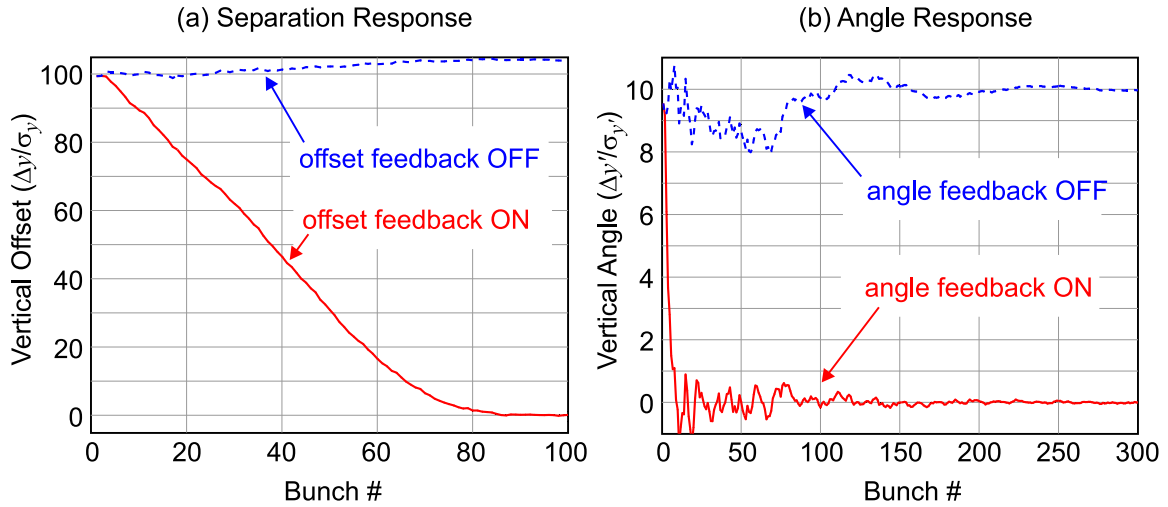
Figure 7.3.3: *Results of simulations of the IP fast feedback for (a) a $100\sigma_y$ offset step function and (b) a $10\sigma_{y'}$ angle step function. Included in the simulation are: residual effects of multi-bunch wakefields in the linac; signal BPM noise of $5\,\mu m$ and $1\,\mu m$ for the position and angle respectively; 0.1% kicker field imperfections; a 10% random variation in the beam-beam kick.*

or $\sim 10\sigma_{y'}$ at the IP. A BPM at a high β_y point in the VCCS (450 m downstream of the kicker) is used to correct any incoming vertical betatron oscillation. The resulting feedback delay is approximately $3.4\,\mu\text{sec}$, or 10 bunches, which is still considered acceptable. In order to achieve the required resolution of $0.1\sigma_{y'}$, the signal BPM requires a spatial resolution of $1\,\mu\text{m}$. Although the correction is effectively removed from the IP, there is virtually no source of angle jitter downstream of the kicker in the FFS itself, since nearly all the magnets are $\pi/2$ out of phase with the IP [16].

Since the fast inter-bunch feedback system (section 7.3.1) is expected to correct the offset of each of the 5 Hz bunch trains independently, only the effects on the beam size (σ_y^*) will be considered in the following sections. Details of the fast IP feedback system can be found in [22].

7.3.2   Effects of fast quadrupole motion

In this section the effects of random uncorrelated quadrupole vibration on σ_y^* will be considered. Due to the 5 Hz repetition rate, these effects cannot be corrected. As a (pessimistic) reference, we will take an RMS quadrupole motion of 70 nm RMS, which corresponds to recent measurements at HERA ($f > 2\,\text{Hz}$) [23]. A detailed account of the results presented here can be found in [16].

At any given instant, the magnets (quadrupoles) in the BDS will have random alignment errors due to vibration. The resulting kicks from these offset quadrupoles cause an ever increasing orbit amplitude in the downstream magnets. To estimate the effect on σ_y^* from the perturbed (vertical) orbit, the following aberrations must be
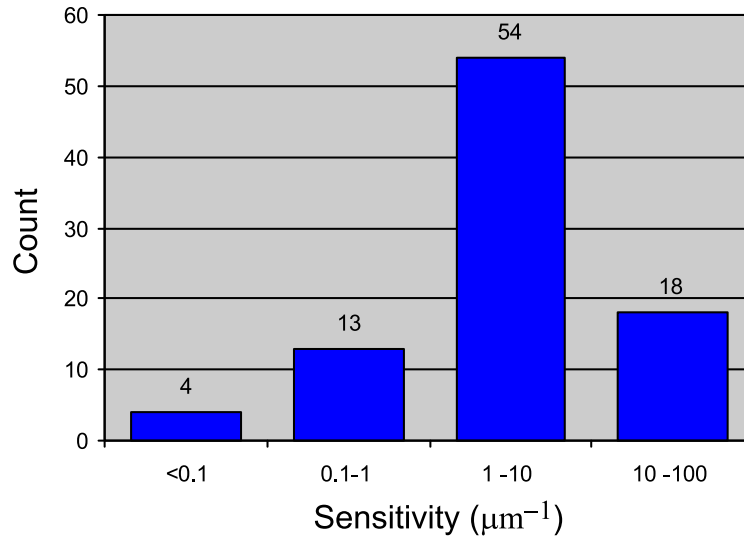
Figure 7.3.4: *Summary of quadrupole sensitivity calculations. The sensitivity (μm^{-1}) is calculated as the inverse of the vertical quadrupole motion required to increase σ_y^* by 2%.*

Aberration	contribution to $\Delta L/L$	comments
xy coupling	4.5%	both beams
linear dispersion	5.5%	e^- only
2$^{\mathrm{nd}}$-order dispersion	2%	e^- only
total	12%	

Table 7.3.1: *Summary of expected luminosity loss due to fast uncorrelated quadrupole motion (70 nm RMS). The loss is estimated only from an increase in σ_y^* (no beam-beam effects).*

considered:

magnet type	aberration
quadrupole, sextupole	linear dispersion
quadrupole, sextupole	second-order dispersion
sextupole	xy coupling

In figure 7.3.4, the results of the vertical motion of single quadrupoles is summarised. The majority of the magnets have a sensitivity in the range of 1–$10\,\mu\mathrm{m}^{-1}$, corresponding to a $\Delta\sigma_y^*/\sigma_y^* = 2\%$ alignment tolerance of 100–$1000\,\mathrm{nm}$. 18 magnets have a tolerance $< 100\,\mathrm{nm}$.

Table 7.3.1 summarises the expected luminosity loss (no beam-beam effects) for

70 nm RMS quadrupole vibration. For the energy dependent terms (first- and second-order dispersion), only the contributions from the electron beam ($\sigma_{\Delta P/P} \approx 0.15\%$) to the luminosity loss are considered, since the energy spread in the positron beam is much smaller ($<0.05\%$)[1]

The total of 12% luminosity loss scales quadratically with the RMS vibration amplitude. Hence an amplitude of 35 nm would decrease the total to $\sim$3%. Should it be necessary, certain key quadrupoles can be actively stabilised to $\sim$20 nm RMS using fast piezo-electric micro-movers [24].

7.3.3   Slow alignment drifts due to ground motion

Low-frequency motion (ground motion, $f < 1$ Hz) can be compensated using an orbit correction system (feedback), having a sample rate equal to the machine repetition rate of 5 Hz. For the current studies, the so-called ATL ground motion model has been used [25]:

$$\langle Y^2 \rangle = A \cdot T \cdot L$$

where Y is the relative offset of two points separated by a distance L after a time T. A is the constant of proportionality, and is generally quoted with the units $\mu\text{m}^2\text{m}^{-1}\text{s}^{-1}$. For the DESY site, a value of $A \approx 4 \times 10^{-6} \mu\text{m}^2\text{m}^{-1}\text{s}^{-1}$ has been measured [23], and this value will be assumed throughout the following section.

For the orbit correction, a simple one-to-one algorithm has been studied. An upstream corrector is used to steer the beam through the magnetic centre of the downstream magnet. For the simulations, it is assumed that

- each quadrupole has an additional horizontal and vertical dipole corrector associated with it;

- each magnet (quadrupole and sextupole) has an integrated BPM with a given resolution (noise);

- the BPM offsets with respect to the (magnetic) centre of the associated magnets have been accurately determined using beam-based alignment techniques;

- systematic residual BPM offsets are assumed to be zero.

The last item requires some clarification: after applying beam-based alignment techniques, there will be some finite residual BPM offsets. These offsets are considered to be static, and so their effects on the luminosity can be initially 'tuned out' using the tuning knobs described in section 7.3.5. To study the effects of *random* BPM noise, we set the *static* offsets to zero.

---

[1]the electron energy spread comes from the undulator for the positron source (see 4.3).
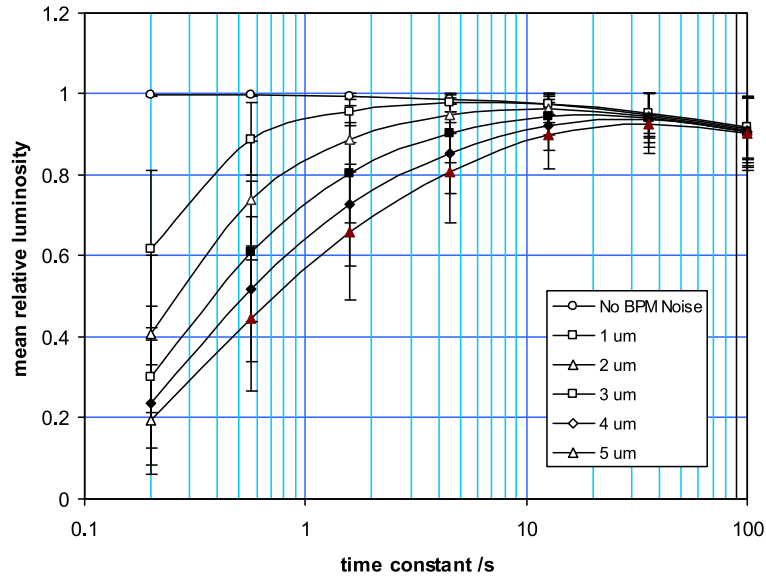
Figure 7.3.5: *Results of simulations of the effect of ATL-like ground motion on luminosity, as a function of the orbit correction feedback time constant and RMS BPM noise. Each point represents the average over 1000 simulated pulses (200 seconds).*

Figure 7.3.5 shows the results of simulating 1000 pulses at 5 Hz. The plot clearly shows the trade-off between random BPM noise and the feedback time constant[1]. As the time constant is increased, the BPM noise is effectively integrated away. Above $\tau \approx 20$ s, all the curves come together, and the effects of the ground motion itself begin to dominate. Assuming that we will have a BPM resolution of $1\mu m$, a time constant of ~ 8 s would seem to give the minimum luminosity loss ($\sim 2\%$).

Figure 7.3.6 shows the results of simulating the effects of ground motion over a longer time scale (~ 10 days). Since the time steps taken represent many 5 Hz pulses, the orbit corrections are applied 'one-shot' with a gain of 1. No BPM noise is included in the simulation. The results are plotted for three different cases:

1. no correction — shows the effects of ground motion on the luminosity if no correction is applied. The luminosity rapidly drops to zero as the beams move out of collision.

2. IP fast feedback on — shows the results with the fast feedback on, effectively keeping the beams in collision (section 7.3.1). The luminosity stability is increased by more than two orders of magnitude, but still falls off due to aberrations generated by the orbit in the BDS.

---

[1]the feedback time constant is adjusted using a 'gain' factor ($0 < g < 1$) which defines how much of the calculated correction should be applied per 5 Hz pulse. A gain of 1 (100% correction) corresponds to a time constant of 0.2 s, while a gain of 0.1 corresponds to 2 s.
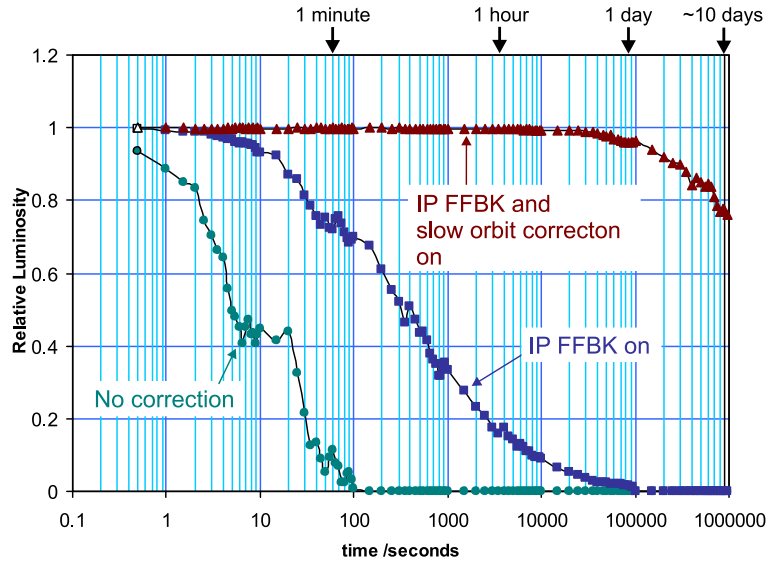
Figure 7.3.6: *Luminosity loss due to ATL-like ground motion as a function of time. Each curve represents an average over 20 random seeds of simulated ground motion (see text for more details).*

3. both IP feedback and orbit correction on — represents the full stabilisation of the BDS. The luminosity is now constant and only begins to slowly fall off after several days.

The drop in luminosity for the fully corrected case is a direct result of the one-to-one steering algorithm: such algorithms are not 'dispersion free', and eventually the residual dispersion generated by the corrector kicks will begin to degrade the luminosity. A dispersion-free steering algorithm would certainly result in longer time stability. On the time scale of days, however, it is a relatively simple task to re-tune the IP dispersion using a dispersion tuning knob (section 7.3.5). For more details of the simulations see [16].

> *Note: the results shown in figures 7.3.5 and 7.3.6 were based on an electron energy spread of 0.18%. As of writing, a re-design of the positron undulator (section 4.3) has now reduced the estimated energy spread to $\sim 0.15\%$. Since the luminosity loss $\Delta L/L \propto (\Delta P/P)^2$, this will reduce the effects by $\sim 30\%$.*

7.3.4   Power supply tolerance requirements

Where possible, the magnets are placed in series and connected to a single power supply, resulting in a total 52 power supplies for a single BDS. The power supplies are divided into three stability groups: 10^{-4}, 5×10^{-5} and 10^{-5}. The requirements are summarised in table 7.3.2. The partition of the tolerance budget was made to minimise the number

of high-stability supplies, while keeping the total expected luminosity loss to less than 3%. All supplies can be obtained commercially to the required specification [28].

Stability	Num. of PS	Num. of Magnets	Comments
10^{-4}	41	80	
5×10^{-5}	6	28	MES bend string CDS quad* CCS quad* weak FT doublet
10^{-5}	5	178	s.c. final doublet, CCS bend strings, ARC bend strings
totals	52	286	

* *specific quadrupoles only*

Table 7.3.2: *Summary of power supply stability requirements. The total luminosity loss from the specified tolerances is ~3% (taken from [16]).*

7.3.5   Initial luminosity tuning

In order to achieve the design luminosity, it will be necessary to perform two initial tuning steps:

beam-based alignment of the type successfully used at the FFTB [26] will be initially required to (a) align the magnets to within some accuracy over a long baseline, and (b) to accurately determine the BPM offsets;

orthogonal IP tuning is used to tune out the effects of residual (static) BPM offsets and magnet alignment after beam-based alignment.

Due to ground motion and vibration effects, it will be necessary to re-apply the orthogonal tuning at specific time intervals ($\sim$ 10 days, see 7.3.3). Eventually it may even be necessary to repeat the beam-based alignment procedure, although current simulation results suggest that this is unlikely within a typical luminosity run period ($\sim$5000 hours).

For the IP tuning, five orthogonal optics knobs are required:

- x- and y-waist

- x- and y-dispersion

- x-y coupling

Aberration		Sextupole pair	Motion Type	3β Range (μm)	2% limit (μm)
waist	x	HCCS		52	7
		VCCS	horizontal	413	58
	y	HCCS	symmetric	346	48
		VCCS		3.6	0.5
dispersion	x	HCCS	horizontal	121	18
		VCCS	anti-symmetric	465	70
	y	HCCS	vertical	19	2.6
		VCCS	anti-symmetric	2.6	0.4
coupling		HCCS	vertical	7.4	1
		VCCS	symmetric	2.1	0.3

Table 7.3.3: *Summary of the various CCS sextupole mover combinations and their effects. The 3β range is the typical scan range required, while the 2% limit gives that motion needed to reduce the luminosity by 2% (taken from [27]).*

The above knobs can be constructed by moving the strong sextupole pairs in the two CCS sections. By selecting various combinations of horizontal or vertical, symmetric or anti-symmetric motion of a specific sextupole pair, all five required aberrations can be cleanly generated (corrected) at the IP. Table 7.3.3 summarises the motions required.

It is currently foreseen to place all eight CCS sextupoles on mechanical movers. The movers will have a resolution (step size) of $\sim 1\,\mu$m and a range of $\pm 1\,$mm. Three of the combinations listed for the VCCS pairs have 2% limits below $1\,\mu$m: it is probably therefore better to only use the less sensitive HCCS sextupole pairs to provide the required knobs.

Beam-based alignment has been successfully demonstrated in several machines, and particularly at the FFTB [26], where quadrupole alignment errors of $50\,\mu$m to below $1\,\mu$m were achieved. In [27] an estimate of the required precision of initial alignment was made, based on the maximum allowed residual second-order dispersion generated after alignment and one-to-one steering[1]. The precision varies depending on the 'wavelength' or baseline length over which the alignment is to be applied. For the current BDS, the alignment requirements range from $<20\,\mu$m RMS over short distances ($<10\,$m) up to $\sim 80\,\mu$m RMS over longer baselines ($\sim 500\,$m). While short magnet-to-magnet alignment tolerances on the order of 10-20 μm should be achievable with the methods used at the FFTB, the longer baseline tolerance may well prove difficult: second-order dispersion knobs, or better steering and tuning algorithms will probably be required.

---

[1]the tolerance is based on a 2% increase in σ_y^* due to the residual second-order dispersion.

7.4 Interaction Region and Beam-Beam Effects

The beam-beam interaction at the IP of a linear collider will be very intense. To minimise the effects, flat beams with large aspect ratios $R = \sigma_x^*/\sigma_y^*$ are used at the IP, resulting in a strong beam disruption only in the vertical plane. Disruption is quantified by the *disruption parameter*, D_y, defined as the ratio of the bunch length σ_z to the vertical beam-beam focal length f_y:

$$D_y \equiv \frac{\sigma_z}{f_y} = \frac{2\,r_e\,N_b\,\sigma_z}{\gamma\,\sigma_x^*(\sigma_x^* + \sigma_y^*)}$$

where N_b is the bunch population. The relatively high TESLA value of $D_y \approx 25$ indicates that particles undergo several vertical oscillations while crossing the opposing bunch. *Beamstrahlung* (i.e. the emission of synchrotron radiation in the coherent e.m. field of the opposing bunch) is also considerable at these high beam energies. It is usually characterised by the *Upsilon* parameter:

$$\Upsilon \equiv \frac{2}{3}\frac{\langle E_c \rangle}{E_0} = \frac{5\,r_e^2\,\gamma\,N_b}{6\alpha_e\sigma_z\,(\sigma_x^* + \sigma_y^*)}$$

where $\langle E_c \rangle$ and E_0 are the average photon critical energy and the beam energy respectively. With a photon yield of about $1.6/e^{\pm}$, beamstrahlung causes a significant energy loss in the spent beam, resulting in a 3–4% average energy loss characterised by a long tail. The associated luminosity spectrum $d\mathcal{L}/d\sqrt{s}$ is also degraded (see section 7.4.1). A small fraction of the beamstrahlung photons are converted into low energy e^+e^- pairs which form the most numerous background source to the detector. On the positive side, the pair flux is proportional to the luminosity and can therefore be used to monitor relative luminosity variations on a bunch to bunch basis[30, 31].

Beam-beam effects are analysed in more detail in [29]. They influence the collider performance in essentially three ways described in the following sections.

7.4.1 Luminosity enhancement and luminosity spectrum

Results of beam-beam simulations using GUINEA-PIG [18] show that the mutual focusing of the bunches at the IP leads to a luminosity enhancement factor of ~ 2 with respect to the geometric luminosity. Figure 7.4.1 shows (a) the luminosity as a function of the longitudinal position of the vertical waist, and (b) the corresponding number of pairs striking a forward detector at a radius of $r > 12\,\mathrm{mm}$. The luminosity is maximum when the bunches are focused to vertical waists located about $0.63 \times \beta_y^* \simeq 250\,\mu\mathrm{m}$ in front of the IP. Figure 7.4.1(b) shows that the detected pairs can be used to achieve the optimum (maximum) luminosity. The gain from the luminosity enhancement is somewhat offset by the dilution due to beamstrahlung of the luminosity spectrum $d\mathcal{L}/d\sqrt{s}$ towards lower centre of mass energies (figure 7.4.2). However, about 60% of the total luminosity is still produced at energies higher than 99.5% of the nominal c.m. energy.

cm energy	[GeV]	$\sqrt{s} = 2E_0$	500	800
Luminosity	$[10^{34}\text{cm}^{-2}\text{s}^{-1}]$	L	3.4	5.8
Bunch population	$[10^{10}]$	N_b	2	1.4
Transverse bunch sizes	[nm]	σ_x^*, σ_y^*	553, 5	391, 2.8
Transverse bunch divergences	[μrad]	Θ_x^*, Θ_y^*	37, 12	26, 7
Bunch length	[mm]	σ_z	300	300
Disruption parameters		D_x, D_y	0.22, 25	0.20, 27
Upsilon parameter		Υ	0.06	0.09
Average relative energy loss		δ_B	3.2	4.3
Number of photons/$e^\pm$		n_γ	1.6	1.5
Spent beam power	[MW]	P_{SB}	11	17
Beamstrahlung photon power	[kW]	P_γ	360	760
Number of pair particles		N_P	129 000	153 000
Average pair particle energy	[GeV]	$\langle E_P \rangle$	2.8	5.3

Table 7.4.1: *TESLA IP Parameters.*
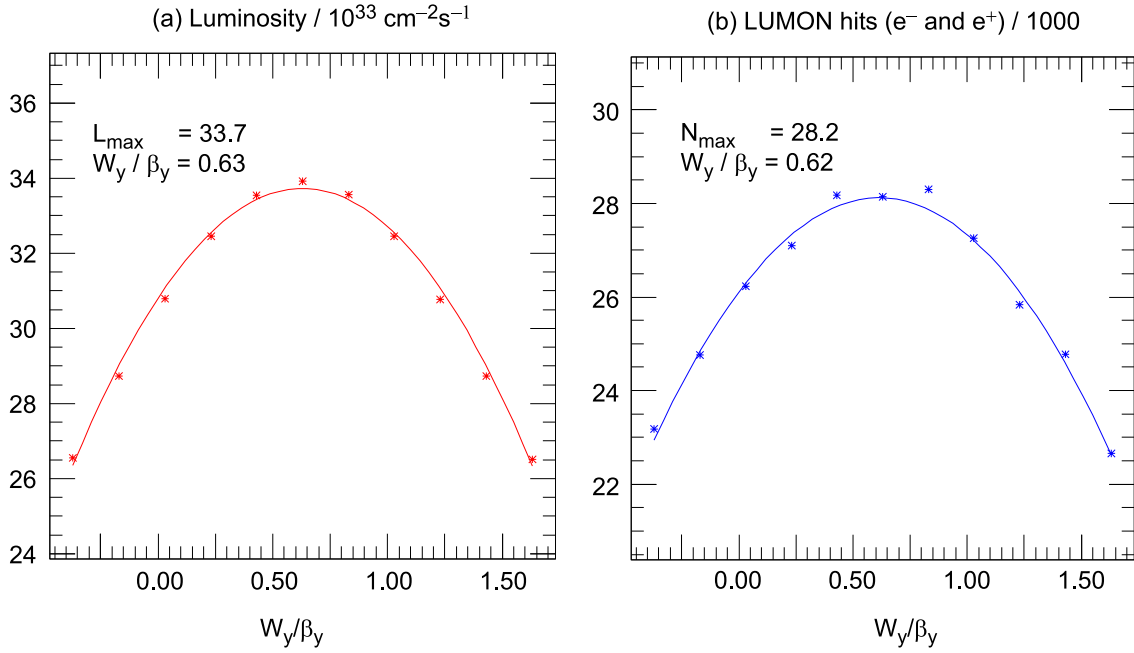
Figure 7.4.1: *Luminosity optimisation relative to the longitudinal position of the vertical waist for TESLA 500 GeV c.m. energy. (a) shows the actual luminosity as a function of waist position (relative to the IP, $W_y/\beta_y = 0$), while (b) shows the numbers of e^+e^- pairs detected in the fast luminosity monitor. Solid lines show the parabolic fits through the 11 data points.*
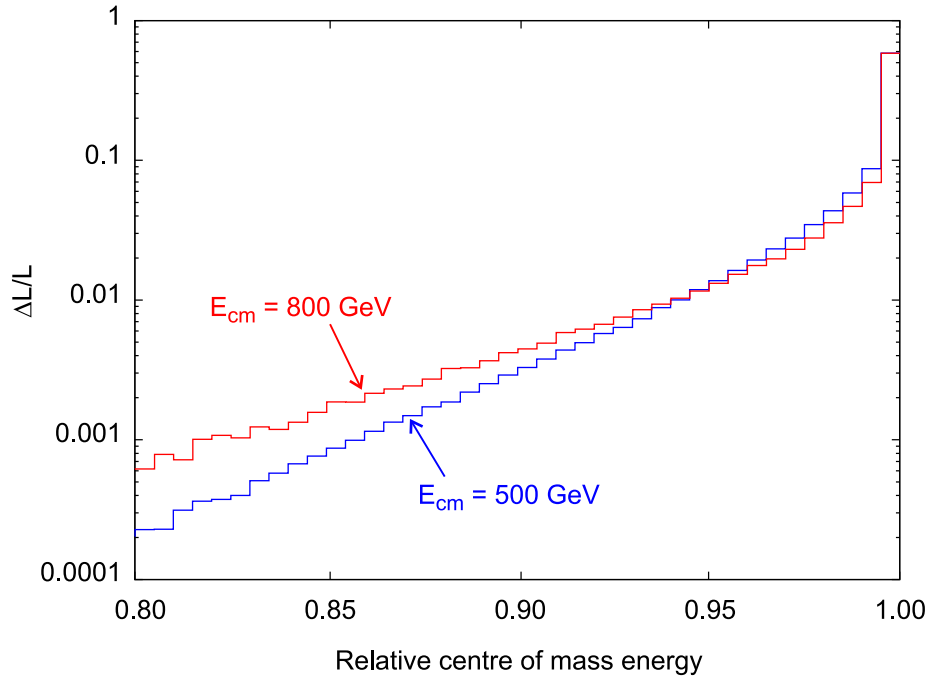
Figure 7.4.2: *Luminosity spectra for 500 GeV and 800 GeV centre of mass energy.*

7.4.2   Sensitivity to vertical displacements and angles

The high disruption regime ($D_y \approx 25$) results in a high sensitivity of the luminosity to both vertical beam-beam offset and crossing angle. The luminosity loss for offset and angle errors is shown in figure 7.4.3, where simulation results[18] are compared to the analytic expressions without beam-beam forces. The sensitivity is enhanced by a factor of five for small offsets, and by a factor of ten for small angles with respect to the simple geometric factor. The aggressive optimisation of the IP parameters into this high disruptive regime is justified by the use of the fast inter-bunch orbit feedback system (section 7.3.1), which will be capable of maintaining the beams in collision to within the specified tolerances.

   Given the extreme sensitivity to offset and angle, some loss of luminosity is also expected from internal bunch deformations, such as those induced by single-bunch wakefields in the linac (the so-called 'banana effect'). The single-bunch *correlated* emittance growth from wakefields is expected to be 6% on average (see section 3.2). Figure 7.4.4 plots the luminosity obtained from colliding electron and positron bunches with a 6% correlated emittance growth. The bunches are initially generated with the correlated emittance growth either entirely in the displacement (y) plane or in the angle (y') plane, including all six sign combinations. In all cases, the nominal luminosity can almost be recovered by optimisation of the beam offset (figure 7.4.4(a)) followed by an angle scan (figure 7.4.4(b)). The optimum set point can be found by monitoring the luminosity on a bunch to bunch basis using the pair signal. The impact of beam-beam instability is discussed in more detail in [32].
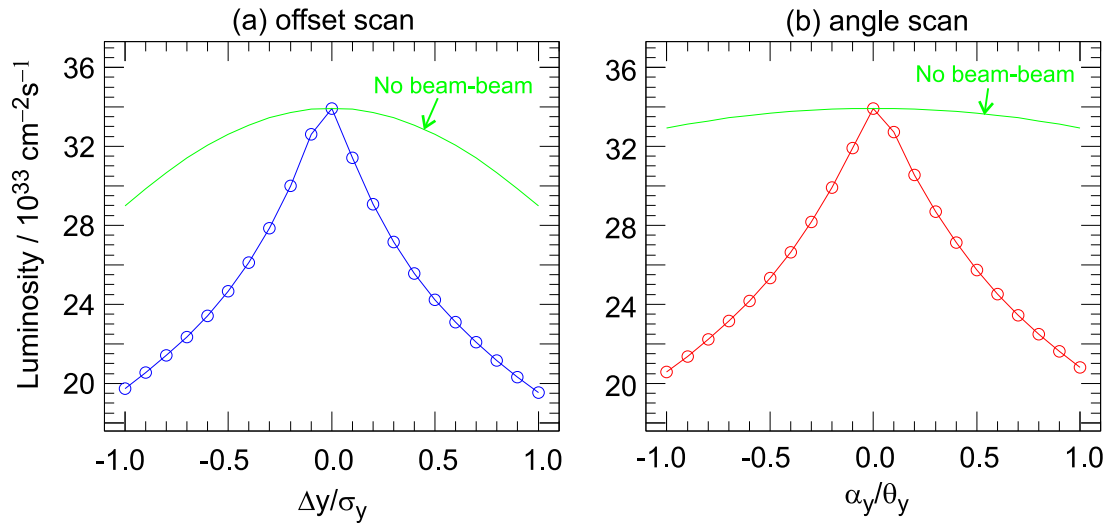
Figure 7.4.3: *Luminosity loss as a function of normalised IP vertical offset and angle for TESLA 500 GeV.*
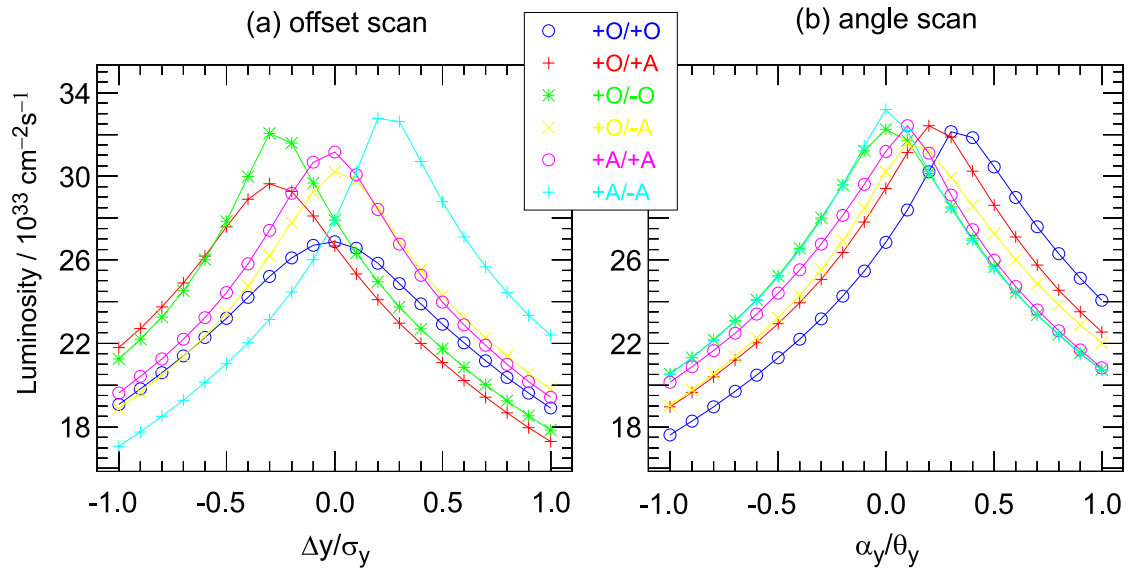
Figure 7.4.4: *(a) Offset followed by (b) angle scans of the luminosity for various combinations of vertical to longitudinal correlations leading to 6% $e^{\pm}$ correlated emittance growth. $\pm O$ = offset (y-plane) correlated, $\pm A$ = angle (y'-plane) correlated*
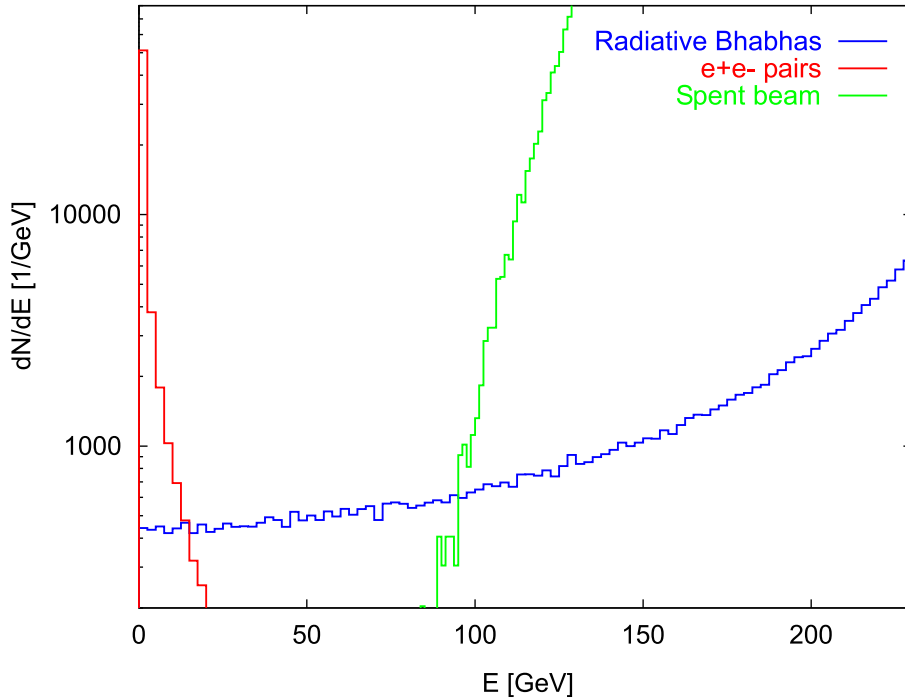
Figure 7.4.5: *Energy spectrum of charged particle backgrounds for 500 GeV c.m. energy.*

7.4.3 Beam-beam backgrounds

The charged particle beam-beam background is essentially the result of three basic processes:

1. beamstrahlung emission — the energy-degraded spent beam dominates the spectrum of charged particles above 100 GeV;

2. pair creation — e^+e^- pair particles dominate the spectrum below 20 GeV;

3. Radiative Bhabhas or (beam-beam) bremsstrahlung — this incoherent process creates same sign e^+or e^-particles moving along with the beam.

The various energy spectra are plotted in figure 7.4.5 for 500 GeV c.m. energy. The rate of radiative Bhabha in the intermediate energy range around 50 GeV provides a signal proportional to luminosity which — although less powerful than the pair signal — can also be used for machine tuning [30]. In addition, beamstrahlung photons carrying 3–4% of the beam power are emitted in a narrow forward cone of about ±0.15 mrad. The extraction and disposal of these background sources is discussed in section 7.7; their impact on the detector is discussed in Part IV chapter 6 of this report.

7.4.4 Interaction region (IR) and last doublet design

The layout of the IR is shown in figure 7.4.6. The most important regions are:
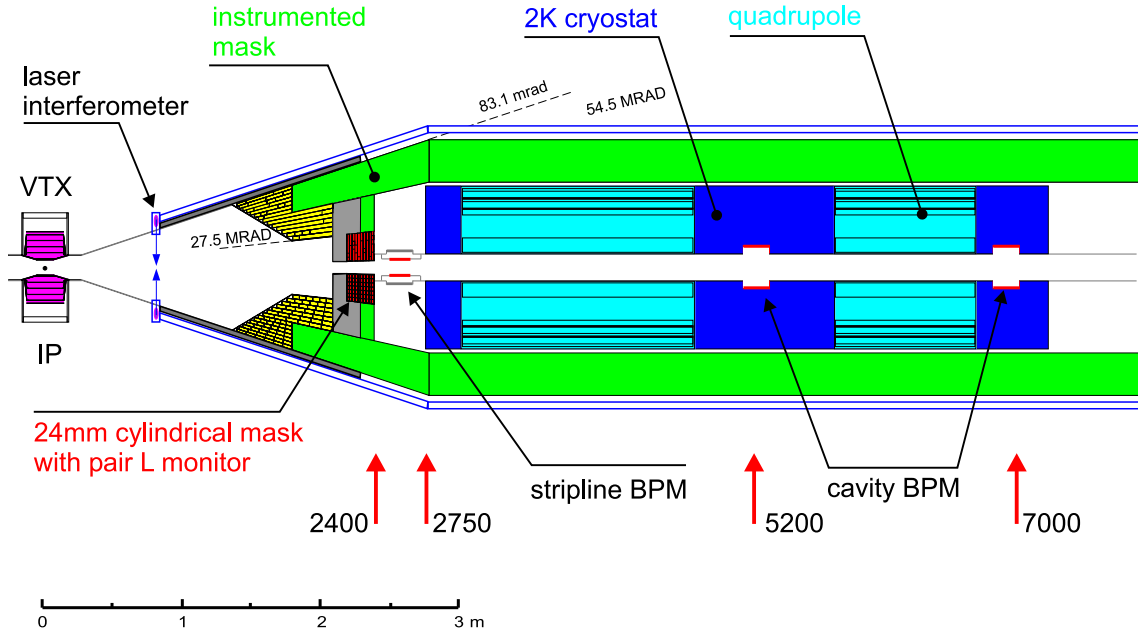
Figure 7.4.6: *Interaction region layout.*

- the instrumented mask constructed from high Z material to absorb most of the e^+e^- pairs and their secondaries; and

- the cryostat housing the final super-conducting quadrupole doublet.

In the beam direction, the aperture limitations are set by the forward cylindrical mask of 24 mm diameter housing the pair luminosity monitor, and by the super-conducting quadrupole doublet itself, consisting of a 1.7 m and a 1.0 m long quadrupole ($dB_y/dx = 250\,\mathrm{T/m}$), with an inner diameter of 48 mm. A schematic cross-section of the doublet is shown in figure 7.4.7, and a detailed design is described in [33].

Figure 7.4.6 also shows the instrumentation required for beam tuning:

- one stripline and two cavity beam position monitors (BPM), which are primarily used by the inter-bunch fast feedback system (section 7.3.1);

- a laser interferometer [34] for single beam profile measurement at 0.8 m from the IP;

- one luminosity monitor (pair counter) on each side of the IP located at the lowest aperture radius of 1.2 cm on the inner mask;

Finally, a slower luminosity monitor, integrating the bremsstrahlung signal over about 10 bunch crossings, is foreseen around the beam pipe at 8.5 m from the IP (not shown).
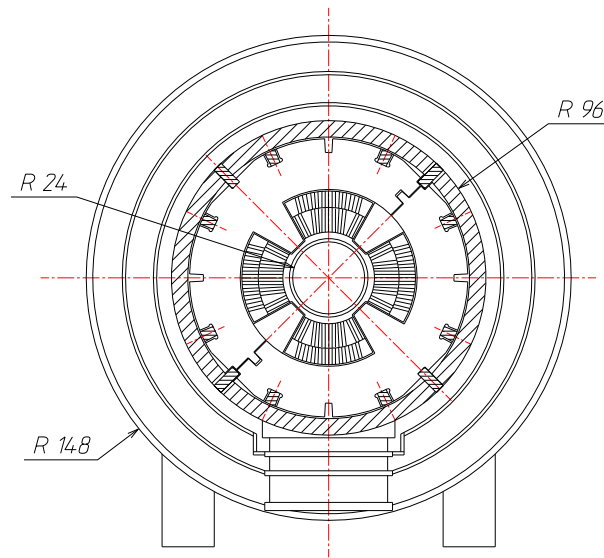
Figure 7.4.7: *Cross-section of the super-conducting final doublet quadrupole and cryostat.*

7.5   Collimation System

The collimation system uses thin mechanical spoilers followed by thick absorbers to physically scrap the halo particles off the beam. The design of the optics are constrained by:

- the required physical aperture for the given collimation depth;

- spoiler survival considerations in the event of a direct hit from the beam;

- wakefield effects from the narrow aperture of the spoiler jaws.

Since it is the spoilers which effectively define the collimation aperture, we will interchangeably use the word collimator and spoiler in the following sections. The absorbers are large blocks of material ($\sim$20 radiation lengths), which sit in the geometric shadow of the spoilers. The exact (most efficient) location of the absorbers is still to be determined. For the spoilers, we assume that one radiation length of titanium will be used.

The following sections give a concise synopses of the current status of the collimation system. More detailed information can be found in [3].

7.5.1   Required collimation depth

Halo particles with large amplitudes will radiate photons in the quadrupoles close to the IR; in particular, photons generated within the strong final doublet may strike inner parts of the detector and cause unacceptable background. The required collimation depth is defined as the aperture within which photons generated by halo particles pass
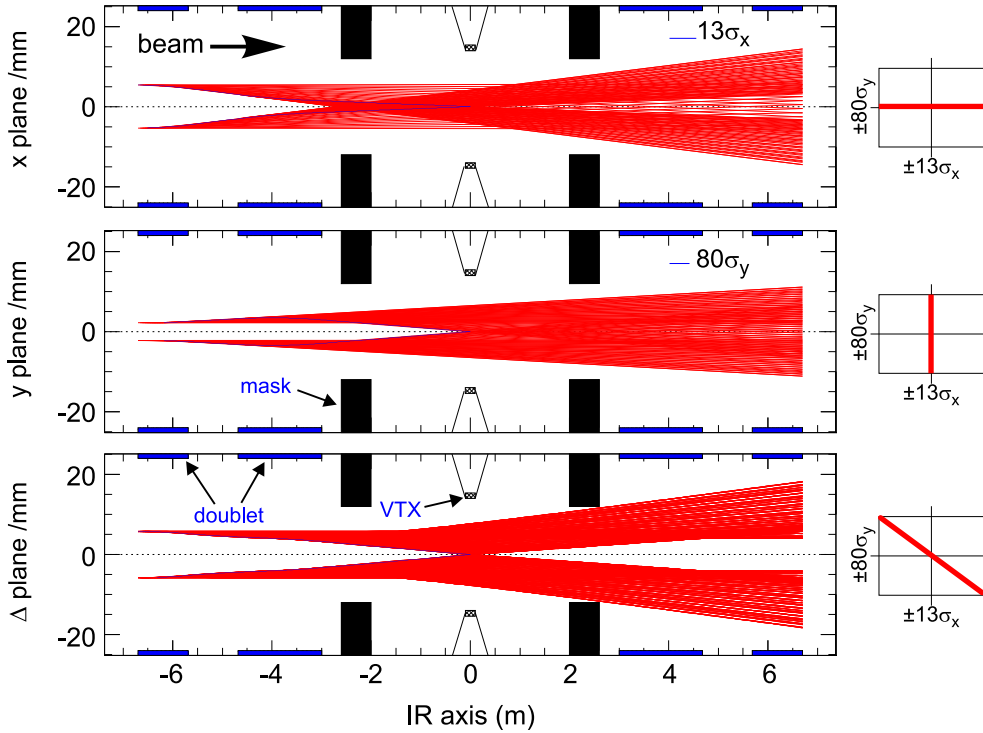
Figure 7.5.1: *Synchrotron radiation fan generated by the last quadrupoles and traced through the IR. The envelope defines the required collimation depth of $\pm 13\sigma_x$ and $\pm 80\sigma_y$. The limiting aperture is defined in the diagonal (Δ) plane by the exit 24 mm mask (see section 7.4.4 for more details of the IR region).*

cleanly through the IR. Figure 7.5.1 shows the limiting case for photons generated by an incoming halo in the final doublet; the resulting collimation depth is $\pm 13\sigma_x$ and $\pm 80\sigma_y$, where $\sigma_{x,y}$ are the nominal transverse beam dimensions at 250 GeV [35].

7.5.2   Optics

The main (primary) collimation section consists of a series of five identical cells, with $\beta_x = \beta_y = 800$ m at the symmetry points where the spoilers are located. The phase advance per cell (spoiler) is effectively 45° in both planes[1]. Figure 7.5.2 shows the optics. The first spoiler is at a high dispersion point ($D_x = -100$ mm), and is used as the momentum collimator. The remaining four spoilers are located in a zero dispersion region, and are referred to as the betatron collimation system; they effectively define an octagon in phase space as depicted in figure 7.5.2. The physical apertures of the spoilers are set to a factor $\cos(45°/2) \approx 0.92$ smaller than the required collimation depth, which fits the octagon defined by the spoilers inside the ellipse defined by the collimation depth. A second set of spoilers are located at the high β-points in the

---

[1]due to optics constraints, the actual phase advance is $\phi_x = 45°$ and $\phi_y = 315°$.
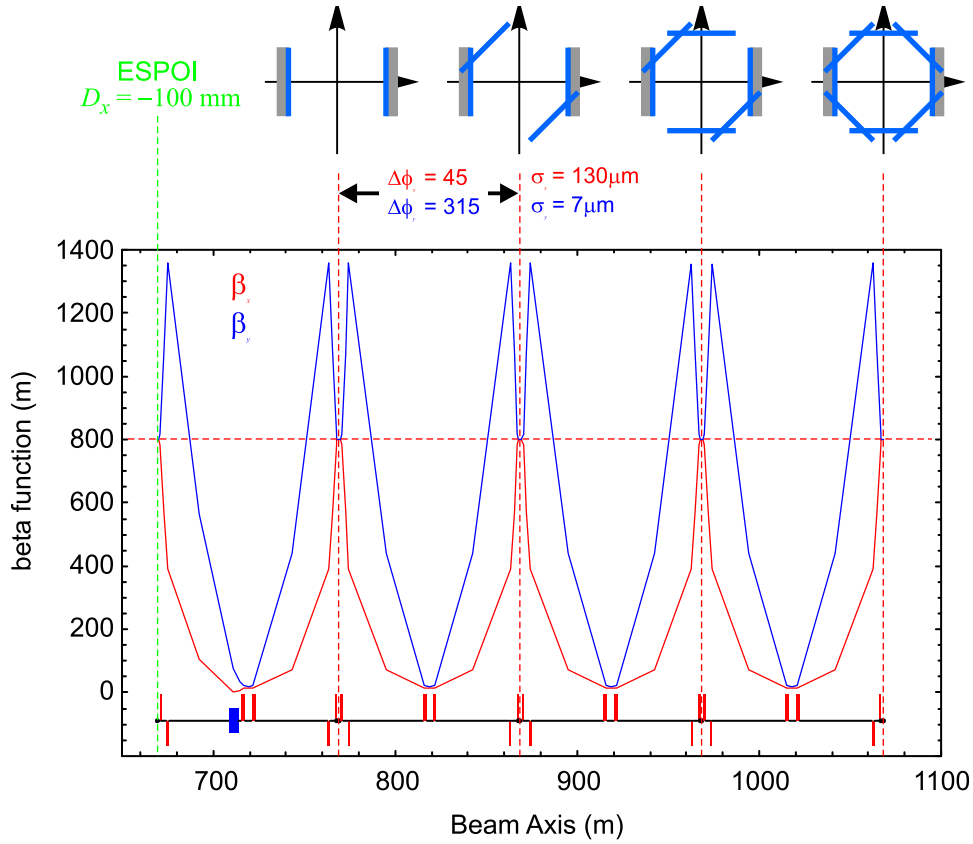
Figure 7.5.2: *The primary collimation and diagnostics system (CDS).*

| Spoiler | Aperture | | Acceptance | | |
	x/mm	y/mm	$\pm x/\sigma_x$	$\pm y/\sigma_y$	$\pm\Delta P/P$ (%)
ESPOI	3	-	12	-	1.5
XYSPOI	3	1	12	74	-
COLX	3.9	0.6	13	80	5.7
COLY	0.9	2.7	13	80	2.9

Table 7.5.1: *Physical apertures (gaps) and the* linear *acceptance of the various spoilers in the BDS. ESPOI = energy spoiler, XYSPOI = betatron spoilers (CDS), COLX(Y) = CCS spoilers.*

HCCS and VCCS; these collimators are positioned at the sine-like phase with respect to the IP, and so directly shadow the final doublet aperture. They are set to collimate exactly at $\pm 13\sigma_x$ and $\pm 80\sigma_y$. The physical apertures of all the spoilers are listed in table 7.5.1.

The values in table 7.5.1 represent the phase space acceptance *for a linear system*

only: the relatively strong chromaticity of the lattice and the non-linear elements in the MES (section 7.5.3) cause off-momentum particles to be driven to large (betatron) amplitudes. Particle tracking was performed to check that the system collimates correctly. All physical apertures were treated as 'hard' edges (i.e. no scattering). Figure 7.5.3 summarise the results of tracking 10^5 particles; figure 7.5.3(b) shows that there are no particles remaining outside of the required collimation aperture at the entrance to the final doublet.

7.5.3   Spoiler protection

The spoilers are by design the limiting apertures in the machine: when a bunch train comes out of the linac with a large orbit or energy error, it is the spoilers that should intercept the beam first. In the event of some upstream error, the fast emergency extraction line (FEXL, section 7.2.6) should safely extract the beam after one or two bunches: hence the spoilers need only survive at most two bunches from the bunch train.

The current spoiler design uses one radiation length of titanium (3.56 cm). Studies using GEANT4 [3] have shown that the spoiler should withstand a single *design* bunch ($128 \times 7 \mu\text{m}^2$) with some safety margin. The calculation uses the ultimate tensile strength (σ_{UTS}) as the survival criterion for the spoiler [83, 3, 36]. However, recent experiments using the SLAC linac have indicated that failure tends to occur at lower instantaneous power densities than the GEANT studies would suggest [37], and so an additional level of protection seems prudent.

The original collimation system reported in [83, 36] reflected the philosophy that *all* spoilers should be able to survive a direct hit from some number of bunches. The beam size at each spoiler was blown up using linear optics to reduce the peak energy particle density to an acceptable level. The system was characterised by large (km) β-functions, resulting in relatively long systems with extremely tight tolerances. Such systems eventually proved to be impractical and have been abandoned. The current philosophy is to protect the spoilers from energy errors, since these are the most likely (frequent) type of error we can expect from the linac. Large orbit (pure betatron) oscillations of sufficient amplitude to strike a spoiler are probably rare events by comparison: the typical scenarios tend to be magnet failures, which occur relatively slowly ($> 100 \, \mu\text{sec}$), and can be detected by direct monitoring.

A non-linear magnet system referred to as the magnetic energy spoiler (MES) is incorporated just upstream of the collimation system. Figure 7.5.4 indicates how the system works. An off-momentum bunch receives a horizontal kick from the octupole at the high dispersion point ($D_x = -100 \, \text{mm}$), which translates into a (momentum dependent) horizontal offset at the downstream skew-sextupole[1]. The effective *skew-quadrupole* generated couples the horizontal emittance into the vertical plane. The result is a significant increase in the vertical beam size at the energy collimator, placed $(n + 1/2)\pi$ downstream in both x- and y-phase. From a simple thin-lens analysis, the

---

[1]the octupole effectively generates third-order dispersion at the skew-sextupole.
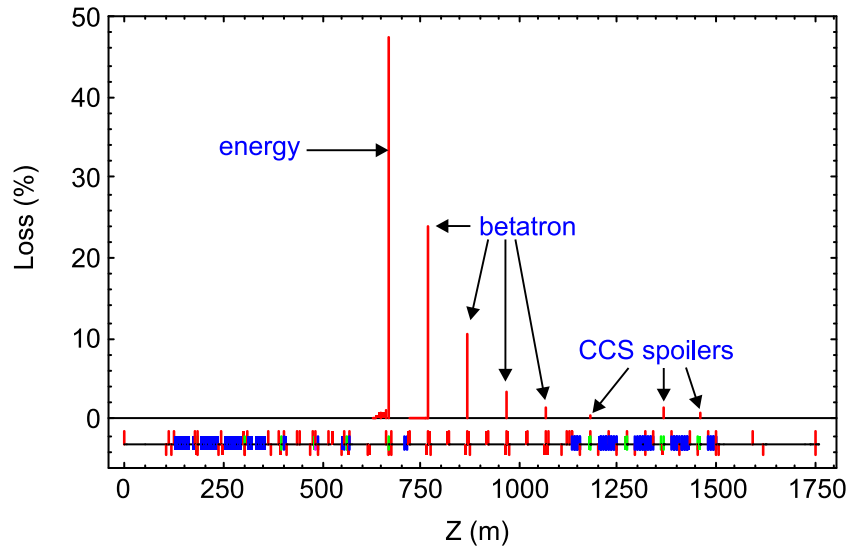
(a) Particles 'losses' along the beamline, expressed as a percentage of the initial particle number tracked.
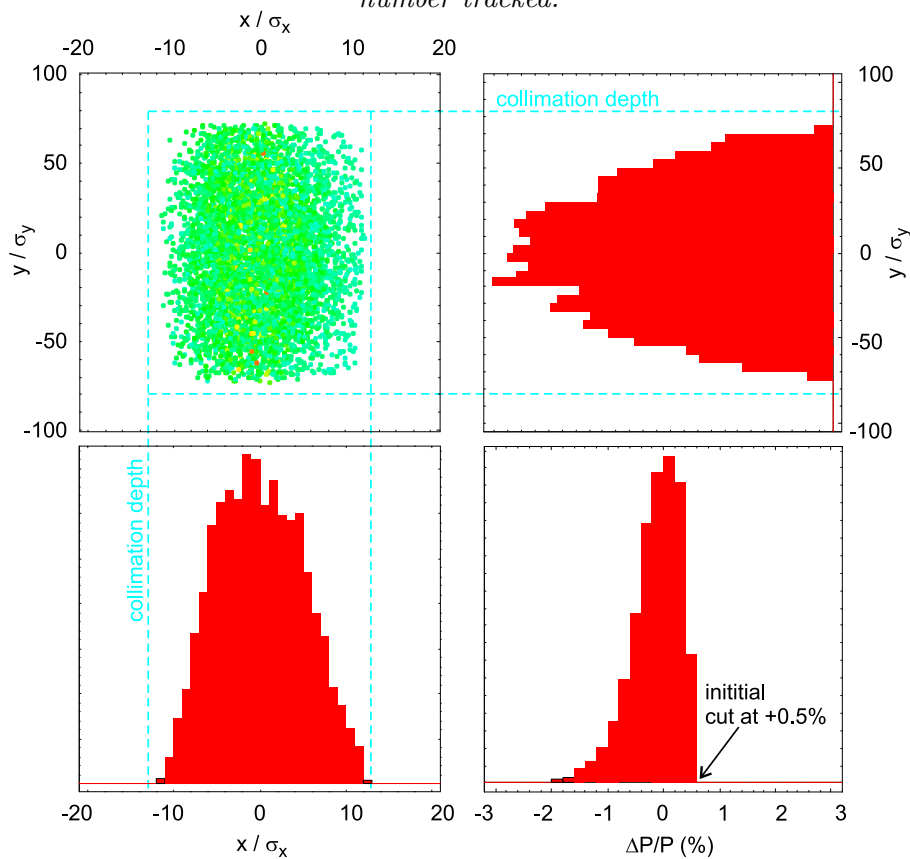
(b) Particle distribution at the entrance to the final doublet after tracking through the entire BDS.

Figure 7.5.3: *Results of particle tracking through the BDS. All apertures are treated as 'hard' edges, i.e. a particle outside of a given aperture is deemed lost. An initial flat distribution of 10^5 particles was generated, with a transverse extent of $\pm 16.25\sigma_x$ and $\pm 100\sigma_y$ (collimation depth plus 25%). The momentum distribution was $-3\% < \Delta P/P < +0.5\%$. Effects of scattering and transmission through material are not included.*
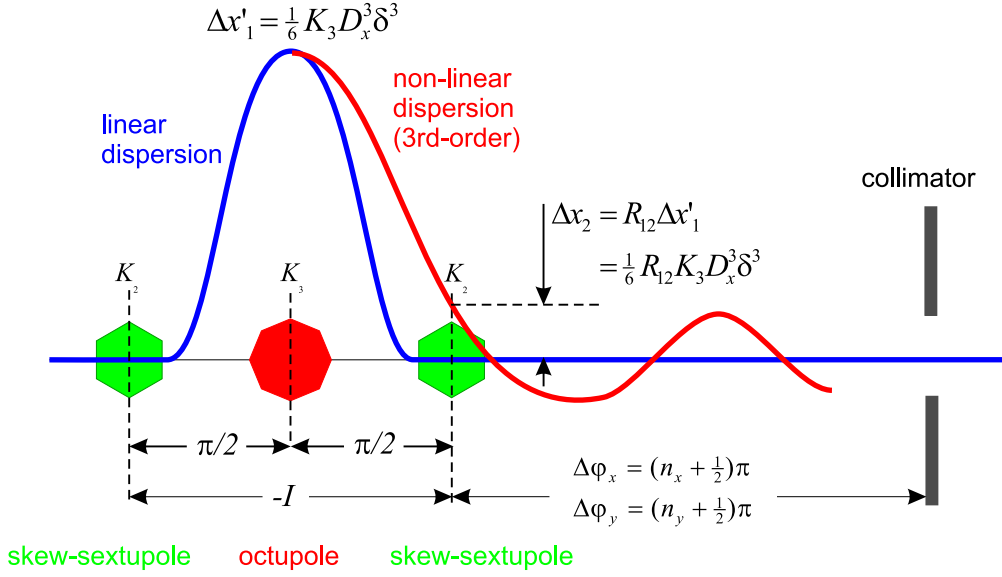
Figure 7.5.4: *Concept of the magnetic energy spoiler (MES). See text for details.*

increase in vertical beam size at the spoiler as a function of momentum error $\delta = \Delta p/p$ is

$$\frac{\sigma_y(\delta)}{\sigma_y(\delta = 0)} \approx \frac{1}{6} K_2 K_3 R_{12} \sqrt{\beta_x \beta_y} \sqrt{\frac{\epsilon_x}{\epsilon_y}} D_x^3 \delta^3$$

where K_2, K_3 are the integrated strengths of the skew-sextupoles and octupole respectively, D_x is the linear dispersion at the octupole, R_{12} is the linear Green function from the octupole to the skew-sextupole, and $\beta_{x,y}$ are the β-functions at the skew-sextupole. The system also generates centroid kicks to the beam, resulting in third-order horizontal dispersion and sixth-order vertical dispersion. These energy dependent orbits eventually cause the beam to strike a betatron collimator in CDS section. If the collimator apertures are set at $\pm N_x \sigma_x$ and $\pm N_y \sigma_y$, the maximum relative increase in beam size, defined at the point when the beam hits a betatron spoiler, is given by

$$\left. \frac{\sigma_y(\delta)}{\sigma_y(0)} \right|_{max} \approx 2 \frac{N_y}{N_x}$$

For the current system, the limit corresponds to $2 \times (80/13) \approx 12$. However, chromatic effects in the downstream CDS lattice that are not included in the above analysis constrain the maximum obtainable factor still further. The current values of $K_2 = 5\,\mathrm{m}^{-2}$ and $K_3 = 640\,\mathrm{m}^{-3}$ are set to give a factor of ~ 6 increase in vertical beam size, which has been confirmed using tracking (see figure 7.5.5).

7.5.4   Wakefield considerations

For one radiation length of titanium at the specified apertures, the resistive wall wakefield can be ignored. To reduce the geometric wakefield to an acceptable level, the
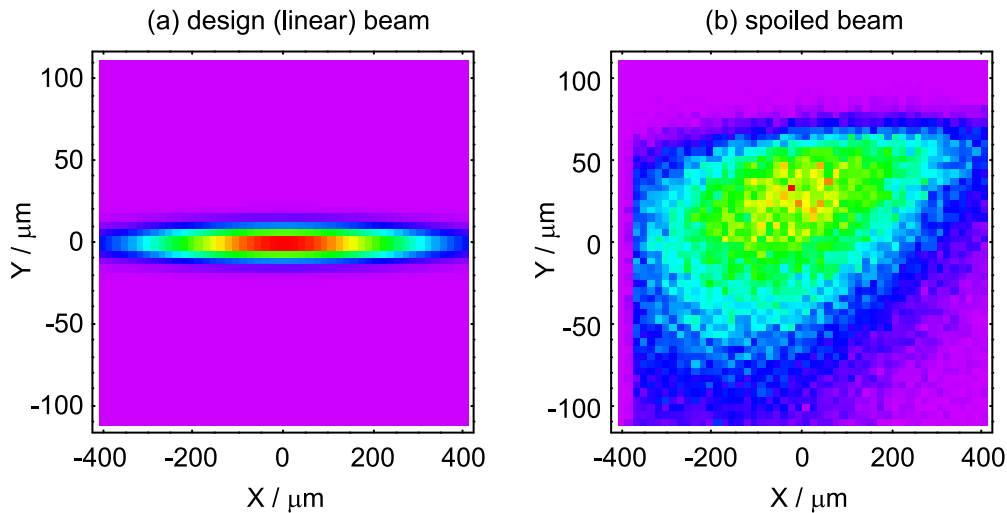
Figure 7.5.5: *Results of tracking a design beam with a momentum centroid error of $\Delta P/P = -2\%$. (a) shows the* design *beam on the energy spoiler (ESPOI), while (b) shows the results of the tracking. The beam area is increased by a factor of 6.*

spoilers will be constructed with tapers approximately $1\,\mathrm{m}$ long. Simple estimates based on calculations presented in [36] suggest that vertical beam offsets on the order of a few σ_y cause less than a 2% emittance growth. In addition, recent experimental results from SLAC [38] have shown that such theoretical estimates are pessimistic by as much as a factor of ten. Even with the conservative theoretical estimates, however, there appears to be no significant wakefield effects.

7.6 Beam Extraction

After collision at the IP, the highly disrupted beams must be cleanly extracted from the IR and transported without significant losses to the main dump. In addition, the intense beamstrahlung generated during the beam-beam interaction must be cleanly extracted and dumped. A third requirement is to safely transport the undisrupted charged particle beams to the main dump in the event that there is no collision (i.e. no beam-beam interaction); in this case, the optics of the extraction line must generate a large enough beam size on the dump window to prevent single pulse damage. The various extracted beam parameters are summarised in table 7.6.1. A detailed description of the extraction system design can be found in [39].

With the exception of the energy spread for the undisrupted beam case (see table 7.6.1), the extraction systems are identical and symmetric about the IP. Unless explicitly stated, the following description applies to both e^+ and e^- systems.

			Spent $e^\pm$	Beamstrahlung	Undisrupted $e^\pm$
$E_{cm} = 500\,\mathrm{GeV}$					
Av. Power	[MW]	P	10.9	0.360	11.3
Av. Energy	[GeV]	$\langle E \rangle$	242	5.1	250
Divergence	[μr]	$\Theta_{x,y}$	245, 27	151, 36	37, 12
Emittance	[10^{-12} m]	$\epsilon_{x,y}$	67, 0.18	–	20, 0.061
Energy Spread	[%]	σ_E/E	5.5	–	$0.15(e^-)/0.032(e^+)$
$E_{cm} = 800\,\mathrm{GeV}$					
Av. Power	[MW]	P	16.8	0.760	17.5
Av. Energy	[GeV]	$\langle E \rangle$	283	11.4	400
Divergence	[μr]	$\Theta_{x,y}$	152, 17	94, 21	26, 6.8
Emittance	[10^{-12} m]	$\epsilon_{x,y}$	28, 0.68	–	10, 0.019
Energy Spread	[%]	σ_E/E	7.4	–	$0.15(e^-)/0.032(e^+)$

Table 7.6.1: *Main characteristics of the disrupted spent beams, beamstrahlung photons and undisrupted (low emittance) beams at the IP.*

7.6.1   Electron and positron beam extraction

The charged beam extraction line (figure 7.6.1) is based on the following concepts:

- The beams are transported to water dump systems (section 7.7) located 240 m downstream of the IP.

- The beams are *vertically* extracted outside of the IR (i.e. outside of the final s.c. quadrupoles) and before the first parasitic bunch crossing[1].

- 20 m of electrostatic separators (ESEP1 and ESEP2) provide an initial separation of incoming and outgoing (extracted) beams, with an angle of 0.8 mrad. The separators have both a d.c. electrostatic and magnetic deflectors combined in the same unit; the electric and magnetic deflections add up for the outgoing beam while they cancel each other for the incoming one.

- A total downward angle of 15 mrad is primarily achieved by a magnetic septum MSEP and the dipoles BV1 and BV2; the angle is constrained by the need to minimise the muon rate at the surface.

- The beam optics shown in figure 7.6.2 is designed to limit the disrupted beam losses to less than 0.1% along the beam line. This is done by controlling the

---

[1]The first parasitic bunch crossing is at 50 m and 26 m for 500 GeV and 800 GeV c.m. energy respectively.
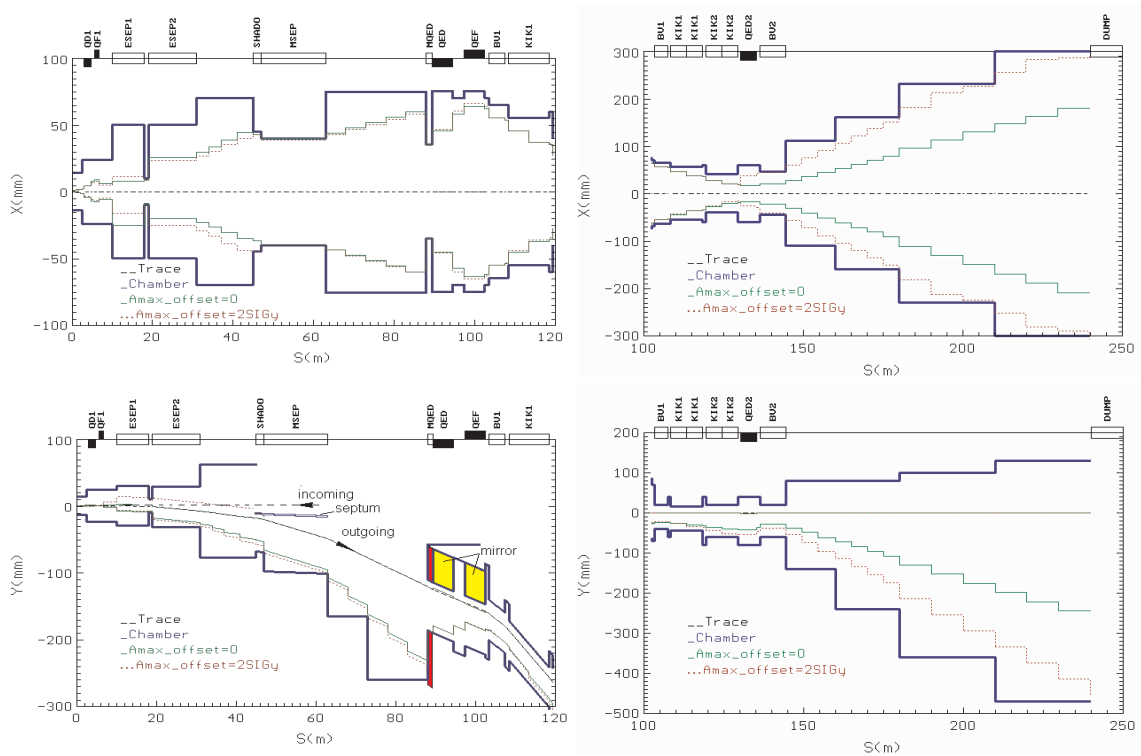
Figure 7.6.1: *Horizontal (top row) and vertical (bottom row) layouts and beam pipe apertures of extraction beam line.*

vertical dispersion generated by the extraction bends with a proper arrangement of septum quadrupoles (QED, QEF, and QED2) with magnetic mirror blades. About 0.01% of beam power is lost at the collimator embedded in the separator and at the magnetic-septum shadow (SHADO), and 0.1% at the quadrupole collimator (MQED).

- The same optics blows up the spot size of the undisrupted (low emittance) beams above $0.4\,\mathrm{mm}^2$ at the dump window (see figure 7.6.3). To increase the effective beam size still further, two $10\,\mathrm{m}$ long fast-sweeping magnets (KIK1, KIK2) sweep the bunch train in a circle of $5\,\mathrm{cm}$ radius; the water temperature rise is then limited to $40°\,\mathrm{C}$ (see section 7.7).

The electrostatic separators are constructed from $5 \times 4\,\mathrm{m}$ units based on the design used in LEP[40], where they have reached the $50\,\mathrm{kV/cm}$ field needed for the $500\,\mathrm{GeV}$ c.m. energy machine. For the upgrade to $E_{cm} = 800\,\mathrm{GeV}$, either the field or the length or both need to be increased: while a field of $80\,\mathrm{kV/cm}$ is feasible, it has yet to be demonstrated and requires further R&D. The field of the $16\,\mathrm{m}$ long vertical septum
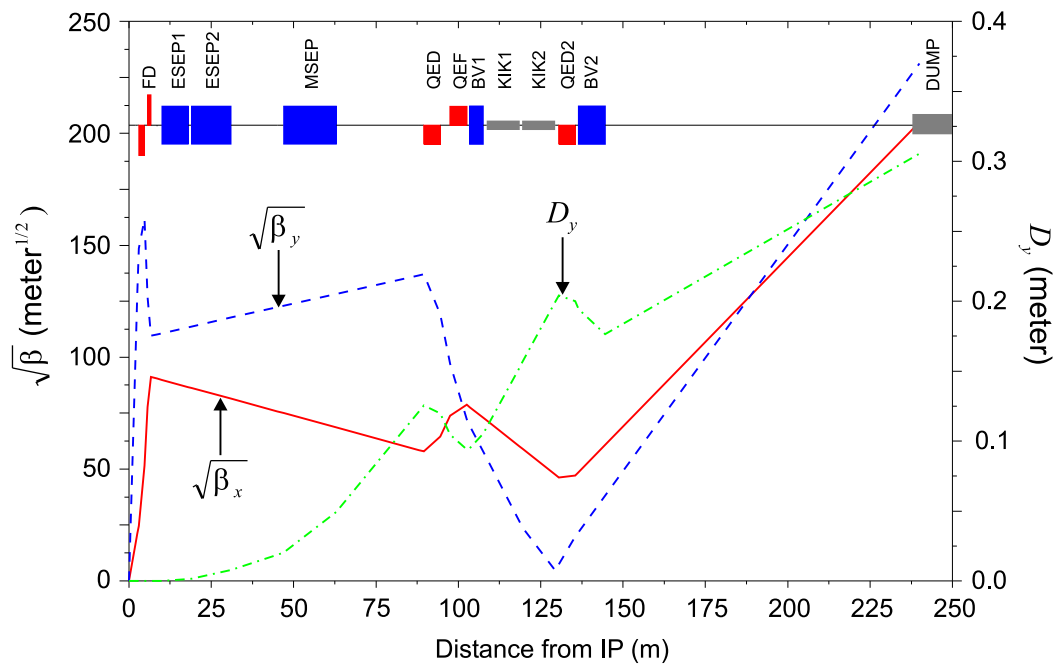
Figure 7.6.2: *Optics of the charges particle extraction line.*
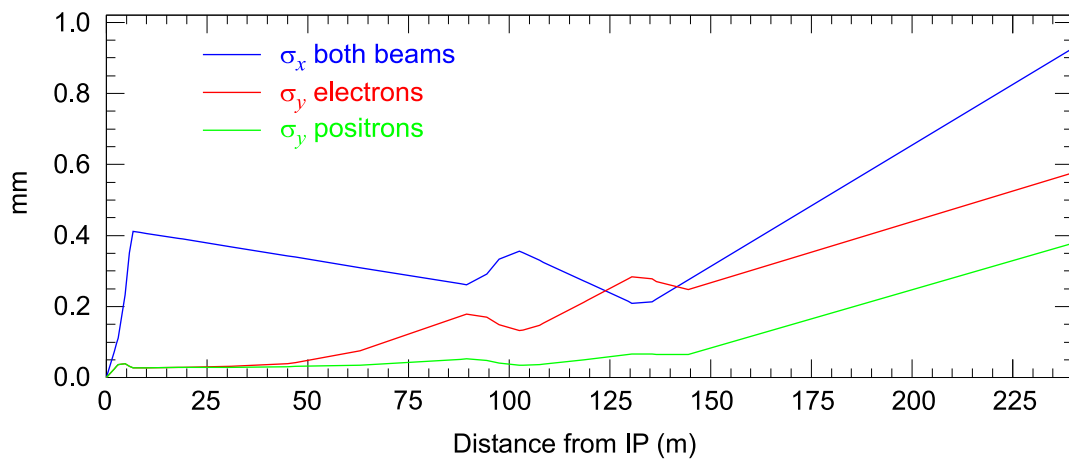
Figure 7.6.3: *Beam sizes of the undisrupted (low emittance) electron and positron beams along the extraction line. The blow-up of the vertical emittances due to synchrotron radiation in the vertical bends is also included.*
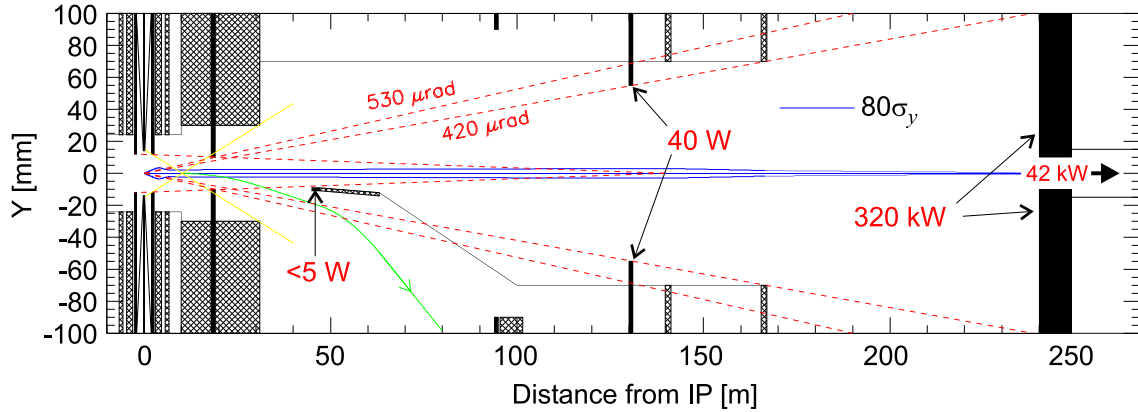
Figure 7.6.4: *Vertical layout of the final transformer region. The beamstrahlung power levels on the collimators are for the $E_{cm} = 500\,GeV$ machine.*

magnet is kept low ($\sim$0.1 Tesla) to allow for a thin septum blade of a few millimetres; a complete description can be found in [13].

7.6.2   Beamstrahlung photon extraction

The 360 kW of beamstrahlung power is extracted cleanly through the large aperture final telescope to a water dump. To localise the main power deposition in one heavily shielded area, the beamstrahlung dump is located (integrated) at the same position as the main spent beam water dump (240 m downstream of the IP)[1]. The key features of the system (shown in figure 7.6.4) are:

- a 10 mm radius collimator located 18 m from the IP (designed to mask the detector from the incoming synchrotron radiation) intercepts less than 1 W of beamstrahlung power;

- the intermediate quadrupole doublet ($\sim$150 m from the IP) with 70 mm bore radius is shielded by a 55 mm radius collimator which intercepts about 40 W of beamstrahlung power;

- the main beamstrahlung collimator (dump), which has a central 20 mm diameter aperture to allow for the incoming beam; the $\sim$40 kW of low-angle beamstrahlung which passes though this aperture is dumped in a smaller (solid) beam dump located directly after the first C-dipole of the CCS.

7.6.3   Pairs and radiative Bhabhas power deposition

Although the $\pm$10 m region around the IP is free from spent beam loss, lower energy radiative Bhabhas and e^+e^- pairs — which experience large disruption during the

---

[1]This results in the stretching of the final telescope optics discussed in section 7.2.5.
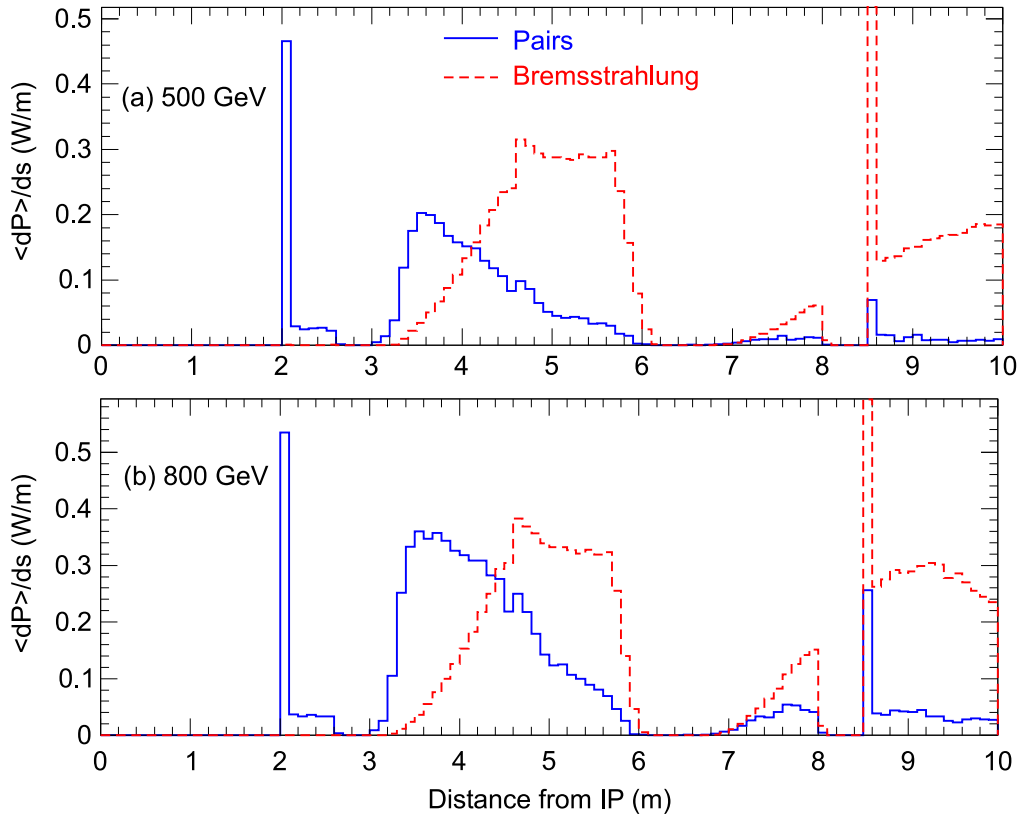
Figure 7.6.5: *Average power density (W/m) deposited by the e^+e^- pairs and the radiative Bhabhas (bremsstrahlung) in the IR.*

bunch collision — are over-focused by the IR doublet quadrupoles. The power densities deposited on the beam pipe (shown in figure 7.6.5) are smaller than the $3\,\mathrm{W/m}$ limit set by cooling capacity of the cryogenic system for the s.c. IR quadrupoles [33].

7.7   Main Beam Dump System

This section discusses the main characteristics, features and safety aspects of the main beam dump system. Many of the basic considerations of the dump system are discussed in detail in [83]: in the following, therefore, emphasis is placed on those aspects that differ or are new. A more detailed description of certain subcomponents of the system can be obtained from the cited references. The numbers quoted are for the design beam power for the $500\,\mathrm{GeV}$ machine ($11.3\,\mathrm{MW}$). Where necessary, comments concerning the $800\,\mathrm{GeV}$ upgrade ($17.5\,\mathrm{MW}$ beam power) are included.

E_0, particle energy	250 GeV	400 GeV
N_t, particles per bunch train	$5.64 \cdot 10^{13}$	$6.84 \cdot 10^{13}$
ν_{rep}, repetition rate	5 Hz	4 Hz
I_{ave}, average beam current	45 μA	43.8 μA
W_t, energy per bunch train	2.3 MJ	4.4 MJ
P_{ave}, average beam power	11.3 MW	17.5 MW

Table 7.7.1: *Beam parameters relevant to the beam dump system for the* 250 GeV *main linac beam and its* 400 GeV *upgrade option.*

7.7.1   Requirements and basic concept

The important beam parameters relevant to the dump are given in table 7.7.1. The current high-luminosity parameter set represents a 50% increase in the average power requirement compared to the CDR parameters [83]. Solid dumps are ultimately limited by the thermal conductivity of the material, and already become technically difficult beyond several hundred kW of beam power: in the MW regime, therefore, the only reasonable and technically feasible solution is a water dump, which can handle the high power by a sufficient mass flow of water towards an external heat exchanger [87].

   Figure 7.7.1 shows the conceptual layout of the main parts of the dump system. The same dump is used for the main spent beam, and for the fast emergency extraction line (FEXL), described in section 7.2.6 (the main extraction line is described in section 7.6); as a result the dump requires an entrance window at both ends of the water vessel. A single cooling system (per side) is intended to serve both the main spent beam dump and the beamstrahlung collimator (section 7.6.2); if a second IR is constructed, then the same cooling plant can also be used for the additional dumps, since the *total* power at any given time can never exceed the maximum single beam power.

7.7.2   Design of water vessel

Most of the beam power should go into the water and not into the mechanical container: hence the vessel must be built from a minimum amount of mechanically strong and corrosion resistant material, which in addition represents a small source of induced radioactivity. The dump consists of about 11 m^3 of water, which is housed in a 10 m long (27.7 radiation length) cylindrical titanium vessel, with a radius of 60 cm (6.3 molière radii), and a wall thickness of 15 mm.

   According to 250 GeV shower simulations using the MARS code, energy escaping from the absorber is at the 1–2% level, and is dominated by radial leakage. Since penetration of the shower varies only logarithmically with energy, we can assume that the leakage power out of the vessel and into the surrounding shielding scales approximately linearly with incident beam power: an increase of ∼50% is therefore expected for the 800 GeV upgrade.
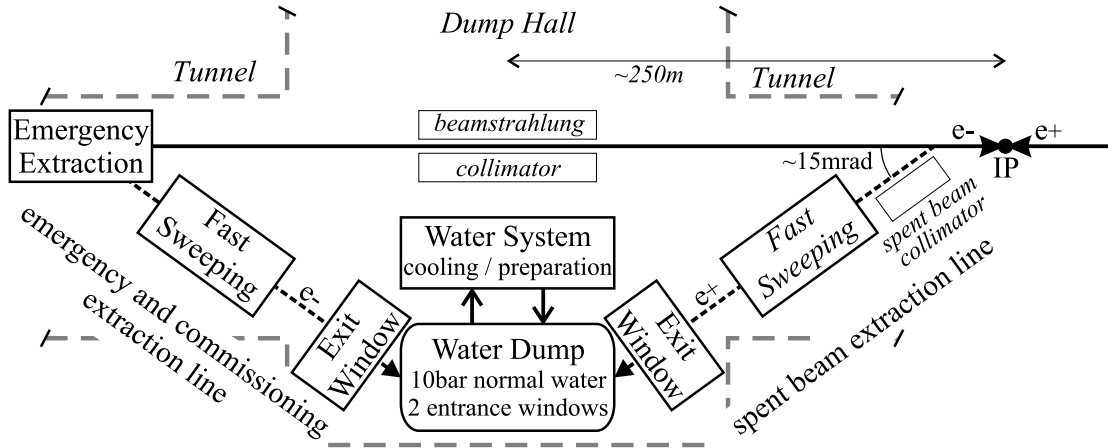
Figure 7.7.1: *Schematic side view of the main linac beam dump system and its subcomponents.*

Although relatively small, the leakage power is still more than $100\,\mathrm{kW}$, and an inner shell of aluminum is required to significantly reduce the power density on the outer concrete shielding [86]. Aluminium was chosen because of its low residual radioactivity and high thermal conductivity. The removable shield will be thermally coupled to the water vessel. Gaps between the vessel and shielding, or within the shielding volume must be kept to a minimum to reduce air activation. For further details on radiation safety issues see section 8.3.

The absorption of all N_t particles of one bunch train leads to a certain energy distribution in the water, which directly translates into an instantaneous temperature rise with its maximum $(\Delta T_{inst})_{max}$ somewhere on the shower axis. If E_0, N_t and the absorber material are fixed, $(\Delta T_{inst})_{max}$ only depends on the area of the incoming beam. The risk of boiling is avoided by:

- pressurising the water to $10^6\,\mathrm{Pa}$ ($10\,\mathrm{bar}$), which pushes the boiling point to about $160°\mathrm{C}$; and

- limiting the instantaneous temperature rise to $< 40°\,\mathrm{C}$ (assuming that the water has a temperature of $\sim 50°\,\mathrm{C}$ before the arrival of the beam).

The latter constraint sets a minimum RMS beam radius at the dump of $19\,\mathrm{mm}$ and $30\,\mathrm{mm}$ for $E_{beam} = 250\,\mathrm{GeV}$ and $400\,\mathrm{GeV}$ respectively. For an *undisrupted* beam (i.e. no collision), the RMS beam size at the dump is only $1 \times 0.4\,\mathrm{mm}^2$ which is far too small: therefore the effective spot size has to be increased by using a fast sweeping system [88], that distributes all the bunches of the bunch train around a circle of radius $5\,\mathrm{cm}$ at $250\,\mathrm{GeV}$ ($8\,\mathrm{cm}$ at $400\,\mathrm{GeV}$) on the face of the dump. The fast sweeping system consists of a set of orthogonal deflectors excited with a sinusoidal current of the same frequency but with a $90°$ phase shift. The frequency needs to be at least $1\,\mathrm{kHz}$ in order to evenly
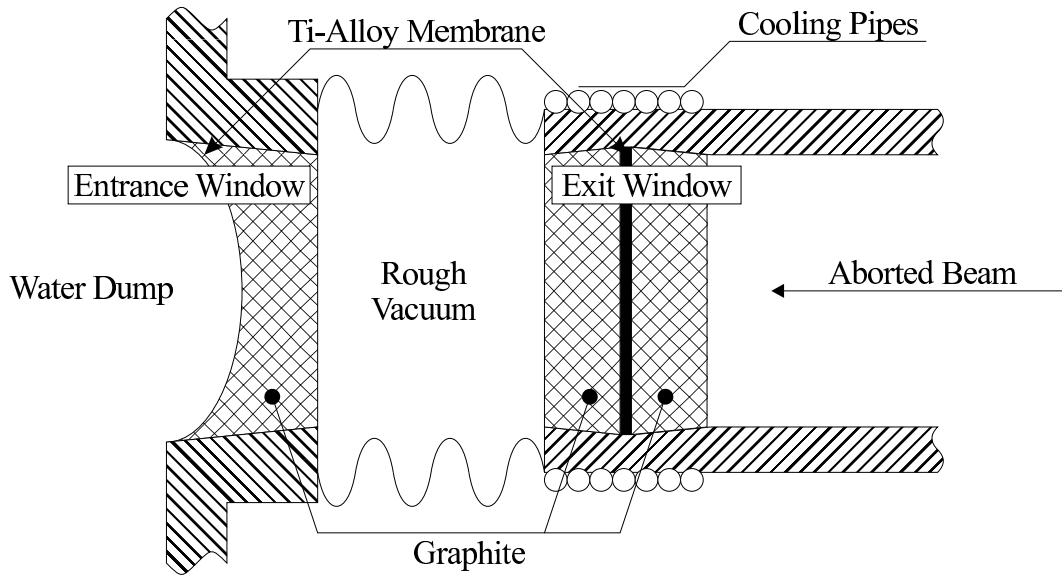
Figure 7.7.2: *Concept of the (vacuum) exit and (water) entrance window, which is based on a titanium-graphite sandwich design.*

distribute all the bunches from a single bunch train ($950 \, \mu$sec). Pulsed iron yoke dipoles sitting outside of the vacuum chamber will be used. Several independent modules in each plane are foreseen to allow safe operation should one fail. As an additional safety measure, the sweeper system will be triggered early enough to prevent the extraction of the bunch train from the damping ring should a failure in the system be detected.

7.7.3   Entrance and exit windows

Figure 7.7.2 shows the concept of the dump window. The beam passes through an exit window at the end of the vacuum system before it enters the water absorber through a second (separate) window: using two windows provides a level of redundancy in the event of a leak. The volume between the two windows requires a rough vacuum to avoid air activation. Windows for pulsed beams suffer from cyclic mechanical stress due to instantaneous heating. A $5 \, \text{Hz}$ operation and a $10 \, \text{year}$ lifetime gives in total about 10^9 cycles. Normally materials with high specific heat like beryllium are preferred; but given the required high number of cycles titanium alloys are good candidates. Available data for such alloys shows that the maximum allowed particle density $(dN/dA)_{max}$ at the window as a function of the number of cycles (before failure) tends to a constant value of $\sim 4 \times 10^{12} \, /\text{mm}^2$ after $\sim 10^4$ cycles [89]. Unfortunately data only exists up to 10^7–10^8 cycles. However, even for the undisrupted beam, the particle density on the window is a factor of ten less than this limit due to the constraint from the instantaneous temperature rise of the water.

The titanium membranes in both windows are reinforced by graphite disks as shown

in figure 7.7.2. In the case of the (vacuum) exit window, the graphite (which is located on either side of the membrane) will help to conduct away the average power[1] of $30\,W/mm^2$ towards the heat sink at the circumference of the window. For the (water) entrance window, average heating is not a problem since the membrane is cooled directly from the dump water.

The performance of the window is only dependent on the peak particle density and average beam current, and *not* on the beam energy: therefore, the window can also be used for the 800 GeV upgrade, since the average beam current remains roughly the same, and due to the increased sweep radius, the peak particle density is also approximately constant. Since the performance is not energy dependent, experience can be obtained from tests at the TESLA Test Facility Phase 2 (TTF2), where such a graphite-titanium sandwich-like window will be installed as an exit window.

7.7.4 Water system

Removal of the heat dissipated by the beam in the water vessel will be done by a special water in- and outlet system. The flow of water though the vessel is dictated by two constraints:

- to renew the volume of water that the shower sees for each beam pulse, a flow of $\sim 0.5\,m/s$ perpendicular to the shower axis (at the critical longitudinal position) must be guaranteed; and

- a continuous (bulk) flow of $100\,kg/s$, or $360\,m^3/h$ of water towards an external heat exchanger is required to handle the average power.

The temperature drop between in- and outlet is $\sim 30°\,C$. The heat exchanger is part of an ambitious water preparation plant, schematically shown in figure 7.7.3; the system must also handle the radiological and chemical aspects of the dump water.

It is expected that the dump water will remain in the closed system for the entire lifetime of the collider. For pure water, The following radioactive nuclei will be produced (half-life in brackets): ^{15}O (2 minutes); ^{13}N (10 minutes); ^{11}C (20 minutes); ^{7}Be (54 days); and ^{3}H (12 years). The activity of the ^{7}Be and ^{3}H saturate at 66 TBq and 7.3 TBq respectively. After decay of the short-lived isotopes, the outside dose rate is mainly determined by the $478\,keV$ γ particles from the ^{7}Be decay, since the $20\,keV$ electrons from tritium decay will not penetrate the walls of the water system. If distributed evenly in a total water volume of $10\,m^3$, the estimated dose rate at the surface of a 300 mm diameter tube is about 500 mSv/h; this value will be reduced by two to three orders of magnitude if a few percent of the total water flow is passed through a resin filter which removes the ^{7}Be. In addition, the filter removes other particles and therefore maintains the purity of the water, which is essential for avoiding corrosion. Radiolytical damage of the filter material is reduced by a delay line in front of the filter to allow the short-lived products to decay.

---

[1]Assuming an average current of $45\,\mu A$
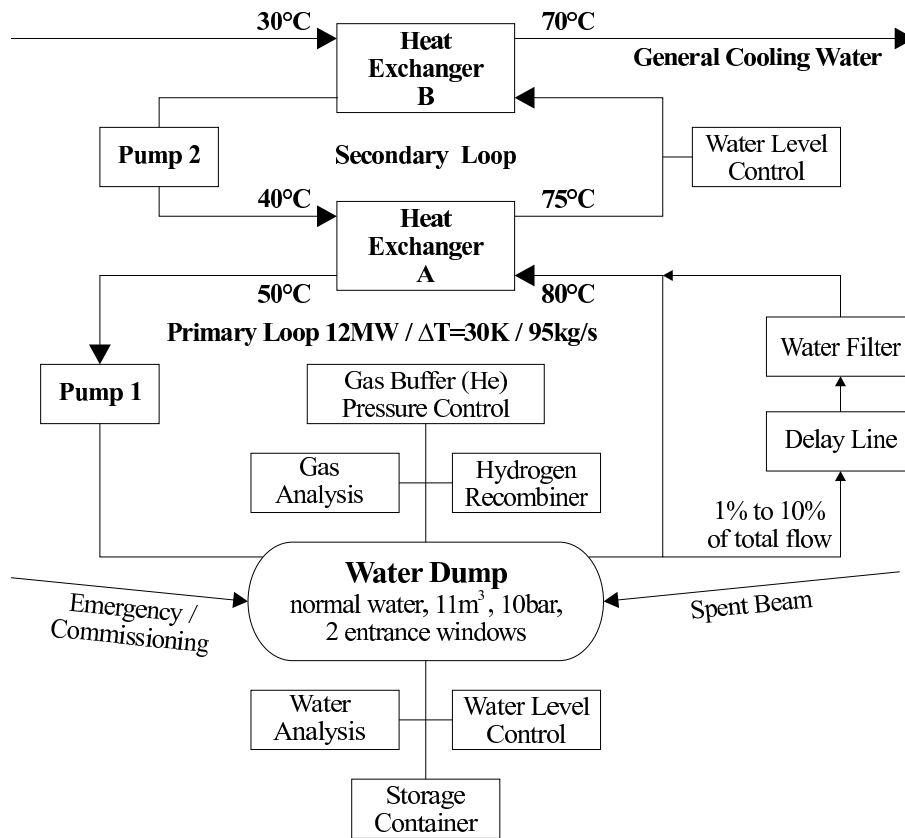
Figure 7.7.3: *Schematic overview of the water system required for the main beam dump.*

There will be a small gas volume (most probably He) at the top of the dump vessel; it will protect the vessel from pressure waves induced by instantaneous heating in the event of a failure of the fast sweeping system. The gas buffer will also maintain the static pressure and compensate for slow expansion due to different average temperatures of the dump water. All gaseous constituents not dissolved in the water will accumulate in the buffer: special attention must be paid to hydrogen, which is produced via radiolysis with a rate of 3.6 l/s [85]. A catalytic hydrogen recombiner and a gas analyzing station will be connected to the buffer volume.

The system needs to be leak-tight at the level typically found in vacuum systems; this requires gas-tight components (pumps, heat exchangers, etc.), welded or metal sealed connections, and a proper choice of materials to avoid harmful water-chemical reactions. A water analysis station will monitor relevant parameters such as acidity, ion concentrations and conductivity. However the possibility of a leak requiring a repair or exchange of a component has to be foreseen. Once a leak has been detected by monitoring water pressure and level, the system will first be flushed into the storage container to remove the dominant source of radiation, allowing work to proceed on the necessary mechanical parts after a relatively short cool-down period.

All walls of the hall for the system have to be sealed with a special paint to collect leaking water. The primary cooling circuit is separated from the the general cooling

water by an intermediate secondary loop, which has a higher pressure than the primary one. The loop protects the general cooling water from being contaminated, in the event of leaks in either of the heat exchangers. The whole water system will be housed in the dump hall.

The design and fabrication of such a complex water dump represents a significant technical challenge. However, similar systems already exist: e.g. the 25 GeV, 2.2 MW water dump at SLAC [84]; spallation neutron sources like the SINQ at Paul Scherrer Institute (PSI); or research reactors. By using the experience gained at these and other facilities, a safe and technically feasible design can be achieved.

Bibliography

[1] R. Brinkmann, G. Materlik, J. Roßbach and A. Wagner (eds.), *Conceptual Design of a 500 GeV e+e- Linear Collider with Integrated X-ray Laser Facility*, DESY-97-048 and ECFA-97-182, chapter 3: http://www.desy.de/lc- cdr/tesla/tesla.html, 1997.

[2] J. Payet, O. Napoly, *A Proposal for the TESLA High Energy Switchyard*, DESY TESLA-2000-24, 2000.

[3] R. Brinkmann, N. Walker, G. Blair, *The TESLA Post-linac Collimation System*, DESY TESLA-01-12, 2001.

[4] M. D. Woodley, P. E. Emma, *Measurement and Correction of Cross Plane Coupling in Transport Lines*, Proc. 20th Int. Linac Conference, Monteray, CA, Aug. 2000, LINAC2000-MOC19, SLAC-PUB 8581, 2000.

[5] K. Wittenberg, *Conventional Wire Scanners for TESLA*, DESY TESLA-00-18, 2000.

[6] W. Inman et al., *A Laser-Based Beam Profile Monitor for the SLC/SLD Interaction Region*, Nucl. Instrum. Meth. **A379** (1996) 363.

[7] K. L. Brown, *Basic Optics of the SLC Final Focus System*, presented at Workshop on Physics of Linear Colliders, Capri, Italy, June 1988, and Int. Workshop on the Next Generation of Linear Colliders, Stanford, CA, Nov. 1988, SLAC-PUB-4811, 1988.

[8] D. Burke for the FFTB Collaboration, *Results from the Final Focus Test Beam*, Proc. 4th EPAC, London 1994, Vol. I, p. 23.

[9] V. Sytchev et al., *Concept of an Emergency Extraction Kickersystem for TESLA*, DESY TESLA-01-06, 2001.

[10] O. Napoly, J. Payet, N. Walker, *Emergency Extraction High-Energy Beamline for TESLA*, DESY TESLA-01-13, 2001.

[11] E. Bondarchuk et al., *A Technical Proposal for the Development and Manufacturing of the Electromagnets for the TESLA BDS*, DESY TESLA-00-23, 2000.

[12] E. Bondarchuk et al., *A Technical Proposal for the Development and Manufacturing of the Electromagnets for the TESLA Fast Emergency Extraction Line*, DESY TESLA-01-20, 2001.

[13] E. Bondarchuk et al., *A Technical Proposal for the Development and Manufacturing of the Electromagnets for the TESLA Main Extraction Line*, DESY TESLA-01-21, 2001.

[14] A. Brenger et al., *The Vacuum System for the TESLA Beam Delivery System*, DESY TESLA-01-14, 2001.

[15] A. Sery, O. Napoly, *Influence of Ground Motion on the Time Evolution of Beams in Linear Colliders*, Phys. Rev. **E 53** no. 5 (1996) 5323.

[16] N. Walker, A. Wolski, *Luminosity Stability Issues for the TESLA Beam Delivery System*, DESY TESLA-00-22, 2000.

[17] F. Rouse, T. Gromme, W. Kozanecki, N. Phinney, *Maintaining Micron Size Beams in Collision at the Interaction Point of the Stanford Linear Collider.*, Proc. IEEE Particle Accelerator Conf., San Francisco, CA, May 1991, IEEE 1991:3222-3224 (QCD183:P3:1991), SLAC-PUB-5512, 1991.

[18] D. Schulte, *Beam-Beam Simulations with Guinea-Pig*, CERN-PS-99-14, CERN-CLIC-NOTE-387, 1999.

[19] C. Magne, M. Wendt, *Beam Position Monitors for the TESLA Accelerator Complex*, DESY TESLA-00-41, 2000.

[20] F. Obier, *TTF Feedback Kicker*, DESY-M-002, 2000.

[21] J. Rümmler, *Kicker Systems for the TESLA Transverse Feedback*, DESY-M-003, 2000.

[22] I. Reyzl, *Stabilisation of Beam Interaction at the TESLA Linear Collider*, Proc. 7th EPAC, Vienna 2000, p. 315.

[23] V. Shiltsev et al., *Measurements of Ground Vibrations and Orbit Motion at Hera*, DESY-HERA-95-06, 1995.

[24] C. Montag, *Active Stabilization of Mechanical Quadrupole Vibrations for Linear Colliders*, Nucl. Instrum. Meth. **A378** (1996) 369.

[25] B. A. Baklakov et al., INP 91-15; Tech. Ph. **38** (1993).

[26] P. Tenenbaum et al., *Beam Based Alignment of the Final Focus Test Beam*, Proc. 4th International Workshop on Accelerator Alignment (IWAA95), Tsukuba 1995, p. 393; SLAC-PUB-7058, 1995.

[27] N. Walker, *Linear Tuning and Estimates for the Initial Beam Based Alignment Requirements for the TESLA Beam Delivery System (BDS)*, DESY TESLA-00-29, 2000.

[28] H.-J. Eckoldt, *Magnet Power supplies for Tesla*, DESY TESLA-00-37, 2000.

[29] O.Napoly et al., *Beam-beam effects at the TESLA Linear collider*, DESY TESLA-01-15, 2001.

[30] O. Napoly, D. Schulte, *Luminosity monitor options for TESLA*, Proc. 19th Int. Linac Conference, Chicago, Illinois, Aug. 1998, CERN-OPEN-2000-135 (1998).

[31] O. Napoly, *Luminosity Stability, Possible Feedback, and Background at Future Linear Colliders*, Proc. 7th EPAC, Vienna 2000, p. 53.

[32] R. Brinkmann, O. Napoly, D. Schulte, *Beam-Beam Instability driven by Wakefield Effects in Large Disruption Linear Colliders, to be published as DESY TESLA-01-16, 2001.*

[33] A. Devred et al., *Conceptual Design for the Final Focus Quadrupole Magnets for TESLA*, DESY TESLA-01-17, 2001.

[34] T. Shintake et al., *Experiments of Nanometer Spot Size Monitor at FFTB using Laser Interferometry*, Proc. Particle Accelerator Conf., Dallas 1995, Vol. 4, p. 2444.

[35] O. Napoly, *Collimation Depth Requirements for the TESLA IR*, DESY TESLA-01-18, 2001.

[36] R. Brinkmann et al., *The TESLA Beam Collimation System*, DESY TESLA-95-25, 1995.

[37] M.C. Ross et al., *Single Pulse Damage in Copper*, Proc. 20th Int. Linac Conf., Monteray, CA, August 2000 (LINAC2000-MOA06); SLAC-PUB-8605, 2000.

[38] P. Tenenbaum et al., *Direct Measurement of Geometric Wakefields from Tapered Rectangular Collimators*, Proc. 20th Int. Linac Conf., Monteray, CA, August 2000 (LINAC2000-MOA09); SLAC-PUB-8563, 2000.

[39] E. Merker et al., *The TESLA High-Power Extraction Line*, DESY TESLA-2001-19, 2001.

[40] B. Balhan, B. Goddard, M. Sassowsky, *Engineering Considerations for the Proposed Beam Extraction System at TESLA*, CERN Preprint, SL-Note-2000-002 MS, 2000.

[41] R. B. Neal et al., *The Stanford Two-Mile Accelerator*, chapter 20-2 W. A. Benjamin Inc., New York, 1968.

[42] D. R. Walz, E. J. Seppi, *Radiolysis and Hydrogen Evolution in the A-Beam Dump Radioactive Water System*, SLAC-TN-67-29, 1967.

[43] D. Dworak, J. Łoskiewicz, *Direct Energy Deposition in the Lateral Concrete Shielding of the TESLA Water Dump and the Rise of Shielding Temperature*, Report No 1854 / PH, The Henryk Niewodniczánski Institute of Nuclear Physics, Kraków, Poland, 2000.

[44] M. Maslov et al., *Concept of the High Power $e^{\pm}$ Beam Dumps for TESLA*, DESY TESLA-01-04, 2001.

[45] V. Sytchev et al., *Concept of the Fast Beam Sweeping System for the $e^{\pm}$ Beam Dumps of TESLA*, TESLA 2001-05, 2001.

[46] M. Maslov et al., *Concept of Beam Entrance and Exit Windows for the TESLA Water based Beam Dumps and its related Beamlines*, DESY TESLA-01-07, 2001.

8 Infrastructure and Auxiliary Systems

8.1   Introduction

Different conventional facilities have to be set up for TESLA. This chapter describes the buildings and infrastructure, which are necessary for the construction and operation of the Linear Collider and the integrated X-ray Free Electron Laser facility. Radiation safety aspects are also discussed (section 8.3). Tunnels must be constructed to house the linear accelerators and the beam distribution system of the X-ray lasers. Underground buildings are needed for the High Energy Physics detector and the beam absorbers. The helium plants (section 8.7), the cooling water supply (section 8.5) and the modulators for the klystrons are, as the X-FEL experiments, in halls above ground. In addition halls have to be built for the tests of various components. In total eight new areas outside of the DESY site are necessary for TESLA.

Before describing the different buildings and plants some basic considerations will be made.

There is a consensus in the TESLA collaboration that the Linear Collider and the X-ray FEL facility must be built at an existing laboratory to make optimal use of available know-how and infrastructure. In the 1997 Conceptual Design Report two sites had been presented, Fermilab and DESY. This report describes the civil engineering of the TESLA facility at DESY in Hamburg as a detailed layout. The resulting costs are site dependent. The selected site is favourable with respect to costs as the area is flat, and the soil conditions are well suited for a tunnel boring technique.

TESLA is a Linear Collider with one head on collision point for the annihilation of electrons and positrons. However, an option for a second interaction point with a crossing angle of 34 mrad is included. This experimental section is intended either for electron-positron and electron-electron collisions or for photon-photon collisions. The first section of the electron accelerator is used for the integrated X-ray laser facility. As a further option HERA could be operated as a stretcher ring for nuclear physics experiments, using part of the electron linac as an injector (see chapter 4 in part VI). Additionally the positron linac could be operated as an accelerator for electron scattering experiments at a gas target similar to the HERMES experiment at HERA (see chapter 3 in part VI). A future option is the collision of protons stored in HERA with electrons accelerated in both TESLA linacs with a three to five times higher centre of mass energy than today (see chapter 2 in part VI). For this option TESLA must be orientated in the direction of one of the HERA straight sections. From these considerations it was concluded that the tunnel starts on the DESY site and runs in direction North-Northwest, parallel to the straight section West of HERA.
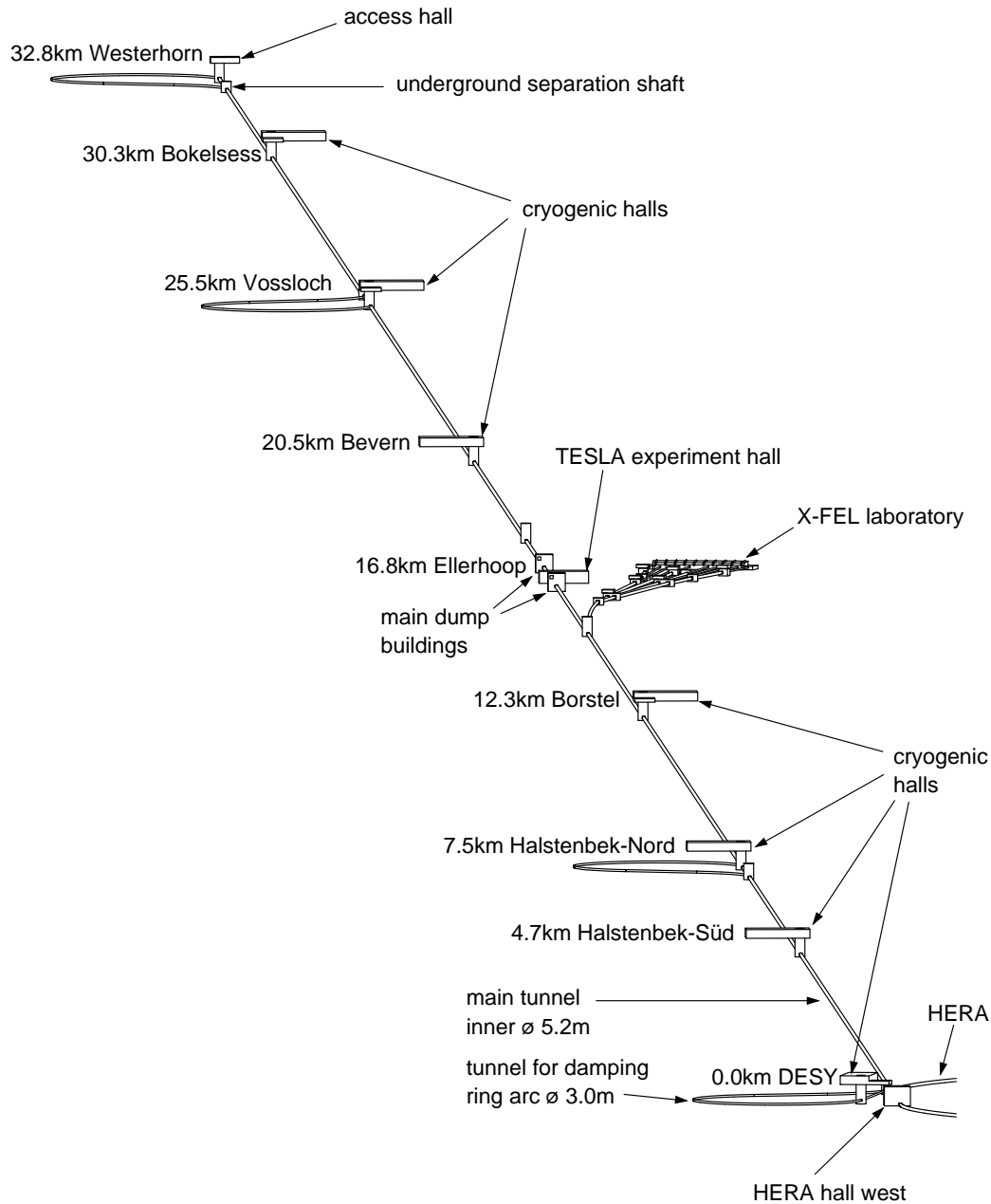
Figure 8.1.1: *Schematic layout of the TESLA facility.*

By far the largest building element is the main tunnel for the accelerators, beam lines and the various auxiliary components like klystrons, waveguides, power supplies, cables, electronics racks and water distribution. This tunnel has a total length of about 33 km and is built by a Tunnel Boring Machine (TBM). This technique is the same method as uses for the HERA tunnel. Tunneling has the smallest impact on

the existing surface buildings and infrastructure and on the natural environment. The technique is ideally suited for the soil conditions (mainly sand along the entire length of the linac). The inner diameter of the tunnel is 5.2 m. This size is the result of an optimisation process between the required space for installations and the construction costs, part of which scale linearly with the tunnel diameter.

Four additional tunnels with 3 m diameter and 1 km length each are needed for the return arcs of the damping rings.

An underground experimental hall for the Particle Physics detector is located on the campus in the centre, which also accommodates the X-ray laser facility and some additional office buildings and workshops.

Seven cryogenic plants are distributed along the main tunnel, four for the southern electron linac and three for the northern positron linac. This asymmetry is due to the operation of the FEL facility.

In 1998 the two federal German states "Freie und Hansestadt Hamburg" and "Land Schleswig-Holstein" passed a law to create the planning basis for the construction and the operation of TESLA. The legal procedure in Germany is known as 'Planfeststellungsverfahren'.

8.2   Site Layout and Civil Construction

8.2.1   Overall layout

The linac tunnel, including the beam delivery system, has a total length of about 33 km and is straight in the top view. In the side view the tunnel is mainly horizontal. This means it follows the curvature of the earth surface. Due to the constraint for the electron proton option the tunnel runs parallel to the HERA straight section West. The tunnel starts on the DESY site to make use of the existing infrastructure. Figure 8.2.1 shows an overall view of the Linear Collider site. From DESY close to the border of Hamburg the tunnel crosses the whole county of Pinneberg. Over a large fraction, the tunnel runs parallel to the motorway A23 from Hamburg to Itzehoe. The end of the tunnel is near the village Westerhorn. The tunnel starts laterally shifted beside the HERA hall West and bends with a radius of 500 m after several hundred meters into the main direction. The initial section of the tunnel houses the injectors for the High Energy Physics and X-FEL operation. The machine runs under two districts in the city of Hamburg and fifteen towns and villages in the county of Pinneberg. The campus in the centre of TESLA is south of the village Ellerhoop. An underground experimental hall for the particle physics detector and two underground halls for the beam dumps are located in this area. The site also accommodates the X-FEL underground beam distribution system and experimental hall, which is above ground.

Seven cryogenic halls are distributed along the main linac tunnels. They are connected to the tunnel via shafts. One plant can supply a 5 km long tunnel section. In the first part of the electron linac the heat load is higher than in the rest of the machine due to the additional acceleration of an electron beam for the X-FEL operation. Here a cryogenic plant supplies only a 2.5 km long tunnel section. This is the reason for the
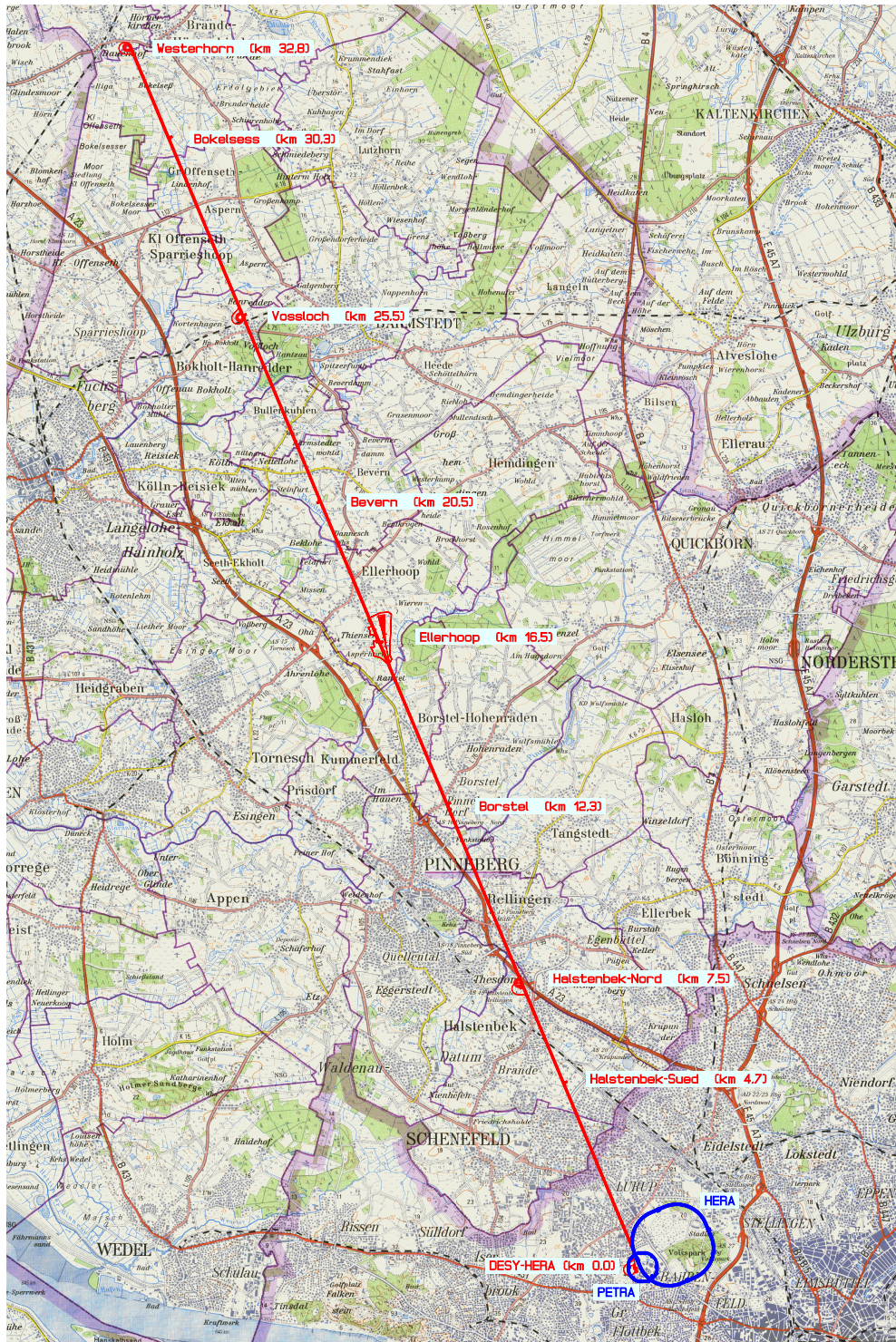
Figure 8.2.1: *Site map of the Linear Collider and X-FEL at DESY in Hamburg.*

Westerhorn (km 32.8)   **Bokelsess (km 30.3)**   **Vossloch (km 25.5)**

Bevern (km 20.5)   **Ellerhoop (km 16.5)**   **Borstel (km 12.3)**

Halstenbek-Nord (km 7.5)   **Halstenbek-Süd (km 4.7)**   **DESY (km 0.0)**
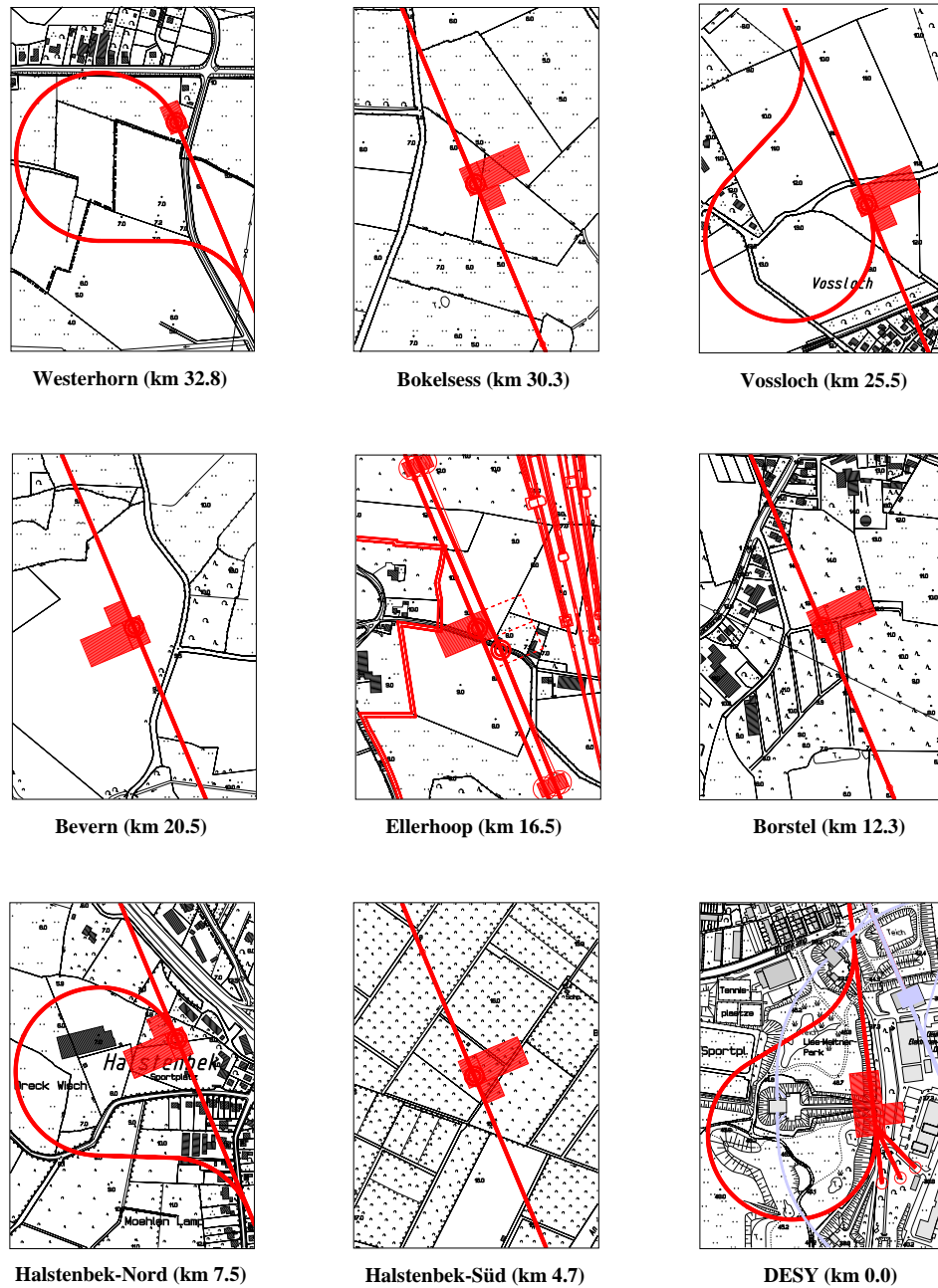
Figure 8.2.2: *The various stations along the TESLA site.*
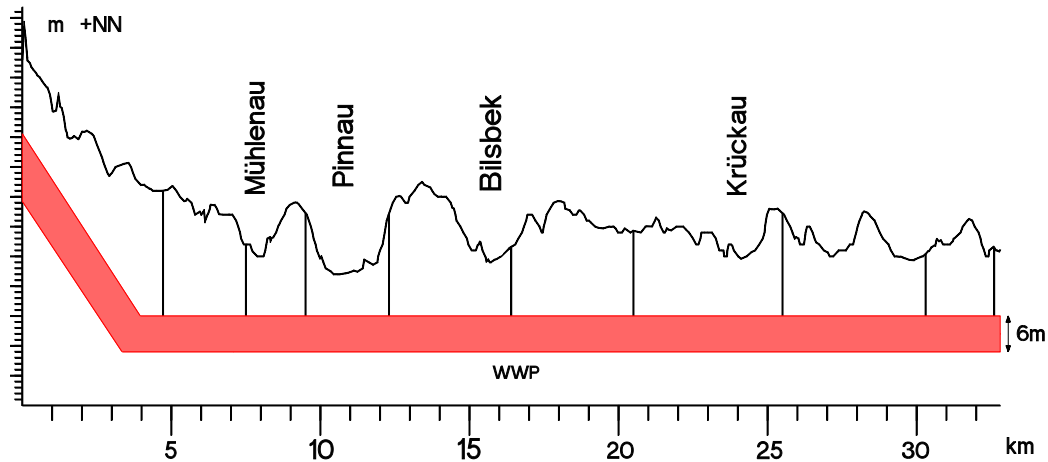
Figure 8.2.3: *Elevation of the linac tunnel.*

asymmetric distribution of the cryogenic halls along the TESLA route, namely four halls in the south electron linac and three in the north positron linac.

Each tunnel section ends in a shaft. In Westerhorn, at the end of TESLA, an entrance hall comparable to an external HERA ground building covers the shaft. The hall has $20\,\mathrm{m} \times 20\,\mathrm{m}$ floor space and $10\,\mathrm{m}$ height. The cryogenic halls cover the other shafts. Some shafts serve also as a connection for the damping ring return arc to the main tunnel. All shafts can be used for mounting and dismounting of the Tunnel Boring Machines (TBMs) and for access to the tunnel during machine installation and maintenance. Further temporary shafts are necessary for the connection of the damping ring return arcs and for the beam delivery to the X-FEL laboratory.

The main part of the tunnel is bored in quaternary sand and a smaller part is in marl. The whole tunnel is below the ground water table over nearly the entire length. With the well-proven tunnel boring technology buildings at the surface remain completely unaffected.

The interaction point HERA West is about $20\,\mathrm{m}$ above sea level. The axis of the linac tunnel lies at $8\,\mathrm{m}$ below sea level. Additionally, the HERA plane is tilted by $1\,\%$ and the straight section HERA West has a vertical slope of $8\,\mathrm{mrad}$. The tunnel follows the slope for about $3\,\mathrm{km}$ and then bends with a radius of $5\,\mathrm{km}$ into the horizontal direction at $8\,\mathrm{m}$ below sea level. In figure 8.2.3 the elevation of the linear collider tunnel is shown. The thickness of the ground above the tunnel is between $7\,\mathrm{m}$ below the level of the Pinnau and $23\,\mathrm{m}$ between Borstel-Hohenraden and Kummerfeld, sufficient to guarantee radiation shielding.

A special situation is given in the village Rellingen about $8.5\,\mathrm{km}$ away from DESY. In Rellingen the TESLA tunnel runs directly under an 18th century church. The tower was founded on much older buildings and the church is a historical monument. The distance between the top of the tunnel lining and the church foundations is $14\,\mathrm{m}$. This is a very safe distance for a tunnel construction by a TBM in soil. Nevertheless it

was investigated whether there could be any risk to the ancient building [1], [2]. As a reference the motion of the church will be monitored starting in 2001.

8.2.2 Main tunnel

The inner diameter of the main TESLA tunnel is 5.20 m as at HERA. The achievable precision of a bored tunnel with this diameter is about 10 cm in the transverse directions. Therefore a diameter of 5 m can safely be used for the installation of machines and beam lines. The tunnel will be bored with a tunnel boring machine and lined with precast watertight concrete segments called tubbings. The TBM will be similar to the HERA boring machine. A cutting head rotates in a compartment filled with a pressured liquid called bentonite. The bentonite suspension resists the soil and hydraulic pressure to avoid displacements on the surface above the tunnel. The liquid also stabilises the sand in front of the boring machine and transports the soil, which is removed by the rotating cutting wheel. Above ground the soil is separated from the bentonite. The regenerated suspension is pumped back to the machine. In the steel cylinder behind the milling wheel (called the shield) a complete tunnel ring is assembled from tubbings 30 cm thick and 1.20 m long. A ring consists of seven tubbings and has a weight of 15 t. The diameter of the wheel is 6 m. The slit between the soil and the tubbings will be filled with concrete. Minimal settings on ground are not avoidable but are below 1 cm.

Based on HERA experience the TBM speed is assumed to be 10 m per day on average and 14 m per day maximum. The machine will run 24 hours a day, five days a week, 250 days a year: hence one TBM will bore 2.5 km of tunnel per year. With four machines running in parallel the total tunnel construction time will be about 3.5 years. Twenty trucks per day per access shaft will be required to transport the earth away; eight trucks per day are required to deliver the tubbings.

During the installation time and the shut down periods the whole tunnel will be ventilated with dried air. The ventilation will be stopped during accelerator operation. For smoke exhausting the ventilation can be sped up, reversed and exhausted at the next shaft or hall. The northern and southern tunnel sections form separate fire compartments. The longest escape route has a length of about 5 km. Fire protection walls shield the shafts. The fire load in the tunnel will be minimised. Unavoidable fire loads will be shielded by small fire compartments or protected by a fire extinguishing system, if necessary. Smoke and fire detection systems are installed in all tunnels.

8.2.3 Damping ring tunnels

For the arc of the damping rings four additional tunnels are necessary. These tunnels have an inner diameter of 3 m and a total length of approximately 4 000 m. They are separated from the main TESLA tunnel via special separation shafts, which can be built as caisson cylinders of approximately 15 m inner diameter. Four of these separation shafts are accessible from the surface through cryogenic halls. These access shafts are also used for maintenance and supply (water, cryogenics, modulator cables
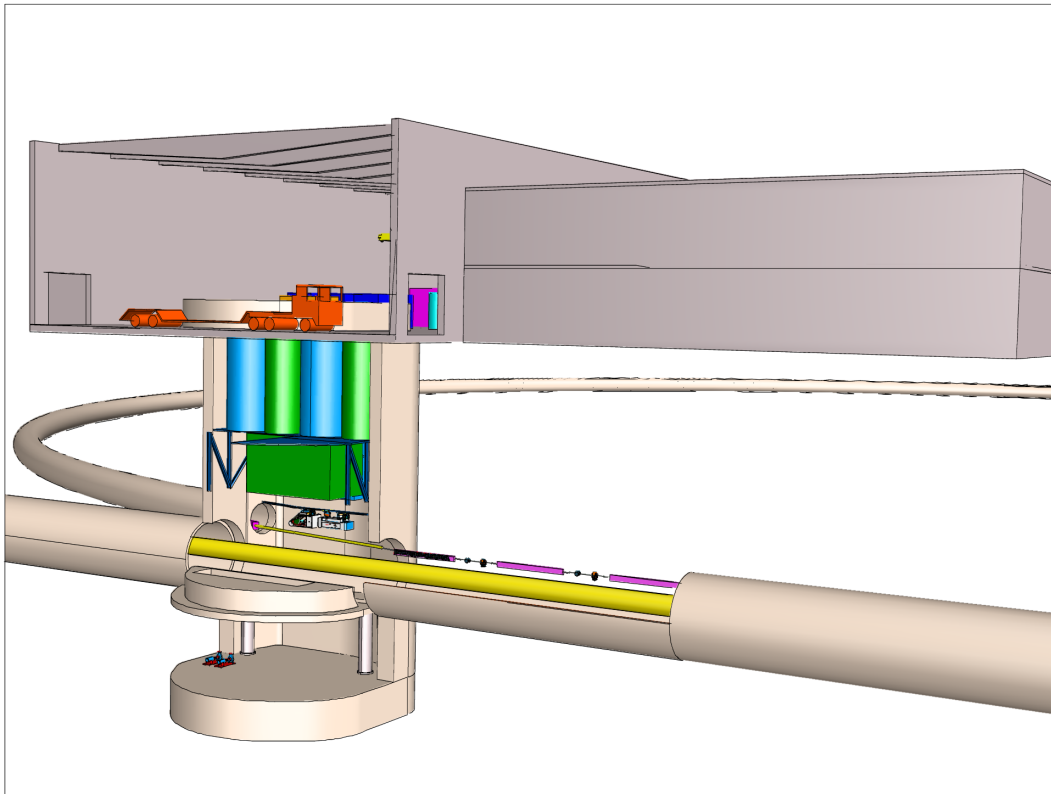
Figure 8.2.4: *Access shaft and damping ring tunnel.*

and electrical power). The remaining four separation shafts are only accessible during the construction time. They will be closed after the tunnel is finished and the surface area will be reconstructed.

The damping ring tunnels have a bending radius of 148 m at the tunnel axis. Because of the small bending radius they have to be constructed from tubbings. Ring segments formed from tubbings are capable of following a much narrower curvature than full tubes.

8.2.4   DESY site and external areas for the cryogenic plants

The Linear Collider tunnel starts on the DESY site (figure 8.2.5) in Hamburg-Bahrenfeld. The first access shaft is next to the HERA hall West. The tunnel boring machines for the main tunnel and the electron damping ring arc will be assembled in this shaft. A second temporary shaft is necessary to reconnect the arc into the main tunnel and to dismount the small TBM. A third shaft in the main tunnel is necessary to enable the connection between TESLA and HERA. This shaft must be finished before the arrival of the TBM. The connection to HERA will be made later. The starting point for the main tunnel is laterally shifted from the HERA hall. After a distance of several hundred meters the tunnel bends into the main direction with a radius of 500 m.
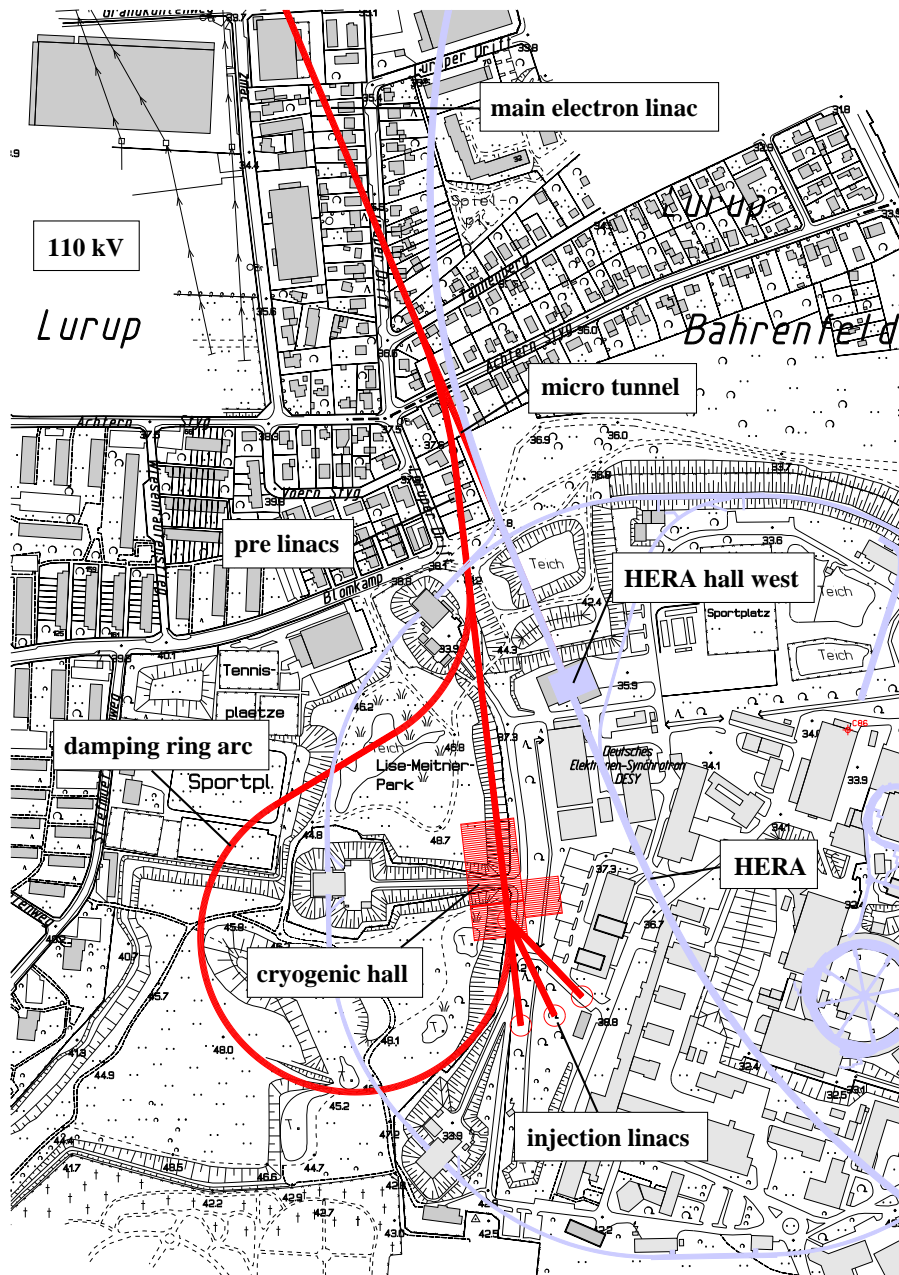
Figure 8.2.5: *The station at the DESY site.*

From this point on, the tunnel is straight from the top view. Here also starts the main electron linac. The initial section houses the injectors for the collider and X-ray lasers. The cryogenic plant, modulator hall and cooling water systems for the first 2.5 km of the electron linac are on the DESY site. The next 2.5 km section is supplied by the cryogenic plant located at the 5 km point. Each of the other five plants supplies about 5 km of the superconducting linacs. The total of six areas distributed along the linac

are named after the villages nearby. In the table 8.2.1 all sites are summarised. Each site has an area of about 40,000 m².

An access shaft connects these ground buildings with the tunnel. The shaft has an inner diameter of about 15 m. The cryogenic and water pipes and HV, power and auxiliary cables pass through the shaft into the tunnel. For installation and maintenance a hall crane will lift heavy components through the shaft. All service halls will be connected separately to the public main high voltage grid (see section 8.4). Optionally, high voltage power supply through the tunnel is conceivable.

Site	Position L/km
DESY	0
Halstenbek-Süd	4.7
Halstenbek-Nord	7.5
Borstel	12.3
Ellerhoop	16.8
Bevern	20.5
Voßloch	25.5
Bokelseß	30.3
Westerhorn	32.8

Table 8.2.1: *Names and positions of the stations along the linac.*

8.2.5   Central site in Ellerhoop

The underground experimental hall for collider experiments at the interaction point is located south of the village of Ellerhoop and north of the creek Bilsbek. Figure 8.2.6 shows the arrangement of the experimental and dump halls. The area has a size of about 540,000 m². In tunnel direction the site is roughly 800 m long. The surface lies between 6 and 10 m above sea level. The groundwater table (depending on rainfall) is about 6 m above sea level. The soil in Ellerhoop consists of quaternary layers of sand and marl on the top and tertiary layers of sand and clay below.

The underground hall for the High Energy Physics detector has a floor space of 82 m × 30 m and a height of 19 m below the hook of the 80 t portal crane. For the option of a second interaction point with a crossing angle of 34 mrad, the tunnels can be separated in an underground shaft. The southern shaft will also be used to separate the X-FEL beams. These shafts are constructed together with the first interaction region. The tunnels and buildings for the second interaction region could be constructed at at later date. The second experimental hall could be an extension of the first one or shifted in beam direction. In the first case the available space for the two detectors is limited, for the shifted version the distance between the two halls is fixed by the bunch spacing.
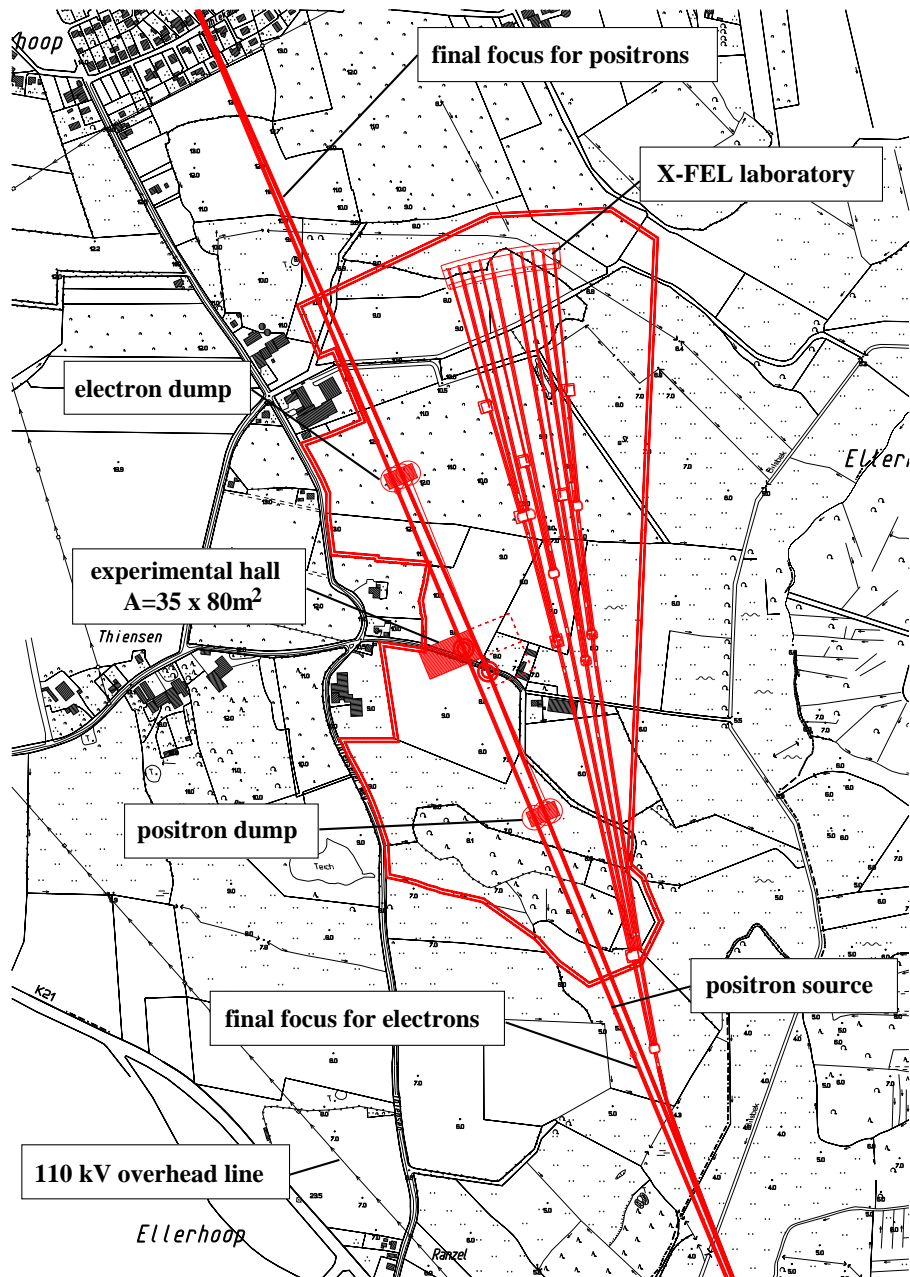
Figure 8.2.6: *Overview of the campus area in Ellerhoop.*

The two beam dump halls are located 250 m away from the interaction point. The beams are orientated downwards with an angle of 15 mrad into the dumps. The floor space of both halls is 35 m × 25 m and the available hall height is 15 m. Additional dump buildings will have to be constructed for the second interaction region.

The positron source is installed in the southern beam delivery section. A bypass tunnel below the experimental hall houses the transport line to the positron linac. The bypass tunnel connects the two dump halls.
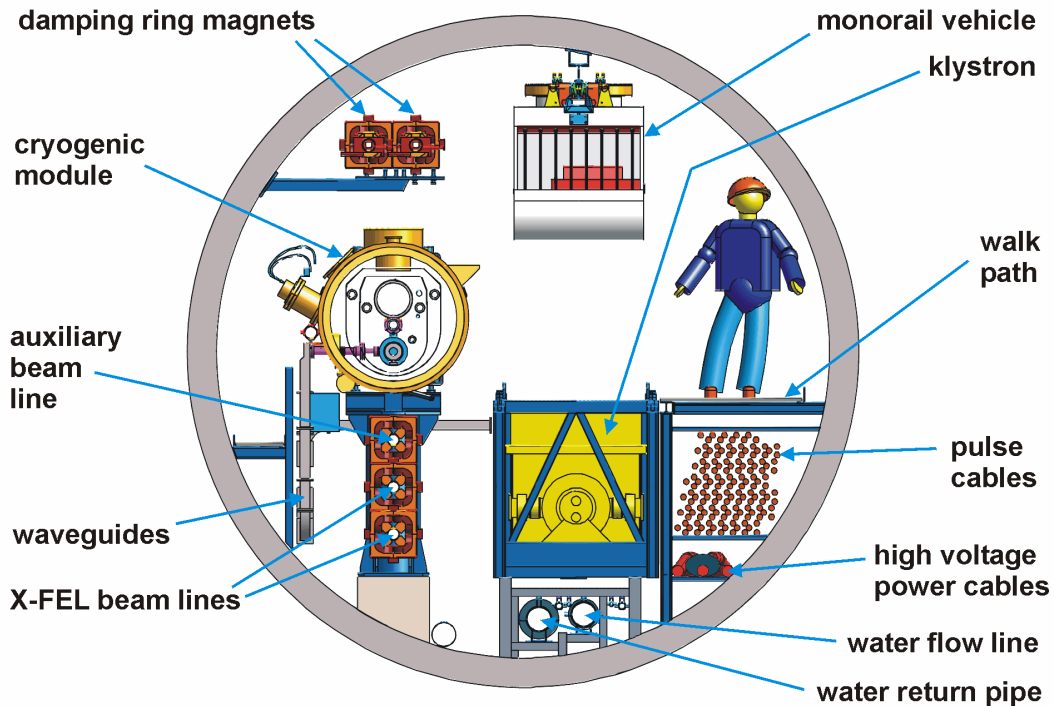
Figure 8.2.7: *Cross-section of the TESLA tunnel.*

The X-ray Free Electron Laser laboratory is also located on the central area, east of the main tunnel. After separation from the linac tunnel, the beams for the FEL are guided upwards in a tunnel to the switchyards with a slope of about 10 mrad. For the tunnel separation in the X-FEL switchyard shafts are necessary. Some of the shafts can be used for access, others will be covered after construction. The inner tunnel diameter for the electron beam lines is 4 m and for the photon beam lines 2 m. The beam dumps are installed in four underground halls. They are similar to the dumps for the main linac. There are ten photon beam lines which supply the experiments in the X-FEL hall. The floor space of this hall is about 200 m $\times$ 45 m and the available hall height 15 m.

In addition to the experimental halls workshops, administrative and social buildings and streets have to be constructed on the central area. The planned floor space covers 20 000 m^2 in total.

8.2.6   Tunnel layout

The cryogenic modules of the superconducting linac, the beam lines for the damping rings and X-FEL and the auxiliary components are installed in the 5.2 m diameter tunnel. A tunnel cross section is shown in figure 8.2.7 and a virtual view into the tunnel
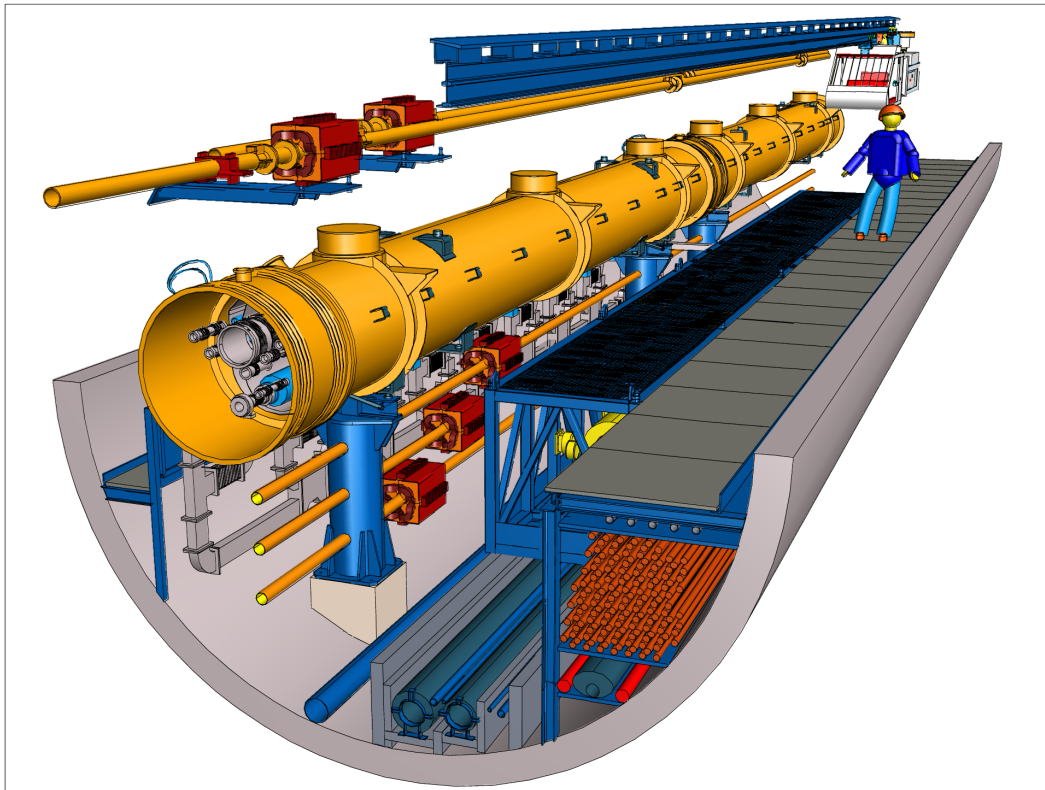
Figure 8.2.8: *Virtual view into the TESLA tunnel.*

in figure 8.2.8. The tunnel cross section is divided basically in three vertical and two horizontal areas. Referring to figure 8.2.7, the left section is reserved for the sensitive accelerator and beam line components and for the RF-distribution. A walk path is located on the left side for installation and maintenance. The central area is reserved for the transport system and all auxiliary components. These components like klystrons, power supplies, electronics, water and vacuum pumps are installed in special containers. This arrangement guarantees quick exchange during the short regular maintenance periods. The transport system for personnel and material is a monorail. The rail is an I-beam bolted to the top of the tunnel. The forward and return pipes for water-cooling are mounted in small channels on the floor. The channel collects the leakage water. The third area of the tunnel cross section is reserved on top for the main walk path and below for the pulse power cable trays. The walk path is kept free at any time for emergency reasons. In addition the free space will be used for the lines-of-sight for optical survey.

The lifetime of the electronic components is limited by radiation background. The selected electronics are operable up to an integrated radiation dose of $100\,\mathrm{Gy}$. The radiation background is mainly determined by the dark current of the cavities, which is limited by the additional heat load of the $2\,\mathrm{K}$ helium circuit. Most of the power of the lost electrons is absorbed in the cold mass, namely the cavity, the $2\,\mathrm{K}$ helium and the

helium container. A value for the required shielding to suppress radiation damage was calculated [7]. The result is that the lifetime of the electronics components is about 10 years without any additional shielding. However, space for additional radiation shielding is reserved.

8.2.7   Safety and Rescue Systems in the Tunnel

Safety of personnel and equipment in the tunnel have to be provided during construction, shutdown, maintenance, and operation of TESLA. The tunnel has segments between access shafts with a longest distance of 5 km. The resulting escape and access times largely determine the organisational and technical means for rescue as well as for fire protection.

- Access to the tunnel is restricted to instructed personnel.

- Rescue and transportation of persons is speeded up by the monorail train system used for transportation of equipment.

- Fire loads are minimised and kept in compartments or small hermetic containers acting as fire compartments.

- Several levels of fire control and fire fighting are in place which react very early and keep fires well localised. The automated or remotely controlled levels foreseen include (1) component malfunction detection and very early smoke detection, (2) cutting the electric power per component and (3) per tunnel segment, (4) local fire control or suppression, and (5) remotely controlled fire fighting with the monorail trains. Only a final level includes human emergency intervention in the tunnel.

The technology available for tunnel safety is developing fast following the experience of fire hazard in the recent past. TESLA will benefit from this ongoing development. The measures considered for TESLA which are described in the following are available with present-day systems and satisfy the goals as to protection of personnel and equipment in the tunnel.

- The pulse cables constitute the main fire load in the tunnel. Each cable is covered with fire protective coating. Two containment options are considered: (1) longitudinal compartment for the cables within the tunnel, (2) fire shields in the cable area in ≈ 50 m intervals along the tunnel. The cable area is equipped with its own very early smoke detection and fire fighting system. Fire detection levels cut the power and activate the fire fighting system.

- Hermetic electronic and electric containers located along the tunnel in about 50 m intervals are each equipped with early smoke detection in the internal air cooling circuit. Fire detection cuts the power of the container.

- Other fire loads like magnets and electronics are more distributed along the tunnel. The transformers positioned at ≈ 50 m intervals are shielded in two-layer

hermetic containers. For all of these fire loads and for temporary fire loads present during maintenance work, a very early smoke detection and fire fighting system covers the full cross section of the tunnel. Detectors have a resolution of about 50 m along the tunnel. Fire detection levels cut the power and activate the fire fighting system. The system is effective whether people are in the tunnel or not and ensures sufficient time for rescue or monorail intervention.

- The monorail trains are primarily used for transportation of equipment in the tunnel which includes remote control operation. In addition, for their safety tasks, they are equipped with (1) space for injured people, (2) battery backup for the motors, (3) fire fighting system with a reservoir of water / foam agent on the train. Radiation hard cameras and sensors for vision within smoke-filled areas are considered for remotely controlled fire fighting.

- During installation, shutdowns and maintenance the tunnel is ventilated with dried air over the full length. The ventilation is stopped during operation. To exhaust smoke the ventilation can be switched to maximum speed, with the direction of air flow chosen according to smoke situation, and with exhaust to the next shaft or hall.

- Access control and communication systems are installed at the access points and in the tunnel for normal operation. The communication system integrates personnel distress equipment which allows localisation of persons needing help.

Staff specially trained for rescue and for fire fighting in the tunnel as well as in the experimental halls will be made available.

8.2.8   Plan approval procedure

The two federal German states of 'Freie und Hansestadt Hamburg' and 'Land Schleswig-Holstein' will host the TESLA project. In 1998 they passed a law (Gesetz zum Staatsvertrag) allowing the formation of the planning basis for the construction and operation of a linear accelerator [4]. A common plan approval procedure will be used for both states. The approval authority (Planfeststellungsbehörde) is the Head Bureau of Mining (Oberbergamt) in Clausthal-Zellerfeld. At a meeting held by the authority and attended by all parties concerned (both public and private), the next steps towards a formal planning procedure were agreed upon. The tunnel route was fixed, and the scope was defined as the boundaries of the single central and seven external sites, together with the maximum volume of the ground buildings. Within this scope the design can be changed even after planning approval. An environmental impact study is also mandatory and is currently in progress, with completion expected in 2001. The formal procedure, for which preparations are under way, will begin after the general project approval is given. Based on a Europe-wide tendering procedure, contracts for the planning of all TESLA buildings will be awarded in the first quarter of 2001. The first step of hydro-geological report is finished [6]. The tunnel and the underground

halls have negligible impact on the ground water. In principle the pumping of $50\,\mathrm{m}^3$ water per hour for cooling purpose is acceptable. The detailed impact of the wells in the neighbourhood has to be studied in a further step. An additional result of the study is a hydro geological profile along the TESLA route. The tunnel runs in soil formed by ice-age (quaternary) deposits essentially. This is water-conducting sand covered by non-water-conducting marl. However, in Ellerhoop the tunnel lies in tertiary layers hardened during the ice-time by the glacier cover, which was several hundred meters thick.

The planning of the ecological compensation of the areas covered by buildings will be started in 2001. By 2002 all documents for the plan approval procedure will be completed.

8.3   Radiation Safety

This section describes the radiation safety requirements for the TESLA linear collider. The main potential locations of beam loss were identified from the point of view of radiation safety. Different scenarios of beam losses at these locations were formulated and both the impact on the environment and public and consequences for machine operation and access to the machine were investigated. The main emphasis was put on the impact of the collider operation on the public (local population) and the environment. Most important are here the limitation of the radiation level (doses) to the public originating directly from stray radiation or indirectly through a potential activation of soil and groundwater or air and coolants released from the facility.

Following the German regulation and the ALARA (As Low As Reasonably Achievable) principle planning goals in terms of dose limits for all following studies were set for the DESY site and for the public. The German regulation requires for surveyed areas ("Überwachungsbereich") local doses to be below $15\,\mathrm{mSv/a}$, whereas for the public the maximum allowed personal dose due to direct radiation and radiation from radioactive release (activated air, water etc.) is $1\,\mathrm{mSv/a}$ and for radiation from radioactive release alone $0.3\,\mathrm{mSv/a}$. Considering the ALARA principle our planning goals for TESLA are to stay bellow $1/10$ of the above limits. This results in $1.5\,\mathrm{mSv/a}$ local dose for the DESY site, $0.1\,\mathrm{mSv/a}$ personal dose for the public from direct radiation and radiation from radioactive release and $30\,\mu\mathrm{Sv/a}$ from radiation from radioactive release alone, whereas the natural doses in the northern part of Germany are about $1\text{-}2\,\mathrm{mSv/a}$. Most of the single dose contributions given below occur at different locations along the facility; therefore one has to keep in mind that these single dose contributions must not be added together.

In comparison to the CDR [8] already two major design changes with positive impact on radiation safety were done: 1. The positron source will now be in front of the IP. Therefore the proposed $2\,\mathrm{MW}$ collimator system in the extraction line is avoided. 2. All main beam absorber are now concentrated in dump halls and therefore shielding and handling of activated material are much easier.

The studies of the radiological impact on the environment carried out by the DESY

radiation protection group (summarized in [15, 16]) were evaluated by two independent German institutes (Technischer Überwachungs-Verein Nord e.V. [21] and Öko-Institut e.V. [22]). Both institutes agreed on our basic assumptions and calculations and found no major problems for an implementation of TESLA in the foreseen way. In their opinion the following items have to be studied in more detail: leakage in dump water system, beam loss and evaporation of activated material, losses at collimators, soil and groundwater studies near the dump halls.

8.3.1   Basic parameters and main locations of beam loss

The basic parameters for all following simulations and calculations concerning radiation safety are as follows: The beam energy will be 250 GeV and the total power of one beam will be 11.3 MW. The total operation time per year is assumed to be 5000 hours. In table 8.3.1 the main locations of beam loss, power, beam loss scenarios, resulting implications, consequences and references to the studies done are given. One has to keep in mind that the dump and collimator designs are still in progress. For all main locations of beam loss different scenarios were formulated and the impact on and consequences for the public and environment and operation and access are given.

8.3.2   Stray radiation due to neutrons

There are two different kinds of secondary radiation capable of penetrating thick material layers. High energetic neutrons are considered here, muons follow in the next subsection.

The maximum annual dose for the public living above the main linacs is estimated as follows: The worst possible scenario with respect to radiation safety is a failure of the beam loss monitor system in the tunnel during a loss that is just not large enough to damage the accelerator and so to terminate the operation. The inherent safety mechanism is based on the fact that more than 3/4 of the lost power is absorbed by the cold mass. That means dramatic pressure rise in the 2 K cooling circuit and therefore the loss of superconductivity and acceleration over a 2.5 km long section. To cover such a very unrealistic worst case scenario a loss of 100 W/m is assumed during 100 h of operation per year. This leads to an annual dose equivalent of 0.6 μSv for the minimal thickness of the soil layer above the tunnel of 8 m and 5×10^{-6} μSv for the average thickness of 14 m [14, 15, 16] The acceptable average power loss of 0.1 W/m for the main linacs during 5000 h per year leads to values by a factor of 20 less than those mentioned above.

Local loss points such as emergency dumps and collimator sections can be additionally shielded inside the tunnel according to the maximum local beam power loss.

For shielding of the dumps a few options were worked out [14, 15, 16]. The basic one consists of 3 m ordinary concrete and 7 m sand leading to a maximum annual dose equivalent of 120 μSv on the earth surface directly above the dump halls, which will not be on public ground.

location of loss	power of loss	scenario	main implications	consequences	ref.
main e$^+$e$^-$ dump	11.3 MW	5000 h/a	muons	depth of tunnel	[9, 12]
main $\gamma\gamma$ dump	11.3 MW	5000 h/a	activation of soil/groundwater	shielding	[10, 15, 16, 23]
Beamstrah.dump (in dump hall)	320 kW	5000 h/a	activation of air/cooling water	requirements on air release/water cooling system	[15, 16, 13, 23]
γ dump (from e$^+$ source, 100 MeV, in dump hall)	130 kW	5000 h/a	residual activities γ and neutrons	no access possible (robotics) shielding	[13, 23] [15, 16]
Beamstrah.dump (at 500 m from IP)	42 kW	5000 h/a	0.4% of main dump power	local shielding	-
e$^-$ dump (from e$^+$ source, 100 MeV)	15 kW	5000 h/a	0.1% of main dump power	local shielding	-
e$^+$ source target (28 MeV)	5 kW	5000 h/a	γ and neutrons activation of target	local shielding access restricted	[24] [24]
damping rings (warm sections, 5 GeV)	24 kW (local)	5000 h/a	0.2% of main dump power	local shielding	8.3.2
cold linac sections	100 W/m (accidental)	100 h/a	γ and neutrons	shielding and emergency system	[15, 16]
	0.1 W/m (permanent)	5000 h/a			8.3.2
septum (at 45 m from IP)	1 kW	5000 h/a	0.01% of main dump power	local shielding	[11, 19, 20]
collimator (at 100 m from IP)	0.1 kW	5000 h/a	0.001% of main dump power	local shielding	[11, 19, 20]
XFEL dumps (e$^-$,γ, 50 GeV)	2.0 MW	5000 h/a	21% of main dump power	see main dumps	-
primary collimation (5 GeV)	2.4 kW	5000 h/a	0.02% of main dump power	local shielding	-
beam delivery collimation	12 kW (accidental)	100 h/a	0.1% of main dump power	local shielding	-
	120 W (permanent)	5000 h/a	0.001% of main dump power		

Table 8.3.1: *Main locations of beam loss, power of losses, scenarios, main implications, consequences and references to the detailed studies. All numbers given are for 250 GeV beam energy.*

8.3.3 Stray radiation due to muons

Muons with maximum energies of 250 GeV are capable of penetrating 400 m of soil. Those muons can hardly be shielded artificially. Thus, the muon radiation leads to the direct constraint on how deep under the surface the tunnel must be. The most intense muon sources are the main beam dumps. To reach the planning goal of 0.1 mSv for the annual dose equivalent on the earth surface the thickness of the soil layer above the tunnel should be more than 11 m up to a distance of 1 km in both directions from the dump halls and therefore the $e^+ e^-$ beams have to be deflected with an angle of 15 mrad downward to compensate for changes of the relief [9, 12].

In case of the $\gamma\gamma$ dumps, where the γ beams are coming from the second interaction point, the tunnel has to be deeper by 3 m at the dump position to fulfill the same requirements as mentioned above.

Loss points inside the tunnel such as collimators are acceptable as long as they absorb less than 1% of the total beam power ($\approx$100 kW), assuming the minimal thickness of the soil layer above the tunnel to be 8 m.

The XFEL dump must absorb a 50 GeV electron beam with 2.4 MW power. The dump position has to be chosen such that there is an undisturbed soil cylinder in direction of the beam with 8 m radius and 150 m length.

8.3.4 Activation of soil and groundwater

Around the main beam dumps the activation of soil and groundwater was estimated by means of a simple model [10, 15, 16] and compared to limits derived from a very conservative assumption. New Monte Carlo simulations of soil and groundwater activation behind a 3 m thick concrete shielding of the dump halls, and a more realistic model of transformation of soil and groundwater activation in the first 50 cm around the dump shielding into activation concentration of drinking water and doses for the public can be found in [23]. It has been shown that even taking the big entrance hole of the main dump into account, the production of Tritium and Sodium-22 in groundwater for one year of operation is 3.2 Bq/g and 0.56 Bq/g respectively. Assuming a dilution of 1/500 this transforms to a total personal dose of 14 μSv/a [23]. This is well below the legal limit of 300 μSv/a and our planning goal of 30 μSv/a.

Soil and groundwater can also be activated around a collimator inside the tunnel (or other significant loss points) where a small fraction of the beam gets continuously lost. A Monte Carlo simulation has been made for a 100 kW collimator [19]. In case of the Beamstrahlung dump at 500 m from the IP (see table 8.3.1) with the largest power loss of 42 kW and without any additional shielding (except the tunnel wall), the activity concentrations are comparable to the above mentioned numbers for the main dump shielded with 3 m of concrete. Therefore also for all other components in the tunnel from table 8.3.1 with less power loss no additional shielding inside the tunnel is necessary with respect to soil and groundwater activation.

8.3.5   Activation of air

In the above mentioned studies [11, 19] also the activation of air was investigated. On that basis another study [20] is in progress to develop ventilation concepts for the tunnel section nearby the IP, where in total about 100 kW of losses are expected. Two different ventilation concepts are examined to keep the activity concentration of the air at such a low level that it can be blown out without using a chimney according to the expected new German regulation. Both concepts are based on additional shielding around the loss points and delay times to let the short living nuclides decay. In the first concept (open loop) the air flows continuously through the tunnel with a velocity of 0.6 m/s. The release point has to be about 4 km away to reach sufficient decay times. The other concept is a closed loop system. The air circulates inside the tunnel during an operation time of 1 month. After stopping the operation the air has to be kept inside the tunnel for additional 3 hours before the release could start.

With respect to the dump halls all possible actions will be taken to keep the air activation at the same low level or even lower as described above for the 100 kW collimator case. This requires a closed ventilation system for any air in direct contact to the dump components.

8.3.6   Activation of coolants

The highest activity concentration is expected in the dump medium which is water. It circulates in a closed loop as it is described in section 7.7. Two long-living radioactive isotopes have to be considered: Tritium and Beryllium-7. Their saturation activities for 12 MW are 146 TBq and 60 TBq respectively and after 1 year of operation 4.6 TBq Tritium and 56 TBq Beryllium-7 are produced. Therefore all parts belonging to the primary cooling system are expected to be inside restricted areas ("Sperrbereich"). A more detailed list of activation products can be found in [23]. Special safety requirements have to be put on the dump water cooling system. Hence standard safety techniques from nuclear industry will be applied to design the water system and handle the activated cooling water.

The superconductive cavities are cooled with liquid helium. The coolant is continuously transported within a loop consisting of accelerator structures in the tunnel and a cryogenic plant outside. In shut-down periods a storage outside the tunnel should also be possible and therefore the activation of helium may be of radiological interest. The only possible activation product is tritium. An average beam loss of 0.1 W/m (see table 8.3.1) leads to a specific activity of 70 Bq/g after 20 years of operation [18], which is well below the release limit of 1000 Bq/g.

8.3.7   Other studies

The kryo shafts of the main tunnel are expected to allow access for DESY staff without limitations. Shielding calculations were done in [17] with a power loss of 100 W/m during 100 h per year (compare subsection 8.3.2). They led to a horizontal shield of

2.4 m and a vertical shield of 1.2 m made out of ordinary concrete to reach 1.0 mSv/a and therefore less than the planning goal of 1.5 mSv/a local dose.

As it is the case for the HERA accelerator also for the TESLA machine a radiation monitoring system is needed to survey online dose rates at several locations along the beam line. Therefore studies have been started to design new radiation monitoring detectors to handle the timing conditions and a new data acquisition system to manage the large distances at the TESLA collider.

8.4 Power Distribution

The electrical power consumption is dominated by the pulsed RF power supplies (modulators) and the cryogenic plants, which are located at the seven service halls along the TESLA site. Additional consumers are sub-systems such as the damping rings and beam delivery system (BDS), FEL user facility beam lines, power supplies and electronics racks in the tunnel (magnets, klystron auxiliaries, low level RF, etc.), and infrastructure components (e.g. water cooling, ventilation). An overview of the power consumption for the different components and at the different locations is given in table 8.4.1.

For the power distribution to the service halls the existing infrastructure of 110 kV and 220 kV power lines will be used. Along the TESLA site, there are three distribution stations (locations Hamburg-West, Halstenbek and Steinburg) and four overhead lines (near Borstel, Ellerhoop, Bevern and Offenseth) available (figure 8.4.1). The existing distribution stations will be upgraded by additional transformers. Four new distribution stations will be built under the power lines, equipped with high-to-medium (20 kV) voltage transformers. The power will be transported to the service stations by 20 kV power cables buried in the ground along existing roads. There is no need for cables at high voltage (110 kV or 220 kV) level in the linac tunnel.

8.4.1 Medium and low voltage supplies

The choice of medium (20 kV) and low (400 V 3-phase, 230 V single phase) voltages follows the industrial standard in Germany. There will be a switchboard plant with 20 independent 20 kV to 400/230 V transformers. The 20 kV transformers are air cooled and installed outside next to the service buildings. An auxiliary supply from the public grid is also foreseen. The modulators will be supplied from 690 V switchboard plants installed in service rooms in the modulator halls. The helium compressors as single high-power consumers require a special switchboard at 6 kV.

8.4.2 Power supply of the linac tunnel

Since the spacing between service halls is about 5 km, power has to be transported into the tunnel over a maximum distance of 2.5 km. This is too long to be efficiently done at low voltage level. Therefore only the first $\approx$500 m tunnel will be supplied

Component	Sum	DESY	Halst. N	Halst. S	Borstel	Central	Bevern	Vossloch	Bokels.	Westerh.
Modulators	79.2	13.2	10.0	8.8	11.3	-	13.0	11.3	11.8	-
Cryo plants	24.4	2.5	2.3	3.4	3.4	0.5	3.1	3.7	3.4	-
Infrastructure	3.5	0.4	0.4	0.4	0.3	1.0	0.3	0.4	0.4	0.03
PS, racks in tunnel	12.1	1.0	1.6	1.6	2.0	-	2.0	2.0	2.1	-
Damping Rings	18	4.5	-	4.5	-	-	-	4.5	-	4.5
Injectors	0.5	0.5	-	-	-	-	-	-	-	-
BDS	8.1	-	-	-	-	8.1	-	-	-	-
Detector	2.0	-	-	-	-	2.0	-	-	-	-
FEL facility	6.1	-	-	-	-	6.1	-	-	-	-
Sum	154.7	22.1	14.3	18.7	17.0	18.0	18.5	21.9	17.7	4.5

Table 8.4.1: *Overview of power consumption (in MW). The total power for the 500 GeV collider is 140 MW, about 14 MW of the total power are due to FEL operation.*
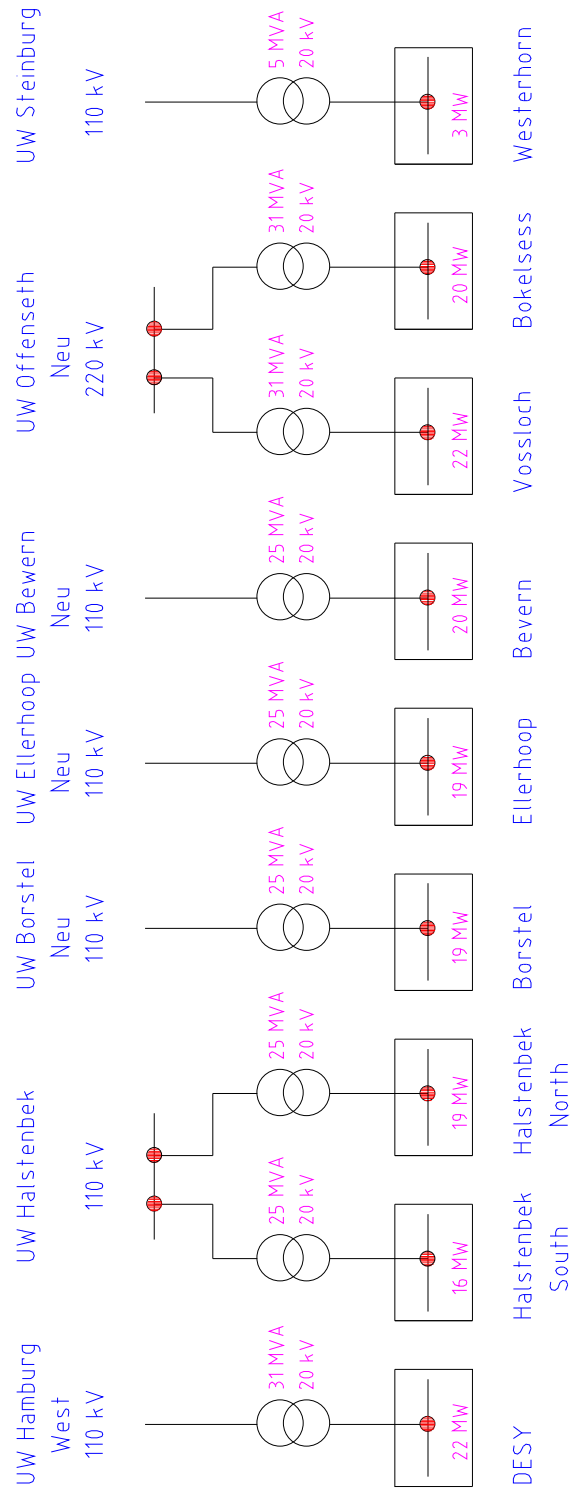
Figure 8.4.1: *Sketch of the power distribution from the existing grid to the service stations.*

with low voltage cables from each hall. For the remaining 2 km two medium to low voltage transformer stations are foreseen in the tunnel, supplied by 20 kV cables. Each station consists of two 315 kVA transformers, one for the klystron auxiliary systems (e.g. focusing solenoid, filament heating) and one for the magnet power supplies and electronics racks. The 20 kV cables and the cables for the distribution at low voltage level are installed under the walkway in the tunnel (see figure 8.4.2). The transformers are air cooled dry resin types with low stray field. The magnetic stray field of the cables can reach up to $2\,\mu\text{T}$ at 1 m distance. The impact of the stray field on the beam is drastically reduced by using stranded cables with a twist length of 1 m, short compared to the typical betatron wavelength in the linac and in the damping ring.

In order to reduce the fire risk, fire retarded and non-corrosive (FRNC) cables will be used. In addition, they will be covered with fire-proof paste. The current density in the cables is relatively low, which keeps the heat load to the tunnel low and reduces the fire risk. The total average heat load to the tunnel from the medium and high voltage cables and the transformers amounts to about 24 W/m.

The tunnel lighting system will be supplied by a power distribution at 1 kV level. There are 10 transformers installed under the ceiling per 2.5 km of tunnel section.

8.5 Watercooling and Air Conditioning

8.5.1 Watercooling System

The layout for the cooling circuits of the TESLA accelerator is divided up into separate sections in the same way as the cryogenics system. Each cooling station has cooling towers, pumps and control systems. The inlet water temperature into the tunnel will be 30 °C and the outlet temperature will be approximately 70 °C. All klystrons and magnets will be cooled directly and therefore deionised water with a conductivity of $1\,\mu\text{S/cm}$ must be used.

There are three possibilities for the recooling plant: wet, dry and hybrid systems. The wet cooling tower works by water evaporation. It is a well-known system and it is possible to have the required inlet temperature throughout almost the whole year. The disadvantages are: the loss of water due to evaporation (in this case for each hall $50\,\text{m}^3/\text{h}$), the requirement of an extra water loop with pumps, heat exchanger, control-systems etc, cooling tower plume during winter time, the necessity for cleaning the heat exchanger to avoid calcification.

The alternative dry cooling system has the advantage of simplicity and therefore low-maintenance, because there is no requirement for an extra water loop. The disadvantages are the higher investment costs and approximately double floor space requirement in comparison with the wet cooling system.

The hybrid cooler system which we choose for TESLA is a combination of these elements: Dry cooling is used throughout the year, unless the ambient temperature rises above 15 °C. At higher temperatures, which according to statistics occur in Northern Germany only during less than one third of the year, the finned surface of the cooling elements is wetted with water. The average water evaporation is thus only about 30 %
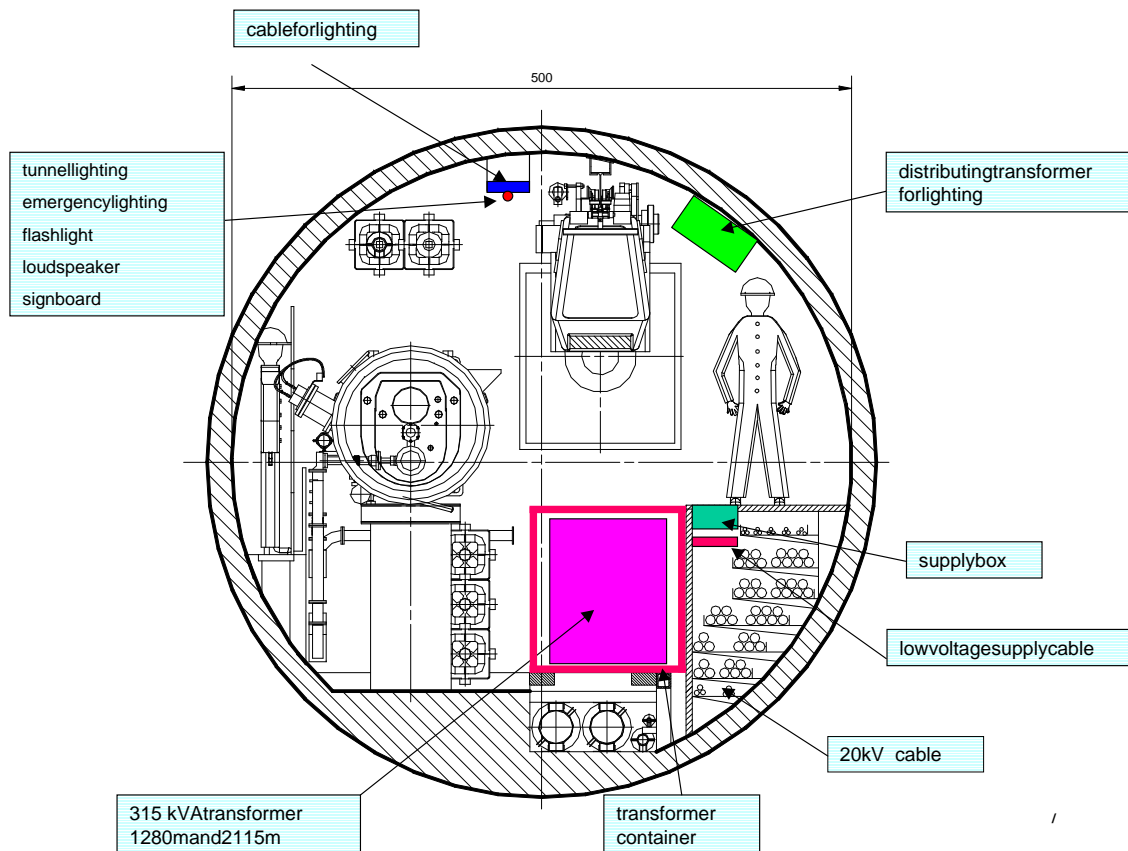
Figure 8.4.2: *Power distribution in the tunnel.*

of that for wet cooling tower and the plume is avoided. Still the system is compact and, if automatic desludging is incorporated, the maintenance requirements can be as low as for a dry cooling tower.

The dominant part of the heat load to the cooling system in the tunnel comes from the RF stations, with the klystron collectors and the absorbers for reflected RF power being the main sources. For simple maintenance in the tunnel the elements for the cooling system are installed in containers (figure 8.5.2) next to the klystrons (about every 50 m) and equipped with quick connections to the local cooling circuits and the main water distribution pipes. The collector cooling circuit requires enhanced water flow and has therefore an additional booster pump. The conventional magnets for the beam delivery system and transfer lines are directly connected with the main tubes with a flow switch and a valve.

The use of deionised water with a conductivity of $1\,\mu\mathrm{S/cm}$ as coolant restricts the choice of material for the pipes to stainless steel, copper and bronze; stainless steel will be used for the main pipelines. Booster pumps will pump the return water from the tunnel level back to the surface level where the water cooling plant is installed. This
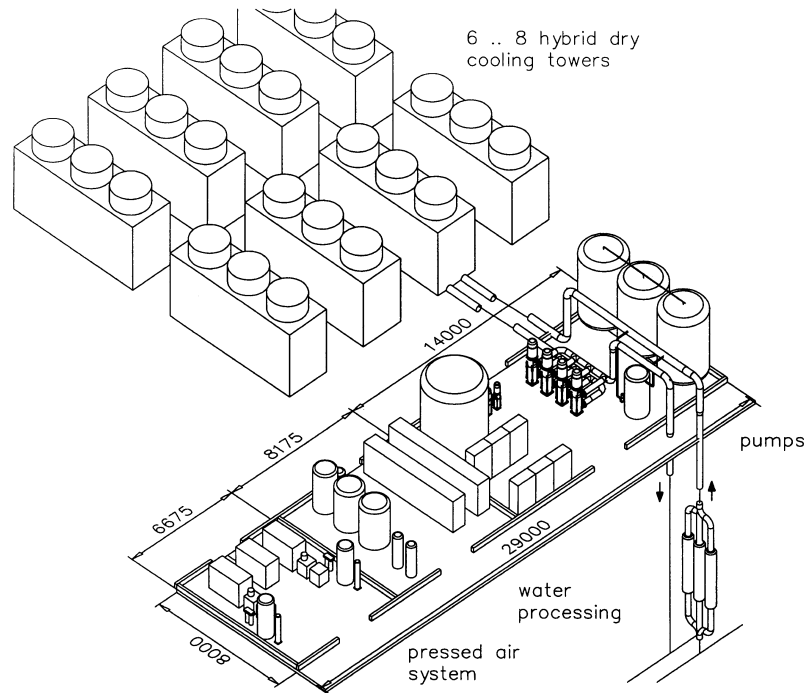
Figure 8.5.1:   *Sketch of the cooling station for one service hall.*

keeps the pressure of the return pipe as low as required by some of the RF system components. The diameter of the tubes, installed on the tunnel floor (figure 8.5.4), is 200 mm over the whole length of the linac tunnel. For operation at 500 GeV the pressure in the supply water pipe is approximately 7.5 bar and goes up to 10 bar at 800 GeV.

The temperature of the return water is 70 °C . Therefore the return water tube will be insulated with mineral wool of 70 mm thickness, which reduces the heat loss into the tunnel to about 30 W/m. To minimise the mechanical stress in the tubes due to thermal expansion there are compensators in the tubes. Every six metres is a sliding support and between pairs of compensators a fixed support. The last or direct connections to all elements (e.g. magnets, klystrons etc.) are done by EPDM-rubber tubes. The advantages are: resistance against radiation, high flexibility for the connections, quick installation, direct connection between elements at high electrical potential and grounded tubes.

8.5.2   Air conditioning

A ventilation and exhaust system is foreseen for each of the 9 halls along the TESLA site (two end stations, 6 service halls, central site), see figure 8.5.5. Each of the tunnel sections between two halls is operated independently and with 100 % fresh air (no recycling). It is also possible to bypass a hall and feed the air from one tunnel sec-
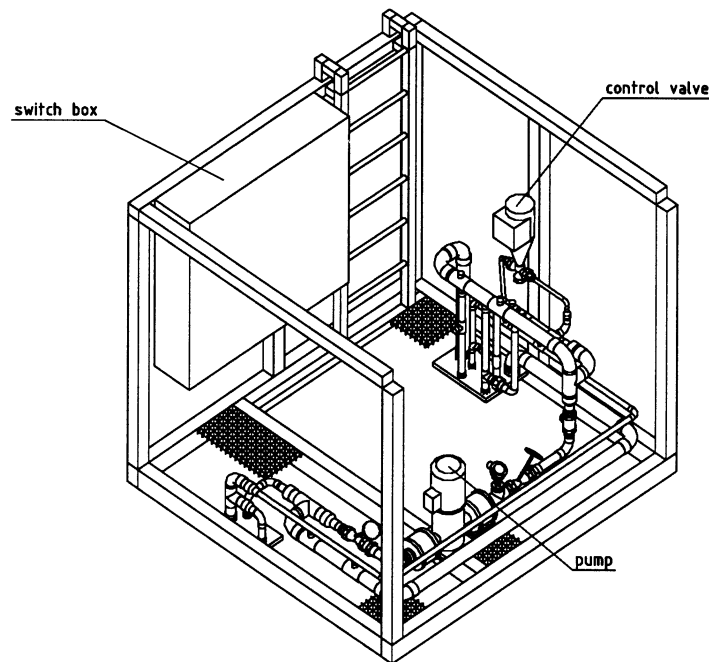
Figure 8.5.2:   *The cooling system container installed in the tunnel next to the klystrons.*

tion directly into the next. The air speed in the tunnel under normal conditions is 0.8 m/s. An air-drying system will be used in each of the halls which reduces the dew point of the air to 4 °C, well below the tunnel wall temperature of about 12°C. The ventilation will be switched on only during the construction and installation phase and during maintenance or temporary access periods. During beam operation the tunnel ventilation will be switched off.

In case of an emergency (fire, smoke in the tunnel), additional fans can be switched on which increase the air speed to 3 m/s. The fans are reversible to change the direction of air flow and can stand a gas temperature up to 600 °C for up to 2 h. A similar ventilation system is foreseen for the damping ring arc tunnels.

Special air conditioning is required for the tunnel sections accommodating the undulators of the FEL facility, for which the ambient temperature must be kept constant at 22±0.3 °C. These sections will be equipped with local recirculating air conditioning systems, installed in the tunnel.
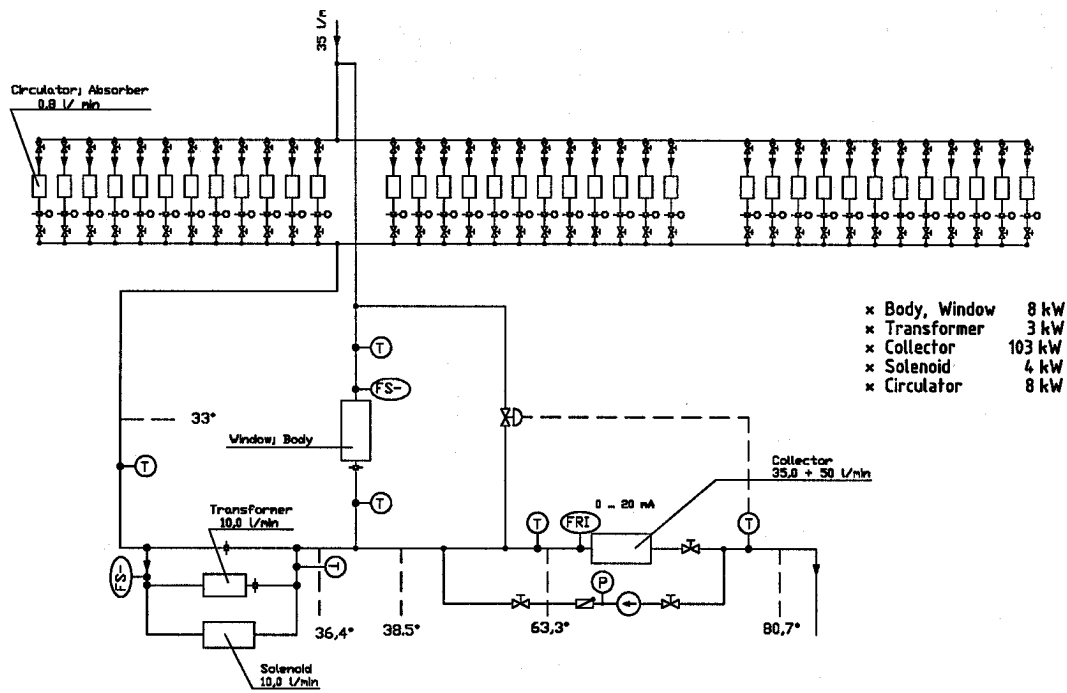
Figure 8.5.3:   *The cooling circuits for one RF station.*
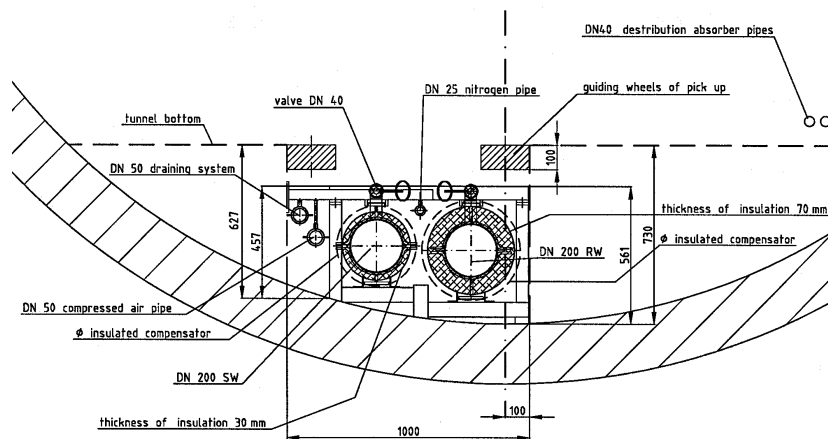
Figure 8.5.4:   *Main water pipes in the tunnel.*

8.6   Survey and Alignment

8.6.1   Basic network

In order to mark any installation of the facility a basic network has to be established. Coordinates of reference points along the linear collider have to be determined on
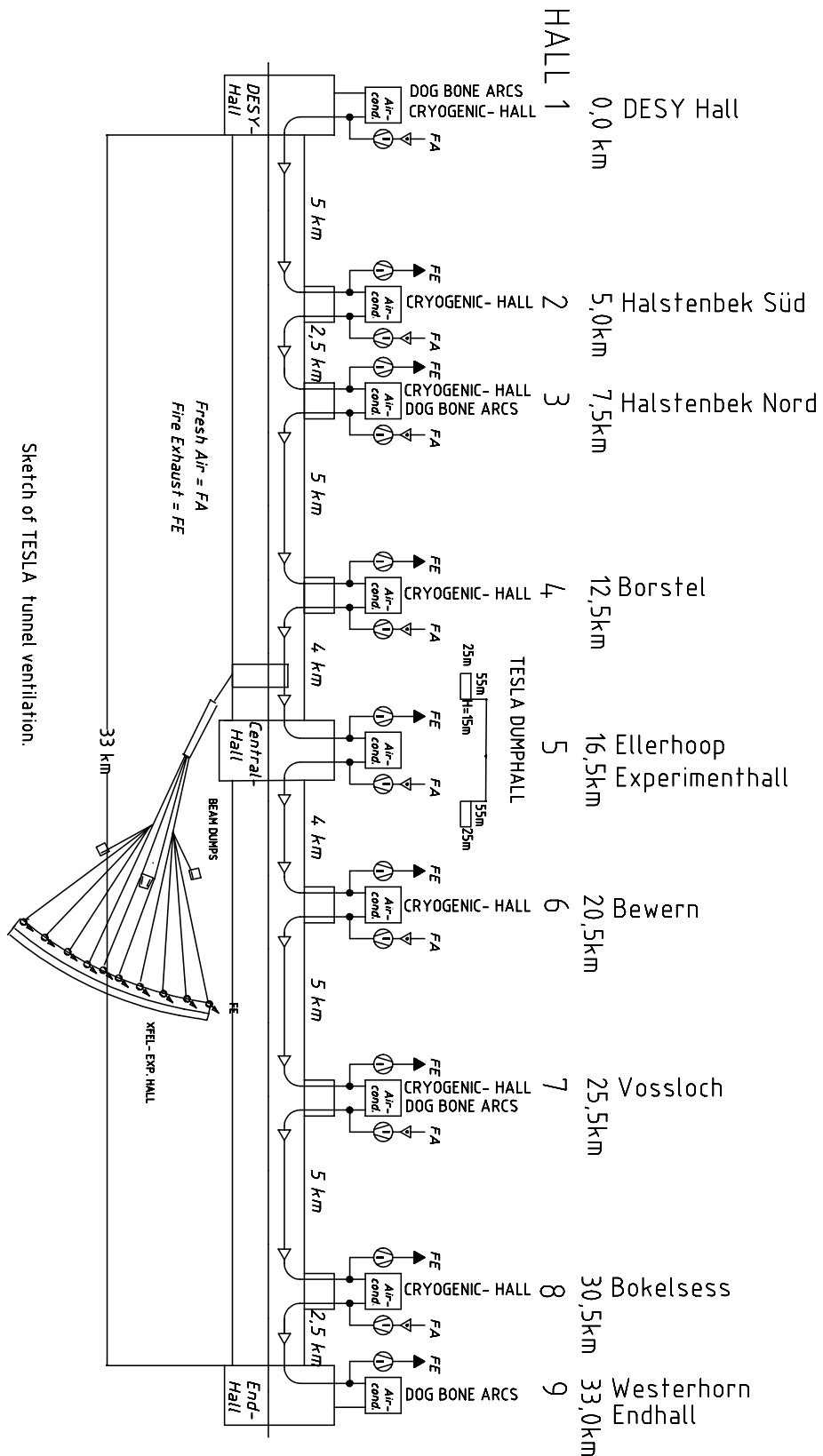
Figure 8.5.5: *Overview of the ventilation system.*

earth's surface with respect to the existing coordinate system at the respective site. In case of DESY this will be the HERA coordinate system. The coordinates will be determined by using geodetic receivers of the GPS satellite system. The demanded global precision (standard deviation) of every reference point in the whole area of the linear collider has to be better than 5 mm. The reference points serve as a basis to mark the buildings e.g. the halls or to control the tunnel boring machine. Therefore coordinates have to be transferred into the tunnel via the halls or shafts. The vertical network has to be established by a precision levelling. In the ground plan the tunnel axis is a straight line. In the vertical plane the axis of the tunnel follows the earth's curvature except for the first 3 km. The heights are referenced to the geoid and thus depend on earth's gravity field / mass distribution.

8.6.2   Requirements for the alignment of the components

The reference points which have been transferred from the basic network into the tunnel have to be refined in order to match the demanded accuracy for the alignment of the accelerator components. The standard deviation of every component has to be within 0.5 mm horizontally and 0.2 mm vertically over a range of 600 m (betatron wave length). Since there are several separate beam lines to be aligned with high accuracy, the most efficient survey will be to carry out only one basic alignment providing a suitable reference structure and then to connect each beam line to that basic structure.

8.6.3   Basic alignment

The reference points for the basic alignment will be fixed to the tunnel wall every 20 m to 40 m and serve as target points only. Since neither the causeway nor the reference points are suitable to put geodetic instruments on, the instrument will be mounted on a moveable carriage which runs on beams fixed to the tunnel wall above the causeway (see figure 8.6.1). The carriage can be fixed to the tunnel wall at certain equi-distant positions. The basic alignment will be carried out with tachymeters. A tachymeter does simultaneous measurements of horizontal angle, vertical angle and distance to marked target points (table 8.6.1). Taylor-Hobson-Spheres or prisms mounted into Taylor-Hobson-Spheres serve as suitable target marks for that purpose.

Parameter	Accuracy
Horizontal angle	0.2 mgon (3 μrad)
Vertical angle	0.2 mgon (3 μrad)
Distance	0.1 mm

Table 8.6.1: *Tachymeter accuracy.*

In order to determine the coordinates of the reference points the tachymeter can be positioned close to any of the reference points and then measurements to a certain
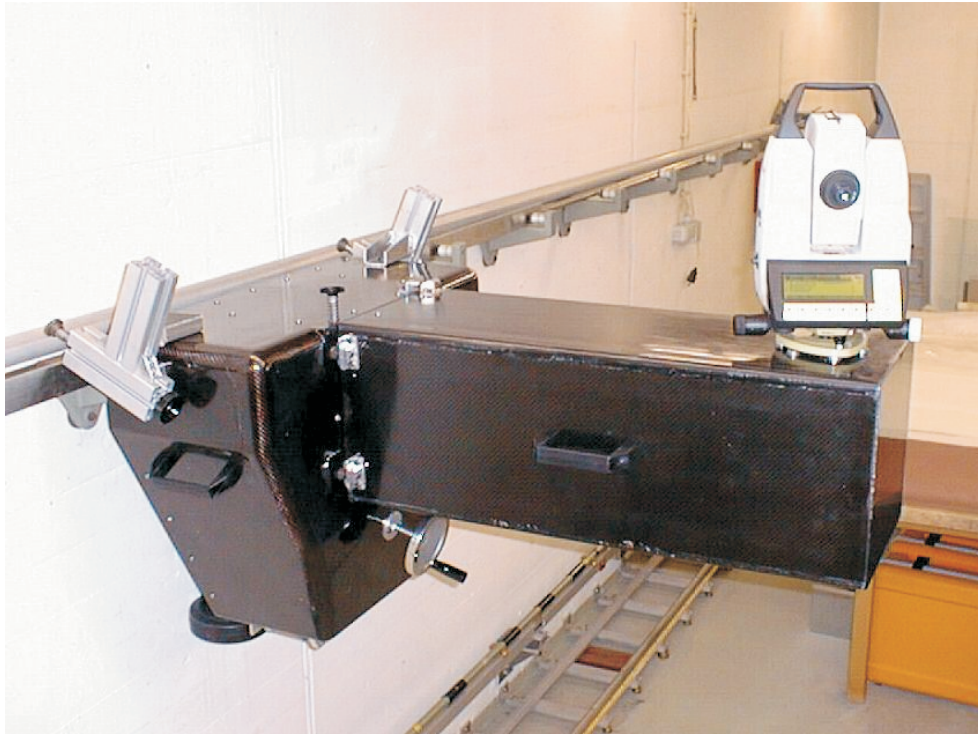
Figure 8.6.1: *Installation of the tachymeter on a moveable carriage.*

number of neighboring points can be carried out. The quantity of reference points to be aimed at depends on the demanded accuracy. If only random errors are taken into account, figure 8.6.2 shows the expected accuracy in the middle of a 600 m section as a function of the number of measured targets and the distances between the reference points.

Apart from random errors, whose influences can easily be reduced by increasing the number of measurements, there are also systematic errors which degrade the results. The main error in optical survey is caused by refraction, which means that the line of sight does not follow a straight line due to density variations of air. The density mainly depends on the temperature of air. If one assumes a constant temperature gradient of only $0.1\,\mathrm{K/m}$ which is perpendicular to the wave propagation of the line of sight, then a line of sight of 600 m length will be bent to a circular curve with a displacement of 4.5 mm to the straight line between instrument and target. Thus the demanded tolerance for the alignment of components is exceeded by far. The reference points provided by optical methods will be sufficient for any installation purposes like marking the supports of the beamline components. Refining the reference structure in order to achieve the above mentioned accuracy for alignment purposes has to be done by different measurement techniques which reduce or avoid the effects of refraction:

- angle measurements with a two-color laser to determine the amount of refraction (under development)
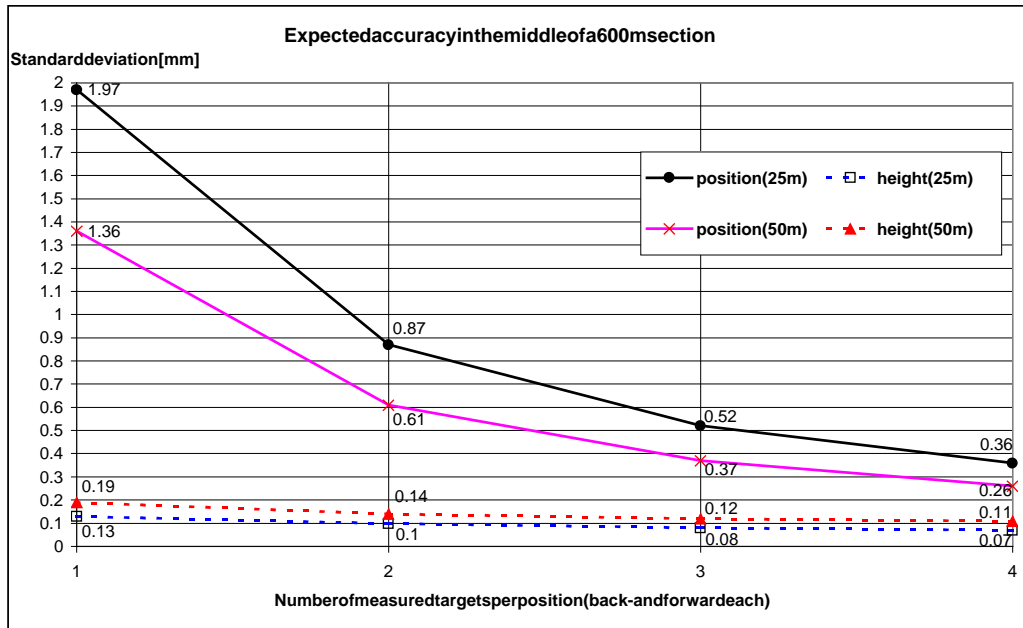
Figure 8.6.2: *Expected accuracy in the middle of a 600 m long section versus number of measued targets.*

- stretched wires in an overlapping arrangement (horizontal position only)

- multi-point alignment by distance measurements (horizontal position only)

- hydrostatic levelling (vertical position only).

In the following the hydrostatic levelling system and the multi-point alignment will be described in detail.

8.6.4   Hydrostatic levelling system

A hydrostatic levelling system will be installed in the tunnel in order to provide an exact vertical position of the reference points. Basically this can be done by installing a sealed pipe half filled with fluid, half with air. The surface of the fluid levels to an equipotential and thus serves as height reference. In the sloping section of the tunnel (first ≈ 3 km) the levelling system has to be installed in a staggered manner. With capacitive or ultrasonic sensors the clearance between reference point and the surface of the fluid can be determined. The above mentioned sensors show an accuracy of better than $5\,\mu$m. With that setup the height of the reference points can be determined to 0.1 mm along a 600 m section. First tests of a 42 m installation led to satisfying results. Currently a 1 km installation is under study.
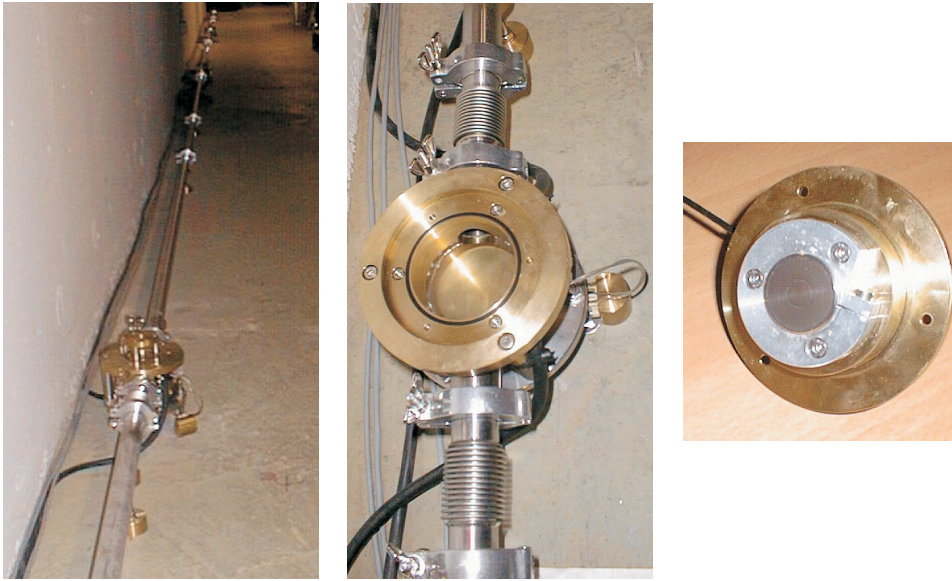
Figure 8.6.3: *Test installation (42 m section) of a hydrostatic levelling system.*

8.6.5   Multi-point alignment

A technique to avoid the effects of refraction is given by the multi-point alignment. This method replaces angle measurement by distance measurement to at least three points (see figure 8.6.4). A moveable bar serves as a fundamental structure for straightness measurements. From this straight line the distances a to target marks at the tunnel wall are determined. With known distances s the horizontal angle w can be determined. To enhance redundancy the number of target marks can be increased.
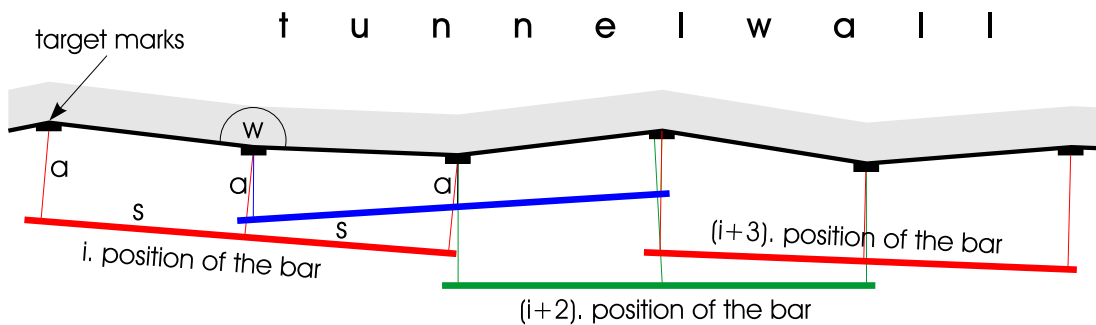
Figure 8.6.4: *Straightness measurements with multi-point alignment.*

The distances will be determined by photogrammetric methods by means of 3 CCD-cameras. The overall accuracy depends on the straightness of the bar, the resolution of the distance measurements and the number and spacing of target marks. First test assemblies have been performed with a 2 m long bar. To accomplish better efficiency one can increase the length of the alignment unit. The straightness reference then has

to be assured by a stretched wire and wire detectors. For further testing a 25 m unit is currently under development.

8.6.6   Transferring the coordinates

After having performed the above mentioned measurements, a reference structure with the demanded accuracy has been established inside the tunnel. The coordinates of the reference points now can be transferred to the components of each beamline. In order to determine the three-dimensional position every component has to be equipped with two reference plates suitable to put target marks on and a support to determine the roll angle. Now the geodetic instrument mounted to the moveable carriage is positioned close to the components which have to be aligned. First the coordinates of the instrument are calculated by surveying a certain number of reference points, then the components are to be aligned. One can use a tachymeter or a laser tracker to carry out that survey. As practiced at other accelerators (e.g. HERA), a second survey of the same components should be carried out from a neighboring instrument placement to increase redundancy and to verify the alignment of components. Finally, it is advisable to provide a control survey throughout an aligned section of beamline including both reference points and components simultaneously.

8.7   Cryogenics

About 21000 TESLA 9-cell cavities along the 33 km long linear collider have to be cooled in a superfluid helium bath to $\leq 2\,\mathrm{K}$, to achieve a cavity quality factor $Q_0 = 10^{10}$ at 23.4 MV/m. The cavities are grouped into 1781 cryomodules in total, almost all of which are of the standard type described in section 3.3 (a small number of shorter modules is required for the pre-accelerators, see section 4).
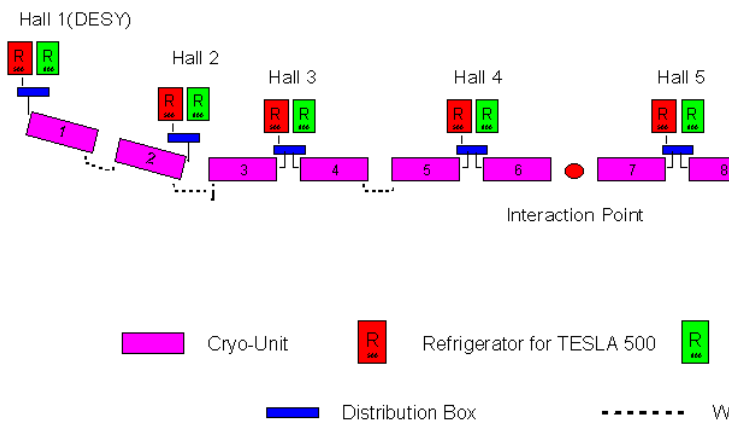
Figure 8.7.1: *Cryogenic system overview.*

The modules are placed horizontally (following the earth's curvature) in the un-

derground TESLA tunnel, except for the first part of the e$^-$ linac, where the string of modules is declined by ~ 8 mrad (see section 3.2).

Strings of modules of about 2.5 km length (cryo-units) are supplied from one end with 2 K helium from a single refrigerator which has to provide also 5–8 K one-phase helium as well as 40–80 K helium, both for radiation shield cooling.

There are 12 cryo-units in total (see figure 8.7.1). Generally, with the exception of units 1 and 2, two of them are supplied from a common cryogenic hall, sitting above ground, with one refrigerator serving both cryo-units through a distribution box. Units 1 and 2, in which the FEL electron beam will be accelerated in addition, will be supplied from individual refrigerators, one on the DESY site, the other at 4.7 km from DESY. The refrigerators in hall 1 and 6 also supply cooling for the damping ring RF-system for electrons and positrons (section 5).

8.7.0.1   Layout of cryo-units and cryo-strings

In each unit (figure 8.7.2) every 10 cryomodules are grouped in a cryogenic "string". One cryomodule in each cryo-string (figure 8.7.3) will be equipped with valves, tubing, flow meters and instrumentation.
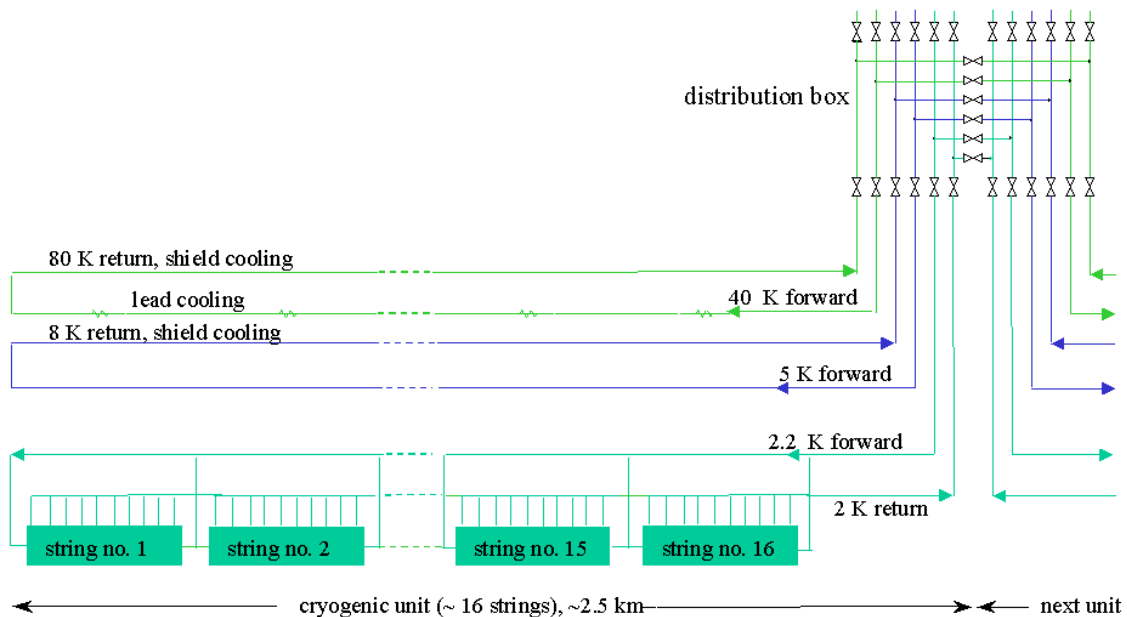
Figure 8.7.2: *Cryogenic unit.*

Each cryo-unit contains 4 vacuum barriers which separate the insulation vacuum into sections of ~ 500 m length. This is necessary to limit the pressure increase in the cold tubing to acceptable values in case of an accidental break of the insulation vacuum [25] and to make leak checking more easy.

A warm helium gas line connects all cryo-units of each linac for ease of helium
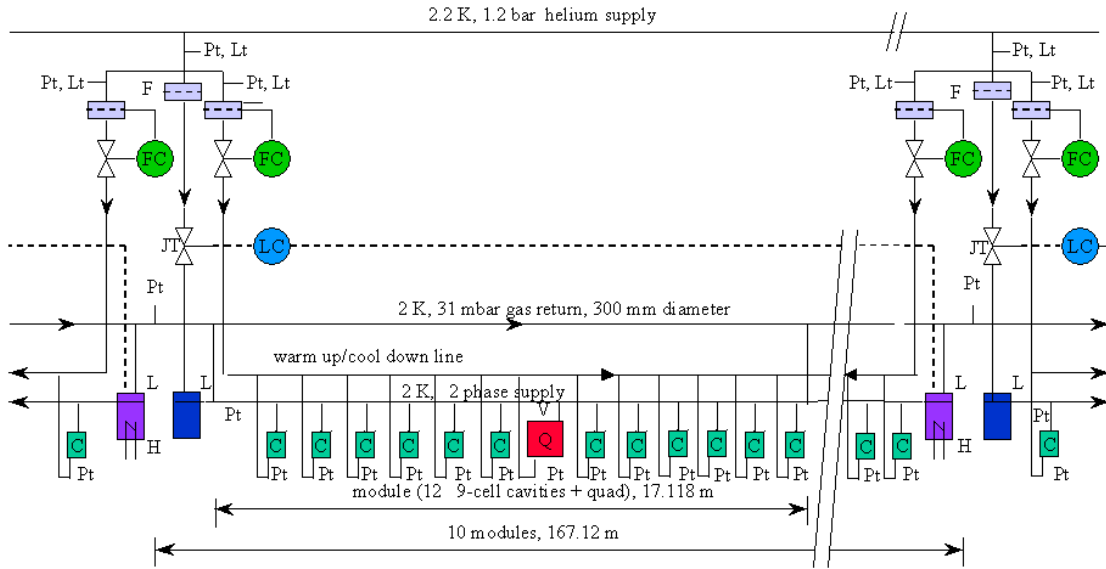
Figure 8.7.3: *Cryogenic string.*

exchange between the cryo-plants. Table 8.7.1 shows a list of the major cryogenic components of TESLA.

standard modules (12 cavities)	1004
modules (12 cavities) with 1 magnet package	742
modules with 8 cavities and 1 magnet package	27
modules with 4 cavities and 4 magnet packages	8
vacuum barriers	48
feed boxes	19
end boxes	19
injector feed boxes	3
cryo-plants	7
standard distribution box (2 units)	6
single distribution box	1
injector distribution box	1
transfer lines	824 m

Table 8.7.1: *Major cryogenic components.*

8.7.0.2   Heat loads

Static and dynamic heat loads have been determined for the 500 GeV collider mode of operation and for the FEL mode (section 3.3). The requirements for the cryo-units are shown in Table 8.7.2. A safety factor of 1.5 has been applied to determine the design

capacity of the plants. Operation at maximum energy (800 GeV) with high luminosity (see section 1.4) requires an upgrade of the 2 K plant capacity by up to a factor of two, depending on the dependence of the cavity quality factor on gradient.

	hall 1	hall 2	hall 3	hall 4	hall 5	hall 6	hall 7
2 K							
static	460	372	628	624	598	619	659
dynamic500	789	1159	2190	2181	1984	2138	2190
dynamicFEL	551	517					
st.+dyn.500/FEL	1800	2049	2818	2804	2582	2756	2814
design500/FEL	2700	3073	4227	4206	3873	4134	4220
5–8 K							
static	1554	1914	3530	3511	3296	3449	3518
dynamic500	508	748	1418	1428	1294	1386	1391
dynamicFEL	427	401					
st.+dyn.500/FEL	2488	3064	4949	4929	4590	4835	4909
design500/FEL	3733	4596	7423	7394	6884	7252	7363
40–80 K							
static	12548	14345	26183	25661	24316	25467	26520
dynamic500	9997	14619	27584	27431	25264	26918	27175
dynamicFEL	7162	6732					
st.+dyn.500/FEL	29707	35696	53768	53092	49580	52415	53695
design500/FEL	44561	53544	80652	79638	74370	78622	80543

Table 8.7.2: *Calculated heat loads and design plant capacities (in* W*) for cryogenic units and unit pairs (cryo-halls).*

8.7.0.3   Cooling of cryo-units

In steady state operation one-phase helium of 2.2 K and about 1.2 bar is flowing from the refrigerator through all cryomodules of a cryo-unit. At the end of each cryogenic string a fraction of this is expanded in a JT-valve into a gas separator at $\leq$ 31 mbar. Liquid and gas is flowing through a 76 mm diameter 2 K two-phase tube used to fill the cavity and magnet helium vessels. Heat generated in the cavities is conducted through the liquid in the helium vessel supply tube to the liquid surface in the two-phase tube where it evaporates helium. The helium gas is transported to the module interconnections where it enters into the 300 mm diameter gas return pipe. It is finally pumped back to the refrigerator through this pipe. Excess liquid – if any – at the end of each string is collected in a helium bath and evaporated there by an electric heater. Proper control of the JT-valve will assure that there is nearly no excess liquid helium entering this bath.

The pressure drop in the worst case (unit no. 3, 2.8 km long) is 0.94 mbar at a mass flow of 108 g/s. In addition a pressure drop of 2 mbar occurs in the about 20 m long shaft connecting the cryo-plant with the tunnel.

For cool down and warm up, helium at appropriate temperature is pumped through the 2.2 K one-phase tube and to a gas header above the cavities and magnet packages. From this header the gas runs through small tubes connected to the bottom of the helium vessels. The smallest cool down section is here one half of a string (5 modules). After running through the helium vessels the gas returns back to the refrigerator through the 300 mm gas return pipe.

One-phase helium of 5 K and 5 bar is flowing from the refrigerator through the cryomodules to the end of the unit. On its way back to the refrigerator it is cooling the 5–8 K radiation shield to which all the heat intercepts are connected.

Helium gas of 40 K and 19 bar is flowing from the refrigerator through the cryomodules cooling the high temperature end of the HTS current leads. On its way back to the refrigerator it is cooling the 40–80 K radiation shield with all the heat intercepts (HOM absorber, input coupler, instrumentation).

8.7.0.4   Instrumentation

Because of the large numbers involved the instrumentation in the cryo-units is kept to the necessary minimum. In the standard modules there are platinum sensors (Pt) at each input coupler, as well as cables to the motor and piezo-quartz of each tuner. Each cavity is equipped with two HOM antennas, one RF-pick-up and one secondary emission electron sensor. The modules with magnet package have a platinum sensor at the current lead heat intercept (50 K) and voltage taps across each HTS part in addition. The BPM has 4 antennas for signal readout. Modules with valves at the string ends, feed and end boxes have platinum thermometers, low temperature sensors (Lt) and flow meters (F) at each 2.2 K line and each cool down/warm up line as well as level sensors (L, superconducting, and carbon-glass resistor chains) and heaters at the local liquid helium reservoirs. A list of the foreseen instrumentation is shown in table 8.7.3.

8.7.0.5   Plant reliability and redundancy

The refrigeration system needs to have a very high availability of over 95 %. Because the refrigerators in all 7 refrigeration halls have to be working at the same time, each single hall has to have an availability of at least $(0.95)^{1/7} = 99.3\%$. So availability has highest priority in all design considerations.

The first questions, which one has to address, is, whether in each refrigerator hall one should install one large refrigerator or multiple refrigerators with eg $2 \cdot 100\%$ or $3 \cdot 50\%$ redundancy.

The sources of unavailability in existing cryogenic refrigeration systems have been investigated, whether the installation of multiple refrigerators increases the availability. Table 8.7.4 shows the main causes of unavailability in existing systems, in order of the frequency of their occurrence.

	standard mod.	mod. with magn.	mod. with valves	mod. 8 cav.	mod. 4 cav.	feed boxes	end boxes	sum
Pt sensors	20064	19292	5376	486	128	114	114	45574
Lt sensors			1008	162		76	76	1322
sc level sensors			672			38	38	748
carb. res. chains			336			19	19	374
cold flow meter			504			38	38	580
heater			336			38		374
HOM antennas	20064	17808	4032	432	64			42400
pick-up antennas	10032	8904	2016	216	32			21200
e$^-$ sensors	10032	8904	2016	216	32			21200
BPM antennas		2968		108	32			3108
voltage taps		7420		270	320			8010
motor steering	10032	8904	2016	216	32			21200
piezo quartz	10032	8904	2016	216	32			21200

Table 8.7.3:   *Number of sensors and other instrumentation in each TESLA linac.*

Rating	Topic	Example	Multiple refrigerators ...
1	External utility failures	Electrical power, cooling water, instrument air failure	bring no advantage
2	Blockage by frozen out gaseous impurities	Air and/or water vapour	provide somewhat larger tolerance
3	Operational problems	Controls, instrumentation, operators	would be detrimental, because of higher system complexity
4	Single component failure not leading to total plant shut-down	Electrical motor burnout, compressor bearings, leaking oil pump seal, turbine bearing trouble	bring no advantage over component redundancy within a single refrigerator
5	Catastrophic component failure leading to plant shutdown	Loss of insulation vacuum, rupture of heat exchanger, oil spill into cold process piping	would have a positive effect

Table 8.7.4: *Rating of refrigerator system unavailability.*

When one inspects table 8.7.4, it turns out that concerning the four most frequent sources of unavailability the effect of multiple plants is either small, negligible or even detrimental. Only in case of a catastrophic component failure like loss of vacuum or oil

spill into the cold box piping, there would be a clear advantage of multiple refrigerators, but these effects have occurred so far very seldom in existing refrigerators.

So after consulting with experts at CERN, who were confronted with a similar question when a decision had to be made for the LHC cryogenic system, and with refrigerator manufacturers, we decided to go for just one single large refrigerator at each of the seven refrigerator halls with some built-in component redundancy and a clear strategy to fight impurities. Further discussions with manufacturers showed that the required size of refrigerator is about 20 % larger than the largest existing refrigerator, but the cold components still fit within a single cold box, which is transportable across the road.

So we are convinced that in this case the lowest cost solution also provides the maximum possible availability. Of course all technical details have to be executed in high quality.

8.7.0.6   Refrigerator size

The design refrigeration loads in halls 3, 4, 5, 6 and 7 are about equal, whereas the requirements in halls 1 and 2 are somewhat smaller. It is suggested to install seven refrigerators, which are identical in those components which are difficult to replace or to modify (coldbox, heat exchangers, expander and cold compressor housings, adsorbers and piping). Adjustment to the special needs, like the lower design loads of the refrigerators in halls 1 and 2, can be covered by a different number of compressors and special turbine and cold compressor nozzles and wheels.

As usual for refrigerators of this size, the plants will be designed for very high energy efficiency at the design point, i. e. the highest expected refrigeration load. The present state of the art is a Carnot efficiency of about 27 %, which translates for a 4.5 K refrigerator into a COP[1] of 245 W of input power for each W of refrigeration.

The TESLA refrigerators are designed for a very good partial load efficiency. So if e. g. the accelerator is operated at reduced load, the electrical power consumption is reduced proportionally down to about 60 % of the highest refrigeration load.

For the upgrade to 800 GeV, space will be left in all halls for additional refrigerators. They may have a capacity up to the same size as the refrigerators of the first phase; but the actual size can be determined at a later stage. The only investment, which will be done already in the beginning, are additional connections in the distribution boxes.

8.7.0.7   Technology of large helium refrigerators

Over the last forty years, accelerator projects have been instrumental to push helium refrigerator technology into the direction of higher reliability, better efficiency and lower cost. All major components of the TESLA helium refrigerators have been used successfully in similar systems before.

While the design of the mechanical components is already fixed, continuous progress is going on concerning quality assurance, instrumentation, diagnostics and computer

---

[1]The coefficient of performance, COP, is the inverse of the overall refrigerator efficiency.

simulation of operational conditions.

The special challenge of the TESLA refrigeration system is the remote operation of several such refrigerators from a central operating room without any service persons on site. It is of advantage for TESLA, that the LHC cryogenic system will be in operation a number of years earlier. The TESLA refrigeration system has many similarities with the LHC system, like number of plants, distance between plants, superfluid helium cooling and the helium inventory of about 100 t. The TESLA system has about an eight times smaller cold mass, so cool-down and warm-up will be simpler.

8.7.0.8   Helium storage

When in full operation the TESLA cryosystem will contain about 100 t of helium. When the cryostats are warmed up, this helium has to be handled outside the cryostats. In principle one has the following options:

- Gaseous storage at 200 bar (very expensive compressors needed)

- Gaseous storage at 20 bar (investment about 150 Euro/kg)

- Liquid storage (investment about 60 Euro/kg)

- Reselling of the helium to the market (Depends strongly on market conditions)

For the TESLA system, it is proposed to provide a combination of gaseous storage at 20 bar and liquid storage. Gaseous storage will be provided for about 25 % of the inventory in 31 storage vessels with a geometric volume of $250\,\mathrm{m}^3$ each, working between 1 bar and 23 bar. On the other hand, nearly 100 % of the inventory can be stored in liquid form in seven $120\,\mathrm{m}^3$ liquid helium dewars.

Halls 1 and 2 will be equipped with one dewar and 3 gas tanks each, whereas stations 3 to 7 will be equipped with one dewar and 5 gas tanks each. All tanks and dewars will be installed outside the refrigerator halls.

The dewars are shielded by liquid nitrogen and have nevertheless a boiloff-rate of 0.28 %/day, i.e. 14 l/h. This load is negligible, when the associated refrigerator is in operation. When the refrigerator is not in operation, the boiloff has to be compressed into gaseous storage, preferably by a compressor, which is on emergency power.

The ambient temperature helium systems of halls 1, 2, 3 and 4 on one side and 5, 6 and 7 on the other side are interconnected by ambient temperature pipes through the tunnel. In an extended standstill period, about once per month one of the plants on each side of the accelerator has to be started to reliquefy the collected boil-off gas from 20 bar storage vessels into its dewar.

In case of an unplanned refrigerator shutdown and an associated pressure rise in all cold systems, the helium inventory of the portion of the system, which has a high design pressure, will be directed directly to the 20 bar buffer. This includes the helium in the refrigerator itself and in the 40–80 K shield of the cryostats. The 5–8 K shield will be treated as part of the low pressure system to keep it operational for the purpose described in the next paragraph.

The helium of the part of the system with lower design pressure, i. e. mainly the inventory of the cavity cryostats, will be allowed to rise in pressure and temperature by the "2 K static heat load". Such a warm-up from 2 to 4.4 K will take about 10 to 20 hours. If the pressure in the cryostat exceeds a pressure of about 1.2 bar, vapour is allowed to leave the cryostat, partially also through the 5–8 K shield line. So additional static heat load to the cryostat is avoided. All emerging vapour will be warmed up to ambient by an air-heated exchanger and compressed by a compressor, which works on emergency power, into the 20 bar storage.

The evaporation of all liquid from the cryostats by the static heat load would take about 80 hours. But already after about 20 hours, the gaseous storage of the respective station will be full. So at this moment either the refrigerator itself should come online again, or the warm compressed helium has to be transferred to a neighbour hall for reliquefaction into the dewar of that station.

8.7.0.9   Model refrigerator

A model refrigerator has been designed, with valuable advice from CERN and from industry. The model refrigerator allows

- to get information an component sizes, number of compressors, flow rates in different loops etc.

- to get provisional data on power consumption for the specification of utility systems and the operating budget

- to get the approximate size of components for the building layout.

This model refrigerator (figure 8.7.4, table 8.7.5) was discussed extensively with the industrial companies, which are presently building the LHC refrigerators. The following important aspects of the model refrigerator are a correct basis of the planning of TESLA:

- The design loads can be covered by a single refrigerator with a single horizontal coldbox.

- The number of foreseen screw compressors is adequate.

- The power consumption estimates are realistic.

- The intended Technical Specification leaves industry sufficient freedom to incorporate their best components.

- The estimated cost is adequate.

Helium is compressed at ambient temperature by a two-stage screw compressor group to a pressure in the 20 bar range. After recooling to ambient temperature and
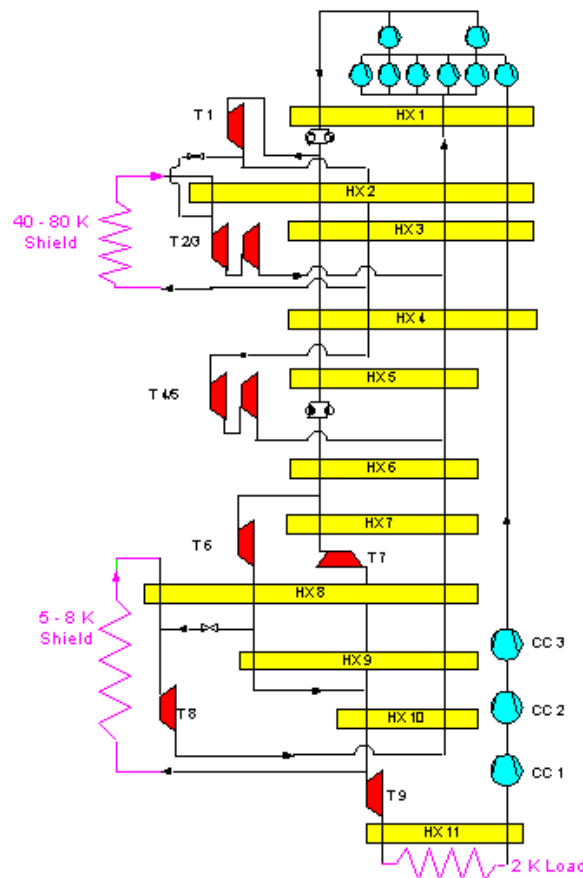
Figure 8.7.4: *Flow diagram of model refrigerator.*

careful oil removal and drying from residual water vapour, the high pressure helium is cooled in HX 1 to 80 K, where it is purified from residual air in switchable adsorbers.

Then a part of the flow is split off and expanded in turbines T1, T2 and T3 to about atmospheric pressure. After T1 a part of the stream is split off and cooled in HX 3 to 40 K. Here one part of the flow leaves the coldbox and cools the 40–80 K shield in the cryostats. It returns back, is cooled in HX 2 and enters T2. A pressure drop of about 1 bar is foreseen for this shield flow.

One part of the flow already expanded in T1 and precooled in HX 3 is further cooled in HX 4 and expanded in T4 and T5 to atmospheric pressure. The main high pressure stream leaving the 80 K adsorbers is cooled in HX 2, 3, 4, 5 and 6 and in between purified from neon and hydrogen in the switchable "20 K adsorbers". The high pressure stream is expanded in two parallel turbines T6 and T7 to an intermediate pressure of about 5 bar. The major part is further cooled in exchangers 8, 9 and 10 and is then used for the 5–8 K shield. After return from this shield, the gas is expanded in T8 to atmospheric pressure.

Another part of the 5 bar flow is expanded in T9 and subcooled in HX 11 before flowing to the cavity cryostats. After throttling to the 30 mbar pressure level and evaporation in the cryostats, the low pressure helium vapour returns to the refrigerator through the 300 mm line in the cryostats. After superheating in HX 11, the gas is compressed in a three or four-stage cold compression system to a pressure close to atmospheric pressure, but not necessarily to above atmospheric pressure. This stream is separately warmed up to ambient in exchangers 4, 3, 2 and 1 and enters its own low pressure screw compressor.

The indicated power consumption of 5147 kW (table 8.7.5) is the power consumption of the biggest refrigerator for the design case. The power at smaller refrigerators or at part load operation can be calculated by using the indicated COPs for the individual temperature levels.

A possible layout of a cryogenic hall is shown in figure 8.7.5.

		Mass flow	Outlet	Return
2 K Load	4253 W	199.4 g/s	1.1 bar 2.2 K	0.0275 bar 2.0 K
5 – 8 K Shield	7465 W	249.8 g/s	5.5 bar 5.16 K	5.0 bar 8.2 K
40 – 80 K Shield	80788 W	383.3 g/s	16.0 bar 40 K	14.0 bar 80 K
Compressor				
LP I		199.4 g/s		0.92 bar 295 K
LP II		1369 g/s		1.4 bar 295 K
HP		1568.4 g/s	24.0 bar 300 K	
Power Consumption	Refrigeration	COP	Specific Load	% of Power
2 K	4.253 kW	588 W/W	2500 kW	49 %
5 – 8 K	7.465 kW	168 W/W	1254 kW	24 %
40 – 80 K	80.788 kW	17 W/W	1373 kW	27 %
Total			5147 kW	100 %

Table 8.7.5: *Process parameters of the model refrigerator.*
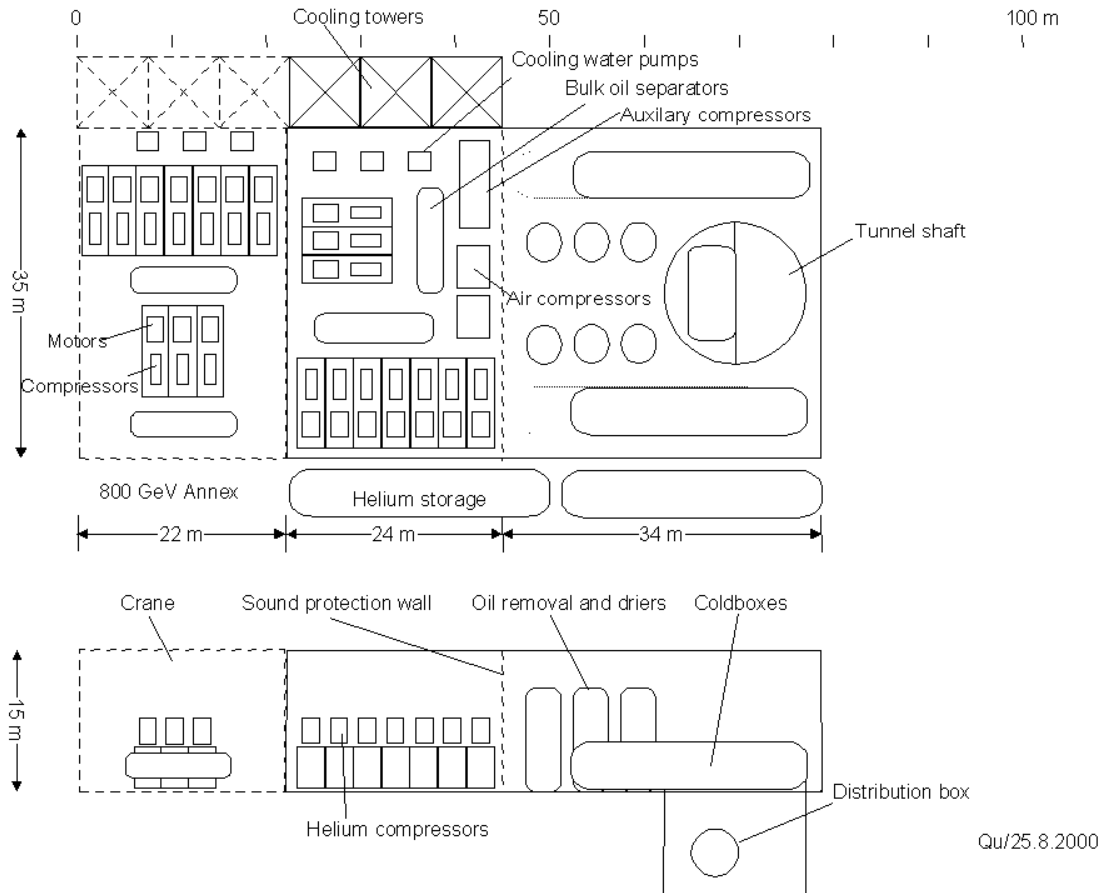
Figure 8.7.5: *Layout of the refrigerator hall.*

8.7.0.10 Additional Refrigeration for Damping Rings

In addition to the refrigeration requirements of the main linac with the FEL, there are the two damping rings, where each of them requires refrigeration at 2 K for superconducting RF cavities. The present estimate is, that 720 W of additional refrigeration at 2 K will be needed. The damping rings are close to refrigeration halls 1 and 6. Whereas the refrigerator in hall 1 has sufficient spare capacity, the foreseen safety margin for the refrigerator in hall 6, which covers units 9&10, would be reduced from a factor of 1.5 to 1.3 regarding the 2 K plant capacity. If that is found unacceptable, one has to envisage an "oversize" refrigerator for this particular cryo hall.

8.8 Accelerator Module Test Facility

8.8.1 Objectives of the Accelerator Module Test Facility

In order to detect systematic faults in the production process, 9-cell cavities have to be tested before assembly of the accelerator modules. Furthermore, a certain amount

of scattering in the maximum gradient per cavity has to be expected and the energy reach of the linear accelerator can be improved by sorting of the cavities according to their performance. We therefore plan to test all of the $\approx$21,000 single cavities, at a rate of about 24 cavities per day.

In addition, about 800 packages of superconducting quadrupoles have to be tested in the vertical dewars on an average rate of one quadrupole per day.

Before their installation in the TESLA tunnel, the accelerator cryomodules have to be qualified after the assembly in random tests. The qualification includes the check of the general mechanical dimensions and the measurement of the cryogenic performance of all systems, in particular, the performance of the cavities. At the start of the cryomodule series production the tests will cover 100 % of the cryomodules, in order to check and adjust the fabrication. After that, only about 25 % of the cryomodules will be tested. These random tests can be applied with low risk for the commissioning of the accelerator, because all main single components, like cavities and quadrupoles, will be tested to an extent of 100 % before the assembly of the cryomodules.

In general, with the exception of the tests of prototypes, the tests will aim only at quality insurance. For the cavities as well as for the cryomodules the test results from the test facility will be used as a fast feed back into the series production in order to avoid failures and to increase the performance.

8.8.1.1   Test Programme for the Cavities and Quadrupoles

The maximum accelerating field and the corresponding unloaded quality factor Q_0 of each single cavity will be measured at a temperature of 2 K in a bath cryostat. To increase the throughput of the vertical tests stands, eight cavities will be assembled at one cryostat insert. Each cavity will be equipped with a fixed coupler antenna ($Q_{ext} = 1 \cdot 10^{10}$) and a pick up probe ($Q_{ext} = 1 \cdot 10^{13}$). The cavities will be locked in the accelerator mode. The accelerator field will be increased to the maximum value in steps. At each step the cavities will be powered for 20 s in cw-operation mode. According to estimates of the test schedule, about 20 hours are needed for one complete test run for eight cavities, including the assembly and disassembly of the insert to the cryostat and the cool down and warm up procedures.

The inserts will be assembled at the cavity preparation site and delivered to the test facility. Cavities, which have passed the tests successfully will be sent to the cryomodule manufacturer. Cavities with low performance will be returned to the cavity preparation.

The superconducting performance of the quadrupoles will also be tested in the bath cryostats. Two quadrupoles will be tested at a time in one cryostat.

8.8.1.2   Test Programme for the Accelerator Module Test Benches

The cryogenic performance tests include the integral leak check of all vacuum systems and cryogenic process tubes, the test of the instrumentation, measurements of the static heat loads, of the maximum accelerating field of the cavities and the corresponding unloaded quality factor Q_0. The quality factor will be monitored by means of cryogenic

measurements of the dynamic heat load. The cryogenic measurement of the Q_0-value has been demonstrated as well in the horizontal cryostat (CHECHIA) [26] as for the cryomodules of the linear accelerator of the TTF. During the performance tests of the cavities, also the X-ray radiation and the related dark currents will be measured by means of two ionisation chambers at each test bench and monitors at both ends of the beam tube of the cryomodules, respectively.

The pre-conditioned RF-couplers will be further conditioned. The RF-phase will be adjusted in the order of ± 20 degrees. There will be also the possibility to process the cavities.

The instrumentation of superconducting quadrupoles will be tested in those cryomodules which contain quadrupoles.

About 170 cryomodules will be equipped with cryogenic valves, temperature sensors, flow sensors and liquid level indicators (string interconnection equipment). Also this instrumentation will be tested on the test benches.

According to estimates of the test schedule, about eight days are needed for the complete test of one accelerator cryomodule, including the mechanical assembly and disassembly on the test bench [27]. To fulfil this schedule, it is assumed that the pre-conditioned RF main couplers will be pumped and heated before the installation on the test bench.

8.8.1.3   Layout of the Accelerator Module Test Facility

Hall Layout

From the given test rates and the estimates of the test schedules it follows that 6 test benches for cryomodules and at least 3 vertical dewars have to be installed in the module test facility.

The number of test benches includes an overcapacity of about $20\,\%$ for the test of $25\,\%$ of the modules. In order to increase the efficiency of the vertical tests, 6 vertical dewars will be foreseen.

The overcapacities will compensate for shut down periods, maintenance and repairs. In addition, depending on the detected failure rates, capacities for the repetition of tests have to be foreseen.

Beside the test areas there will be areas for the intermediate storage of cryomodules and cavity test inserts, a test area for "warm" measurements of cryomodules, transport areas, infra structure areas and workshops. Also control rooms, offices and social rooms have to be provided. The test hall will have an overall size of $135\,\mathrm{m} \times 85\,\mathrm{m}$ ground area and a height of about $12\,\mathrm{m}$. Two parallel hall cranes, each with a capacity of $20000\,\mathrm{kg}$, a span of $36\,\mathrm{m}$ or $40\,\mathrm{m}$ respectively, and a hook height of $9\,\mathrm{m}$ will be installed (see figure 8.8.1).

There will be under floor channels leading from the cryogenic and RF supply equipment to the test benches and to the test dewars in order to take all supply tubes and cables.

Each individual module test bench has to be surrounded by a concrete shielding of $0.8\,\mathrm{m}$ thickness. The test benches will be covered by a roof shielding of $0.8\,\mathrm{m}$ thickness
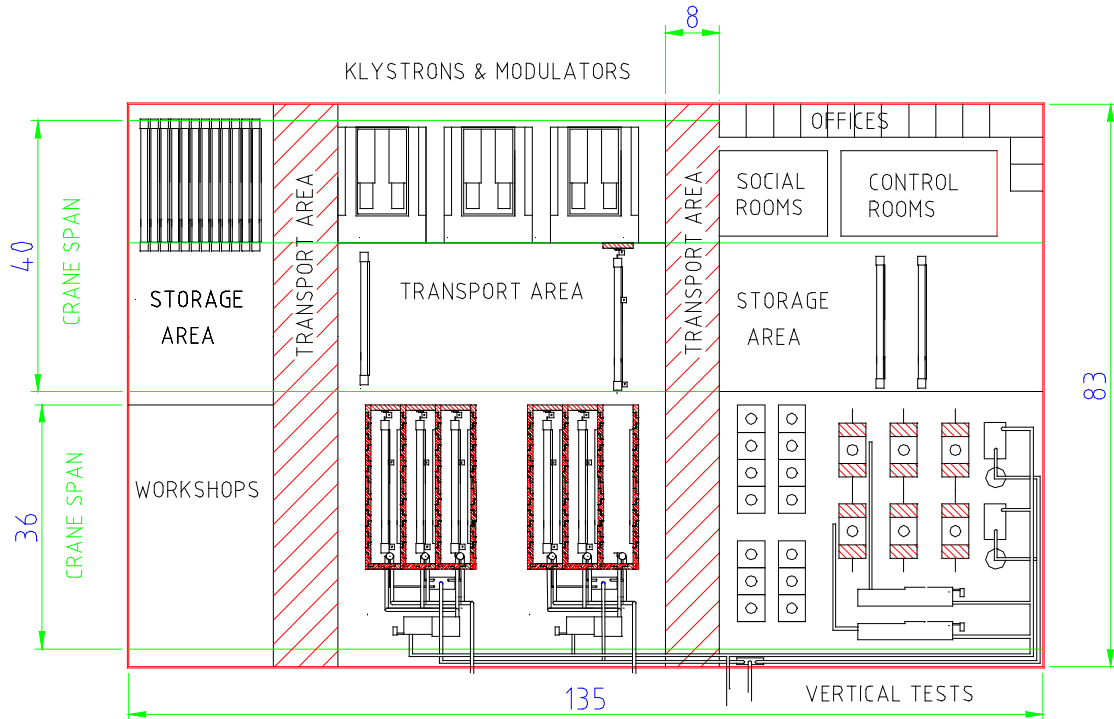
Figure 8.8.1:   *Ground plan of the accelerator module test facility.*

in order to establish radiation safety in all parts of the test hall. There will be an inner space of $23\,\mathrm{m} \times 4.4\,\mathrm{m} \times 2.5\,\mathrm{m}$ for one test bench. Three test benches will be grouped together as a block.

The front door of each test bench together with a module support structure can be moved horizontally on railways into the transport area. For the installation of a cryomodule on a test bench, the cryomodule will be moved by the hall crane from the storage area to the front of one test bench and will be installed on the support structure. After installation, the support structure will be moved back into the shielding of the test bench. During the installations inside the shielding, the front door can be shifted relatively to the support and will stay open.

The vertical dewars will be inserted into the ground and covered by movable concrete shielding blocks of $1.2\,\mathrm{m}$ thickness. The cryostat inserts will be moved from the storage area into the cryostats by use of the hall crane.

Cryogenic Systems

For the continuous operation of the test hall, cooling capacities of about $10\,\mathrm{kW}$ at $40/80\,\mathrm{K}$, $1.0\,\mathrm{kW}$ at $4.5\,\mathrm{K}$ and $0.6\,\mathrm{kW}$ at $2.0\,\mathrm{K}$ are needed. In order to reduce the effort of the helium distribution system, only the $40/80\,\mathrm{K}$ and $4.5\,\mathrm{K}$ circuits will be branched to the test benches and the test dewars. At the cryomodule test benches as well as at the vertical cryostats the $2\,\mathrm{K}$ liquid helium will be supplied by the isenthalpic
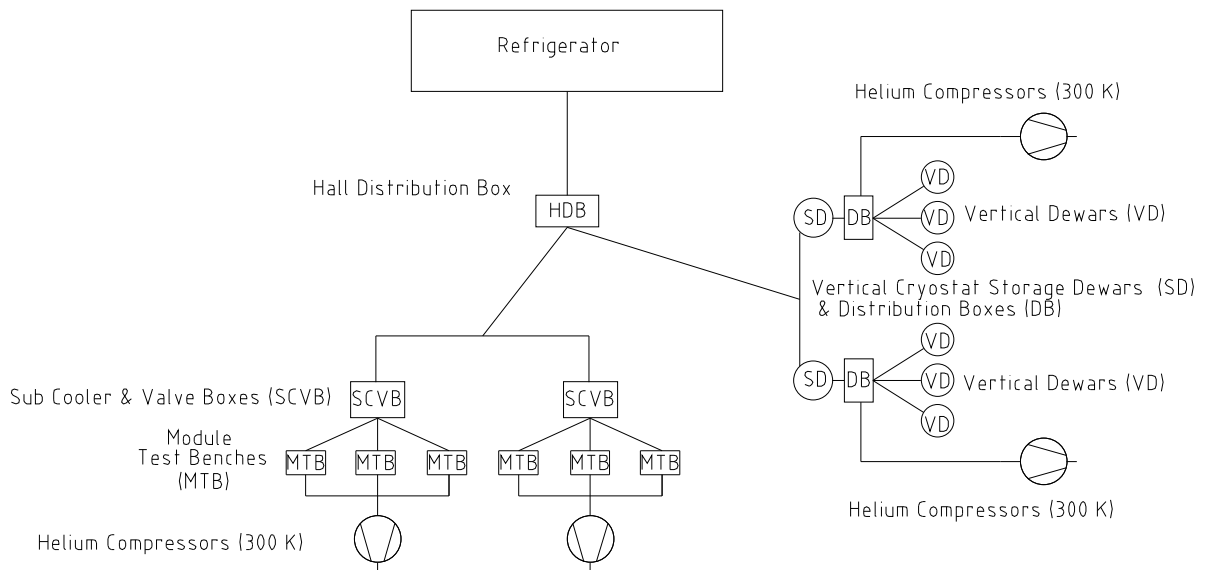
Figure 8.8.2:   *Block Diagram of the Cryogenic System.*

expansion of the $4.5\,\mathrm{K}$ helium, which will be sub cooled to $2.2\,\mathrm{K}$ before the expansion by means of counter flow heat exchangers. The average $2\,\mathrm{K}$ heat loads will be small in comparison to the capacity of the cold compressors of a TESLA refrigerator plant, and these loads will always vary. Therefore distributed warm compressor systems will be used to lower the vapour pressure of the helium baths to $31\,\mathrm{mbar}$ [28]. As a result, a helium liquefaction rate of about $50\,\mathrm{g/s}$ has to be supplied on average from the helium plant. Peak liquefaction rates will be buffered by means of two $10\,\mathrm{m^3}$ liquid storage reservoirs.

The cryogenic system of the test facility will be designed in a modular structure (see Fig. 8.8.2). The test facility can be connected to any helium refrigerator plant, which can supply the capacities mentioned, in particular to the HERA refrigerator or TESLA refrigerator on the DESY site.

a) Cryomodule Test Benches

The cryogenic supply of the test benches is divided into two "layers", in order to operate the test benches independently from each other, to avoid air condensation on cryogenic valves during the exchange and installation of modules, and to reduce the consequences of leaky valves. One layer are the feed boxes of each test bench, the other layer are the sub cooler & valve boxes, to which a group of 3 feed boxes will be connected (see figure 8.8.2).

In order to supply the cryogenic $40/80\,\mathrm{K}$ and $4.5\,\mathrm{K}$ shield circuits as well as the $2\,\mathrm{K}$ circuit, each cryomodule test bench has to be equipped with a feedbox, including a feed cap and an end cap [27, 29]. The feed box will be fixed inside the shielding of the test bench and will contain cryogenic valves for each supply and return tube, a small

4.5 K sub cooler and a 2 K counter flow heat exchanger. The 4.5 K sub cooler of the feedbox is used to stabilise the supply temperatures of the 4.5 K and 2 K circuits. The safety vent lines and relief valves are connected to the feed box. The feed cap, which is attached to the feedbox will contain all connection flanges to the cryomodule. The end cap will be fixed to the module support structure and will contain only the short circuits of all cryogenic tubes and a 2 K liquid reservoir. The position of each end cap can be adjusted easily to the different length of cryomodules.

Each cryogenic supply tube in the feedbox is equipped with a Venturi flow meter. As well in the feed cap as in the end cap all supply and return tubes are equipped with redundant thermometers. Redundant liquid level indicators and pressure sensors are installed in the 2 K reservoir of the end cap. The pressure of all cryogenic circuits will be monitored.

Each group of three feed boxes will be supplied via transfer lines from one sub cooler & valve box. The connecting transfer lines consist of 4.5 K supply, 4.5 K return, 40 K supply and 80 K return tubes. The sub cooler & valve box contains one 4.5 K sub cooler and cryogenic valves for all process tubes of the different transfer line branches and all corresponding warm up and cool down tubes and valves connected to the transfer lines. The sub cooler has to compensate the heat losses of the transfer lines, leading from the refrigerator to the test benches.

As a result of the combination of feed boxes and sub cooler & valve boxes all cryogenic supply and return tubes are separated by two cryogenic valves in series from the test bench.

The sub cooler & valve boxes will be supplied from the test hall distribution box (see figure 8.8.2).

The 2 K vapour return tubes of three test bench feed boxes are connected to one 300 K helium compressor unit. In the exhaust of the compressor unit the pumped mass flow can be measured by warm gas flow meters. By means of this flow meters, the heat load of the 2 K circuit can be monitored with a resolution of better than ± 0.1 W at a constant liquid helium level in the 2 K reservoir of the test bench.

b) Vertical Test Cryostats

As for the supply of the module test benches also for the vertical dewars two "layers" of valves in the dewars and in distribution boxes will be installed (see figure 8.8.2). The design of the vertical dewars can be scaled from the vertical test dewars of the TTF [28, 30]. The vertical dewars will consist of a $2.2\,\text{m}^3$ liquid helium volume, cryogenic valves and a 2 K counterflow heat exchanger, installed in the vacuum jacket. Three dewars will be connected to one distribution box respectively. The distribution boxes will contain all warm up and cool down connections and valves. One $10\,\text{m}^3$ liquid storage dewar will be connected to each distribution box respectively, in order to buffer the loads for the refrigerator. The storage dewars will also be used as sub coolers. The storage dewars will be supplied from the test hall distribution box.

The 2 K vapour return tubes of the vertical dewars will be connected to warm helium compressor units.

RF Systems

According to the test schedule of the cryomodules [27], up to 4 test benches have

to be supplied with RF power in parallel and independently from each other at a time for the conditioning of the couplers and the dynamic measurements of the cavities. It is supposed that all couplers of one cryomodule will be conditioned in parallel.

In order to avoid time consuming installations of the RF equipment in between the test benches and to obtain redundancy, one 10 MW klystron and modulator set will be connected to each test bench, including a fixed RF distribution system.

Vacuum Systems

a) Insulation Vacuum

For the insulation vacuum of the cryogenic systems standard turbo molecular pump units are foreseen. Each cryomodule test bench will get its individual turbo molecular pump unit. The other cryogenic equipment will be connected to a net of pump stands according to the experience of the HERA and TTF insulation vacuum systems.

b) Main Coupler Vacuum

The main RF couplers of one cryomodule will be equipped with one pumping tube connected to the pumps without individual valves. There will be only one manual valve at the pumping tube. The set of pumps and pumping tube will stay at each individual cryomodule from the assembly, during the tests until the installation in the TESLA tunnel.

c) Cavity Vacuum

During the tests on the module test benches, one oil-free turbo pump unit will be connected to the cavity vacuum.

One getter pump will be connected to the coupled vacuum system of the eight cavities of each vertical dewar insert. In addition there will be oil free turbo molecular pump units at the vertical dewars as a back up.

Controls

There will be different control sub-systems for the RF-, vacuum- and cryogenic systems, which have to be integrated by an industrial visualisation and data management system. In general, standard industrial components will be used as far as possible. The transfer of data between the different systems and the data management will be mandatory for the operation of the test facility.

Infrastructure

The installation of the test facility will require 4.5 MW of electrical primary power, 2.7 MW equivalent of water cooling capacity and about $500 \, \text{m}^3/\text{h}$ of instrument air. About 0.7 MW of heat will be dissipated into the air of the test hall.

8.9 Global Control System

A powerful control system is important for a successful commissioning and operation of TESLA. Experience with such control systems exists from the operation of the present accelerators HERA and TTF. A challenge for the design of the control system is the rapidly changing hardware and software over the last several years and the changes will continue during the course of constructing the linac. On the other hand, a software development for such a big machine has to start early to be ready in time. Most of the

investment goes into computer software and into front-end electronics. As to the front-end components, investing in industrial standards is a safe path to follow. Systems such as VME have a long lifetime, for example. Software developments should be based on new industrial methods and standards. A modular design of the software is required to allow to adapt new standards and products for a smooth development of the whole system during its lifetime. Special consideration of the huge amount of equipment, (due to the length of the machines) has to be taken. The software and the hardware layout of the control system must allow for this. On the software and communication side, an efficient access to device data is necessary. A lot of similar devices must be readable with little overhead and short response times. Higher levels in the control system should provide summary information on device groups. Good and automatic monitoring of all devices is essential. This includes a complete remote debugging and control of all front-end hardware to high degree of detail. The control system layout should be fault tolerant. Failing hardware and software components should not in general stop larger segments. This can be achieved by a modular design and by using redundant units of key components. All these principles will allow an operation of TESLA in a global accelerator network.

8.9.1   Architecture

The overall architecture consists of three layers of computers (figure 8.9.1). A top level with display or client programs, a front-end layer with device servers and I/O and a middle layer with powerful group servers. The upper layer is the interface to the operators. These top-level services should be available to the consoles in the control room, the experts working in the tunnel and the specialists of the collaborating institutes in their offices and development labs. All such users should be able to use the same programs, where the level of details presented might be different for different categories of users. Modifications of device data must be protected with access rights.

Since a lot of users and client programs access a lot of data from the front-end and the middle layer, a fast network is necessary to decouple the display stations. Ethernet switch technology that routes packets from the clients to their servers provide the important bandwidth. Client programs often need a go/no-go information from a group of devices only. In such a big system it is necessary to ask a large number of front-ends to get this information. A middle layer server should provide such collective reports. Likewise, the middle layer should supply frequently requested data of all its front-end computers in a single block transfer. In general, the middle layer implements higher services to provide integrative functionality and to improve the performance of the system. This becomes more important as the size and complexity of accelerators increase. The middle layer is the natural level at which to implement sequencing, automation, and global features such as data bases.

TESLA will need a real-time accelerator model which uses data from magnets, BPMs, and cavities to generate a picture of the current optics and beam envelope; this can be used to predict the effect of modifications and to block potentially destructive
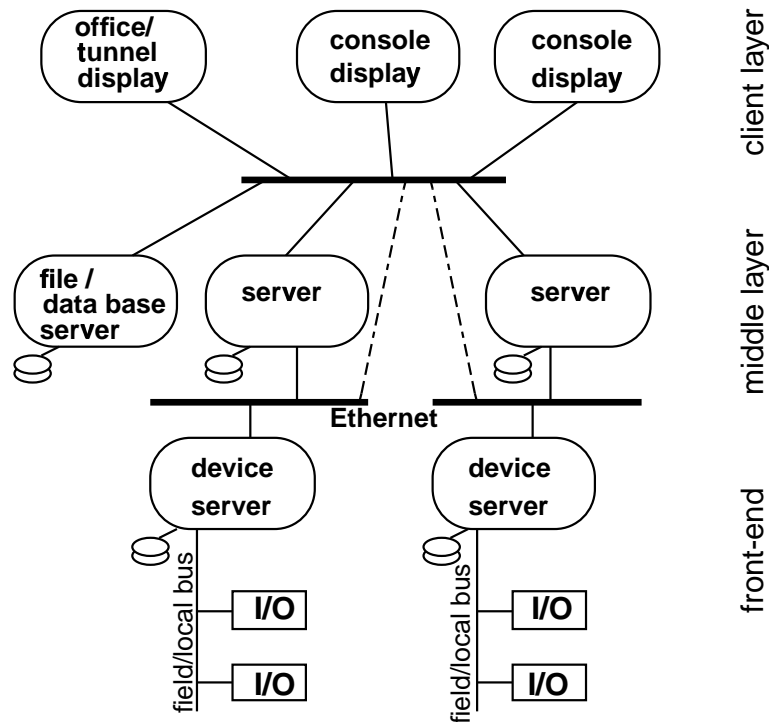
Figure 8.9.1: *Sketch of the control system layers.*

actions. The challenge for the next generation of control systems will be effective implementation of these automation features.

The front-ends are distributed and close to the devices of the linac. Some hardware is directly connected to the device servers, other equipment use field busses or Ethernet to connect the front-end electronics to the device servers. Programmable Logic Controller (PLC) and 'intelligent' devices, e.g. magnet power supplies, are examples of stand-alone units. They introduce a further level of computers in the system. If a front-end has to run stand-alone in case of a network problem, it should have a direct connected disk or must have the program and data files in memory. A huge number of devices can reduce the overall up-time of the machine. Malfunctions of a single device should not stop machine operation. A fault-tolerant or redundant layout must be used. The organisation depends very much on the individual device type. Low level RF systems for the klystrons can be grouped to serve one klystron only. A single failure would switch off the cavities of one klystron only and the machine could continue to operate. In order to be able to analyse, understand, and optimise all details of the machine a fast data acquisition system must be provided. This requires all front-end electronics including ADC and bus systems to be able to process the linac data with 5 Hz rate and single bunch resolution. The network has to provide the necessary bandwidth to transfer the data to a central diagnostic archive.

8.9.2   Network

Devices servers connect to the group servers via standard local area networks (LAN). The devices get their timing and synchronisation signal on a dedicated network and the machine protection system is connected to a further separate line. Standard LAN technology is also used in the links between the servers and all client processors. Clients are distributed in the control room, the tunnel and the offices. And the whole network is connected to the DESY and outside nets. Networks between the consoles, group servers and front-end servers will be based on standard LAN technology. This is today the 100 Mbit Ethernet. The servers in the middle layer should be connected by a faster network i.e. about 1 to 10 Gbit/s. All these network components are or will be standard items from many suppliers and can easily be integrated in the control system since they are based on the TCP/IP communication.

Remote configurability and maintainability is mandatory. For the long distances fibre optical links will be used to prevent ground loops and to isolate the subsystems. Local connections use less expensive twisted pair cabling to the active hubs that link to the fiber optics. In order to keep the network load low and reliable, the network is switched and redundant with two parallel lines to the front-end distributions.

During the installation and maintenance of all components of the machines, mobile terminals will be used. These terminals connect to the standard network and allow access to all devices in the system. A wireless network should be used in order to be more flexible and to save installation costs compared to a wall plug system. Such a wireless system will be used for audio communications i.e. telephones also. It can be based on the UMTS standard. A few receivers/transmitters inside the tunnels will connect the terminals to the controls network and telephone system.

8.9.3   Software

Throughout the development time of the software for the machines the computer industry will introduce a lot of new products. A main challenge for the design will be to create the software modular with good interfaces to allow easy migrations to new environments. Modular means that some submodules must be changeable without interference with other part. It also means to design reusable objects. The 'heart' of the control system is the communication protocol. All client and server programs communicate by it. Requirements are:

- must be based on standard protocols on top of TCP/IP

- has to transport a well defined set of data objects

- needs to convert the data between different computer architectures

- provides common methods e.g. translations of the data structures

- access to all data (including archived data) of devices in a consistent way

- interface to standard desktop applications like spread sheets and to special controls applications

- has to provide an on-line names service to query existing devices and their properties

- defines a unique way for names of device addresses and their parameters

- provides access to data from other systems

Whenever possible standard industrial components should be used for front-end hardware up to the display programs. And the software should be designed with the common tools and programming languages. Our experience in the TTF control system showed that object oriented languages (like C++) are adequate design environments to create reusable modules. Object orientation leads to a clean frameworks and follows the industrial paradigm. In addition to apply object orientation, an implementation on more than one computer platform leads to a better design and helps migrating to new operating systems. A good design with standard methods allows to create generic programs. These programs don't have to be modified in a changing environment. They allow access to all devices in a standard way and therefore, can save software investment.

8.9.4   Machine Protection System

The complete accelerator complex and the various beam transfer and delivery lines etc. have to be equipped with a machine protection system to prevent beam operation e.g. in case of technical failures. The machine protection system is an independent alarm system. It is remotely controlled, configured and read out by the main accelerator control system. The structure of the machine protection system follows the structure of the TESLA complex having separate section permits for the different machine sections. The section permits can change from pulse to pulse and must exist for all sections the beam will pass in a pulse. The machine protection system acts on the gun, the ejection elements of the damping rings and on the various beam abort kickers. It reacts to trigger events, e.g. from beam loss detectors, beam current measurements, RF systems, collimators and spoilers, vacuum valves, etc. The remaining beam pulse after a trigger event should be as short as possible. To prevent for example the damage of spoilers or collimators of the beam delivery system the beam has to be re-directed to the final beam dump within a few microseconds. The machine protection system consists of distributed interlock modules. These interlock modules have digital I/O channels and interfaces to a redundant fibre-optic alarm line as well as to the main Ethernet network. It is desirable to use industrial interface chips or boards. An embedded CPU running for local control, self-testing, error logging, configuring of I/O channels and trigger events to react on etc. should be integrated.

Bibliography

[1] F. Wenzel, W. Blübaum, S. Szaktilla, *Die Rellinger Kirche: Gutachten über den statisch-konstruktiven Zustand und über mögliche Auswirkungen des Tunnelbaus für einen neuen Linearbeschleuniger*, Wenzel · Frese · Pörtner · Haller, Büro für Baukonstruktionen, Karlsruhe, Oktober 1999.

[2] *Baugrunduntersuchungen im Bereich der Rellinger Kirche*, Grundbauingenieure Steinfeld und Partner GbR, Hamburg, September 1998.

[3] R. Windels, G. Timm, K. Morgen, *Planung eines Linearbeschleunigers: Vorstudie ber die baulichen Anlagen*, Windels · Timm · Morgen, Beratende Ingenieure VBI, Hamburg, Februar 1997.

[4] *Staatsvertrag über die Schaffung der planerischen Voraussetzungen für die Errichtung und den Betrieb eines Linearbeschleunigers*, Hamburgisches Gesetz- und Verordnungsblatt, Juli 1998

[5] *Umweltverträglichkeitsstudie für TESLA*, Planungsgruppe Ökologie + Umwelt Nord, Hamburg, to be published in 2001.

[6] *Hydrogeologisches Fachgutachten: Stufe 1*, Grundbauingenieure Steinfeld und Partner GbR, Hamburg, September 2000.

[7] A. Leuschner, S. Simrock *Radiation Field inside the Tunnel of the Linear Collider TESLA*, DESY internal report D3-113, 2000.

[8] R. Brinkmann, G. Materlik, J. Rossbach, A. Wagner, *Conceptual Design of a 500 GeV e^+e^- Linear Collider with integrated X-ray Laser Facility*, DESY 1997-048 (1997), ECFA 1997-182 (1997).

[9] G. Baur, A. Leuschner, *Bethe-Heitler Cross-Section for Very High Photon Energies and Large Muon Scattering Angles*, Eur. Phys. J. C. 8 (1999) 631.

[10] K. Tesch, *Production of Radioactive Nuclides in Soil and Groundwater Near the Beam Dump of the Linear Collider*, DESY Internal Report D3-86 (1997).

[11] K. Tesch, H. Dinter, *Production of Radioactive Nuclides in Air Inside the Collider Tunnel and Associated Doses in the Environment*, DESY Internal Report D3-88 (1998).

[12] A. Leuschner, K. Tesch, *Muon Doses at Earth Surface Above the Linear Collider*, DESY Internal Report D3-89 (1998); G. Baur, A. Leuschner, K. Tesch,*Muon Doses at Earth Surface above the Linear Collider: Improved Calculations*, DESY Internal Report D3-91 (1998).

[13] A. Leuschner, K. Tesch, *The Residual Radioactivity of Water-copper Beam Dump for the TESLA Test Facility*, DESY Internal Report D3-92 (1998).

[14] H. Dinter, A. Leuschner, K. Tesch, D. Dworak, J. Loskiewicz, *Calculation of Hadron Yields around Thick Targets and Doses behind Concrete Shielding of High Energy Electron Accelerators*, DESY Internal Report D3-95 (1999) and Nucl. Instr. Meth. **A455** (2000) 460.

[15] H. Dinter, *Radiologische Auswirkungen auf die Umwelt beim Betrieb des Linear Colliders*, DESY Laboratory Note D3-97 (1998).

[16] B. Racky, H. Dinter, A. Leuschner, K. Tesch, *Radiation Environment of the Linear Collider TESLA*, DESY Laboratory Note D3-98 (1998).

[17] H. Dinter, *Abschirmung des Linear Collider TESLA im Bereich der Kryohallen*, DESY Laboratory Note D3-99 (1999).

[18] A. Leuschner, K. Tesch, *Production of tritium in the liquid helium of the TESLA Linear Collider*, DESY Laboratory Note D3-101 (1999).

[19] H. Dinter, A. Leuschner, *Induced radioactivity and dose rates in the vicinity of a collimator at the Linear Collider TESLA*, DESY Laboratory Note D3-104 (1999).

[20] A. Leuschner, B. Racky, *A Ventilation Concept for Activated Air in the TESLA Tunnel*, DESY Laboratory Note D3-104a (2001).

[21] Technischer Überwachungs-Verein Nord e.V., *Gutachten über radiologische Arbeiten für den Linear Collider TESLA*, Nr. 50-98-004 (1998).

[22] Öko-Institut e.V., *Radiologische Auswirkung des Linear Collider Projekts des Deutschen Elektronen-Synchrotrons (DESY) auf die Umwelt*, Darmstadt (1999).

[23] N. Tesch, *Soil, Groundwater and Cooling Water Activation at the TESLA Beam Dump*, DESY Laboratory Note D3-114 (2001).

[24] N. Tesch, *Activation and Fluxes at the TESLA Positron Source*, DESY Laboratory Note D3-115 (2001).

[25] B. Petersen, S. Wolff, *Numerical Simulations of Possible Fault Conditions in the Cryogenic Operation of the TTF/FEL and TESLA Linear Accelerators*, Proceedings International Cryogenic Engineering Conference ICEC 18, p. 67, February 2000, Mumbai, India, Narosa Publishing House, New Delhi.

[26] P. Clay et al., *Cryogenic and Electrical Test Cryostat for Instrumented Superconductive RF Cavities (CHECHIA)*, Adv. in Cryogenic Engineering, Plenum Press, New York (1996), Vol. 41 a, p. 905.

[27] W. D. Möller, B. Petersen, B. Sparr, *A Proposal for a TESLA Accelerator Module Test Facility*, DESY TESLA-01-08, 2001.

[28] G. Grygiel et al., *Status of the TTF Cryogenic System*, Adv. in Cryogenic Engineering, Plenum Press, New York (1996), Vol. 41 a, p. 847.

[29] W. D. Möller, B. Petersen, B. Sparr, *A Proposal for the Cryogenic Supply of a Single TTF/FEL-Cryomodule Test Bench*, DESY TESLA-01-09, 2001.

[30] T. H. Nicol et al., *TESLA Vertical Test Dewar Cryogenic and Mechanical Design*, IEEE Proceedings of the 1993 Particle Accelerator Conference, Vol. 2, p. 989, Piscataway, N.J., 1993.

9 Free Electron Laser and its Sub-Systems

9.1 Introduction and Overview

9.1.1 Introduction

Most of the information humans receive from their environment is carried by light. Thus it is not surprising that also for research in natural sciences photons not only in the optical regime but ranging from radio frequencies to hard γ-rays are among the most important tools to study nature. For the photon range beyond the narrow optical spectral window up to the hundred keV γ-regime synchrotron radiation has provided over the past forty years an increase in flux and brightness by more than ten orders of magnitude. The development of storage rings including special magnetic components, called wigglers and undulators, has led to third-generation machines specially designed for synchrotron radiation research, which are exceeding by far their design goals. This illustrates impressively how successful accelerator technology has become today.

Most recent successes in development of linear accelerators have opened the route to a new quantum jump in photon source quality. The progress of the various Linear Collider R&D projects over the last years not only forms the basis for the construction of a Linear Collider, but it also contributes significant knowledge on how to build a Free Electron Laser (FEL) at wavelengths much shorter than the visible. The reason is that for both instruments it is crucial to generate and accelerate electron beams of unprecedented quality. Taking into account the progress in other fields of accelerator technology (such as the development of photoinjectors and advanced undulators), it now seems possible to construct such a laser (called XFEL for short in this report) providing coherent X-ray radiation at spectacular brilliance. Rapid progress was achieved during the past years in successfully proving the required FEL process at $12\,\mu$m (1998) [1], $530\,$nm (1999) [2] and $108\,$nm (2000) [3] thus demonstrating that the theoretical concepts and crucial accelerator technologies are well under control.

The basic principle [4] makes use of the fact that an electron beam of sufficient quality, passing a long undulator magnet, amplifies an initially existing radiation field, if the photon wavelength λ_{ph} matches a resonance condition determined by undulator parameters and the beam energy:

$$\lambda_{ph} = \frac{\lambda_u}{2\gamma^2}(1 + K_{rms}^2) \qquad (9.1.1)$$

Here, γ is the electron energy in units of its rest mass, λ_u is the undulator period, $K_{rms} = eB_u\lambda_u/(2\pi m_e c)$ is the undulator parameter, and B_u is the rms magnetic field in the undulator. Due to the interaction between the radiation field and the electron

bunch in presence of the magnetic field of the undulator, a density modulation (micro-bunching) of the electron bunches at the electro-magnetic wavelength builds up, which enhances the power and coherence of radiation during the passage of the bunch through the undulator. In this "high-gain mode" [5, 6, 7], the radiation power $P(z)$ grows exponentially with the distance z along the undulator:

$$P(z) = AP_{in} \exp\left(2z/L_g\right) \quad , \tag{9.1.2}$$

where L_g is the gain length for the electro-magnetic radiation field, P_{in} is the effective input power, and the constant A is equal to $1/9$ in one-dimensional FEL theory with an ideal electron beam [6, 7].

If the desired wavelength is very short, one can, instead of providing the "initially existing radiation field" by a conventional laser, consider the undulator radiation radiated spontaneously in the first part of the undulator as an input signal, see figure 9.1.1.
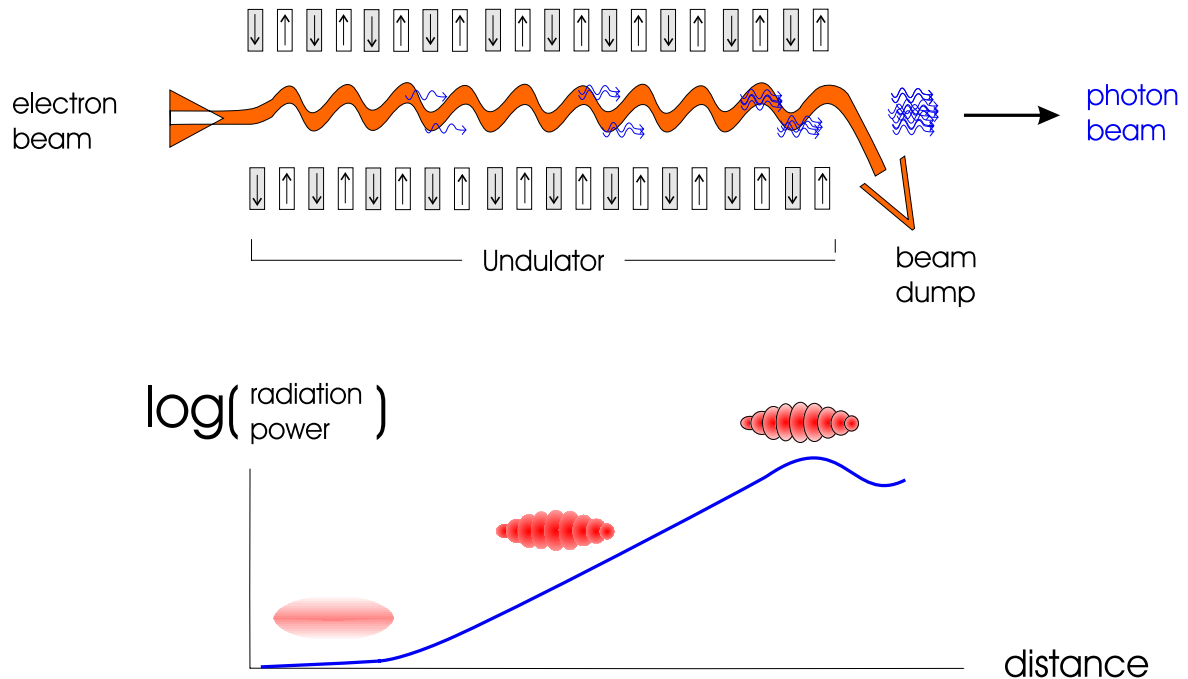
Figure 9.1.1: *Schematic Diagram of a Single-Pass Free Electron Laser (FEL) operating in the Self-Amplified-Spontaneous-Emission (SASE) mode. The bunch density modulation ("micro-bunching"), growing up in parallel to the radiation power, is schematically shown in the lower part of the figure. Note that in reality the number of slices is much larger.*

This principle of Self-Amplified-Spontaneous-Emission (=SASE) [8, 9] does not require the optical cavity resonator normally used in multi-pass, longer wavelength FELs and can hence deliver light with wavelengths down to the Ångstrøm regime, where optical mirrors are ineffective. One expects a transversely fully coherent beam, larger average brilliance and, in particular, a pulse length of about 200 fs FWHM with

eight or more orders of magnitude larger peak brilliance [1] compared to state-of-the-art synchrotron radiation sources, see figure 9.1.2. The peak power is of the order of 100 GW. As the SASE FEL is completely independent of atomic excitation levels, it can be tuned over a wide range of wavelengths. This tunability was recently demonstrated at the TESLA Test Facility in the wavelength range between 80 nm and 180 nm [10], see section 9.2.

If we assume undulator periods of the order of a few centimetres, eq. 9.1.1 requires multi-GeV electron energies to achieve photon wavelengths in the Ångstrøm regime. A high energy is also required to sufficiently reduce the beam emittance provided by the injector. Hence the electron accelerator required for an XFEL would be a major investment. The most cost-effective solution is to use the the linac of the linear collider. In addition there is a large overlap of the considerable expertise required to construct, commission and operate the two facilities. Last but not least, a large laboratory site will be needed to accommodate the various user facilities. In conclusion, there are good reasons for combining an XFEL facility into a linear collider installation [11], which is possible without serious mutual interference (see below).

For an XFEL, electron beam properties like high phase space density and bunch charge, small energy spread, and, as requested by many users, large average beam current (see part V) are essential. A superconducting, low frequency accelerator is the ideal device to produce such a beam. It provides very good beam quality, because each electron bunch extracts only a small fraction of the large energy stored in the big cavity volume (small beam loading and small wakefield effects, see section 3.2). Due to the low losses in the superconducting niobium cavities, large beam currents can be accelerated at high power efficiency. In addition, because of the possibility to accelerate long bunch trains and since its duty cycle of 1% is orders of magnitude larger than it could be with a normal conducting linac, a large variety of timing patterns can be realized, see section 9.1.4 and figure 9.1.6.

The present chapter discusses all accelerator components and accelerator physics issues specific to the XFEL at TESLA. Accelerator components used by both the High Energy Physics and the XFEL, in particular the superconducting accelerator, its performance and its infrastructure, are presented in chapters 3 and 8.

---

[1] For partially coherent light sources (wigglers and undulators) the brilliance is calculated from the spectral flux divided by the photon beam sizes and divergences, convoluted with the electron beam sizes and divergences:

$$spectral\ brilliance = \frac{spectral\ flux}{4\pi^2 \cdot \sum_x \cdot \sum_x' \cdot \sum_z \cdot \sum_z'}; \quad \sum = \sqrt{\sigma_e^2 + \sigma_{ph}^2}, \sum' = \sqrt{\sigma_e'^2 + \sigma_{ph}'^2}$$

For fully coherent sources (FELs) it is the spectral flux divided by the transverse photon phase space volume:

$$spectral\ brilliance = \frac{spectral\ flux}{(\lambda/2)^2}$$
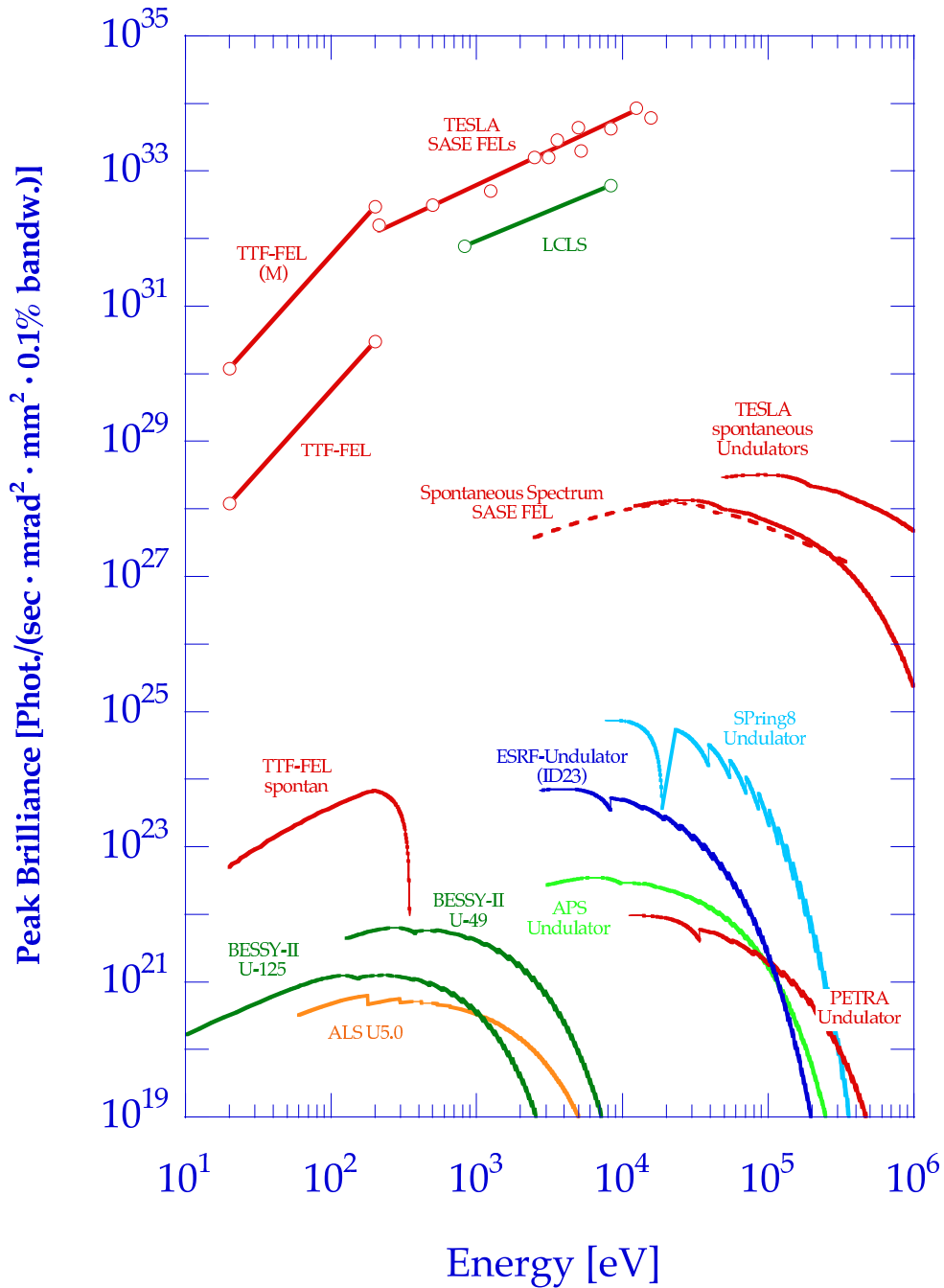
Figure 9.1.2:   *Spectral peak brilliance of X-ray Free Electron Lasers (XFEL) and undulators for spontaneous radiation at TESLA, in comparison with third-generation synchrotron radiation sources. For comparison, also the spontaneous spectrum of an XFEL undulator is shown. The label TTF-FEL indicates design values for the FEL at the TESLA Test Facility, with (M) for the planned seeded version. First lasing was demonstrated at TTF FEL in the year 2000 at 11 eV photon energy, and a peak brilliance of $(6 \pm 4) \cdot 10^{25}$ in the above units has been achieved up to now.*

The production of FEL and spontaneous undulator radiation is discussed in part V, together with the scientific case, photon optics issues, FEL physics and civil engineering for the FEL laboratory. Although undulators are discussed in part V, the present chapter also includes a synoptic version of the undulator chapter for the convenience of those readers particularly interested in technology issues.

9.1.2 General layout

The FEL laboratory building is located at the new campus close to the collider inter-action region. The electron beam is extracted from the regular acceleration structure at the desired energy level and then transferred by a long beam transport line parallel to the linac, until it is deflected into the X-ray experimental area, see figure 9.1.3 and section 9.6.
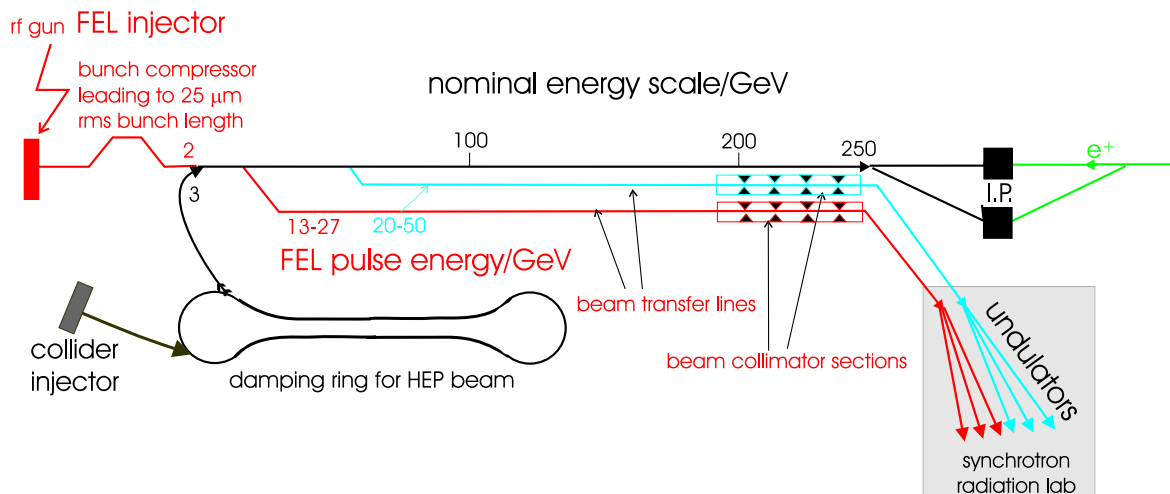
Figure 9.1.3: *Sketch of a coherent X-ray source laboratory based on the TESLA linear collider installation. The XFEL electron beam is produced by a dedicated injector followed by a sequence of bunch compressors. The beam can in principle be extracted at any energy between 2 and 250 GeV and is transferred inside the linac tunnel to the X-ray lab located close to the interaction points (I.P.). Multiple extraction lines can be utilised in parallel, so that various beam energies are available in the X-ray lab quasi-simultaneously. In the present design, two beam lines with electron energies up to 50 GeV are foreseen.*

Several such extraction lines can be built in parallel, so that various beam energies can be made available in the XFEL laboratory quasi-simultaneously. The scientific requirements (presented in part V) can be satisfied with 30 GeV maximum electron beam energy. Since the cost increase is very small, one of the electron beam transport lines is designed for a max. energy of 50 GeV in case new experiments require this energy in future. Thus, our design provides two beam lines for energies between 13 - 27 GeV and 20 - 50 GeV, respectively. The 800 m long beam collimation system (see section 9.6.4) which protects the undulators from radiation damage is also part of the

transfer line. 900 meters before the XFEL laboratory, these beams are deflected into a 4 m diameter tunnel, thus separating the beams from the linac tunnel.

At the end of the extraction tunnel, a beam switchyard is foreseen distributing the beams to different undulators, see figure 9.1.4 and section 9.8.
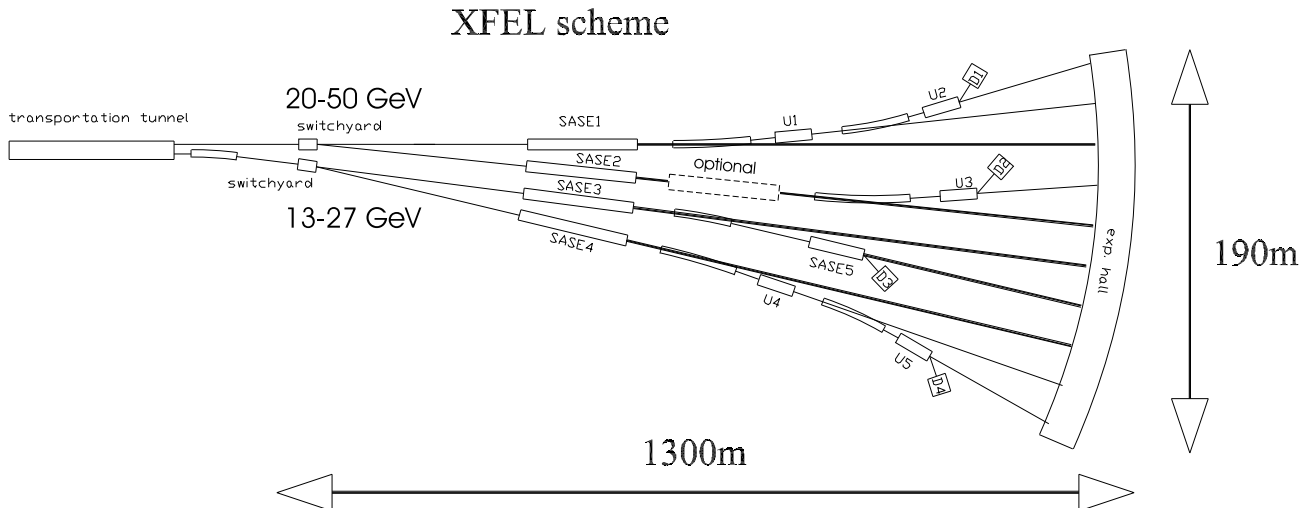
Figure 9.1.4:   *Beam switchyard distributing two electron beam lines of different energies to various undulators. SASE1 through SASE5 are FEL undulators while U1 through U5 are undulators for spontaneous radiation. The scheme sketched can be extended to serve many more undulators. It displays also the long drift lines necessary for the photon beams.*

Having left the FEL, the quality of the electron beam is still very attractive, so that it is passed through another FEL or through further undulators generating spontaneous radiation. As described in section 9.6, all electron beam transfer lines have been designed with large bending radii (> 2000 m for the 50 GeV branch) in order to keep degradation of beam quality due to quantum fluctuation of spontaneous synchrotron radiation in these bends in tolerable limits. The over-all size of the XFEL lab is determined by the length of the electron beam switchyard, the length of FEL undulators, and by several hundred meters of drift lines for the intense photon beams to let them grow by their natural divergence until they can be handled by the first optical elements. Including the actual experimentation area, a total length of 1300 meters is required.

While the linac tunnel is about 20 meters below ground, there is no problem to build the XFEL lab above ground or at a more moderate depth. The present design has been optimised taking into account civil engineering costs, radiation shielding requirements, and environmental considerations.

9.1.3   Combined operation for collider and XFEL

Due to the large accelerating gradient foreseen, only pulsed RF operation is possible for both technical and economical reasons. Thus, the electron pulse structure consists of

trains of electron bunches, repeated at the linac repetition rate of 5 Hz. It is proposed to run in an interleaved pulse mode, where RF pulses for high-energy physics and those for X-ray physics alternate, as shown in figure 9.1.5. This means that the first part of the electron linac which is used for both XFEL and collider pulses, operates at a total repetition rate of 10 Hz, and dipole magnets pulsed at 5 Hz extract the XFEL electron beam from the main linac at the desired beam energy.
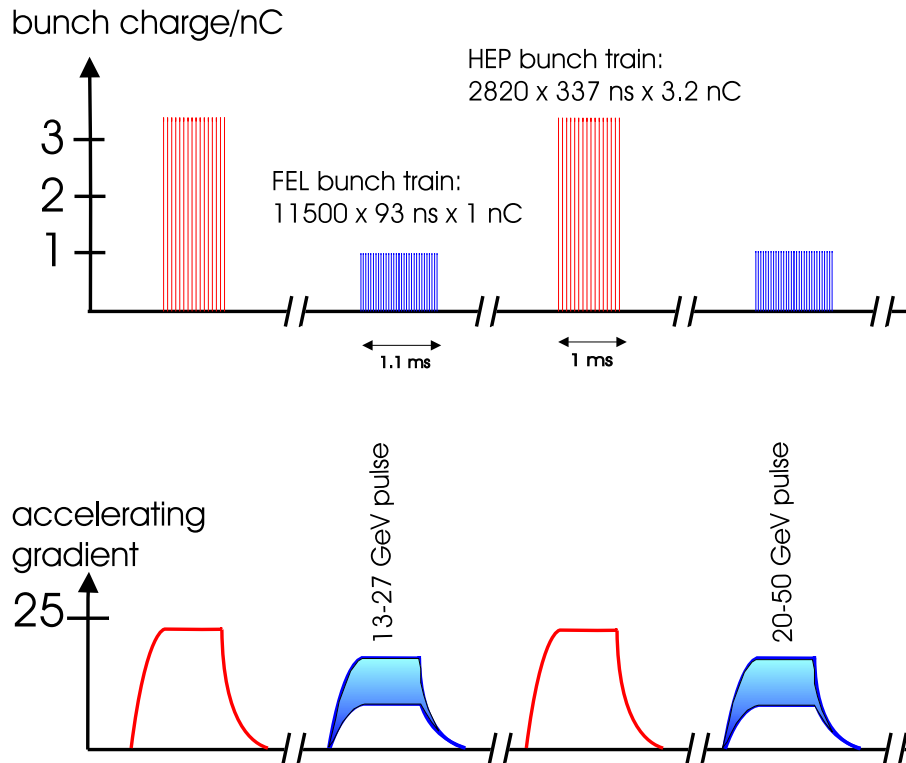
Figure 9.1.5:   *TESLA pulse structure for combined high energy physics (HEP) and XFEL operation.*

   The proposed pulse structure for combined high energy physics (HEP for short) and XFEL operation minimises the interference between beam properties for HEP and XFEL physics, and all pulsed magnets required to switch beam lines can be made slow. In particular, the beam energy of the XFEL pulse in each extraction line can be varied from pulse train to pulse train within a range determined by the tuning speed of the extraction beam line magnets, and is independent of the collider energy. The basic operation mode could be that both XFEL electron beam lines are fed alternately by full bunch trains, so that both the 27 GeV and the 50 GeV branch are actually operating at 2.5 Hz. Note that such an operation mode consisting of alternating beam pulses for HEP and X-rays is different from joint use of HEP storage rings by synchrotron radiation users: Both users can define beam properties like energy, emittance, current, time structure, etc. of their electron pulse independent of each other to a very large

extent, since they use different injectors and since it is feasible for RF components to change power and pulse length from pulse to pulse.

In principle, both pulse length and repetition rate of the XFEL pulse could be increased within a certain limit, but one should keep in mind that, already in this scheme, the *average* electron beam power of the XFEL pulse alone is of the order of 2 MW, resulting in AC power consumption of roughly 6 MW, see Table 9.1.1. In the context of power efficiency it is certainly an advantage of TESLA that the AC power for compensation of the static cryogenic losses have to be invested anyway for the collider pulse, so that the overall power efficiency for the XFEL electron beam pulse can be made as large as 28%. This optimum efficiency occurs at 18 MV/m accelerating gradient.

Variable	Unit	Value
Linac Parameters		
optimised gradient for XFEL operation	MV/m	18
linac repetition rate f_{rep} for XFEL	Hz	5
bunch length (rms)	fs	80
bunch spacing	ns	93
number of bunches per train		11500
bunch train length	μs	1070
bunch charge	nC	1
normalised emittance at undulator entrance	mrad mm	1.6
uncorrelated rms energy spread	MeV	5.1
RF duty cycle	%	0.5
average electron beam power (27 GeV branch)	MW	≤ 0.8
average electron beam power (50 GeV branch)	MW	≤ 1.4
over-all power efficiency AC to electron beam	%	28
FEL Parameters		
typical saturation length	m	100 - 220
photon energy range	keV	0.2 - 12.4
photon beam power range	GW	20 - 100
number of photons per bunch	10^{12}	1 - 20
typical photon beam divergence (rms)	μrad	1
typical photon beam diameter (rms)	μm	20

Table 9.1.1:   *Key parameters for XFEL operation with TESLA. More detailed tables on XFEL operation are given in part V.*
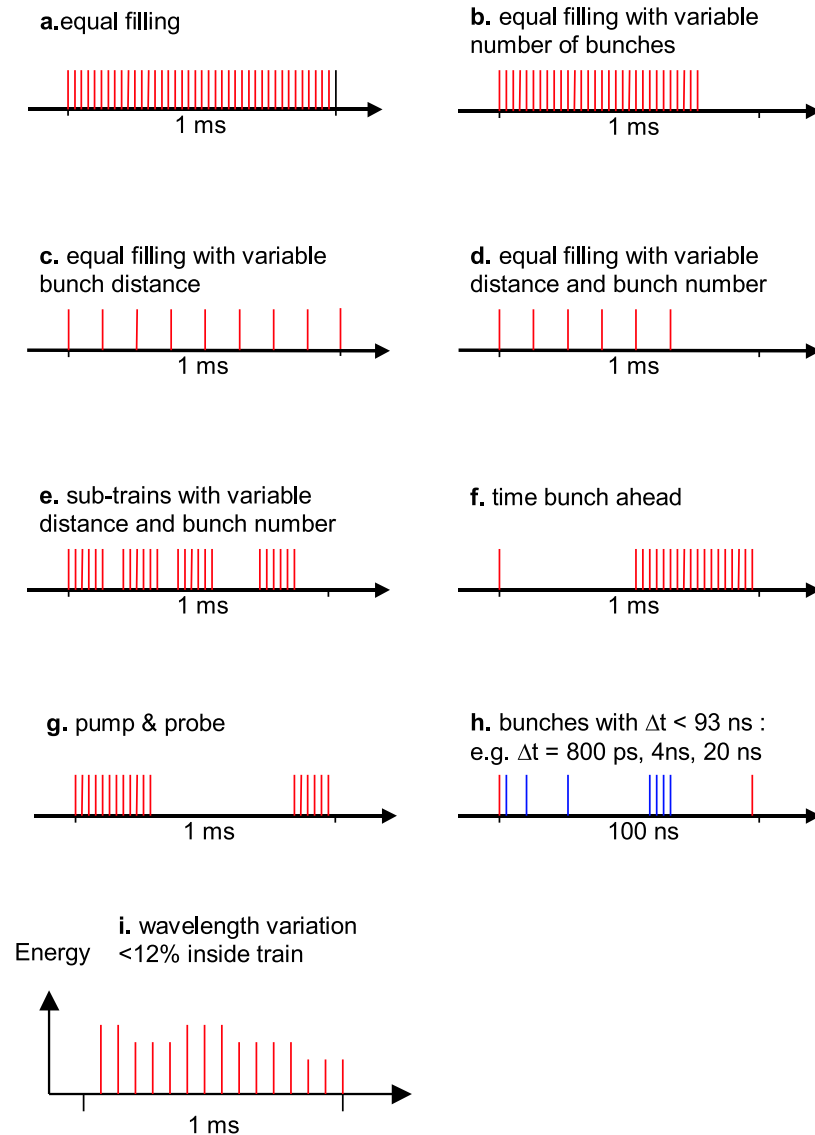
Figure 9.1.6: *Possible pulse train patterns for the TESLA XFEL.*

9.1.4 Pulse pattern and energy variation

There is considerable flexibility in choosing the bunch-to-bunch spacing inside the pulse train, the fundamental limitation only given by the RF period of 770 ps. Figure 9.1.6 illustrates some of the possibilities. The distribution of bunch trains among different undulators can be done in many ways. To be specific, in this report the most straightforward solution is presented, namely a dipole magnet pulsed at 1.25 Hz located in the "switchyard" (see figure 9.1.4) of each electron transfer line. It directs every other electron bunch train into a second branch of undulator lines, so that each undulator actually receives bunch trains of full length at 1.25 Hz repetition rate. Each of the four resulting electron beam lines ends into its own beam dump, see figure 9.1.4 and section 9.9.

The distribution could alternatively be done by either fast kicker magnets, by deflecting-mode-cavities synchronised with the accelerating RF [13], or by subharmonic cavities followed by a dispersive section. Each of these systems has different capabilities with respect to the pulse structure delivered to the respective users, so the choice will be made depending on the user requirements. Space is reserved in the switchyard area to keep this choice open. Naturally, the procedure of bunch train distribution reduces the average brilliance to be generated by each undulator, but the peak brilliance remains untouched. Note also that even if the pulse train is distributed among many undulators, the average brilliance from *each* undulator will still be three or more orders of magnitude higher than at state-of-the-art 3rd generation synchrotron radiation sources.

In principle, the linac is capable of rapidly changing the beam energy from RF pulse to RF pulse. Even within each bunch train some well-controlled energy variation is possible. However, changing the beam energy by a large amount requires also adjustment of magnet settings in the transfer lines which typically takes a few minutes. To keep the possibility of very fast tuning within at least a small energy range, the entire electron beam lines are designed such that within a $\pm 3\%$ momentum bandwidth there is only small emittance dilution due to chromatic and dispersive mismatch, see section 9.6. Consequently, the wavelength can be tuned within 12% range at a speed only limited by RF regulation, without any adjustment of magnet settings, and beyond that range with a time constant of minutes. In addition, wavelength tuning by undulator gap variation is foreseen, see section 9.8.

9.1.5   Electron beam parameters

Choice of injector   While the electron beam size delivered from a radiation damping storage ring perfectly matches the requirements of the collider pulse, such a beam cannot be utilised for an XFEL. A beam with smaller horizontal emittance and much smaller longitudinal emittance is required, which can be provided by an RF photocathode gun. With the present state of technology of RF guns, an XFEL could be made operating in the several Ångstrøm range. Anticipating improvements in gun performance by about a factor of 4 in terms of minimum emittance, a normalised emittance of less than $\epsilon_n = 0.8\,\mathrm{mrad}\,\mathrm{mm}$ (for $1\,\mathrm{nC}$ bunch charge) and a longitudinal emittance of $26\,\mathrm{keV}\cdot\mathrm{mm}$ becomes feasible, see section 9.3. It is important to understand that in a linac the *normalised* emittance ϵ_n is a conserved quantity (provided wakefield and space charge effects are small, see below), so that the *geometrical* emittance ε (which determines the diffraction limit) decreases linearly with energy: $\varepsilon = \epsilon_n/\gamma$, $\gamma = E/m_0 c^2$ being the relativistic factor. In contrast, the geometrical emittance of a storage ring is not determined by initial conditions but by quantum fluctuation effects and *increases* with the square of the energy. This dependence limits the generation of high-energy, very low-emittance beams in storage rings and makes, together with peak current limitations in storage rings, circular machines unsuitable for XFELs.

Bunch compression In order to achieve laser saturation within a single passage, XFELs require peak currents of a few kiloamperes. Because of space charge effects, such high currents cannot be generated directly in the RF gun cathode without blowing up the transverse emittance. Instead, a 20 ps long beam with 50 A peak current is produced, accelerated, and longitudinally compressed by a factor of 100. This compression takes place in several steps at different energies, see section 9.4.

Bunch compressors are beam line sections which longitudinally compress the bunch using path length differences in a magnetic chicane. Although simple in first-order theory, the physics of bunch compression becomes very challenging if collective effects like space charge forces and wakefields (so-called coherent synchrotron radiation forces, CSR) are taken into account [15, 16]. Considerable progress has been made during recent years on detailed understanding (including computer simulation) of transverse and longitudinal electron beam properties in presence of these forces [43]. In particular, bunch compression has been performed and analysed at the TESLA Test Facility, proving the validity of computer modeling tools, see section 9.2. The actual design of the bunch compressor sequence for the TESLA XFEL is determined to a large extent by a careful balance of CSR effects, see section 9.4.

Wakefields Wakefields are electro-magnetic fields (transverse or longitudinal) generated by the interaction of the electron bunch charge with the vacuum chamber. Bunch compression requires perfect control of the longitudinal energy distribution inside each bunch. For very short bunches, this energy distribution is distorted or even dominated by longitudinal wakefields. Wakefields of bunches as short as 25 μm have never been measured and are challenging to predict.

Fortunately, the wakefields in the low-frequency accelerating structures of TESLA are quite small in comparison with higher-frequency linacs, which is certainly an argument in favour of a superconducting accelerator like TESLA, as mentioned before (see also section 3.2).

Wakefields in the beam transfer lines are discussed in section 9.7. Their main effect is a systematic variation of beam energy along the longitudinal position within each bunch, sometimes called correlated energy spread. A considerable correlated energy distribution due to wakefields exists at the entrance of the undulators, see table 9.1.2, where the contributions of beam line sections are listed. Figure 9.1.7 shows the accumulated longitudinal wake potential at the undulator entrance. Within $\pm 1\,\sigma$ longitudinal distance from the bunch centre, there is a $\pm 20\,\mathrm{MeV}$ correlated energy distribution. In contrast to uncorrelated energy spread present within each longitudinal slice of the bunch (i.e. present in each micro-bunch, see figure 9.1.1), such a correlated energy distribution is not necessarily a problem for FEL operation, but it nevertheless widens the linewidth of the XFEL beam because such electron beam "chirp" is transferred into a photon beam chirp, see eq. 9.1.1. On the other hand, the chirp (at least the linear part of it) might be used for a further photon beam compression. It can also be used to compensate partly the wakefields which grow during the passage of the bunch through the undulator due to the resistivity and the surface roughness of the vacuum chamber (see section 9.7). It should be noted that the bunch compressor design leaves some

flexibility in the amount of the energy chirp by appropriately setting the initial RF phase, thus being able to respond to requirements on FEL operation, on user requests, or on beam parameter variation.
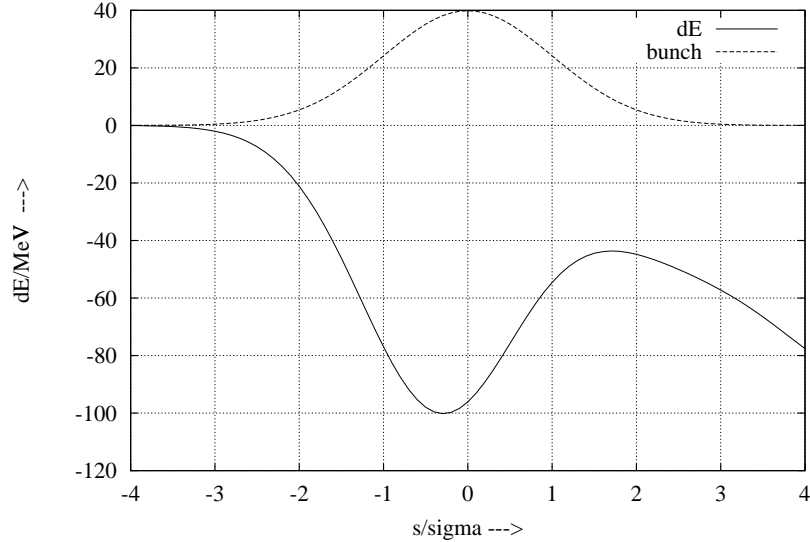
Figure 9.1.7:   *Accumulated longitudinal wake potential at the undulator entrance versus the longitudinal position s (in unit of rms bunch length) inside the bunch. The broken line indicates a Gaussian bunch profile with $\sigma = 25\,\mu m$ bunch length (1 nC charge) which was used in the calculation. The bunch tail is to the right.*

Transverse emittance   The RF photoinjector produces a round beam, just as it is needed for the FEL. Compared to the HEP beam (provided by the damping ring), the FEL beam emittance is smaller in the horizontal plane, but much larger in the vertical. It has been demonstrated in section 3.2 that the tiny vertical emittance of the HEP beam can be preserved in the linac, hence emittance in the linac is not an issue for the FEL beam. However, as mentioned above, there will be emittance growth in the bunch compressors and in the beam transfer lines, and chromatic effects due to the strong longitudinal wakefields might occur.

Similar to the energy spread, emittance growth within each slice of the bunch is much more dangerous to the FEL process than a slice-to-slice variation of the slice-centroid transverse position. The latter leads to growth of the over-all emittance projected along the longitudinal coordinate, which is the quantity normally determined by emittance measurement techniques. As seen from table 9.1.2, our simulation codes predict a slice emittance of 0.9 mrad mm at the entrance of the undulator, while the projected emittance becomes as big as 2.6 mrad mm, mainly due the coherent synchrotron radiation (CSR) in the bunch compressors. Note that the contributions to emittance growth (both slice and projected) downstream from the bunch compressors are all below 1% and are thus neglected in table 9.1.2.

Since the slice emittance determines the required undulator length to a large extent, we believe a conservative approach is appropriate for the assumption on this key parameter. We therefore allow for a considerable contingency margin and assume 1.6 mrad mm slice emittance at the undulator entrance. This choice guarantees that a major part of the bunch reaches saturation in the FEL process. It takes also into account that for commissioning and tuning of the machine experimental verification of the slice emittance will be needed, but will be difficult to measure precisely if it is much smaller than the projected emittance.

Section	driving effect	slice/projected emittance [mrad mm]	slice/ correlated energy spread	energy loss	bunch length (rms)
Cathode	therm. emitt.	0.65/0.65			1.7 mm
Injector	space charge	0.7/0.8	15/0 keV		1.7 mm
Compressor	CSR	0.9/2.6	2.5/0 MeV		25 μm
Main linac	geometric wake	"	2.5/<19 MeV		"
Transfer line	resistive wake	"	2.5/5.9 MeV	12 MeV	"
Transfer line	roughness wake	"	2.5/25 MeV	7.7 MeV	"
Elevation	resistive wake	"	2.5/8.6 MeV		"
Undulator	resistive wake	"	2.5/12 MeV	2.9 MeV	"
Undulator	roughness wake	0.9/2.6	2.5/14 MeV	12 MeV	25 μm

Table 9.1.2: *Development of electron beam parameters along the beam line. In the undulators there are, in addition to resistive and roughness wakes, further contributions to the energy spread and energy loss, depending on undulator parameters and beam energy. These contributions are intimately related to the radiation process and are thus discussed in part V. For wakefields in the main linac, see also section 3.2.*

9.1.6 Undulators

The undulator length L_u required to reach the FEL saturation increases with decreasing photon wavelength. Most XFEL parameter sets call for L_u of at least 100 m. A high field quality (or corresponding correction elements) is required to guarantee, for instance, that the electron beam centroid does not depart from a straight line by more than 10 μm within some 10 meters of undulator length. Finally, a periodic quadrupole focusing lattice has to be superimposed to achieve the small beam diameter required. Such an undulator has not yet been built, and it is believed that one should proceed step by step towards the challenging goal [17, 18]. All undulators are designed for variable gap to permit maximum wavelength tuning flexibility for users.

A very attractive alternative to planar undulators are helical undulators. They radiate circularly polarized photons, which are of interest for some users, and they can

be shorter than planar devices. Section 9.8 contains a synoptic description of concepts
and technology of XFEL undulators while more details can be found in part V. Finally
it is noted that here is again a common interest with the linear collider in terms of
technology. As discussed in section 4.3, a 100 m long planar undulator or a 150 m long
helical undulator is needed for the high brilliance positron source.

9.1.7   FEL Theory and Photon Beam Properties

The prediction of the photon beam parameters of an X-ray FEL is based on an elaborate
theory and on various computer codes. Table 9.1.1 contains only a few numbers on
the expected FEL performance, a much more detailed discussion is given in part V, as
well as a justification for the choice of design parameters. The values quoted on the
FEL performance should be used as a guideline only, since there is no experimental
experience yet in this wavelength regime. As mentioned before, the average brilliance
generated by each undulator is accordingly smaller than the number quoted if the
electron beam is distributed to many undulators.

   According to eq. 9.1.1 there are two fundamentally different methods for wavelength
tuning: One can either change the electron beam energy or the undulator K parameter.
As discussed before, a linac has excellent possibilities for energy variation, but energy
variations beyond the bandwidth of the beam transfer lines will apply for all undulators
served by the respective extraction line. To provide additional tuning flexibility, all
undulators will provide variable K parameters by variable gap size. Since at TESLA
the electron energy is (practically) a free parameter for radiation users, one could think
of further increasing the photon energy by increasing the electron beam energy. There
are two effects limiting the energy:

- At this electron energy level there is a large energy loss by spontaneous undulator
  radiation, which both detunes the resonance condition and represents a significant
  source of background to the FEL radiation.

- When increasing the electron energy to achieve shorter and shorter wavelength, a
  serious limitation due to the quantum fluctuation of spontaneous radiation is en-
  countered [19]. For any set of electron beam parameters and tolerable undulator
  length a minimum photon wavelength exists which corresponds to a well-defined
  electron energy. For the electron beam parameters assumed here and an undula-
  tor length of $L_u = 200$ m this limit is 0.64 Ångstrøm.

   Thus there are two potential ways to make use of the high electron energy available
at TESLA: To increase the XFEL brilliance at a not too small wavelength, or to use
the spontaneous undulator spectrum in the hard X-ray regime that can extend up
to the multi-MeV range and that provides an enormous peak brilliance even without
the FEL process. The presented layout includes both options. The bending radii of
all electron transfer tunnels are large enough that beam lines could be installed with
tolerable synchrotron radiation losses up to approx. 100 GeV beam energy. Presently,
the beam lines are laid out for an energy range up to 50 GeV.

9.1.8   The VUV FEL Project at the TESLA Test Facility

At the TESLA Test Facility (TTF) linac, a proof-of-principle experiment is running to demonstrate the SASE principle at wavelengths below 100 nm [14]. The TTF FEL includes all major components and techniques necessary for an XFEL, and the electron beam parameters are in many respects not too far away from those needed for an XFEL:

- The RF photoinjector has achieved $\varepsilon_n = 3.5$ mm mrad at 1 nC bunch charge.

- The bunch compressor has successfully demonstrated compression to $< 500\,\mu$m rms bunch length.

- Coherent synchrotron radiation (CSR) effects and roughness wakefields have been studied experimentally.

- A 15 m long undulator including quadrupole focusing and a collimator section for undulator protection was installed and successfully commissioned.

- Linac operation with bunch trains as long and at the same beam current as needed for the XFEL was demonstrated with tolerable losses in the undulator. The peak energy variation was kept below 0.3% by active beam loading compensation.

First lasing was achieved at wavelengths ranging from 80 to 180 nanometers in accordance with FEL theory [3]. An upgrade is being prepared for FEL operation with pulse trains identical in length and current to XFEL parameters, including feedback systems to stabilize beam energy and beam position at the undulator entrance. Section 9.2 presents some details on the TTF FEL operation experience.

A project to upgrade the TTF to a user facility producing photons with wavelengths down to 6 nm is under way. This upgrade raises the electron energy to 1 GeV and reduces the bunch length to 50 μm. The injector will be modified to a scheme very similar to the XFEL injector, and the undulator will be extended to a total length of 30 m.

Since the photoinjector has a large impact on the saturation length and performance of the FEL, a stand-alone test facility for high-performance RF photoinjectors (PhotoInjector Test stand in Zeuthen, PITZ) is under construction at DESY-Zeuthen. Each progress on gun development will readily be transferred to TTF FEL to improve its performance and to investigate operation properties at a full scale facility.

9.1.9   The FEL collimation and protection system

Collimators in the FEL beam line serve two purposes: Reduction of the dark current contents in the beam and protection of the undulators from radiation damage.

Dark current may lead to radiological problems in the beam line and the undulators if it is lost in an uncontrolled way, and produces a background signal for the FEL users. Due to its low phase space density, the spontaneous radiation produced by dark current in the undulators is not amplified by the SASE process. The integrated light output might nevertheless be non-negligible since each RF bucket may contain electrons.
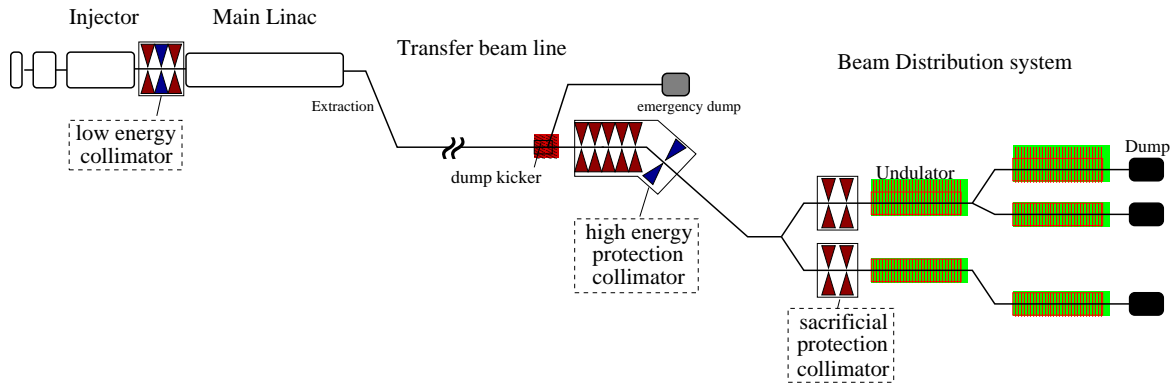
Figure 9.1.8:   *Schematic layout of the FEL collimator and protection system.*

The collimation system is separated into two parts. Low energy collimators in the injector and the bunch compressors reduce the dark current produced in the RF gun and the first accelerator modules. High energy collimators at the end of the transfer line scrape off dark current from the main linac (figure 9.1.8). The high energy collimation is rather simple due to the large energy difference between the dark current produced in the main linac and the actual beam. Dark current produced in the gun is quite difficult to collimate, since it has similar energy as the real beam, and requires a set of collimators to reduce the acceptance of the beam line in the transverse and the longitudinal phase space. It is of utmost importance to keep the production of dark current, especially from the back plate of the gun, at a minimum. Experience at TTF has shown that a dark current contents as low as 10^5 electrons per bucket (corresponding to $20\,\mu$A in the RF pulse) at the undulator entrance is achievable.

In case of a machine failure that is not detected by the control system, the the FEL beam lines have to be protected from the very intense electron beam. Especially the undulator magnets are sensitive to beam losses and can degrade by radiation damage even from a small loss over a long period. The collimator sections are equipped with fast beam loss monitors (szintillators and photomultipliers) which trigger the emergency dump kicker and the laser beam shutter of the RF gun.

In order to detect a beam loss at the lowest possible energy the collimators in the injector have the smallest acceptance. The acceptance of the collimators is increasing along the beam line so that downstream collimators are in the shadow of all upstream collimators. The undulators are in the shadow of all collimators. The largest part of the XFEL installation is protected by the high energy collimation section which is described in more detail in section 9.6.4. In order to save length only sacrificial collimators are employed in front of the undulators. They will not survive a beam loss in the section downstream of the high energy collimators if the emittance of the beam stays at the nominal value during the loss.

9.2   Experience from TTF FEL Operation

This section deals with the experience gained on FEL issues at the TESLA Test Facility (TTF). For discussion of superconducting accelerator matters and the integrated systems test, see section 2.

The first lasing of the high gain FEL at the TTF linac was achieved in February 2000 [3], which served as a proof-of-principle for high gain SASE FEL at VUV photon wavelengths. Since then, an FEL photon beam has been delivered over several hundreds of hours at wavelengths between 80 and 180 nm [10], corresponding to electron beam energies between 270 and 180 MeV (figure 9.2.1), demonstrating stable operation and energy tunability of TTF FEL.
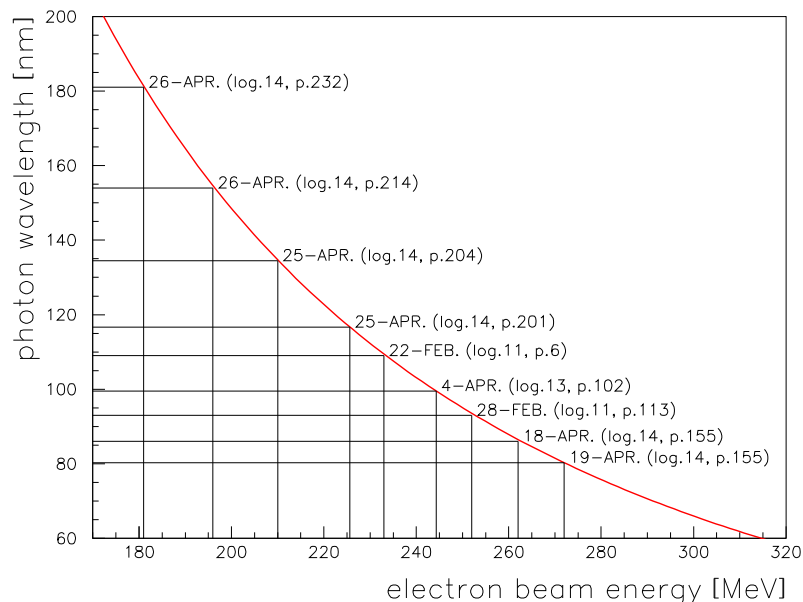
Figure 9.2.1:   *SASE FEL wavelengths obtained at TTF FEL versus electron beam energy. The red curve is the prediction according to eq. 9.1.1.*

9.2.1   FEL results

The characteristics of the FEL photon beam were studied in great detail at photon wavelengths of around 108 nm, with an FEL gain of a few thousands over the undulator spontaneous emission. The observed wavelength spectrum (see figure 9.2.2), the angular spread and photon intensity fluctuations agree very well with the expectations [3]. Gain saturation has not yet been observed. A fundamental characteristic of the FEL process is the strongly non-linear dependence of the photon intensity on bunch charge, shown in figure 9.2.3.

In September 2000, SASE with a gain of 10^5 was observed at 108 nm with bunch charges of 3.5 nC. Additionally, experiments varying the electron beam trajectory inside
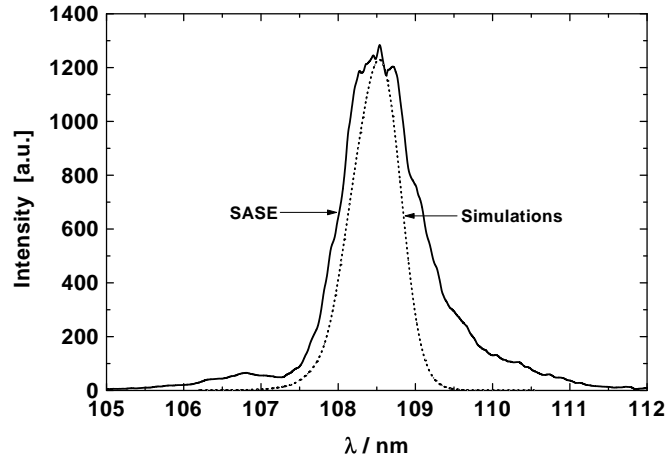
Figure 9.2.2:   *Typical wavelength spectrum of the central SASE FEL radiation cone (collimation angle ± 0.2 mrad), taken at the TESLA Test Facility. The dotted line is the result of numerical simulations. The bunch charge is 1 nC. The larger width of the measured spectrum is consistent with the energy spread of the beam.*

the undulator have demonstrated the strong dependence of the FEL process on the overlap between the electron and the photon beam along the undulator axis.

9.2.2   TTF FEL performance

The operation of the linac in the 'FEL mode' has been sustained over a period of more than two months, demonstrating the stability and reproducibility of the various linac components (magnets, injector system, RF systems, superconducting cavities, etc.) for delivering small emittance and short electron bunches with good alignment to the undulator axis. The superconducting cavities, the RF control and the cryogenics system showed an excellent performance at moderate gradients of about $15\,\mathrm{MeV/m}$ during the entire period of commissioning and operation of TTF FEL. Moreover, the FEL action was recovered within only a week of the linac startup after the shutdown of June-July 2000.

The two most relevant technical factors that have made possible the successful test and operation of the high gain FEL are the field quality of the undulator magnet, which assures a good interaction between the photon and the electron beams, and the capability of the linac components to generate electron bunches with small emittance, compress them to a few tenths of a millimetre and accelerate them while preserving their high charge density.

9.2.3   Undulator magnet quality

An FEL gain of several thousands over the undulator spontaneous emission has been achieved with a $13.5\,\mathrm{m}$ long undulator magnet without the help of additional mag-
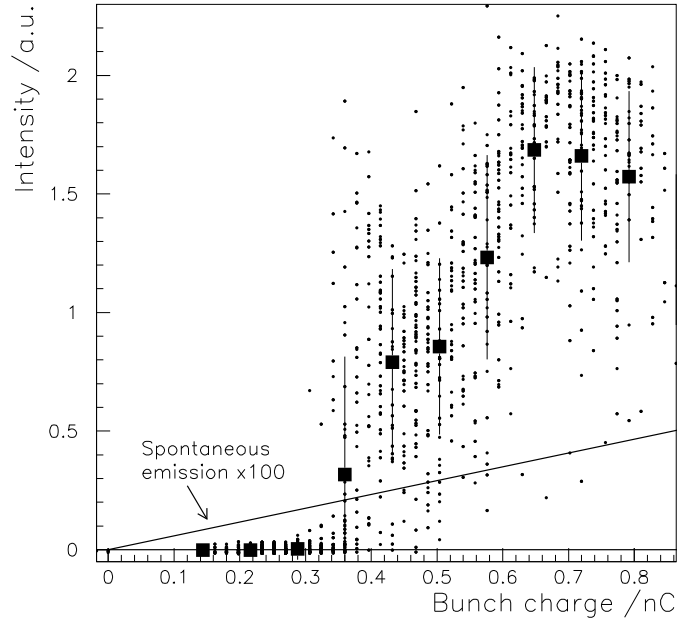
Figure 9.2.3: *SASE FEL intensity versus bunch charge. The straight line is the spontaneous intensity multiplied by a factor of 100. To guide the eye, mean values of the radiation intensity are shown for some bunch charges (full squares). The vertical error bars indicate the standard deviation of intensity fluctuations, which are not an indication of machine instability but are due to the statistical character of the SASE process. For this measurement all accelerator settings were kept constant, except for the bunch charge. Above 0.6 nC there is no further increase of gain without readjustment of accelerator settings which would be necessary to compensate for the changed phase space distribution of the electron bunch.*

netic correction. This is the result of careful design, fabrication, quality control and installation of the undulator modules.

An undulator with high magnetic field, and a very good overlap between the photon and the electron bunches are essential for SASE FELs. The magnetic field quality realized at three 4.5 m long undulator modules installed in the TTF linac represents the state-of-the-art for production and quality control of such devices [18]. The undulator field alone was measured to have deviations in the second field integral $\int_0^{L_u} \int_0^s B(s')ds'ds$ from an ideal field between 3 and 6 T·mm² rms [20], which would induce an rms orbit deviation of about 5 μm at 300 MeV. These undulator modules are equipped with strong quadrupole magnets to keep the beam focused within very small dimensions. The alignment of these quadrupoles is better than 50 μm, which reduces their kicks to the electron beam trajectory along the undulator. The installation and alignment of the three modules with respect to each other and with respect to the linac and the vacuum chamber [21] was accomplished using laser alignment techniques.

9.2.4   Electron beam quality

Bunches with very small transverse beam emittances and high peak current (longitudinal density) are needed for a high gain FEL. This is achieved using a two-step strategy: generation of bunches with small transverse emittances using an RF photocathode, and longitudinal compression at high energy using a magnetic chicane (see below).

The laser-driven photo-injector [22, 23, 24] (see also section 9.3) is capable of generating bunches of electrons of 1 nC with transverse emittances of 3.5 mrad mm (normalized) in agreement with simulation results [25, 26]. A strong RF field at the cathode provides a rapid acceleration to relativistic energies to reduce space-charge effects (which can blow up the beam). The operation of this injector and its subsystems (laser, cathode, RF, etc.) started in May 1999 and since then they have proven to be very reliable. (For details concerning the laser see section 9.3.7.) A major concern has been the increase of dark current within several weeks of run with beam. The origin of the dark current and its effects on the linac have been understood to a large extent [27]. In the recent months, several technical solutions were applied, which reduced the amount as well as the effects of dark current.

In the first accelerator module, which contains eight TESLA cavities, the electron bunches are accelerated to 125 MeV and a correlated energy distribution within the bunch is generated by shifting the phase of the RF field by about 10° from the crest value. Thereby the particles at the tail of the bunch gain more energy than particles at the head and take a shorter path in the following magnetic chicane (see also section 9.4). A compression factor of about five has been achieved routinely, shortening the bunch from 2.5 to 0.5 mm rms.

Several methods to measure the longitudinal charge distribution of the electron bunch have been developed and tested in the TTF linac: coherent transition radiation interferometry [28], longitudinal phase-space tomography and streak camera [29]. The first method employs a Martin-Puplett interferometer to measure the autocorrelation function of the coherent transition radiation emitted when an electron bunch goes through a very thin aluminum foil. The autocorrelation yields by Fourier transformation the absolute magnitude of the bunch form factor. For the reconstruction of an asymmetric bunch, such as shown in figure 9.2.4, also the phase of the form factor is needed which is computed from a dispersion-relation integral. In the longitudinal tomography method, the phase of the accelerating cavities downstream the bunch compressor is varied in several steps in the range of ±45°. The energy profile resulting from each phase is measured at a screen downstream the spectrometer dipole. The charge density in the longitudinal phase space can be reconstructed from the measured projections on the energy axis using a tomography method. The longitudinal bunch profile is obtained by projecting the phase space in the longitudinal axis. Measurements of the longitudinal profile of the electron bunches obtained from the two methods described above are shown in figure 9.2.4. All measurements reveal a non-Gaussian longitudinal profile with one peak containing about half of the total bunch charge when the bunch is longitudinally compressed. Moreover, the energy distribution measured after a spectrometer dipole, breaks up into several peaks indicating a fragmentation of the
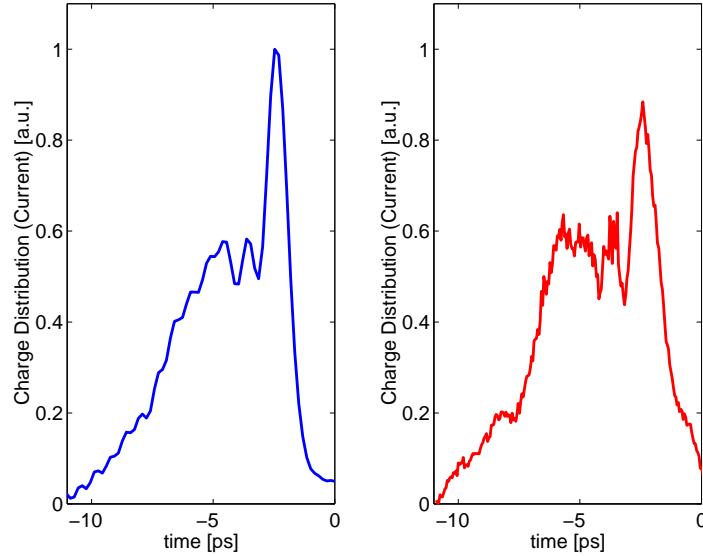
Figure 9.2.4:   *Longitudinal profile of the electron bunches as measured with two different methods. Left: A measurement using the coherent transition radiation interferometry method. Right: Projection of the longitudinal phase-space reconstructed by means of the tomography method. Both measurements were taken with a few days separation.*

longitudinal phase-space when the bunch is fully compressed [30]. Theoretical studies [31] point to coherent synchrotron radiation causing the fragmentation when the radiation emitted by the tail particles in the dipoles interacts with the particles at the head of the bunch. According to these studies, full compression leads to an rms bunch length well below $0.5\,\mathrm{mm}$ rms which is consistent with an observed FEL radiation pulse length of only $100\,\mu\mathrm{m}$ [3]. Since such fragmentation would be detrimental to further compression, less aggressive compression in the first compressor chicane and further stages of compression at higher beam energy are foreseen for the second phase of TTF and for TESLA (see section 9.4). Since detailed understanding of longitudinal dynamics in this new domain of accelerator physics is of paramount importance for FEL performance, further studies and experiments on this subject are planned at TTF. A system of wire scanners is installed at both ends of each undulator module in order to measure the transverse profile of the electron. For a transverse emittance of $4\,\mathrm{mrad\,mm}$ (normalized) the expected beam size at the undulator is about $0.1\,\mathrm{mm}$ rms. A horizontal and vertical beam profile measurement taken with the wire scanner is shown in figure 9.2.5.

   The prototype of an orbit correction feedback system installed at TTF consists of a pair of fast vertical kicker magnets controlled by a digital signal processor. This processor takes the signals from a pair of beam position monitors located downstream and provides two feedback loops: A feed-forward loop corrects beam orbit deviations that appear on every macro pulse and applies a correction to the following macro pulse. The second feedback loop corrects the position deviations from bunch to bunch. A first test (see figure 9.2.6) demonstrates the possibility to correct fast bunch instabilities
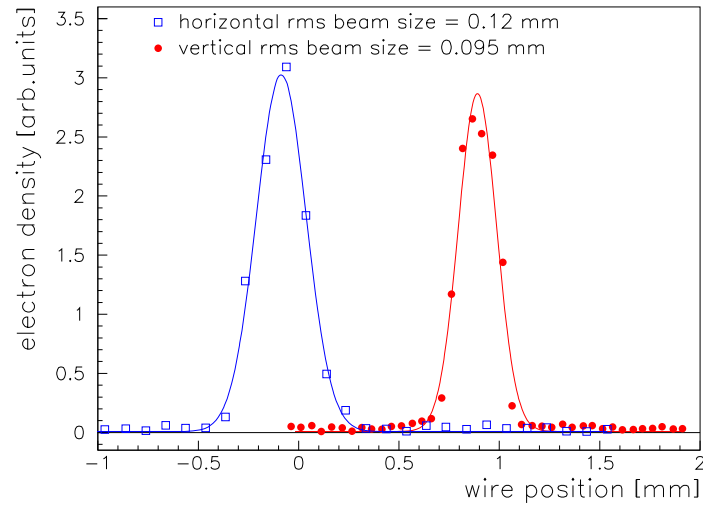
Figure 9.2.5:   *Typical transverse beam profiles measured with the wire scanners installed at the undulator section.*

appearing at each bunch train as well as slow drifts of the beam position along the bunch train.
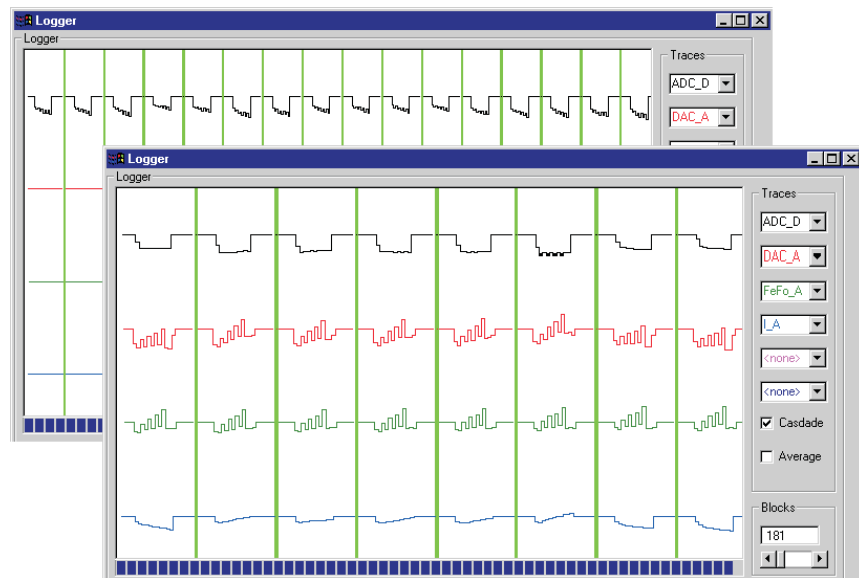
Figure 9.2.6:   *Results of the first test of the fast orbit feedback system on a 10 μs long bunch train. Back window: beam position monitor signal with feedback off. Each bunch train is separated by a vertical green line. The first kicker is used to introduce a noise signal of 0.5 MHz in the bunch train. Front window: Signals for the feedback on. from top to bottom: Beam position monitor signal for eight consecutive bunch trains, the amplitude signal applied to the second kicker, the feed forward signal and the bunch-to-bunch regulation signal.*

9.3   The XFEL Injector

9.3.1   Introduction

The high electron beam brightness, necessary to drive a SASE FEL, has to be generated in the FEL injector and then accelerated to higher energy and transported to the FEL laboratory with a minimum of emittance dilution. Only the development of RF photoinjectors makes it possible to generate a bunch with the required transverse emittance at a rather high charge and short bunch length. The bunch length has to be further compressed in the downstream beam line when the effects of space charge forces are reduced due to the higher beam energy. The new injector layout presented here is based on experience with existing injectors and new simulation tools as well as an improved theoretical understanding of the beam dynamics of space charge dominated beams.

9.3.2   General layout

A schematic layout of the injector is shown in figure 9.3.1.
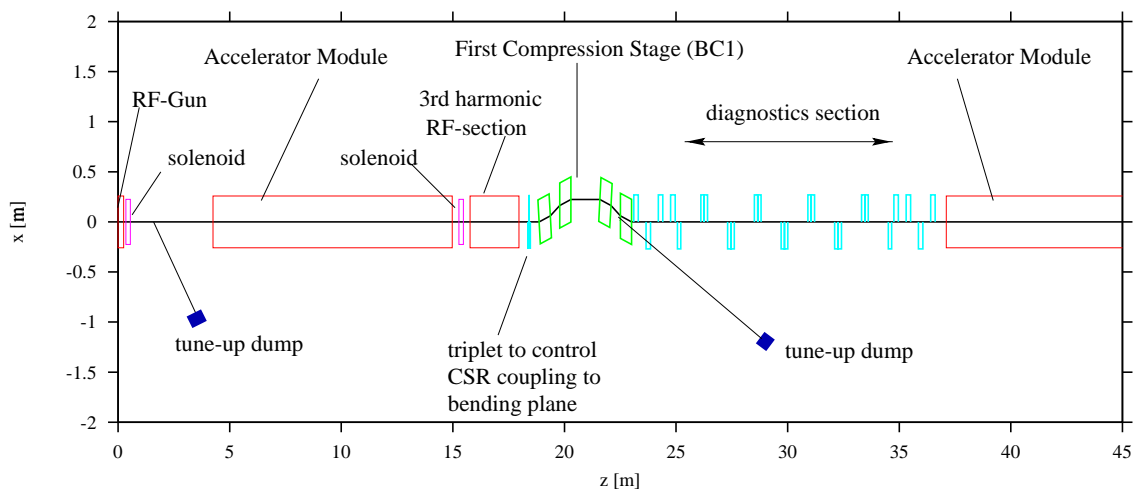
Figure 9.3.1:   *Schematic layout of the FEL injector.*

The electron bunch is emitted by a Cs_2Te cathode illuminated by a UV laser pulse in a high accelerating field (60 MV/m on the cathode, corresponding to 30 MV/m average gradient in the gun cavity) and accelerated up to 6.6 MeV in the normal conducting 1.3 GHz RF gun cavity. The gun cavity is about 0.25 m long (one and a half cell) and is powered by a standard 10 MW klystron. A solenoid, centred 0.4 m downstream of the cathode, focuses the beam into the first accelerator module which is located after a 3 m long drift. Even without a bucking coil the solenoid field on the cathode is negligible. The accelerator module, consisting of 8 superconducting 9-cell structures

(standard TESLA design), increases the energy to 140 MeV and also provides the required correlated energy spread for the subsequent magnetic bunch compression by running off crest. Before injecting the bunch into the first bunch compressor a third order harmonic (3.9 GHz) accelerating section, located 2 m downstream of the accelerator module exit, compensates for the non-linear energy distribution in the bunch arising from the cosine-like dependence of the accelerating field in the first module. The bunch compressor is followed by an elaborated diagnostic section which allows to tune the injector and to measure the transverse and longitudinal beam parameters. Table 9.3.1 summarises the important parameters of the injector. More details on the layout can be found in [32].

Charge	1 nC
Laser pulse length (total)	20 ps
Laser spot radius	1.5 mm
Peak electric field on the cathode	60 MV/m
Solenoid centre (w.r.t. cathode position)	0.4 m
Solenoid peak field	0.2 T
Solenoid field on cathode	0.0 T
Accelerator module:	
- Gradient: Cavity 1-4	12 MV/m
- Gradient: Cavity 5-8	25 MV/m
- Phase	-13.6°
Third harmonic section:	
- Gradient	14 MV/m
- Phase	-173°

Table 9.3.1: *Parameters of the FEL injector.*

9.3.3   Development of the transverse emittance.

The development of the projected transverse emittance in the gun region is dominated by space charge induced correlations in the phase space distribution due to the variation of the transverse space charge force along the longitudinal position within the bunch. A proper focusing allows to compensate these correlations and thus to reduce the projected emittance downstream of the gun [33, 34]. Figure 9.3.2 shows schematically the development of the phase space.

A new working point, very suitable to damp emittance oscillations, has been found recently [35] in the context of the LCLS FEL project [36]. By a proper choice of RF gun and solenoid parameters, the emittance evolution shows a double minimum in the drift section behind the gun. If the booster, i.e. the first accelerator module, is located where the relative emittance maximum and the envelope waist occurs, the second emittance minimum can be shifted to the booster exit and frozen at a very low level, preventing
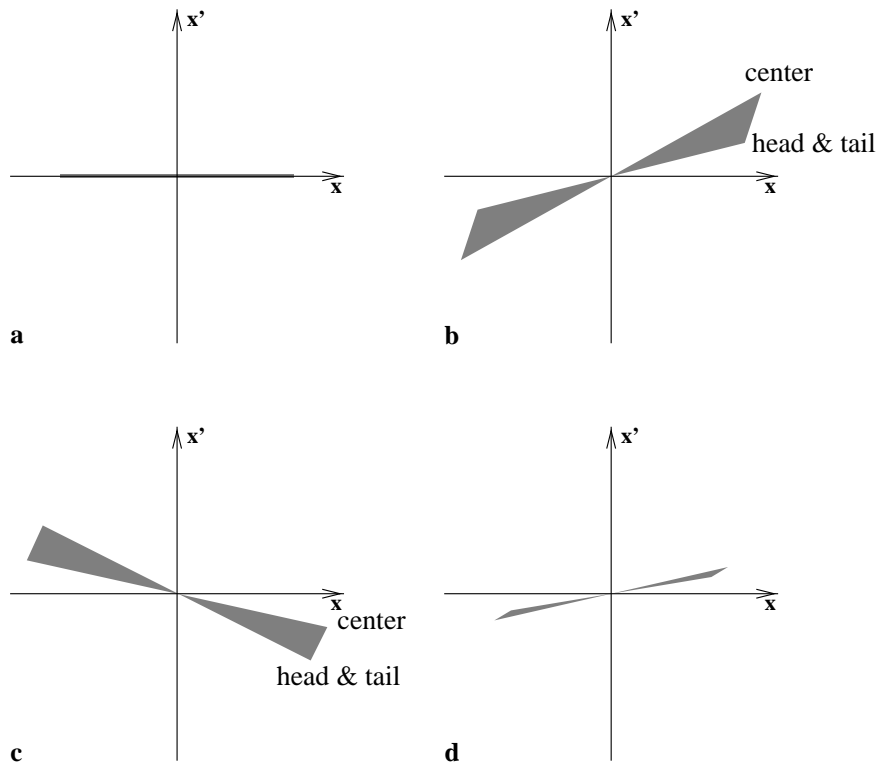
Figure 9.3.2:   *Transverse phase space plots showing schematically transverse emittance growth and reduction due to space charge forces. (a) Initial phase space with small (zero) emittance at the gun. (b) Phase space after transport up to the solenoid lens, showing the growth of the projected emittance due to the different focusing strength at the bunch centre and the tails. (c) The phase space distribution has been rotated by an external focusing kick. (d) Phase space after a drift behind the lens. The projected emittance is decreased due to the action of the space charge forces.*

additional emittance oscillations in the subsequent beam line. In this configuration the location of the solenoid can be shifted downstream of the gun cavity exit. At the same time the drift section between gun and accelerator module has to be increased and the gradient in the first part of the module lowered. The increased drift section is useful to accommodate the laser input port, basic diagnostic, vacuum components and the cold-warm transition for the superconducting accelerator module. Starting from a scaled LCLS injector the design was optimised with two codes: the macro-particle tracking code ASTRA [37] and the multi-slice envelope code HOMDYN [35]. In HOMDYN, space charge fields are described analytically for a uniformly charged hard-edge cylinder with a linear off-axis approximation of the transverse electric field. ASTRA allows the simulation of arbitrary cylindrically symmetric particle distributions and includes non-linear fields. HOMDYN on the other hand is much faster than ASTRA and hence allows large parameter scans to be performed. Figure 9.3.3 shows the development of the transverse emittance as calculated with ASTRA and HOMDYN. Besides a general agreement of both codes, small differences are found which are due to non-linear space

charge fields in the region close to the cathode. The transverse emittance compensation process is clearly visible in the plot: the emittance reaches an absolute maximum in the centre of the solenoid and is reduced to a first minimum in the drift section before it begins again to increase. The booster entrance is located at the following relative emittance maximum at which the beam envelope reaches a laminar waist. The emittance oscillation is reduced by a properly matched accelerating field in the first cavities of the accelerator module to an absolute minimum of 0.5 mrad mm. At the booster exit the average bunch energy is 140 MeV, high enough to suppress space charge forces, so that standard optics applies downstream of the booster. The thermal emittance is not included in this simulation. Theoretical estimates [38] give an upper limit of 0.74 mrad mm for the thermal emittance with the present parameters of the injector. Adding both contributions in quadrature yields 0.9 mrad mm as the predicted transverse emittance of the injector.
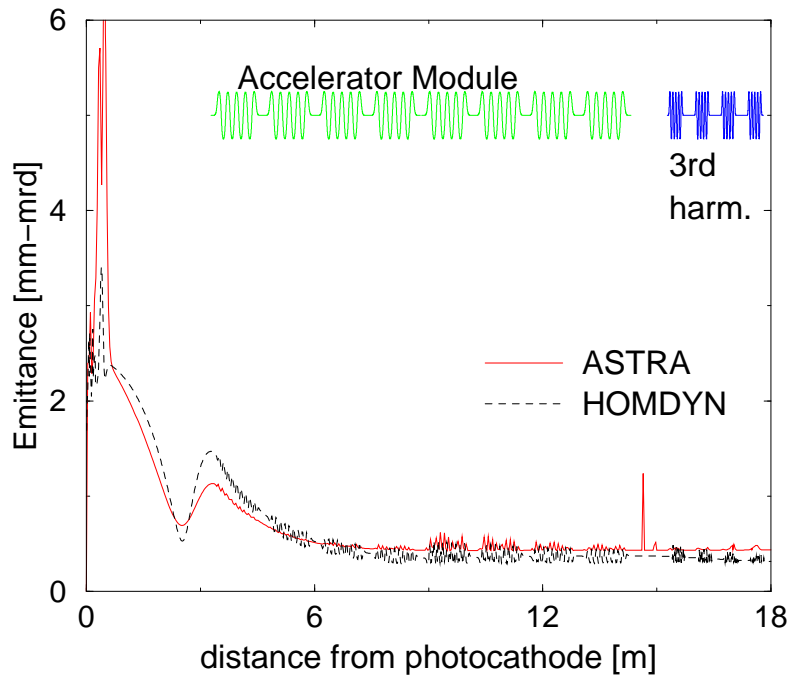
Figure 9.3.3: *Development of the transverse emittance in the gun, the accelerator module and the third harmonic section.*

9.3.4 Development of the longitudinal emittance.

The main drawback of injecting a long electron bunch directly into the booster linac resides in the longitudinal phase space distortion induced by the RF wave curvature. This cosine-like distortion obstructs the compression process and sets a lower limit on the achievable bunch length. A possibility to correct this distortion is to use a third harmonic RF accelerating field (i.e. at 3.9 GHz). The operating point of this higher

harmonic accelerating section (amplitude V_3 and phase φ_3) is closely related to the booster linac parameters (V_1, φ_1): Given the incoming kinetic energy E_0 (at the gun exit), the relative energy spread at the exit of the third harmonic section takes the form:

$$\delta(s) \;=\; \frac{1}{E_0 + V_1 \cos(\varphi_1) + V_3 \cos(\varphi_3)} \cdot [V_1 \left(\cos(k_{rf}s + \varphi_1)\right. \tag{9.3.1}$$
$$\left. - \cos(\varphi_1)\right) + V_3 \left(\cos(3k_{rf}s + \varphi_3) - \cos(\varphi_3)\right)],$$

where s is the longitudinal coordinate w.r.t. the bunch centre.

On the other hand, a downstream compression section (i.e. a single bunch compressor or a chain of bunch compressors) maps an electron with initial position (s_i, δ_i) to (s_f, δ_f) according to:

$$s_f = s_i + R_{56}\delta_i + T_{566}\delta_i^2 + U_{5666}\delta_i^3 + \mathcal{O}(\delta_i^4), \text{ and } \delta_f = \delta_i, \tag{9.3.2}$$

where the Taylor coefficients of the transfer map are written as: $R_{56} = \partial S^{i \to f}/\partial \delta$, $T_{566} = 1/2\partial^2 S^{i \to f}/\partial \delta^2$, and $U_{5666} = 1/6\partial^3 S^{i \to f}/\partial \delta^3$, defining $S^{i \to f}$ as the path length through the compressor. Note that the maximum compression occurs when $s_f = 0$ in equation (9.3.2).

From the two latter equations, and under the assumption that the longitudinal phase space upstream of the compressor can be expanded as a polynomial form: $\delta(s_i) = \alpha_1 s_i + \alpha_2 s_i^2 + \alpha_3 s_i^3$, longitudinal matching conditions of the type $\alpha_i = 1/i! \left[\partial^i \delta(s)/\partial s^i\right]_{s=0}$ ($i \in \mathbf{N}$), can be derived, which, in turn, yield functional dependences of the amplitude and phase of the third harmonic section:

$$V_3 \;=\; \sqrt{\left(\frac{V_1 \sin(\varphi_1)\left[1 - \hat{A}/\hat{C}\right]}{3\left[9\hat{A}/\hat{C} - 1\right]}\right)^2 + \left(\frac{BE_0 - (1 - \hat{B})V_1 \cos(\varphi_1)}{9 - \hat{B}}\right)^2},$$

$$\tan(\varphi_3) \;=\; -\frac{V_1 \sin(\varphi_1)(1 - \hat{A}/\hat{C})(9 - \hat{B})}{3(\hat{B}E_0 - (1 - \hat{B})V_1 \cos(\varphi_1)(1 - 9\hat{A}/\hat{C})}. \tag{9.3.3}$$

where $\hat{A}$, $\hat{B}$ and $\hat{C}$ are coefficients depending on the compressor parameters (e.g. R_{56}, ...) and RF wavelength λ_{RF} [32]. The latter equations can be fed back into the matching conditions to finally yield the operating phase of the booster linac:

$$\varphi_1 = \arcsin\left(\frac{\mu\kappa - \nu\sqrt{\mu^2 + \nu^2 - \kappa^2}}{\mu^2 + \nu^2}\right). \tag{9.3.4}$$

where the coefficients are $\mu = (8\hat{A}V_1)/(9\hat{A} - \hat{C})$, $\nu = (8\hat{A}V_1)/(\hat{B} - 9)$, and $\kappa = 9\hat{A}E_0/(9 - \hat{B})$. The equations (9.3.3) and (9.3.4) are used to find the optimum setup of the first and third harmonic section given an amplitude for the accelerating field V_1 and an incoming beam energy E_0. The longitudinal phase space before and after the third harmonic RF section is shown in figure 9.3.4. The downstream longitudinal

phase space has a second order curvature that is matched (in absolute value but with opposite sign) to the second order distortion introduced by the T_{566} of the first stage bunch compressor. This setup was computed using the aforementioned relations and then further optimised via numerical simulations. It should be noted that the linearised RF potential leads to a reduced sensitivity to phase errors.
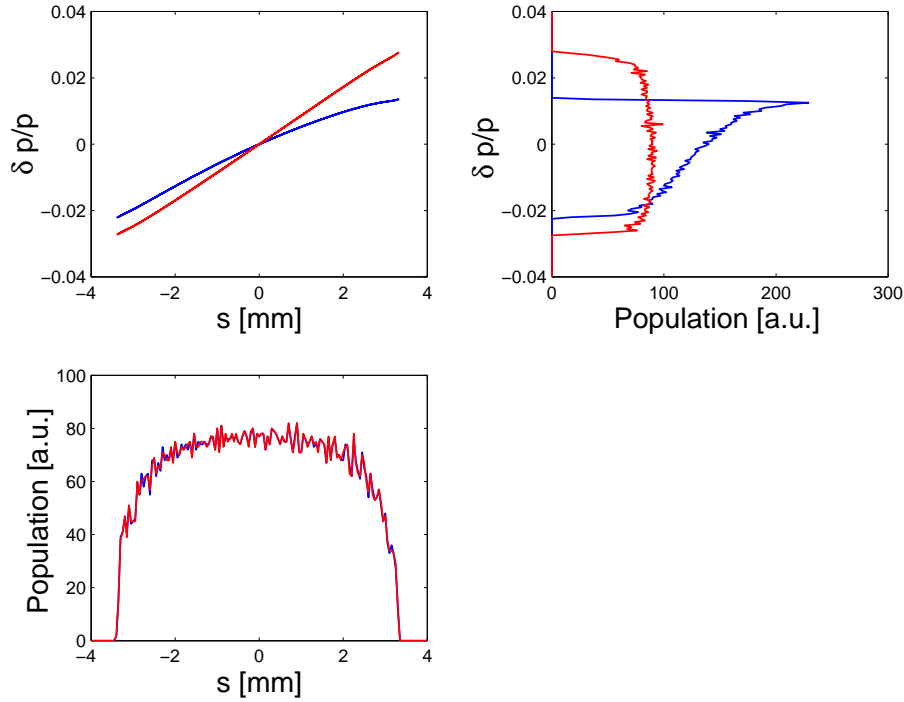
Figure 9.3.4: *Longitudinal phase space upstream (blue) and downstream (red) of the third harmonic RF section. The longitudinal phase space distribution is linearised by the combined action of the first and third harmonic RF. The remaining curvature is matched to the second order compression factor of the bunch compressor.*

9.3.5   Matching and bunch compression section

The beam line downstream of the third harmonic section propagates the beam to the next accelerating section and provides three main functions: compression, transverse matching and diagnostic. The compression system reduces the bunch length from 1.7 mm to 250 μm (rms). It consists of an achromatic four-dipole chicane with a bending angle of 14.2 ° yielding a momentum compaction of $R_{56} \simeq -10$ cm. The compression of a high density bunch has been studied using the TraFiC^4 code [43] to include bunch self-interaction via radiative tail-head effects (i.e. coherent synchrotron radiation, CSR). A quadrupole triplet upstream of the chicane allows to control the beta function through the compressor: it is desirable to create a waist of the horizontal beta function between the third and fourth dipole of the chicane. Hence, the CSR induced rms angular kick,

$\langle \delta x'^2 \rangle^{1/2}$ in the last dipoles leads to the smallest possible emittance growth according to $\Delta \varepsilon / \varepsilon_0 \simeq \beta \langle \delta x'^2 \rangle / \varepsilon_0$.

Downstream of the chicane the beam line consists of 17 quadrupole magnets arranged as two quadrupole telescopes separated by a four-FODO-cell lattice with a betatron phase advance of $\mu_{x,y} = 45\,^\circ$ in both planes. The first telescope provides a Twiss parameter match from the chicane to the periodic solution of the FODO lattice, while the second telescope is used to match the Twiss parameters to the downstream accelerating section. The FODO cell incorporates diagnostics (see next section), and the FODO half length, L, was chosen to obtain an rms beam size of $\geq 100\,\mu$m in order to avoid significant transverse space charge effects, resulting in $L = 0.7$ m. The evolution of the beta functions in the section is presented in figure 9.3.5.
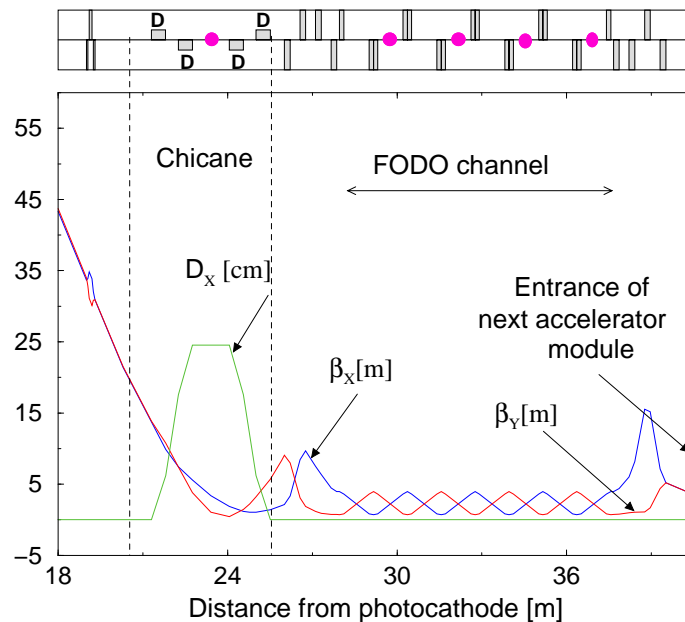
Figure 9.3.5: *Optical lattice functions along the compressor and matching/diagnostic section. The dipoles and quadrupoles are indicated by rectangular boxes (D: dipole) and beam profile monitors by magenta bullets in the upper part.*

9.3.6   Diagnostics for injector commissioning

The beam diagnostics section includes devices that allow both the measurement of the absolute beam and lattice properties and also relative measurements which are helpful for monitoring the accelerator stability and setting-up the injector in a reproducible fashion.

Beam charge   A Faraday cup inserted between gun and booster allows an absolute charge measurement, while toroidal AC transformers are used to monitor the charge

along the beam line and to detect beam losses. Four toroids are foreseen for the injector: (1) upstream and (2) downstream of the first accelerator module, (3) downstream of the compressor chicane, and (4) in front of the second accelerating section.

Transverse diagnostics: Direct measurements   The beam position must be known in order to steer the beam onto an ideal orbit, and to measure the transverse transfer functions of the lattice. In the FEL-injector the beam position will be measured with electro-magnetic pickups.

The beam distribution is determined by means of observation screens. At low energy, i.e. directly downstream of the RF gun, Yttrium:Aluminum:Garnet (YAG) screens are suitable due to their high electron-to-photon conversion efficiency. Downstream of the booster section optical transition radiation (OTR) screens will be used. The images will be recorded with CCD cameras. With a single lens optics a resolution of $10\,\mu$m can be achieved [40]. In the bunch compressor area, synchrotron radiation in the optical regime (the critical wavelength is $\simeq 300\,$nm), permits non-interceptive measurements of the transverse density both at high (second and third dipole) and low (first and fourth dipole) dispersion points.

Transverse diagnostics: Indirect measurements   The transverse projected emittance will be measured with two different techniques: (1) the so-called quadrupole scan and (2) the multi-monitor method:

- For the first method the gradient of a quadrupole is varied and the corresponding beam size variation downstream is recorded. The beam size is a function of the Twiss parameters and emittance at the quadrupole entrance and of the transfer matrix between the quadrupole entrance and the observation point. Using standard fitting techniques and provided the transfer matrix is known, the Twiss parameters and emittance can be computed.

- For the second method the beam size at different locations along the beam line is measured. The betatron phase advance between the observation points is crucial: it should be chosen to sample one half a betatron period as well as possible. Thus a 45° phase advance FODO cell lattice accommodates four OTR monitors. Using four monitors separated by 45° instead of the three monitors with 60° phase advance strictly needed to determine the three independent parameters ϵ, α and β, provides information about the measurement error of the calculated emittance. Though the multi-monitor method is less precise than the quadrupole scan technique, it provides an almost on-line measurement without any optics tune-up; thus it is well suited for regular checking and tuning.

The slice emittance can also be measured at the end of the first accelerator module. Operating the last cavity of the linac at zero-crossing, an almost linear correlation between the longitudinal position of an electron in a bunch and its relative energy offset is introduced. In a dispersive section this correlation translates into a correlation between the horizontal offset of the electron and its longitudinal position. By

transversally filtering the beam, i.e. using a mechanical slit with variable width and position, it is possible to select a longitudinal slice with a variable size. A variable slit, installed in the symmetry point of the bunch compressor, will therefore allow to measure the emittance of longitudinal slices by means of the aforementioned quadrupole scan technique.

Longitudinal diagnostics: Direct measurements Two spectrometers will be used for energy and energy spread measurements. The first one downstream of the RF gun will provide a horizontal dispersion of $D_x \simeq 1 \, \text{m}$. For the second one the bunch compressor chicane is modified by switching the fourth dipole off (see figure 9.3.1). It provides a dispersion of $D_x \simeq 0.6 \, \text{m}$.

To quantify the compression process it is planned to measure the longitudinal transfer maps $\partial s_{in}/\partial s_{out}$ between the photocathode and the bunch compressor exit (∂s indicates the longitudinal position in the bunch). This technique provides a way of setting-up the machine in a very reproducible manner and yields quantitative information on the Taylor expansion of the lattice map (i.e. R_{55}, T_{555}). The hardware consists of two pickup cavities (one in front of the accelerator module, the other behind the compressor), which measure the relative time-of-flight while the timing of the photocathode laser is shifted with respect to the RF-phase [39]. A phase variation of the booster linac and the third order harmonic section at the 1° level can be detected. A similar technique, but this time varying the gradient of a cavity and measuring the relative time-of-flight, can provide the same kind of diagnostics for the $\partial \delta_{in}/\partial s_{out}$ map which in turn gives quantitative information on the coefficients R_{56} and T_{566} (and higher order) i.e. the linear and quadratic momentum compaction factors ($\partial \delta_{in}$ indicates the relative incoming energy offset).

Longitudinal diagnostics: Indirect measurements The relative energy spread δ is measured by observing the spatial beam density in a dispersive section. At this location the rms beam size can be written as $\sigma_x \simeq \sqrt{\beta_x \varepsilon_x + (D_x \delta)^2}$, so by tuning the upstream optics to reduce the beta function, β_x, at the observation point, and by choosing sufficiently high dispersion D_x, the beam projection directly gives the energy profile from which δ can be extracted. Energy spread measurements can be performed in the two spectrometers and at the compressor chicane symmetry point.

The bunch length σ_s is measured (absolute or relative) using several techniques:

- At the gun exit, and downstream of the bunch compressor with compressor operated on or off, the bunch length will be measured with a streak camera of 200 fs resolution.

- After the compressor, for various settings of the compressor magnets (with σ_s down to approximately $50 \, \mu\text{m}$ for max. compression), coherent synchrotron or transition radiation (i.e. at wavelengths $\lambda \gtrsim \sigma_s$) will be analyzed with an interferometer. The spectrum of the radiation can directly provide information on the bunch form factor (BFF) (i.e. $|\mathcal{F}[S(t)](\omega)|^2$, $S(t)$ being the charge density

and $\mathcal{F}$ stands for the Fourier transform). The technique allows even to reconstruct the longitudinal bunch asymmetry if the spectrum can be measured over a broad range of frequencies [41] and has been successfully used at the TTF (see section 9.2).

- The bunch length remains constant within the booster linac and up to the compressor entrance. It can be measured using the zero-phasing technique: the last cavity of the linac is operated at zero-crossing to introduce a linear correlation between δ and s. The energy profile, measured in a downstream dispersive section, depends on the longitudinal bunch profile and can thereby provide information on the bunch length and longitudinal phase space slope before the "zero-phasing" cavity entrance [62].

Most of the diagnostic tools described above have been routinely used or are under test at the TTF (see section 9.2) and other accelerators.

9.3.7   RF Gun Laser

The design of the laser system for the FEL RF gun is based on the photoinjector laser system in operation at the TESLA Test Facility. A description of the laser and running experience can be found in [23]. Basic specifications of the laser system are listed in table 9.3.2.

Wavelength	262 nm
Train rep. rate	5 Hz
Pulse Train Structure:	
Pulse train length	1070 μm
Nb. of pulses per train	11500
Pulse spacing	93 ns
Pulse energy on cathode	1 μJ
Pulse length	20 ps (flat top)
Flat top rise time	< 4 ps
Spot radius on cathode	1.5 mm (flat top)
Synchronization	to reference RF signal
Phase stability	< 1 ps (rms)
Energy stability	< 2 % (rms)
Control	fully remote
Uptime	>99 %

Table 9.3.2: *Basic specifications of the laser system for the FEL electron source.*

The Cs_2Te photo cathode used in the RF gun has a quantum efficiency of at least 0.5 %, thus 1 μJ of UV laser energy is sufficient to produce an electron beam of 1 nC. However, since the number of pulses per train is 11500, a total energy of 11.5 mJ per

train has to be achieved in the UV wavelength. With a repetition rate of 5 Hz, the average UV laser power is 55 mW, achievable with present laser technologies. The present running TTF laser system fulfills this requirement already.
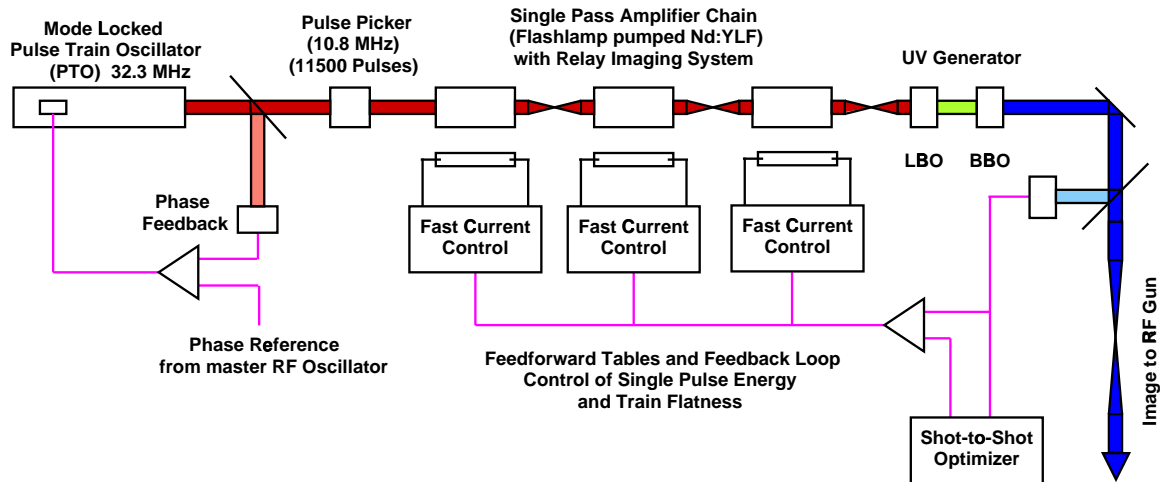
Figure 9.3.6: *Schematic overview of the photoinjector laser system.*

The laser is based on flashlamp pumped Nd:YLF rods lasing at 1047 nm. This material has a long fluorescence lifetime, high induced emission cross section, and very small thermal lensing, which is favourable for long pulse trains. A mode-locked pulse train oscillator (see figure. 9.3.6) synchronized with the reference RF signal generates a pulse train with a suitable multiple of the required pulse train frequency: 32.3 MHz has been chosen. The pulse spacing of 31 ns is large enough to allow a Pockels-cell based pulse picker to run at 10.8 MHz. The train is amplified by a single pass amplifier chain to 30 μJ per single pulse. This corresponds to an average laser beam power of 1.7 W at the fundamental wavelength of 1047 nm. The UV wavelength (262 nm) is generated with two non-linear, commercially available crystals (LBO and BBO). The conversion efficiency is 15 to 20%, which leads to a UV single pulse energy of 5 μJ. This gives an overhead by a factor of 5, sufficient to account for regulation reserve and losses in the transport beam line to the cathode.

The pulse length of the laser in operation at TTF is 7 ps rms. The bandwidth of Nd:YLF is sufficiently large to achieve a pulse length down to 2 ps. An upgrade of the pulse train oscillator is in development. An additive mode-lock technique is used to shorten the pulses. A pulse length of 3 ps has already been achieved and a field test at TTF will follow within the first half of 2001. Several pulses have to be stacked with a small time delay in a so-called pulse-stacker, in order to generate a longitudinally flat-top profile out of the short Gaussian laser pulses. The pulse train oscillator is pumped by laser diodes and has a high average power, in the 1 W range within the pulse train. A diode-pumped pre-amplifier follows to increase the power to about 30 W.

The amplifier chain consists of 3 single pass flashlamp pumped Nd:YLF amplifiers with an adjustable gain around 10. Programmable power supplies allow to set the

flashlamp current on a time scale of $10\,\mu$s width predefined feedforward tables. This is essential to obtain a flat pulse train and gives in addition the opportunity for an efficient amplitude feedback system [42]. An energy stability in the UV of better than $\pm 2\%$ (rms) has been achieved. Figure 9.3.7 shows an oscilloscope trace of the phase with respect to the reference phase of the $1.3\,$GHz RF signal. Also shown are the output of the pulse train from the pulse train oscillator and the amplified train after conversion into the green, measured with fast photodiodes.
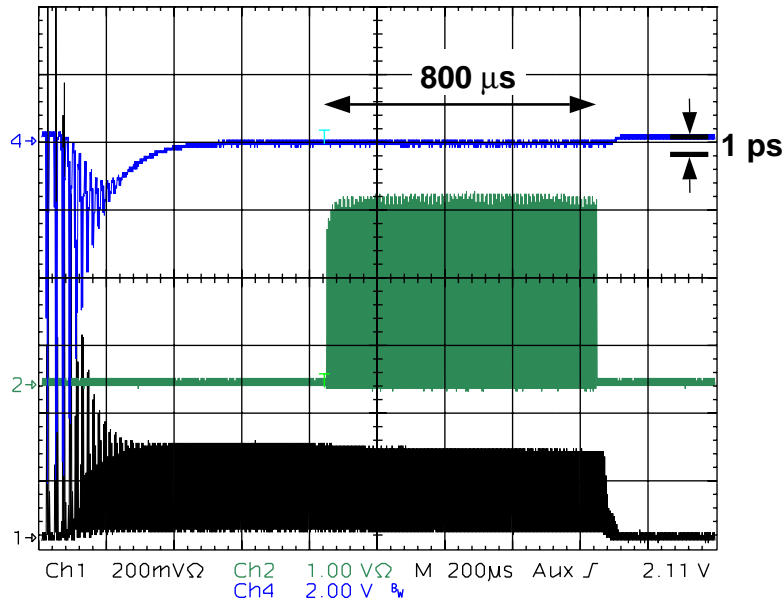
Figure 9.3.7: *Oscilloscope trace of the output of the pulse train oscillator (PTO) (trace 1), the phase of the pulses relative to the reference (trace 4), and the pulse train after amplification measured in the green with a fast photodiode (trace 2). The data have been taken at the TTF laser system, which is running with $800\,\mu$s long pulse trains. Note, that due to the scale ($200\,\mu$s per div.) individual pulses in the train are not resolved.*

The laser uses the relay imaging technique in combination with spatial filtering to obtain a clean transverse flat profile on the cathode and to improve the pointing stability. A wavefront correction system using an adaptive mirror is in development to correct for wavefront distortions due to the frequency conversion into the UV. The laser beam slightly overfills the sensitive cathode area in order to be insensitive to residual tails in the profile and to beam jitter.

Complete remote control and integration into the TESLA control system is mandatory. Since December 1998, the TTF laser system has been operated for $6000\,$h for electron beam production. A total uptime of 99% and an availability for beam of 98% has been achieved.

9.4 Bunch Compressors

9.4.1 Introduction

The SASE FEL process requires high peak currents and very small normalised transverse beam emittance of about 1 mrad mm to keep the undulator length within reasonable limits. It has not yet been possible to design an electron gun which delivers ultra short bunches of very small emittance. Thus a relatively large bunch length of 1.7 mm (rms) has to be accepted and a compression to the final length of 25 μm is carried out at higher energy.

Bunch compression for relativistic bunches can only be achieved by inducing a correlation between longitudinal position and energy offset with an RF system and using the path length differences in a magnetic bypass section (a so-called magnetic chicane) to bring head and tail of the bunch closer together.

Figure 9.4.1 shows an overview of the TESLA XFEL bunch compression scheme. At a beam energy of 140 MeV, the bunch is compressed from its initial length of 1.7 mm (rms) down to 250 μm. Compression at beam energies below 100 MeV is excluded because the effects of space charge forces are too strong. On the other hand, longitudinal emittance growth, due to the cosine-like shape of the RF, scales with the third power of the bunch length [46]. To reduce the requirements on the higher order RF system which is used to decrease the longitudinal emittance (described in section 9.3), the first compression stage is at a rather low energy.

The beam coming from the gun has a small uncorrelated energy spread of some 10 keV. To achieve sufficient compression, only very little correlated energy spread would be needed; at 140 MeV, an rms of 10^{-3} would be sufficient.

This, however, would require a high longitudinal dispersion (described by the matrix element $R_{56} \sim \int D/\rho ds$ in the transfer matrix) in the compressor chicane, which makes it difficult to preserve the transverse emittance. This is because the emittance growth due to energy losses in a dispersive section scales with D^2, and the strength of the coherent synchrotron radiation (CSR) fields scales with $1/\rho^{2/3}$.

From that point of view we prefer compression with a small R_{56} and large energy distribution. An upper limit for the energy spread is given by the XFEL requirements. Since the electron beam in an undulator has an energy of at least 10 GeV, that limit is fairly loose. A tighter restriction stems from the non-linearities of particle orbits with large energy deviations in the chicane, causing distortions in longitudinal and transverse phase space. Induced energy correlations with rms values of above 2% can hardly be handled without excessive phase space distortion.

The second bunch compressor at the end of the 500 MeV injector linac with an R_{56} of 0.05 m reduces the bunch length to 100 μm (rms). The next section describes the two first compression stages in more detail. The final compression to a peak current of 5000 A, which would correspond to an rms bunch lengths of 25 μm for a Gaussian distribution with 1 nC bunch charge, takes place at higher energy and is discussed in section 9.4.3. In the last section, simulation calculations of the beam dynamics from the gun cathode through the entire bunch compression system are presented.

σ_s=1.7mm $\longrightarrow$ σ_s=0.27mm $\longrightarrow$ σ_s=0.1mm

3rd Harmonic RF

Gun

BC-I
R56=0.1

BC-II
R56=0.045

2.5 GeV Linac

σ_s=0.1mm $\longrightarrow$ σ_s=0.025–0.1 mm $\longrightarrow$ σ_s=0.025mm

fifteen degrees arc

Main Linac

BC-IIIa
R56=0.02

FEL-Beam extraction
@ max. 27 or 50 GeV and
FODO-Compressor
R56= 0.001-0.02

:Acc. Module   :Bending Magnet
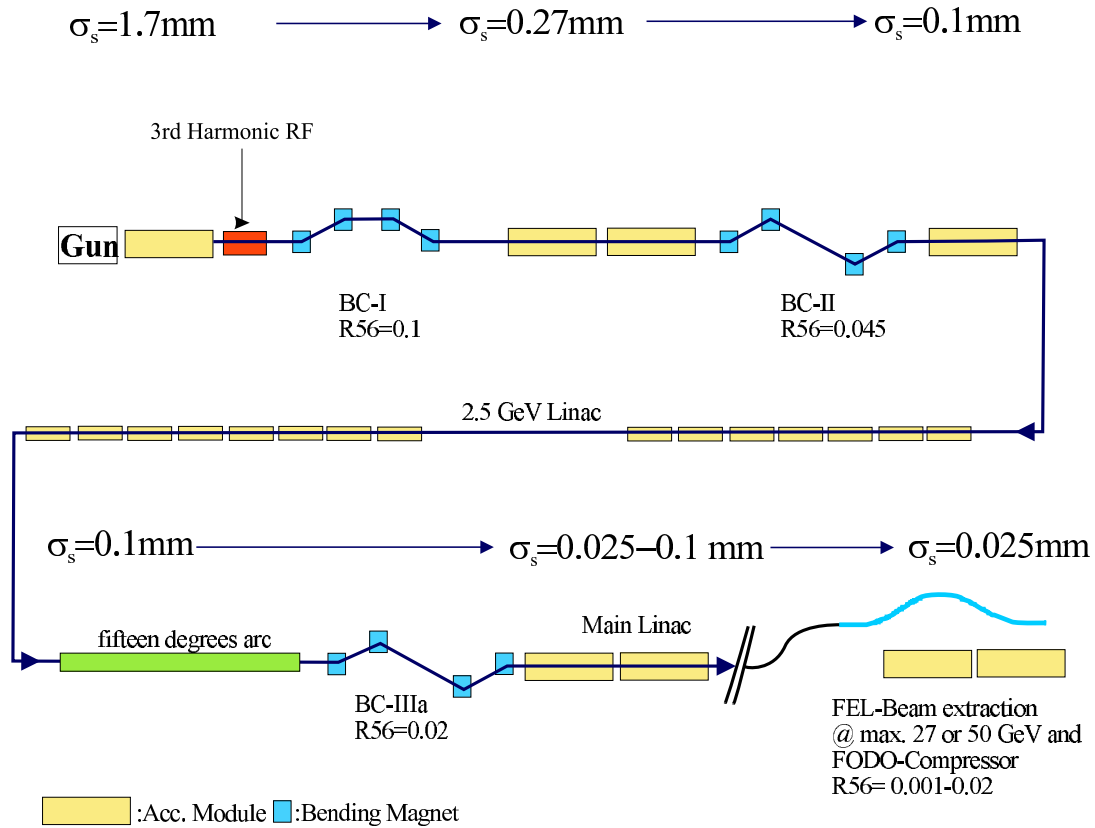
Figure 9.4.1: *Bunch compression scheme for the TESLA XFEL. The "FODO compressor" is optional.*

9.4.2   Compression in the 500 MeV injector linac

As explained in section 9.3, the curvature of the RF wave is compensated using the third harmonic RF system. The rms value of the induced correlated energy distribution is 1.5%. The first chicane (BC-1) has an R_{56} of 0.1 m with four dipole magnets of 0.5 m length, deflection angles of 14.2° and a total length of 4 m. The bunch compressor (BC-2) follows after two regular accelerator modules and is laid out as an s-shaped chicane with an overall length of 14 m. The parameters for the bunch compression system are summarized in table 9.4.1. In the chicanes there are no quadrupoles interleaved with the rectangular bending magnets; the dispersion is therefore closed to all orders. Several matching quadrupoles upstream of the chicane are needed to provide the special optics required for emittance preservation. Computer studies with the code TraFiC[4] [43] have shown that a beam waist in the region with strong coherent synchrotron radiation is needed to prevent transverse emittance growth [44]. Figure 9.4.2 shows the optics in the BC-1 region.

The complete 500 MeV injector linac with the first two bunch compressors is shown
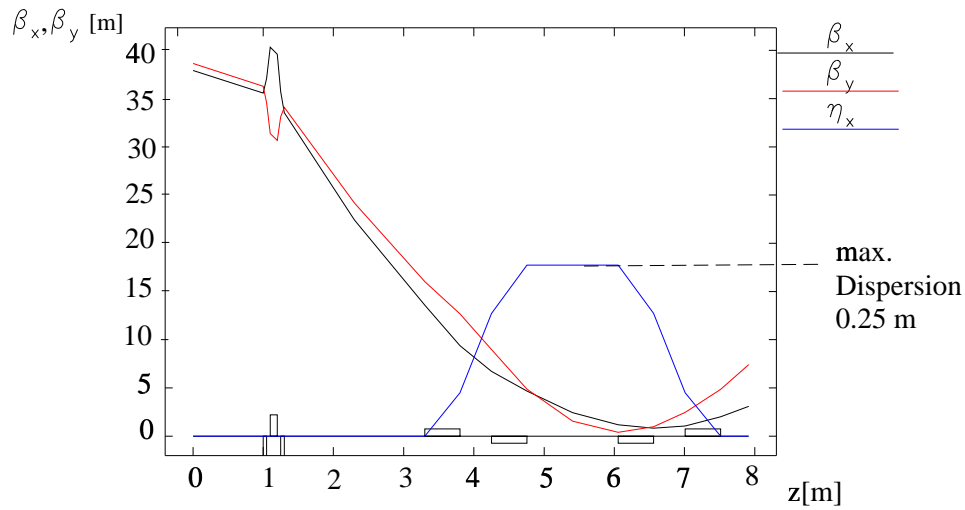
Figure 9.4.2: *Optics in the region of Bunch Compressor 1.*

in figure 9.4.3.
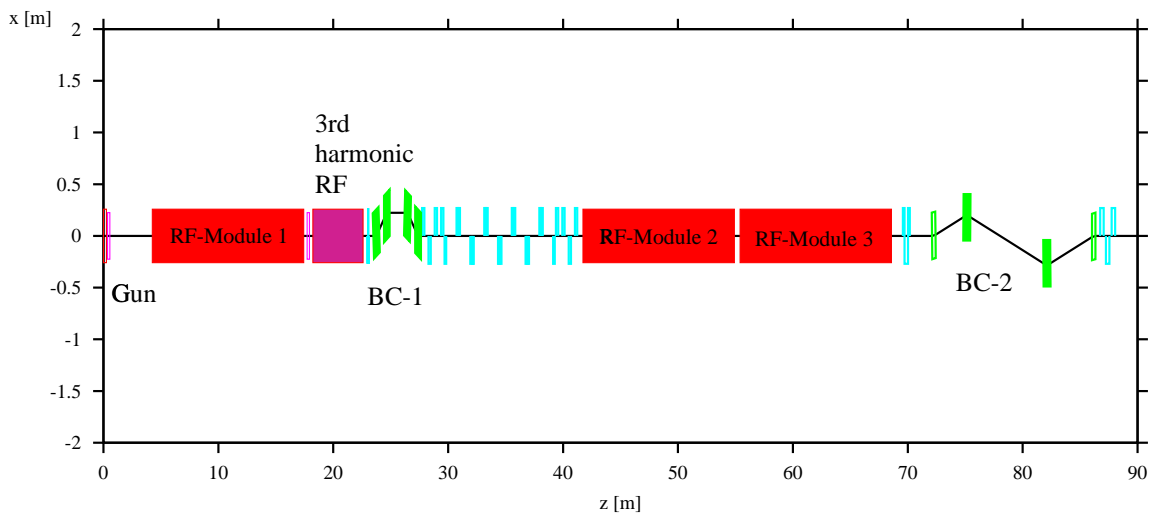
Figure 9.4.3: *Floor plan of the 500 MeV XFEL pre-injection linac with the first two bunch compression stages.*

9.4.3   Final compression to 5000 A peak current

The geometry of the beam line up to the main linac injection point at the XFEL beam energy of 2.5 GeV is shown in figure 9.4.4. After leaving BC-2, the beam is accelerated to 2.5 GeV by an accelerator section also used for the collider pulse in a time sharing

mode. The beam line is then bent by 15° into the main TESLA tunnel. BC-3 is located at the end of this bend, just before joining the damping ring extraction line for injection into the main linac. It is an S-shaped chicane and compresses the bunch to a peak current of up to 5 kA. Note that for short bunches, the rms length is not a good measure for the peak current any more, since due to the non-linearities of the bunch compression the longitudinal beam profiles become strongly non-Gaussian.

It is not foreseen to use the 15° arc as bunch compressor, since simulation calculations have shown that at rms bunch lengths below $100\,\mu$m the transverse slice emittance starts to grow. The cell length of the 15° arc is therefore chosen to reduce the longitudinal dispersion R_{56} so that the bunch length does not reduce by more than 10%.

At max. 27 GeV and 50 GeV, respectively, the XFEL beams are extracted from the main linac and enter transport lines, which guide them to the undulators in the FEL laboratory located near the collider interaction point.

At the beginning of these transport lines, bunch compressors consisting of many periods of weak, S-shaped chicanes including periodic quadrupole focusing (called FODO compressor in figure 9.4.1) [45] are optionally foreseen. Since such compressors can be adjusted for *negative* R_{56}, they can use the energy correlation induced by the wake fields of the TESLA RF structures to compress the bunch further to achieve peak currents even higher than the required 5 kA and to generate bunch lengths even below 80 fs rms, which would be highly desirable for the users. Also, according to simulations, the correlated transverse emittance could be further reduced by redistributing the compression factors between the compressors. We leave this as an option because we believe it needs more experience on the beam dynamics of ultra-short bunches for a reference design.

Bending Magnets	Quantity	Mag. Length [m]	Defl. Angle [deg]	Mag. Field [T]	Gap [mm]
BC-1	4	0.5	14.2	0.17	20
BC-2	6	0.3	3.4	0.36	20
BC-3	6	0.6	2.4	0.90	20
FODO	8/4	3.	1.0/2.0	0.5/1.0	20

Quadrupoles	Quantity	Mag. Length [m]	Max. Gradient [T/m]	Bore [mm]
	38	0.2–0.4	25.0	20

Correctors	Quantity	Mag. Length [m]	Max. Defl. [deg]	Max. Field [T]	Gap [mm]
	50	0.1	0.009	0.025	20

Table 9.4.1: *Magnet parameters for the bunch compression system.*
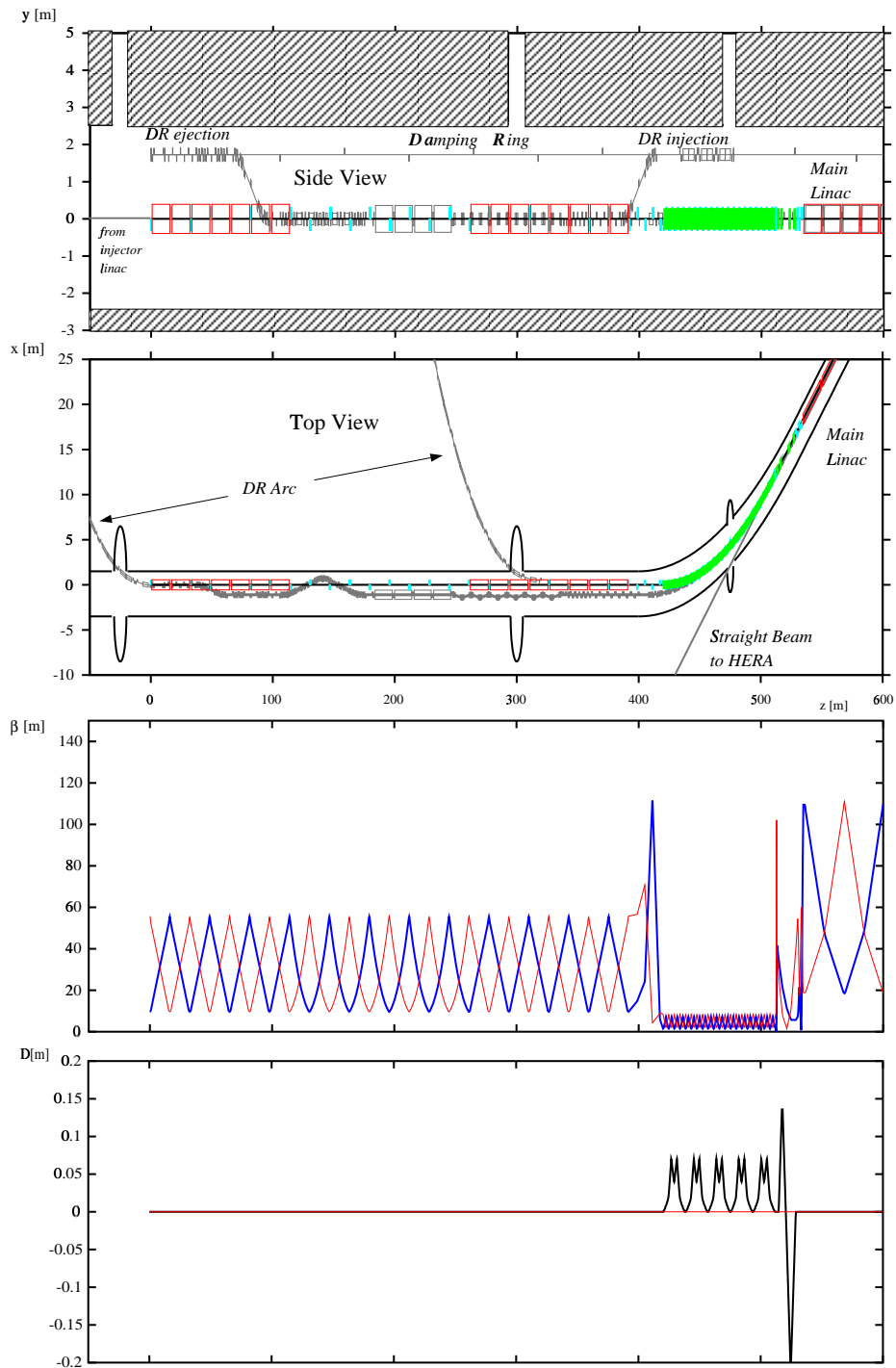
Figure 9.4.4: *Layout for the TESLA XFEL injector from the 500 MeV point (exit of BC-2, see figure 9.4.3) to the main linac injection. Bending magnets are green, quadrupoles blue and RF modules red. The beam lines for damping ring ejection/injection are shaded grey.*

9.4.4   Complete simulation of the TESLA XFEL

To obtain a realistic beam distribution at the entrance of the XFEL undulator, tracking has to be done from the cathode through the whole accelerator. Non-Gaussian beam profiles have to be taken into account as well as non-linear effects such as space charge, Coherent Synchrotron Radiation (CSR) and wake fields.

We have done this with the help of several codes: ASTRA [37] for the low energy, space-charge dominated regions, TraFiC[4] for the bunch compressor chicanes where CSR influences the particle trajectories and the code *'elegant'* [47] for the tracking with wakefields [51, 52] in the linac(s) and transport lines.

The greatest concern about the preservation of emittance is the bunch compression. The CSR fields acting on the short bunches in the chicanes can increase the transverse emittance by orders of magnitude if the parameters are not chosen with great care [49].

One has to take into account that the transverse distribution as well as the position of its center can vary along the bunch. Therefore the bunch is treated as a sequence of slices, where each slice has its own transverse emittance, optical functions and centroid position. The projected emittance, which is usually measured, can grow via two different mechanisms:

- the emittance of the single slice increases (slice emittance growth)
- the slice centers are shifted differently ("correlated emittance growth").

The combination of both contributions gives the projected emittance. The correlated emittance can be much bigger than the slice emittance before it starts to degrade the XFEL performance. The cooperation length of the SASE process is a few hundred optical wave lengths long but several thousand times smaller than the bunch length. Since the correlated emittance stems from CSR fields with wave lengths comparable to the bunch length, no strong variation of slice center positions will occur on the scale of a cooperation length which is less than a micrometer. Too big a projected emittance, however, should be avoided since it complicates tuning and operation of the XFEL.

The simulation starts with ASTRA which tracks point-like particles from the gun cathode through the first module to the entrance of BC-1.

The CSR simulation code TraFiC[4] uses 3-dimensional Gaussian sub-bunches to model the beam. Computer time limitations make it impossible to use more than a few hundred sub-bunches. The phase space has to be 'condensed'. For the results which are presented in this section we model the beam as a longitudinal chain of 3-D sub-bunches that generate the CSR fields. In the bunch center several hundred particles populate a short slice and are tracked through the chicane under the influence of the CSR fields. The moments of this ensemble are used to calculate slice emittance growth and optical mismatch.

Optics matching and tracking to the entrance of Bunch Compressor 2 is done again in 'elegant', before TraFiC[4] tracks the beam through BC-2. In the scenario presented in this section, BC-3 is used to achieve the final peak current of 5 kA. The beam is transported to the XFEL undulator, where an FEL code like GENESIS [50] can predict the laser performance. The interplay of the different codes and the optics used in between the bunch compressors is shown in figure 9.4.5.
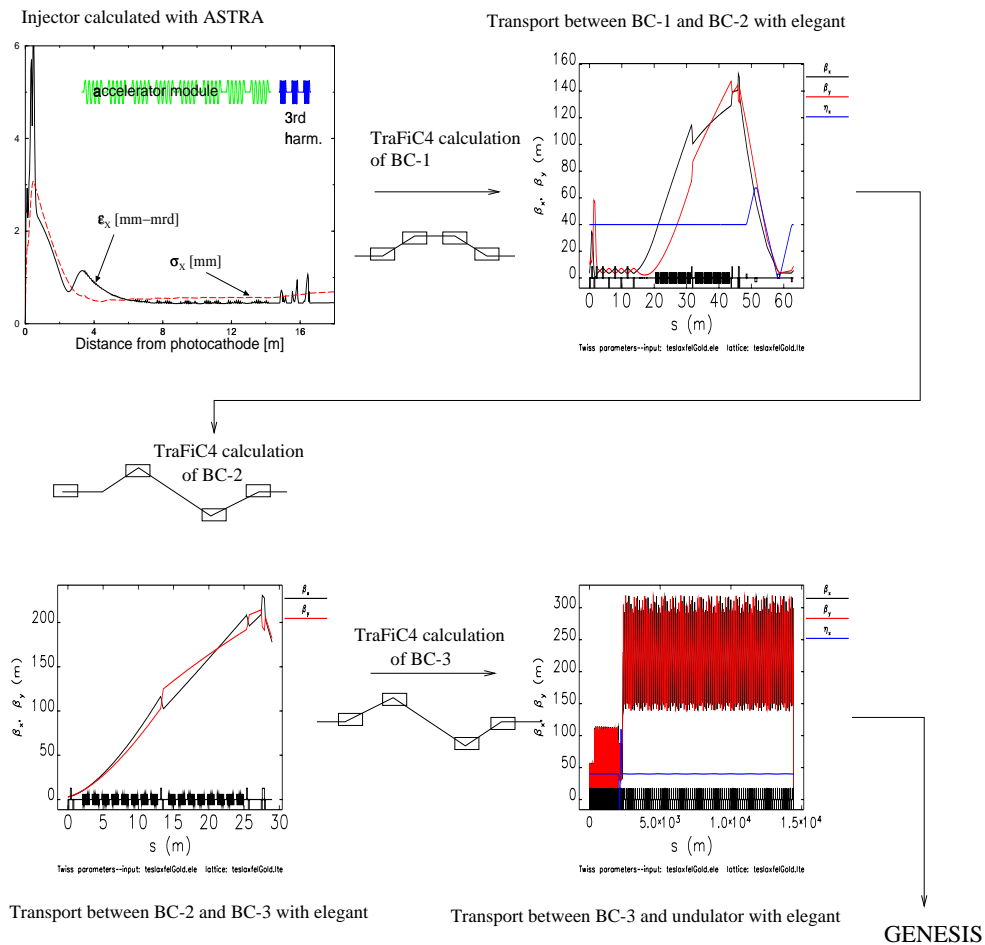
Figure 9.4.5: *Complete beam dynamics simulation for TESLA XFEL.*

The next figures (9.4.6 - 9.4.8) show the results of the complete simulation at the exits of the bunch compressors. Table 9.4.4 lists the peak current and the transverse emittances after the different stages of compression.

	Slice Emittance [mrad mm]	Correlated Emittance [mrad mm]	Projected Emittance [mrad mm]	Peak Current [A]
BC-1	0.4	0.05	0.7	400
BC-2	0.4	0.3	0.9	1250
BC-3	0.6	1.7	2.5	5000

Table 9.4.2: *Normalized horizontal emittance and peak current for the different TESLA XFEL bunch compression stages. The simulation includes the entire beam line starting at the gun.*

s_rms (initial):   1763.440 µm

s_rms (final):   268.926 µm

δ_rms (initial):   1.540 [%]

δ_rms (final):   1.555 [%]

x_rms (CSR):   89.689 µm

x_rms (w.o. CSR):   72.876 µm

xp_rms (CSR):   121.302 µrad

xp_rms (w.o. CSR):   113.398 µrad
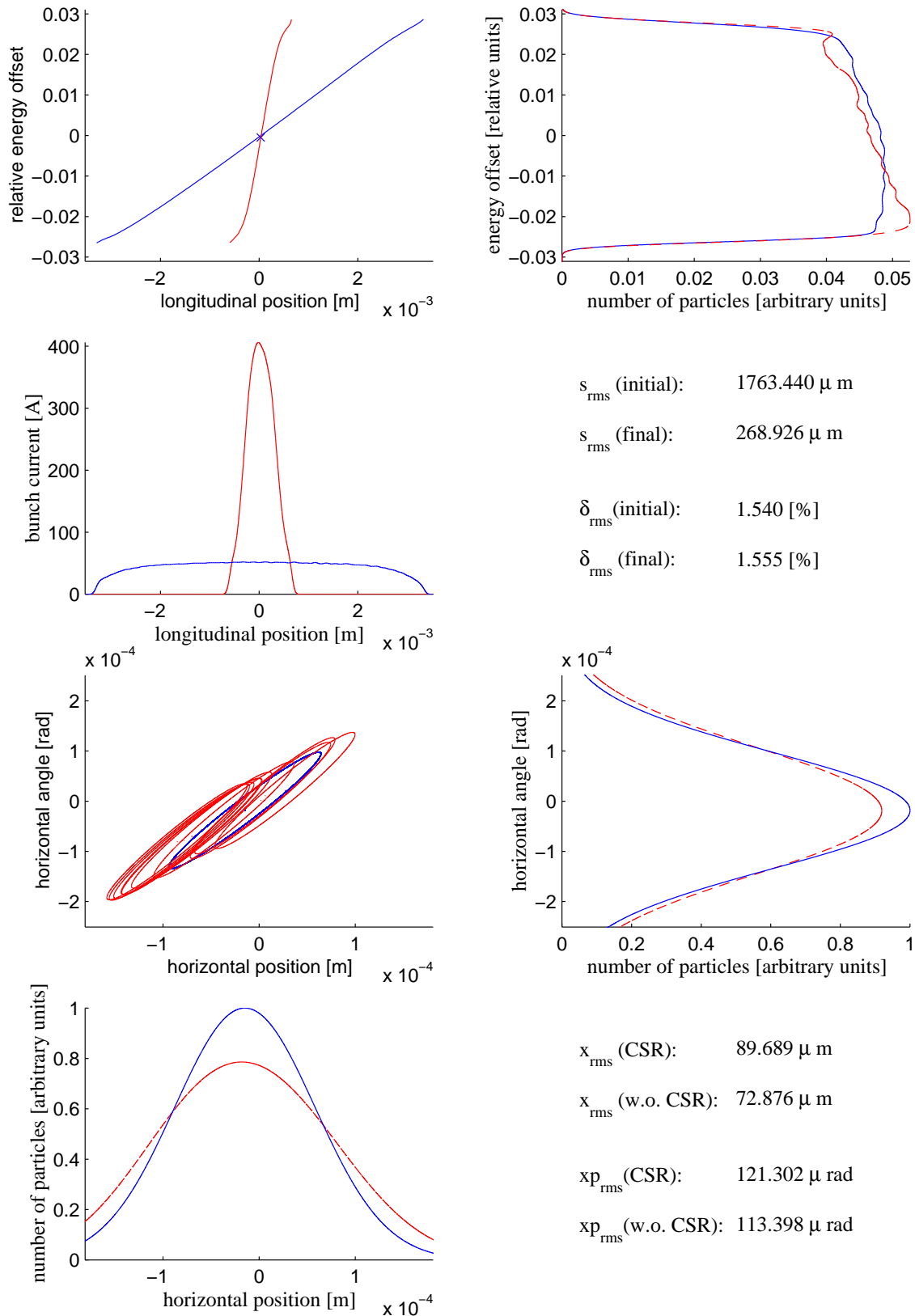
Figure 9.4.6: *Longitudinal phase space before (blue) and after (red) Bunch Compressor 1 and transverse phase space at the compressor exit without (blue) and with (red) CSR, respectively.*
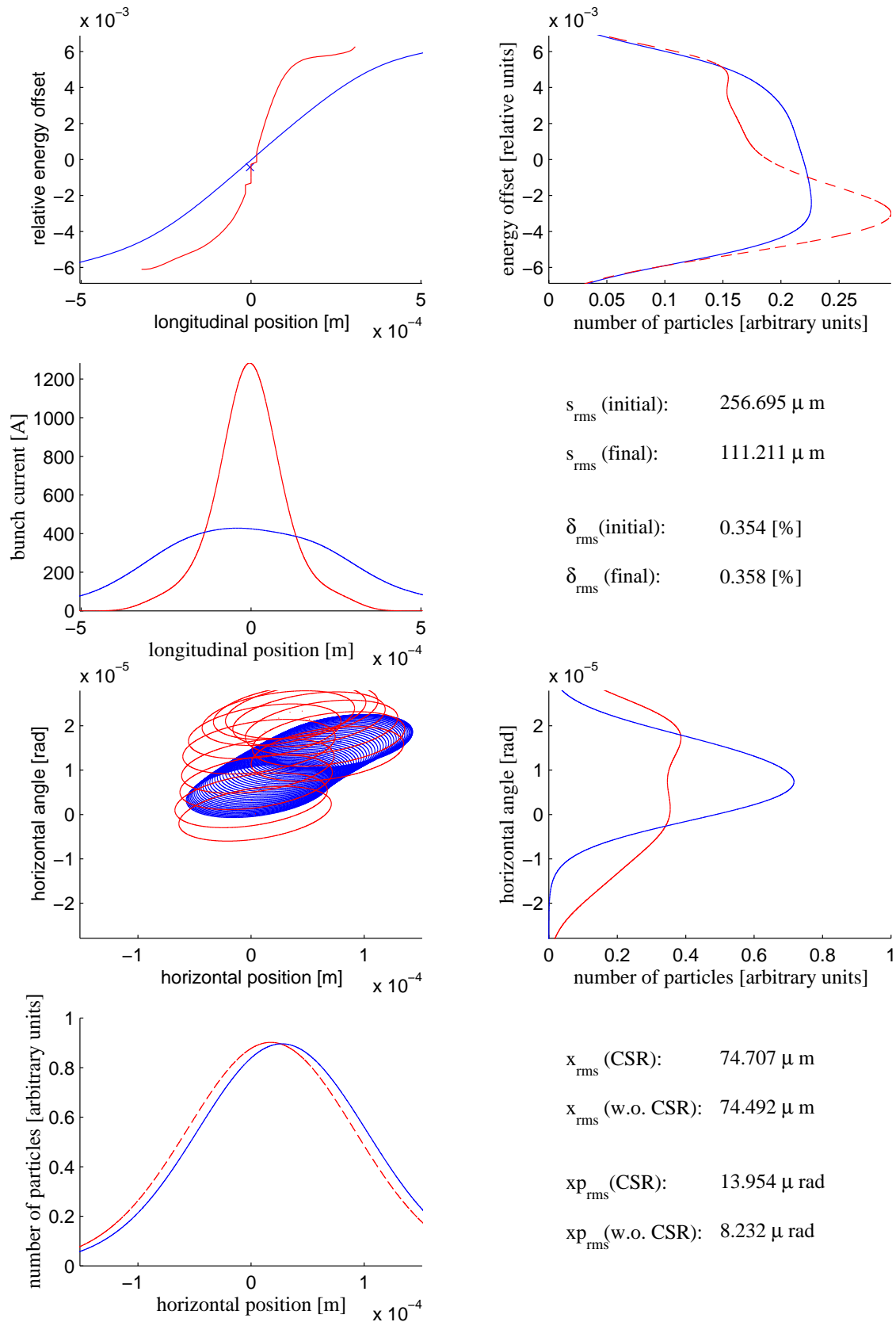
Figure 9.4.7: *Longitudinal phase space before (blue) and after (red) Bunch Compressor 2 and transverse phase at the compressor exit space without (blue) and with (red) CSR, respectively.*

s_rms (initial):   101.606 μ m

s_rms (final):   66.908 μ m

δ_rms (initial):   0.223 [%]

δ_rms (final):   0.217 [%]

x_rms (CSR):   90.433 μ m

x_rms (w.o. CSR):   61.603 μ m

xp_rms (CSR):   27.058 μ rad

xp_rms (w.o. CSR):   16.331 μ rad
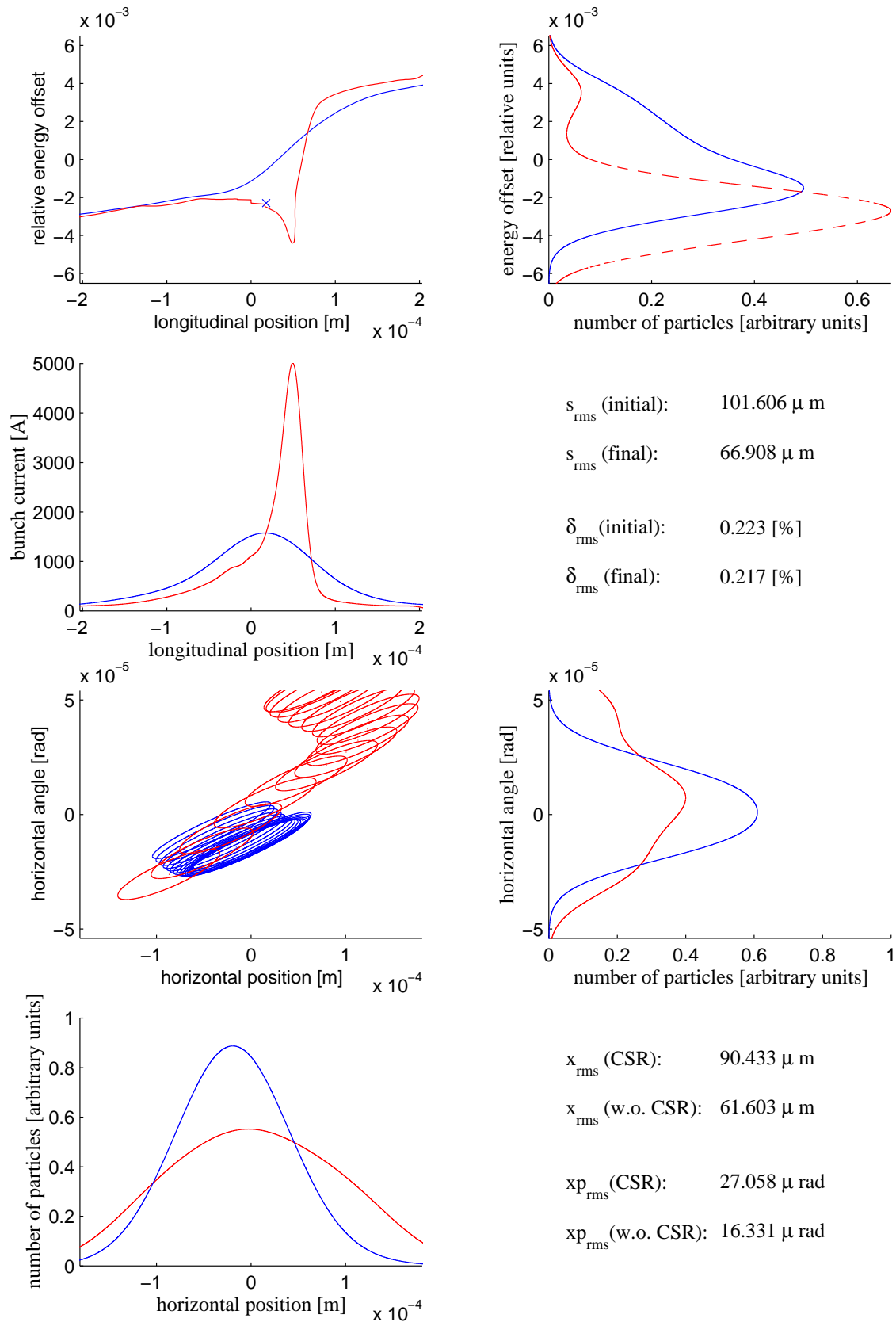
Figure 9.4.8: *Longitudinal phase space before (blue) and after (red) Bunch Compressor 3 and transverse phase space at the compressor exit without (blue) and with (red) CSR, respectively.*

9.5   Beam Dynamics in the Main Linac

The low energy part of the main linac will be used to accelerate the beam for the X-Ray Free Electron Laser facility in an interleaved pulse mode with the collider beam. To provide a maximum energy range for the FEL beam (13-50 GeV) with a minimum number of extraction points, the betatron phase advance per FODO cell for the HEP beam is chosen to be $\mu_T = 45°$. An energy range of the FEL beam of 13-50 GeV is provided by two extraction points from the main linac. In this part of the linac, the beam for high energy physics is accelerated by a gradient of 22 MV/m both for the TESLA-500 and the TESLA-800 options. The acceleration gradient for the FEL operation lies then between 9.2 and 23.4 MV/m, where an optical solution for the FEL beam exists. The overall AC-to-beam power efficiency for the FEL operation is above 20% in the entire range of accelerating gradients between 9.2 and 23.4 MV/m.

The first extraction point covers the energy range of 13-27 GeV, and the second extraction point covers the range of 20-50 GeV. Due to the overlap in the range 20-27 GeV, both beam lines may be operated at the same energy in that range, if desired. Table 9.5.1 presents the main parameters of the beam at the extraction points from the main linac.

Extraction ports	Port 1	Port 2
Energy range E(GeV)	13÷27	20÷50
Acceleration gradient G(MV/m)	9.2/23	9.2/23.4
Number of FODO cells	21	38
Extraction position along the main linac L_1 (m)	1365	2470
Phase advance in last FODO cell μ	125° − 47°	127° − 45°

Table 9.5.1:   *Linac parameters relevant for beam dynamics up to the extraction points.*

The minimum and maximum values of the phase advance per cell along the linac for the FEL beam with different acceleration gradients is presented in figure 9.5.1. The 22nd and 39th FODO cells are used for the extraction magnets.

The maximum emittance growth of the FEL beam is expected to occur for the lowest operation gradient of 9.2 MV/m. In a two beam operation mode with large energy difference, the FEL beam will perform large coherent betatron oscillations when the quadrupoles are misaligned and the trajectory of the HEP beam is corrected by a one-to-one correction method. Hence the information of the trajectories of both beams with different energies will be used to minimise the difference orbit by fitting the strength of the corrector dipoles, using the method of "dispersion free correction".

The simulation study [53] shows that the application of the two-beam correction scheme stabilises both the HEP and the FEL beam trajectories at the level of the BPM resolution. The maximum orbit amplitude for given rms misalignments (quadrupoles 0.3 mm, beam position monitors (BPM) 0.1 mm, BPM resolution 10 μm) is at the level of 25 μm at the end of the linac section operated in two-beam mode. Accordingly the
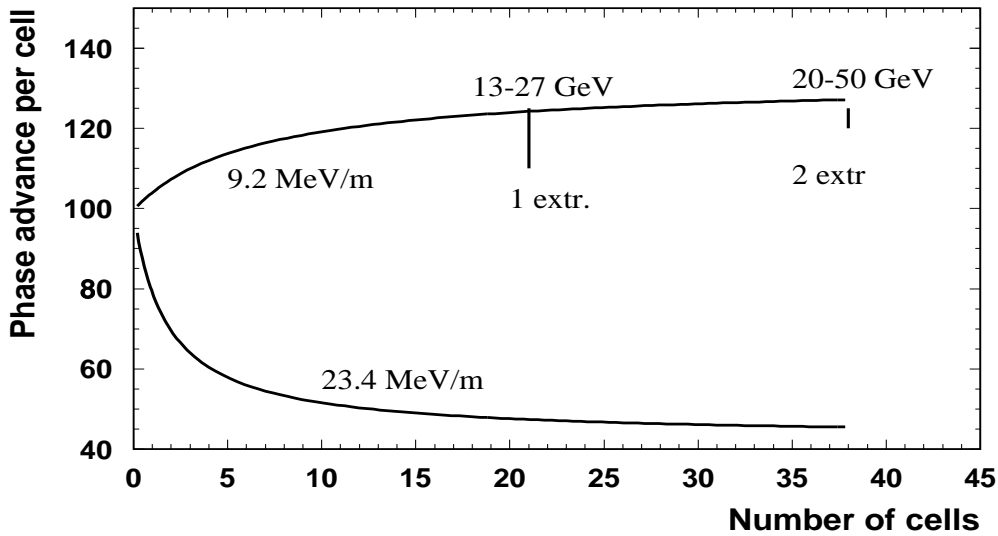
Figure 9.5.1: *Phase advance per FODO cell (in degrees) of the main linac for the FEL beam operating at different acceleration gradients.*

relative FEL beam emittance growth is below 10^{-3} with the application of a two-beam based trajectory correction algorithm for any acceleration gradient foreseen. Verification of dispersion-free correction of the orbit can be done continuously during routine operation and will be profitable to both XFEL and collider operation.

The correlated energy distribution of the FEL beam, induced in the main linac, is dominated by geometric wakefields. It amounts to 10.5 MeV rms at the first extraction point and 18.8 MeV rms at the second extraction point, corresponding to a relative energy spread of $1.1 \cdot 10^{-3}$ for a gradient of 9.2 MV/m and of $4 \cdot 10^{-4}$ at 23.4 MV/m, see also table 9.1.2 and section 3.2 for more details on the beam dynamics in the main linac.

9.6 Electron Beam Transport and Distribution

9.6.1 Introduction

The FEL performance depends strongly on the electron beam parameters such as phase space density, bunch charge and narrow energy spread. Once the design parameters have been established, the downstream magneto-optics systems should handle the beam "carefully" to avoid any degradation of the beam quality, such as growth of energy spread or emittance due to uncorrelated synchrotron radiation. The energy acceptance is another important property for a transport and distribution system. To scan the FEL radiation wavelength within a bunch train one must be able to vary the energy inside the train. Therefore, the transport and distribution system should accept bunches with

different energies and transport them without deterioration.

9.6.2   Extraction

Two transfer lines are provided for the FEL beam transport [54]. Beam energies ranging from 13 GeV to 27 GeV are extracted from the linac at position 1365 m (as measured from the injection point to the main linac), and energies from 20 GeV to 50 GeV at position 2470 m, respectively. These lines are designed for an energy acceptance of max. ±3%, to allow fast tuning of the undulator radiation.

Three sections of each transfer line are considered here. A 390 m long achromatic arc deflects the beam out of the linac into a 150 m long matching section. Here the beam optics is adapted to the 12 km long transfer line of which is parallel to the linac. All magnetic elements of the arc are excited according to the beam energy. The matching section follows a more complicated excitation pattern and the quadrupoles of the long transfer lines are powered independently of energy. Finally the beam is bent to the ground level, distributed by a switch yard to different undulators and then directed to the beam dump.

The achromatic arc starts with a pulsed dipole magnet (for the technical design of a similar magnet proposed for the FEL distribution system, see ref. [63]) following a defocusing linac quadrupole. The first dipole has tight field tolerances: neither the undeflected HEP beam, nor the deflected FEL beam should get a directional jitter of more than $0.06\,\mu$rad (10% of the beam divergence). This corresponds to a tolerance of $\delta B/B \leq 10^{-4}$ for the pulsed dipole, if the identical dipole downstream at 180° phase
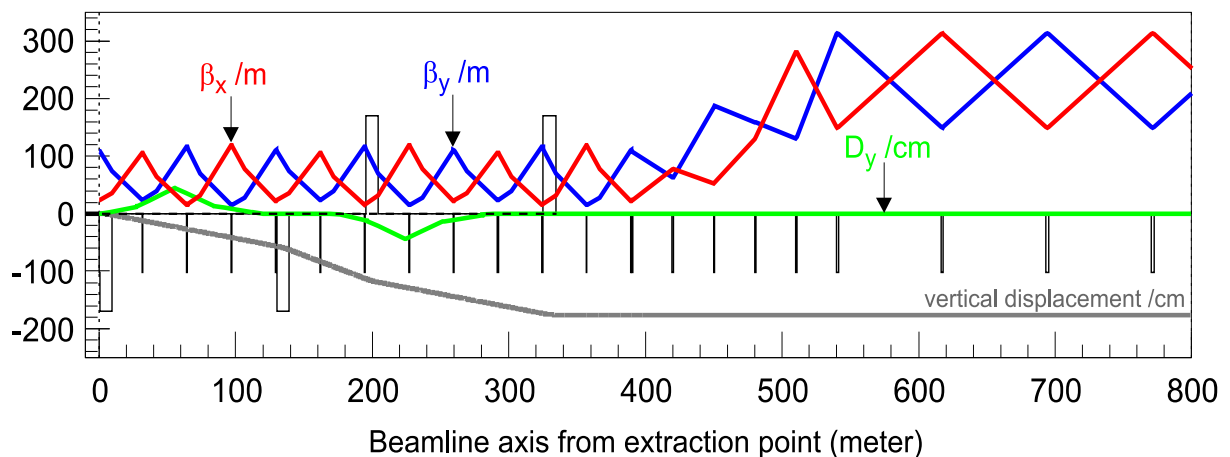
Figure 9.6.1:   *Electron optics in the first part of the transfer line. Quadrupoles and dipoles are marked by vertical boxes (dipole boxes are field sign dependent). The vertical orbit displacement (black curve, scale in cm) is shown versus the distance from the extraction point in the lower part of the figure. The achromat ranges from 0 to 390 m, the matching cells extend up to 540 m followed by the first cells of the transfer line.*

advance is powered in series. A suitable pulsed power supply has been designed [63]. Altogether 4 dipoles are used to achieve a dispersion free beam displacement of 1.7 m. The bending radii of the dipoles are 2000 m to keep synchrotron radiation heating low, the increase in energy spread is estimated at < 0.1 MeV (rms) for a 40 GeV beam.

Quadrupoles of the arc are arranged in 6 FODO cells with the same geometrical structure as in the linac. The phase advance over the full arc is 540 $^\circ$ in both planes. These quadrupoles are excited in proportion to the beam energy, to preserve the achromatic condition. The same scaling has to be applied to 12 sextupole and 2 octupole correction elements of moderate strength within the arc, necessary to improve the chromatic orbit. In this way all pulse trains with an energy modulation of $\pm 3\%$ are deflected into the transfer line with chromatic orbit errors of less than a few μm, to be compared to an rms beam size of approx. 60 μm. Inside the achromat the chromatic orbit deviations are defined by the linear dispersion function reaching extrema of ± 0.45 m and yielding an R_{56} matrix element of 0.12 mm. Figure 9.6.1 shows the arrangement of the dipoles, quadrupoles and the optical functions in the first part of the transfer line, figure 9.6.2 shows an example of chromatic beating of the optical functions.

9.6.3   Transfer channel

Following the achromat there is a matching section with 6 independently tunable quadrupoles. These are required to focus the beta functions at the exit of the arc to the correct, energy dependent entrance values of the energy-independent FODO
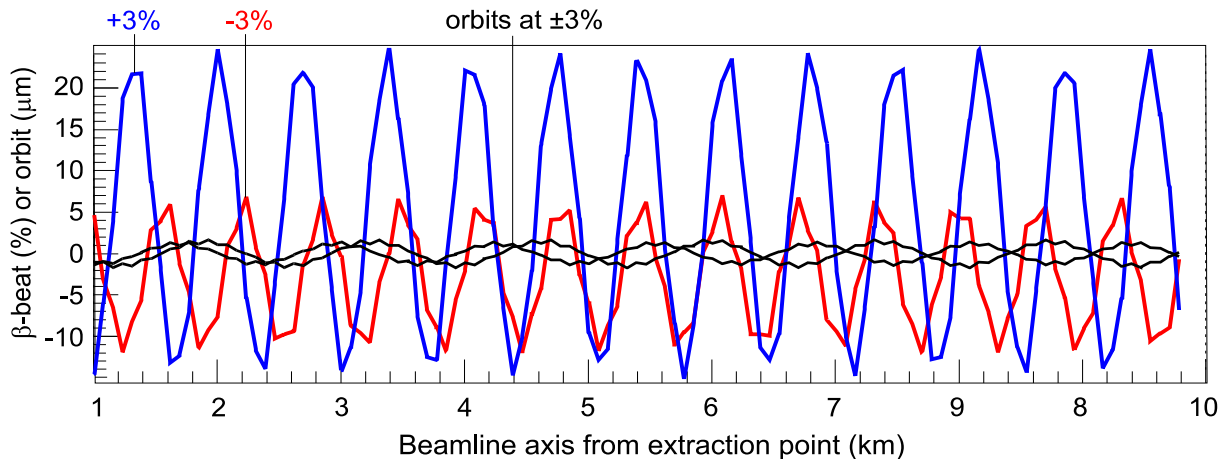
Figure 9.6.2:   *Chromatic beta beat $\Delta\beta/\beta$ in % of the vertical beta function at 30 GeV for $\Delta p/p = +3\%$ (blue) and -3% (red) in the 12 km transfer line. The 2 curves of smaller amplitude (black) show examples of not perfectly corrected chromatic orbits at $\Delta p/p = \pm 3\%$ (in μm). Beta functions and orbits both have a chromatic phase dependency. The horizontal beta function (not shown) reaches 8% beat.*

magnet type	units	location	length	max. field	half aperture
dipole (pulsed)	2	arc	9.0 m	0.085 T	4 cm×2.25 cm
dipole	2	arc	9.0 m	0.085 T	4 cm×2.25 cm
quadrupole	12	arc	2.0 m	3.7 T/m	4 cm
quadrupole	6	match. cell	2.0 m	5.0 T/m	2.25 cm
quadrupole	160	FODO	0.3 m	3.0 T/m, const.	2.25 cm
sextupole	6	arc	0.5 m	65 T/m^2	4 cm
sextupole	6	arc	0.5 m	170 T/m^2	4 cm
octupole	2	arc	0.5 m	500 T/m^3	4 cm
corrector	173	quadrupole	0.3 m	0.03 T	2.25 cm

Table 9.6.1:   *Main parameters of the magnetic elements for the high energy beam line at 50 GeV. Values of the FODO channel are energy-independent.*

channel. This FODO channel has been designed for fixed gradient to retain the freedom of choosing permanent magnet quadrupoles for cost saving reasons. In principle, this concept even suggests that both long transfer lines could be combined into one (still keeping two extraction points!), which would require a few more pulsed magnets and is considered as a cost saving option which needs more investigation.

There is already a chromatic dependency of the beta functions at the achromat entrance, because the FEL beam in the linac is accelerated by a variable gradient but constant strength of the linac quadrupoles. This leads to energy dependent beta functions at the entrance of the arc (see section 9.5). This chromatic dependency is enhanced at the exit of the arc. These values have to be matched to the correct beta functions in the FODO channel. For all energies considered this can be achieved without residual beta beat in the transfer line. However, any energy variation within a bunch train will lead to a beta beat depending on the bunch train energy and the amount of energy variation.

The present scheme was optimized for minimum beat beat in the FODO channel at 30 GeV, corresponding to the most demanding FEL conditions which are found at that beam energy level. At magnet settings for 30 GeV and ±3% momentum variation, the beta beat is ≈ 20% in the vertical plane and 8% in the horizontal plane. A ±1.5% momentum variation results in a beat of 8% in both planes.

The FODO channel has 80 cells with quadrupoles separated by a drift of 73 m. The optics is tuned to keep the beta functions for all energies below 500 m, which ensures low sensitivity to time dependent magnetic stray fields. Each quadrupole includes a dipole corrector for orbit correction, allowing for a 0.05 mrad kick to a 50 GeV beam (equivalent to 5 mm quadrupole misalignment at 50 GeV). This would be also sufficient to correct for an ambient stray field of 10^{-4} T. Residual effects of time dependent stray fields will be corrected by an orbit feedback system, see section 9.6.6.

A parameter list of the magnetic elements at the strongest field excitation (50 GeV) is presented in table 9.6.1.

9.6.3.1   Vacuum system for the transfer line

The vacuum requirements in the transfer line are relaxed, since the effect of the fast beam-ion instability is negligible for a vacuum pressure below 10^{-6} mbar as has been shown in [55]. An average vacuum pressure of the order of 10^{-8} mbar is expected in the beam line. A large beam pipe radius of 12.5 cm and a good electrical conductivity (aluminum) is required to keep the contribution of resistive wake fields to the correlated energy spread in the long transfer line small. The resistive wake field contributions are discussed in more detail in section 9.7.1. In the quadrupole magnets the chamber radius is reduced to 17 mm.

9.6.4   The electron beam collimation

Transverse phase space and an energy collimation of the electron beam is foreseen before it is guided to the switchyard. The collimation has two functions: First to remove halo particles (dark current) during normal operation, usually with particle losses small compared to the total beam, second to protect the undulators in case of a machine failure, when the total beam is outside the acceptable parameter range.

While halo collimation is necessary to avoid radiation damage and activation of the undulators and other components of small aperture, protection collimation is even more critical since it has to prevent the destruction of the vacuum chamber. In case of a failure, kickers will be fired in order to guide the beam into the emergency beam dump and hence to reduce the load on the collimators. The overall concept of the machine protection is described in the overview section 9.1.9, here details on the layout of the high energy collimation section will be presented.
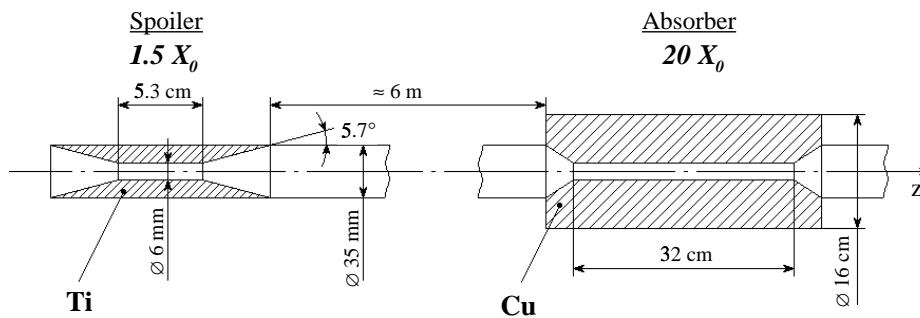
Figure 9.6.3:   *The spoiler and the absorber scheme.*

For the high energy electron beam collimation a spoiler-absorber scheme is employed, see figure 9.6.3. Titanium alloy is chosen as spoiler material to improve the

spoiler survival time, in case of being hit by the full beam.

After the spoiler an absorber for the secondary particles is installed at a distance of ≈ 6 m. Copper was chosen as the absorber material for its short radiation length (X_0) and high electrical conductivity. The electrical conductivity of Cu is useful to reduce the resistive wall wakefield kick. To absorb secondary particles, the Cu absorber is $22\,X_0$ thick (or 32 cm) and 16 cm in diameter. The aperture of the absorber is chosen in a way, that the absorber is just in the shadow of the spoiler, i.e. it efficiently scrapes secondary particles but cannot be hit by primaries.

To minimise wakefields, spoiler and absorber are tapered. The direct measurements of the wake field effect [61] show that the chosen geometry for the spoiler and the absorber is reasonable. The spoiler with $1.5\,X_0$ thickness withstands 70 bunches with a spot size of $\sigma_x \cdot \sigma_y \approx 72\,\mu\mathrm{m} \cdot 72\,\mu\mathrm{m}$. The time delay of $\approx 6.5\,\mu$s) is sufficient to trigger the emergency system placed upstream of the collimating sections. For a response time of the emergency system electronics of ≈ 300 ns, including the kicker rise time, and a typical signal velocity in the cable, the tolerable kicker position is at a distance of ≈ 1200 m from the spoiler. The collimation efficiency has been determined with extensive Monte-Carlo calculations with the EGS4 code for the 50 GeV primary beam with $5 \cdot 10^9$ particles [63]. To be able to enter the downstream line, the secondary particles would have to pass the absorber aperture, i.e. only particles within a solid angle ≈ 2 msterad are accepted (assuming no magnetic elements between the spoiler and the absorber). The relative number of secondary electrons within the energy acceptance and within the solid angle of 2 msterad is estimated at $< 5 \cdot 10^{-7}$.

Transverse phase space collimation   The transverse phase space collimation system is placed downstream of the long transfer line before the arcs which elevate the beam to the ground surface level. A FODO structure is chosen for the transverse phase space collimation, since it has more favourable chromatic properties than, for example, a triplet chain [63]. A FODO lattice with a cell length of 166 m and a phase advance of $\pi/6$ per cell in both planes is used, resulting in maximum beta functions of 418 m. Weak quadrupoles with a gradient of 1.05 T/m at 50 GeV and an effective length of 1.0 m are used. The collimators are placed between quadrupoles, to ensure that the beam spot size at the spoiler position, at an energy of 50 GeV and for a normalised emittance $\varepsilon_x = \varepsilon_y = 1.6$ mrad mm will be $\sigma_x \sigma_y \simeq 5250\,\mu\mathrm{m}^2$.

The full betatron collimation system consists of 6 FODO cells of 996 m length and collimates in two planes. Figure 9.6.4 shows the behaviour of the beta functions for the six-cell FODO lattice and the collimator positions. The energy acceptance of the transverse collimation section exceeds $\pm 5\%$.

Energy collimation   The transverse phase space collimation is followed by an energy collimation section. The dispersion in the arc of the elevation beam line, following the collimation section, could be utilised for this purpose. However, the beta functions have to be kept small in the arc to suppress emittance growth due to spontaneous synchrotron radiation. Hence a sweeping system would be required to guarantee the survival of the spoilers. Instead a magnetic chicane is foreseen in between the transverse
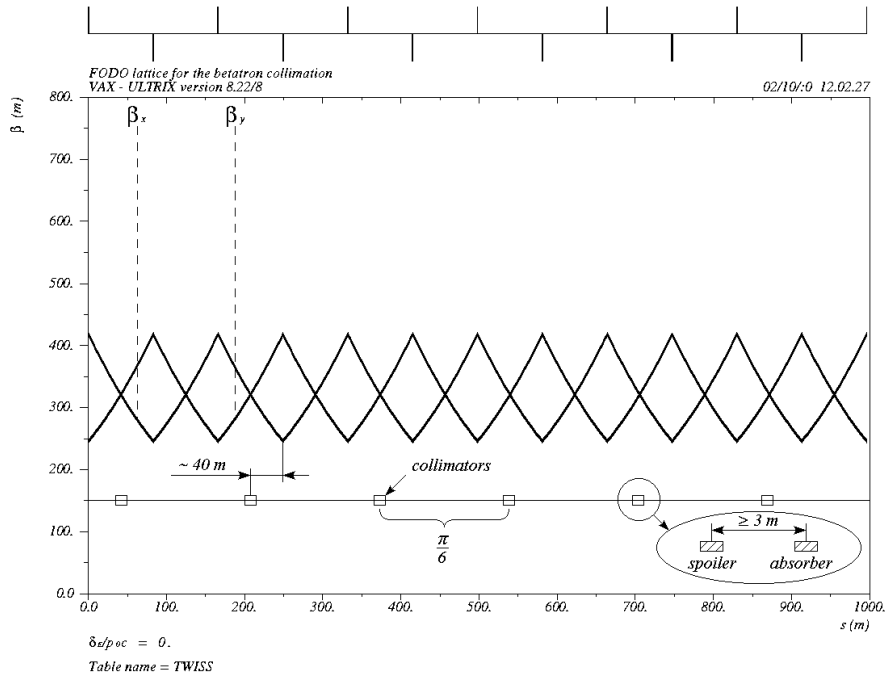
Figure 9.6.4:   *The optical functions of the FODO lattice for the transverse collimation.*

collimation section and the arc, followed by a matching telescope, which reduces the large β-functions of the transport line to the small β-functions required in the arc.

Figure 9.6.5 shows the optical functions in the chicane and in the telescope. The chicane, consisting of only four rectangular dipole magnets, is intrinsically achromatic and has a large bandwidth which is limited by the vacuum chambers rather than by chromatic effects. Equipped with movable jaws, the energy acceptance can be adjusted according to the requirements of the FEL operation. The simple telescope, consisting of only three quadrupoles, is limited in bandwidth to $\approx \pm 3\%$ and needs more investigation.

9.6.5   Beam elevation to ground level

The magnet lattice of the system to elevate the beam from the tunnel level to ground level has to fulfil a number of requirements, both in terms of beam dynamics and geometry. Top and side views of this "elevation system" are shown in figure 9.6.6. The general design criteria are:

- Generation of a horizontal angle of $8.36°$ between the linac and the mean axis of the X-ray beam lines.
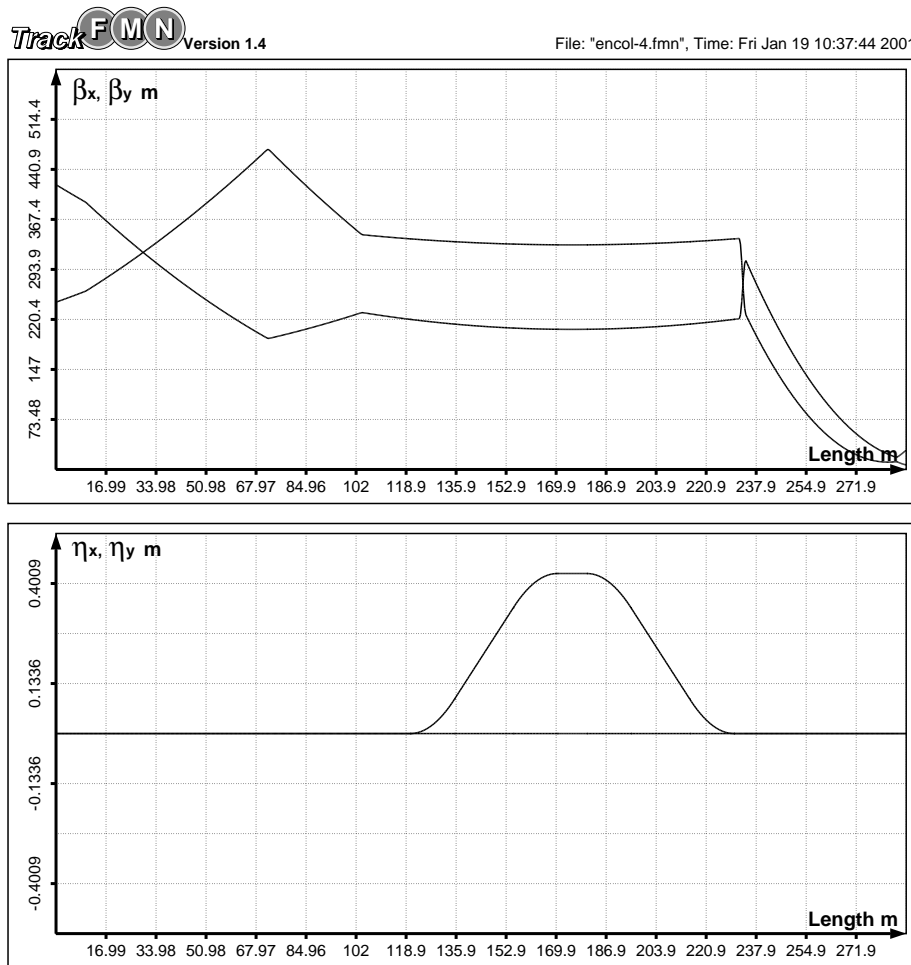
Figure 9.6.5: *Optical functions in the energy collimation section and the matching telescope, connecting the transverse collimation section (on the left side) and the beam elevation arc (on the right side).*

- Generation of a vertical displacement of the beam by 15.154 m relative to the collider beam line.

- Provision of the required energy acceptance.

- Introduction of neither significant transverse emittance growth nor additional energy spread.

The system consists of the horizontal arc, the vertical arc and the matching section between them. The horizontal deflection and vertical displacement are separated and composed of four identical arcs called A1 in figure 9.6.6.

The design of the A1 arc is based on geographical considerations, on the experimental area and the beam distribution system, and on the requirement of a large energy acceptance for the bunch train.
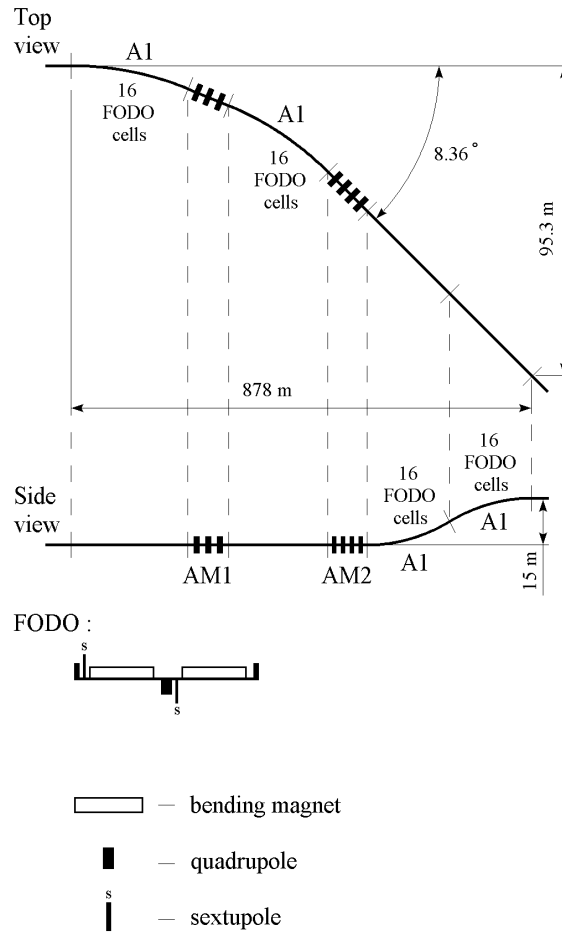
Figure 9.6.6: *Schematic layout of the elevation system.*

The A1 arc unit consists of 16 FODO cells and has a length of 208.6 m. In both transverse planes the A1 arc constitutes a second-order achromat and is symmetrical about the centre. A total of 32 sextupoles arranged in two families are needed in all FODO cells. Thus, two out of four free spaces (the length of which is 0.51 m) in each FODO cell are occupied by sextupoles, see figure 9.6.6. The other two free spaces may be used for correction elements. The transverse emittance dilution in the A1 arc unit is $\Delta(\varepsilon_n)/\varepsilon_n = 0.21\%$ at an energy of 40 GeV.

Each arc, horizontal and vertical, is constructed from two A1 units, using different types of symmetries to achieve the required value of energy acceptance. Between the two horizontal A1 units is a special section (AM1) with minus identity transfer matrix located. The horizontal arc provides a deflection angle of 8.36° in accordance with the

geometrical requirements of the experimental area.

The vertical arc is build of two A1 units rotated by $+90°$ and $-90°$, respectively. It provides a vertical displacement of $15.154\,\mathrm{m}$. A matching section called AM2 is located between the horizontal and vertical arcs.

The lattice of the complete arc fulfils the general design requirements listed above. The tracking results prove that the energy acceptance is $\pm5\%$, see figure 9.6.7 which presents trajectories of particles with energy offsets of $\pm3\%$ and $\pm5\%$. The maximum amplitude of the dispersive trajectory displacement in the arc is approximately $\pm0.013\,\mathrm{m}$ for a $\pm5\%$ energy offset.
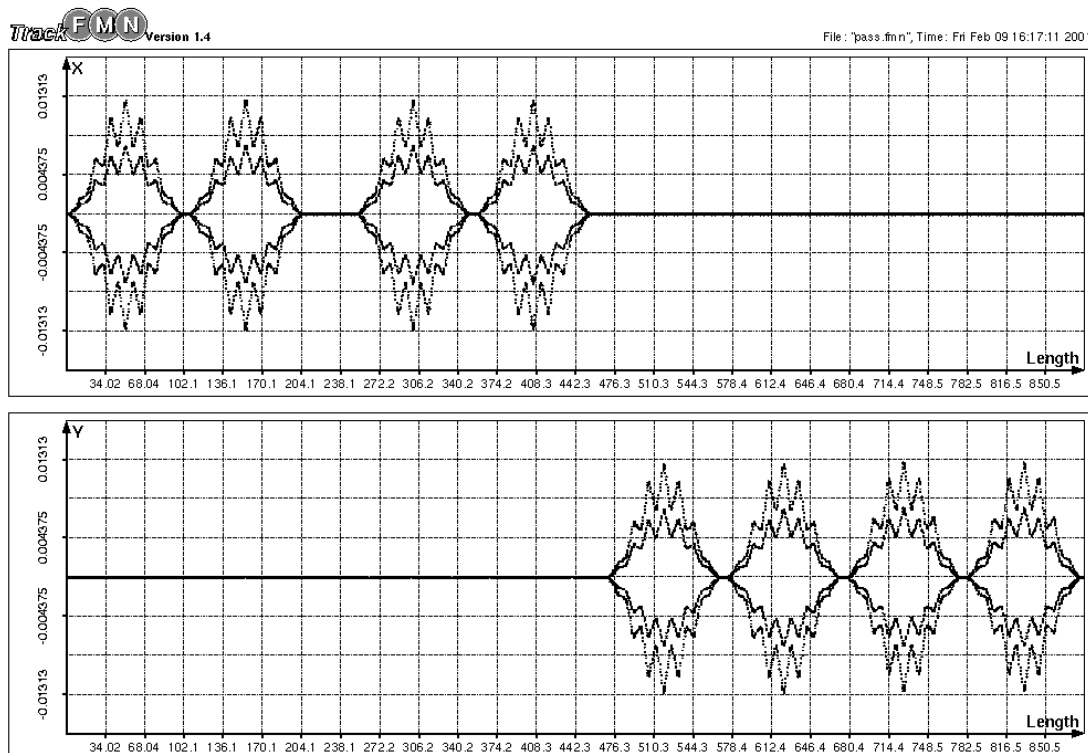
Figure 9.6.7: *Tracked trajectories of off-energy particles, taking into account all non-linearities, along the complete arc deflecting and elevating the XFEL electron beam from the TESLA collider tunnel. The energy deviation is $\pm3\%$ (inner trajectories) and $\pm5\%$.*

9.6.6 Electron beam distribution system

The schematic layout of the FEL beam transport lines for the separation of the bunch trains and distribution to several FEL users is shown in figure 9.6.8.

The beam distribution system to the various undulators consists of two transport lines. The first beam line (BDL1) directs one bunch train, coming through the arc to the FEL hall level, to SASE1 and undulators U1 and U2. The second line (BDL2)

takes every other bunch train and delivers it to SASE2 and undulator U3. The design requirements of the distribution system are:

- A horizontal separation of the bunch trains with a 1.4° bending angle for one branch of the transport line to deliver beams for two separate FEL undulators (SASE1 and SASE2 in figure 9.6.8).

- A separation of the trains with pulsed dipole magnets ($\leq 5\,\mathrm{Hz}$).

- A horizontal deflection of $\approx 2.6°$ between the downstream undulators (U1, U2 and U3 in figure 9.6.8).

- An energy acceptance of at least $\pm 3\%$.

- Insignificant contributions to transverse emittance and energy spread.

- Integration of a fast feedback system to control the beam position jitter at the entrance of the FEL undulators.
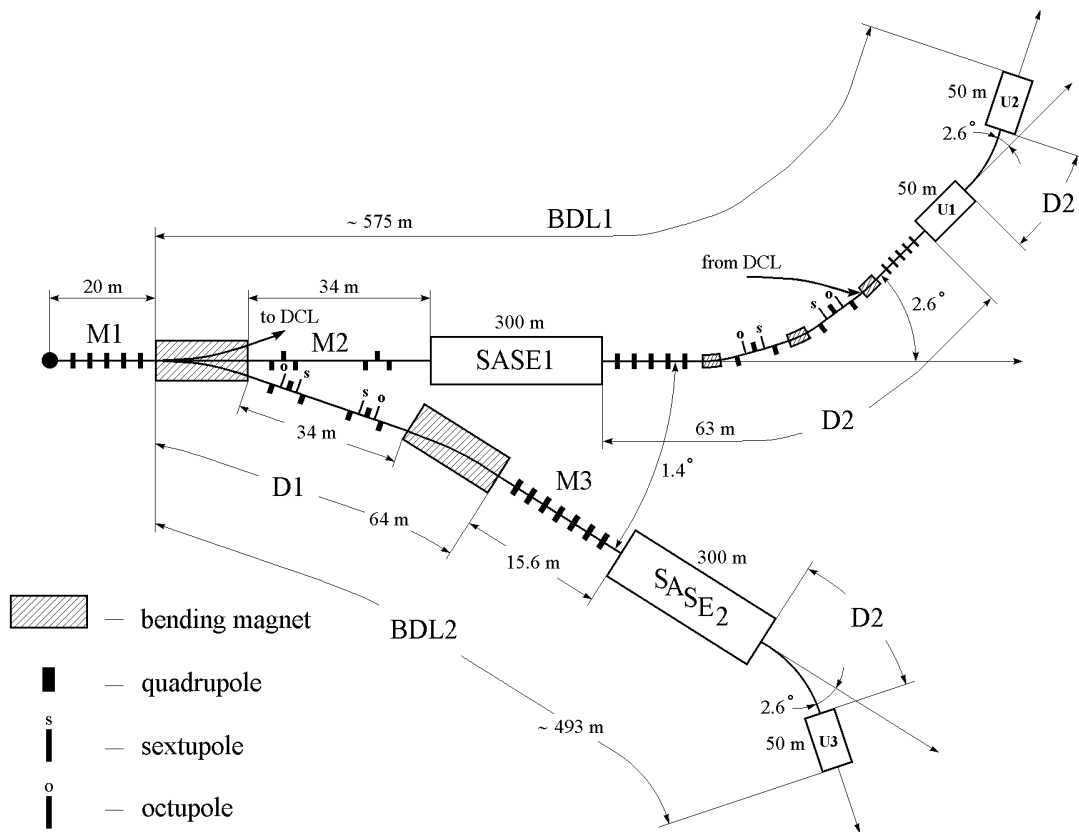
Figure 9.6.8: *Layout of the beam distribution system for the high energy beam line. An equivalent beam distribution system is set up for the low energy branch.*

Two parts of the transport lines include bending magnets:
    - The separation section D1 which uses the pulsed dipoles, powered in series,
    - and the section D2 with DC dipoles.

The photon beams of the different undulators have to be separated by a distance of 17 m in the experimental hall, which is realized by a deflection angle of 1.4° in the separation D1. The section is composed of two pulsed dipole magnets of 15 m length (powered in series), separated by two quadrupole triplets to produce a linear achromat with a mirror symmetry with respect to the centre of the section. To provide the energy acceptance the dispersion is corrected to third order by two sextupoles and two octupoles. The choice of two triplets between the dipoles was made to facilitate beam matching into and out of the system and to obtain a behaviour of the beta functions which allows to achieve a large energy acceptance.

The beam line D2 deflects the beam to various undulators using a triple-bend structure. Two quadrupole triplets between the dipole magnets are required with one sextupole and one octupole placed between the quadrupole lenses in each triplet. The 11 m long matching sections to the undulator on both sides of the bending are composed of five equally spaced quadrupoles ($\Delta l = 1.5$ m).

The beam distribution system contains the three matching sections M1, M2 and M3. The optics of the M1 section includes the kickers for the fast orbit feedback system. Consumable or sacrificial spoilers [60] are foreseen in sections M2 and M3 for the protection of the undulators, as well as additional feedback kickers. The optics of the sections M1, M2 and M3 is very flexible with respect to the parameters of the in- and outgoing beams. The energy acceptance of the transport lines up to SASE1 and SASE2 is ±5% and ±3% up to the undulators U1, U2, U3. The optics of the beam elevation and distribution system, as well as technical parameters are described in more detail in ref. [63].

Integration of the fast orbit feedback system   Orbit distortions due to fast vibrations of quadrupoles and cavities can not be detected and controlled by the usual orbit correction. In order to correct the position and angle of every bunch in a train a fast feedback system for both the horizontal and vertical plane is required. Each system consists of two pairs of kickers. One pair of kickers is used to correct either the angle or the position error of the beam. The length of the kicker magnets is assumed to be 1.1 m and the maximum magnetic field is up to 0.1 mT. The feedback system for the FEL undulator SASE1 is located in the matching section M1 and M2 while the system for SASE2 is located in section M1 and D1 or M3. An equivalent system is set up in the low energy branch of the distribution system. The fast feedback system for SASE1 and SASE2 can correct position and angle errors corresponding to two sigma of the beam width or divergence. The expected uncorrected orbit variations are below 0.5 sigma in position and divergence. A similar feedback system is under test at the TTF (see section 9.2).

9.6.7   The diagnostic commissioning line

The performance of the FEL depends critically on the parameters of the electron beam. The optics before and in the beam distribution system is especially designed to ensure the desired beam quality. Due to space restrictions a complete beam characterisation in front of the undulators is impractical. Thus a special Diagnostic Commissioning Line (DCL) is integrated into the beam distribution system permitting precise measurements of all beam parameters during commissioning.

A general layout of the DCL is shown in figure 9.6.9. The DCL is placed at a distance of $1.135\,\mathrm{m}$ parallel to undulator SASE1. The bending magnet CM_1 is normally operated in pulsed mode and distributes the electron beam between the SASE1 and SASE2 undulators. To bend the beam into the DCL, it operates in a DC mode with improved field stability. At the end of the DCL the electron beam returns back into the branch of the distribution system by means of bending magnet CM_5.
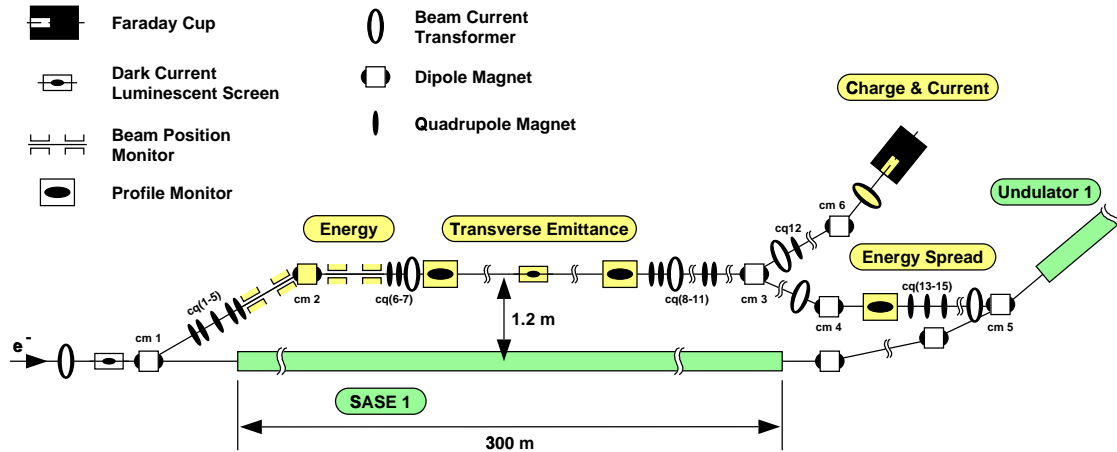
Figure 9.6.9: *The layout of the Diagnostic Commissioning line (DCL).*

In the first DCL section, the bending magnets CM_1 and CM_2 provide the parallel shift of the beam axis by a distance of $\approx 1.135\,\mathrm{m}$. The average beam energy is measured by means of two pairs of Beam Position Monitors (BPMs), installed before and behind dipole CM_2.

The next part of the DCL, the drift space between the doublets CQ_{6-7} and CQ_{8-9} is used for the transverse emittance measurement. Because a beam with equal emittances in both planes is foreseen for the FEL, the $2D$ projected beam emittances ϵ_x and ϵ_y are determined in the drift space with a length of $L_d = 150\,\mathrm{m}$ by means of spot size measurements with three wire scanners.

The last DCL section delivers the beam to the undulator U1 and further into the beam dump. The dipole magnets CM_3 and CM_4 provide a parallel shift of the beam axis by a distance of $\approx 0.36\,\mathrm{m}$, then the beam reaches the entrance of dipole CM_5.

An energy spectrometer with a resolution of $0.4 \cdot 10^{-4}$ is realized in the drift down-

stream of dipole CM_4. Bunch length measurements can be performed with the energy spectrometer by applying the zero-phasing technique [62].

A Faraday cup is used for absolute bunch charge measurements and beam current monitor calibrations. The section consisting of the magnets CM_3, CM_6 and quadrupole CQ_{16} delivers the beam achromatically to the Faraday cup. At the Faraday cup entrance the beam is defocused to $\sigma_x = \sigma_y = 300\,\mu$m.

More details of the DCL design, the proposed diagnostic tools and methods and the technical layout can be found in ref. [63].

9.7 Wakefield Effects in the Transfer Line and in the Undulator

Wakefields describe the interaction of the electron beam with the surrounding vacuum chamber. Two effects are distinguished: wakefields due to the finite conductivity of the chamber material (= resistive wakefields) [56, 57] and wakefields due to the imperfect surface of the vacuum chamber (= roughness wakefields). Longitudinal wakefields become increasingly important for the short bunches considered for FEL operation, while the effects of transverse wakes on the beam tend to become weaker with decreasing bunch length. Geometric wakes due to variations of the chamber geometry (bellows, ports etc.) can be controlled by an appropriate design of the vacuum chamber and are not discussed here. Wakefields are the main source for the correlated energy distribution of the electron beam. They build up in the long transfer line and in the beam elevation arc up to the entrance of the undulators. While this correlated energy distribution degrades the FEL performance only by an increased line width, the additional energy spread that the beam collects while passing the undulator can interfere with the SASE process since it detunes the resonance condition (see part V).

9.7.1 Resistive wakefield effects

After the extraction from the main linac at energies of 13 - 27 GeV (first beam line) and 20 - 50 GeV (second beam line), the FEL beam is transported to the user laboratories located about 12 km downstream. Substantial sources of resistive wakes are

1) the round chamber (radius $B =$ 12 cm) for the beam transfer over $\sim$12 km.

2) the elliptical chamber of the bending magnets in the beam elevation section with a total length of about 900 m and small vertical half-aperture ($b = 1.2$ cm).

3) the round chamber in the undulator with a beam pipe radius of 5 mm.

We first concentrate the discussion on the resistive wakefield effects of the transfer line and the elevation arc. The wakefield in the undulator chamber is presented together with the roughness wakefield in the next section.

The total induced energy spread is the superposition of the induced spread according to

$$\Delta E(s) = eQ \left[L_b W_z^b(s) + L_B W_z^B(s) \right] \tag{9.7.1}$$

where L_b, L_B are the length of the small and large vacuum pipes, respectively, and $W_z^b(s)$, $W_z^B(s)$ are the respective wake potentials. These two sources produce different types of wakes: The wake in the small-height pipe can be computed in the so-called long range model, while the wake in the large cylindrical pipe is describe by the so-called short range model [58]. Figure 9.7.1 shows the computed energy deviation induced in a Gaussian bunch by the two wakefield contributions after the FEL beam has passed a 900 m long pipe of 12 mm radius and a 12 km long pipe of 12 cm radius. The wall material is aluminum and the wakes are computed using a frequency dependent conductivity model [58].
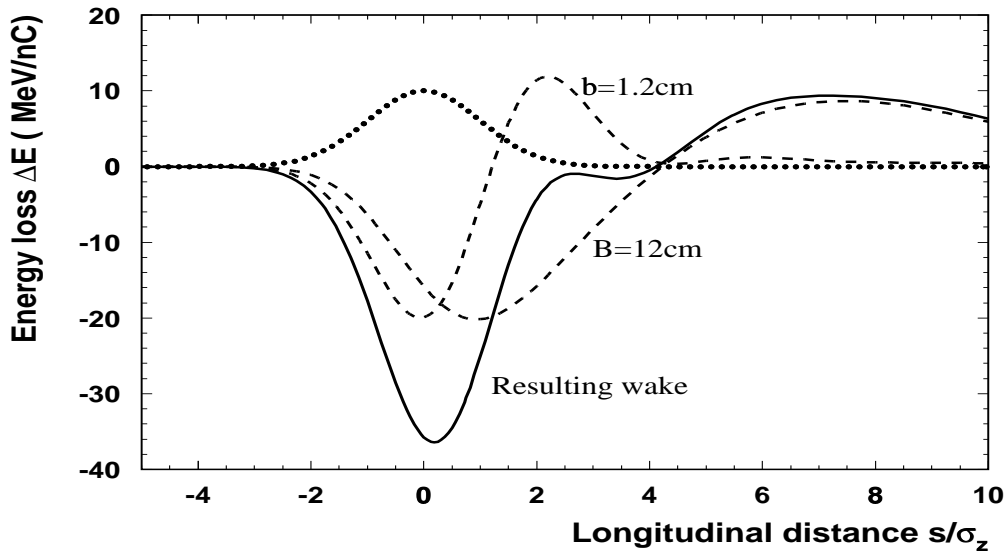
Figure 9.7.1:   *Longitudinal resistive wake potentials of the FEL beam in the transfer line ($\sigma_z = 25\,\mu m$). Shown are the wakes in the small pipe ($b = 1.2\,cm$), the large pipe ($B = 12\,cm$) and the resulting induced wake potential. The dotted line indicated the longitudinal Gaussian bunch profile. The bunch tail is to the right.*

An off-axis beam in a resistive tube produces a transverse wake potential that affects the trailing particles. Figure 9.7.2 shows the dipole wake potential in a cylindrical tube at a longitudinal distance $s = 2\sigma_z$ versus the tube radius.

The longitudinal and transverse wake potentials are summarised in table 9.7.1. While longitudinal wake fields lead to a considerable systematic longitudinal energy variation within the bunches, it will be shown below that transverse wakes have only small effects.

Correlated emittance growth due to transverse resistive wakefields   The 12 km long transfer lines consist of 40 symmetrical FODO cells. The growth of the projected emittance ("correlated emittance") due to coherent beam oscillations with an offset of
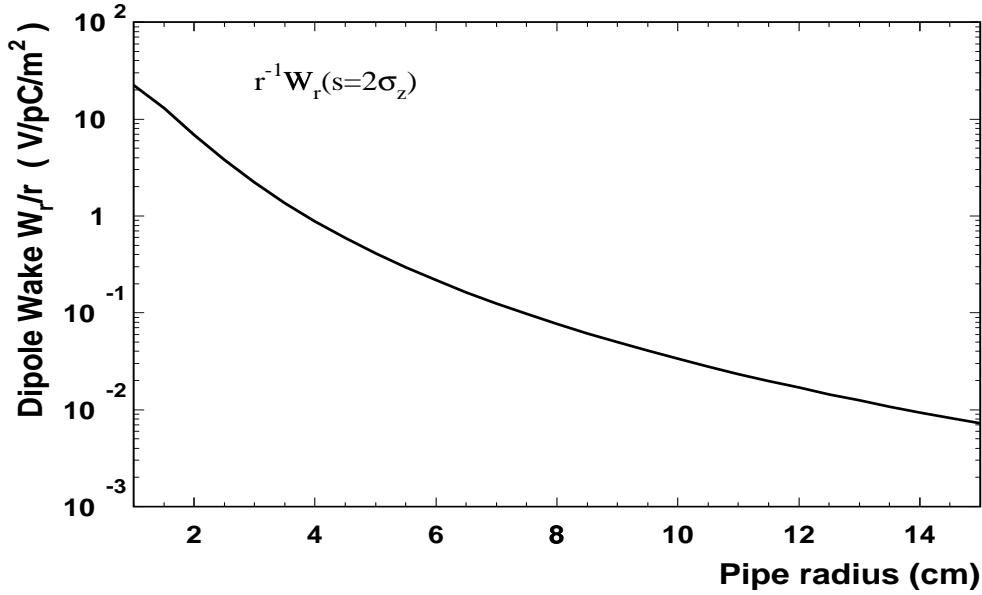
Figure 9.7.2:   *Transverse resistive wake potential $W_\perp\,(s = 2\sigma_z)$ versus tube radius. It is normalised to 1 m transverse orbit displacement and 1 m tube length.*

	Small pipe	Large pipe	Combined
Peak-to-peak (MeV/nC)	31.77	20.16	36.33
rms (MeV/nC)	8.55	5.90	10.56
Transverse wake ($V/nC\,m^2$)	$19.4 \cdot 10^3$	14.8	-

Table 9.7.1:   *Energy variation ("correlated energy spread") due to longitudinal resistive wakefields. The bottom line shows the transverse wake potential in the transfer line at a longitudinal distance of $s = 2\sigma_z$ from the bunch centre, see figure 9.7.2. It is not reasonable to simply add the two contributions for this wake, because the actual value depends on the transverse orbit displacement which changes over the long distances considered here.*

one standard deviation of beam size (σ_r) is given by

$$\frac{\Delta\varepsilon}{\varepsilon_0} = \frac{1}{2}\left(\frac{eQW_\perp}{8E_0}\right)^2 \frac{1}{sin^2\mu}\frac{L^4}{N_{cell}^2} \qquad (9.7.2)$$

with $W_\perp$ the transverse dipole wake at a longitudinal distance of two sigma ($s = 2\sigma_z$) and bunch charge Q, ε_0 the original beam emittance, E_0 the design particle energy, μ the phase advance per FODO cell , L the total length of the beam line and N_{cell} the number of FODO cells.

The same effect has also been estimated for the arc. Although the transverse wake is larger due to the smaller beam pipe radius, its effect on the emittance growth is still

negligible, see table 9.7.2.

Correlated emittance growth due to longitudinal resistive wakefields   Since focusing depends on energy ("chromaticity"), growth of the projected emittance occurs, if particles in the head and in the tail of the bunch have different energies. The relative correlated rms energy spread along the beam line increases linearly with distance and the emittance growth for one σ_r offset is given by

$$\frac{\Delta\varepsilon}{\varepsilon_0} \approx \left(\frac{\sigma_\in L}{E_0}\right)^2 (N_{cell} - 1)^2 \cdot tan^2\frac{\mu}{2} \tag{9.7.3}$$

where $\sigma_\in$ is the induced (correlated) rms energy spread in the pipe per unit length.

Uncorrelated emittance growth   A similar effect takes place if uncorrelated energy spread is considered, which leads, however, to uncorrelated emittance growth (i.e. growth of slice emittance). For an initial uncorrelated rms energy spread δ_{un}, this emittance growth is

$$\frac{\Delta\varepsilon}{\varepsilon_0} = 2\delta_{un}^2 N_{cell}^2 \cdot tan^2\frac{\mu}{2} \tag{9.7.4}$$

The emittance growth of the FEL beam in the transfer line for one σ_r transverse offset is summarised in table 9.7.2. It is seen that for a beam energy of 13 GeV (worst case) the expected overall emittance growth due to resistive wake fields in the transfer line is below 1%.

Number of FODO cells	40
Cell length	300 m
Max β value E=13 GeV	537 m
Relative emittance growth (correl.) by trans. wake in long trans. line	$2.1 \cdot 10^{-7}$
Relative emittance growth (correl.) by trans. wake in dipoles	$1.8 \cdot 10^{-3}$
Relative emittance growth (correl.) by long. wake	$3.2 \cdot 10^{-4}$
Uncorrelated relative emittance growth	$4.5 \cdot 10^{-3}$

Table 9.7.2: *Relative emittance growth $\Delta\varepsilon/\varepsilon_0$ for an FEL beam with an energy of 13 GeV; $\sigma_z = 25\,\mu m$, $\sigma_\in = 0.2\,keV/m$, $\delta_{un} = 10^{-3}$, $\mu_1 = 100°$.*

9.7.2   Surface roughness wakefield effects

Different models exist [73, 74, 75] to compute wakefields caused by the surface roughness in the beam pipe. All models assume that the radial and transverse dimensions of the surface structure are small compared to the bunch length. Figure 9.7.3 shows the longitudinal surface variation δr of a sample measured at DESY [76]. With respect

to surface roughness, it represents the state-of-the-art of a commercially available, extruded aluminum profile.

The model to be applied depends on the size of the surface structure compared to the bunch length. The amplitude of δr is everywhere small compared to the bunch length. Its longitudinal autocorrelation length has however two components, one with structures small compared to the bunch length and other contributions with larger dimensions. The roughness parameter δr is therefore split into a slowly varying part δr_1 and a rapidly varying part $\delta r_2 = \delta r - \delta r_1$ as shown in figure 9.7.4. The effects of both parts are estimated separately by the wakes of periodic surfaces δr_{p1}, δr_{p2} with the same rms roughness $\delta_1 = \sqrt{\langle (\delta r_{p1} - \langle \delta r_{p1} \rangle)^2 \rangle} = \sqrt{\langle (\delta r_1 - \langle \delta r_1 \rangle)^2 \rangle}$ (δ_2 accordingly) and similar transverse dimensions as the original functions (see figure 9.7.5).

The slowly varying part δr_1 is obtained by low pass filtering the experimental data using a Gaussian filter function with $15\,\mu$m rms width. The properties of the measured surface and the periodic model surface functions are listed in table 9.7.3. The

function	rms amplitude	wavelength	comment
δr_1 (meas.)	$0.5\,\mu$m	low pass filter	slowly varying random component
δr_{1p}(model)	$0.5\,\mu$m	$100\,\mu$m	rectangular periodical
δr_2 (meas.)	$0.1\,\mu$m	high pass filter	fast random component
δr_{2p}(model)	$0.1\,\mu$m	$10\,\mu$m	sinusoidal periodical

Table 9.7.3: *Properties of the original and the periodic surface functions.*

electro-magnetic wakefields have rather different properties for periodic surfaces with period $\lambda > 3\sigma$ as δr_{1p} and $\lambda < \sigma$ as δr_{2p} (σ being the bunch length) so that different methods are used to calculate the wake potentials [79]. The longitudinal wake potential w_{z1} of δr_{1p} is obtained by numerical integration [77] using a periodic rectangular model function with $100\,\mu$m period for the slowly varying part, see figure 9.7.5. The rapidly varying surface function δr_{2p} excites essentially one synchronous mode for each azimuthal order with a group velocity close to c. The longitudinal and transverse wake functions of the synchronous monopole and dipole modes are

$$w_z\left(s\right) = 2\kappa_0 \cos ks, \qquad w_r\left(s\right) = 4\kappa_0 \sin ks, \qquad (9.7.5)$$

with $\kappa_0 = Z_0 c/2\pi b^2$ [75] and the wave number $k = \sqrt{\frac{\lambda}{\pi b \delta_{\text{rms}}^2}}$ [78]. For a Gaussian bunch distribution the longitudinal wake potential is then

$$W_z(s) = -\frac{\kappa_0}{2} e^{-s^2/2\sigma_z^2} \left\{ \xi\left(\frac{-is - k\sigma_z^2}{\sqrt{2}\sigma_z}\right) + \xi\left(\frac{-is + k\sigma_z^2}{\sqrt{2}\sigma_z}\right) \right\} \qquad (9.7.6)$$

with a complex error function $\xi\left(z\right) = e^{-z^2} \text{erfc}\left(-iz\right)$.

The longitudinal wake potentials of the surfaces with δr_{1p} and δr_{2p} and of a smooth surface with the conductivity of aluminum ($\sigma = 3.65 \cdot 10^7\,\Omega^{-1}\text{m}^{-1}$) are plotted in figure 9.7.6 and figure 9.7.7 for the undulator pipe (radius $b = 5\,$mm) and the transfer pipe

$b = 5\,\text{mm}$	$\min(w)$ V/pCm	$\max(w)$ V/pCm	$< w >$ V/pCm	rms(w) V/pCm
$w_{\delta r_{1p}}$	-60.3	54.9	-9.6	41.1
$w_{\delta r_{2p}}$	-9.04	9.04	0	6.5
$w_{\text{resistive}}$	-82.3	45.0	-40.4	39.6
$\sum w$	-143.2	99.3	-50.0	82.5

$b = 12\,\text{cm}$	$\min(w_z)$ V/pCm	$\max(w_z)$ V/pCm	$< w_z >$ V/pCm	rms(w_z) V/pCm
$w_{\delta r_{1p}}$	-2.65	2.38	-0.41	1.80
$w_{\delta r_{2p}}$	-1.07	1.09	-0.23	0.36
$w_{\text{resistive}}$	-1.55		-0.97	0.48
$\sum w$	-3.56	1.33	-1.61	1.67

Table 9.7.4: *Summary of roughness wakefield induced energy spread for small and large beam pipe radii.*

($b = 12\,\text{cm}$). The peak, average and rms values of these wakes and of their sum are summarised in tables 9.7.4.

The resulting values for the induced correlated energy distribution are large compared to the uncorrelated energy spread of 2.5 MeV. In particular in the undulator the energy spread could be a problem since it grows when the beam passes the undulator and thus the resonance condition is detuned while the SASE process is taking place, see eq. 9.1.1 and the discussion of FEL physics in part V.

The present wakefield calculations are, besides radiation safety considerations, the basis for our specification of the undulator vacuum chamber size and thus of the minimum undulator gap. In spite of missing experimental experience on beam dynamics in this parameter range, we believe our design is on the safe side, because our wakefield calculations are based on fairly conservative assumptions. Valuable knowledge is being gained on this issue at the TESLA Test Facility by wakefield measurements on well-defined pipe surfaces. First measurements agree encouragingly well with our model calculations [80].
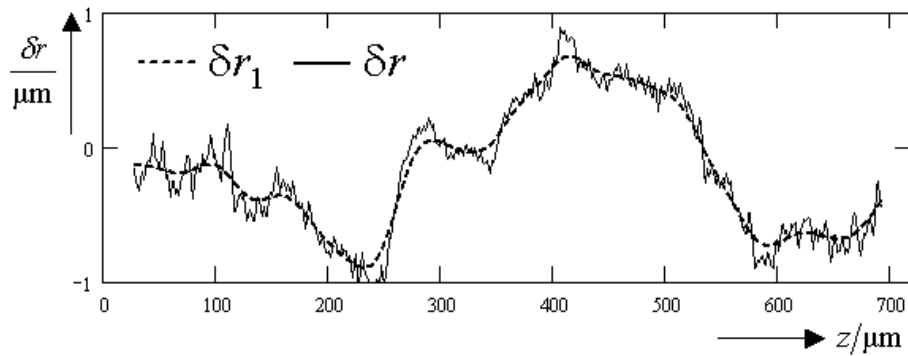
Figure 9.7.3: *Measured surface function δr and the slowly varying contribution δr_1.*
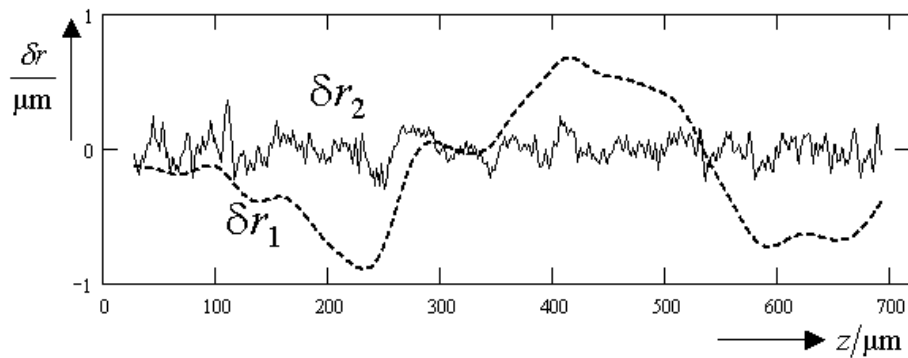
Figure 9.7.4: *The slowly and rapidly varying contributions δr_1 and δr_2.*
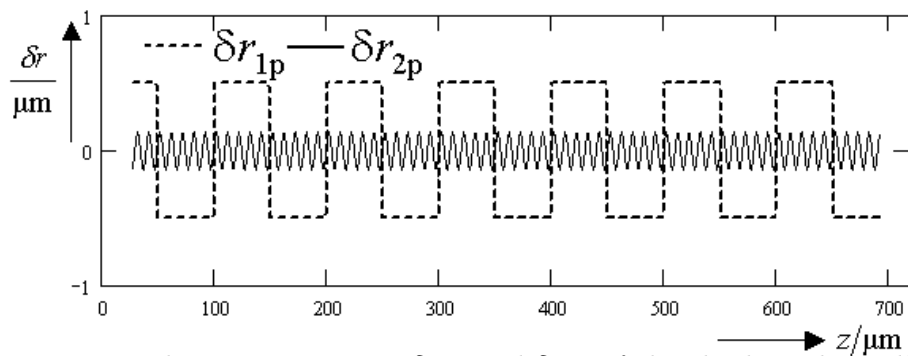
Figure 9.7.5: *Periodic approximations δr_{1p} and δr_{2p} of the slowly and rapidly varying contributions to the surface function.*
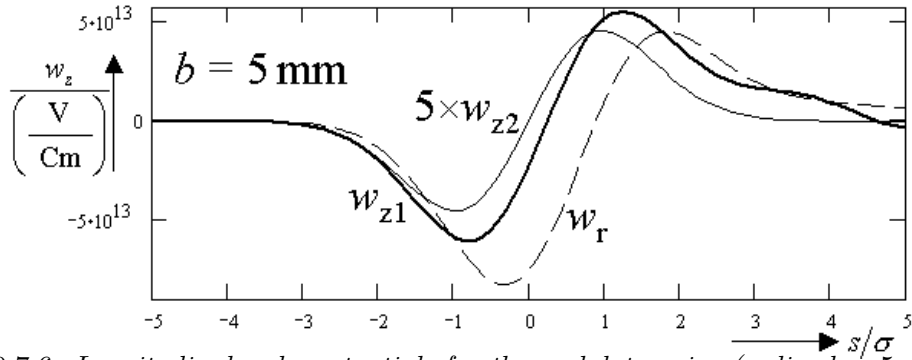
Figure 9.7.6: *Longitudinal wake potentials for the undulator pipe (radius $b = 5\,mm$). w_{z1} and w_{z2} are the wakes caused by the model surface structures δr_{1p} and δr_{2p} (figure 9.7.5) describing the measured surface shown in figure 9.7.3. For comparison, the resistive wake potential w_r is shown. The bunch tail is to the right.*
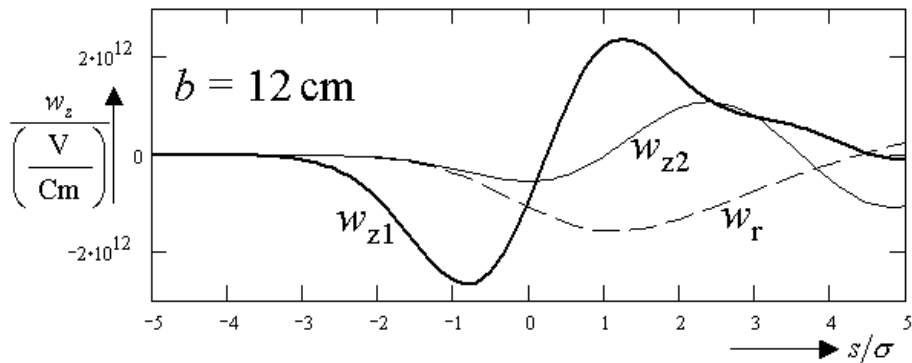
Figure 9.7.7: *Longitudinal wake potentials for the transfer pipe ($b = 12\,cm$).*

9.8 Undulators for the XFEL

9.8.1 Introduction

This section summarises technical design considerations and parameters of the undulators for the TESLA XFEL. A more detailed presentation can be found in part V of this TDR.

The undulators provide the periodic magnetic field so that the FEL process can take place. SASE FELs in the X-ray regime need undulator lengths of approx. 200 m. Such devices cannot be built in one piece, but are divided into 5 m long segments. Additional components like focusing quadrupole magnets, optical phase shifters, electron beam correctors, position monitors are needed as well. The complete undulator system is a periodic arrangement of these elements. Figure 9.8.1 shows a 3D view of three periods which are part of a much larger system. Table 9.8.1 summarises the parameters of the undulator systems for the TESLA XFEL, resulting from extensive parameter optimisations [64, 65].
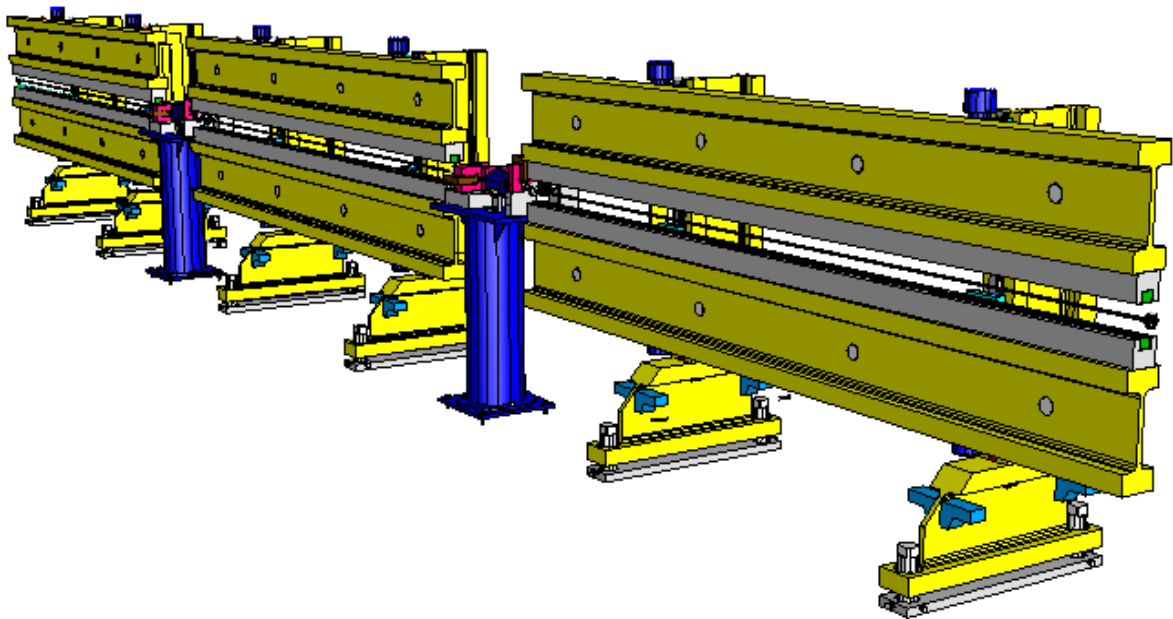
Figure 9.8.1: *3D view of 3 cells of the undulator system.*

Five SASE FELs are planned in total. Four of them, SASE1 through SASE4, are primary FELs using the fresh electron beam delivered from the electron beam distribution system (see section 9.6.6). They produce linearly polarised light and operate primarily in the 0.1 nm wavelength regime. SASE5, a helical undulator, uses the spent beam of SASE3 and operates in the soft X-ray regime at wavelengths up to 5.8 nm. The five spontaneous radiators, U1 through U5, use the spent electron beam of the remaining three SASE FELs, see figure9.1.4.

With respect to undulator design, there is no significant difference between SASE

Device	Type	E_e [GeV]	Wavelength [nm]	Photon Energy [keV]	λ_U [mm]	ρ^+ [10^{-4}]	K_{min}-K_{max}	B_{min}-B_{max} [T]	Gap [mm]	β [m]	L^*_{sat} [m]	L^{**}_{tot} [m]	F^{++}_{mag} [kN]	Segm. [+++]
SASE-1	planar	30	0.1-0.25	12.4-4.9	60	4.3-5.9	4.6-7.5	0.82-1.33	19-12	45	220-150	323.5	26.7-70.2	53
		25	0.1-0.35	12.4-3.5		4.2-6.3	3.4-7.5	0.66-1.33	22-12		220-120			
		20	0.15-0.5	8.25-2.5		5.1-7.7	3.4-7.0	0.66-1.25	22-13		175-100			
SASE-2	planar	25	0.085	14.4	45	3.6	4.0	0.95	12	45	210	311.1	35.8	51
		20	0.13	9.3		4.1	4.0	0.95	12		155			
SASE-3	planar	23	0.1	12.4	45	3.8	4.0	0.95	12	45	185	274.5	35.8	45
		15	0.13	5.2		4.1	4.0	0.95	12		115			
SASE-4	planar	25	0.1-0.35	12.4-3.5	60	4.2-6.3	3.7-7.5	0.66-1.33	22-12	45	220-120	323.5	26.7-70.2	53
		15	0.3-1.0	4.1-1.24		7.1-10.3	3.9-7.5	0.70-1.33	21-12		125-80			
SASE-5	circular	23	0.4-2.5	3.1-0.5	107	14.5-26.8	3.8-9.6	0.38-0.96	35-12	15	120-60	176.9	11.5-73.2	29
		15	1.0-5.8	1.2-0.21		19.2-35.7	3.8-9.6	0.38-0.96	35-12		95-50			
U-1/U-5	planar	50	0.003-0.009	420-140(1.harm)	30	-	0-3.1	0-1.1	∞-6	45	50***	61.0	0-51.6	10
		30	0.0083-0.025	150-50(1.harm)										
			0.0028-0.0083	450-150(3.harm)							total	total		total
		15	0.033-0.1	37-12(1.harm)							250	305		50
			0.0123-0.033	111-37(3.harm)										
										Sum	1405	1714.1		281

*The saturation length is taken as the net magnetic length of the undulator.

**The total length of an undulator system includes the saturation length plus 1.1 m for intersections (Quadrupoles, phase shifters, correctors, diagnostics pumps etc) and 20 % contingency for field errors, misalignment etc. For the spontaneous radiators no contingency for the device length is considered.

***For the spontaneous radiators U-1 – U-5, the "saturation length" represents the assumed magnetic length of each device. The summation in the bottom line includes 5 devices.

$^+$For SASE-1 to SASE-4 a normalised emittance ϵ_n of $1.6 \cdot 10^{-6}$ m, an energy spread of 2.5 MeV and a peak current of 5000 A is used. For SASE-5 due to the spent beam an energy spread of 6.0 MeV is used. For the definition of the FEL ρ-parameter, see Part V of this TDR.

$^{++}$A pole width of 40 mm and an undulator segment length of 5.0 m is assumed. Load values for max./min. gaps are given. The total magnetic length including 20 % contingency is 1405 m, the total undulator length, intersection inclusive is 1714.1 m.

$^{+++}$Length assumptions : Undulator segment 5.0 m, Intersection 1.1 m, cell length 6.1 m

Table 9.8.1: *Key undulator parameters for the TESLA X-ray laboratory.*

and spontaneous undulators. As seen from table 9.8.1, only four different types of devices are required, thus allowing cost efficient production and operation.

The undulator systems for TESLA will be large and complex, the most delicate and expensive components being the magnetic structures. Their design and construction will benefit from the progress made on 3rd generation storage rings during the past 20 years. Nowadays, devices with almost ideal properties can be built. There is, however, a big difference: a 3rd generation X-ray source such as the ESRF has a total installed length of insertion devices of about 110 m which have been built over the past 15 years. In contrast, the total length of the undulator systems for TESLA is 1700 m, see table 9.8.1. The challenge is therefore to find a design which allows industrial production of the large number of undulator segments.

9.8.2   Hardware setup

Overall design.   A sequence of focusing and defocusing quadrupole magnets forming a so-called FODO lattice keeps the electron beam size small over the entire undulator length and provides the optimum beta-function for FEL operation. These quadrupoles are placed in the 1.1 m long intersections connecting subsequent undulator segments which are 5 m long each.

Wavelength tunability by variation of the undulator gap is required for three of the SASE undulators and for the spontaneous undulators as well. This has mainly two consequences to the mechanical design. First, since the longest SASE saturation length is expected at the shortest wavelength at which the FEL is to operate, (thus at the smallest K-parameter,see eq. 9.1.1), the required undulator length is determined by the comparatively weak magnetic field at the upper gap position. Thus the undulator must be longer than needed for a fixed (i.e. 12 mm) gap device optimized for short wavelength.

Second, the match of the optical phase between subsequent undulator segments changes when the gap is changed. While a proper phase match at a fixed gap device can be guaranteed by a proper choice of the distance between subsequent undulator segments, phase matching for variable gaps needs tunable, magnetic chicanes in the intersections, called phase shifters in figure 9.8.2 [71].

Besides more flexibility for wavelength tuning, there are more arguments for a variable gap design [72]. It allows a simple way of undulator gap fine tuning during FEL operation, including a systematic variation of the gap along the undulator ("tapering"), and since any part of the undulator can be effectively switched off by fully opening the gap, various ways of photon beam based diagnostics become feasible, see also section 9.8.3 below. Finally, fully opening the gap to 200 mm will minimize radiation damage during commissioning.

The large number of identical components calls for standardization. Ideal candidates are

- The gap separation drive system, including motion control, motors, etc.

- Girders.
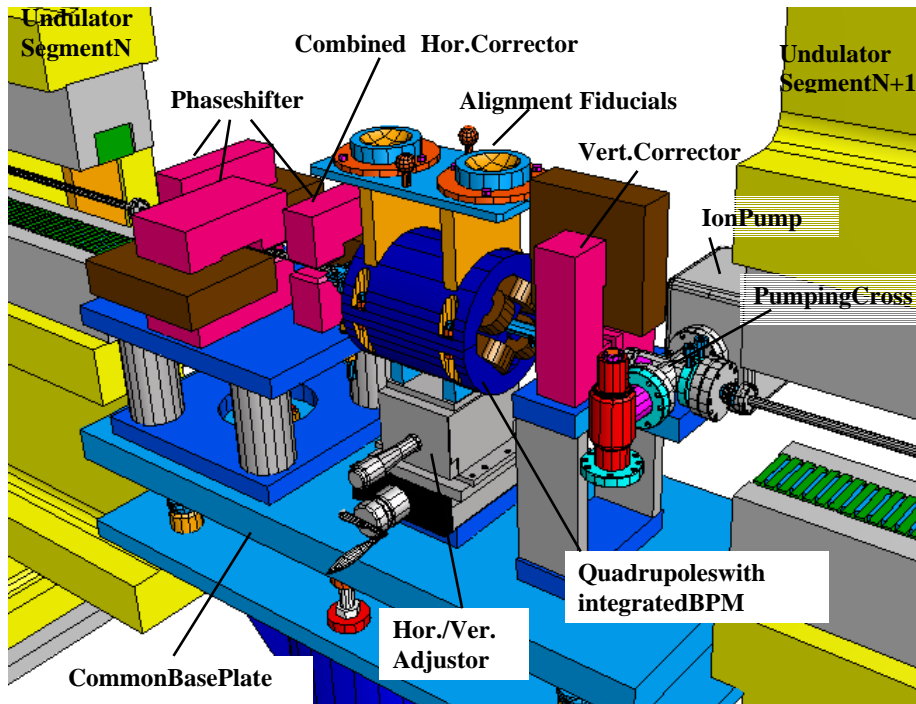
Figure 9.8.2:   *3D view of an undulator intersection.*

- Components of the intersections such as phase shifters, steerer magnets, quadrupole magnets, and beam position monitors (BPMs).

- Control systems for gap motion, gap dependent magnet settings and BPM read-out.

- Vacuum chambers and other vacuum equipment.

Undulators for linear polarization.   In view of the present state of the art, permanent magnet (PM) technology is sufficiently matured and perfectly suited to be the design basis for all TESLA undulators. Permanent magnet hybrid technology is proposed for all undulators generating linear polarization. It uses highly permeable soft iron blocks to concentrate and direct the flux created by PM blocks. A prototype planar structure based on NdFeB permanent magnets has been developed for the SASE1 undulator [66]. At a gap of 12 mm and a period length of 60 mm the peak magnetic field is 1.33 T. The width of poles and PM blocks was determined for a transverse good field region of ± 1 mm where the relative field variation is less than the FEL ρ parameter (see the FEL theory section in part V), i.e. $< 4.2 \cdot 10^{-4}$ in the most critical open gap position. 400 cm^3 of PM volume is required per undulator period, resulting in 13300 kg of PM material for the 53 undulator segments (5 m long each) of SASE1 or SASE4.

Undulators for circular polarization.   A photon beam with adjustable circular polarization will be provided by SASE5. A Sasaki type undulator [67] is proposed. It

provides lateral access to the gap for precise magnetic field measurement as well as an adjustable degree of polarization, see figure 9.8.3. It is based on a pure permanent magnet structure cut along the electron beam axis in four parts. These parts can be moved longitudinally with respect to each other. Depending on the relative longitudinal position, radiation with left or right handed circular polarization, elliptical polarization or linear polarization is produced. The design for SASE5 [68] is based on an existing magnet at BESSY [69].
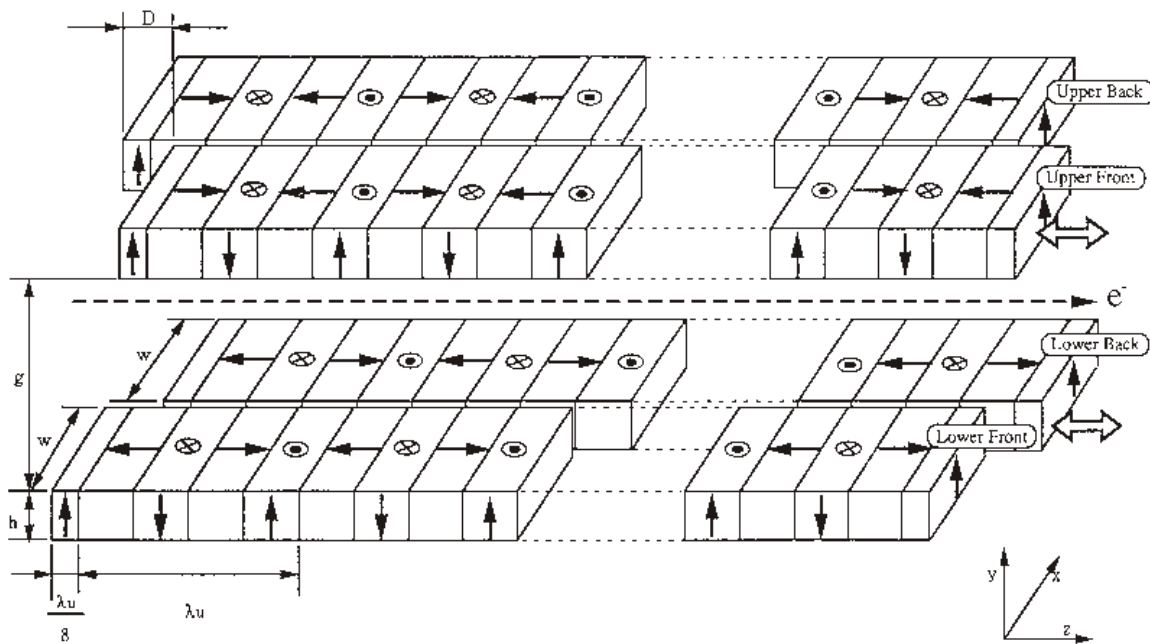
Figure 9.8.3: *Magnetic design principle of a Sasaki type undulator, a planar helical structure providing adjustable polarization.*

Tolerances. For optimum FEL performance, tight tolerances have to be met. The gap height of undulator segments has to be controlled within $\pm 2\,\mu$m. This can be achieved by absolute length encoders mounted to frames mechanically separated from the undulator girders [72]. The tolerances on undulator field integrals are well within state-of-the-art technology. Quadrupole magnets would have to be centered with an accuracy of $1\,\mu$m with respect to a straight line if no beam based alignment procedure will be applied. This well-established technique has been adapted to XFEL undulator needs, see section 9.8.3, and permits relaxed initial quadrupole alignment tolerance of $\pm 0.2\,$mm.

Industrial manufacturing. Manufacturing of 281 undulator segments in a reasonable time at sufficient quality and at minimum costs will be a challenge. The entire production process will be split into two parts, starting with an extensive R&D phase to

prepare the production phase and to address critical issues including:

- Improvement of the manufacturing process, in particular of the PM quality (spread of magnetization performance).

- Development of reliable magnetic measurement techniques suitable for industrial environment.

- Design optimization and streamlining for large scale production.

- Prototyping including support systems, motion control and magnet assembly.

The subsequent industrial production phase has been planned and analyzed in cooperation with industry [70].

9.8.3   Beam based alignment procedure for the undulator

Electron beam based alignment.   In order to reach saturation in the wavelength range of the TESLA X-ray FEL, an undulator length of approximately $200 \, \mathrm{m}$ is required (see part V). Out of this length, 78% is covered by the undulators and 22% is needed for phase shifters and quadrupoles (see section 9.8). The latter are needed to focus the beam in order to obtain a small beam radius. The simulations determining this undulator length assume the electron and radiation beams to be perfectly aligned over the entire undulator length. Simulations of the FEL amplification process including quadrupole misalignments (see part V) have shown that, even assuming perfect undulator fields, quadrupole magnets need to be aligned on a straight line with an accuracy of about $1 \, \mu\mathrm{m}$. In this case, the beam deviation from a straight line results in an rms value of $6 \, \mu\mathrm{m}$ or less (for more details, see part V). Quadrupoles and beam position monitors (BPM) attached to them can be aligned by conventional means with an accuracy of about $200 \, \mu\mathrm{m}$. For this reason, beam based alignment based on varying quadrupole gradients is proposed to align the quadrupole axis to the required tolerances. The simulations presented here do not include residual errors in first and second magnetic field integrals. The method can, however, be easily adapted to include these errors. A complete study can be found in [82]. In order to vary the quadrupole gradients individually, an independent current loop (or a shunt) for each quadrupole is required. In the present design, all quadrupoles are connected in series to a single power supply, and an additional power supply changes the gradient of an individual quadrupole which can be selected arbitrarily.

The beam based alignment procedure is described in the following. All quadrupoles in the undulator beam line are initially set to zero current. The growth of the β-function along the undulator is then given by

$$\beta(z) = \beta_0 \Big(1 + \frac{z^2}{\beta_0^2} \Big),$$

where it is assumed that the waist is put at the undulator entrance. β_0 is approximately $45 \, \mathrm{m}$. From the entrance to the end of the $300 \, \mathrm{m}$ beam line the beam radius

grows in both planes from $35\,\mu$m to $250\,\mu$m, which is still acceptable for the alignment procedure.

The alignment of each quadrupole is done by varying its gradient around its nominal value by $\pm 20\%$ and changing the position of the electron beam inside the quadrupole in a certain range (here between $\pm 100\,\mu$m). The latter can be done with a steerer 6 meters upstream from the quadrupole. The beam position Δx downstream of the quadrupole with an offset δx is given by

$$\Delta x = \frac{\delta x}{f} L \,,$$

with f the quadrupole focal length and L the distance downstream from the quadrupole causing the kick. For the TESLA FEL undulators, the nominal focal length is approximately $20\,$m (for all beam energies), resulting in a $\Delta x = 1.5\,$mm offset per $100\,\mu$m offset of the quadrupole at the end of a $L = 300\,$m long beam pipe. Moving the beam at the quadrupole position, for instance, between $\pm 100\,\mu$m at the settings of $\pm 20\%$ around its nominal value, results in two lines (in the plane Δx versus δx) that cross at the position where the quadrupole does not deflect the beam. At this point, the reading of the BPM associated to this quadrupole gives its offset with respect to the magnetic centre of the quadrupole. For quadrupole offsets smaller than $50\,\mu$m, the kick can be compensated by steerers placed close to the quadrupole (within 300 mm). For larger offsets, the quadrupoles have to be moved in order to avoid angles of the electron beam with respect to the undulator axis of more than $1\,\mu$rad. As discussed in [81], the magnetic center changes with the quadrupole gradient. To avoid systematic errors from this effect, this procedure is performed around the quadrupole nominal gradient. All other quadrupoles are set to zero gradient in order to avoid the effect of orbit distortions due to residual offsets in upstream quadrupoles. When putting all quadrupoles to zero, the measurement is independent of BPM position and calibration, and independent of the applied shift to the quadrupole. It is assumed, however, that the BPM is linear in the applied range.

Simulation results of the procedure are shown in figure 9.8.4. As can be seen, for a BPM resolution of $4\,\mu$m, the rms orbit deviation is still within the tolerance limit of $6\,\mu$m. As long as the rms values of first and second field integrals of each undulator segment are small and their integrals at the undulator exit are zero, the orbit deviation will not increase significantly if the undulator field errors are included.

Photon beam based alignment.   A complementary method to align the quadrupole magnets is to observe the direction of the photon beam radiated from individual undulator segments instead of the electron beam orbit. The basic idea is to open all undulator gaps except for one. Observing the spontaneous undulator radiation emitted by the activated segment provides information on the electron beam trajectory at the location of emission. Only one X-ray diagnostic station is needed downstream of the undulator. It measures the spatial distribution of the spontaneous radiation emitted from one undulator segment after the other, which should, ideally, all overlap. In addition, it can be used to determine the correct gap for each of the undulator segments
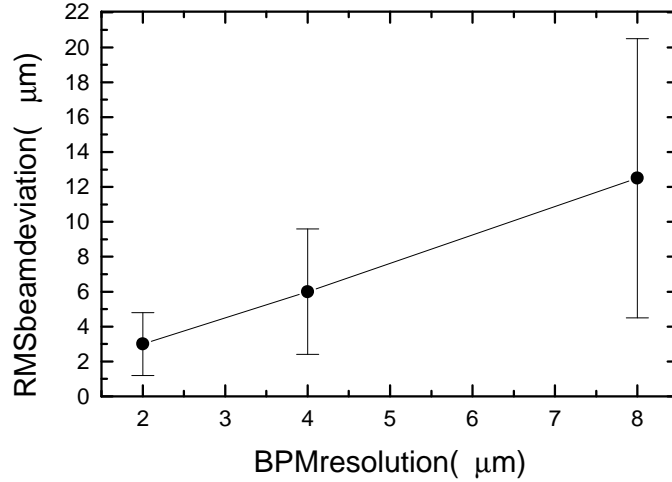
Figure 9.8.4: *RMS value of the electron beam orbit deviation after beam based alignment along a 300 m long undulator for different values of the BPM resolution. Initial quadrupole offsets are within $\pm 200\,\mu m$. Beam based alignment has been performed for 1000 samples of random quadrupole offsets for each BPM resolution.*

from the spectrum of the spontaneous radiation. Furthermore, the phase matching between electrons and photon beam at the entrance of each undulator module can be determined. Further details on this method are described in part V.

9.9   Beam Dumps

The design of the beam dumps for the XFEL takes into account the operational flexibility needed by the users. We first discuss the decision on a water based absorber concept and then its characteristics and safety aspects.

9.9.1   Requirements and basic concept

1 ms long bunch trains with $N_t = 7 \cdot 10^{13}$ electrons are guided to the FEL facility at at 5 Hz repetition rate. Extraction from the linac at two positions either into the low energy (13 to 27 GeV) or the high energy branch (20 to 50 GeV) transfer line guides the beam to the FEL user facility, where each of both lines again splits up into two arms, to allow for installation of several radiators before the particle beam is going to be aborted. Hence 4 electron dump systems are needed. Assuming an operation mode, in which every FEL bunch train is sent into the same arm, table 9.9.1 lists the maximum requirements for the dump system.

Since routine operation aims for a balanced distribution towards all 4 beam lines, i.e. only $I_{ave}/4$ into each arm, it is not reasonable to require full current capability at maximum energy in single arm mode. Therefore the maximum power will be restricted

to 2 MW, although at 50 GeV a max. power of 2.9 MW could be delivered. For a given absorption efficiency the length of a homogeneous cylindrical absorber depends only logarithmically on the primary particle energy E_0 and its radius is independent of it. Thus 4 identical and independent abort systems capable of handling the 50 GeV / 2 MW case will be installed.

Besides the radiological aspects the design of high power beam absorbers beyond several hundreds of kW is ruled by the question of heat transfer. Since heat conduction defines the power capability of solid absorbers, extending them in one transverse dimension and distributing the incoming beam with a slow sweep in that direction across the dump face enables sufficient heat transport with a tolerable temperature drop towards the water cooled surface of the dump. A carbon based absorber would need a slow sweep path length of about 2 m for the 50 GeV / 2 MW mode. Although favoured in the TESLA Conceptual Design Report, it became obvious in the meantime, that a technical solution of a solid absorber will result in a highly impractical and complicated design [87] (weight, possibility of exchange, piping for water cooling, noble gas containment, protection absorber for sweeping failures, ...) and additionally requires a huge exit / entrance window to enable several meters of beam sweeping. Thus being the only reasonable and technically feasible solution a dump system based on a water absorber will be used for the MW-beams of the FEL facility. The same concept as for the 250 GeV / 12 MW main linac dump (see section 7.7) will be applied and therefore all 4 identical 50 GeV / 2 MW abort systems for the FEL facility can be considered as scaled version of the HEP dump system. The main features of this system are described below.

9.9.2 Dump system layout

Figure 9.9.1 shows schematically the main components of the beam dump system. Behind the last undulator the spent electron beam is separated from the X-ray beam by a vertical deflection and sent into the abort transfer channel with a water beam dump.

Water beam dump and fast sweeping system Water absorbs most of the incident beam power to minimise activation of the solid materials enclosing the water volume, such as the water vessel and the shielding. After the system is flushed into a storage

N_t, particles per bunch train	$7.2 \cdot 10^{13}$ electrons	
I_{ave}, average beam current	$57.7 \, \mu A$	
E_0, particle energy	27 GeV	50 GeV
W_t, energy per bunch train	310 kJ	575 kJ
P_{ave}, average beam power	1.55 MW	restricted to 2 MW

Table 9.9.1: *Maximum beam parameters relevant to the electron beam dump systems of the FEL facility.*

container, this strategy enables and simplifies exchange and repair on components with
finite lifetime, e.g. the water vessel. Except for the second entrance window a vessel
identical to the one installed at the main linac dump system will be used. It is a 10 m
long (27.7 radiation length) cylindrical container with a radius of 60 cm (6.3 molière
radii) carrying about 11 m^3 of water. Sticking to the mentioned philosophy this vessel
must be built from a minimum amount of mechanically strong and corrosion resistant
material, with the property of being a small source of induced radioactivity. A titanium
wall of 15 mm thickness is required for stability reasons.

According to 50 GeV shower simulations (MARS code) $\sim 1\%$ radial and $\leq 0.1\%$
longitudinal leakage is expected from such an absorber. In absolute numbers this is
still 20 kW in total, resulting in heating of the concrete shielding and activation of the
air. For its low residual radioactivity and high thermal conductivity an inner shield
of aluminum, thermally coupled to the dump vessel but removable, is proposed [86]
to reduce the power density on the adjacent outer concrete shielding. The aluminum
layer perfectly fills the volume between dump vessel and rectangular shaped concrete
blocks in order to avoid gaps within the shielding volume and therefore minimises air
activation. For further details on radiation safety issues see section 8.3.

The absorption of all N_t particles of one bunch train leads to a certain energy
distribution in the water, which directly translates into an instantaneous temperature
rise with its maximum $(\Delta T_{inst})_{max}$ somewhere on the shower axis. If E_0, N_t and
the absorber material are given, it only depends on the size of the incoming beam.
Assuming 50 °C before the bunch train enters, the risk of getting gaseous is avoided
by pressurising the water at 10^6 Pa (10 bar), which pushes its boiling point to about
160 °C, and by limiting instantaneous heating at $(\Delta T_{inst})_{max} \leq 40$ °C. For the 50 GeV
beam parameters a Gaussian beam entering the dump with $\sigma_x = \sigma_y = 7.9$ mm meets
the latter requirement. Unfortunately a smaller beam arrives at the dump and its
spot size needs to be artificially increased by means of a fast sweeping system [88],
that distributes all particles of the macro pulse along a circular line with radius r_{fast}
over the entrance window of the dump. Given the 50 GeV beam with a 1 mm rms
radius, a sweeping radius of $r_{fast} \approx 15$ mm is sufficient to keep $(\Delta T_{inst})_{max} \leq 40$ °C.
The fast sweeping system is located several 10 m upstream of the dump in the abort
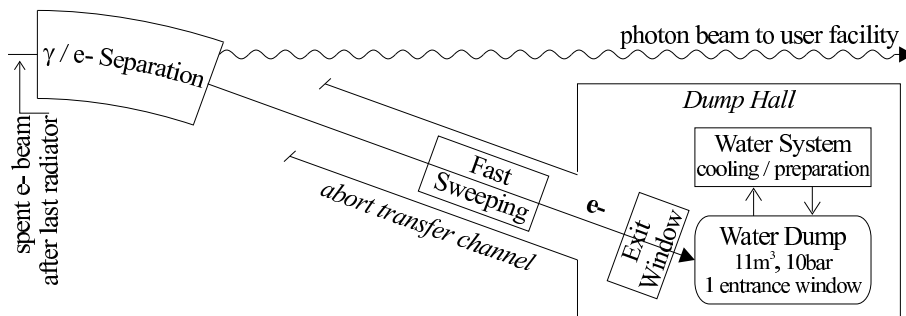
Figure 9.9.1: *Schematic view of the beam dump system for the electron beams at the FEL
facility.*
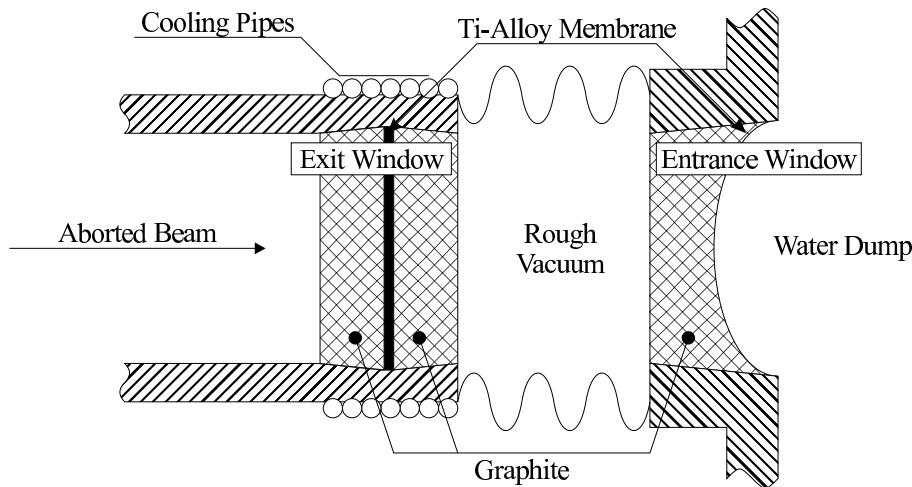
Figure 9.9.2: *Concept of (vacuum) exit and (water) entrance window, using a titanium-graphite sandwich design.*

line. It consists of a set of orthogonal deflectors excited with a sinusoidal current of same frequency but with a 90° phase shift between horizontal and vertical deflector. This frequency needs to be at least 1 kHz in order to provide a homogeneous particle distribution within the bunch train passage time of about 1 ms. Pulsed iron yoke dipoles sitting outside of the vacuum chamber can be used. They are triggered early enough so that, when recognising a failure of this system, release of the next bunch train from the injector can be inhibited. In addition several independent modules in each plane with a total length of ≤ 20 m allow safe operation even if one module fails.

Entrance and exit windows   As indicated in figure 9.9.2 the aborted beam leaves the vacuum system through an exit window before it enters the water absorber through a separate entrance window. The volume between both windows needs to be evacuated for reasons of air activation and will be used to detect window leakage. Double safety against dump water leaking into the vacuum system in case of a window failure is achieved. Windows for pulsed beams suffer from cyclic mechanical stress due to instantaneous heating. A 5 Hz operation in a 10 year lifetime gives in total about 10^9 cycles. Normally materials with high specific heat like Beryllium are preferred, but including considerations on mechanical strength under cyclic conditions titanium alloys are good candidates. On the base of 10^7 - 10^8 cycles the maximum allowed particle density $(dN/dA)_{max}$ at the window is about $4 \cdot 10^{12}/$mm^2 for such a material [89]. For reasons of instantaneous heating of the dump water the particle density at the dump entrance is less by a factor of 10 due to the fast sweeping, assuming $N_t = 7.2 \cdot 10^{13}$, $r_{fast} = 15$ mm and $\sigma_x = \sigma_y = 1$ mm. In this respect the tolerable spot size entering the dump system is not determined by the window but given by instantaneous heating of the dump water.

In order to withstand static pressure either from the dump water relevant to the entrance window or from the atmosphere relevant to the exit window, the titanium

membrane is reinforced by graphite. Especially for the exit window, where graphite is applied on either side of the membrane it helps to conduct the average power of $39\,\mathrm{W/mm}$, which is dissipated in the titanium assuming an average current of $I_{ave} = 57\,\mu\mathrm{A}$, towards the heat sink at the circumference of the window. For the entrance window average heating is not a challenge since the membrane is exposed to the dump water and will be cooled across its whole area from there.

Since the capability of a window is dependent on the peak particle density (i.e. N_t and spot size) and average beam current but not on energy, a lot of experience can be obtained from tests at the TESLA Test Facility Phase 2 (TTF2), where such a graphite-titanium sandwich-like window will be installed as an exit window.

Water system   An especially designed geometry of water in- and outlets at the vessel has to combine two tasks. On the one hand it has to introduce a sufficiently high water flow in the $0.5\,\mathrm{m/s}$ range perpendicular to the shower axis, so that the water in the shower core is exchanged within subsequent bunch trains. Each bunch train enters a quasi "fresh and cold" absorber and pulse to pulse accumulation of instantaneous heat in areas of high energy deposition is avoided. On the other hand a continuous flow of $16\,\mathrm{kg/s}$, or $60\,\mathrm{m^3/h}$ of vessel water towards an external heat exchanger handles the $2\,\mathrm{MW}$ average heat load with a $30\,^{\circ}C$ temperature drop between in- and outlet. The heat exchanger is part of a sophisticated water preparation plant, schematically shown in figure 9.9.3, which besides cooling also handles the radiological and chemical aspects of the dump water.

It is expected that the dump water will remain in the closed system for the entire lifetime of the FEL facility. For pure water, the following radioactive nuclei will be produced (half-live in brackets): ^{15}O ($2\,\mathrm{minutes}$), ^{13}N ($10\,\mathrm{minutes}$), ^{11}C ($20\,\mathrm{minutes}$), ^{7}Be ($54\,\mathrm{days}$) and ^{3}H ($12\,\mathrm{years}$). With $2\,\mathrm{MW}$ beam power the activity of ^{7}Be and ^{3}H saturates at $11\,\mathrm{TBq}$ and $1.2\,\mathrm{TBq}$, respectively. After decay of the short-lived isotopes, the outside dose rate is mainly determined by the $478\,\mathrm{keV}$ γ-particles from the ^{7}Be decay, since the $20\,\mathrm{keV}$ electrons from tritium decay will not penetrate the walls of the water system. If distributed evenly in a total water volume of $10\,\mathrm{m^3}$, the estimated dose rate at the surface of a $100\,\mathrm{mm}$ diameter tube is about $28\,\mathrm{mSv/h}$; this value will be reduced by two to three orders of magnitude if a few percent of the total water flow is passed through a resin filter in which the ^{7}Be is removed. In addition, the filter removes other products and therefore maintains the purity of the water, which is essential for avoiding corrosion. Radiolytical damage of the filter material is reduced by a delay line in front of the filter to allow the short-lived products to decay.

There will be a small gas volume (most probably He) at the top of the dump vessel; it will protect the vessel from pressure waves induced by instantaneous heating in the event of a failure of the fast sweeping system. The gas buffer will also maintain the static pressure and compensate for slow expansion due to different average temperatures of the dump water. All gaseous constituents not dissolved in the water will accumulate in the buffer. Special attention must be paid to hydrogen, which is produced via radiolysis with a rate of $0.6\,\mathrm{l/s}$ at $2\,\mathrm{MW}$ [85]. Thus a catalytic hydrogen recombiner and a gas analyzing station to monitor its proper functioning are connected to the buffer volume.
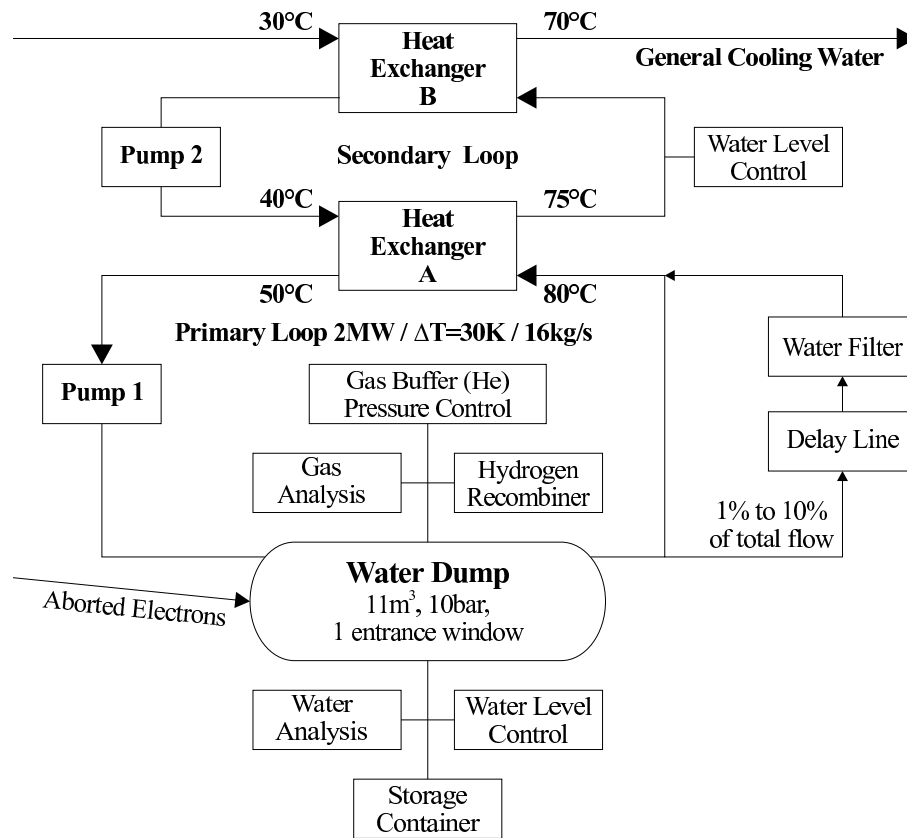
Figure 9.9.3: *Schematic overview of the water system required for each of the four FEL electron beam dumps.*

Obviously the system needs to be leak-tight at the level typically found in vacuum systems; this requires gas-tight components (pumps, heat exchangers, etc.), welded or metal sealed connections and a proper choice of materials to avoid harmful water chemical reactions. A water analysis station will monitor relevant parameters such as acidity, ion concentrations and conductivity. However the possibility of a leak requiring a repair or exchange of a component has to be foreseen. Once a leak has been detected by monitoring water pressure and level, the system will first be flushed into the storage container to remove the dominant source of radiation, allowing work to proceed on the necessary mechanical parts after a relatively short cool-down period. All walls of the hall for the system have to be sealed with a special paint to collect leaking water. The primary cooling circuit is separated from the general cooling water by an intermediate secondary loop, which has a higher pressure than the primary one. The loop protects the general cooling water from being contaminated, in the event of leaks in either or both of the heat exchangers.

The whole water system will be housed in the dump hall. The design and fabrication of such a complex facility represents a significant technical challenge. However, experience on a safe and careful technical design can be taken from existing plants which have to deal with similar problems: e.g. the $25\,\mathrm{GeV}\,/\,2.2\,\mathrm{MW}$ water dump at

SLAC [84], spallation neutron sources like the SINQ at Paul Scherrer Institute (PSI), or research reactors.

Bibliography

[1] M. Hogan et al., *Measurements of Gain Larger than 10^5 at $12\,\mu m$ in a Self-Amplified Spontaneous-Emission Free-Elektron Laser*, Phys. Rev. Lett. **81**, 4867, 1998.

[2] S. Milton et al., *Observation of Self-Amplified Spontaneous Emission and Exponential Growth at $530\,nm$*, Phys. Rev. Lett. **85**, 988, 2000.

[3] J. Andruszkow et al., *First Observation of Self-Amplified Spontaneous Emission in a Free-Electron-Laser at 109 nm wavelength*, Phys. Rev. Lett. **85**, 3825, 2000.

[4] J. M. Madey, *Stimulated Emission of Bremsstrahlung in a Periodic Magnetic Field*, J. Appl. Phys. **42** 1906, 1971.

[5] K. J. Kim, *Three-dimensional analysis of coherent amplification and self-amplified spontaneous emission in free-electron lasers*, Phys. Rev. Lett. **57**, 1871, 1986.

[6] S. Krinski, L. H. Yu, *Output power in guided modes for amplified spontaneous emission in a single-pass free-electron laser*, Phys. Rev.**A 35**, 3406, 1987.

[7] E. L. Saldin, E. A. Schneidmiller, M. V. Yurkov, *The Physics of Free Electron Lasers*, Springer, New York 1999, and references therein.

[8] A. M. Kondratenko, E. L. Saldin, *Generation of Coherent Radiation by a Relativistic Electron Beam in an Ondulator*, Part. Accelerators, **10**, 207, 1980.

[9] R. Bonifacio, C. Pellegrini, L. M. Narducci, *Collective Instabilities and High-Gain Regime in a Free Electron Laser*, Opt. Commun. **50**, No. 6, 373, 1984.

[10] J. Rossbach, et al., *Observation of Self-Amplified Spontaneous Emission in the Wavelength Range from 80 nm to 180 nm at the TESLA Test Facility at DESY*, Proc. of the FEL 2000 Conf., to be published in Nucl. Instr. Meth. A, 2001.

[11] R. Brinkmann, et al., *An X-Ray FEL Laboratory as Part of a Linear Collider Design*, Nucl. Instr. Meth. **A 393**, 86, 1997.

[12] G. A. Loew (Ed.), *International Linear Collider Technical Review Committee Report*, SLAC-R-95-471, 1995.

[13] R. Wanzenberg, *A Fast Switchyard for the TESLA FEL-beam using a Superconducting Transverse Mode Cavity*, Proc. of the Linac 2000 Conf., (to be published).

[14] T. Åberg, et al., *A VUV Free-Electron Laser at the TESLA Test Facility at DESY, Conceptual Design Report*, DESY TESLA-FEL 95-03, 1995.

[15] Ya. S. Derbenev, et al., *Microbunch Radiative Tail-Head Interaction*, DESY TESLA-FEL 95-05, 1995.

[16] E. L. Saldin, E. A. Schneidmiller, M. V. Yurkov, *On the Coherent Radiation of an Electron Bunch Moving in an Arc of a Circle*, DESY TESLA-FEL 96-14, 1996.

[17] R. Tatchyn, et al., *Design considerations for a 60-meter pure permanent magnet undulator for the SLAC linac coherent light source (LCLS)*, SLAC-PUB-6106 and Proc. of the PAC 1993 Conf.

[18] J. Pflüger, *Undulators for SASE FELs*, Nucl. Instr. Meth. **A 445**, 366, 2000.

[19] J. Rossbach, et al. *Interdependence of Parameters of an X-Ray FEL*, Nucl. Instr. Meth. **A 374** 401, 1996.

[20] J. Pflüger et al., *Magnetic Characterization of the Undulator for the VUV-FEL at the TESLA Test Facility*, Proc. of the FEL 1999 Conf., II-87.

[21] U. Hahn et al., *Design and Performance of the Vacuum Chambers for the Undulator of the VUV-FEL at the TESLA Test Facility at DESY*, Nucl. Instr. Meth. **A 445**, 442, 2000.

[22] S. Schreiber et al., *First Running Experience with the RF Gun based Injector of the TESLA Test Facility Linac*, Proc. of the FEL 1999 Conf., Hamburg, II-113.

[23] S. Schreiber et al., *Running Experience with the Laser System for the RF Gun based Injector at the TESLA Test Facility Linac*, Nucl. Instr. Meth. **A 445**, 427, 2000.

[24] D. Sertore et al., *First Operation of Cesium Telluride Photocathodes in the TTF Injector RF Gun*, Nucl. Instr. Meth. **A 445**, 422, 2000.

[25] H. Edwards et al., *Transverse Emittance Measurements in the TTF Injector*, Proc. of the FEL 1999 Conf., II-75.

[26] A. Cianchi et al., *Transverse Phase Space Studies in TTF photoinjector during run 00-01: A comparison between Simulation and Experiment*, DESY TESLA-FEL 2000-04, 2000.

[27] S. Schreiber et al., *Performance Status of the RF-gun Based Injector of the TESLA Test Facility Linac*, Proc. of the EPAC 2000 Conf., Vienna.

[28] M. Castellano et al., *Bunch Length Measurements at TTF Using Coherent Diffraction Radiation*, Proc. of the EPAC 2000 Conf., Vienna.

[29] M. Geitz et al., *Determination of the Longitudinal Phase Space Distribution pro-duced with the TTF Photo Injector*, Proc. of the FEL 1999 Conf., Hamburg, II-83.

[30] M. Huening et al., *Observation of Longitudinal Phase Space Fragmentation at the TESLA Test Facility Free-Electron Laser*, Proc. of the FEL 2000 Conf., to be published in Nucl. Instr. Meth. A, 2001.

[31] T. Limberg et al., *An Analysis of Longitudinal Phase Space Fragmentation at the TESLA Test Facility*, Proc. of the FEL 2000 Conf., to be published in Nucl. Instr. Meth. A, 2001.

[32] P. Piot et al., *Conceptual desgin for the XFEL Photoinjector*, DESY TESLA-FEL 01-03, 2001.

[33] B. E. Carlsten, *New Photoelectric Injector Design for the Los Alamos National Laboratory XUV Fel Accelerator*, Nucl. Instr. Meth. **A 285**, 313 1985.

[34] L. Serafini, J. B. Rosenzweig, *Envelope Analysis of Intense Relativistic Quasilam-inar Beams in RF Photoinjectors: A Theory of Emittance Compensation*, Phys. Rev. **E 55**, 7565, 1997.

[35] M. Ferrario, et al. *HOMDYN Study For The LCLS RF Photo-Injector*, Proc. of the 2nd ICFA Adv. Acc. Workshop on 'The Physics of High Brightness Beams', UCLA and SLAC-PUB-8400, 1999.

[36] The LCLS Design Study Group, *Linac Coherent Light Source (LCLS) Design Study Report*, SLAC-R-521, 1998.

[37] K. Flöttmann, *ASTRA user manual*, http://www.desy.de/∼mpyflo/Astra_dokumentation.

[38] K. Flöttmann, *Note on the Thermal Emittance of Electrons Emitted by Cesium Telluride Photo Cathodes*, TESLA-FEL 97-01, 1997.

[39] G. A. Krafft, *Correcting the M_{56}, and T_{566}*, Proc. of the AIP Conf. **367**, 46, 1995.

[40] W. S. Graves, E. D. Johnson, P. G. O'Shea, *A High Resolution Electron Beam Profile Monitor*, Proc. of the PAC 1997 Conf.

[41] R. Lai, U. Happek and A. J. Sievers, *Measurement of the longitudinal asymmetry of a charged particle bunch from the coherent synchrotron or transition radiation spectrum*, Phys. Rev. **E 50**, 4294, 1994.

[42] I. Will, A. Liero, D. Mertins, W. Sandner, *Feedback-stabilized Nd:YLF amplifier system for generation of picosecond pulse trains of an exactly rectangular envelope*, Journal of Quantum Electronics 34, 2020, 1998.

[43] A. Kabel, M. Dohlus, T. Limberg, *Using TraFiC-4 to Calculate and Minimize Emittance Growth due to Coherent Synchrotron Radiation*, Nucl. Instr. Meth. **A 455**, 185, 2000.

[44] M. Dohlus, A. Kabel, T. Limberg, *Optimal beam optics in the TTF-FEL bunch compression sections: Minimizing the emittance growth*, Proc. of the PAC 1999 Conf., New York.

[45] R. Brinkmann, T. Limberg, *Features and usage of the extended COMFORT beam optics code with space charge*, DESY TESLA-FEL 99-08, 1999.

[46] A. Loulergue, A. Mosnier, *A simple S-chicane for the final Bunch Compressor of TTF-FEL*, Proc. of the EPAC 2000 Conf., Vienna.

[47] M. Borland, *Elegant User Manual*, http://www.aps.anl.gov/asd/oag/manuals/elegant_ver14.1.

[48] E. L. Saldin, E. A. Schneidmiller and M. V. Yurkov, *On the coherent radiation of an electron bunch moving in an arc of a circle*, Nucl. Instr. Meth. **A 398**, 373, 1997.

[49] Ya. S. Derbenev, V. D. Shiltsev, *Transverse Effects of Microbunch Radiative Interaction*, FNAL internal report FNAL-TM-1974 and SLAC-PUB-7181, 1996.

[50] S. Reiche, *GENESIS 1.3: A fully 3D time dependent FEL simulation code*, Nucl. Instr. Meth. **A 429**, 243, 1999.

[51] K. Bane, M. Sands, *The short-range resistive wall wakefields*, SLAC-PUB-95-7074, 1995.

[52] A. Novokhatski, A. Mosnier, *Short Bunch Wake Potential for a Chain of TESLA cavities*, DAPNIA/SEA-96-08, CEA-Saclay, 1996.

[53] V. Tsakanov, *Beam Dynamics Study for TESLA with the Integrated FEL*, DESY TESLA 99-21, 1999.

[54] J. Feikes, D. Krämer, G. Wüstefeld, *Optics of the Beam Transfer Line for the TESLA FEL*, BESSY-TB Nr.223/00, BESSY, 2000.

[55] C. Montag, *Simulation of the Fast Beam-Ion Instability in the TESLA FEL Transfer Line*, DESY TESLA 2000-17, 2000.

[56] A. Chao, *Coherent Instabilities of a Relativistic Bunched Beam*, Technical Report 2946, SLAC-PUB, 1982.

[57] K. L. Bane, *The Short range resistive wall wake fields*, SLAC-AP-087, 1991.

[58] M. I. Ivanyan, V. M. Tsakanov, *Summary of the Resistive Wakefield Effects in TESLA-FEL Transfer line*, TESLA-FEL 00-25, 2000.

[59] P. Tenenbaum et al., *Studies of beam optics and scattering in the next linear collider post-linac collimation system*, Proc. of the Linac 2000 Conf., Monterrey, USA (to be published).

[60] J. Frisch et al., *Advanced collimator systems for the NLC*, Proc. of the Linac 2000 Conf., Monterrey, USA (to be published).

[61] P. Tenenbaum et al., *Direct measurement of geometric wakefields from tapered rectangular collimators*, Proc. of the Linac 2000 Conf., Monterrey, USA (to be published).

[62] D.X. Wang, G. A. Krafft, *Measuring Longitudinal Distribution and Bunch Length of Femtosecond Bunches with RF Zero-Phasing Method*, Proc. of the PAC 1997 Conf., Vancouver
K. L. Bane et al., *Measurement of the Longitudinal Wakefield and Bunch Shape in the SLAC Linac*, SLAC-PUB-7536, 1997.

[63] K. Flöttmann, V. Paramonov (Eds.) *Study of a Beam Transport and Distribution System for the TESLA X-ray Facility*, DESY TESLA-FEL 2000-21, 2000.

[64] P. Elleaume, J. Chavanne, B. Faatz, *Design considerations for a 1 Ångstrøm SASE Undulator*, TESLA-FEL 2000-16 and Nucl. Instr. Meth. **A 455**, 503, 2000.

[65] Hasylab Annual Report 1999, p 103 ff,1999.

[66] M. Tischer, J. Pflüger, *Magnetic design of a prototype structure for the X-ray FELs at TESLA*, TESLA-FEL 2000-12, 2000

[67] S. Sasaki, *Analysis for a planar variably polarizing undulator*, Nucl. Instr. Meth. **A 347**, 719, 1991.

[68] J. Bahrdt, et al., *Conceptual design of a planar helical undulator for the TESLA SASE FEL*, TESLA-FEL 2000-11, 2000.

[69] J. Bahrdt, et al., *Elliptically polarizing insertion devices at BESSY II*, Proc. of the SRI2000, Aug. 21-25, 2000, Berlin, Germany 2000.

[70] R. Cremer, F. J. Boergermann, J. Pflüger, M. Tischer, *Manufacturing considerations of the magnetic structures for the undulators of the X-FEL at TESLA*, TESLA-FEL 2000-10, 2000.

[71] J. Pflüger, M. Tischer, *A prototype phase shifter for the undulator system at the TESLA X-ray FEL*, TESLA-FEL 2000-08, 2000

[72] M. Rüter, J. Pflüger, *A prototype gap separation system for the TESLA undulator*, TESLA-FEL 2000-07, 2000

[73] K. L. Bane, C. K. Ng and A. W. Chao, *Estimate of the impedance due to wall surface roughness*, SLAC-PUB-7514 and Proc. of the PAC 1997 Conf., Vancouver.

[74] G. V. Stupakov, *Impedance of small obstacles and rough surfaces*, Phys. Rev. ST-AB **1**, 1998.

[75] A. Novokhatsky, M. Timm and T. Weiland, *The surface roughness wakefield effect*, DESY TESLA 99-17 and ICAP 98, 1998.

[76] U. Hahn, DESY, T. Rymarczyk, Fa. Nanofocus Meßtechnik GmbH, Duisburg, private communication.

[77] The MAFIA Colaboration, CST GmbH, Buedinger Str. 2a, D-64289 Darmstadt, Germany.

[78] G. V. Stupakov, *Surface Impedance and Synchronous Modes*, SLAC-PUB-8208, 1999.

[79] M. Dohlus, V. Tsakanov, M. Ivanyan, *The roughness study for TESLA-FEL*, DESY TESLA-FEL 2000-26, 2000.

[80] M. Huening, et al., private communication, to be published

[81] P. Tenenbaum, T. O. Raubenheimer, *Resolution and Systematic limitations in beam-based alignment*, Phys. Rev. ST-AB, 2000.

[82] B. Faatz, *Beam-based alignment of the TESLA Free Electron Laser Undulator*, DESY TESLA-FEL 01-04, 2001.

[83] R. Brinkmann, G. Materlik, J. Rossbach, A. Wagner, *Conceptual Design of a 500 GeV* $e^+ e^-$ *Linear Collider with Integrated X-ray Laser Facility*, DESY 1997-048, ECFA 1997-182, 1997.

[84] R. B. Neal et al., *The Stanford Two-Mile Accelerator*, chapter 20-2, W. A. Benjamin Inc., New York 1968.

[85] D. R. Walz, E. J. Seppi, *Radiolysis and Hydrogen Evolution in the A-Beam Dump Radioactive Water System*, SLAC-TN-67-29, 1967.

[86] D. Dworak, J. Łoskiewicz, *Direct Energy Deposition in the Lateral Concrete Shielding of the TESLA Water Dump and the Rise of Shielding Temperature*, Report No 1854 / PH, The Henryk Niewodniczánski Institute of Nuclear Physics, Kraków, Poland, 2000.

[87] M. Maslov et al., *Concept of the High Power* $e^\pm$ *Beam Dumps for TESLA*, TESLA 2001-04, 2001.

[88] V. Sytchev et al., *Concept of the Fast Beam Sweeping System for the* e$^{\pm}$ *Beam Dumps of TESLA*, TESLA 2001-05, 2001.

[89] M. Maslov et al., *Concept of Beam Entrance and Exit Windows for the TESLA Water based Beam Dumps and its related Beam Lines*, TESLA 2001-07, 2001.

10 Project Costs and Schedule

10.1 Overview

The investment costs given in this chapter include all components necessary for the baseline design of TESLA, as described in chapters 3 to 9. Not included are the costs for the High Energy Physics detector (part IV) and the X-ray FEL experimental stations (undulators, photon beam lines, etc., see part V). All numbers are quoted at year 2000 prices.

It is assumed that the manpower required for the various stages of the project (i.e. preparation, procurement, testing, assembly and commissioning) will be supplied by the existing manpower in the collaborating institutes: however some of this manpower may have to be hired. For this reason the manpower is quoted separately, and is not included in the total cost.

To allow a comparison with other e^+e^- linear collider projects, the costs for the linear collider and X-FEL have been separated as follows:

- the costs for the linear collider part of the TESLA project amount to **3136 million EUR**;

- the costs for the *additional* accelerator systems and civil engineering required for the X-FEL are **241 million EUR**.

The total cost is divided up by the major sub-systems as shown in table 10.1.1 (see also figures 10.1.1 and 10.1.2). To assure full competition in future bidding procedures, no further cost breakdown is given in this public report.

Several collaborating institutes were responsible for evaluating parts of the cost. A planning group consisting of the persons responsible for each of the major sub-systems, together with experienced senior scientists from the collaboration, has been continuously reviewing the technical layout of the system and the cost evaluations.

In the following section we will describe the various procedures used for the cost evaluation of the major components.

10.2 Cost Estimate Basis

The cost estimates for all major components (see below) have been obtained from studies made by industry, and are based on a single manufacturer supplying the total number of a given component. A production schedule of three years peak production

Sub-system	cost [M-EUR]	components included
Main linac modules	1131	cavity string, cryostats, input couplers, HOM couplers, tuning systems, quadrupoles and steering magnets, instrumentation
Main linac RF system	587	RF power supplies, modulators, HV pulse cables, transformers, klystrons, waveguide system, low level RF controls, interlocks, cables
Injection systems	97	RF gun system, accelerator modules and RF system for 5 GeV linac for electrons and positrons, positron source, conventional preaccelerator, beam transfer lines, bunch compressors, diagnostics
Damping rings	215	magnets, permanent magnet wigglers, vacuum systems, RF systems, power supplies, beam instrumentation, injection and ejection systems
Collider beam delivery systems	101	beam transport lines, magnets, s.c. final doublet, beam collimation, beam extraction and dump systems, vacuum systems, power supplies, feedback systems, diagnostics
Civil engineering	546	33 km tunnel, surface buildings, connecting shafts, hall for experimental detector, damping ring tunnels, beam dump halls, civil construction for injectors
Infrastructure	336	tunnel infrastructure, cable trays, power distribution, main power connection, cryoplants and cryogenic distribution system, cooling and ventilation systems, safety systems, module and RF test facility
Auxiliary systems	124	control systems, vacuum pump stations, cabling, interlocks, magnet supplies, miscellaneous
Incremental cost for X-FEL	241	RF photoinjector and 500 MeV linac, upgrade of 50 GeV linac to 10 Hz rep. rate (RF system and cryoplants), bunch compressors, FEL and LC beams merging and separation, beam transport and delivery, civil construction for beam lines and experimental hall

Table 10.1.1: *Cost overview for the major sub-systems of the project. All numbers are given in million Euro at year 2000 prices.*
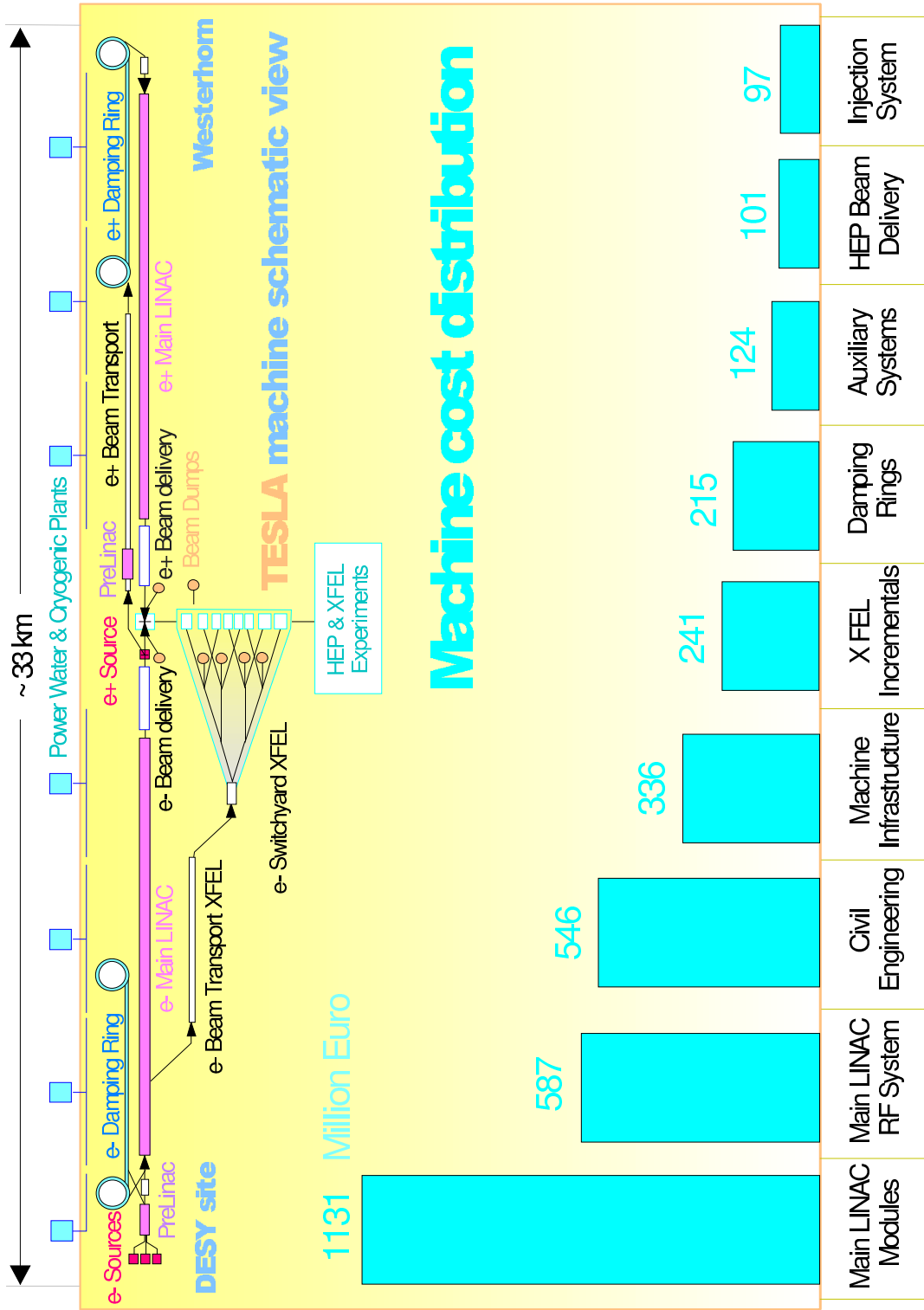
Figure 10.1.1: *Overview of the accelerator investment costs.*
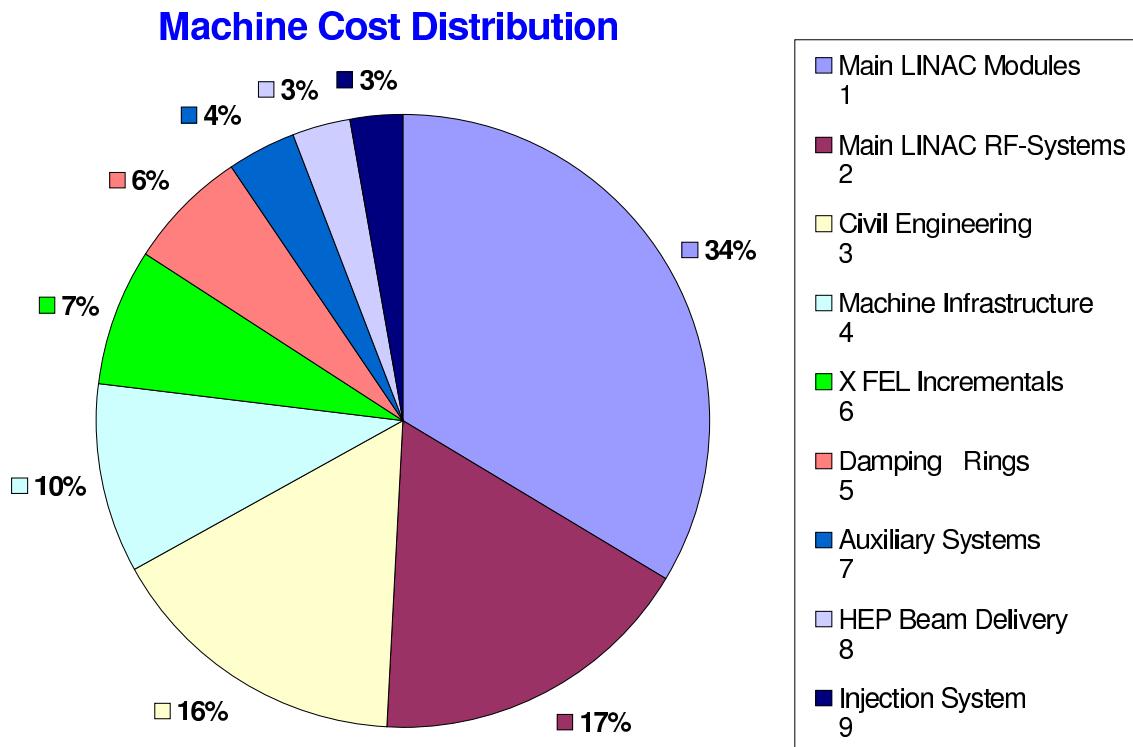
Figure 10.1.2: *Contribution of the accelerator sub-systems in percent of the total cost.*

plus one year for start-up for each component was specified. The four-year production cycles required for the various components are scheduled within the total construction time of 8 years (see figures 10.5.1 and 10.5.2). The schedule was considered feasible by the companies involved in the study.

A core production period of three years plus one year for start-up corresponds to an average production rate of 32 m of machine per working day. The corresponding numbers for the proton storage ring of HERA were about 25 m/day; for the LHC about 40 m/day are planned.

10.2.1   Main linac modules

The TESLA cryomodules for the main linac (chapter 3) with the superconducting cavities are the largest cost item with 1131 million EUR. The cost is dominated by the s.c. cavities, the cryostat and the assembly of the module. Niobium, cavity fabrication and treatment procedures each constitute a substantial part of the cavity costs.

It should be mentioned that the goal set to the TESLA collaboration in 1992 by Bjørn H. Wiik of 2000 US-\$/MV for the complete accelerating modules (including s.c. cavities, power couplers, cryostat, s.c. quadrupoles etc.) has been achieved[1] within 8%.

---

[1] using the current exchange rate of 0.95 US-\$ per Euro

10.2.1.1   Superconducting cavities

The cost of cavity fabrication for TESLA has been estimated using industrial studies made by companies with expertise in niobium production, cavity fabrication, and the planning of mass production plants.

Niobium production

The amount of material needed for the TESLA cavities is about 500 tons of high purity (RRR 300) niobium. According to the response of a questionnaire sent to the leading four niobium sheet producers, there is no shortage of raw material or facilities for niobium sheet metal handling. However, new melting furnaces specifically for TESLA production will be required to guarantee the time schedule of 3 years.

Quotes from two companies (Wah Chang, Albany, OR, USA, and Cabot Corp., Boyertown, PA, USA) indicate that the price per kg of niobium is substantially lower than the present market price for the large quantity required for TESLA. This is due to savings on sheet cuts for re-melting and streamlining of facilities for continuous production. There is an uncertainty in the price of niobium as prices are quoted in US-\$: the price used in the cost estimate is based on 1 US-\$/Euro.

Cavity fabrication

Within an industrial study (Babcock Noell Nuclear GmbH, Würzburg, Germany) the TTF cavity production was analyzed in terms of cost driving and critical procedures. Mass production costs were determined by offers from suitable companies. In the fabrication of TTF cavities, electron beam welding is the dominant cost driving procedure. A new fabrication facility is planned with three vacuum chamber welding installations. The facility, together with the use of multiple welding tooling, substantially reduces the welding costs. The total facility costs were determined in detail (planning, investment, effort for ramping up and closing the facility, personnel, repair and maintenance, consumption, quality insurance) and were compiled in a report.

10.2.1.2   Cryomodules

The costs for the 2500 required cryomodules are based on the 12.2 m long TTF module, and then extrapolated to the 17 m TESLA module. Two industrial studies were made for the mass production:

- the costs for the vacuum vessel and cold mass were taken from an industrial study by E. Zanon SpA, Schio, Italy;

- the costs for the cavity preparation and cryomodule assembly were derived from an industrial study by Babcock Noell Nuclear GmbH.

The manpower requirements reported from the second study have since been reduced in accordance with recent experience with assembled TTF modules. Costs for other

components were derived from the experience gained from the procurement of similar components for TTF.

10.2.2   Main linac RF system

The RF system (chapter 3.4) is the second largest cost item with 587 million EUR. The most relevant parts with respect to cost are: klystrons; modulators and pulse transformers; wave guide distribution system; interlock and controls; low level RF system; HV cables. The cost estimates are based either on industrial studies or established costing procedures.

Klystron

The cost estimate is based on the production of the total number of klystrons by one manufacturer. A mass production study was made by the present prototype manufacturer (Thomson Tubes Electroniques, Velizy, France).

Prices for auxiliary power supplies (solenoid, filament, core bias, vacuum pump, electronics racks) were scaled from TTF costs using a standard industrial mass production costing rule, which states that a price reduction of 5 % is achieved for each factor of two in production number (95 % learning curve). The cost estimate for the racks is based on an estimate by a manufacturer.

Interlocks and controls

The cost estimate makes use of an established industrial costing procedure based on the number of channels to be interlocked, monitored or controlled. The procedure produces a cost based on the use of an industrial standard PLC (Programmable Logic Circuit) system. An alternative approach where all the costs for the required interlock hardware and cable connections are summed up gives a similar price.

Low level RF system

The cost is based on TTF experience scaled for mass production. The cost estimate for the 400 W preamplifiers is based on the production of the total number by one manufacturer (an informal quote on 750 units was received).

Waveguide distribution system

The cost estimate is based on experience with the existing TTF system, adjusted for mass production. Different parts of the system will be supplied from different manufacturers. Informal quotes and estimates on cost saving based on mass production exist from some manufacturers.

Modulator and Pulse transformer

The cost estimate is based on the production of the total number of modulators (HV power supply, pulser, internal modulator interlock) and pulse transformers by one manufacturer. A mass production study was made by PPT Puls-Plasmatechnik GmbH, Dortmund, Germany.

Cables

A cost estimate of a manufacturer (Nexans Deutschland, Mönchengladbach, Germany) exists for 1000 km of HV pulse cable (connecting klystrons in the tunnel to modulators in the external halls). The in-tunnel connection cost of the RF units is estimated on the basis of TTF experience.

10.2.3   Injection systems

The costs for the injection systems amount to 97 million EUR. They include all systems described in chapters 4 and 6. The biggest single cost items are the accelerator modules and the RF system for the 5 GeV injector linacs; these are taken directly from the costs of the main linac. Cost estimates for the other parts are based on existing components at TTF or at conventional linacs. The injector components for the X-FEL are given in the FEL incremental cost budget.

10.2.4   Damping Rings

The costs for the damping rings (chapter 5) amount to 215 million EUR. All components required for the two rings are included except for the costs of the infrastructure of the arc tunnels (which are included in the infrastructure budget), and the cryogenic supply for the superconducting cavities (which is included in the main cryoplant costs). A detailed technical study including technical drawings of every section of the vacuum and magnet system has been made by Ansaldo Ricerche, Genua, Italy. The biggest cost driving components have been handled most thoroughly. Based on this study, industrial companies have determined the costs for most of the damping ring components. The costs for sub-systems which have not been specified to this level of detail have been estimated based on similar present day installations.

10.2.5   Collider beam delivery system

The costs for the beam delivery system (BDS, chapter 7) for the baseline design with one interaction point amount to 101 million EUR. Costs for diagnostics, feedback and vacuum systems are based on TTF and HERA experience. The major cost items are the magnet and the beam dump systems.

Magnet system

The preliminary cost estimate of the magnets were made on the assumption that all conventional magnets will be produced by one supplier with the appropriate experience and facilities: the cost of tooling sets will then be minimised. The current estimate has been made by the D. V. Efremov Institute, St. Petersburg, Russia, which has a long history of magnet production.

For the superconducting Final Doublet, the cost estimate has been supplied by the superconducting magnet group in Saclay (CEA/Saclay DAPNIA/STCM, France), and is based on HERA and LHC quadrupole magnet experience.

All power supplies in the BDS are commercially available. The cost of the cables is based on locating the supplies in the tunnel. The estimate also includes a level of redundancy, allowing one power supply to fail in the tunnel without the need to make an access for repair.

Electrostatic separators

The cost estimate has been supplied by the LEP ES separator group (CERN/SL/BT) at CERN, and is based on existing LEP electrostatic separator experience.

Main dump system

The dump vessel, fast sweeping system and shielding have been evaluated on the basis of industrial quotes or experience with similar systems at HERA. The most complicated part of the dump is the water cooling system. This has been evaluated on the basis of the experience with a similar system at the target station at SINQ (Paul Scherrer Institute, Villigen, Switzerland).

Costs for the kicker magnet and pulser system have been evaluated from the experience with the HERA beam dump system.

10.2.6 Civil engineering

Civil engineering (chapter 8) is a major cost item amounting to 546 million EUR. It includes all tunnels, shafts, underground and surface buildings for the linear collider. The dominant cost item is the 33 km long linac tunnel. Civil engineering cost for the X-FEL are included in the FEL budget.

A certain percentage of the total construction cost has been taken into account for the services of architects and civil engineers according to HERA experience and public regulations. The costs for the land were estimated using present market prices.

Main tunnel

The construction cost estimate for the TESLA tunnel is taken directly from the actual costs of the HERA tunnel. The TESLA tunnel has the same diameter as the HERA

tunnel, which is constructed from concrete segments called tubbings. The soil conditions (mainly sand) are comparable at both sites. At HERA the tunneling speed was 10 m per day on average and 14 m per day maximum. The speed of the TESLA machine will be similar. One tunnel-boring machine will bore 2.5 km TESLA tunnel in one year, and four tunnel boring machines are necessary to limit the tunnel construction time to about three years.

Damping ring arc tunnel

The inner diameter of the arc tunnels is 3 m. The price for these tunnels is based on the construction price for a cable tunnel in the centre of Berlin, which has a similar diameter and soil conditions.

Underground buildings and shafts

All TESLA underground buildings are immersed in the ground water. The situation is similar to the HERA section North, which extends nearly 20 m into the water table. The price per unit volume of this HERA hall was therefore used as a basis for the cost estimate for the construction of the underground buildings and shafts required for TESLA.

Surface buildings

The size of the TESLA cryogenic halls are similar to the HERA cryogenic hall (72 m × 33 m, with a height of about 15 m). The price per unit volume of this hall is taken as the basis for the price estimation of the construction costs for the TESLA surface buildings.

10.2.7   Infrastructure

The infrastructure (chapter 8) costs amount to 336 million EUR. The major cost items are the cryogenic plants, distribution lines, and connection boxes. Additional items included are: the main power connection and distribution; water cooling and ventilation systems; safety installations; test equipment for cryomodules and RF components.

Cryogenic Plants

From the design heat loads for TESLA the cooling capacity requirements (4.5 K equivalent) for the 7 individual TESLA cryoplants were derived. The cost for the cryoplants was then calculated using the following formula, which was found in 1998 at CERN during the procurement of the similarly sized cryogenic plants for LHC:

$$\text{cost [MCHF]} = 2.2 \text{ [MCHF]} \times (\text{cooling capacity [kW]})^{0.6}$$

The costs in Euro for the year 2000 were obtained by using the Euro/CHF exchange rate of 1.634, assuming a rate of inflation of 4% over the last 2 years. For the cost of

most auxiliary components the experience of CERN was also used. The costs for the distribution boxes are based on the number of cold, warm and safety valves, taking into account the cost for valves of different size and type. The resulting costs are in agreement with both the experience at CERN and at DESY[1].

The costs for helium transfer lines and feed- and end-boxes were estimated from recent experience with the procurement of similar components for DESY (TTF/FEL).

Connection to main grid and power distribution

The installed power for TESLA will be about 200 MVA and the design power consumption 155 MW. The mains connection has been evaluated by two local power companies, and the power distribution by an outside engineering consulting firm in collaboration with DESY.

Water cooling and ventilation

The costs for cooling and ventilation were estimated on the basis of prices for HERA and the TESLA Test Facility equipment.

Test Facility for accelerator modules and RF components

The basic equipment costs are given by the number of cryogenic valves and the lengths of transfer lines. Prices were taken from recent procurement of similar equipment for the cryogenic supply of the TTF/FEL-linac and of the HERA luminosity upgrade.

For the supply boxes for the module test benches, the results of the call for tender for the CERN LHC magnet test benches was used.

For the RF-equipment the costs from the evaluations for the linac components has been used.

10.2.8   Auxiliary systems

A total cost of 124 million EUR was budgeted for the auxilliary systems, which covers (as major items) the accelerator control system and the main linac external vacuum systems. Costs for these systems have been evaluated on the basis of HERA and TTF experience. The budget also collects a number of smaller items like spare linac modules.

10.2.9   Incremental cost for the X-ray FEL

The additional costs of the accelerator components required for the X-ray FEL (chapter 9) amount to 241 million EUR, the dominant part being the civil engineering of the FEL experimental hall and the beam distribution system. Costs for the FEL injector, bunch compressors, beam line magnets, vacuum systems, beam dumps, diagnostics, water cooling and ventilation systems were evaluated on the same basis as the injector

---

[1]from recently purchased valve boxes for the HERA Luminosity Upgrade and TTF/FEL

and beam delivery systems for the collider. The undulator and photon beam line costs are given in part V.

10.3   Manpower Requirements

The manpower required for the different stages of the project (design, procurement, fabrication and assembly, testing, installation and commissioning) has been estimated mainly on the basis of the experiences gained at TTF and in large projects like HERA. It is assumed that this manpower will be supplied by the collaborating institutes.

A total of 6,933 man years will be required. Figure 10.3.1 shows the time profile of the total (collaboration) manpower needed until the completion of the installation, divided up by the major sub-systems.
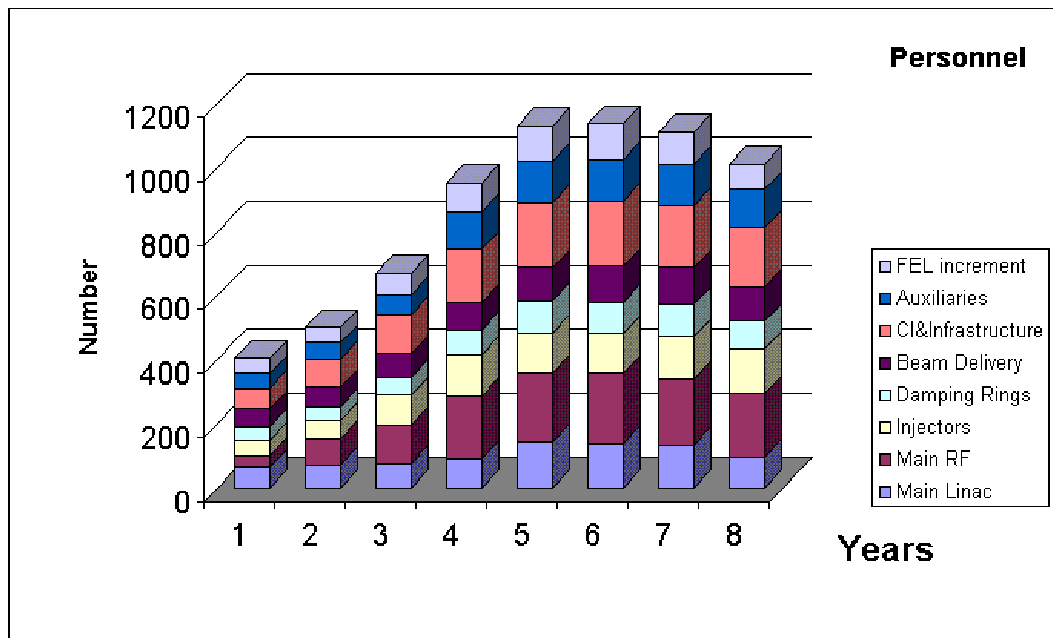
Figure 10.3.1: *Laboratory manpower requirement for TESLA during the 8 years of construction.*

10.4   Time Schedule

The construction time of TESLA is 8 years. The evaluation is based on industrial studies and the experience gained at the construction of HERA and TTF.

Figures 10.5.1 and 10.5.2 show the construction schedule, indicating the major activities which are briefly explained in the following:

- Based on HERA experience an average tunneling speed of 10 m per day can be safely assumed. Thus the total civil construction will be completed after 3.5 years using 4 tunneling machines.

- Two years after the start of civil construction on the DESY site, the tunneling machine will have reached the shaft for the next service hall 5 km away. The tunneling base and support infrastructure will then be moved to this hall, and installation can begin in the first tunnel section.

- Installation of the first cryoplant, watercooling systems and other infrastructure into the service hall on the DESY site will start after 2.5 years.

- Orders for major components (s.c. cavities, cryostats, etc.) will be placed at the same time as the civil construction starts. According to the industrial studies, between 2 and 3.5 years will be needed to set up the production facilities. Full production rate will be reached after one additional year. The first cryomodules will be assembled and ready for tunnel installation 4 years after the start of civil construction.

- After 5 years the production and installation of all components proceeds at full design rate. The first 16.5 km tunnel section of the linear collider and the beam lines for the FEL will be completed after 6.5 years. The positron side of the collider will be completed after 8 years. The installation period of 3 years plus one year for start-up corresponds to an average installation rate of 32 m accelerator structure per day for all sub-systems. The corresponding numbers for the HERA proton storage ring HERA were about 25 m per day, and 40 m per day are planned for the LHC.

We expect that no more than one year will be required (between financial approval and the beginning of construction) for the public planning approval procedure ("Planfeststellungsverfahren") and the bidding and awarding of contracts.

10.5   Operating Costs

The total cost for operation has been estimated at 120 Million Euro per year. This includes the electrical power consumption, the regular replacement or refurbishing of klystrons, and the helium losses. The numbers are determined assuming current prices and an annual operation time of 5,000 h. Costs for general maintenance and repair have been estimated assuming 2 % per year of the original total investment costs corresponding to the DESY experience.

For critical components (such as accelerator modules) a number of spares will be produced; these costs are included in the investment costs.
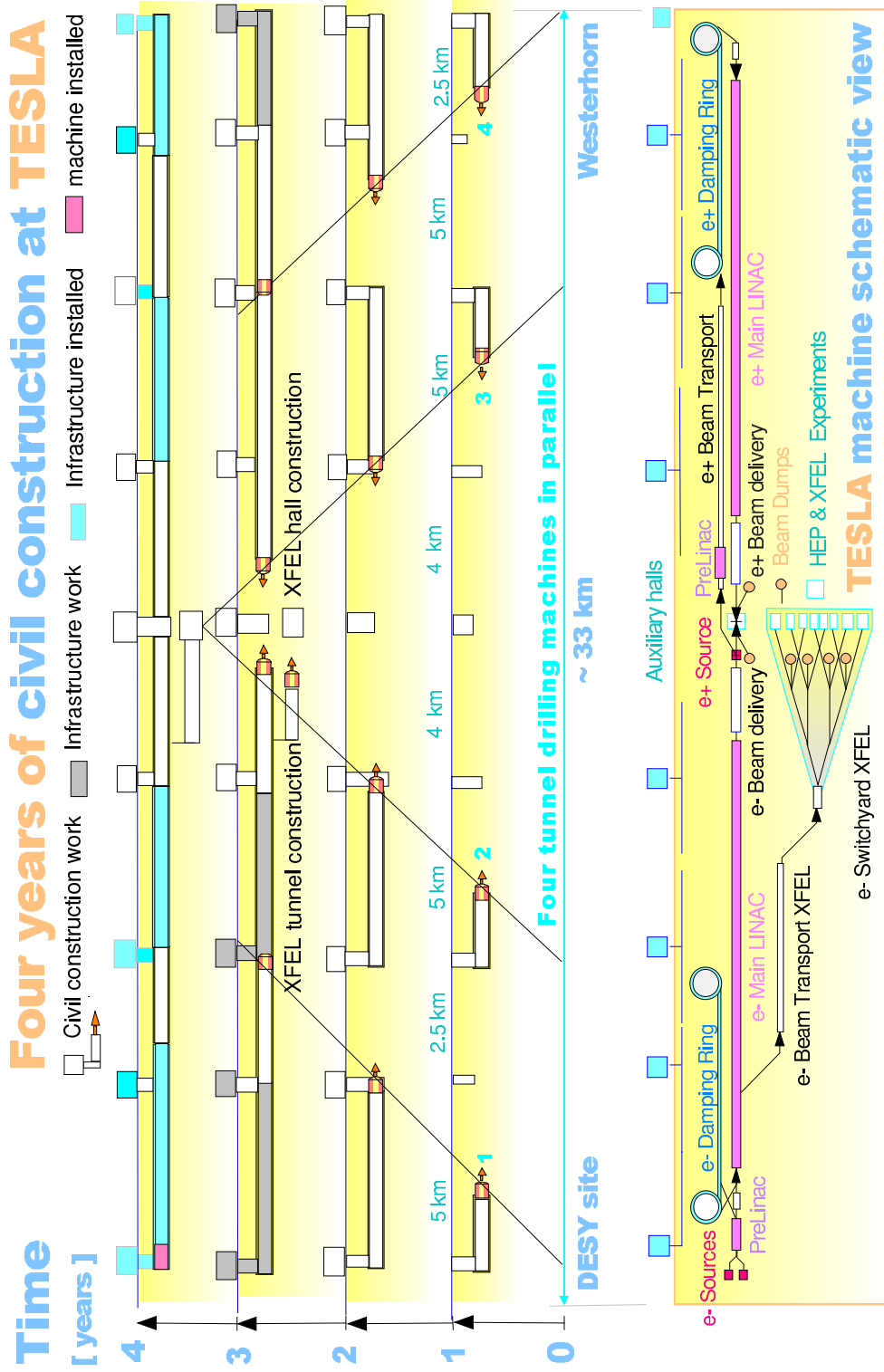
Figure 10.5.1: *Time schedule for civil construction.*
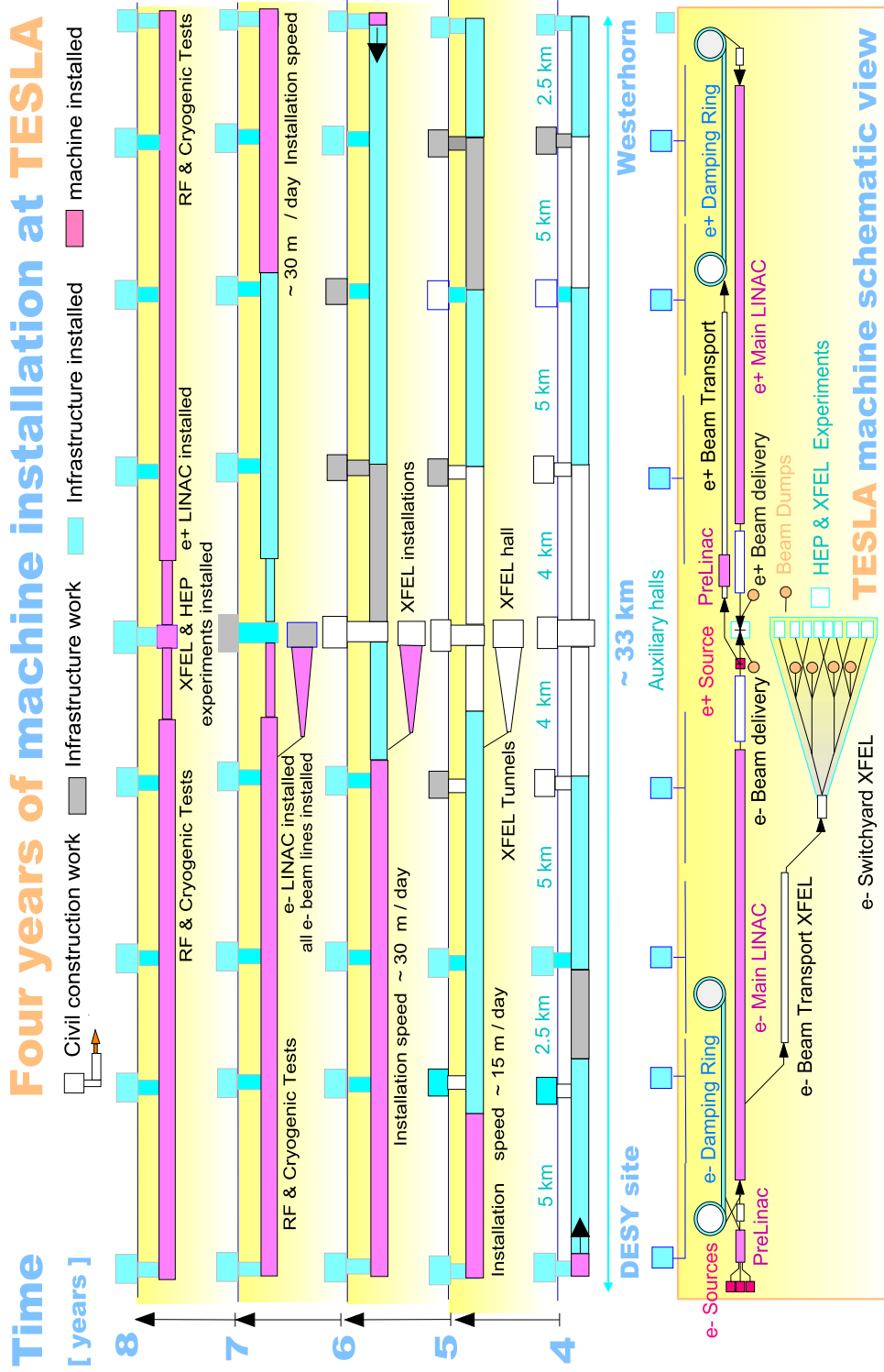
Figure 10.5.2: *Time schedule for machine installation.*